CALIFORNIA INSTITUTE OF TECHNOLOGY

SOIL MECHANICS LABORATORY

PHYSICAL SCALE MODELING OF GEOTECHNICAL STRUCTURES AT ONE-G

BY

ANDREW D. GIBSON

REPORT NO. SML 97-01

A REPORT ON RESEARCH SUPPORTED BY GRANTS FROM THE NATIONAL SCIENCE FOUNDATION, THE NATIONAL AERONAUTICS AND SPACE ADMINISTRATION, AND THE EARTHQUAKE RESEARCH AFFILIATES OF THE CALIFORNIA INSTITUTE OF TECHNOLOGY

PASADENA, CALIFORNIA

1997

PHYSICAL SCALE MODELING OF GEOTECHNICAL STRUCTURES AT ONE-G

Thesis by

Andrew D. Gibson

In partial fulfillment of the requirements for the

Degree of Doctor of Philosophy

California Institute of Technology

Pasadena, California

1996

(Submitted October 4, 1996)

ACKNOWLEDGMENTS

To my family, colleagues, and the many friends who have offered encouragement and support, I am most grateful. To acknowledge the contribution of each would require yet another tome exceeding the size of this thesis itself. I also acknowledge the financial support from Caltech, the National Science Foundation, and Woodward Clyde Consultants, all of which has enabled me to undertake and complete this work.

From my associates at Woodward Clyde, I extend a special thanks to Larry Rapp who has been a steadfast friend for many years and who willingly submitted himself to the torture of proofing the initial drafts of this thesis. Also of Woodward Clyde, my thanks to Yoshi Moriwaki whose mentor-ship has been invaluable and who has taught me by example the value of diligence, care, and a good sense of humor.

To my advisor, Professor Ron Scott, I thank him for his patience, encouragement, and friendship. I will never forget the many hours he freely gave to give direction and assistance in my work. Neither will I ever forget the innumerable hours of discussion spent on all and sundry topics. His insight, intelligence and acute sense of humor are indeed rare and I will sorely miss experiencing these attributes on a daily basis.

For my wife, Mary, words alone cannot express my gratitude for her tolerance, support, and companionship during the final stages of the completion of this thesis.

Lastly I wish to acknowledge my parents, Betty and Warren. To my mother, for her unquestioning support and quiet wisdom. To my father, for instilling in me the desire to question and learn. To them, I dedicate this thesis.

ABSTRACT

The use of physical scale modeling techniques for geotechnical applications is investigated. The scaling laws to relate a prototype structure to a model are developed for the centrifuge modeling technique and for the laboratory (or one-g) environment. A theory based on critical or steady state concepts for the constitutive scaling of the behavior of the soil in a one-g model is investigated. A series of one-g models of varying configurations was constructed in a laminar box and subjected to earthquake like motions on a shake table. A total of 73 tests was performed. Most tests were constructed of saturated Nevada sand placed in a loose and dense state in adjacent halves of a laminar box, and the results of these tests were compared with a similar centrifuge test (Model 3) which was performed as part of the VELACS study. Some of the one-g models were constructed with an alternate model sand and an alternate pore fluid to investigate these modeling variations. One-g models were also constructed with the sand at a uniform density throughout the laminar box.

The research indicates that there is a significant conflict between the time scaling for dynamic processes and dissipation processes in both the centrifuge and one-g techniques, which means that excess pore pressures generated in the model saturated sand by a simulated earthquake will be less than what would occur in the same sand in the real prototype. This effect is generally more severe in the centrifuge. This implies that model tests performed to investigate liquefaction, flow failure problems, and/or deformation problems in saturated sands may significantly underestimate the potential behavior of the prototype. In addition to the above, the research provides insight into the behavior of adjacent loose and dense sands and indicates the potential for high excess pore pressures to develop in the dense sand. Current practice ignores the potential for liquefaction in dense sands or the development of cyclic mobility in the assessment of the seismic performance of geotechnical structures.

TABLE OF CONTENTS

Page

LIST OF TABLES

LIST OF FIGURES

NOMENCLATURE AND SYMBOLS

Symbol	Meaning
a_v	Coefficient of compressibility
c_v	Coefficient of consolidation
D	Damping force
D_r	Relative density (%)
D_{ro}	Initial relative density (%)
ΔD_r	Relative density increment from the SSL
e	Void ratio
e_{max}	Maximum void ratio
e_{min}	Minimum void ratio
e_0	Initial void ratio
Δe	Void ratio increment from the SSL
g	Gravitational acceleration
H	Thickness of layer or effective length of drainage
i,j,k	Subscripts for orthogonal components (Einstein's convention for summation)
k	Coefficient of permeability
k_s, k_l	Spring constants
K	Absolute or specific permeability of the soil
n	Ratio of prototype to model length or dimension (equivalent to x^*)
m	Parameter subscript denotes model value
p	Parameter subscript denotes prototype value
p'	Mean effective stress
SSL	Steady state line
t	Time

t_c	Time for consolidation or diffusion processes
t_d	Time for dynamic processes (e.g.: earthquake)
T	Non-dimensional time
u	Excess pore fluid pressure
u_i	Displacement component
u_o	Initial arbitrary excess pore fluid pressure
v_i	Velocity component
V	Volume of body
W	Non-dimensional excess pore pressure
x	Spatial coordinate or position
X	Body force
$X(t)$	Forcing function
z	Vertical coordinate or depth within soil deposit
Z	Non-dimensional depth
γ_f	Unit weight of pore fluid
μ	Dynamic viscosity of pore fluid
ρ	Mass density
σ	Stress tensor
σ_v	Total vertical stresses
σ'_v	Vertical effective stresses
$\sigma'_1, \sigma'_2, \sigma'_3$	Principal effective stresses
*	Denotes scale factor or ratio of prototype to model parameter

Chapter 1

INTRODUCTION

1.1 General

The ability to predict the behavior of soil is often critical to the successful design and performance of civil engineering projects. Soil that occurs in natural deposits or that has been reworked as an engineered fill usually provides the foundation for buildings, bridges, highway pavements, and airports. Soil is also the basic material encountered in geotechnical structures such as slopes, embankments, reclamations, tunnels, and earth dams.

Evaluating the strength of the soil and its deformation (or stress-strain) behavior under imposed loading conditions are typically of primary concern. The non-linear plastic behavior of soil and its generally anisotropic heterogeneous properties make the task of prediction very difficult. The addition of fluid (usually water) within the soil matrix and imposition of dynamic loading (from earthquakes, for example) compounds the problem by orders of magnitude. Soil behavior can range from stable (such as creep, consolidation, and settlement) to highly unstable (such as landslides, liquefaction, and flow failures).

In industry the practice of geotechnical engineering continues to be dominated by empirical procedures of design, even though over the last 30 years considerable effort has been made to develop more sophisticated analytical techniques, including numerical models which incorporate non-linear, elastic-plastic, constitutive models. While numerical modeling can be useful, it is still generally expensive to undertake and its success is varied, especially in complex problems. The continued reliance on empirical data and semi-empirical design methods reflects the complex behavior of soils and the diverse conditions encountered in nature.

To complement empirical methods and numerical models, physical modeling of soil structures is becoming more common. On large, complex projects, or on high risk projects, the practicing

geotechnical engineer may undertake all three approaches of design: empirical, numerical, and physical modeling, and attempt to balance the results of each to arrive at a 'consensus' of opinion.

In modeling terminology the actual structure is called the prototype, and a model is built to represent the prototype.The geometry of the model is similar to the prototype but the model is typically a smaller version of the prototype.

Models have been used to investigate the qualitative behavior of soil structures for many years. However, to obtain quantitative results from a model, it is necessary to have a set of scaling relations which will enable the behavior of the model to be translated to a predicted behavior of the prototype. Basically the testing consists of subjecting the model to a stress condition which represents the stress condition expected in the prototype. The deformation and strain response of the model is recorded, and with the scaling relations this data is used to predict the behavior of the prototype.

The key to the success of the modeling is the scaling relation used to relate the model and prototype. For soils, obtaining an appropriate set of scaling relations is complicated by an incompatibility between the stress scaling and the constitutive behavior of soil. It is the constitutive behavior which governs the stress-strain response of the soil. Essentially the stresses scale linearly, but the constitutive behavior is non-linear. In general, a model constructed from the same soil as the prototype in exactly the same state (density, layering, etc.) will not behave in the same way because of the non-linear constitutive behavior of the soil. If the model is constructed at the same scale, then presumably it will behave in a similar manner to the prototype. As the disparity in scale between the model and prototype increases, the divergence in behavior will increase also.

A modeling method which avoids the scaling incompatibility described above requires the use of a centrifuge. The centrifuge method has become generally accepted as a valid technique and its use is becoming relatively widespread. However, it is capital intensive and performing tests is difficult, complex, and ultimately costly. There are also some issues regarding the applicability of the method to more complicated problems, and a continuing concern with the boundary conditions imposed by test containers.

1.2 Object of Present Study

The primary object of this study is to explore aspects of scaling relations for models, and to investigate a proposed method which would overcome the scaling incompatibility described above without the use of a centrifuge. The proposed method can be used in a normal laboratory environment (which will be referred to as a one-g condition to distinguish it from the centrifuge); however, it also has a potential application for centrifuges to overcome size limitations for models. The merits of the one-g model and the centrifuge model are investigated and the advantages or disadvantages are explored.

In addition to the above, the dynamic response of soils when subjected to earthquakes is of interest because of the potential impacts to the infrastructure. In particular the phenomenon of liquefaction, which can occur in saturated soils, can potentially cause catastrophic failures. During the research described herein, some insights and observations as to the process of liquefaction have been possible and are described with reference to possible implications for design and evaluations.

1.3 Background and Previous Work

There are three basic areas of research that are relevant to this thesis topic: model theory; the centrifuge method; and the one-g method. A brief discussion of these areas including some background of previous work is presented below.

1.3.1 Model Theory

Model testing has been employed in all areas of engineering and two commonly used techniques which are used to derive appropriate scaling relations are dimensional analysis and similarity theory (Sedov, 1959). The application of such general techniques to civil engineering has been performed since the 1920's, and has been used to develop model theories for given applications. The centrifuge method is an example of a model theory which is governed by a set of scaling relations.

The centrifuge was first used to perform model tests for geotechnical structures in the 1930's. Specifically the centrifuge was proposed independently by P. B. Bucky in the United States (Bucky, 1931) and by N.N. Davidenkov and G.I. Pokrovsky in 1932 (Pokrovsky and Fyodorov,

1975) in the former USSR. The method was used by Bucky primarily for mining applications (Bucky and Fentress, 1934) and extensively in the former USSR on a wide range of applications since the mid 1930's (Pokrovsky and Fyodorov, 1975).

A more general model theory for soils which could be applied in one-g conditions was apparently first suggested in the 1950's (Rocha, 1953). Rocha illustrated some example applications (Rocha, 1957) using very simplified assumptions regarding soil properties. However, he concluded that attempting to model a two phase soil (i.e., a matrix of solid grains having pore fluid within the matrix) and the non-linear relations between stresses and strains would make the mathematical analysis "insuperably complicated."

This observation goes to the heart of the problem with models at one-g and can be explained as follows. Usually body forces (such as gravity and seepage) are the dominant factors in geotechnical problems, influencing the strength and stresses through the self weight of the soil. When a model is constructed at a reduced size, the stresses in the model at geometrically similar points to the prototype are reduced also. The different stresses will cause different strain behavior in model from prototype because of the complex non-linear stress-strain (constitutive) behavior of soil. This assumes the same soil is used in the model and the prototype. Finding the correct mapping between model strains and the projected prototype strains is extremely difficult and open to many questions; this is what Rocha alludes to.

Rocha also discussed the difficulty of reproducing in a model the heterogeneity and anisotropy that exists in natural and manmade prototype soils. The subtleties of the soil structure can have a major bearing on its behavior, and therefore this is a potential source of significant errors. This problem exists for both one-g models and centrifuge models.

Given these difficulties, Rocha went on to make an interesting assertion: physical modeling requires simplifications and assumptions; however; the design techniques (analytic and numeric) used at that time also required simplifications and assumptions.

It is worth considering that Rocha's assertion may still have validity in today's design environment even though numerical, and to a lesser extent, analytic, tools have improved over the last 40 years in soil mechanics.

1.3.2 Centrifuge Testing

In the centrifuge method the apparent incompatibility in the stress scaling and constitutive behavior of the model and prototype soil is avoided by making the model have the same magnitude of stresses as the prototype. This is achieved by imposing a centripetal acceleration field across the model. If the model size is n times smaller than the prototype, then the magnitude of the acceleration field is n times greater than gravity. If the density of the model and prototype are the same, this creates identical stresses in the model at geometrically similar points to the prototype. The presumption is that similar strain behavior will be observed because the same soil is used in the model and prototype.

After the centrifuges' initial use in the 1930's, it was not extensively used in US again until the 1970's, where it has now gained significant popularity. It has also been used extensively in Japan and Europe. The centrifuge has been used to study particular mechanisms in soil structures, to verify numerical models, and in some cases to predict the actual behavior of prototype geotechnical structures. Over the last 10 years the use of centrifuge testing has become increasingly accepted as an appropriate modeling technique for geotechnical problems. Both in research and industry, considerable capital is being devoted to construct centrifuges and complete centrifuge studies.

The scaling relations appropriate for the centrifuge have been defined by numerous authors using different derivation methods. For example, Pokrovsky and Fyodorov (1975), Roscoe (1968), Scott (1978), and Fuglsang and Ovesen (1988).

While the centrifuge apparently maintains compatibility between the model and prototype stresses and constitutive behavior, there are several other issues of concern which have been raised by various researchers over the years. These are summarized in the following items:

1) Variation in the acceleration field across the model in the centrifuge due to Coriolis effects and to the variation in the radius of rotation. This effect is accentuated on centrifuges with relatively small diameters with respect to the depth of the model being tested.

2) The impossibility of reproducing the exact soil structure of the prototype in the model and its stress history.

3) Correctly scaling time-dependent effects, and the fact that three different time scales exist for dynamic, dissipative, and viscous effects respectively.

4) Grain size effects created by using a dimensionally smaller model without adjusting the model material to have a smaller grain size also.

5) Soil-structure interaction and boundary effects.

6) The possibility that different centrifuge test equipment will give different results for an otherwise identical test due to, for example, variations in the input earthquake, boundary conditions, and preparation methods.

A detailed discussion of these potential criticisms is beyond the scope of this review; however, some of the items have been partly addressed in the available literature and are briefly described below.

Item 1 will always remain an issue with the centrifuge; however, the introduction of larger diameter centrifuges is reducing this potential effect by decreasing the ratio of the radial distance to depth of the model. The Coriolis effect is of concern in certain situations (Tan and Scott, 1985) such as in-flight deposition of materials and the liquefaction phenomenon.

For Item 2 it is, of course, possible to recreate the stress history of the prototype in the model by trying to emulate the prototype development or construction by building the model in a similar fashion while it is in flight (Scott, 1989). Attempts to do this for simple prototype histories have been made with varying success [(Pokrovsky and Fyodorov, 1975), (Kimura, 1988), and (Bassett and Craig, 1988)].

The varying time scaling cited in Item 3 can be an advantage of the centrifuge technique, or not a critical issue when the physical process being modeled is dominated by only one time scale. For example, problems of consolidation are controlled by dissipation, and in this case the centrifuge has a great advantage because the scaling effect dramatically shortens the dissipation process in the model compared to the prototype (Steenfelt, 1992). The varying time scales do become a problem when two physical processes governed by different time scales are important to the mechanism being studied. For example, liquefaction in sands involves a dynamic time scale from earthquake excitations, and also a dissipative time scale due to the generation of pore fluid pressure above hydrostatic pressures. In an attempt to overcome this, researchers have modified one of the time scales to conform with another time scale. The dissipative time scale can be

matched to the dynamic time scale by changing the pore fluid viscosity (Schofield, 1988) or reducing the grain size of the model material (Fuglsang & Ovesen, 1988). However, both these options potentially violate other similitude requirements between model and prototype. This problem is discussed in further detail in Chapter 2.

Item 4 was investigated for sands (Fuglsang and Ovesen, 1988), and it was concluded that the grainsize effect was negligible for pullout tests on anchors, and negligible for footing models provided the model size to mean grainsize ratio exceeded 30. It appears that there has been little else research completed to investigate this potential effect (Scott, 1977).

For Item 5, the introduction of the laminar box (Hushmand et al., 1988) and stacked ring boxes (Whitman and Lambe, 1985) attempts to minimize the boundary effects created by test boxes under simple one-dimensional shearing modes. Placing damping materials between the model and test box has also been employed in an attempt to attenuate dynamic boundary effects. In tests where a model structure is placed on or in a model soil (e.g., a footing or pile), care must be taken to ensure the boundary of the container does not influence the model structure behavior (Ferguson and Ko, 1981).

The final Item 6 was not studied until relatively recently when several major centrifuge facilities in the US and UK completed a variety of prescribed liquefaction type tests (Arulanandan and Scott, 1993, 1994). This program was referred to as "Verification of Numerical Procedures for the Analysis of Soil Liquefaction Problems" (VELACS). In general, the results of testing indicated that repetition of the same test at various facilities yielded comparable results (Scott, 1994). However, several problems were identified in relation to the soil preparation, placement of transducers, saturation, and excitation for each test facility.

The centrifuge has been used to model a wide array of geotechnical problems over the last 55 years (Craig et al., 1988), (Arulanandan and Scott, 1993, 1994). The validity of technique has been verified by comparison with prototype behavior where available, and by completing models of models. However, the reliability of the modeling technique is less certain for more complex dynamic problems, when the soil is partially or fully saturated with a pore fluid, or when conflicting time scales must be considered.

1.3.3 One-g Testing

Model tests of geotechnical structures have been performed under one-g conditions probably for as long as engineers have had the challenge of dealing with soil as a building material. However, even with the knowledge of similitude and dimensional theory, few one-g tests were performed with regard to scaling considerations (Roscoe, 1968), (Scott, 1988).

Scaling relations governing dynamic equilibrium can be derived regardless of the model material behavior. The scaling derivation is the same for the one-g conditions and the centrifuge. However, the constitutive behavior of the model and prototype material must also be matched. As discussed in Section 1.2.2, the centrifuge achieves this by developing the same stress state in the model and as in the prototype, and the presumption is that similar constitutive behavior will also be observed. In one-g tests the magnitude of the stresses is obviously different in the smaller model, and the behavior of the soil under these conditions will be quite different from the prototype. A possible solution to this dilemma is to use a different material for the model soil and attempt to match the constitutive behavior under the different stress conditions. This task is formidable and poses many problems even when dealing with a linearly elastic material, let alone the complex non-linear behavior of soil. If the model is required to have a pore fluid, the alternative material must also accurately represent the behavior of two phases (solid and liquid) which compounds the problem. These issues and the scaling relations for one-g conditions have been discussed in depth by a number of authors including Rocha (1957), Roscoe (1968), and Scott (1989).

Another option to account for the different behavior of model and prototype soils is to scale the constitutive behavior of the soil to account for the differing stress regimes between model and prototype. This requires a knowledge of the functional relationship between the soil strain and stress. Rocha assumed that the stress and strain of the model was linearly related to the prototype (Rocha, 1957) and introduced two constant scaling factors: one for stress, and one for strain. This was later extended to the more general case (Kagawa, 1978), (Iai, 1989). Iai applied constant scaling factors (prototype to model) to the key parameters of general equations for a saturated soil as proposed by Zienkiewicz et al. (1980). With this approach, the details of the constitutive behavior for a particular soil type are avoided as they are essentially embodied in a single parameter denoted as the tangent modulus. The tangent modulus is one of the parameters which is assumed to have a constant scaling factor from model to prototype. After reducing the

equations three independent scaling factors are defined for length, density, and strain. The method assumes the soil matrix acts as a continuous medium, and that deformations and strains are small.

The scaling relations derived using the approach above were applied to some triaxial laboratory test data (Iai, 1989) which demonstrated the applicability at least under small strains. While the method has been extended to liquefaction type problems (Iai, 1989), it is also stated the method is not applicable to (1) phenomena in which soil particles lose contact, (2) where deformation or strains are too large. Unfortunately, the method has not been applied to models of models, that is where a test is repeated at progressively smaller scales, which would help verify its validity. The main concern with the method proposed by Iai is that it requires conjecture about the constitutive behavior (even at low strains) and is certainly limited if larger strains do occur.

An alternate approach to deal with the scaling of soil behavior from model to prototype was suggested by Roscoe (1968). He proposed that if the model soil was placed at a different density or state, then the prototype behavior could be emulated without requiring a scaling factor to transform model strains to prototype strains. Roscoe suggested the appropriate scaling could be achieved considering the critical state behavior observed in soils. Scott (1989) independently arrived at a similar conclusion and proposed a systematic method by which the state of the model soil could be selected. Scott presented data to support the hypothesis and demonstrated the method by completing a one-g test on a model which was constructed to represent a centrifuge test. The proposed method is described in detail in Chapter 2.

In Section 1.2.2 six items were described as fundamental concerns or issues with centrifuge testing. All of these items, with the exception of the first (which was the variation of the acceleration field across the centrifuge model), are also of concern for a one-g test. In addition, the one-g method has the added concern of constitutive scaling. However, one inherent advantage with one-g modeling tests is that they are easier to perform and generally the scaling of size is less than what would be employed in a centrifuge test. The larger model size usually employed in the one-g environment reduces the divergence in many of the scaling relations as will be elucidated in Chapter 2.

1.4 Scope of Present Study

The primary focus of this study described herein is to explore the validity of the scaling methodology proposed by Scott (1989) for the one-g conditions. This has been undertaken by performing a series of one-g tests on models which represented a test performed in the centrifuges as part of the VELACS project (Arulanandan and Scott, 1993, 1994). This project was briefly described in Section 1.2.2 above. In effect, the centrifuge test has been used as a prototype for this study. The centrifuge and one-g tests consisted of saturated soil placed at two densities subjected to an earthquake input motion that had sufficient intensity to cause liquefaction. Multiple tests were conducted in the one-g environment on a shake table with varying parameters.

The one-g model tests performed are considered adequate to explore the limits of the proposed scaling hypothesis. At the time this thesis was prepared, this study was the first to attempt a systematic modeling method evaluation employing a liquefaction type mechanism.

In addition to the one-g method, the study shed light on the performance of the centrifuge with respect to modeling liquefaction. The conflict between the time scaling for dynamic and diffusion behavior is accentuated in the centrifuge, but it is also an issue in one-g environment. The array of tests performed has permitted some conclusions to be drawn regarding the limitation of the methods when modeling soil problems involving two phases. These issues have been raised as concerns in prior work, but this is the first study which provides experimental evidence indicating the limitation of the methods.

A byproduct of the investigation has been some insights into the liquefaction phenomenon itself, especially with respect to the generation and dissipation of excess pore fluid pressures. To date, the diffusion process has been considered a function of the permeability of the soil; however, the tests performed indicate that the compressibility of the soil is an essential item requiring consideration. This approach may explain the behavior observed in liquefaction phenomenon which have been attributed to an unexplained increase in permeability (Ishihara, 1994).

The tests performed also provide some insight into the behavior of liquefaction when dense and loose soils are adjacent to each other. Generally current practice ignores liquefaction effects in denser soils if they are assessed to be non-liquefiable. The test results indicate, however, that excess pore pressures migrate from a loose liquefiable layer into an adjacent dense layer, and

under certain configurations may cause significant degradation of strength in the dense layer. The current design practice is not conservative for this situation.

1.5 Thesis Format and Units

Each chapter of this thesis is prefaced with brief introduction describing its contents. The list of references cited are contained in the final section of each chapter. The referenced tables and figures follow the chapter text. The units used in this thesis are consistent with S.I. metric. A list of notations and symbols used in this thesis are included in the preface.

1.6 References

Arulanandan, K. and R. F. Scott, eds., 1993, 1994, "Verification of Numerical Procedures for the Analysis of Soil Liquefaction Problems," Vol. 1, 1993; Vol. 2, 1994, Balkema, Rotterdam.

Bassett, R. H., and W. H. Craig, 1988, "The development of geotechnical centrifuges in the United Kingdom, 1965-1985," in Centrifuges in Soil Mechanics, W. H. Craig, R. G. James, and A. N. Schofield, eds., pp. 119-138, Balkema, Rotterdam.

Bucky, P. B., 1931, "Use of Models for the Study of Mining Problems," Trans. Am. Inst. Min. Metall. Engrs., Tech. Publ. No. 425.

Bucky, P. B., and A. L. Fentress, 1934, "Application of the Principles of Similitude to Design of Mine Workings," Trans. Am. Inst. Min. Metall. Engrs., pp. 109, 25-50, 1934.

Craig W. H., R. G. James, and A. N. Schofield, eds., 1988, "Centrifuges in Soil Mechanics," Balkema, Rotterdam.

Ferguson, K. A., and H. Y. Ko., "Centrifugal Model of the Cone Penetrometer," Proc. Cone Penetration Testing and Experience Symposium, St. Louis, MO., Oct., pp. 108-127.

Fuglsang, L. D., and N. Krebs Ovesen, 1988, "The Application of the Theory of Modeling to Centrifuge Studies," in Centrifuges in Soil Mechanics, W. H. Craig, R. G. James, and A. N. Schofield, eds., pp. 119-138, Balkema, Rotterdam.

Hushmand, B., R. F. Scott, and C. B. Crouse, 1988, "Centrifuge liquefaction tests in a laminar box," Geotechnique 38:2, pp. 253-262.

Iai, S., 1989, "Similitude for Shaking Table Tests on Soil-Structure-Fluid Model in 1g Gravitational Field," Jap. Soc. of Soil Mech. and Found. Eng., Soils and Foundations, Vol. 29, No. 1, pp. 105-119, March.

Ishihara, K., 1994, "Review of the predictions for model 1 in the VELACS," in Verification of Numerical Procedures for the Analysis of Soil Liquefaction Problems, Vol. 2, pp. 1353-1368, Arulanandan, K. and R. F. Scott, eds., Balkema, Rotterdam.

Kagawa, T., 1978, "On the Similitude in Model Vibration Tests of Earth Structures," Soil Mech. and Found. Eng., Proc. of Jap. Soc. of Civil Eng., pp. 69-77, July.

Kimura, T., 1988, "Centrifuge research activities in Japan," in Centrifuges in Soil Mechanics, W. H. Craig, R. G. James, and A. N. Schofield, eds., pp. 119-138, Balkema, Rotterdam.

Pokrovsky, G. I., and I. S. Fyodorov, 1936, "Studies of soil pressures and soil deformations by means of a centrifuge," Proc. 1st Int. Conf. Soil Mech. 1936 1, 70.

Pokrovsky, G. I., and I. S. Fyodorov, 1975, "Centrifugal Model Testing in the Construction Industry," Draft translation prepared by UK Building Research Establishment Library Translation Service.

Rocha, M., 1953, "Similarity conditions in model studies of soil mechanics problems," Laboratoria Nacional de Engenharia Civil, Lisbon, Publ. No. 35.

Rocha, M., 1957, "The possibility of solving soil mechanics problems by the use of models," Proc. 4th Int. Conf. Soil Mech., London 1957 1, pp. 183-188.

Roscoe, K. H., 1968 "Soils and Model Tests," Proc. of Inst. of Mech. Engineers, J. of Strain Analysis, Vol. 3, No. 1, pp. 57-64.

Schofield A. N., 1988, "An introduction to centrifuge modeling," in Centrifuges in Soil Mechanics, W. H. Craig, R. G. James, and A. N. Schofield, eds., pp. 1-10, Balkema, Rotterdam.

Scott, R. F., and N. R. Morgan, 1977, "Feasibility and Desirability of Constructing a Very Large Centrifuge for Geotechnical Studies," report to US National Science Foundation, March.

Scott, R. F., 1978, "Modeling Summary," Proc. ASCE Geotechnical Engineering Division, Specialty Conference, Earthquake Engineering and Soil Dynamics, Pasadena, pp. 1417-1424.

Scott, R. F., 1989, "Centrifuge and Modeling Technology: A Survey," Rev. Franc. Geotech., No. 48, pp. 15-34, July.

Scott, R. F., 1994, "Lessons learned from VELACS project," in Verification of Numerical Procedures for the Analysis of Soil Liquefaction Problems, Vol. 2, pp. 1773-1784, Arulanandan, K. and R. F. Scott, eds., Balkema, Rotterdam.

Sedov, L. I., 1959, "Similarity and Dimensional Methods in Mechanics," translated from the 4th Russian edition by M. Friedman, edited by M. Holt, Academic Press, New York.

Steenfelt, J. S., 1992, "Centrifugal modeling and limit analysis - Reciprocity or adversity?" Proc. XII Int. Conf. Soil Mech. Fnd. Eng. Rio de Jinero, Brazil, 11/27, pp. 987-990.

Tan, T. S., and R. F. Scott, (1985) "Centrifuge scaling considerations for fluid particle systems," Geotechnique 35, No. 4, pp. 461-470.

Whitman, R. V., and P. C. Lambe, 1986, "Effect of Boundary Conditions Upon Centrifuge Experiments Using Ground Motion Simulation," Geotech. Testing Journal, ASTM, Vol. 9, No. 2, June.

Zienkiewicz, O. C., C. T. Chang, and T. Bettess, 1980, "Drained, undrained, consolidating and dynamic behavior assumptions in soils. Limits of validity," Geotechnique, Vol. 30, No. 4, pp. 385-395.

Chapter 2

THEORY

2.1 Introduction

This chapter presents a discussion and, where necessary, the development of the theory necessary to define a modeling method. A general discussion is first given regarding the fundamental behavior of a granular saturated soil and the important parameters which control its behavior. Following this, the scaling relations for the centrifuge and one-g model test are derived and extended. The critical state line and steady state concept is discussed and its use in the constitutive scaling for the one-g model test is explained. The limitations and difficulties which are evident from the theoretical considerations are described.

2.2 Fundamentals of Soil Mechanics

The following discussion is a brief overview of fundamental soil behavior. It is not intended to provide an in-depth review of this complex topic. For this the reader is referred to the many references available, for example, Terzaghi (1943), Scott (1963), and Lambe and Whitman (1969). Some of the basic parameters which influence the soil behavior are initially defined prior to a discussion of some of the important features of soil behavior. The soils used in the model tests were granular soils (i.e., sands) which were saturated, and therefore the discussion is limited to this type of soil condition.

The soil or grain matrix refers to the complex of solid particles. The pore fluid is the fluid which occupies the voids within the matrix. In real soils there is usually a third phase which is the gas content. Typically the pore fluid is water and the gas is air.

If the pore fluid has a negligible gas content, the soil is said to be saturated. As the gas content increases, the soil is said to be partially saturated and the compressibility of the pore fluid

increases. When the gas content is high enough that voids exist within the soil pore fluid mixture, capillary behavior becomes important and in natural deposits this is often referred to as the vadose zone. When the pore fluid content decreases such that the capillary action cannot function around the grains, the soil is often called dry, but in fact, usually has some residual pore fluid.

The vadose zone transitions between saturated and dry states and is typically ignored in most geotechnical engineering applications. It should be noted that in the laboratory a saturated soil has generally less than 1 percent gas content, which must be achieved by complex de-airing and back pressuring procedures. This criterion is not applied to a real soil deposit which is usually assumed to be saturated below a free surface of a pore fluid or groundwater table.

Considering a dry granular soil first, it is composed of a range of irregular grains of varying size, shape, roughness, and hardness. Each soil deposit varies in these attributes and is unique in its composition, though broad definitions are made based usually on the grainsize composition. The behavior of a granular soil is determined primarily by the grain-to-grain contact behavior and the frictional forces which occur between them.

The key parameters controlling such frictional behavior are the grain attributes, the state of the packing of the grains, and the stresses which exist at the grain contacts. The state of packing or density of the soil can range significantly from a loose state to a very dense state. If the applied stresses are high enough, say greater than 700 kPa (or 100 psi), crushing of the grains can occur. However, this range of stresses is usually beyond typical geotechnical considerations.

The maximum density is the state at which minimum voids exist in the soil matrix, and the minimum density corresponds to the loosest state possible at which the void space is maximized. The density, γ, has the conventional definition of the weight of soil per unit volume. There is a dry density and a total density, with total density including the weight of any water within the soil matrix. The void content is usually defined as the void ratio, e, which is the ratio of the volume of voids to the volume of solid particles. The minimum void ratio (e_{min}) and the maximum void ratio (e_{max}) can range widely for different soils. To indicate the state at which a particular soil exists, the relative density (D_r) is often used, where $D_r = \frac{(e_{max} - e)}{(e_{max} - e_{min})}$ and is typically expressed as a percentage.

The stresses from boundary loads and from the self weight of soil due to gravity (or body forces) are transmitted through the soil matrix. These stresses are called total stresses and are calculated using the conventional stress definition assuming the soil matrix is a continuum. The total stress is an average stress because the entire cross-sectional area is used rather than just the area of the grains which are physically in contact. It should be noted that the actual grain-to-grain stresses vary significantly, and will generally be higher than the computed total stress.

Basic strain response of soils to stresses: A general distinction can be made between confining stresses and shearing stresses, which are analogous to the hydrostatic and deviatoric stresses defined in solid mechanics. A soil at a fixed void ratio (same density) will exhibit different behavior under differing confining stresses when subjected to some increment of applied stress. For example, at low confining stresses a granular soil will more likely dilate (increase in volume) when subjected to shearing stresses. Whereas at a higher confining stress the same soil is more likely to exhibit contractive behavior (decrease in volume). If the confining stresses are higher it is more likely the grain structure will adjust to a closer packing and hence the contractive versus dilative behavior which is observed.

In contrast to the above, if the same soil is prepared at two void ratios (a loose and a dense sample) and the applied confining stresses are the same, the denser soil is more likely to dilate when a stress increment is applied. This is a direct consequence of the closer packing of the soil grains, in that displacements caused by the stresses will force grains to move over one another. This is why denser soils generally exhibit higher strengths because more work is required to deform the soil matrix. From the above discussion there are competing effects between the initial state (density or void ratio of the soil) and the confining stresses imposed on the soil.

An increment in the applied stresses can be viewed as a perturbation to the distribution of stresses throughout the soil matrix, and the volumetric behavior (dilatant or contractive) reflects the grain structure adjustment necessary to reach equilibrium under this perturbation. Often a soil will exhibit both dilatant and contractive behavior at different times as stresses are progressively applied. When a soil exhibits no further volumetric change under the continued application of stresses, it is said to be at its critical state, or steady state. This condition is discussed further in Section 2.5.

Generally a soil will behave in a stable manner under applied increments of confining stresses, exhibiting behavior such as creep or settlement. Such behavior is of concern to the geotechnical

engineer, but generally the application of shearing stresses is of greater concern because the soil matrix can behave in an unstable manner. For example, slope failures, foundation shear failures, and landslides. From the above general discussion, the complexity of soil stress-strain behavior is apparent. Soil exhibits non-linear, plastic, strain behavior under applied stresses.

Saturated soils and effective stresses: When a granular soil is inundated with a fluid, the fluid in the pore spaces (or pore fluid) exerts a buoyancy force on the soil grains (in proportion to the density of the fluid) and the stresses due to the self weight of the soil are reduced. Obviously this reduction in stress will also reduce the frictional forces between the soil grains and will affect the soil strength. The pressure (or stress) exerted by the pore fluid is generally termed the "pore pressure", and the difference between this and the total stress is called the is called the"effective stress".

Under steady state static conditions the pressure in the pore fluid (typically water) is hydrostatic and it increases linearly with depth. In this case, the effective stress acting in the vertical direction at any given depth in the soil, will be equal to the difference between the unit weight of the soil and the unit weight of the fluid times the depth. If the pore pressure diverges from the hydrostatic condition, flow will occur within the soil and the pore fluid will exert drag forces on the soil grains as it attempts to return to a hydrostatic state. Essentially the internal fluid pressure within a void space of soil has changed and it in turn changes the stresses acting on the adjacent soil grains. If the divergence from hydrostatic is positive, then it is called the"excess pore pressure" and the effective stress must be reduced accordingly. If the hydrostatic pressure plus excess pressure equals the total stress of the soil, the effective stress is zero and this is a limiting condition. It implies that the average contact stresses between particles in the saturated matrix is zero and the particles are in suspension. This state is often described as a quick condition or under certain conditions liquefaction.

A number of scenarios can cause the pore pressure to diverge from the hydrostatic state. The most common are seepage and consolidation. The seepage behavior in soils will not be described herein. The consolidation behavior of soils is a transient condition, generally induced by increasing the confining stresses on the soil matrix, for example, constructing a building on the soil surface. As described in the discussion on dry soils, when a load is applied the soil structure will compress and the void space will decrease.

In a saturated soil the pore fluid is relatively incompressible with respect to the soil matrix and occupies the void space. Therefore, when the load is applied the pore fluid pressure increases to match the load and diverges from the hydrostatic condition. Flow within the soil matrix will occur as diffusion progresses and pore fluid pressures dissipate returning to a hydrostatic condition. As this occurs the soil matrix will continue to compress as the applied load is transferred to the soil grains. The rate of this process is primarily dependent on the rate of loading, and the compressibility and permeability of the soil. If the loading occurs slowly, the permeability is very high, and the compressibility very low, then diffusion will occur quickly and little change will be observed in the pore fluid pressure. In this case the soil is essentially behaving in a "drained" manner. The converse, that is rapid loading, low permeability, and high compressibility, will generate full pore fluid pressures and is often described as "undrained" behavior. The use of the drained and undrained terminology is essentially defined by the volume change which occurs. A drained condition implies volume change, and an undrained condition, no volume change.

Response of saturated soils under dynamic loading: As discussed previously, any perturbation in the stress state of the soil matrix will potentially cause dilation or contraction. As the confining stresses increase the potential for contractive behavior increases. In a saturated soil in which undrained conditions dominate, the pore pressure will respond to any change in the soil matrix. If dilation occurs, negative excess pore pressures will result and the effective stress will increase. If contraction occurs positive excess pore pressures will occur and the effective stress will decrease. Possible perturbations to the stress state can come from monotonically applied loads or from cyclic loads. An earthquake is an example of a cyclic, dynamic, loading condition.

When earthquake-generated stress waves propagate through the soil, cyclic stresses and strains are applied to the grain matrix which creates a continual disturbance. If the soil density is low (or the void ratio high) and the cyclic stresses and strains are large enough, the grain matrix will want to contract in volume, and, similarly to the consolidation process, excess pore pressures are generated. When this occurs diffusion will also start to occur and dissipation of the pore pressures will begin. As the earthquake continues the generation of pore pressures competes with the diffusion process.

If the repeated cyclic loading of the earthquake is intense enough and diffusion in the soil is low, the pore pressure will progressively increase and it is possible the effective stresses may reach a

zero condition. This is usually called liquefaction; however, the actual exact definition varies from author to author. If the diffusion dominates the generation of pore pressures during the earthquake, or the intensity of the earthquake is low, then only partial pore pressure generation will occur, if any. In this case the soil is dominated by drained behavior rather than undrained.

After the earthquake has stopped, remaining excess pore pressures will begin to dissipate through diffusion, and in many respects this is identical to the consolidation process described earlier. However, it should be noted that in a liquefied state the sand grains are presumably in suspension, and therefore there is an initial period in which the grains are settling in a process similar to sedimentation. Once the grains have re-established contact, then the process is one of consolidation.

From the description of liquefaction above, two comments can be made regarding the potential for liquefaction.

1) A looser soil state (lower density or higher void ratio), higher confining stresses, and higher cyclic stresses or strains, are more likely to generate excess pore pressures under the cyclic loading (Mullis et al., 1975).

2) The rate at which an earthquake can generate pore pressures competes with how quickly diffusion occurs within the soil.

2.3 Model Scaling Relations

In this section the underlying model theory is developed for both the centrifuge and one-g methods. The scaling relations which relate the model to the prototype can be derived by formal dimensional analysis (Fuglsang and Ovesen, 1988), or by direct consideration of dynamic equilibrium (Scott, 1989). The method presented below follows Scott (1989) with some minor refinements to account for density variations between model and prototype.

Using the general equations of dynamic equilibrium (Fung, 1977), Newton's law states that the material rate of change of linear momentum of a body is equal to the resultant applied forces.

$$\int_V \left[\frac{\partial \rho v_i}{\partial t} + \frac{\partial}{\partial x_j}(\rho v_i v_j) \right] dV = \int_V \left[\frac{\partial \sigma_{ij}}{\partial x_j} + X_i \right] dV \text{ where,}$$

$t =$ time

$x =$ spatial coordinate

(2-1) $v =$ velocity

$\rho =$ density (mass per unit volume)

$X =$ body force

$V =$ volume of the body

$\sigma =$ the stress tensor

Since the above must hold for an arbitrary domain V, then it must hold for the integrand,

$$\text{(2-2)} \quad \frac{\partial \rho v_i}{\partial t} + \frac{\partial}{\partial x_j}(\rho v_i v_j) = \frac{\partial \sigma_{ij}}{\partial x_j} + X_i$$

Using conservation of mass the equation reduces to

$$\text{(2-3)} \quad \rho\left(\frac{\partial v_i}{\partial t} + v_j \frac{\partial v_i}{\partial x_j}\right) = \frac{\partial \sigma_{ij}}{\partial x_j} + X_i \Leftrightarrow \rho\left[\frac{\partial^2 u_i}{\partial t^2} + \frac{\partial u_j}{\partial t}\frac{\partial}{\partial x_j}\left(\frac{\partial u_i}{\partial t}\right)\right] = \frac{\partial \sigma_{ij}}{\partial x_j} + X_i$$

which is the Eulerian equation of motion. This equation must be satisfied in the prototype structure, and also in the model that represents the prototype. The equations for the prototype can be written in terms of the model variables if appropriate non-dimensional variables are defined. Using the ratio of prototype to model variables where the subscripts p and m denote prototype and model, respectively, gives the following:

Ratio of length: $x^* = \frac{x_p}{x_m}$

Ratio of time: $t^* = \frac{t_p}{t_m}$

(2-4) Ratio of density: $\rho^* = \frac{\rho_p}{\rho_m}$

Ratio of body forces: $X^* = \frac{X_p}{X_m}$

Ratio of stress: $\sigma^* = \frac{\sigma_p}{\sigma_m}$

Using the definitions of (2-4), the prototype variables can now be written in terms of model variables. Substituting these values into equation (2-3) for the prototype, the following is obtained.

(2-5)
$$\rho^* \rho_m \left[\frac{x^*}{t^{*2}} \frac{\partial^2 u_{im}}{\partial t_m^2} + \frac{x^*}{t^*} \frac{\partial u_{jm}}{\partial t_m} \frac{1}{x^*} \frac{\partial}{\partial x_{jm}} \frac{x^*}{t^*} \left(\frac{\partial u_{im}}{\partial t_m} \right) \right] = \frac{\sigma^*}{x^*} \frac{\partial \sigma_{ijm}}{\partial x_{jm}} + X^* X_{im}$$

$$\frac{x^*}{\sigma^*} \frac{x^*}{t^{*2}} \rho^* \rho_m \left[\frac{\partial^2 u_{im}}{\partial t_m^2} + \frac{\partial u_{jm}}{\partial t_m} \frac{\partial}{\partial x_{jm}} \left(\frac{\partial u_{im}}{\partial t_m} \right) \right] = \frac{\partial \sigma_{ijm}}{\partial x_{jm}} + \frac{x^*}{\sigma^*} X^* X_{im}$$

Equation (2-3) also holds for the model, and can be written as

(2-6)
$$\rho_m \left[\frac{\partial^2 u_{im}}{\partial t_m^2} + \frac{\partial u_{jm}}{\partial t_m} \frac{\partial}{\partial x_{jm}} \left(\frac{\partial u_{im}}{\partial t_m} \right) \right] = \frac{\partial \sigma_{ijm}}{\partial x_{jm}} + X_{im}$$

By subtracting (2-5) from and (2-6), the following is obtained:

(2-7)
$$\left(1 - \frac{x^*}{\sigma^*} \frac{x^*}{t^{*2}} \rho^*\right) \rho_m \left[\frac{\partial^2 u_{im}}{\partial t_m^2} + \frac{\partial u_{jm}}{\partial t_m} \frac{\partial}{\partial x_{jm}} \left(\frac{\partial u_{im}}{\partial t_m} \right) \right] = \left(1 - \frac{x^*}{\sigma^*} X^*\right) X_{im}$$

Equation (2-7) is the condition for dynamic equilibrium. Obviously, this equality must also hold for a static condition or when body forces are zero which implies

$$(2\text{-}8) \quad (1-\frac{x^*}{\sigma^*}X^*)=0 \Rightarrow \frac{x^*}{\sigma^*}X^*=1$$

$$(2\text{-}9) \quad (1-\frac{\rho^* x^{*2}}{\sigma^* t^{*2}})=0 \Rightarrow \frac{\rho^* x^{*2}}{\sigma^* t^{*2}}=1$$

In geotechnical problems the body forces which dominate are due to gravity and may be written as

$$(2\text{-}10) \quad X_i = \rho \; g_i$$

where g_i are the components of the gravitational acceleration in the coordinate directions. If the coordinate system is chosen such that one of the directions is vertical, then the value of g_i is simply the acceleration of gravity in that component direction and all other components are zero.

Gravity is the same in both model and prototype for one-g scale testing; therefore,

$$(2\text{-}11) \quad X^* = \rho^*$$

And equations (2-8) and (2-9) can be reduced to

$$(2\text{-}12) \quad \frac{\rho^* x^*}{\sigma^*}=1 \Rightarrow \frac{x^*}{t^{*2}}=1$$

Now letting $x^* = n$, where n is the ratio of the prototype dimension to the model dimension, or scale of the model, the scaling factors for each of the variables for one-g conditions can be derived as shown in Table 2-1. Note that at this stage no scaling or account has been taken for the different constitutive behavior between the one-g model and prototype. This is discussed in Section 2.3 below.

For the centrifuge modeling technique the body forces are not the same and the centripetal acceleration imposed on the model is higher than gravity. To maintain similar constitutive behavior between the centrifuge model and the prototype, the stresses and soil density in the model and the prototype must be the same. Therefore, the imposed acceleration is equal to ng, where n is the ratio of the prototype dimension to the model dimension. Again the coordinate

system can be chosen such that all other components of the body forces are zero. Given these constraints and (2-9), (2-4) becomes

$$\text{Ratio of length: } x^* = \frac{x_p}{x_m} = n$$

$$\text{Ratio of time: } t^* = \frac{t_p}{t_m} = n$$

(2-13) $$\text{Ratio of density: } \rho^* = \frac{\rho_p}{\rho_m} = 1$$

$$\text{Ratio of body forces: } X^* = \frac{X_p}{X_m} = \frac{1}{n}$$

$$\text{Ratio of stress: } \sigma^* = \frac{\sigma_p}{\sigma_m} = 1$$

The remaining centrifuge scaling factors for other model parameters can now be derived and are presented in Table 1.

The scaling of time for dynamic equilibrium is shown in Table 1, and is referred to as"dynamic" time and is different for the two modeling techniques. As discussed in 2.1, when excess pore water pressures are created in the soil matrix, diffusion occurs. The time scaling for the diffusion process is different from the dynamic time scaling.

To develop a diffusion time scale the consolidation, theory of soil mechanics can be employed, which in one dimension can be described by the equation

$$c_v\left(\frac{\partial^2 u}{\partial z^2}\right) = \frac{\partial u}{\partial t} \quad \text{where}$$

$u =$ excess pore fluid pressure

(2-14) $z =$ dimension or depth within consolidating layer

$t =$ time of diffusion

$c_v =$ coefficient of consolidation

which can also be expressed in non-dimensional terms as

$$\left(\frac{\partial^2 W}{\partial Z^2}\right) = \frac{\partial W}{\partial T} \quad \text{where}$$

Non - dimensional excess pore pressure $W = \frac{u}{u_0}$

(2-15) Non - dimensional depth $Z = \frac{z}{H}$

Non - dimensional time $T = \frac{c_v t}{H^2}$

u_0 = arbitrary constant pore fluid excess pressure

H = thickness of layer, or effective length of drainage

In (2-15), the coefficient of consolidation c_v is a measure of the hydraulic diffusion in a saturated soil, and for a linearized one-dimensional idealization is defined as

$$c_v = \frac{k(1+e_0)}{\gamma_f a_v} \quad \text{where}$$

k = coefficient of permeability

(2-16) e_0 = inital void ratio

γ_f = unit weight of pore fluid

a_v = coefficient of compressibility

Each of the parameters in equation (2-16) has been described in Section 2.2. For equation (2-16) e_0 and γ_f are constants. The coefficients k and a_v are defined indexes which provide a relative scale for each soil type. Both are dependent on the state of stress and void ratio existing at any given time in the soil matrix, which of course changes as consolidation or diffusion progresses. For the linearized solution presented above, they are assumed to be constant and some average value must be chosen. The compressibility coefficient, a_v, is a direct measure of the change in void ratio to the applied stress under radially confined conditions. The permeability k is a function of the fluid viscosity, body forces, and fluid unit weight. The commonly accepted definition of k (Tan and Scott, 1985) is as follows:

$$k = \frac{\gamma_f K}{\mu} \quad \text{where,}$$

(2-17) K = absolute or specific permeability of the soil.

μ = dynamic viscosity.

To determine an appropriate scaling factor for the diffusion process, the non-dimensional solution for consolidation (equation (2-15)) can be employed. To have similitude the non-dimensional parameters W, Z, and T must be the same for homologous points in model and prototype. Certainly Z will be equal from the geometric similitude of the model and prototype. W and T should be equal to maintain similarity of behavior. Therefore, the time scaling factor of model to prototype can be determined as follows:

$$t^* = \frac{H^{*2}}{c_v^*} \quad \text{where}$$

(2-18) $$t^* = \frac{t_p}{t_m} \quad \text{(for diffusion process)}$$

$$c_v^* = \frac{c_{vp}}{c_{vm}}$$

$$H^* = n \quad \text{(defined by the geometric scale of the model)}$$

To determine c_v^*, first consider the conditions which prevail on the centrifuge model. From equation (2-16) and (2-17) the scale factor c_v^* can be determined by each of the scaling factors that would apply for each of the parameters defined in the equations as follows:

$c_v^* = 1$ (assuming the model soil is placed at the same state as in the prototype) where

$$(1+e_0)^* = 1$$

$$a_v^* = 1$$

(2-19) $k^* = n$ for the same pore fluid in model and prototype which follows from

$$\mu^* = 1$$

$$K^* = 1$$

$$\gamma_f^* = \frac{\rho_f g}{\rho_f n g} = \frac{1}{n}$$

This implies that for the centrifuge the solution for equation (2-18), the time scaling for diffusion, is

(2-20) $$t^* = n^2$$

For the one-g environment the scaling ratios are more complex because the soil state of the model will not be the same as the prototype. In fact, as discussed in more detail in Section 2.3, it is desirable to place the model soil at a lower density. Following the same procedure as above, the scaling factor would be as follows:

$$t^* = \frac{H^{*2}}{c_v^*} \quad \text{where}$$

$$H^* = n \quad \text{(defined by the geometric scale of the model)}$$

$$c_v^* = \frac{c_{vp}}{c_{vm}} = k^* \frac{(1+e_0)^*}{\gamma_f^* a_v^*}$$

$$(1+e_0)^* \neq 1$$

(2-21) $$a_v^* \neq 1$$

$$k^* = K^* \quad \text{for the same pore fluid in model and prototype}$$

$$\gamma_f^* = 1$$

$$\Rightarrow t^* = \frac{n^2}{c_v^*} = \frac{n^2 a_v^*}{K^*(1+e_0)^*}$$

For one-g modeling each of the scaling ratios needs to be determined by measurement and in some cases by other laboratory testing. A typical one-g test in which the same soil and pore fluid is used as in the prototype, a_v^* is on the order of n, $(1+e_0)^*$ is approximately equal to 1, and $K^* < 1$. A typical value for the diffusion time scaling, t^*, reported in this thesis would be $2n < t^* < 4n$. The values for the diffusion time scaling are presented in Table 2-1.

In the derivations presented above for the diffusion time scaling, equations and parameters which are based on idealizations have been employed. The accuracy of the derived scaling for the model and prototype where three-dimensional effects and time varying properties exist, can be questioned. Although this is a valid criticism, in defense of the derivation approach, the scaling seeks to define the relative behavior between model and prototype. If the same idealizations are made to both and geometric and material similarity is maintained, the approach followed is reasonable but should be validated by experimental results.

2.4 Constitutive Scaling Technique

The above general scaling relationships derived in Section 2.3 above are valid for any model or prototype material (solid, liquid, gas) regardless of the constitutive behavior of the material itself. As previously described the scaling of the constitutive behavior in the centrifuge technique is achieved by maintaining similar stresses at homologous points. This is not possible in a one-g environment, and as discussed in Section 2.2 the fundamental stress-strain behavior of the model soil will be different from the prototype. To account for this there are two possibilities: 1) scale the constitutive behavior as described in Chapter 1, Section 1.2.3, or 2) modify the model material so that under the different stress conditions it will still exhibit strain behavior similar to the prototype. Scott (1989) has proposed a method for the latter, and this is described herein.

The method relies on the critical state or steady state behavior of a soil, and the existence of a critical state line (CSL) or steady state line (SSL). These concepts are discussed in Section 2.6 below. The significance of the CSL or SSL is the possibility of normalizing the soil behavior with respect to it. For the purposes of discussion, the SSL will be used as it is typically associated with sands.

In general, a unique SSL can be found for given soil if a consistent test methodology is followed to define it. This is discussed further in Section 2.5. Typically the SSL is defined by the void ratio, e, and some measure of the governing stress, for example, the mean effective stress, p' (which is the first stress invariant, I_1).

(2-22) $$p' = \frac{\sigma'_1 + \sigma'_2 + \sigma'_3}{3}$$ where $\sigma'_1, \sigma'_2, \sigma'_3$ are the principal effective stresses

Figure 2-1 shows an example, where the SSL is plotted in an e vs $\log(p')$ space. The SSL is often approximated as linear in this space.

The significance of the SSL (Scott, 1989) for model scaling can be described as follows. If a sand has a given void ratio, e , at a particular value of p' , it is separated from the SSL by an amount Δe . This has also been called the state parameter (Been and Jefferies, 1985). The value of Δe can be positive or negative. If the same soil is subject to a different value of p' and the void ratio, e, is adjusted so that Δe (with respect to the SSL) is kept the same, then the soil will exhibit similar normalized stress-strain behavior. This concept is illustrated in Figure 2-1.

Essentially the soil will have this stress-strain similarity condition for any value of p' as long as its void ratio falls on a line parallel to the SSL. This has an obvious application to one-g modeling where the prototype soil has higher values of stress, p'_p. From Figure 2-1 to maintain similarity at the lower stresses of the model p'_m, the soil is placed at a higher void ratio and is in a looser state than the prototype.

Scott (1989) suggested several steps that could be followed to achieve an appropriately scaled model as follows.

1) The prototype to model scaling ratio, n, is chosen.

2) The void ratio of the prototype soil is determined.

3) A stress (for example, p'_p) is calculated at an appropriate depth in the prototype soil, or is selected to be representative of the load from a structure located in or on the soil.

4) Through triaxial testing the stress-strain behavior of the soil at the prototype void ratio and p'_p is established.

5) A series of triaxial tests is performed at model stress magnitudes, p'_m, at homologous points to the prototype and a void ratio is found at which the same normalized stress-strain behavior is observed.

6) The model test is performed in accordance with the scaling relations presented in Table 2-1 at the void ratio(s) found in 5).

7) The measured model quantities are scaled to prototype values using the scaling relations in Table 2-1.

An alternate approach suggested by Scott (1989) directly uses the SSL and the postulated similarity of behavior if Δe is kept constant. If the same soil is used in the model and the prototype, then the void ratio and stress condition of the prototype and the slope of the SSL are all that are required to select an appropriate void ratio for the model. In his paper Scott assumed the SSL was linear in log space, and that the density difference between model and prototype could be ignored.

Given these assumptions an appropriate model void ratio can be easily selected. However, the slope of the SSL is not necessarily linear and the density difference which occurs when the model is placed at a different void ratio should be accounted for. Given these added factors it is still quite easy to determine an appropriate void ratio for the model but some iteration may be required. For example, tests performed as part of this research (described in Chapter 4) consisted of a layer of sand without any structures on or in it. The prototype stress, p'_p, was calculated for the center of the soil layer, and an initial model stress, p'_m, was estimated for the center of the model layer. Using the SSL an estimate of the model void ratio at the initial estimated p'_m was made. This value was used to compute a revised density for the model soil and a revised estimate of p'_m . The new value of p'_m was in turn used to refine the void ratio selection for the model. This process was repeated until p'_m and the estimated void ratio were compatible. In practice this required only a couple of iterations and was performed on a spreadsheet using a function fitted to the SSL. Again it is emphasized that only the slope of the SSL is required if the same soil is used in both model and prototype, and it does not have to be a linear fit.

Under some conditions, for example, if Δe is positive (above the SSL) and the contrast in model to prototype stresses is large (model scale, n, is large), it may not be possible to place the model soil in a loose enough state. An alternative model soil would be required to overcome this limitation. Scott (1989) has suggested that the postulated normalized stress strain behavior described above would apply to alternate soils as long as the void ratio scaling was performed with respect to the SSL of the alternate model soil. Scott defined the state of the soil in terms of the relative density, D_r , instead of its void ratio, thereby normalizing the soil's behavior with respect to its maximum and minimum void ratios. Figure 2-2 demonstrates a possible methodology for using an alternate model material. It should be noted a different model soil could also be desirable to scale the diffusion properties which will be discussed further in Section 2.6.

The scaling method described above was applied to triaxial test data and a simple one-g model test was performed on a laterally loaded pile (Scott, 1989) in dry sand. The preliminary comparisons between results of this one-g model with a similar centrifuge model appeared to be reasonable. In the discussion of the state parameter (Been and Jefferies, 1985), it is stated that samples of sand with varying composition behaved "similarly if test conditions assure an equal

initial proximity to the steady state" which, in terms of the discussion above, is equivalent to maintaining a constant Δe . These comparisons appear to support the postulated theory.

However, as the tests become more complex, a greater number of issues need to be verified. Some of these are as follows:

1) Under dynamic or cyclic loading is the dynamic response of model and prototype similar?

2) Will settlement recorded at the soil surface due to densification and or deformation reasonably represent the prototype behavior?

3) What is the effect on model soil behavior due to the conflict of time scales, dynamic and diffusion?

4) Are there physical effects present in a small scale model which are not present in a prototype, as is observed, for example, in conventional laboratory triaxial tests which indicate the behavior is affected by sample size?

2.5 Critical or Steady State Condition in Sands

In Section 2.2 the volumetric (dilative or contractive) behavior of granular soil under imposed stresses was briefly described. The point at which the soil shows no volumetric strain or change in effective stresses while subjected to a constant rate of deformation is called the critical state or steady state. The term critical state is usually associated with cohesive soils (e.g., clays) (Roscoe et al., 1958), and steady state with granular soils (e.g., sands) (Castro, 1975). The steady state theory proposes the void ratio and effective stresses measured at a steady state condition will be unique for a given soil. For a single soil a series of points can be found which define a line in a void ratio versus effective stress space. This line is referred to as the steady state line (SSL), and is an essential element of the constitutive scaling method described in Section 2.4 above.

The SSL varies greatly for different soils, and is affected primarily by the grain size content of the soil and the shape of the grains (Poulos et al., 1985). The SSL delineates the potential behavior of a granular soil deposit. If, prior to being subjected to applied stresses, the soil has an initial effective stress and void ratio which plots above the SSL, then the soil is more likely to exhibit contractive behavior. In this state the soil can potentially liquefy, consistent with the definition of Seed and Lee (1966) and Castro (1975). A soil which liquefies exhibits a dramatic

reduction in strength as a result of the collapse of the grain matrix. The soil retains a constant residual strength under continued deformation due to a redeveloped grain matrix.

The condition where the initial soil state lies below the steady state line implies the soil will more likely exhibit dilative behavior. In this state the soil may reach initial liquefaction (Seed and Lee, 1966) and will exhibit cyclic mobility (Castro, 1975) when subjected to cyclic loading. Soils in this state may reach a zero effective stress condition, but an associated sudden reduction in strength and collapse of the soil matrix is not observed.

From laboratory experiments, samples prepared in a contractive state with respect to the SSL do reach a steady state condition under continued applied stresses. However, samples prepared at a less contractive state or at a dilatant state with respect to the SSL often do not reach a steady state condition, at least within the limits of current testing apparatus. Such samples exhibit what is called a phase transformation, at which the sample behavior changes from contractive to dilative. This point usually corresponds to a local minimum in the measured shearing resistance of the sample. This point of phase change is used to define the SSL for tests exhibiting this behavior. References cited by Riemer (1992) conclude that the SSL determined from samples which achieve a steady state condition is the same as the SSL determined from samples which exhibit a phase transformation.

The use of steady state theory for the evaluation of the behavior of sands has been the subject of many papers. The relatively recent work by Riemer (1992) summarizes many of the issues related to steady state concept and SSL. The most important point of debate is the uniqueness of the SSL line.

Points of issue for the uniqueness of the SSL can be summarized as follows:

1) The dependence on the testing method, test apparatus, and the stress path followed before a steady state is achieved.

2) The effect of drainage conditions existing in the tests.

3) Different sample preparation methods.

4) The effects of different consolidation pressures applied to samples prior to testing.

Of the above, Riemer (1992) concluded that Items 1 and 4 were significant factors indicating the SSL is not unique. Item 2 was not an influence and with care Item 3 could be ruled out. From

prior work other factors, such as initial stress anisotropy and the rate of strain applied during the test, have been found to have little or no effect on the SSL.

Given the results of Riemer's study, it is important to note that the factors affecting the uniqueness of the SSL did not appear to affect the slope of SSL. The relative position of the SSL moved up or down in the void ratio stress space but the slope of the SSL remained relatively constant. It was also observed that as long as a consistent laboratory methodology was followed in the testing procedure, there was very little scatter in the data that defined the SSL for a given soil.

These observations are significant for the proposed application of the modeling technique described in Section 2.4 above. If the same soil is used in the model and the prototype, then only the slope of the SSL is required. If an alternate model soil is used, it is reasonable to expect that if the same laboratory testing methodology is followed to determine the model soil SSL and the prototype SSL, then the relative position of the two lines should be correct. While debate about the SSL will continue, the issues do not appear to challenge the constitutive modeling technique proposed by Scott (1989).

2.6 Diffusion Time Scaling

In Section 2.3 the scaling relations were derived for the one-g model and centrifuge model, and from Table 2-1 there is a conflict between the time scaling for the dynamic behavior and diffusion processes. This conflict exists for one-g and centrifuge models and exists regardless of any debate about the scaling of the constitutive behavior of the soil in either method. It should be noted, however, that the scaling incompatibility is less severe for one-g models as indicated on Table 2-1, and one-g models also have an inherent advantage because they are typically larger, and therefore the ratio, n, is smaller. Of course, a one-g model could be constructed at full scale (n=1) which would have exhibited no conflict in the time scaling.

While the time scales can be arbitrarily separated in a model, it is not valid for a test in which both processes play a significant role because they are intrinsically coupled. In model tests of the liquefaction phenomenon, the conflict of these time scales can lead to very misleading results. Under the application of cyclic loading, which is governed by the dynamic time scale, pore pressures will be generated. As described in Section 2.2, diffusion will immediately occur and continue as the cyclic loading continues. In the centrifuge the diffusion process will occur$n$ times

faster than the dynamic scaling would permit, and at one-g would occur $n^{0.5}$ to n times faster. This means that the model is dissipating pore pressure faster than it should. During the application of cyclic loading, the rate of pore pressures generation will be lower than what would occur in the prototype, and after cyclic loading the dissipation of residual pore pressures would be too high. This could result in the following:

1) If the prototype earthquake is sufficient to just induce liquefaction in the real soil, the scaled model will not liquefy. The magnitude of pore pressure generated in the model will be less than the prototype.

2) The dynamic properties of the soil are controlled by the effective stresses and hence pore pressures generated during shaking. If the excess pore pressures are lower, the soil will in general behave more stiffly. Therefore, if the rate of pore pressure increase is too low in the model, the dynamic response will, in general, be higher than the prototype at equivalent times, at least until a liquefied state is obtained.

3) Following the cyclic loading any residual excess pore pressures will dissipate far faster than the prototype, which means the effective stresses will also increase too fast. This will affect fundamental properties such as strength and shear stiffness. Consequently, it can be expected that the behavior of the model will be different from the prototype. For example, the rate of settlement at the soil surface will be faster and the magnitude may be affected. Also, if static shear stresses are high, as in the case of slopes or embankments, failures may not occur and permanent deformations may be underestimated by the model.

The above influences must be considered carefully when performing such tests. Ideally, it would be better to adjust the model properties so that the two time scales concurred. There are two possible choices: alter the model material to adjust its diffusion properties or modify the pore fluid properties to alter the time of dissipation.

If an alternate model material is selected, it would have to have a lower value of c_v than the prototype. From equation (2-19) it would need to be n times less than the prototype value. This would most easily be achieved by using a finer-grained soil which would lower the permeability and, in general, increase the compressibility of the model soil. The problem with the alternate model material then becomes matching its general constitutive behavior to the prototype soil. Potentially this could be attempted using the proposed methodology described in Section 2.4.

If the option of modifying the pore fluid is adopted, then the model pore fluid viscosity must be increased. From equation (2-17) this will have the effect of reducing the permeability. This method appears to be a straightforward solution because the same model and prototype soils could be used. However, there are concerns about the effect that the altered viscosity may have on the behavior of the soil. In general, the scaling requires the viscosity to be increased by a substantial amount. Obviously, in the extreme case where the fluid was very viscous (e.g., tar), the behavior of the fluid within soil grain matrix would be affected, and the soil response would be affected. In addition to this concern, the increased density of the fluid must also be considered, and in the centrifuge there are other factors which require consideration (Tan and Scott, 1985). The degree to which the soil behavior would be affected by a modified pore fluid has not been thoroughly investigated through experimentation to date.

2.7 Digression on Permeability Changes

An issue which is related to diffusion time scaling is the assertion that the permeability of the sand increases during the generation of pore pressures. It is reported that in the centrifuge this effect has been measured (Arulanandan, 1994) and that the permeability increased by up to a factor of four times before returning to the original value. A similar effect has been measured under one-g conditions (Jafarzadeh and Yanagisawa, 1995). It is cited that this effect must be included in numerical models to obtain better estimates of settlement (Ishihara, 1994), (Arulanandan, 1994).

This phenomenon is difficult to explain in light of other observations made during such tests and with respect to the currently accepted definition of permeability. If the viscosity and density of the fluid remain constant, equation (2-17) indicates the permeability during the tests cited above could only increase if the absolute permeability, K, increased. K has units of area and is generally interpreted in sands to correlate with the void ratio which implies the void ratio of the soil would have to increase. Locally, this may occur within a liquefied soil; however, on average this seems unlikely because during these tests surface settlements were measured concurrently which indicated a reduction in the void ratio which implies K will get smaller. Again with reference to equation (2-17), the above implies a reduction in permeability could be expected which is contrary to the increase reported in the cited work.

A factor which would explain an apparent increase in permeability would be the increase in the compressibility of the soil which occurs as the effective stresses decrease as excess pore pressures are generated. Rather than considering permeability as controlling drainage in the tests, a diffusion index such as the coefficient of consolidation, c_v, should be considered as defined in equation (2-16). If the experimenters cited above assumed that c_v was constant, an increase in the compressibility represented by a_v would give an apparent increase in the permeability, k. In fact, c_v is not constant during a test, but is controlled by the compressibility of the soil (which will increase as the pore pressure rises), and the permeability which, in general, is expected to decrease as the excitation continues. This effect is considered further in this thesis and data is presented to support the above conclusion.

2.8 References

Arulanandan, K., 1994, "Why VELACS? (Verification of Liquefaction Analysis using Centrifuge Studies)," in Verification of Numerical Procedures for the Analysis of Soil Liquefaction Problems, Vol. 2, pp. 1239-1266, Arulanandan, K. and R. F. Scott, eds., Balkema, Rotterdam.

Been, K., and M. G. Jefferies, 1985, "A state parameter for sands," Geotechnique 35, No. 2, pp. 99-112, June.

Castro, G., 1975, "Liquefaction and Cyclic Mobility of Sands," J. of Geotech. Eng. Div., ASCE, Vol. 101, GT6, pp. 551-569, June.

Fuglsang, L. D., and N. Krebs Ovesen, 1988, "The Application of the Theory of Modeling to Centrifuge Studies," in Centrifuges in Soil Mechanics, W. H. Craig, R. G. James, and A. N. Schofield, eds., pp. 119-138, Balkema, Rotterdam.

Fung, Y. C., 1977, "A First Course in Continuum Mechanics," Prentice Hall, 2nd Edition.

Ishihara, K., 1994, "Review of the predictions for model 1 in the VELACS," in Verification of Numerical Procedures for the Analysis of Soil Liquefaction Problems, Vol. 2, pp. 1353-1368, Arulanandan, K. and R. F. Scott, eds., Balkema, Rotterdam.

Jafarzadeh, F., and E. Yanagisawa, 1995, "Settlement of sand models under unidirectional shaking," in First Int. Conf. on Earthquake Geotech. Eng., Volume 2, pp. 693-698, K. Ishihara, ed., Balkema, Rotterdam.

Lambe, T. W. and R. V. Whitman, 1969, "Soil Mechanics," Massachusetts Inst. of Tech., John Wiley & Sons, New York.

Mullis, J. P., C. K. Chan, and H. B. Seed, "The Effects of Sample Preparation on the Cyclis Stress Strain Behavior of Sands," Earthquake Eng. Res. Center, Report No. UCB/EERC-75/18, UC Berkeley.

Poulos, S., G. Castro, and J. France, 1985, "Liquefaction Evaluation Procedure," J. of Geotech. Eng. Div., ASCE, Vol. 111, No. 6, pp. 772-792, June.

Roscoe, K. H., A. N. Schofield, and C. P. Wroth, 1958, "On the Yielding of Soils," Geotechnique, Vol. 8, pp. 22-53.

Scott, R. F., 1963, "Principles of Soil Mechanics," Reading, Mass., Addison Wesley.

Scott, R. F., 1989, "Centrifuge and Modeling Technology: A Survey," Rev. Franc. Geotech., No. 48, pp. 15-34, July.

Seed, H. B., and K. L. Lee, 1966, "Liquefaction of Saturated Sands during Cyclic Loading," J. of Soil Mech. and Found. Div., ASCE, Vol. 92, No. SM6, pp. 105-134, November.

Tan, T. S., and R. F. Scott, (1985) "Centrifuge scaling considerations for fluid particle systems," Geotechnique 35, No. 4, pp. 461-470.

Terzaghi, K., 1943, "Theoretical Soil Mechanics," John Wiley & Sons, New York.

Table 2-1: Scaling Factors for the Centrifuge and One-g Modeling.

Quantity to be scaled	One-g Scaling Factor Prototype to Model Ratio	Centrifuge Scaling Factor Prototype to Model Ratio
Displacement	n	n
Time (dynamic)	$n^{0.5}$	n
Velocity	$n^{0.5}$	1
Acceleration	1	n^{-1}
Force	$\rho^* n^3$	n^2
Energy, Moment	$\rho^* n^4$	n^3
Moment of Inertia	n^5	n^4
Frequency	$n^{-0.5}$	n^{-1}
Time (diffusion)	n if $c_v^* = n$ $n^{1.5}$ if $c_v^* = n^{0.5}$	n^2

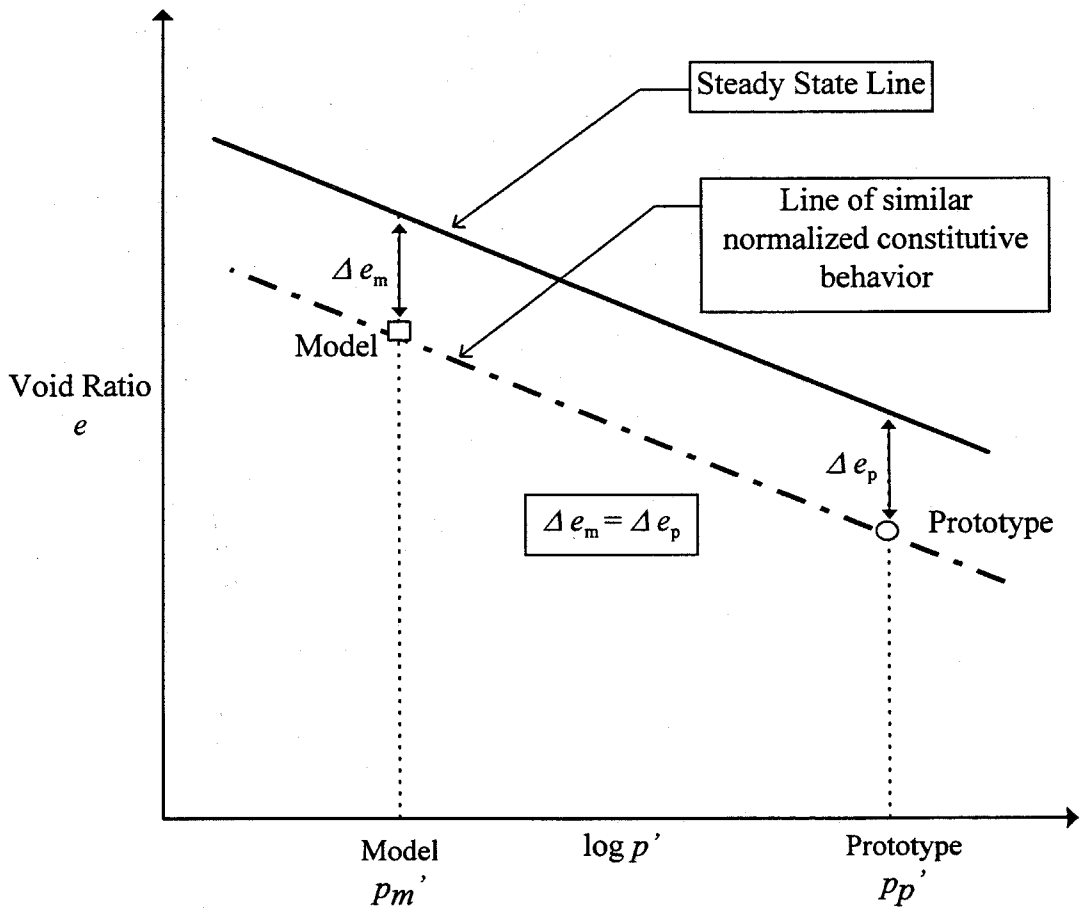

Figure 2-1: Schematic example of the constitutive scaling technique using the Steady State Line.

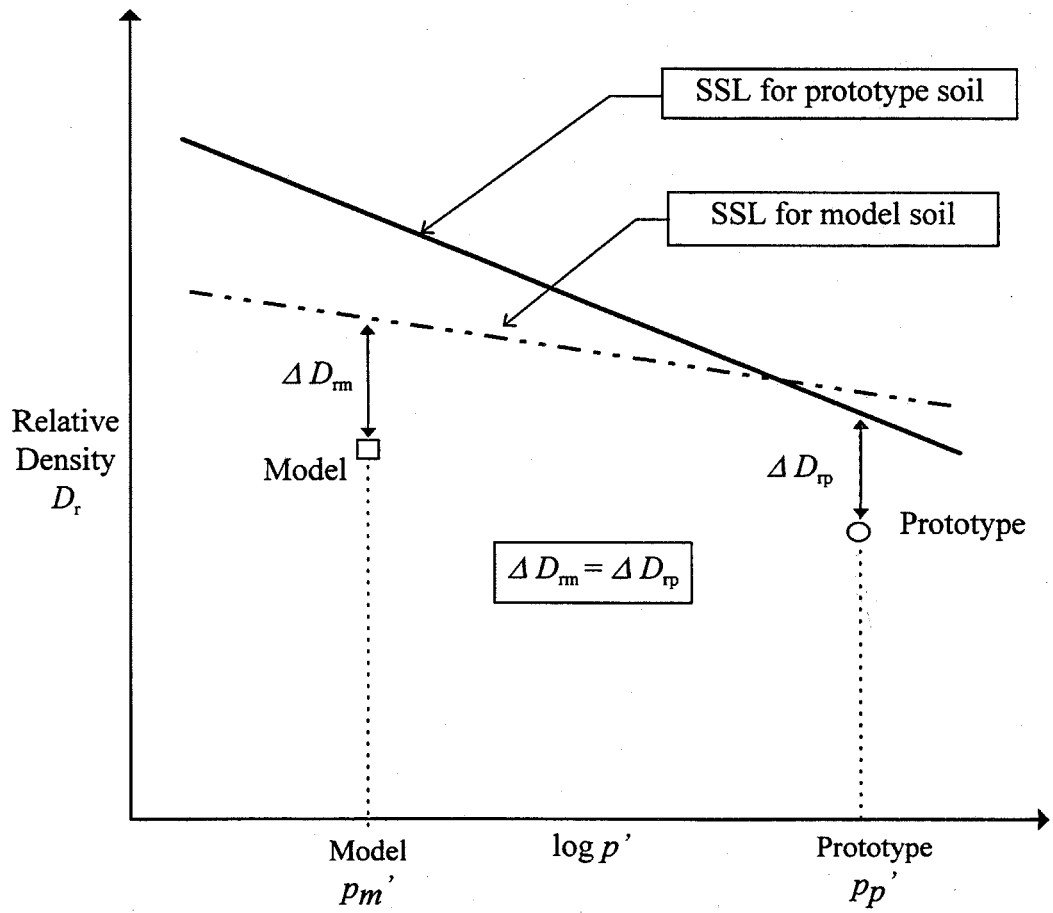

Figure 2-2: Schematic example of the constitutive scaling technique using the Steady State Line (SSL) of the prototype soil and an alternative model soil.

Chapter 3

MODEL TEST MATERIAL CHARACTERIZATION

3.1 Introduction

For the tests described in this thesis two different sands were used: a Nevada fine sand, and a blended beach sand referred to as Blend 6-1.

The Nevada sand was used in the VELACS (Arulanandan and Scott, 1993, 1994) testing program. For that study a single batch of the Nevada sand was prepared and distributed to the test program participants including Caltech. The quantity of material remaining at Caltech after VELACS was approximately 300 kg, which was sufficient to perform the one-g tests described herein. For the VELACS study a comprehensive laboratory testing program was performed to define the properties of the sand (TETC, 1992) and the results of this testing program have been utilized for this study. Specific permeability and confined compression tests were performed in the laboratory at Caltech to supplement this data. In addition, the results of some triaxial tests completed on the Nevada sand at the University of California Davis (Kutter et al., 1994) and by Woodward-Clyde Consultants (Woodward-Clyde, 1989) were used.

The Blend 6-1 sand was a combination of two differently graded sands provided by a local company (Gordon Sand Company)[1] which were both derived from Golden Flint beach sand. About 300 kg of the sands was blended to emulate the gradation of Monterey #0 sand (a beach sand) and Sacramento River sand, both of which have been tested extensively in prior studies [(Seed and Lee, 1967), (Riemer et al., 1990)]. Basic laboratory tests were performed on the Blend 6-1 sand at Caltech, and by Dr. Michael Riemer at UC Berkeley who also performed triaxial tests on the sand.

[1] Address for Gordon Sand Company is 2210 S. Santa Fe Ave., Compton, CA 90221.

The test data for the Nevada and Blend 6-1 sand is presented in the following sections. It should be noted that the sands were re-used in a number of one-g tests which are described in Chapter 5 of this thesis. The low stresses existing in the one-g tests preclude the possibility of any crushing of grains. Throughout the test program the sands were kept in a well mixed condition and procedures were followed to minimize the loss of fines. While it is possible that slight changes to the properties of the sands occurred during the testing program, any modifications are likely to be minor and probably within the error band of the basic laboratory tests originally performed. It should be noted that the sands were air dried in the Caltech laboratory prior to the construction of each new model. This reduced the moisture content, w, (ratio of the weight of water to dry sand) to less than 0.1 % which for the purposes of this research was considered to be "dry".

Finally, some of the laboratory test data contained in this chapter is presented in terms of a magnitude of stress. For the purpose of reference, the vertical effective stress in the one-g models ranged from about 0 to 4 kPa, and in the centrifuge Model 3 ranged from about 0 to 100 kPa.

3.2 Basic Properties

The grainsize distribution for the Nevada sand and the Blend 6-1 are shown on the gradation curves in upper plot of Figure 3-1. The lower plot shown in Figure 3-1 compares the Blend 6-1 sand to the Monterey #0 and Sacramento River sands, which in terms of gradation is quite similar.

The specific gravity, maximum and minimum densities, and maximum and minimum void ratios are presented in Table 3-1. The test methods that were followed are described in the references indicated on Table 1. The specific gravity tests performed at Caltech were performed in general accordance with ASTM D 854-83 (ASTM, 1991) recommended procedures.

3.3 Permeability

The permeability of the test sands was determined using constant head permeability tests, which were performed in general accordance with D2434-68 (ASTM, 1991) recommended procedures. The tests were performed on a number of samples at various void ratios (or densities) reflecting the range expected in the one-g and centrifuge models. The majority of the tests were performed in the Caltech soils laboratory, and the data was supplemented by TETC (1992) tests performed on Nevada sand. There was good agreement between the Caltech and TETC tests.

The permeability data for the Nevada and Blend 6-1 sands are shown in Figure 3-2 as a function of void ratio. Best-fit linear functions with the following equations were found for the range of the void ratio shown.

$$\text{(3-1)} \quad \begin{aligned} &\text{Nevada Sand Permeability (cm / s), } k_N = (0.032894)e - 0.0170283 \\ &\text{Blend 6 - 1 Sand Permeability (cm / s), } k_B = (0.168679)e - 0.0676995 \end{aligned}$$

The Blend 6-1 sand permeability is about eight times greater than the Nevada sand permeability, which can be attributed to the coarser gradation of the Blend 6-1 sand.

3.4 Compressibility

A series of confined compression tests was performed to obtain an index and relative measure of the compressibility of the test sands at a variety of initial void ratios. The tests were performed in the Caltech soils laboratory using a GEOMATIC Consolidometer 8405. Because the materials are sands, the test method was modified from that typically used in more standard confined compression tests as described by ASTM D 2435-90 (ASTM, 1991). Special precautions were taken to isolate the test apparatus from ambient vibrations present in the laboratory. The procedure followed for these tests was as follows:

1) The vertical displacement response of the apparatus under loading and unloading was measured without any sample in place. The measurements were subsequently used to correct the data obtained when soil samples were tested.

2) Samples were pluviated into the sample container in a dry state. An initial seating load was applied to the sample and then water was added until the entire specimen was inundated. The collapse of the sample which occurs as the water is added was measured and the computed initial density of the sample was adjusted accordingly.

3) A load increment was added and the vertical displacement was monitored until the consolidation of the sample was complete and a stable reading was obtained. For the Blend 6-1 sand this typically occurred within a few seconds, and for the Nevada sand within a few minutes. The longer duration required for the Nevada sand is attributed to its finer grainsize distribution.

4) A sequence of loading and unloading was followed to obtain compression, rebound, and re-compression data for each test specimen. A typical worksheet which indicates the

loading sequence followed and the data reduction for one of the tests is presented in Figure 3-3.

5) After each test the wet sand was removed from the test container, oven dried, and weighed to obtain an accurate measure of the initial void ratio.

The tests that were performed and their general parameters are shown in Table 3-2. A set of typical test data of the stabilized readings for the Nevada and Blend 6-1 sand is presented in Figure 3-4. This figure shows the entire loading sequence which is presented in terms of the vertical strain versus the log of the applied vertical effective stress. A summary plot is presented in Figure 3-5 for each test cited in Table 3-2. In Figure 3-5 the data corresponds to the final increment of each loading sequence and the final rebound curve for each of the tests. On Figures 3-4 and 3-5 the initial state of the sand in each test is indicated in the legend in terms of the relative density, D_{ro}.

A couple of general comments regarding the test data can be made. The Blend 6-1 sand was less compressible than the Nevada sand, and over the range of initial relative densities D_{ro} of 10 % to 75 %, the compressibility was essentially the same. In contrast the Nevada sand showed a noticeable variation in compressibility behavior under loading for the range of initial D_{ro} of -15 % to 67 %. The higher compressibility of the Nevada sand is probably due to its finer gradation. It should be noted that the negative value of D_{ro} for the Nevada sand is attributed to the small sample container, which permitted the sand to exist at a lower density than measured for a larger mass of sand. Finally, the rebound behavior for the Nevada and Blend 6-1 sands appeared to be very similar regardless of the initial density.

The above observations are also apparent in the computed values of the one-dimensional coefficient of compressibility, a_v, which is defined as the rate in change of void ratio, e, with respect to the change in vertical effective stress, σ'_v.

$$(3\text{-}2) \qquad a_v = \frac{\partial e}{\partial \sigma'_v}$$

The value of a_v was calculated for each increment in the loading (compression) and unloading (rebound) portions of the tests. These values are plotted on Figure 3-6 for the Nevada and Blend 6-1 sands versus the mean stress for that increment. The compression data was visually fitted

with hyperbolic functions and the rebound data was fitted with a least-squares power function. For the Nevada sand compression data it was possible to fit three curves to represent the variation observed with relative density. For the compression data of the Blend 6-1 sand and the rebound data for both sands, there was little variation with relative density so only one curve was fitted. The equations for the fitted curves are given in Table 3-3 and plotted with respect to the data on Figures 3-7 for the Nevada sand and Figure 3-8 for the Blend 6-1 sand. The range of effective stress shown in Figures 3-7 and 3-8 corresponds to the maximum vertical stress anticipated in the centrifuge model which of course exceeds the range of the one-g model.

The curves for the compression and rebound cycles for the two sands are summarized in Figure 3-9. It should be noted that the curve for the Nevada sand load (compression) cycle corresponds to the range of relative density D_r, 15 to 45 % indicated in Table 3-3.

Lastly, the change in void ratio of the tests at different initial void ratios is of interest because of the significant contrast between stresses of the one-g and centrifuge test methods. Figure 3-10 shows the data from the compression tests described above plotted with void ratio (instead of relative density) versus the vertical effective stress. It is evident from the plot of the Nevada sand data that the compressibility of the sand increases with higher initial void ratio and lower vertical effective stresses. For the Blend 6-1 sand the different initial void ratios had little effect and only the lower vertical effective stresses had a significant influence on the compressibility behavior.

The above data and interpretations will be used as part of the analysis described in Chapter 6.

3.5 Shear Moduli

As part of the TETC (1992) test program a series of resonant column tests was performed on the Nevada sand. In these tests the shear modulus of the saturated sample was measured for very small levels of shear strain. A shear modulus, generally referred to as G_{max}, is the value measured at shear strains less than 0.0001%. The values of G_{max} for the Nevada sand have been plotted on Figure 3-11a versus the mean confining stress for each test. As shown in Figure 3-11a, curves have been fitted to the data with G_{max} versus the square root of the mean confining stress (the constants of the equation are indicated in the legend). This functional relationship is often used in soil mechanics to relate the shear modulus to the stress condition.

As defined above, G_{max} can be considered the initial shear modulus for the sand prior to the development of any significant shear strains. As the shear strains increase, the same sand will soften and the shear modulus values will degrade. A vast amount of experimental work has been completed to investigate this behavior (Seed et al., 1984). Figure 3-11b shows the variation of the normalized shear moduli with shear strain for sands in general, which clearly shows this behavior. The three lines represent different levels of confining stresses and indicate that the rate of degradation in the shear modulus is greater for lower confining stresses.

The implications of these results to the one-g and centrifuge models are two-fold. Firstly, due to the far lower stresses in the one-g model, G_{max} will be about one-tenth of that in the centrifuge model. Secondly, the lower stresses in the one-g model implies that the rate of degradation will be higher than in the centrifuge model. The implications of these trends in the shear moduli will be discussed further in Chapter 5.

Due to budget constraints resonant column tests were not performed on the Blend 6-1 sand, and therefore measurements of the low strain shear modulus, G_{max} , are not available for this material. However, based on the research (Seed et al., 1984) it appears that the void ratio, strain amplitude, and confining stresses mainly determine G_{max} , and that grain size, shape, and distribution, have little effect. Therefore, it is assumed that the shear moduli of the Blend 6-1 sand can be approximated by the curves indicated in Figure 3-11a. The behavior of the Blend 6-1 is certainly expected to follow the trends indicated in Figure 3-11b, which is based on data from a wide range of sands.

3.6 Steady State Line

The concept of the steady state line was discussed in Chapter 2, Section 2.5. For the VELACS study (Arulanandan and Scott, 1993, 1994) an extensive set of triaxial tests were performed on the Nevada sand. Estimates of a steady state line for the sand were made by two participants in VELACS [(Ishihara, 1994) and (Been et al., 1993)]. Both investigators described the difficulty in estimating a steady state condition for the Nevada sand principally because the testing performed by TETC (1992) was not oriented toward obtaining a steady state condition. A wide degree of scatter in the data was evident. Ishihara actually performed quite a few additional tests and defined a line which he refers to as the Quasi Steady State Line (QSSL).

For the research reported herein, only the results of the triaxial tests were used. The TETC (1992) test data completed for VELACS was reviewed and supplemented with additional triaxial data from two other studies [(Kutter et al., 1994) and (Woodward-Clyde, 1989)]. The testing performed by Kutter was completed on the Nevada sand distributed for the VELACS study, and therefore the results should be fully compatible with the TETC (1992) data. The Woodward-Clyde tests were performed on Nevada sand prior to the VELACS study. The sand used in those tests came from the same source as the VELACS sand and has an almost identical gradation curve, and for the purposes of this evaluation has been considered the same material.

Tests, from the various sources cited above, which were used in this study are summarized in Table 3-4. The steady state condition given for each test was estimated at the point of the so-called phase change in the stress-strain path. Unfortunately, none of the tests was performed at very low confining stresses. The steady state behavior of the sand at low confining stresses is of interest for this research because of the relatively low stresses that exist in the one-g model. The steady state behavior of a sand at low stresses has been the subject of some conjecture (Riemer et al., 1990). In their paper, Riemer et al. concluded that the steady state line approaches a limiting maximum void ratio (or minimum density) at low confining stresses and that the steady state shear strength approaches zero at this condition. Based on their research the limiting density appears to occur at a relative density of $D_r \approx 0\%$ to 10%. For this study, a low confining stress was selected to be 1 kPa (which is of the order of the mean stress in the one-g models), and the steady state of the sand at this stress was assumed to be $D_r \approx 0\%$. This implies the sand would be at the maximum void ratio as defined in Section 1.2. While the selection of these arbitrary values could be debated, it turns out the steady state line is quite flat. Therefore, the possible variations in the SSL created by modifying the assumptions above will have little real effect for the purposes of this research effort.

The data listed in Table 3-4 are shown on Figure 3-12. The maximum void ratio for the Nevada sand is plotted at a mean effective stress of 1 kPa. In the upper plot of Figure 3-12 a line is shown based on a least-squares best-fit to all the data, and is denoted as SSL Fit 1. On the lower plot of Figure 3-12 two data points at void ratios of about 0.7 have been removed, and a linear least-squares best-fit (denoted as SSL Fit 2) is shown using the remaining data. A linear fit was selected because the scatter of the data does not permit a rational selection of a curved fit.

The SSL Fit 1 and Fit 2 are shown in Figure 3-13. The SSL's selected by Been et al. (1993) and Ishihara (1994) which have been extrapolated to the lower values of mean effective stress are also shown. Figure 3-13 indicates reasonable agreement between Ishihara's QSSL and the two alternate SSL's, Fit 1 and Fit 2. Considering these were derived using differing data sets, the variation is reasonable. With reference to the SSL of Been et al. it appears to be significantly different especially at low confining pressures. Of all the SSL's, Been et al. has the steepest slope and Fit 2 has the flattest slope. This possible range in the interpreted data is incorporated into the interpretation of the one-g tests discussed in Chapter 6.

For the Blend 6-1 sand, only three triaxial tests were performed to estimate the steady state behavior, which is inadequate to estimate an SSL with confidence. However, extensive testing has been conducted on the Monterey #0 sand and the Sacramento River sand which have similar origins and gradation curves to the Blend 6-1 sand. The SSL's for these two other sands has been reported (Riemer et al., 1990) to be very similar. The three triaxial tests on the Blend 6-1 sand were performed by Dr. Riemer at UC Berkeley following the same test procedures used in prior testing of the Monterey #0 sand (Riemer, 1992). The basic conditions for the Blend 6-1 sand tests are presented in Table 3-5, and the data for each triaxial test are plotted in Figure 3-14. The postulated steady state condition estimated from the triaxial data is indicated on Table 3-5. The data is shown in the upper plot of Figure 3-15 along with steady state data for the Monterey #0 sand (Riemer, 1992). The curves which have been fitted to represent the SSL of the Blend 6-1 sand and the Monterey sand are quite similar in shape which should be expected given the similarity of the sands and test procedures followed. The apparent higher strength of the Blend 6-1 sand (implied by the higher mean effective stress at a given void ratio) is primarily attributed to the more angular nature of the Blend 6-1 sand grains (communication from Dr. M. Riemer). Based on the comparison of the three triaxial tests performed on the Blend 6-1 sand with the large amount of data for the Monterey #0 sand, the Blend 6-1 SSL shown in Figure 3-15 appears to be reasonable.

The SSL for the Blend 6-1 sand is compared with the Nevada sand SSL's of Been et al. and Fit 2 in the lower plot of Figure 3-15. These latter two curves are representative of the range of the steady state condition for the Nevada sand. The relative position of the SSL for the Blend 6-1 sand and Nevada sand is important for some of the one-g tests performed in this study. These will be discussed in Chapter 5.

Further work is required to better define the SSL and resolve some of the discrepancies noted in the various literature on the subject. However, it is emphasized that for the constitutive scaling concepts described in Chapter 2, only the slope of SSL is required if the same sand is used model and prototype. From the literature it appears that the slope is least affected by the discrepancies in test methods and procedures. If an alternative model sand is used in the model test, then its SSL should be determined using the same test methodology as used to determine the SSL of the prototype sand.

3.7 References

Arulanandan, K. and R. F. Scott, eds., 1993, 1994, "Verification of Numerical Procedures for the Analysis of Soil Liquefaction Problems," Vol. 1, 1993; Vol. 2, 1994, Balkema, Rotterdam.

ASTM (American Society of Testing and Materials), 1991, "1991 Annual Book of ASTM Standards, Section 4.0, Construction," Vol. 04.08, Soil and Rock; Dimension Stone; Geosynthetics, ASTM, Philadelphia, PA.

Been, K., M. G. Jefferies, J. E. Hachey, and L. Rothenburg, 1993, "Numerical prediction for Model No. 2," in Verification of Numerical Procedures for the Analysis of Soil Liquefaction Problems, Vol. 1, pp. 331-341, Arulanandan, K. and R. F. Scott, eds., Balkema, Rotterdam.

Ishihara, K., 1994, "Review of the predictions for model 1 in the VELACS," in Verification of Numerical Procedures for the Analysis of Soil Liquefaction Problems, Vol. 2, pp. 1353-1368, Arulanandan, K. and R. F. Scott, eds., Balkema, Rotterdam.

Iwasaki, T., F. Tatsuoka, and Y. Takagi, 1976, "Dynamic Shear Deformations Properties of Sand for Wide Strain Range," Report of Civil Engineering Institute, No. 1085, Ministry of Construction, Tokyo, Japan.

Kutter, B. L., Y. Chen, and C. K. Shen, 1994, "Triaxial and Torsional Shear Test Results for Sand," prepared for Office of Naval Research, Arlington, VA, Report No. CR 94.003, June.

Riemer, M. F., 1992, "The effects of testing conditions on the constitutive behavior of loose, saturated sands under monotonic loading," Ph.D. Thesis at U. C. Berkeley.

Riemer, M. F., R. B. Seed, P. G. Nicholson, H. Jong, 1990, "Steady State Testing of Loose Sands: Limiting Minimum Density," J. of Geotech. Eng., ASCE, Vol. 116, No. 2, pp. 332-337, February.

Seed, H. B., and K. L. Lee, 1967, "Undrained Strength Characteristics of Cohesionless Soils," J. of Soil Mech. and Found. Div., ASCE, Vol. 93, No. SM6, pp. 333-360, November.

Seed, H. B., R. T. Wong, I. M. Idriss, and K. Tokimatsu, 1984, "Moduli and Damping Factors for Dynamic Analyses of Cohesionless Soils," UC Berkeley, EERC Report No. 84/14, September.

TETC (The Earth Technology Corporation), 1992, "VELACS, Verification of Liquefaction Analyses by Centrifuge Studies Laboratory Testing Program Soil Data Report," Project No. 90-0562, prepared for National Science Foundation, Washington, D.C., March.

Woodward-Clyde Consultants, 1989, "Preliminary Results of Shaking Table Tests, Geotechnical Studies Costa Oriental Dikes, Venezuela," prepared for Maraven, S. A., Project No. 8741693F/3000, August.

Table 3-1: Basic properties of the test sands.

Soil Property	Nevada Sand	Blend 6-1 Sand
Specific Gravity	2.67 (1)	2.66 (2)
Maximum Dry Density kN/m^3 (pcf)	 17.33 (1) (110.28)	 16.63 (3) (105.83)
Minimum Dry Density kN/m (pcf)	 13.87 (1) (88.26)	 13.90 (3) (88.46)
Minimum Void Ratio	0.511 (1)	0.569 (3)
Maximum Void Ratio	0.888 (1)	0.877 (3)

Source of data:
1) The Earth Technology Corporation (TETC, 1992).
2) Caltech Soils Laboratory.
3) Dr. M. Riemer, UC Berkeley (Riemer, 1992).

Table 3-2: Test conditions for the confined compression tests.

Test No. and Sand Type.	Initial Void Ratio	Initial Relative Density (%)	Final Void Ratio	Final Relative Density (%)
1DCBL1 Blend 6-1	0.8395	9.9	0.8167	17.4
1DCBL2 Blend 6-1	0.6384	75.4	0.6202	81.4
1DCNS2 Nevada	0.6371	66.6	0.6112	73.4
1DCNS4 Nevada	0.7591	34.2	0.7170	45.4
1DCNS5 Nevada	0.8390	13.0	0.7883	26.5
1DCNS1 Nevada	0.9454	-15.2(1)	0.8688	5.1

(1) The negative relative density is most likely an artifact of the small sample size used in the confined compression tests. The minimum relative density is usually set at 0 % and is based on the minimum density obtained in a larger sample of sand following a standard test procedure.

Table 3-3: Equations for fitted compressibility data.

Sand Type and Range in Relative Density.	a_v Fitted Equation for Compression or Loading Sequence	a_v Fitted Equation for Re-compression or Unloading Sequence
Blend 6-1 Sand, $10\% < D_r < 80\%$	$a_{vc} = 7.2\times10^{-5} - \left[\frac{-(0.093)^2 + (7.22\times10^{-5})\sigma'_v + 3.6\times10^{-4}}{2(\sigma'_v + 5)}\right]$	$a_{vr} = (1.3948\times10^{-4})\sigma_v^{'(-0.40745)}$
Nevada Sand $65\% < D_r < 75\%$	$a_{vc} = 1.6\times10^{-5} - \left[\frac{-(0.11)^2 + (1.6\times10^{-5})\sigma'_v + 4.8\times10^{-5}}{2(\sigma'_v + 3)}\right]$	$a_{vr} = (3.6625\times10^{-4})\sigma_v^{'(-0.65998)}$
Nevada Sand $15\% < D_r < 45\%$	$a_{vc} = 3.6\times10^{-5} - \left[\frac{-(0.148)^2 + (3.6\times10^{-5})\sigma'_v + 1.8\times10^{-4}}{2(\sigma'_v + 5)}\right]$	
Nevada Sand $-15\% < D_r < 5\%$	$a_{vc} = -0.6\times10^{-5} - \left[\frac{-(0.2)^2 - (0.6\times10^{-5})\sigma'_v - 0.3\times10^{-4}}{2(\sigma'_v + 5)}\right]$	

Table 3-4: Triaxial test data used to estimate the SSL for the Nevada sand.

Source of Data	Test Designation	Test Method(1)	Values at Steady State Condition (based on phase change approach)	
			Void Ratio	Mean Effective Stress (kPa)
TETC (1992)	06-01	CIUC	0.8054	725
	13-01	CIUC	0.8092	160
	24-01	CIUC	0.7629	475
	38-01	CIUC	0.6994	750
Kutter et al. (1994)	10N400U	CIUC	0.8193	150
	40N250U	CIUC	0.7103	200
Woodward-Clyde (1989)	Specimen 1	CIDC	0.8215	70
	Specimen 2	CIUC	0.8111	408
	Specimen 3	CIDC	0.8148	311

(1) CIUC denotes isotropically consolidated undrained compression test.
CIDC denotes isotropically consolidated drained compression test.

Table 3-5: Triaxial test data used to estimate SSL for the Blend 6-1 sand(1).

Test Designation	Initial Consolidation Pressure (kPa)	Values at Steady State Condition (based on phase change approach)	
		Void Ratio	Mean Effective Stress (kPa)
Test 1	700	0.807	599
Test 2	300	0.849	221
Test 3	120	0.862	68

(1) Tests were performed by Dr. M. Riemer at UC Berkeley following the general procedures described by Riemer (1992). All were triaxial CIUC (isotropically consolidated undrained compression) tests.

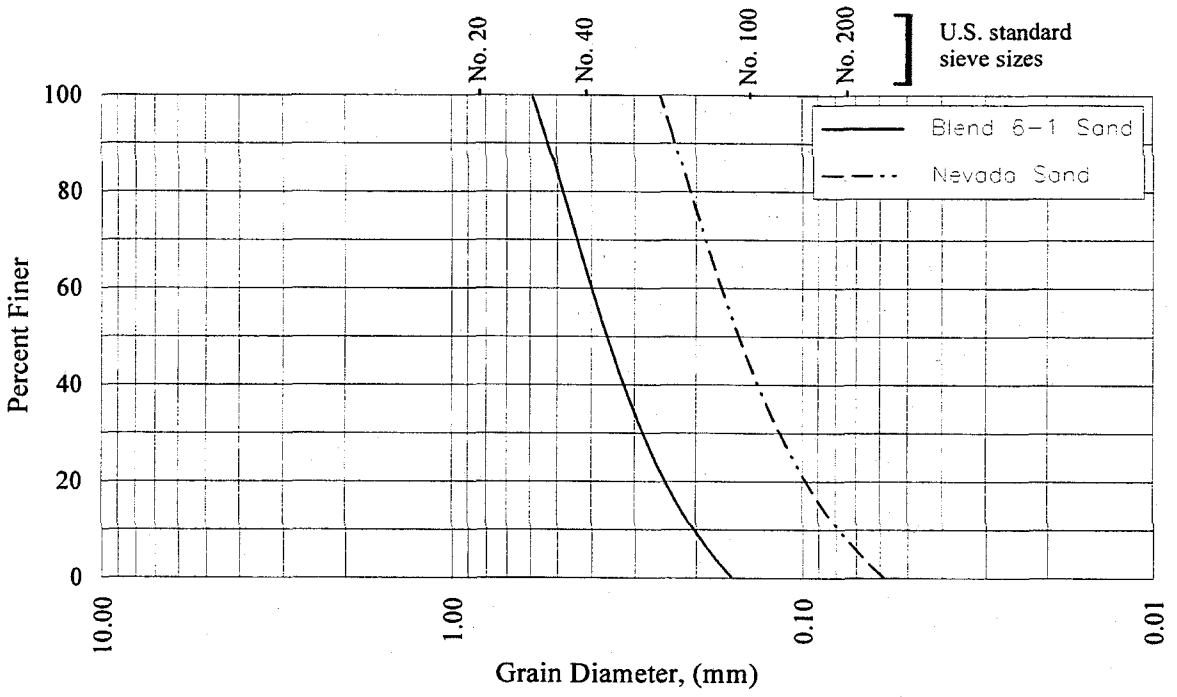

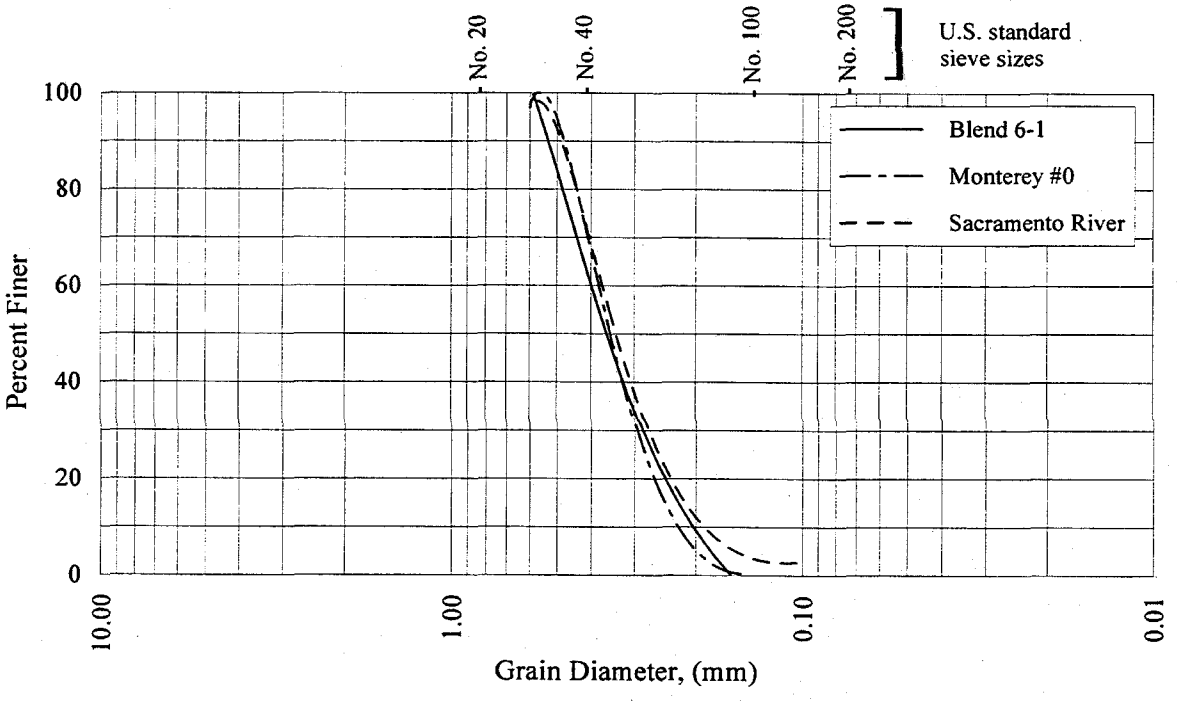

Figure 3-1: Gradation curves for the Nevada and Blend 6-1 Sands, with a comparison of the Blend 6-1 sand with the Sacramento River and Monterey #0 sands.

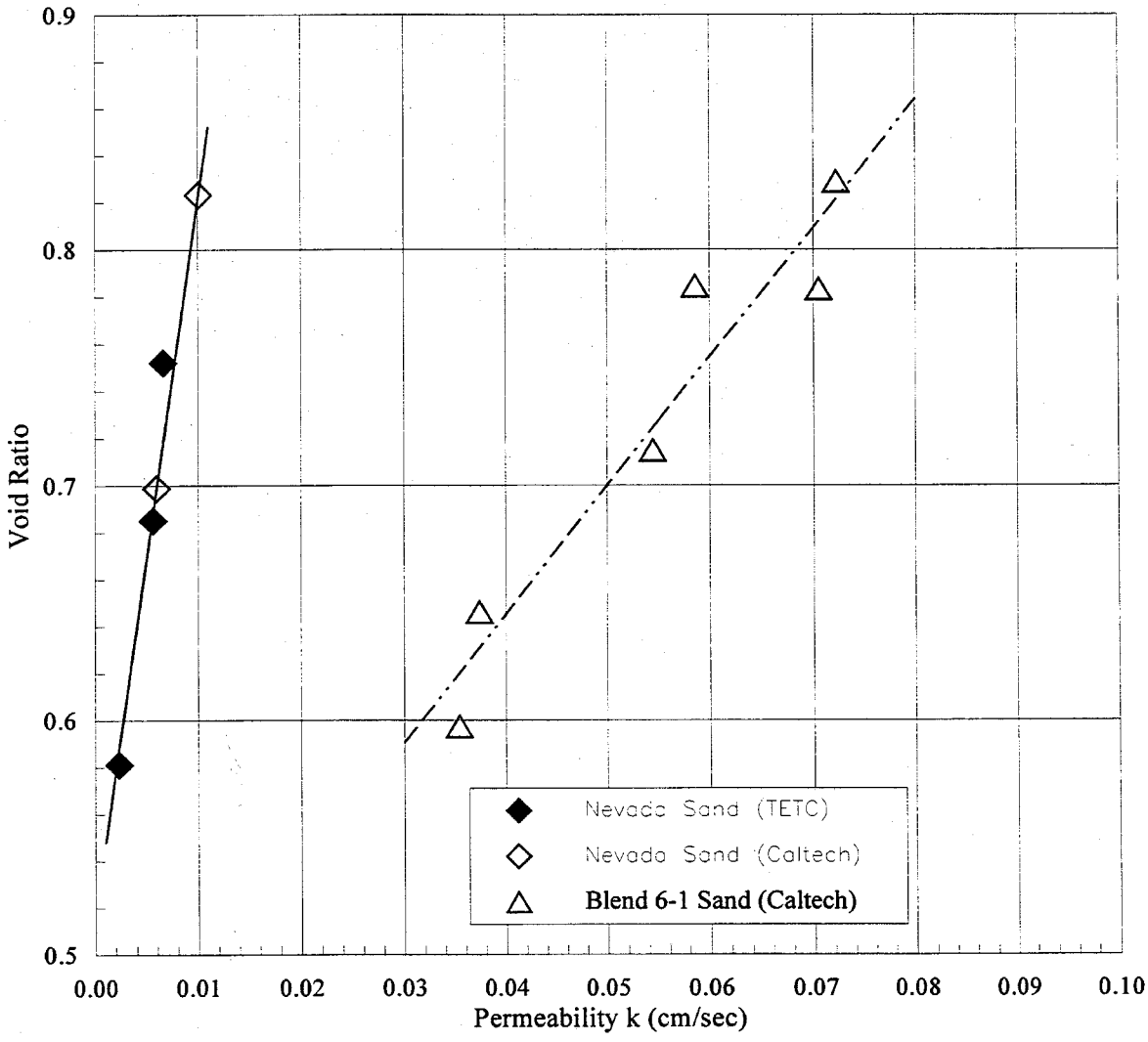

Figure 3-2: Permeability data for Nevada and Blend 6-1 Sands as function of the void ratio.

Spreadsheet to calculate the results of 1-d confined compression test: ADG 1/28/96

Test No: 1DCNS4
Sample Description: Nevada Sand (loose))
Date Tested: 1/28/96

Load (psf)	Load (kN/m2)	Dial Gage Readings (1/10,000 inches) Initial Value	Error Values	Corrected Values	Axial Strain (%)
0	0.00	843.2	0.00	0.00	0.000
10	0.48	839.0	0.27	3.93	0.039
100	4.79	800.0	2.37	40.83	0.406
200	9.58	781.8	4.90	56.50	0.562
400	19.16	750.5	8.73	83.97	0.835
800	38.31	709.2	14.47	119.53	1.189
400	19.16	714.1	16.93	112.17	1.116
200	9.58	719.3	12.73	111.17	1.106
100	4.79	723.7	8.43	111.07	1.105
10	0.48	731.2	3.37	108.63	1.081
100	4.79	727.5	2.37	113.33	1.128
200	9.58	722.5	4.90	115.80	1.152
400	19.16	716.3	8.73	118.17	1.176
800	38.31	701.3	14.47	127.43	1.268
1600	76.63	658.8	21.67	162.73	1.619
800	38.31	666.2	22.07	154.93	1.542
400	19.16	673.1	16.93	153.17	1.524
200	9.58	679.0	12.73	151.47	1.507
100	4.79	683.9	8.43	150.87	1.501
10	0.48	692.2	3.37	147.63	1.469
100	4.79	688.1	2.37	152.73	1.520
200	9.58	685.4	4.90	152.90	1.521
400	19.16	678.8	8.73	155.67	1.549
800	38.31	669.0	14.47	159.73	1.589
1600	76.63	649.5	21.67	172.03	1.712
3200	153.25	599.7	30.57	212.93	2.119
1600	76.63	610.8	27.83	204.57	2.035
800	38.31	619.7	22.07	201.43	2.004
400	19.16	627.3	16.93	198.97	1.980
200	9.58	634.1	12.73	196.37	1.954
100	4.79	639.6	8.43	195.17	1.942
10	0.48	650.0	3.37	189.83	1.889
100	4.79	646.1	2.37	194.73	1.938
200	9.58	642.2	4.90	196.10	1.951
400	19.16	636.7	8.73	197.77	1.968
800	38.31	627.3	14.47	201.43	2.004
1600	76.63	613.5	21.67	208.03	2.070
3200	153.25	588.5	30.57	224.13	2.230
6400	306.51	528.8	46.47	267.93	2.666
3200	153.25	541.9	33.83	267.47	2.661
1600	76.63	553.2	27.83	262.17	2.609
800	38.31	564.8	22.07	256.33	2.551
400	19.16	573.2	16.93	253.07	2.518
200	9.58	582.0	12.73	248.47	2.472
100	4.79	586.8	8.43	247.97	2.467
10	0.48	597.8	3.37	242.03	2.408
0	0.00	600.2	2.50	240.50	2.393

Sample Dimensions:

Dry wt. of soil + tare =	214gm
Wt. of tare =	100gm
Weight of sample =	0.251lbs
Diameter of Cylinder =	2.416in
Area of Cylinder =	4.584sqin
Ht. of sample in Cyl. =	1.005in
Dial gage before H20 =	891.2
Dial gage after H20 =	843.2
Volume of sample =	0.00265cuft
Specific Gravity =	2.67
Minimum Void Ratio =	0.511
Maximum Void Ratio=	0.888
Initial	
Density of sample =	94.71pcf
Void Ratio of sample =	0.7591
Dr (%) of Sample =	34.2%
Final	
Density of sample =	97.04pcf
Void Ratio of sample =	0.7170
Dr (%) of Sample =	45.4%

Figure 3-3: Typical worksheet for a confined compression test.

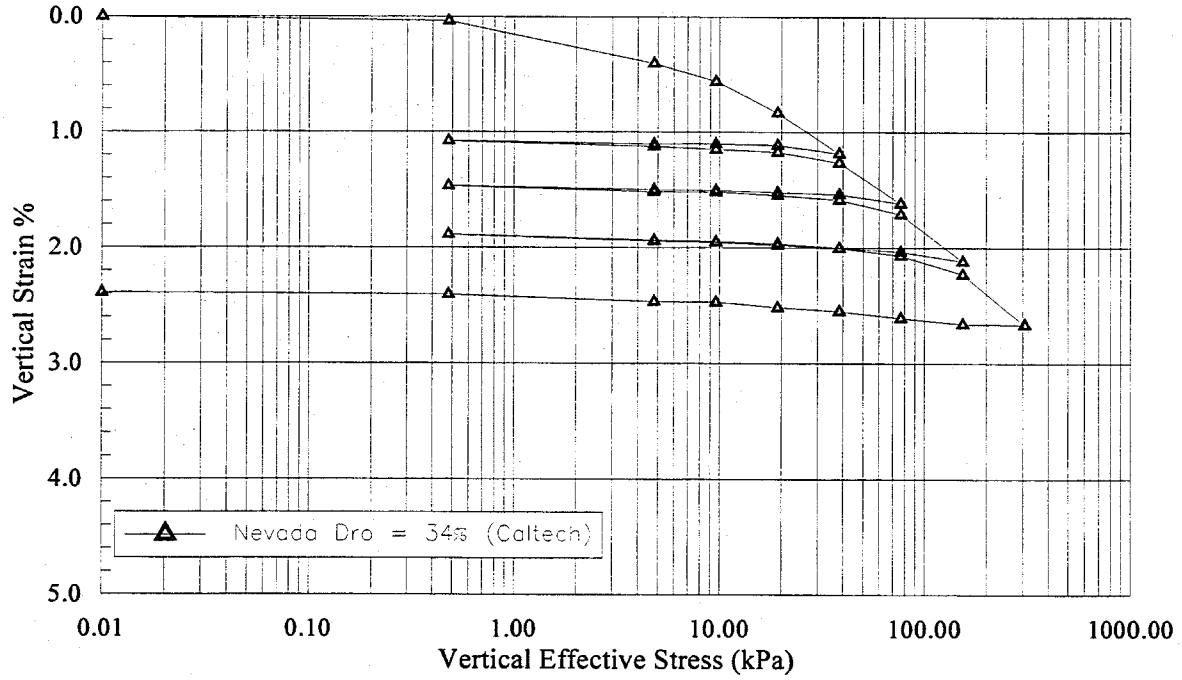

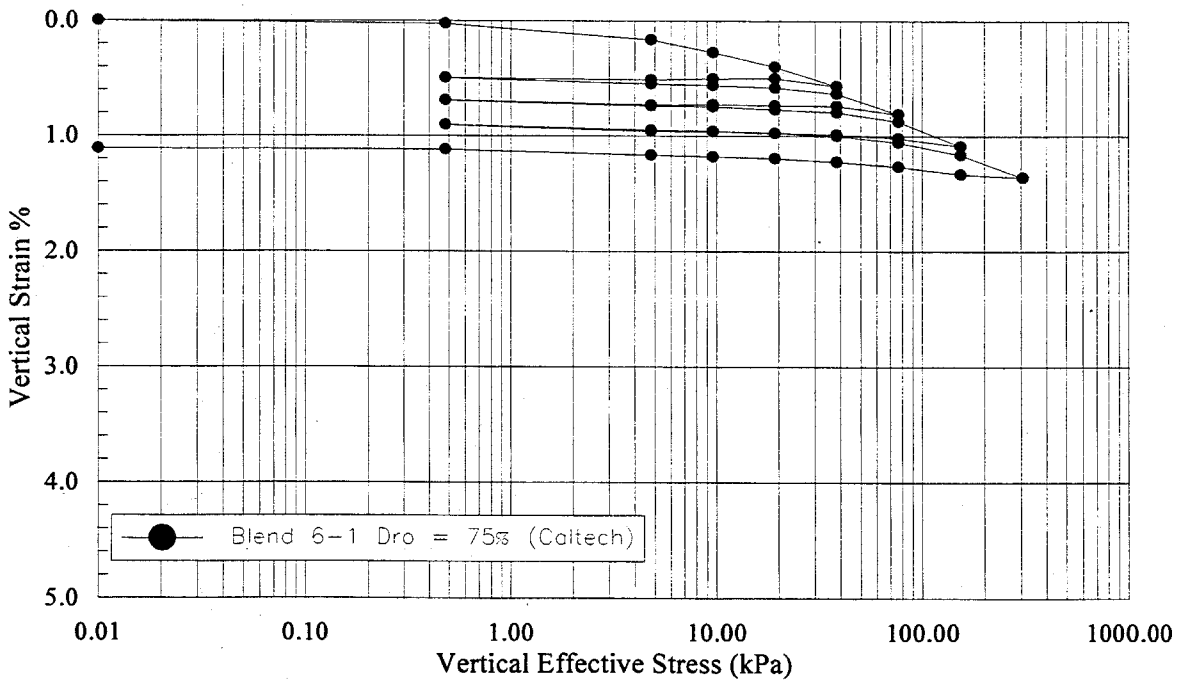

Figure 3-4: Typical confined compression test data for Nevada and Blend 6-1 sands.

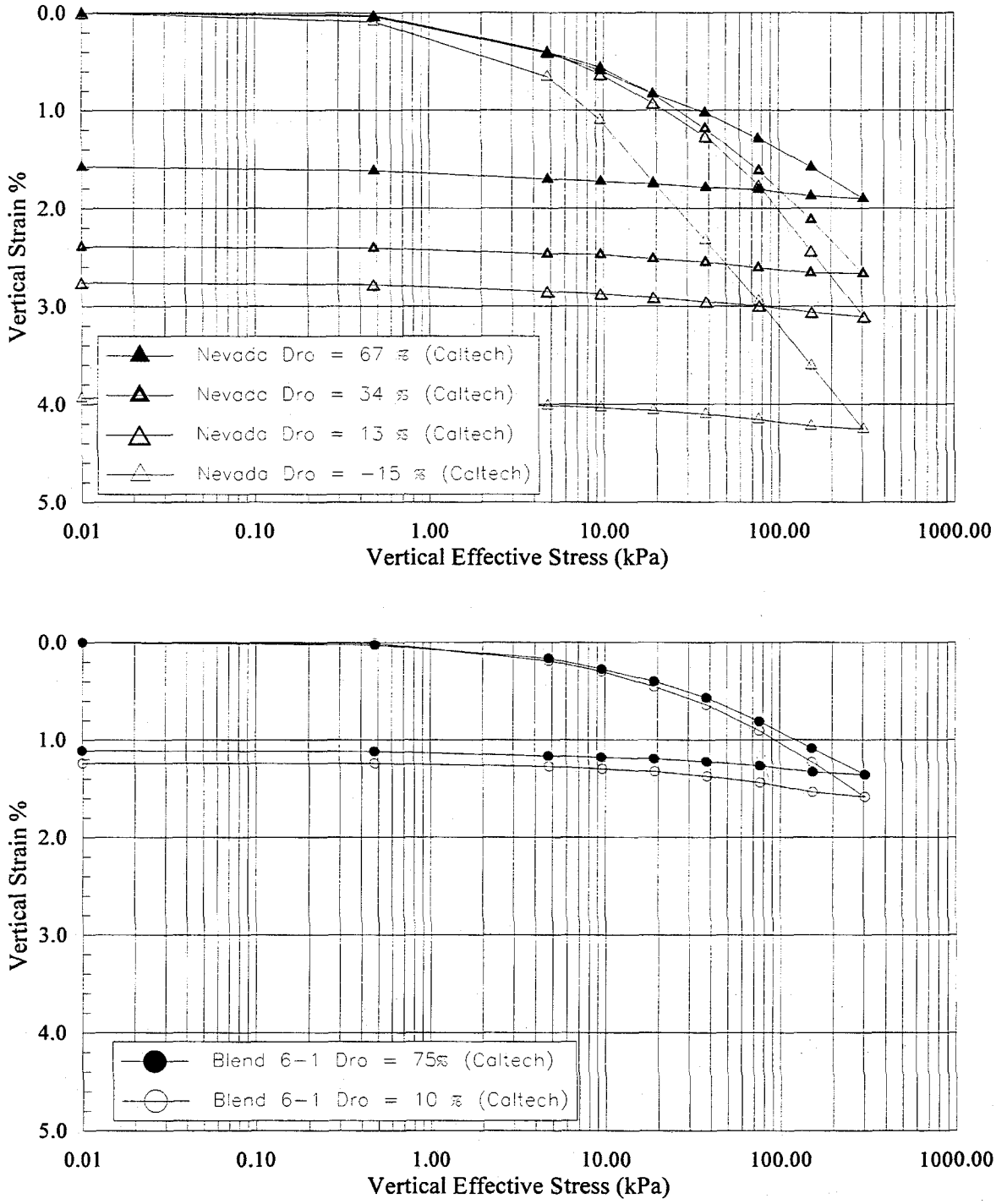

Figure 3-5: Test data from the confined compression tests for the final increment of each load sequence and the final rebound curve.

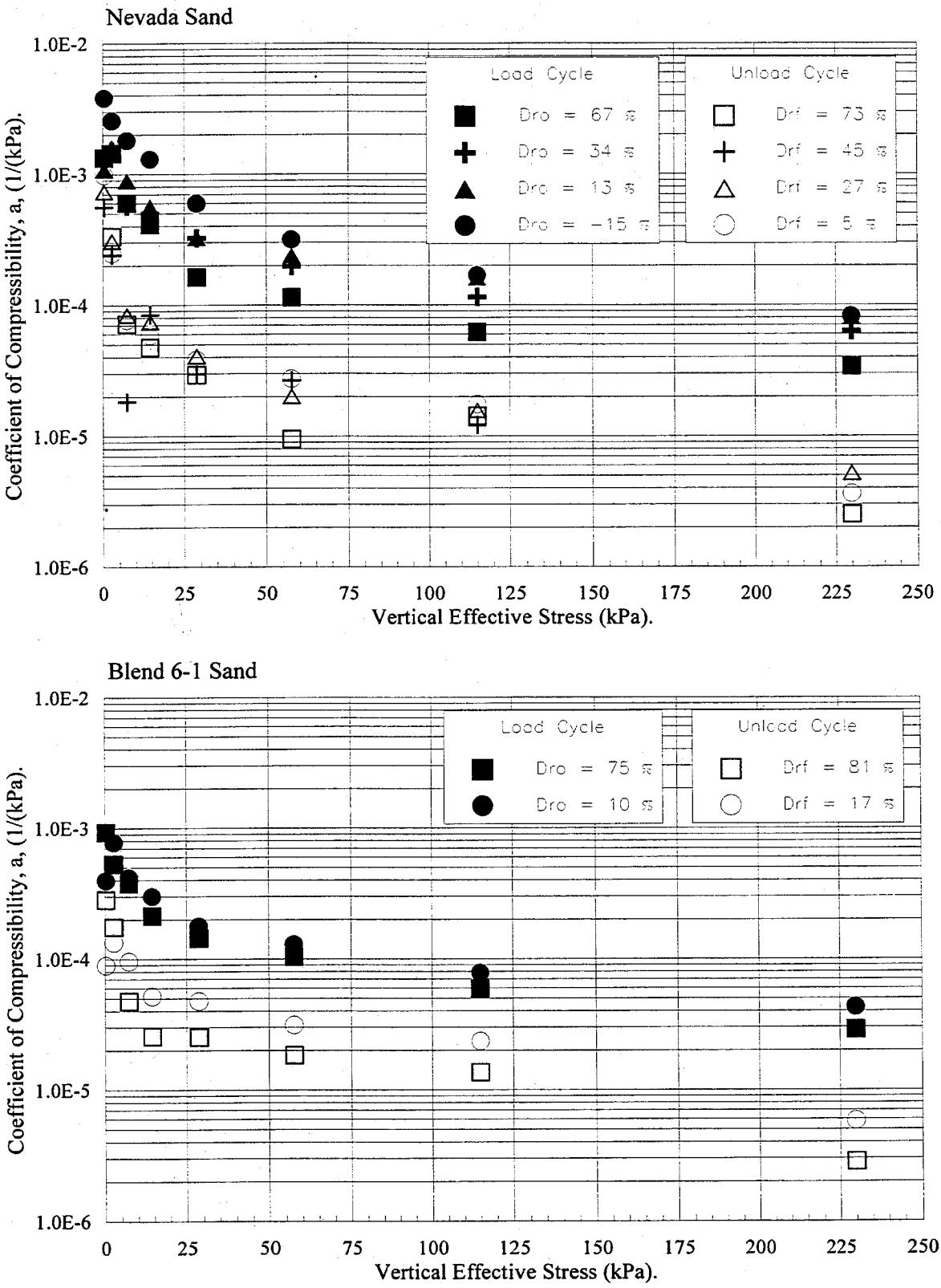

Figure 3-6: Compressibility coefficient, a_v , plotted with respect to the vertical effective stress.

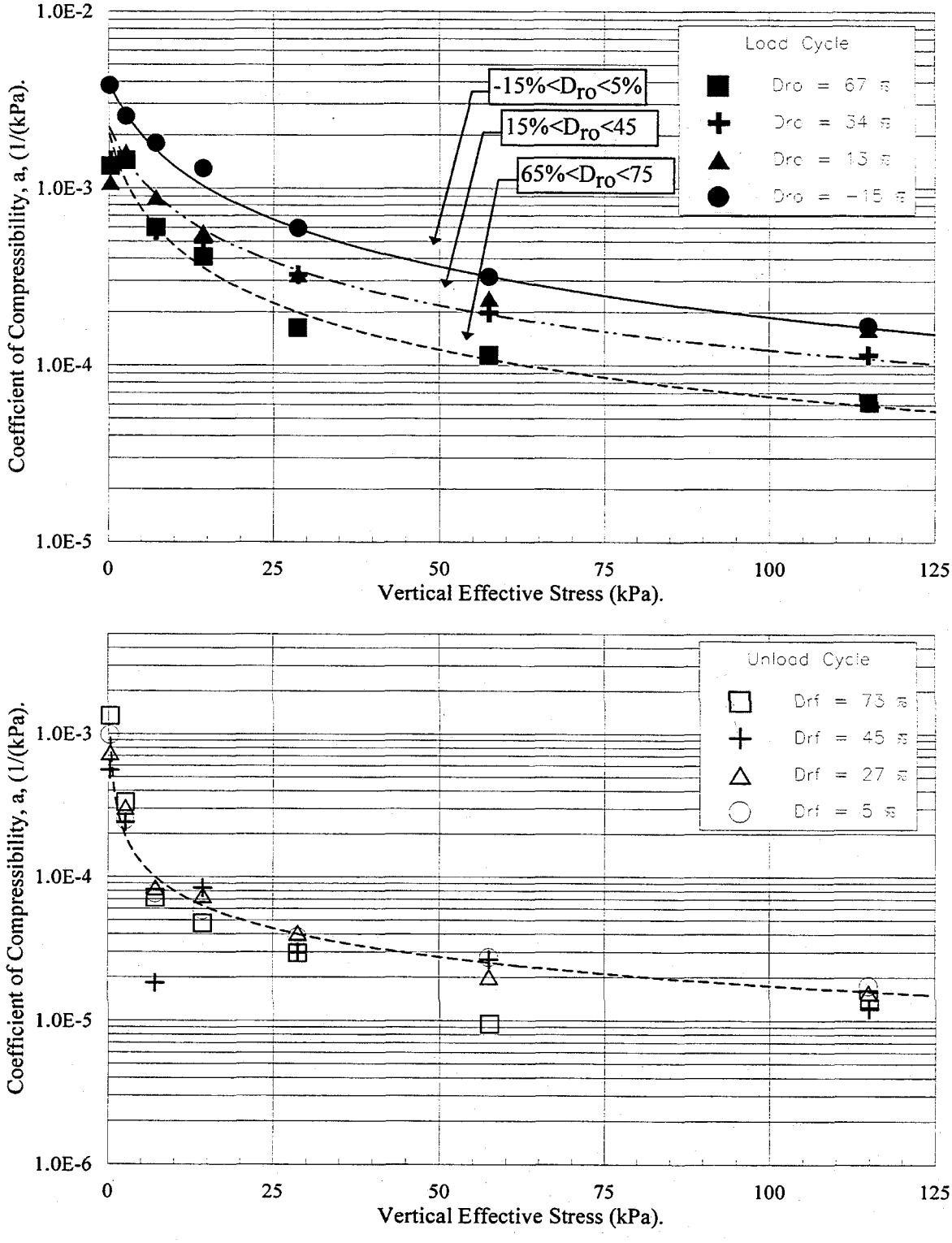

Figure 3-7: Functions fitted to the compressibility coefficient, a_v , in the Nevada sand.

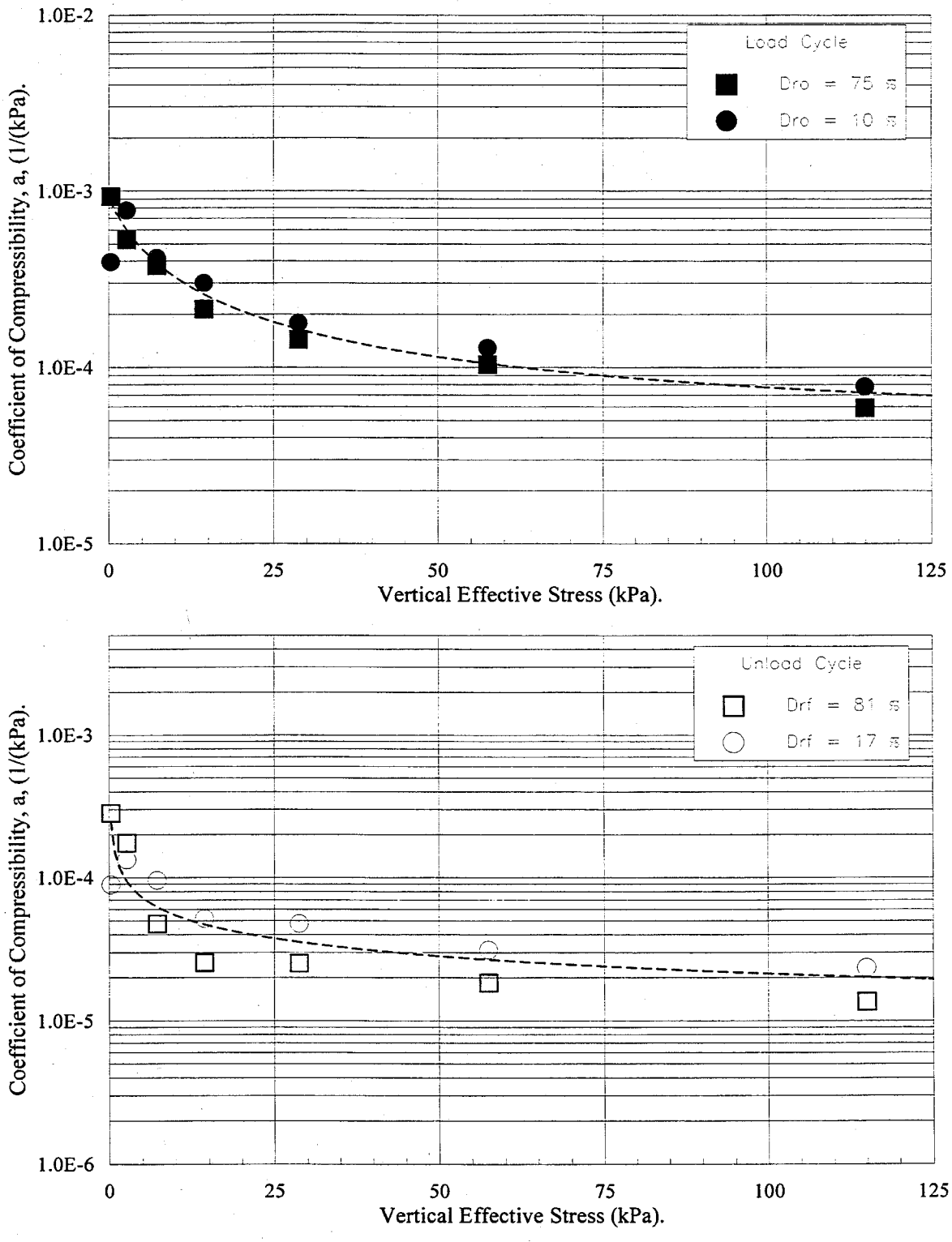

Figure 3-8: Functions fitted to the compressibility coefficient, a_v , in the Blend 6-1 sand.

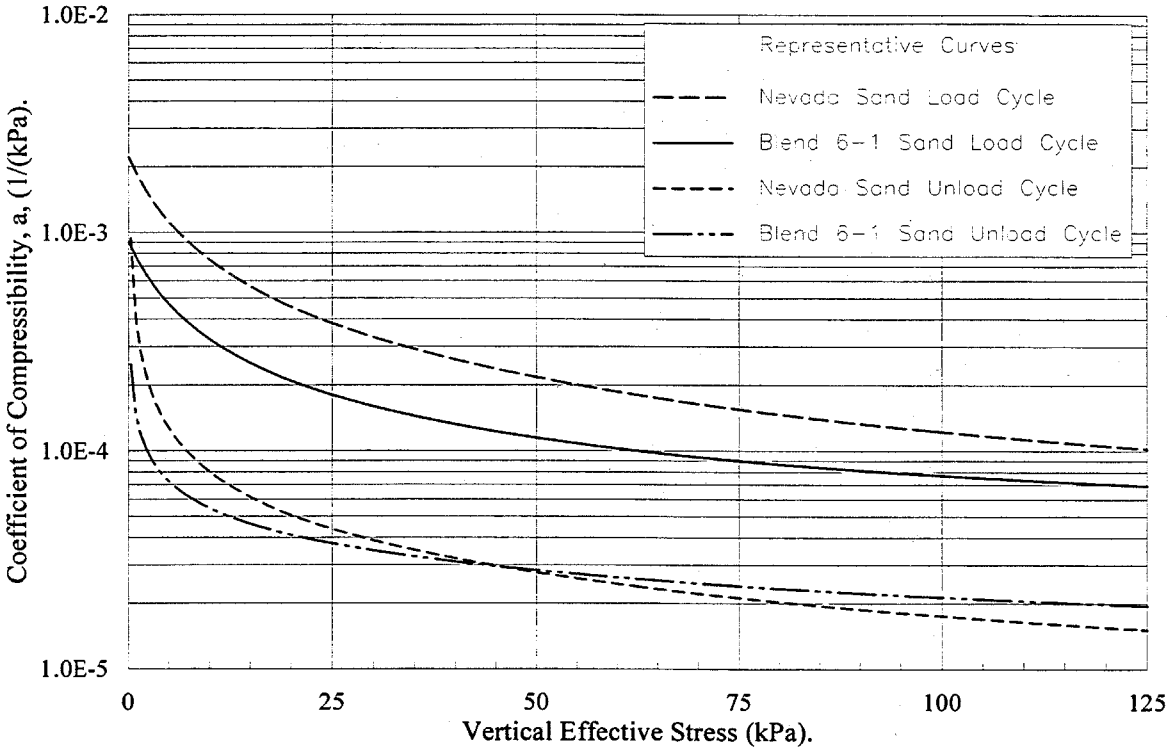

Figure 3-9: Summary of functions fitted to the compressibility coefficient, a_v , in the Nevada and Blend 6-1 sands.

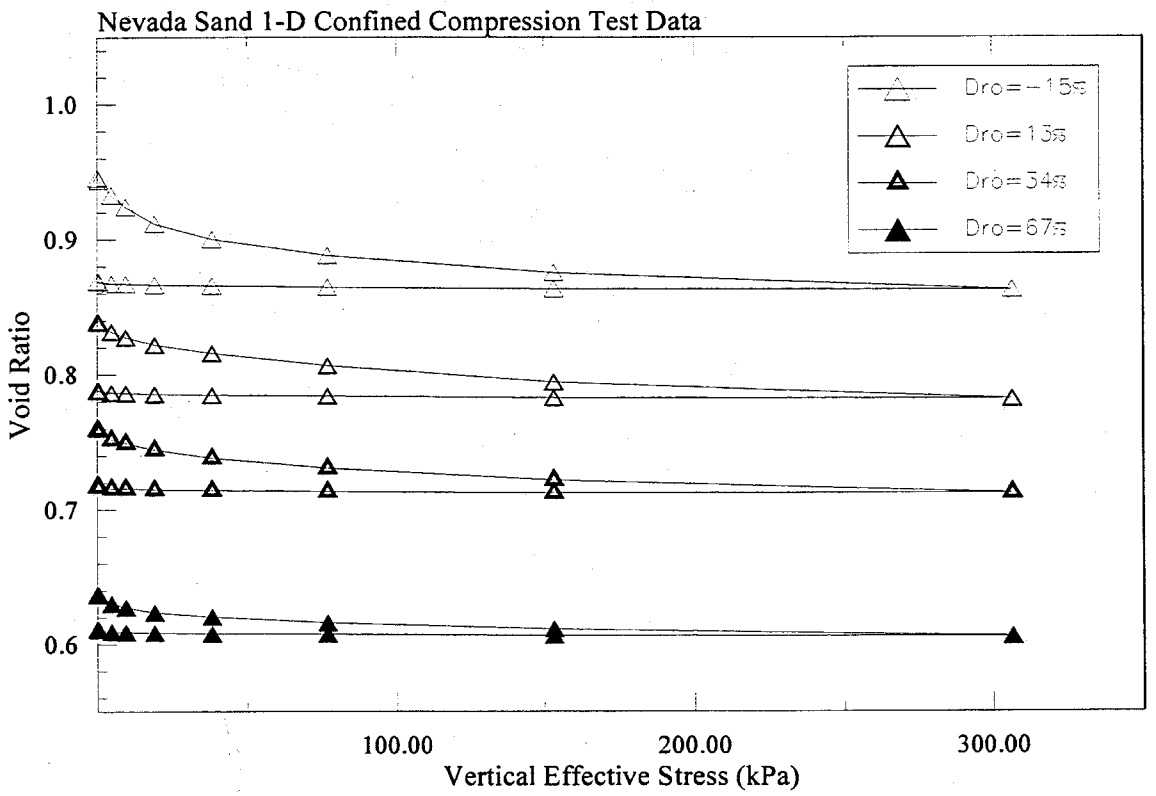

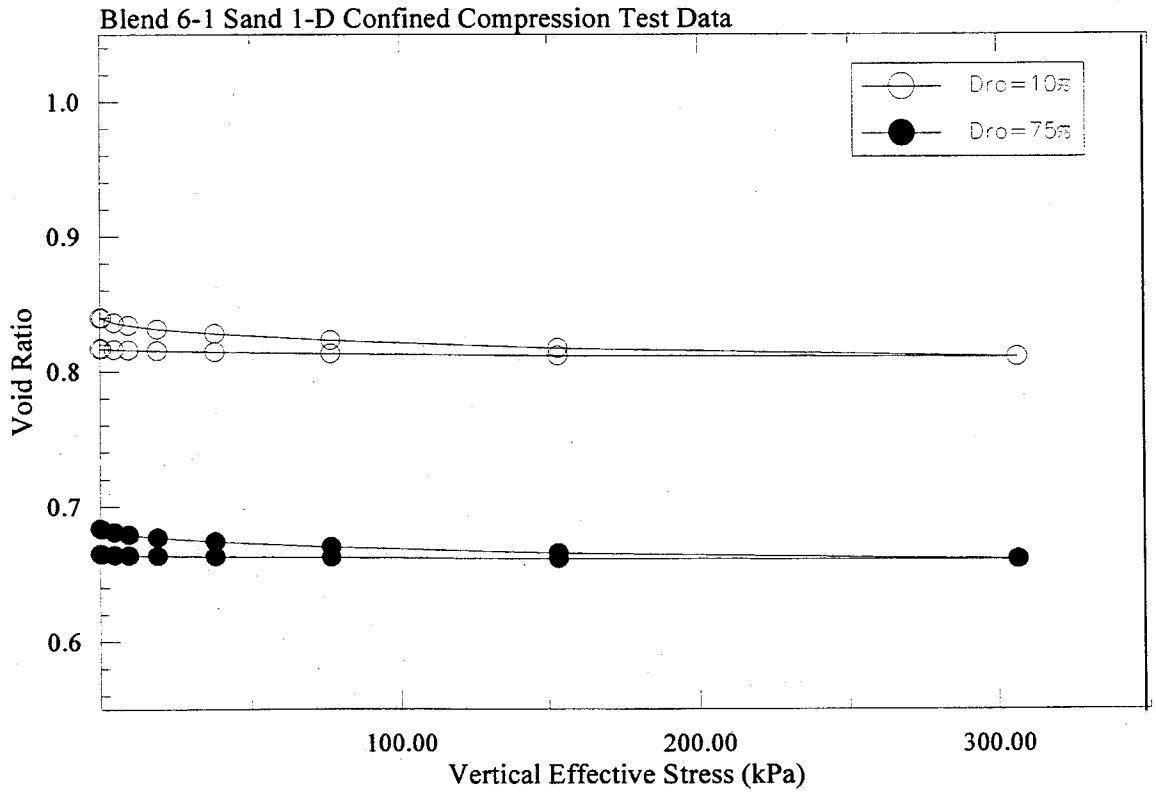

Figure 3-10: Confined compression test data plotted with respect to void ratio and vertical effective stress.

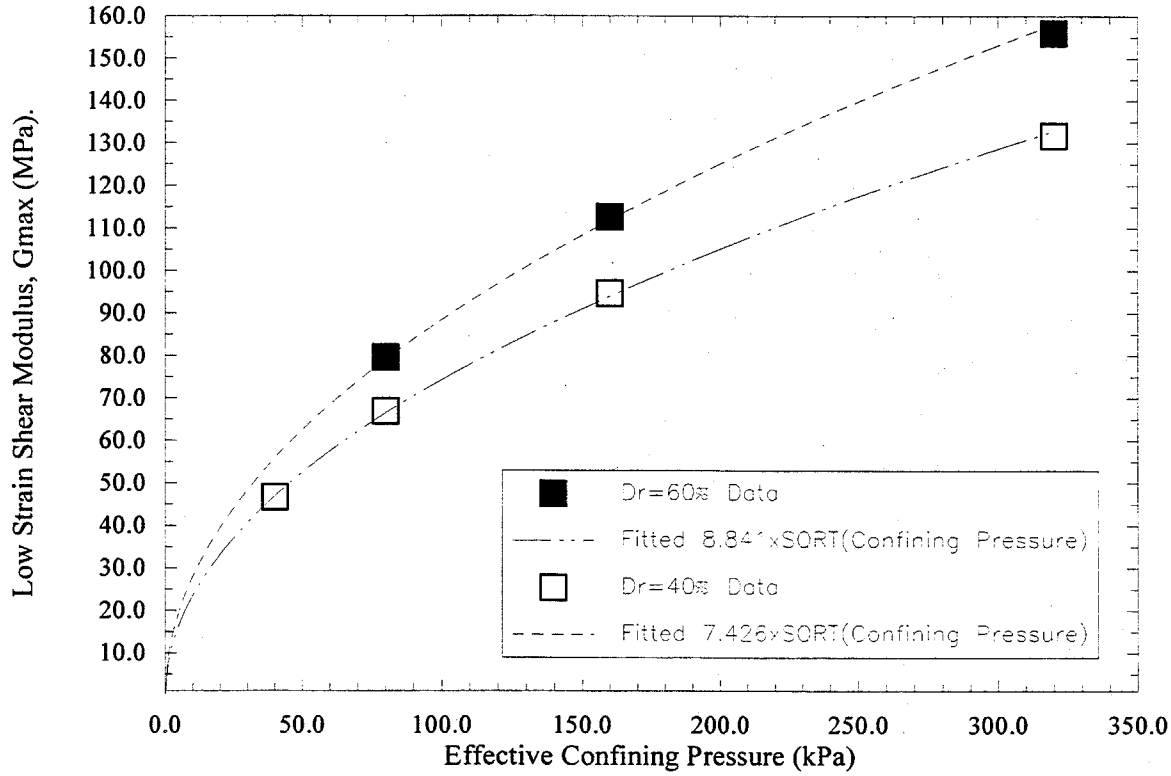

(a): Low strain shear modulus (G_{max}) for relative densities (D_r %) of 40 and 60 percent for various confining pressures. G_{max} values correspond to strain levels ≤ 0.0001%.

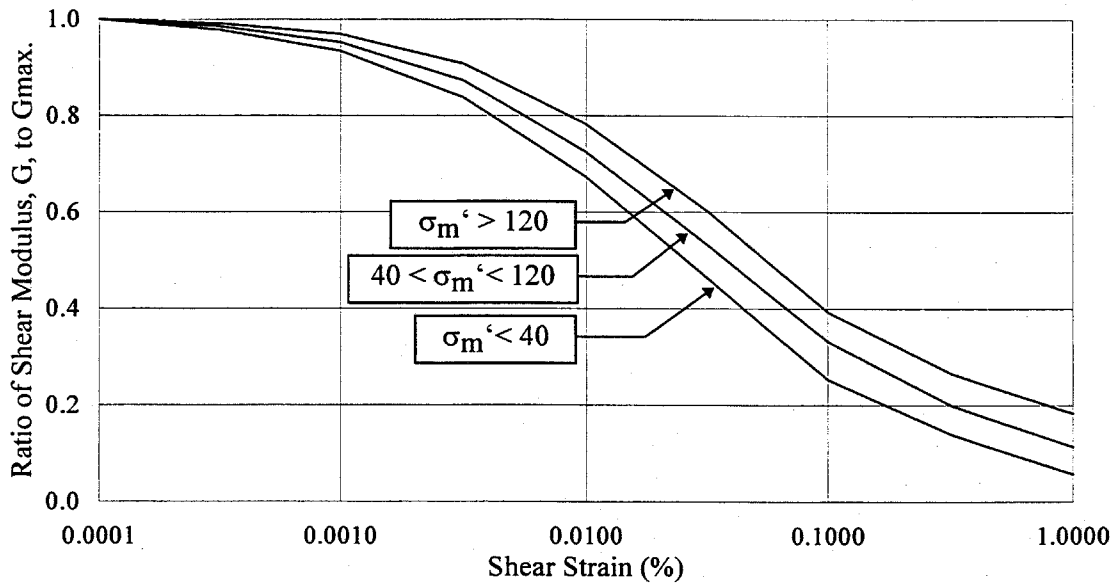

(b): Generalized curves for saturated sands (Iwasaki et al., 1976). Curves are dependent on the effective confining pressure, σ_m' , present in the sand.

Figure 3-11: (a) Low strain shear modulus G_{max} for the Nevada sand, and, (b), the ratio of shear modulus, G, to G_{max} , for sands in general.

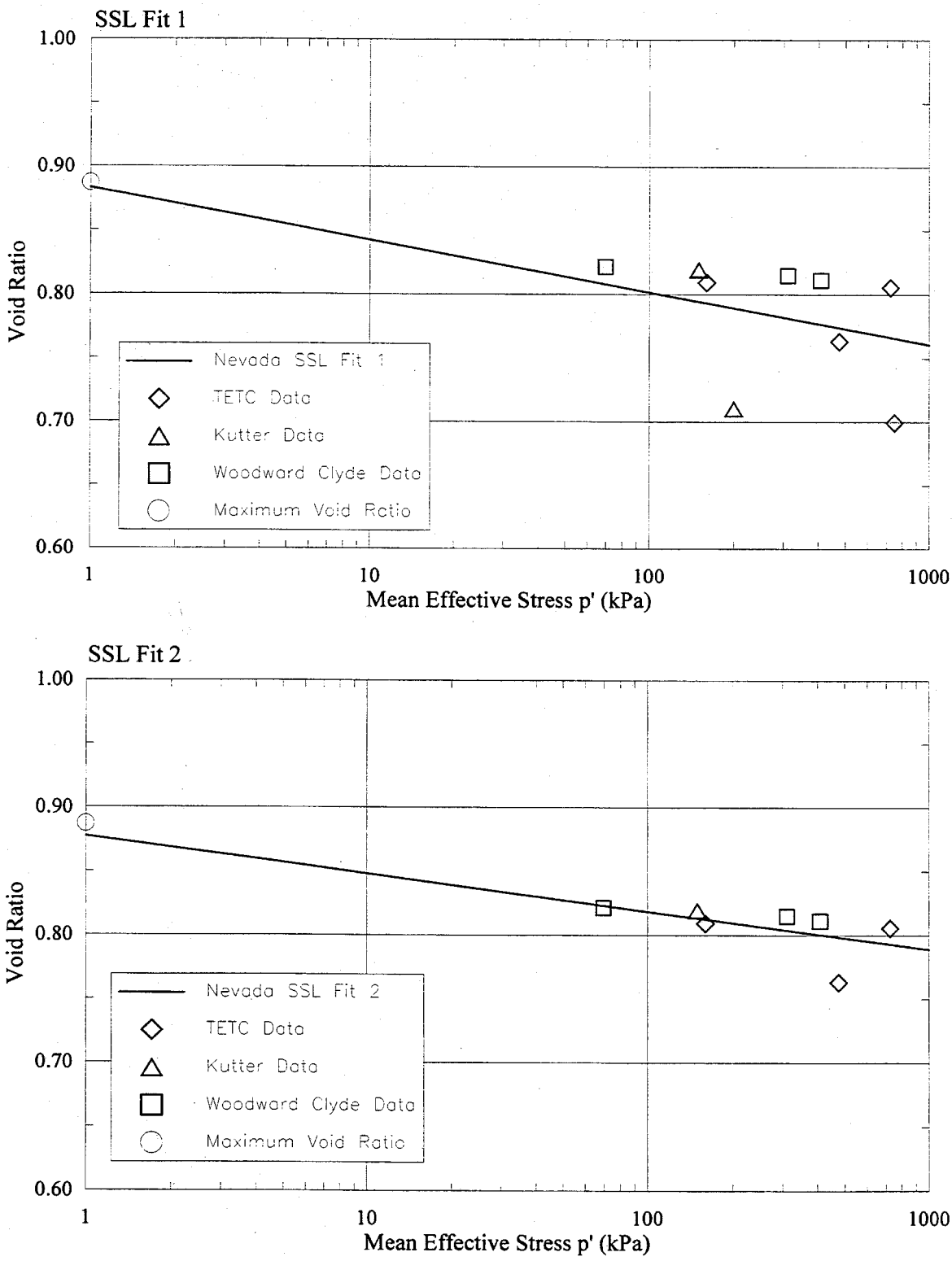

Figure 3-12: Steady state data from Table 3-4 for the Nevada sand fitted with alternate SSL's (Fit 1 and Fit 2).

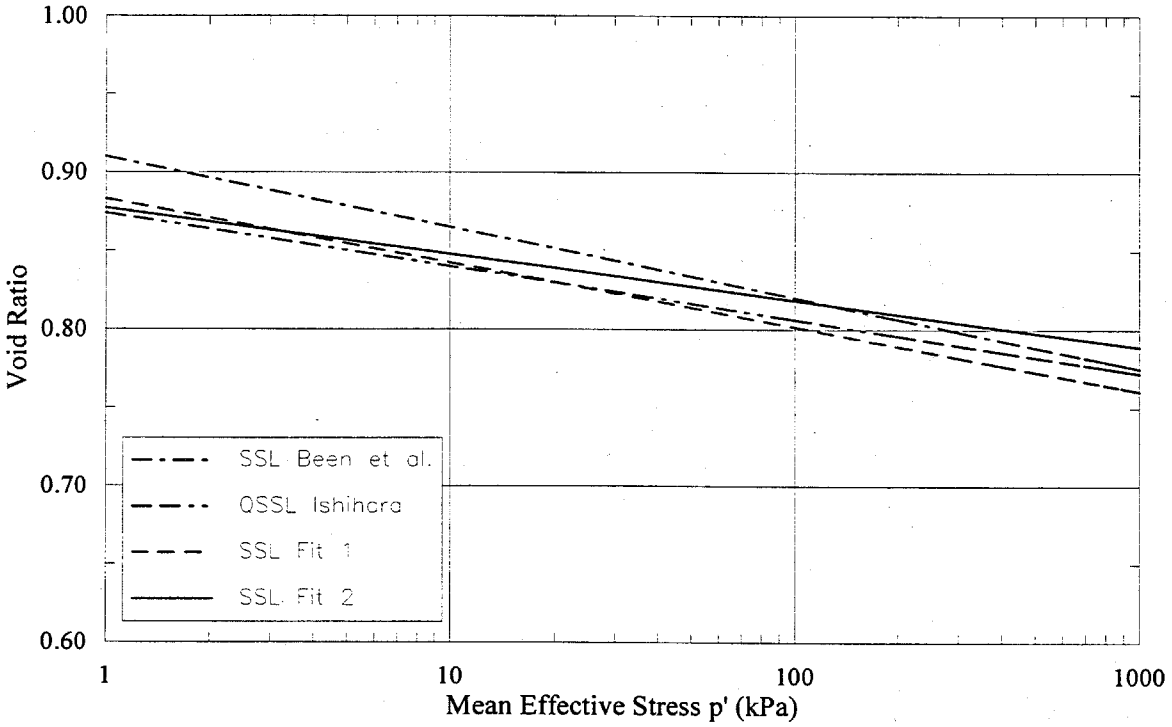

Figure 3-13: Comparison of SSL's for the Nevada sand.

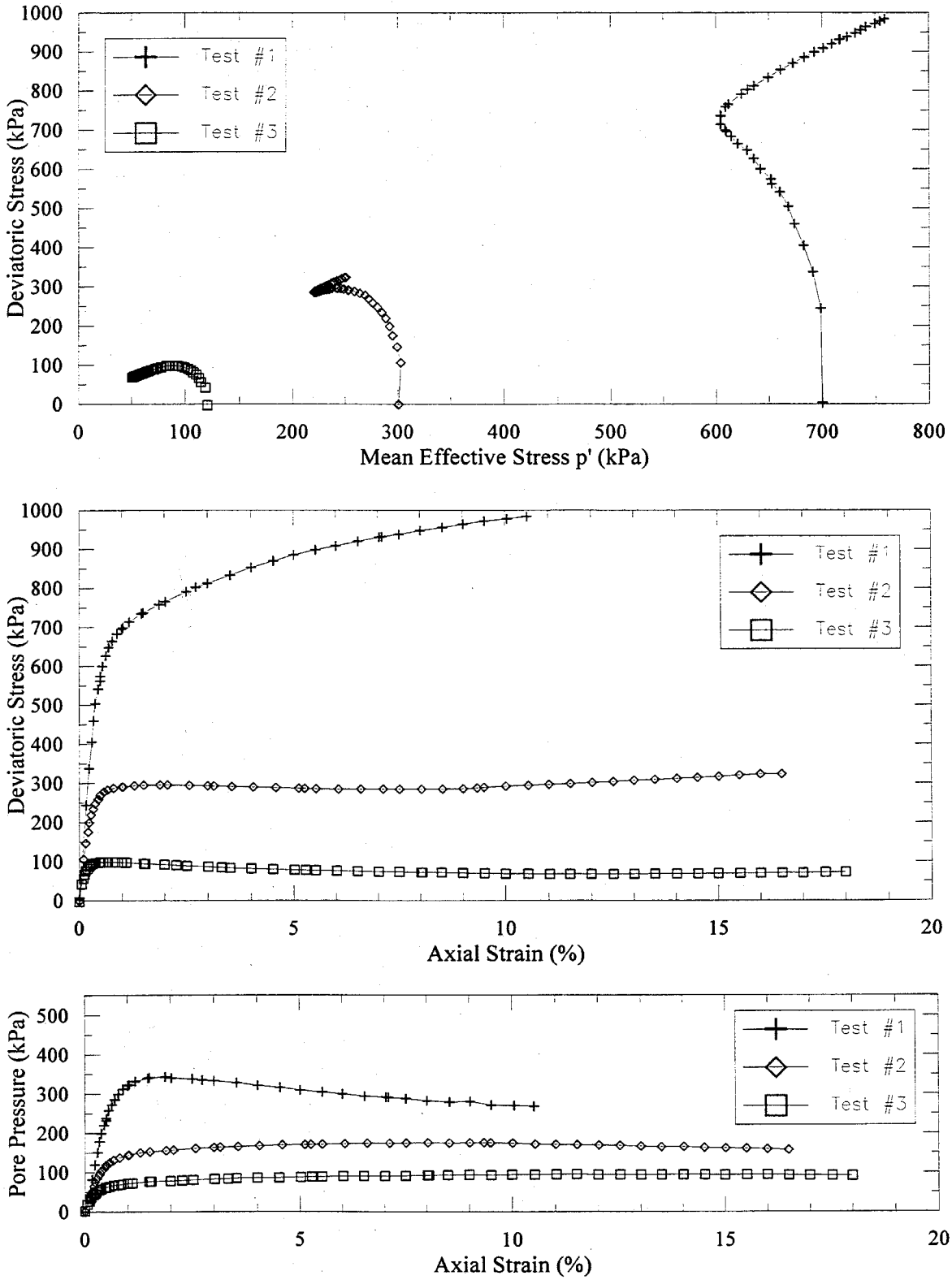

Figure 3-14: Triaxial test data for the Blend 6-1 sand.

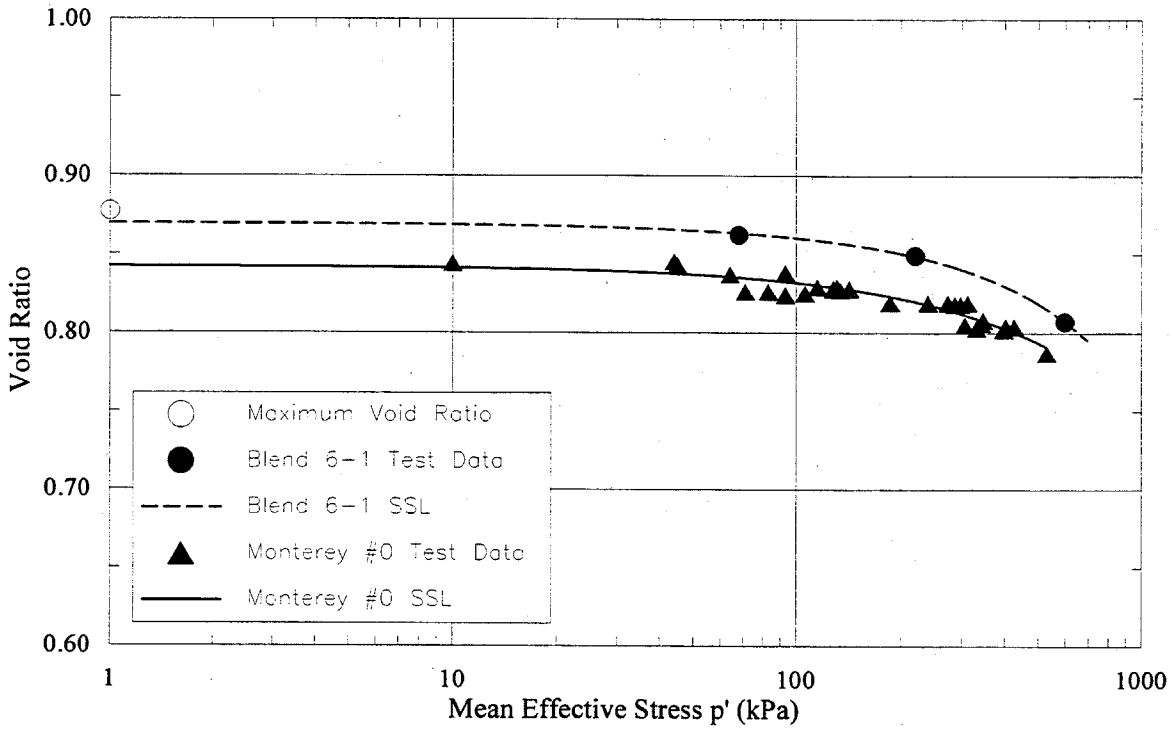

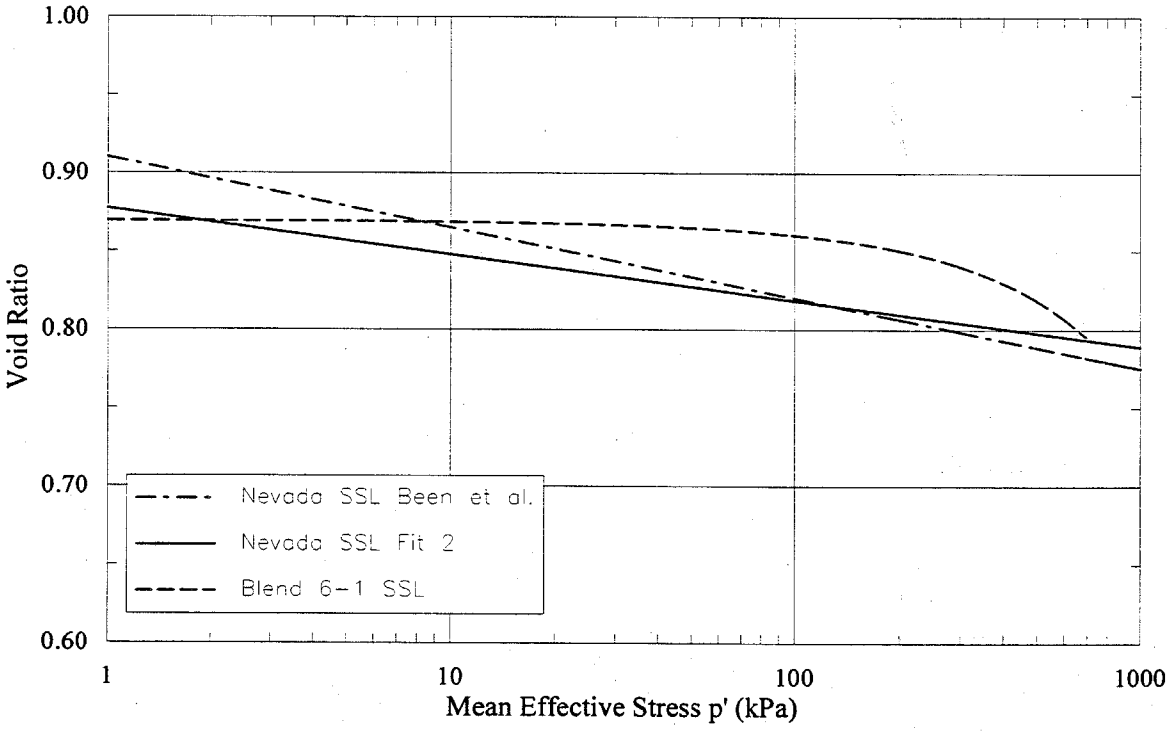

Figure 3-15: Blend 6-1 sand steady state data, fitted SSL, and comparison with Monterey #0 sand SSL and Nevada sand SSL's.

Chapter 4

EXPERIMENTAL METHODOLOGY

4.1 Introduction

This chapter describes the experimental program followed in this study. The background to the physical models selected for testing is discussed, followed by a detailed description of the experiment apparatus and the methodology followed to complete the experiments.

The entire experimental program was formulated to achieve two primary objectives:

1) Investigate the proposed method of modeling for the one-g environment proposed by Scott (1989) as described in Chapter 2, compare this with centrifuge Model 3, and extend the experimental database for verification of the method.

2) Review in general the merits of one-g models and centrifuge models and investigate the advantages or disadvantages and limitations of these modeling methods.

To achieve the first objective, one-g dynamic model tests were performed on a saturated sand using a shake-table. The input motion to the model was an earthquake with sufficient intensity to induce liquefaction in the model sand. These tests have the required complexity of soil behavior to further explore the method proposed by Scott, and in particular the method of constitutive scaling using the steady state line (SSL).

To achieve the second objective and provide a reference for the results of the one-g tests, the model constructed on the shake-table was a replica of a model that was tested in a centrifuge as part of the VELACS project (Arulanandan and Scott, 1993, 1994). The centrifuge test was referred to as Model 3. The primary test was undertaken at Caltech, and duplicate tests were also performed at UC Davis and Rensselaer Polytechnic Institute (RPI) centrifuge facilities (Hushmand et al., 1994).

The results of the centrifuge MODLEL3 test can be scaled to represent a "prototype" using the relations derived in Chapter 2, Table 2-1. The one-g model tests have been performed using this prototype as a reference, and hence the one-g tests are essentially models of the centrifuge test.

4.2 VELACS Model 3 Centrifuge Test

A complete description of the centrifuge testing and the experimental methodology is given by Hushmand et al. (1994). The test configuration and results reported herein have been reproduced from the above source when required for clarity or for comparison purposes.

Figure 4-1 shows a schematic cross-section of the centrifuge model. The centrifuge Model 3 consisted of two saturated columns of loose and dense Nevada sand prepared adjacent to each other in a laminar box. The "loose sand" had a nominal relative density of 40% and the "dense sand" had a nominal relative density of 70%. The entire model was excited at its base with an earthquake input motion of sufficient intensity to induce liquefaction in the upper portions of both the loose and dense columns of sand. The three components of earthquake history, and the Fast Fourier Transforms (FFT's), are indicated in Figure 4-2 and Figure 4-3, respectively. The data in these figures is presented in prototype units.

The model was instrumented with accelerometers, pore pressure transducers, and linearly variable displacement transducers (LVDT's) as shown on Figure 4-4. The results and measurements obtained from the transducer array during the testing of Model 3 and are presented in Chapter 5. The test was performed in the centrifuge at 50-g; therefore, the scale of the ratio of prototype to model dimensions was $n = 50$. A complete set of scaling factors for the centrifuge model is given in Table 4-1 using the relations derived in Chapter 2, Table 2-1. The nominal depth of the sand in the centrifuge model was 220 mm. Therefore, Model 3 represents a prototype deposit of Nevada sand about eleven meters in depth, and the initial state of the prototype sand would be the same as the initial state of the centrifuge model as indicated in Table 4-2. It should be noted that the range of values in Table 4-2 correspond to the reported initial condition of the sand (Hushmand, 1994) and an estimated initial condition that the model may have had prior to being tested. The estimated initial condition considers the possibility that the model sand compressed under the increased gravity field of the centrifuge prior to actually being shaken by the experimental earthquake.

The estimated values were computed using the compressibility data of the Nevada sand reported in Chapter 3, and a mean stress change of about 50 kN/m^2 which the centrifuge model would experience as the body forces increase to 50-g's in the centrifuge. No discussion regarding this potential effect was given in the original paper (Hushmand et al., 1994). The range in initial conditions indicated in Table 4-2 is an important consideration for this study because of the comparison of the centrifuge model with one-g models in which relative densities (or void ratios) play a significant part.

It should also be noted that the centrifuge Model 3 was prepared with a level surface. Due to the radial variation of the body forces over the length of the model in the centrifuge, this would equate to a prototype having a bulged surface profile. This may have a significantl affect on surface settlements recorded in centrifuge Model 3 test.

4.3 One-g Model Test Program

As discussed in Section 4.2 above, the centrifuge Model 3 represented a prototype deposit of sand eleven meters in depth with the sand at an initial state indicated in Table 4-2. In the discussion that follows, the prototype soil deposit represented by the centrifuge test and its input earthquake will simply be referred to as the 'prototype'. The one-g models completed for this research were constructed to represent this prototype and were tested on the shake-table in the Caltech Soils Laboratory.

The laminar box constructed, specifically for the shake-table, was approximately twice the size of the laminar box used in the centrifuge. The maximum practical depth of the sand that could be placed in the shake-table laminar box was 432 mm. Given this, the scale ratio of the one-g models to the eleven meter deep prototype deposit of sand is $n \approx 25$. A full set of scaling factors for the one-g models is given in Table 4-1 based on this value of $n \approx 25$. For the actual models constructed, n varied slightly from model to model due to slight variations in the depth of the model sand. A detailed discussion of the laminar box and its performance is presented in Section 4.4.2.

The function of the shake-table was to produce an appropriately-scaled model earthquake motion for the one-g models which represented the prototype earthquake shown in Figure 4-2. The model earthquake should have the same relative spectral content and magnitude of acceleration as recorded in the prototype earthquake, but in accordance with the scaling factors of Table 4-1,

its total duration should be less. In this respect the model earthquake is like a compressed version of the prototype earthquake. For the given one-g models, the model target earthquake has a duration of about 5 seconds compared to the duration of about 25 seconds in the prototype earthquake. The shake-table specifications and the method used to produce the model earthquake are discussed in Section 4.4.1.

The same array of transducers was used in the one-g models as in the centrifuge model as indicated in Figure 4-4. The specifications of the transducers are presented in Section 4.4.6. To maintain geometric similarity the transducers were positioned with respect to the centerline of the one-g model, and were placed as the sand was progressively added to the model. The initial coordinates of the transducers are given on Table 4-4, which were determined by scaling the centrifuge transducer initial coordinates (Table 4-4) by the ratio of the depths of the one-g and centrifuge models. The tolerance for placement for the transducers in the one-g models was $\pm$ 1 mm. A detailed discussion of the methods employed to place the sand within the model at the required densities is presented in Section 4.4.3.

After the sand and transducers had been placed in the laminar box, the dry sand was de-aired by applying a vacuum through a specially constructed wooden box which encapsulated the entire laminar box and which was sealed to the top of the shake-table. While maintaining a vacuum, de-aired pore fluid was gradually added to the sand until the model was inundated.

Several one-g models were tested on the shake-table. Each model was subjected to the prescribed model earthquake while simultaneously recording the response of the transducers during and after shaking. When all the excess pore pressure had dissipated and no further changes in surface settlements were observed, the model was presumed to have reached a stable quiescent condition. At this time the average final density or void ratio was calculated based on the measured settlement of the surface. The model was then subjected to another earthquake and the transducers were monitored as for the first test. This procedure was repeated several times for each model. In this manner a series of sequential tests was obtained from the construction of single model.

To achieve the objectives of the experimental effort, the one-g models were constructed with a range of initial conditions. The test parameters that were varied are as follows:

1) The initial state (density or void ratio) of the model sand.

2) The type of sand used in the model.

3) The pore fluid used in the model.

Table 4-5 shows the range of one-g models tested, and gives a basic summary of each model configuration. Models SM3B through SM3D were constructed to an initial state which approximated the initial state of the loose and dense columns of sand in the prototype as indicated in Table 4-2. For Model SM3E the sand was not placed at different densities, but at a uniform density corresponding to the initial state of the loose column of sand in the prototype. The models SM3B through SM3E represent the case where no provision for the scaling of the constitutive behavior is made. It should be noted that it was not possible to control the placement of the sand to exactly reproduce the prototype conditions; this is discussed in more detail in Section 4.4.3 below.

Models SM3F through SM3K were constructed at an initial state corresponding to the SSL scaling method proposed by Scott (1989) as described in Chapter 2, Section 2.4, and therefore these models have been adjusted for the constitutive behavior. For Model SM3I the sand was not placed at different densities, but at a uniform density corresponding to the scaled initial state of the loose column of sand in the prototype.

Two different sands, the Nevada sand and Blend 6-1 sands, were used in the testing program models. The majority of the models were completed using the Nevada sand which was used in the prototype. Models SM3D, SM3G, and SM3K were constructed using the alternate Blend 6-1 sand. The purpose of using the alternate sand was to further test the proposed model theory, which potentially can account for using a different model material than the prototype material. If the theory is valid, the scaled results from the models using the Blend 6-1 sand should be the same as the scaled results from the models using the Nevada sand.

All of the models were saturated with water except for SM3H which was dry, and SM3K in which the pore fluid was a mixture of glycerin and water. The model SM3H was completed to obtain data on the model behavior without any pore fluid. The model SM3K had a modified pore fluid to investigate the possibility of scaling the pore fluid properties to address the time scaling incompatibility between dynamic and diffusion processes as discussed in Chapter 2, Section 2.6.

4.4 One-g Experimental Apparatus and Methodology

This following discussion provides a discussion of the apparatus used in the experimental work and the methodology followed to construct and test the models. Figure 4-5 shows a photograph of a typical experimental setup for a one-g model test and identifies the important items of apparatus.

4.4.1 Shake-table and Input Motion to the One-g Models

A typical earthquake generated on the shake-table is shown on Figure 4-6. It has been scaled to prototype units so that a comparison can be made with the prototype earthquake shown in Figure 4-2. The longitudinal components of the earthquakes compare favorably. However, the transverse and vertical components are not well matched. From Figure 4-6, the absence of any significant accelerations in the transverse or vertical components confirms that the shake-table is one-dimensional in its motion. This is in contrast to the centrifuge apparatus which, as indicated in Figure 4-2, generated small but significant accelerations in the vertical and transverse components. From the FFT's shown in Figure 4-3, the vertical component of the prototype earthquake in the centrifuge especially contributes additional energy.

To compensate for the difference between the shake-table and centrifuge apparatus, the amplitude of the earthquake for the one-g models was increased slightly to account for the absence of any motion in the vertical and transverse components. A closer comparison of Figures 4-2 and 4-6 shows the amplitude of the accelerations in the longitudinal component of the shake-table are slightly larger than the prototype longitudinal component. This is better demonstrated in Figure 4-7, which shows the FFT's for all of the one-g model earthquakes compared to the FFT of the prototype earthquake for the longitudinal component.

The one-g model earthquake had greater intensity for frequencies larger than about 2.3 Hz, and is similar to what would be observed if the vertical and longitudinal FFT's of the prototype shown on Figure 4-2 were simply superimposed. While this is not an exact method for matching the model earthquake with the prototype components, it does attempt to keep the intensity of shaking at comparable levels.

From Figure 4-7 it is also evident that some small variations of earthquake motions occurred from each one-g model to another, but that this was limited and is perhaps accentuated by small

shifts in frequency content. Potential reasons for the scatter in the motions and a detailed discussion of the shake-table system and the procedure followed to obtain the earthquake motion follows.

Details of the shake-table: The one-degree-of-freedom shake-table in the Caltech Soils Laboratory was manufactured by The Team Corporation[1]. The table is 900 x 900 mm square with a 25 mm thick aluminum top plate which has tapped holes on 150 mm centers so that apparatus can be securely fastened to the top plate. The table is driven by an electro-hydraulic servo valve and piston arrangement, and its performance specifications are given on Table 4-6. A separate hydraulic oil power supply can deliver up to about 24 MPa (3500 psi) to the electro-hydraulic servo valve.

The table motion is controlled by a displacement feedback loop from a linearly variable displacement transducer (LVDT) located at the servo valve. The desired displacement is input to a servo controller as an analog signal. Based on the feedback from the LVDT, the servo controller modifies the signal to the table to track the desired displacement. The amplitude of the signal to the table is set by a span control on the servo controller and a variable power amplifier. The response of the table under regular sinusoidal inputs is quite good. The frequency response limits are approximately 5 to 2000 Hz before roll off starts to occur.

Under a random input motion the manufacturer's performance specification indicates a frequency band of 20 to 2000 Hz. The frequency range of interest in civil engineering for a typical real (prototype) earthquake is approximately 0 to 15 Hz, and for the prototype earthquake represented in Figure 4-2 this range is a reasonable assumption. For the one-g models this prototype range is scaled (Table 4-1) to approximately 0 to 75 Hz in model terms. Therefore, there is a frequency band mismatch between the model earthquake and table specifications at the lower frequencies, which made it more difficult to control the random response of the table. Adding to the difficulty was the non-linear response of the table and the fact that it was designed principally for higher levels of acceleration than present in a typical earthquake.

Obtaining the scaled earthquake motion: To reproduce the target earthquake motion for the one-g models, a computer algorithm was used in an iterative procedure to obtain a satisfactory result. The servo controller required an analog signal; therefore, a digital-to-analog signal

[1] Address for Team Corporation is 1159 Water Tank Road, Burlington, WA 98233.

conversion PC card was used to convert a digital record to an analog signal. This permitted digital control of the random signal using a computer. The basic elements of the procedure followed are shown in the flow chart of Figure 4-8, and the code written for the procedure is included in Appendix A.

Essentially, the table and control system were approximated as a linear system. An initial input motion for the table was converted to an analog signal and input to the servo controller. The acceleration response of the table caused by this input signal was recorded as the output motion. After converting the initial input and the output motions into the frequency domain using FFT's, a transfer function was computed for the system. It was then possible to calculate a new input signal which would produce a new output motion matching the desired target earthquake. If the system were truly linear, the new input signal would have given the exact target earthquake in one step. However, the table response was non-linear and iterations were required until the recorded response of the table matched the target earthquake. In practice about three to four iterations were necessary to obtain an almost identical match.

In the above process some manipulations of the data were necessary for the numerical procedures. The target earthquake record was used as the initial input motion and was converted to an analog signal. This signal was scaled so that in practice the peak voltages were about $\pm$ 1.5 volts. The normalizing factor required to achieve this level of voltages was applied to all subsequent iterations of new input signals for the servo controller. All the input motions and output motions were processed to have the same number of data points and the same time interval between data points in the time domain. This ensured that in the frequency domain the FFT's had identical band widths. It was also necessary to smooth the FFT's in order to compute reasonable transfer functions. The smoothing was completed by a moving average and the "smoothing factor" corresponded to the number of data points in the moving window. The smoothing factor required was initially about 12 but was reduced to 4 as the iteration proceeded and the output motion more closely approximated the target earthquake. Given the use of the procedure outlined above, it was possible to overcome some of the limitation of shake-table and reproduce the scaled version of the prototype earthquake on the shake-table.

As the experimental work proceeded, other problems were encountered with the shake-table performance. Initially it proved impossible to get repeatable motions from one test to another even though the same input analog signal was used. Eventually the shake-table completely failed

to function and the servo hydraulic valve was serviced by the manufacturer. It was found that the voice coil in the servo valve had completely burnt out and that there was a 1 inch fragment of an O ring in the servo mechanism itself. This explained the erratic behavior and progressive decline exhibited by the table during the initial experiments. Essentially, these experiments were repeated and the affected results were discarded.

After the repairs were completed and the table was reassembled, the performance was very consistent for any given model test. However, some variation in table motion was still observed for different model tests as discussed previously and indicated in Figure 4-7. These variations can be attributed to a number of possibilities, but the most likely causes would be as follows:

1) Differences in the mass and stiffness of the models (which would affect the response of the table).

2) Changes in the hydraulic fluid from test to test, including the temperature of the fluid.

3) Differences in the pressure at the hydraulic servo valve due to progressive clogging of the in-line filters.

4.4.2 Laminar Box Details and Performance

A laminar box for the shake-table was designed and constructed at Caltech to emulate the laminar box used in the centrifuge experiments (Hushmand et al., 1988, 1994). The nominal dimensions of the laminar boxes for the shake-table and centrifuge are compared in Table 4-3. It should be noted that the shake-table laminar box is slightly longer in proportion to the centrifuge laminar box and in this respect the one-g models represent a longer prototype than the centrifuge model. The potential implications of this are discussed in Chapter 6.

The box for the shake-table consisted of a set of rectangular aluminum frames constructed from channel section approximately 25 mm in height. The frames were stacked on top of each other, separated by four aluminum bearings as indicated in the photograph of Figure 4-9. Each bearing was seated in shallow slots milled into the top and bottom faces of the aluminum channel. The locations of the slots were offset for adjacent layers to avoid weakening the aluminum channel section. The bottom frame of the laminar box was attached to a 5 mm thick aluminum base plate which rested on the shake-table and was bolted to it securely. A total of 18 frames were used and

the final inside dimensions of the laminar box were 350 mm wide by 470 mm deep by 900 mm long.

The sizes of the members for each frame were selected to limit the lateral deflection of each member to 1 mm or less under a uniformly distributed load equivalent to that imposed by sand when fully liquefied. It should be noted that the design load of liquefied sand is hydrostatic with an equivalent fluid weight about twice that of water. A short spreadsheet was used to optimize the selection of the end sections and side sections to minimize the weight. Based on this analysis, aluminum channels of section 50 mm in width, 25 mm in height, and 3 mm thick were selected for the lower nine frames. For the upper nine frames the width of the channel was reduced to 40 mm along the sides. The ends of the frames were kept at the full 50 mm width for ease of fabrication and instrumentation. After the frames were constructed, a static test of the mid-side deflection under an equivalent point load was completed and the test showed that the deflection was within the design tolerance. The total mass of the box was approximately 45 kg and each frame weighed about 2.1 kg.

With all the frames and bearings in place, the box easily deformed in a simple shear type mode under very small horizontal loads applied along its axis. The upper photograph in Figure 4-10 shows the empty laminar box in a deformed mode. The maximum travel of each frame with respect to its neighbor was approximately 25 mm. Any raking or torsional mode of the box was negligible. The box was lined with a latex rubber liner approximately 1 mm thick as shown in the lower photograph of Figure 4-10. The liner was custom made by first sealing the inside of the box with masking tape and then painting several coats of the latex on the inside until a 1 mm thickness was obtained. The liner was then removed and used in subsequent tests. The liner was securely taped to the top frame of the box for all the tests completed.

The primary reason for using a laminar box was to maintain a plain strain condition in the soil sample and provide free boundary conditions at the each end of the box for a shear deformation mode. The stiffness and the mass of laminar box had to be low enough so that it did not control or significantly influence the behavior of the sand model being tested. To verify this, however, is not a simple task. The dynamic behavior of the laminar box and latex rubber liner alone are quite complex, without considering the interaction with the saturated sand. Table 4-7 presents some values for the respective masses and range of shear modulus of the sand model and the laminar box. The mass of the laminar box is about 20% of the mass of the sand model, and the range in

shear moduli are of the same order. The shear moduli for the model were taken from Chapter 3, Section 3.5. The higher values correspond to very small shear strains (less than .0001%) and the low values to large shear strains (on the order of 1% which were recorded during the testing of the models).

To obtain shear moduli for the laminar box, a static shear test was performed and the values were calculated using the recorded lateral deflection of the box for a given applied shear stress. The shear behavior of the box was controlled by the latex rubber liner which was held against the frames of the laminar box by filling the box full of water. This is a reasonable representation of the loading condition that would exist when the box is full of sand. The results of the static test showed that as the strains increased, the shear modulus dropped, indicating that the box exhibited strain softening. In addition, the box had a higher shear modulus as the depth increased implying that there is a dependence on the pressures exerted by contents of the box (sand or water). The lower bound of the range of values in Table 4-7 was recorded for the upper part of the box at a level of shear strain on the order of the maximum encountered in the actual model tests (on the order 1%). The upper bound of the values in Table 4-7 was recorded at low shear strains (less than 0.1%) recorded in the lower portion of the box. In general terms the behavior of the box emulates the behavior that might occur in the sand model itself, which also exhibits strain softening and a dependence on pressure or confining stresses. Certainly the shear moduli are of similar magnitude as indicated in Table 4-7.

To evaluate the relative significance of the mass and stiffness of the box to the sand model, some simple physical models can be considered. Probably the simplest idealization and certainly the crudest would be a damped one degree of freedom mass and spring system. Figure 4-11a schematically shows this idealization first for the sand model, and then for the sand model with the addition of the laminar box. For the sand model and laminar box it is assumed that at any time the shear deflection is the same for both (i.e., no separation between the end of the box and the sand) which is supported by observations made during the testing.

In Figure 4-11 the shake-table provides the base excitation to each of the idealizations, and for the analysis the forcing function $X(t)$ is a sinusoidal input. The masses correspond to the masses given in Table 4-7 and the damping, D, has been assumed to be 10% of the critical damping for the system. This level of damping is quite reasonable for a saturated sand. The spring stiffness for the sand, k_S, and for the laminar box, kl, were derived using the upper and lower range of the

shear moduli of Table 4-7. The corresponding values of the stiffness are presented in Table 4-7 and are simply the product of the shear modulus and area of shear divided by the height of the model. The area of shear is the area of a horizontal plane section, and for the sand this is 0.315 m^2 which is 126 times greater than the area of the liner for the laminar box which is 0.0025 m^2. This difference in area explains the contrast in the stiffness values in Table 4-7.

The solution for the idealizations in Figure 4-11b and 4-11c can be obtained from any standard text on dynamics (Housner and Hudson, 1980). In Figure 4-11 a comparison of the solutions for the sand model alone, and the sand model with laminar box, is given in terms of the magnitude of steady state response versus the excitation frequency. The solution shown in the upper plot is for the lower bound shear moduli data presented in Table 4-7 for the sand model and laminar box. The solution shown in the lower plot is for the upper bound shear moduli data in Table 4-7. All of the solutions have been normalized with respect to the static displacement of the sand model. It should be noted that these solutions represent the ends of the range in behavior of a model, which can be expected to move from the upper bound to lower bound behavior as a test proceeds.

A number of general comments can be made regarding the solutions shown on Figure 4-11.

1) The effect of the laminar box is small in the steady state, and is apparently limited to slightly lowering the natural frequency of the system. Given that in the actual tests the excitation is random and that transient conditions will dominate, the effect will be even less than indicated by the steady state solutions.

2) The magnitude of the response is far greater for the lower shear moduli which is the behavior that can be expected as the model softens.

3) The range in natural frequency range is about 8 to 33 Hz, which in terms of the prototype earthquake should be scaled to about 1.5 to 6.5 Hz. With reference to Figure 4-3 this range correlates with the frequency range of the most intense shaking in the prototype earthquake and therefore the response of the model will likely be dominated by the first mode.

For the last item above (3), it is useful to make a comparison with a shear beam idealization for the sand model, which is perhaps a more reasonable idealization of the actual system. The range of the natural frequency or first mode of the model predicted by the shear beam is 13 to 51 Hz (Wakabayashi, 1986) which compares favorably with the 8 to 33 Hz range obtained from the

simple spring and mass idealization. From the shear beam analogy the higher modes occur at 3, 5, 7, ... times the frequency range of the first mode, which implies that higher mode response in the testing of models will not be significant because it is generally outside the frequency range of the earthquake excitation.

4.4.3 Sand Placement Methodology and Equipment

To produce accurate models for comparison, the sand must be placed in the laminar box at or near a target density. Trials were completed using a variety of possible techniques. It was found that the density of the sand was controlled primarily by three factors; the distance the sand free-fell before reaching the surface of the model (or drop height); the flow rate of the sand; and the rate at which accretion occurred at the surface.

Of the various techniques attempted, two were used to construct the models as indicated in the photographs shown in Figure 4-12. The first method used a sand hopper which could be rolled back and forward on a set of tracks, and this technique was used to place the majority of the sand in the models. The second method employed a bucket with a flexible hose through which the sand was poured onto the surface of the model, and this method was used to place the sand at the lowest target densities. The initial sand densities measured for each model were generally within 1.5% of the target densities, which is within the error bound of the density measurement itself (estimated to be ± 1.9% as discussed in Section 4.5).

Sand Hopper: The general elements of the sand hopper system are shown in Figure 4-12. A frame, which supported the rails for the sand hopper, was placed over the entire model and laminar box. The hopper was moved back and forth along the rails at a reasonably constant rate to ensure that the rate of accretion of the sand at the model surface was uniform. The flow-rate from the hopper was controlled by an adjustable slot in the base of the hopper: an inclined back-plate funneled the sand to the slot. The slot extended across the width of the laminar box, and a sliding shut-off plate was used to turn the flow on or off. The sand was laid in about six lifts, each approximately 75 mm in thickness, to construct the full depth of the model. The height of the rails supporting the hopper was adjusted for each lift to maintain a constant drop height from the underside of the hopper to the sand surface of about 500 mm. To minimize the loss of sand when the hopper was raised well above the laminar box, plastic sheeting was stretched from the rails to the sides of the laminar box as indicated in the lower photograph of Figure 4-12. This ensured

that any stray sand particles at the ends of the flowing sand stream reached the surface of the model. The slot width, drop height, and rate of movement of the hopper were selected on the basis of prior trial and error experimentation to obtain the target densities for the model. The sand hopper method proved relatively reliable and resulted in consistent densities for repeated tests to within ± 1.0% of the target densities.

Bucket and flexible hose: During the preliminary experimentation various methods to place the sand were investigated including using a bucket with a variety of modified sand pouring methods such as grates, sieves, funnels, and hoses. None of these methods provided very consistent results, principally due to the difficulty in controlling the accretion rate of sand across the sand surface which was very operator sensitive. However, there was one notable exception. The method employing a plastic bucket as a sand hopper with a flexible hose from its base, as shown in Figure 4-12, did prove reliable only when the sand was being placed at its loosest possible state or lowest density. The end of the flexible hose was kept in contact with the sand surface while being moved gradually side to side and then lengthwise in alternating layers to create a weave type pattern. The sand never developed any appreciable velocity and essentially gradually spilled from the mouth of the hose. This procedure produced consistent results within ± 0.5% of the lowest target density achieved in the models.

Model construction: The models generally required the sand to be placed at two different densities, a loose state, and a dense state as shown on Figure 4-1. To achieve this a thin aluminum plate was located at the centerline of the box to separate the two halves as indicated in the lower photograph of Figure 4-12. Alternating lifts of sand were placed on each side of the plate at the loose and dense target densities.

The mass of the dry sand added to each half of the box was carefully measured. The control of the density within each 75 mm lift appeared to be relatively good. However, the placement of subsequent layers did apparently induce additional densification in the underlying layers of the sand. The increase in density was up to 4 to 5% in the loose material, and this was accounted for when the slot width and drop height were selected. Of this percentage the compression created by the increase in vertical stress as the upper sand layers were placed accounted for a maximum of about 1% of the 4 to 5% density increase. Presumably the remaining 3 to 4% density increase occurred as the upper layers were rained into place, potentially causing micro disturbances within the model sand and densification. Once the sand was placed, there was no discernible change in

the height of the model indicating that no additional densification occurred. This observation was also supported by the one-dimensional confined compression tests which also indicated that the density of the sand remained constant under a steady state sustained load.

The surface of the sand was carefully smoothed and leveled to within about ± 1 mm of the mean final height of the model. The plate separating the loose and dense halves of the model was withdrawn from the sand leaving three lengths of spaghetti embedded at the interface of the loose and dense halves of the box. The spaghetti had been previously tacked to the plate using a few dabs of vacuum grease before the construction of model was started. Figure 4-13 shows the configuration early in the model construction. When the model was subsequently inundated with pore fluid and tested, the spaghetti, which had softened from contact with the pore fluid, followed the deformation which occurred at the loose and dense interface. It should be noted that the addition of pore fluid to the model did induce some additional densification of the sand. In the loose sand the maximum observed increase was about 1.5%, and in the dense about 0.7%.

The laminar box and a completed model are shown in the lower photograph of Figure 4-13 prior to subsequent de-airing and saturation (which is described in Section 4.4.4). The cables from the embedded transducers were coiled and taped to the side of the laminar box, and a piece of geotextile was placed on the surface of the sand to prevent erosion by the pore fluid as it was subsequently added.

4.4.4 De-airing the Model with the Vacuum Box

For model tests in which the generation of pore fluid pressures (and or liquefaction) is present, it is desirable to eliminate as much air as possible from the pore fluid so that the rate of generation and magnitude of the observed pore fluid pressures are not significantly affected by changes in the air volume. If all the air is eliminated, the model would be saturated, a condition which is discussed in Chapter 2, Section 2.2.

For the model tests completed in this study, the first step taken to obtain a saturated condition was to de-air the sand model. A specially designed wooden vacuum box was constructed for this purpose as shown in Figure 4-14. The vacuum box was constructed from 19 mm thick plywood with wooden stiffeners attached to the outside to limit deflections. The joints were sealed with silicon and polyurethane. The inverted vacuum box was placed over the entire model and laminar box, and was sealed to the model base plate with a bead of silicon vacuum or valve grease. A

small Lucite portal located in the top of the box had connections for a vacuum gage, a vacuum line and a pore fluid line from the reservoir.

A vacuum was gradually applied to the box up to a maximum of about -45 kPa (-6.5 psi) over a period of about 1 hour. The vacuum was maintained at this level for at least another hour prior to the addition of pore fluid. To check that this was sufficient, an experiment was performed in which the pressures were monitored in the sand at the base of the model during the de-airing. The results indicated that a uniform negative pressure developed throughout the model within about 20 minutes.

4.4.5 Pore Fluid and Reservoir

To obtain the best possible saturation, only de-aired pore fluid was added to the models. The pore fluid was de-aired in the reservoir (Figure 4-14) under a vacuum of about -90 kPa (-13 psi) for at least 36 hours. The water was heated during this period but was allowed to cool prior to being added to the model. After the model was de-aired as described in Section 4.4.4, the pore fluid was gradually added to the model via a line from the reservoir while a vacuum was maintained at about -45 kPa. The fluid spilled onto the geotextile fabric which was placed on top of the sand surface and seeped into the sand. The flow rate was kept very low and typically a total of about 0.06 m^3 (2 cubic feet) was added over a period of at least 3 hours until the model was fully inundated.

The volume of pore fluid added to each model was estimated by measuring the change in the reservoir volume and measuring the volume of any excess pore fluid removed from the surface of the model prior to testing. Using this estimate of the total volume of water added and knowing the total mass of sand added to the model, a calculation of the degree of saturation can be made. The accuracy of this method is known to be quite poor, but unfortunately it was not possible to complete more accurate tests for saturation (such as the B-value test) because of the size and configuration of the models. The degree of saturation estimated using the above method is reported in Table 4-5 for each model. In general these values are considered low, and the significance of this is discussed further in Chapter 5, Section 5.4.3.

For all the models, with one exception, laboratory tap water was used as the pore fluid. For the model SM3K the pore fluid was a mixture of glycerin and water. The glycerin was added to the water to increase the viscosity of the pore fluid for scaling purposes, and the concentration of

glycerin was 70.8% by weight. A sample of the mixture was removed from the reservoir after the model test had been completed to measure the specific gravity and density. The glycerin-water mixture was heated in a water bath to temperature of 27° C which was the ambient temperature measured in the model SM3K. The dynamic viscosity was measured using a Brookfield Viscometer (Model LV) in the hydraulics laboratory at Caltech, and was 16.0 cps (Mpa.s). For the given temperature this implies the viscosity of the glycerin-water mix is 16.8 times greater than the laboratory water at the same temperature. The specific gravity of the glycerin-water mix was determined using a graduated flask and an accurate mass scale, and was estimated to be 1.176.

4.4.6 Post Test Excavation and Measurement

After each model was subjected to a series of tests, the wet sand was excavated and the positions of the spaghetti strips at the dense and loose sand interface were measured. For some models the final position of the transducers were also measured when it was certain that no disturbance had been created by the excavation itself.

The wet sand which was removed from each model was spread in a clean area of laboratory and left to air dry. In the period of about one week, the residual moisture content of the sand was typically less than 0.1%. Prior to re-using the sand in another model, it was sieved to remove any miscellaneous debris and to fully break up any clumps of dry sand.

4.4.7 Transducer Specifications

Each model was instrumented with a variety of transducers as shown in Figure 4-4 and listed in Table 4-4. The three basic groups of transducers were accelerometers, pore pressure transducers, and linearly varying displacement transducers (LVDT's) which are described in detail below. The initial location of the transducers within the models is given in Table 4-4. The majority of the transducers had been previously used in centrifuge models which in general require a far higher range of measurement than a one-g model. Therefore, the sensitivity of the transducers for the one-g model condition was in general quite poor, requiring certain hardware filtering and post-processing procedures as described in Sections 4.4.7 and 4.4.8. Some transducers were specifically purchased for the one-g models but budget constraints limited this to but a few. A

discussion and an estimate of the accuracy of the measurements made using the transducers is given in Section 4.5.

Accelerometers: Accelerometers were used to record the acceleration response of the shake-table and the model itself. In the early tests (Models SM3B through SM3E) accelerometers A1, A2, and A3 were used to record the longitudinal, transverse, and vertical components respectively of the shake-table-generated model earthquake. They were constructed as a single array as shown in Figure 4-15a, which was bolted to the top of the shake-table at the location indicated in Figure 4-15b.

After several models were tested, it became evident that the transverse and vertical components of the model earthquake were consistently negligible as discussed in Section 4.4.1. Consequently, A2 and A3 were moved to their alternate locations at the end of the laminar box. They were attached to individual frames located midway between LVDT L1 and L2, and midway between LVDT L3 and L4 respectively, to record the longitudinal component of acceleration of the laminar box at different heights. The exact alternate coordinates for A2 and A3 are given in Table 4-4, and are shown in their general positions in Figure 4-15b, though it should be noted that in this photograph accelerometers A2 and A3 are not in the exact positions as used in the model tests SM3F through SM3K.

The accelerometers were manufactured by ICSensors and the range of the transducers A1 and A2 was ±5-g, and of A3 was ±100-g. The 5-g traducers were amplified 10 times and the 100-g range transducer was amplified 200 times. In-line hardware filtering was used as discussed in Section 4.4.7 to remove high frequency noise apparently generated by the servo valve of the shake-table.

Four additional accelerometers, A4, A5, A6, and A7, were placed within the model approximately 85 mm below the surface. These accelerometers were manufactured by DYTRAN and were approximately 10 mm long and 6 mm in diameter with a sensitivity of ±500g. Transducers A4 and A6 recorded the longitudinal components in the loose and dense halves of the model respectively. Transducers A5 and A7 recorded the vertical components in the loose and dense halves of the box respectively. To seal the transducers from the pore fluid, each was coated with silicon sealant prior to being placed in the model. In general this worked well; however, as the testing proceeded some transducers failed and were replaced in subsequent models. The failure presumably occurred due to the ingress of water and such failures are noted

directly on the results described in Chapter 5. The signals from the accelerometers A4 through A7 were amplified by 100 times.

LVDT's: The shake-table uses an LVDT as part of its control system (manufacturer unknown). This was used to obtain the history of displacement of the shake-table top during the application of each model earthquake. A calibration of the LVDT was performed using a micrometer over a range of ± 40 mm, and it was found to be linear. No amplification of the signal from the table LVDT was necessary.

The remaining LVDT's L1 through L6 were all the same type (manufacturer unknown) and no amplification of the signals was necessary. For these one-g tests a short brass rod about 1.5 mm in diameter was used to extend the center rod of each LVDT. With the extension rod in place, each LVDT was calibrated using a micrometer for a range of ±12.5 mm and they were found to be linear over this range. The LVDT's were mounted on a support frame which was aligned along the centerline of the laminar box, as shown in Figure 4-5. LVDT's L1 through L4 were used to record the longitudinal displacement at the end of the laminar box at various heights as given in Table 4-4 and as indicated in Figure 4-16a. They were mounted on the end member of the support frame which is a vertical rod. A detail of this is presented in Figure 4-16a. The vertical location of the LVDT's could be adjusted by sliding them up or down the rod. Once positioned the end of the each brass extension rod was attached to the end of the laminar box using a dab of epoxy. The LVDT therefore tracked the movement of the laminar box frame that it was attached to.

The LVDT's L5 and L6 were used to record the vertical displacement of the sand surface in the loose and dense halves respectively, of each model. They were supported by the horizontal beam of the support frame which ran the length of the laminar box as shown in Figure 4-16b. The position of L5 and L6 could be adjusted longitudinally and vertically. There was also a limited ability to adjust the position laterally, within about 25 mm radius of the support frame. The end of each LVDT brass rod extension was attached to the center of a 25 mm square plate of Lucite which acted as a bearing plate on the sand surface. Once the LVDT was located in the correct position, the mounting bracket was locked and the Lucite plate was buried a couple of millimeters beneath the sand surface. As the sand settled during testing, the LVDT was able to follow freely. Observations from actual tests indicated that the system worked extremely well.

It should be noted that the support frame for the LVDT's was modified during the testing program. Figure 4-15b shows a modified end support which was provided to give added end restraint to the frame to ensure that it moved rigidly with the shake-table top plate. The original frame shown in the lower photograph of Figure 4-16 was found to have some flexibility created by weakened connections at the base plate. It therefore introduced its own dynamic response to the system. This had no effect on the vertical LVDT's L5 and L6 but obviously did affect the measurements made by LVDT's L1 through L4. The modification was used for models SM3F through SM3K and eliminated any measurable flexibility of the system.

Pore pressure transducers: To record the pore pressures that were generated within a model during testing, ten pore pressure transducers were placed as shown in Figure 4-4. The transducers were manufactured by DRUCK and were approximately 6 mm in diameter and 11 mm long. There were two rated capacities for the transducers: a maximum of 690 kPa (100 psi), and a maximum of 35 kPa (5 psi). Four 35 kPa-range transducers were purchased specifically for the one-g tests and their signals were amplified by 500 times. The remaining 690 kPa range transducers, which had been previously used in centrifuge tests, required amplification of the signals by 1000 times. The raw signals from these transducers contained a considerable amount of higher frequency noise, with a noise to signal ratio of about 10%. In-line hardware filtering was used as described in Section 4.4.7 to clean the signals.

Each of the transducers was placed in the model in the initial locations given in Table 4-4. The orientation of each transducer was transverse to the long axis of model. A rather stiff cable connected the transducer to the electronics and data acquisition system which made it difficult to place the transducers accurately. The pore pressure transducers were designed to be waterproof, but in general were not. Even with the added protection of a liberal coating of silicon sealant to protect the exterior of transducer cable connection, several transducers failed during testing as indicated in the results discussed in Chapter 5.

4.4.8 Electronics

A variety of power supplies, amplifiers, and signal conditioners were used for the transducers described above. Basically the LVDT's (L1 through L6) and the DYTRAN accelerometers (A4 through A7) used the manufacturer's custom power supply and amplifier. The ICSensor accelerometers and DRUCK pore pressure transducer's were attached to a Caltech-constructed

16 channel power supply and amplifier. To obtain the amplification for the 690 kPa-range DRUCK pore pressure transducers, it was necessary to add a second in-line amplifier. The first amplifier boosted the signals by a factor of 10 and the second by a factor of 100 which gave the prescribed total amplification of 1000 times.

Due to the relatively high noise to signal ratio of the 690 kPa-range pore pressure transducers and the high frequency noise present in the accelerometers A1 and A3, an additional hardware filter was added in line prior to the data acquisition. For the pore pressure transducers, the filter eliminated frequencies 100 Hz and above, which in prototype scale is a cut-off frequency of about 20 Hz. For the accelerometers the filter eliminated frequencies 1000 Hz and above, which in prototype scale is a cut-off frequency of about 200 Hz.

4.4.9 Data Acquisition

The analog signals from the various transducers were recorded using two IBM PC compatible computers each fitted with 16-channel data acquisition cards manufactured by RCElectronics. Each card has analog-to-digital conversion capability and an on-board buffer of 64k.

To optimize the sampling rate for the tests and preserve the data integrity, the transducers were split into two groups. In the first group 16 channels were recorded at a sampling interval of 2 msec for a total duration of 8 seconds. This group included all seven accelerometers, LVDT's L1 through L4, the shake-table LVDT, and pore pressure transducers P4, P5, P8, P9. The second group of 8 transducers was recorded at a sampling interval of 8 msec for a total duration of 32 seconds. This group included the pore pressure transducers P1, P2 , P3, P6, P7, P10 and the vertical settlement LVDT's L5, L6.

The data from each test was recorded in binary form which was then subsequently converted to an ASCII format. These basic data files were then in turn post-processed to transform the data to a prototype scale. The scaling factors to convert the data were computed for each model based on the length and density ratios determined for that particular model. The methodology followed was consistent with that outlined in Chapter 2, Section 2.3. In addition to the above, the data from the pore pressure transducers were filtered using a software low pass filter of 10 Hz prototype frequency. The data from the accelerometers were filtered using a software low pass filter of 20 Hz prototype frequency. This further cleaned the signals of some spurious higher frequency noise

which was outside the range of general interest for the model response of 0 to 10 Hz prototype frequency.

4.5 Accuracy of Experimental Measurements

There were two basic sets of measurements made in the model tests: measurements of model properties (density, void ratio, and saturation), and the measurements made with the various transducers placed in the model (acceleration, pore pressure, and displacement).

For the measurement of properties, an estimate of the maximum possible error was made by accounting for the potential error in each step of the methodology used to make the measurement. The estimates of the maximum error bound are given in Table 4-8, and it should be emphasized that these are likely maximum values and apply only to the one-g model properties.

For the measurements made with the transducers, there were two potential sources of error. The first was contained in the signal from the transducer itself, which has some calibration error and also amplification (or gain) errors. For this study the calibration errors were taken directly from the manufacturers specifications after prelimnary tests of the transducers confirmed the reported values. For the LVDT's, the manufactuerers specifications were not available and the potential calibration errors were based on measurements made in the Caltech Soils Laboratory. The remaining amplification or gain errors were taken to be 1%. This value was based on some measurements completed in the Caltech Soils Laboratory, and is consistent with values typically reported by manufacturers. The total estimated potential error bound in the signal itself is presented in Table 4-9.

The second source of error for the transducers is the resolution of the data acquisition system itself, which being digital, records the magnitude of the signal in small increments. The resolution corresponds to the smallest increment of data that can be recorded, or the threshold of the measurement. Given the range of the transducer, amplification, and the data acquisition specifications it was possible to calculate the resolution for the one-g model transducers, which is reported in Table 4-9 in prototype units. It should be noted that the magnitude of signal error (computed from the percentages) is linear with the amplitude of signal, whereas the magnitude of resolution is fixed and becomes more significant as the amplitude of the signal decreases.

4.6 References

Arulanandan, K. and R. F. Scott, eds., 1993, 1994, "Verification of Numerical Procedures for the Analysis of Soil Liquefaction Problems," Vol. 1, 1993; Vol. 2, 1994, Balkema, Rotterdam.

Housner, G. W., and D. E. Hudson, 1980, "Applied Mechanics Dynamics," Corrected 2nd Ed., California Inst. of Tech., Div. of Eng., USA.

Hushmand, B., R. F. Scott, and H. Rashidi, 1994, "VELACS model No. 3: Liquefaction in dense and loose sand columns," in Verification of Numerical Procedures for the Analysis of Soil Liquefaction Problems, Vol. 2, pp. 1415-1442, Arulanandan, K. and R. F. Scott, eds., Balkema, Rotterdam.

Scott, R. F., 1989, "Centrifuge and Modeling Technology: A Survey," Rev. Franc. Geotech., No. 48, pp 15-34, July.

Wakabayashi, M., 1986, "Design of Earthquake Resistant Buildings," McGraw Hill Inc., New York.

Table 4-1: Scaling factors for the One-g and Centrifuge Model 3.

Quantity to be scaled	One-g Scaling Factor Prototype to Model Ratio	Centrifuge Scaling Factor Prototype to Model Ratio
Displacement	≈ 25	50
Time (dynamic)	≈ 5	50
Velocity	≈ 5	1
Acceleration	1	0.02
Force	$\approx 16{,}000$	2,500
Energy, Moment	$\approx 390{,}000$	125,000
Moment of Inertia	$\approx 9{,}765{,}625$	6,250,000
Frequency	≈ 0.2	0.02
Time (diffusion)	≈ 25 if $c_v^* = n$ ≈ 125 if $c_v^* = n^{0.5}$	2,500

Table 4-2: Initial state of the Nevada sand in the Caltech Model 3 centrifuge test.

Potential range in the initial condition of the sand	Loose (left hand) column of sand		Dense (right hand) column of sand	
	Reported Values	Possible Values(1)	Reported Values	Possible Values(1)
Dry unit weight kN/m^3 (pcf)	15.13 (96.3)	15.33 (97.6)	16.26 (103.5)	16.45 (104.7)
Void Ratio	0.7305	0.7075	0.6102	0.5922
Relative Density (%)	41.9	48.0	73.8	78.6

(1) Possible values were computed considering the compressibility of the sand in the centrifuge model as discussed in Section 4.2.

Table 4-3: Centrifuge and shake-table laminar boxes.

Nominal dimensions of laminar box	Centrifuge (mm)	Shake-table (mm)	Ratio of Shake-table to Centrifuge box dimensions
Depth of sand	220	432	2.0
Width of box	178	350	2.0
Length of box	355	900	2.5

Table 4-4: Initial coordinate positions of the transducers in the centrifuge and one-g models.

Transducer	Initial position in centrifuge model(2)			Initial position in one-g models(2)		
Name(1)	x	y	z	x	y	z
P1	59.3	88.9	3.3	217.9	175.0	6.5
P2	296.3	88.9	3.3	683.3	175.0	6.5
P3	59.3	88.9	88.4	217.9	175.0	173.6
P4	133.4	88.9	88.4	363.4	175.0	173.6
P5	222.3	88.9	88.4	538.0	175.0	173.6
P6	296.3	88.9	88.4	683.3	175.0	173.6
P7	59.3	88.9	176.8	217.9	175.0	347.2
P8	133.4	88.9	176.8	363.4	175.0	347.2
P9	222.3	88.9	176.8	538.0	175.0	347.2
P10	296.3	88.9	176.8	683.3	175.0	347.2
A1	Array set on base plate of centrifuge model			Array set on base plate of shake-table for one-g models SM3B through SM3E.		
A2						
A3						
A2(3)				950.0	15.0	380.0
A3(3)				950.0	15.0	180.0
A4	88.9	76.2	176.8	276.0	149.9	347.2
A5	88.9	101.6	176.8	276.0	199.7	347.2
A6	266.7	76.2	176.8	625.2	149.9	347.2
A7	266.7	101.6	176.8	625.2	199.7	347.2
L1	368.3	71.1	68.1	950.0	175.0	133.7
L2	368.3	71.1	119.1	950.0	175.0	233.9
L3	368.3	71.1	169.9	950.0	175.0	333.6
L4	368.3	71.1	221	950.0	175.0	434.0
L5	73.7	88.9	223.5	246.2	88.9	432.0
L6	284.1	88.9	224.8	659.3	88.9	432.0

(1) In a transducer name, characters "P", "A", and "L" stand for pore pressure, accelerometer, and LVDT, respectively.

(2) The reference frame for the coordinates is shown on Figure 4-2.

(3) Transducers A2 and A3 were repositioned for the one-g models SM3F through SM3K.

Table 4-5: Description of the One-g models tested on the shake-table.

Model Name	Model Sand	Pore Fluid	Sand Column(1)	Relative Density (%)	Void Ratio	Dry unit weight		Degree of Saturation (%)
						kN/m^3	(pcf)	
SM3B	Nevada	Water	Prototype loose Prototype dense	49 73	0.7041 0.6137	15.36 16.22	(97.8) (103.3)	95.8
SM3C	Nevada	Water	Prototype loose Prototype dense	41 64	0.7336 0.6484	15.10 15.88	(96.1) (101.1)	96.4
SM3D	Blend 6-1	Water	Prototype loose Prototype dense	51 79	0.7203 0.6349	15.16 16.95	(96.5) (101.5)	96.2
SM3E	Nevada	Water	Prototype loose only	41	0.7317	15.12	(96.2)	91.4
SM3F	Nevada	Water	Scaled loose Scaled dense	33 51	0.7632 0.6971	14.85 15.43	(94.5) (98.2)	92.4
SM3G	Blend 6-1	Water	Scaled loose Scaled dense	32 63	0.7787 0.6818	14.66 15.51	(93.3) (98.7)	96.6
SM3H	Nevada	Dry	Scaled loose Scaled dense	22 63	0.8089 0.6819	14.42 15.51	(91.2) (98.7)	-
SM3I	Nevada	Water	Scaled loose only	35	0.7558	14.91	(94.9)	94.4
SM3J	Nevada	Water	Scaled loose Scaled dense	29 62	0.7772 0.6559	14.73 15.81	(93.8) (100.6)	93.7
SM3K	Blend 6-1	Water & Glycerin	Scaled loose Scaled dense	28 57	0.7813 0.6747	14.70 15.63	(93.5) (99.5)	96.9

(1) Loose and dense refer to the left and right-hand sides of the model respectively. "Prototype" implies that no scaling of the initial state of the sand was performed, whereas "Scaled" implies that scaling was completed consistent with the proposed modeling method as described in Chapter 2, Sections 2.3 and 2.4.

Table 4-6: Performance specification for shake-table.

Type of motion generated	Table Capacity		Maximum Stroke
Random	6g (RMS) with 160 kg pay load	12g (RMS) with 45 kg pay load	± 25 mm
Sinusoidal	10g with 160 kg pay load	20g with 45 kg pay load	± 25 mm

Table 4-7: Comparison of sand model and laminar box properties.

	Mass (kg)	Upper bound(1) of shear modulus, $G_{s.}$ (MPa).	Lower bound(2) of shear modulus, $G_{s.}$ (MPa).	Upper bound of equivalent stiffness, *k.* (kN/m)	Lower bound of equivalent stiffness, *k.* (kN/m)
Sand Model	250	15.0	40.0	10,988.4	732.6
Laminar Box	45	1.0	1.0	232.6	5.8

(1) Based on low shear strains and the upper range of confining stresses in the models.
(2) Based on upper range of shear strains observed in the models and the lower range of confining stresses in the model.

Table 4-8: Maximum likely error bounds for the properties of the models.

Property of One-g Model	Estimated Maximum Error
Density	± 1.9%
Void Ratio	± 2.8%
Saturation	± 7.9%

Table 4-9: Maximum likely error bounds for transducer measurements.

Measurement	Transducer Designation	Signal error	Resolution in prototype units
Acceleration	A1 through A3	± 1.1%	0.001 g
	A4 through A7	± 2%	0.005 g
Pore Pressure	P7 and P10	± 1.2%	0.2 kPa
	P1 through P6, P8, P9	± 2.2%	1.3 kPa
Displacement	L1 through L6, and Table LVDT	± 1.5%	0.25 mm

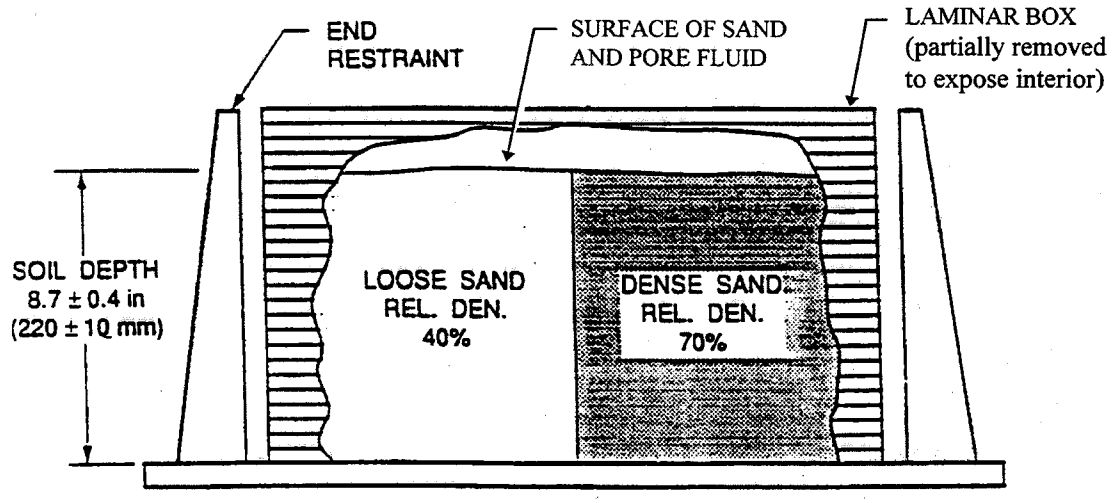

(a) Elevation

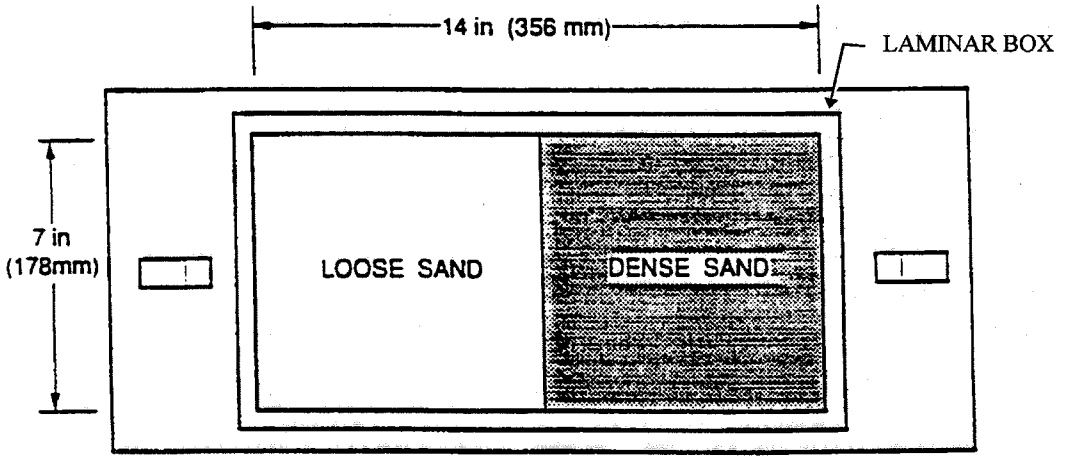

(b) Plan View

Figure 4-1: Geometry of the Caltech Model 3 VELACS Centrifuge test.

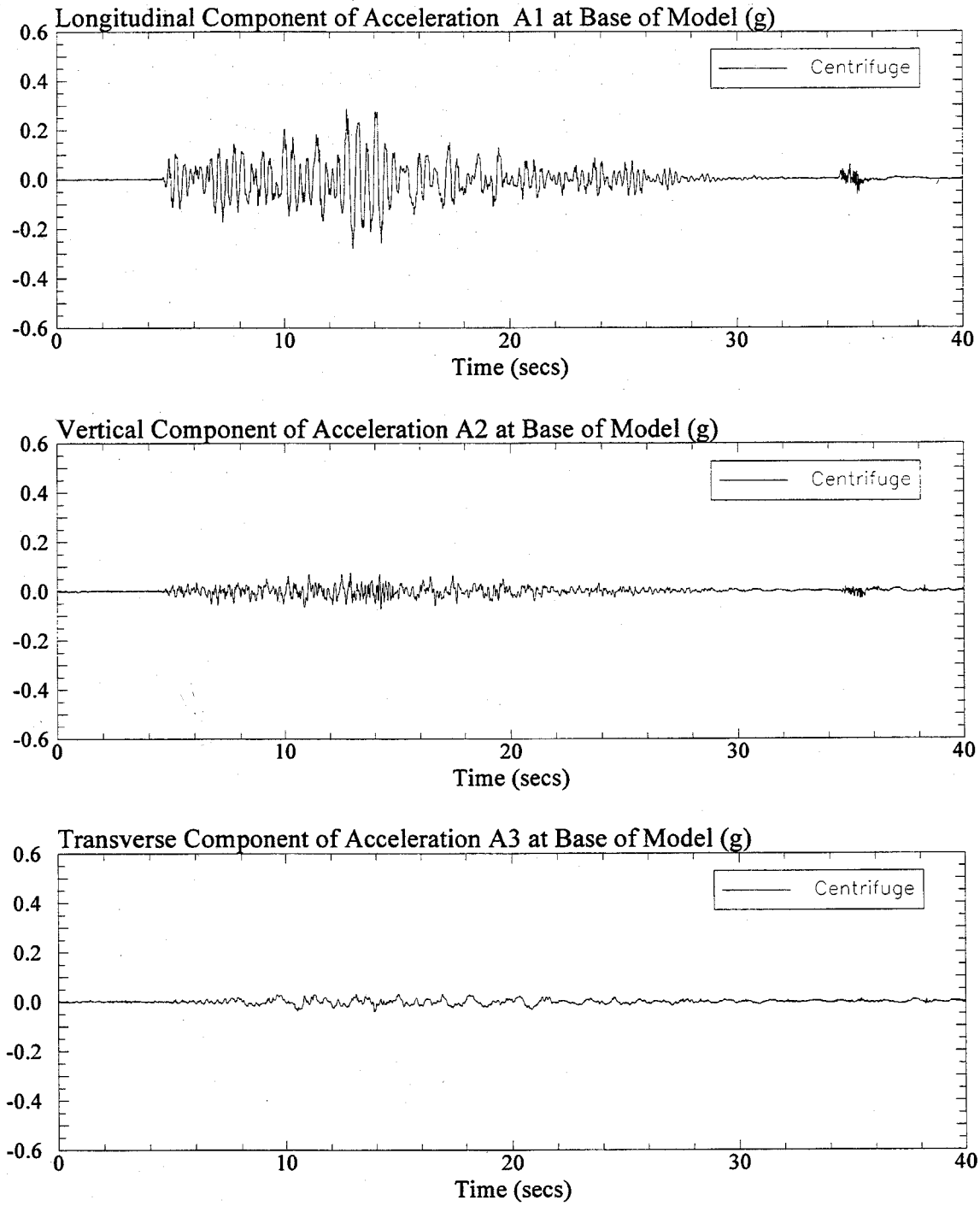

Figure 4-2: Longitudinal, vertical, and transverse components of the recorded acceleration (prototype scale) at the base of the Centrifuge Model 3. Signals were post-processed with a low pass filter of 20 Hz.

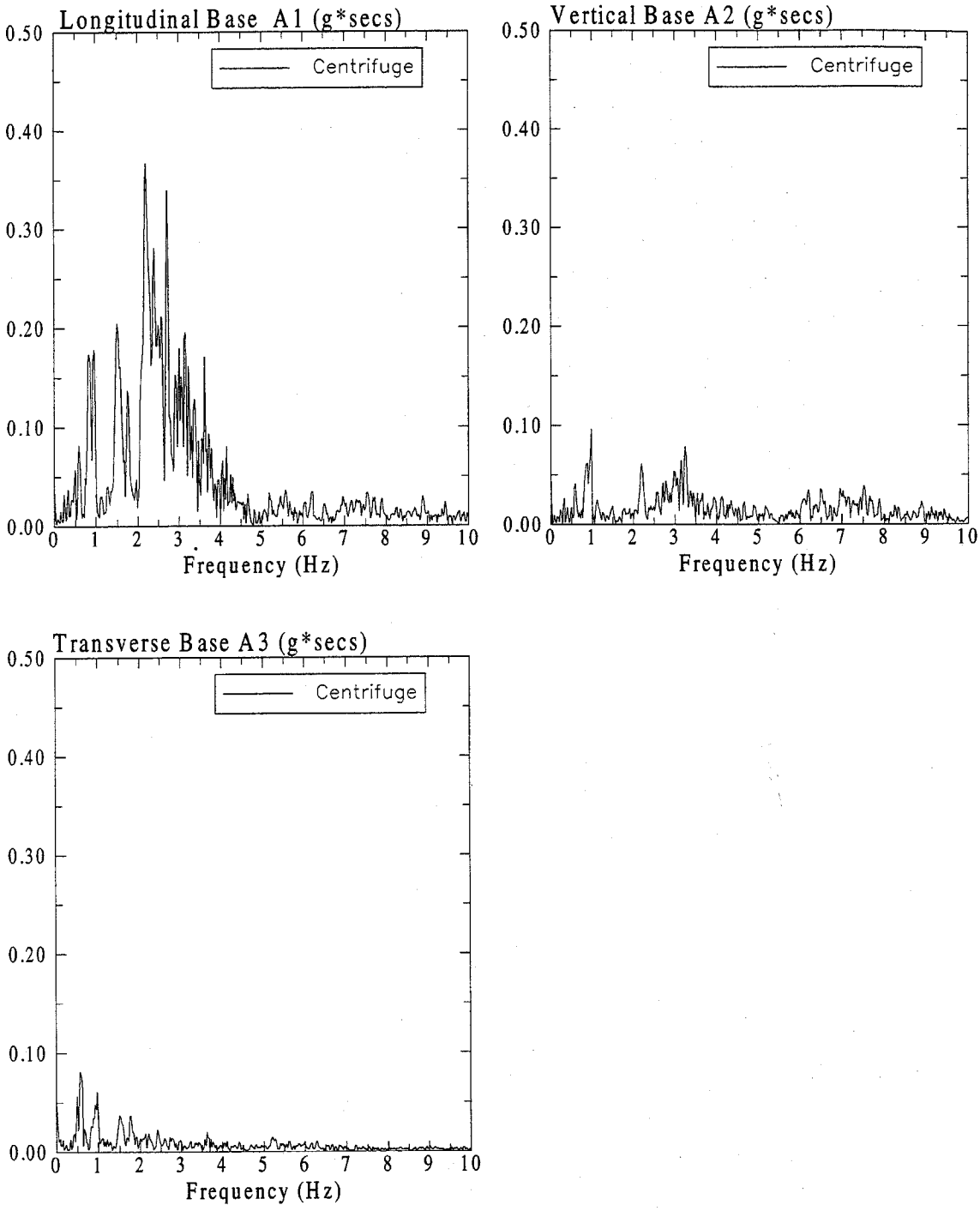

Figure 4-3: Fast Fourier Transforms (prototype scale) of the longitudinal, vertical, and transverse components of recorded acceleration at the base of the Centrifuge Model 3.

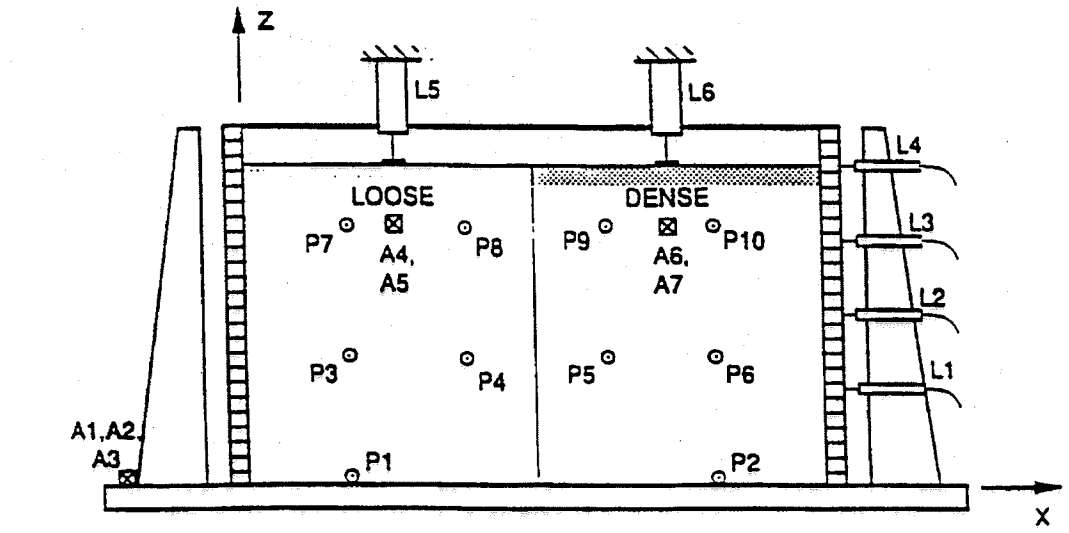

⊙ Pore Pressure Transducer

⊠ Horizontal & Vertical Accelerometers

Displacement Transducer (LVDT)

(a) Front View Elevation

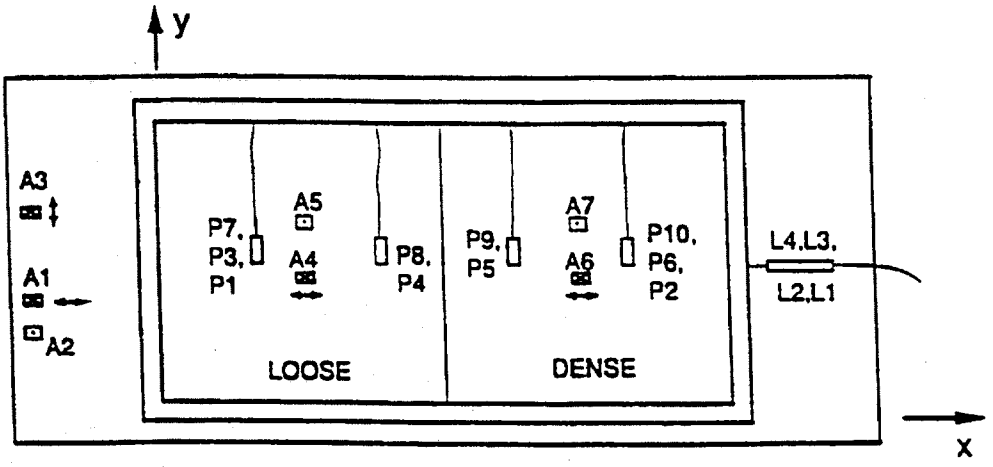

(b) Plan View

Figure 4-4: Array of transducers for the Caltech Model 3 VELACS Centrifuge test. Note that "A", "P", and "L" denote accelerometer, pore pressure transducer, and LVDT, respectively.

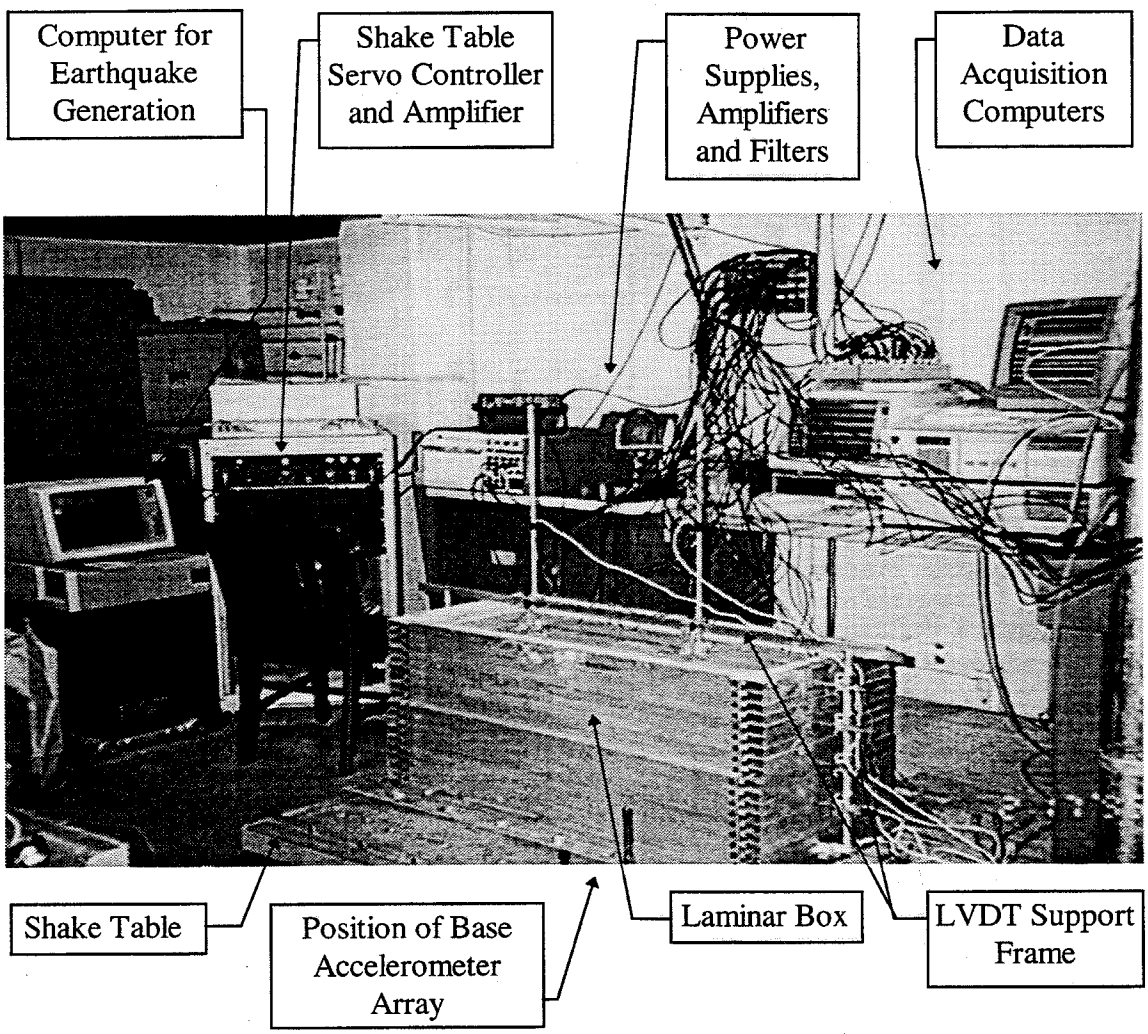

Figure 4-5: Typical experimental setup for a one-g model test.

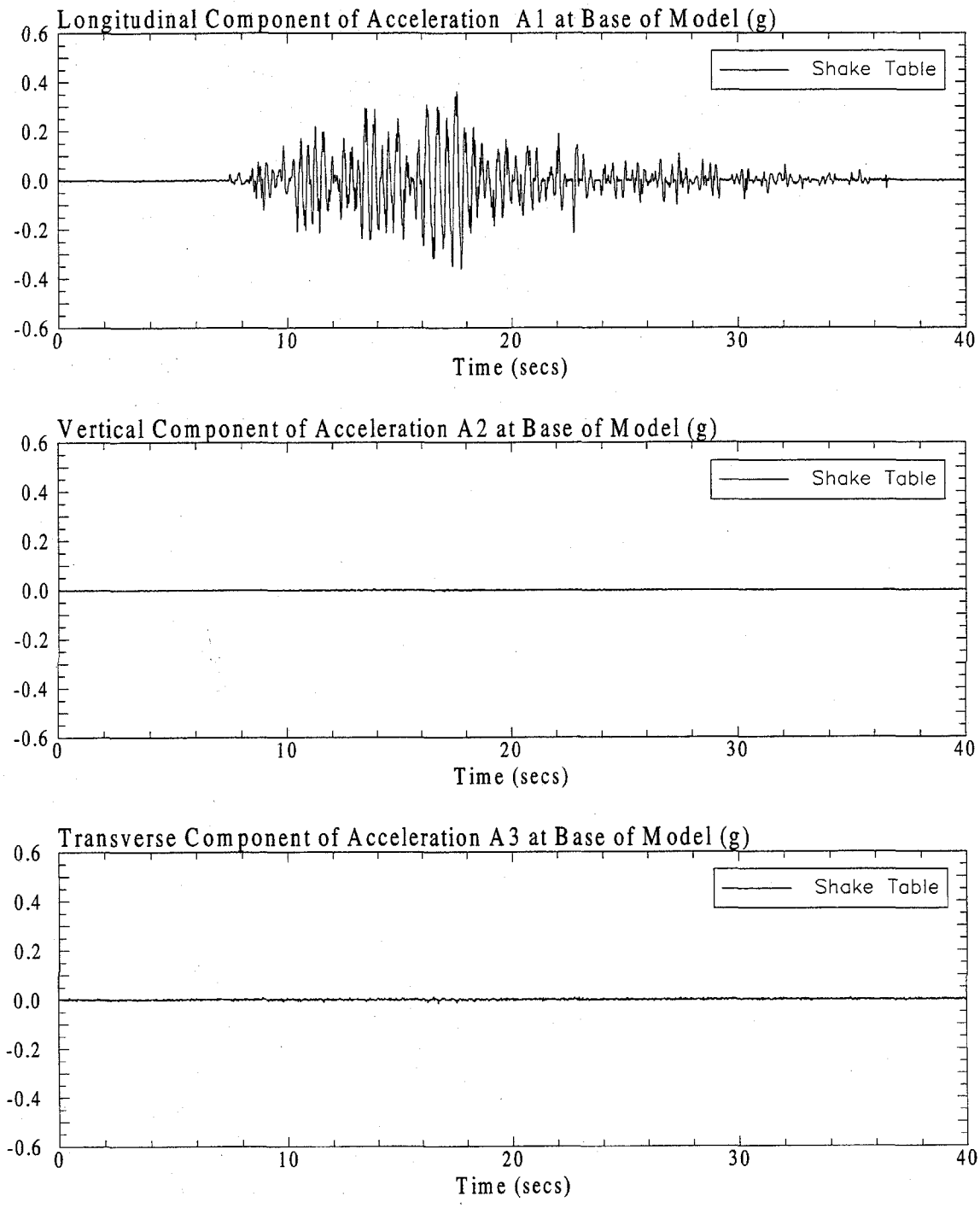

Figure 4-6: The longitudinal, vertical, and transverse components of the recorded acceleration (prototype scale) at the base of the one-g model SM3C. Signals were post-processed with a low pass filter of 20 Hz.

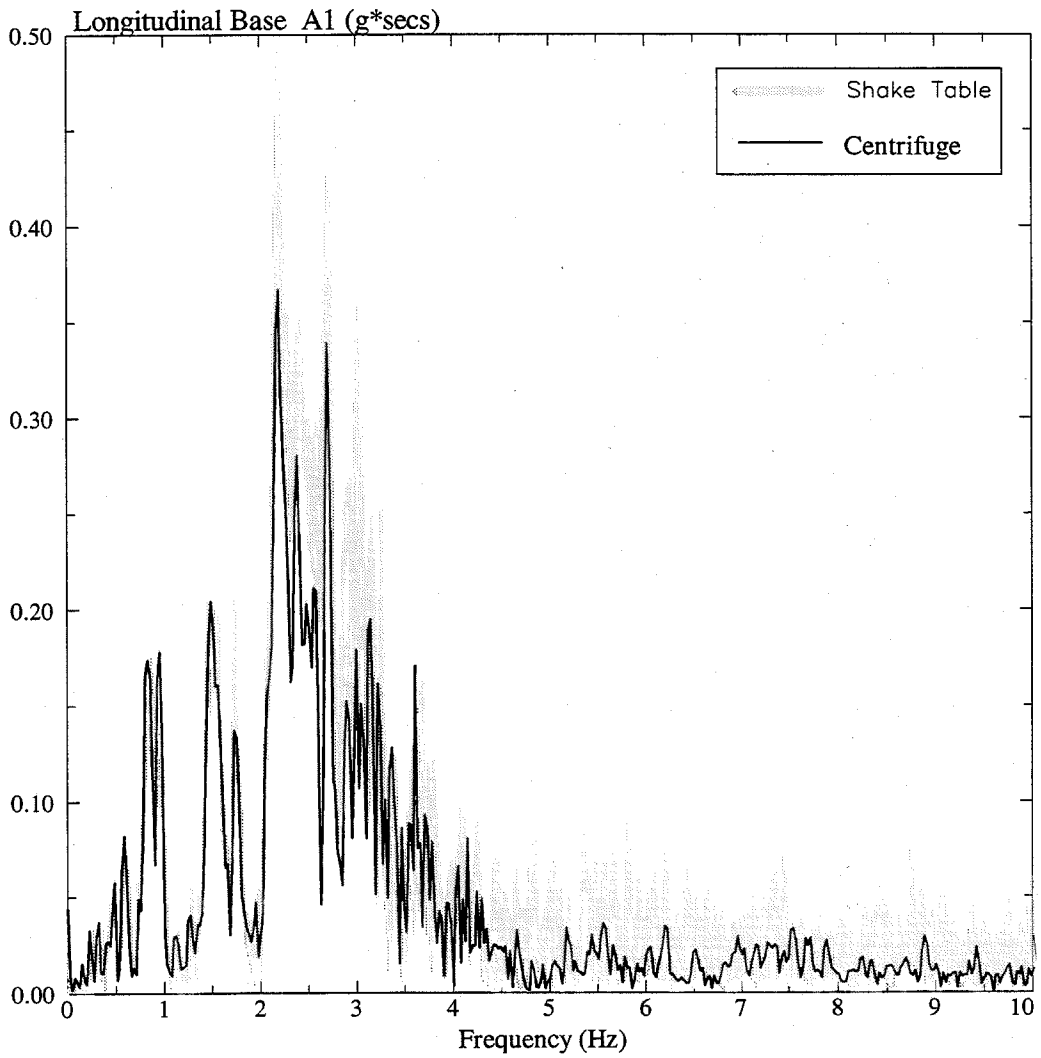

Figure 4-7: Comparison of the FFT's (prototype scale) of the one-g model earthquakes, which were created on the shake table, with the FFT of the longitudinal component of the prototype (centrifuge) earthquake.

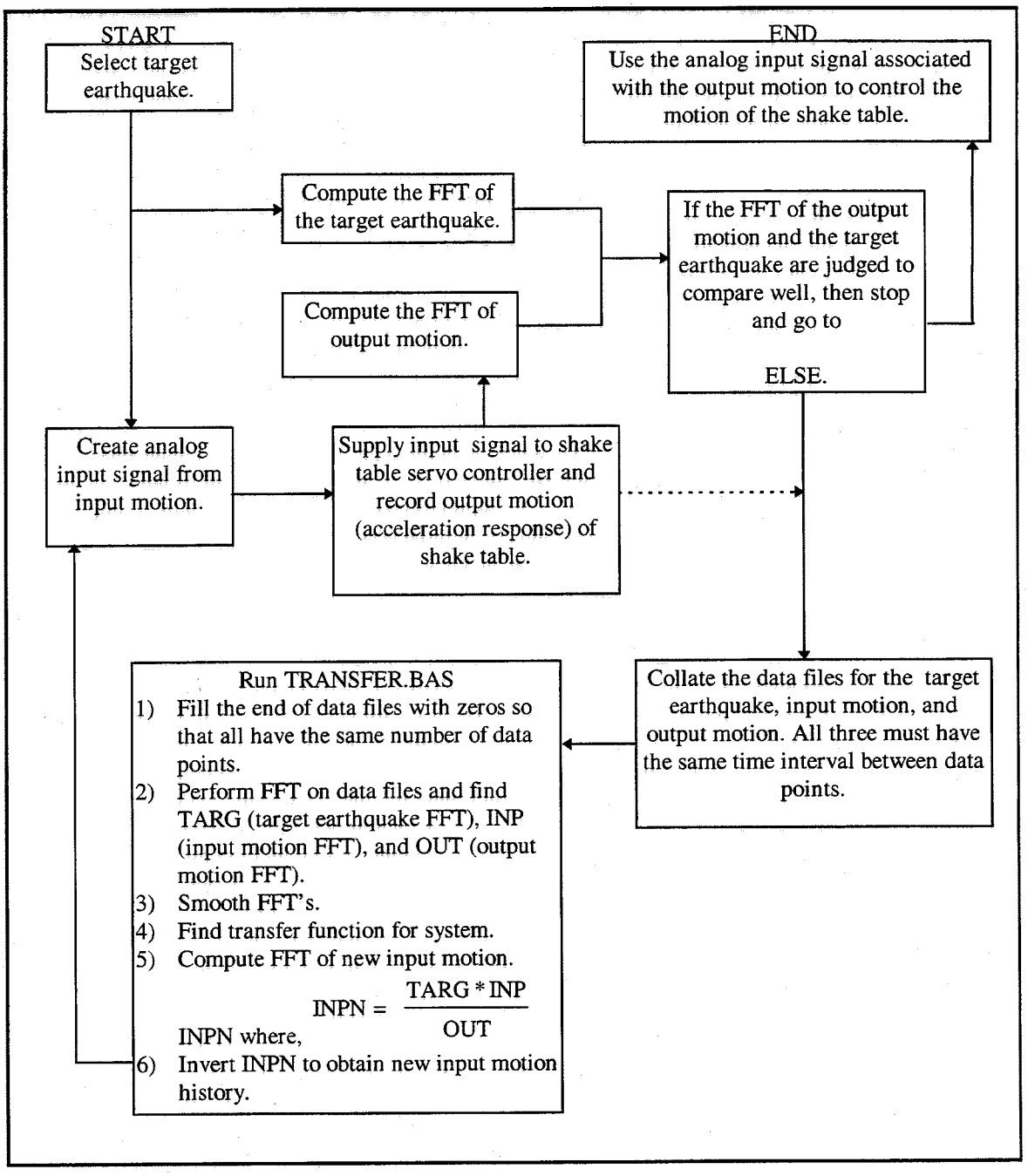

Figure 4-8: Procedure followed to obtain a prescribed earthquake motion for the shake table.

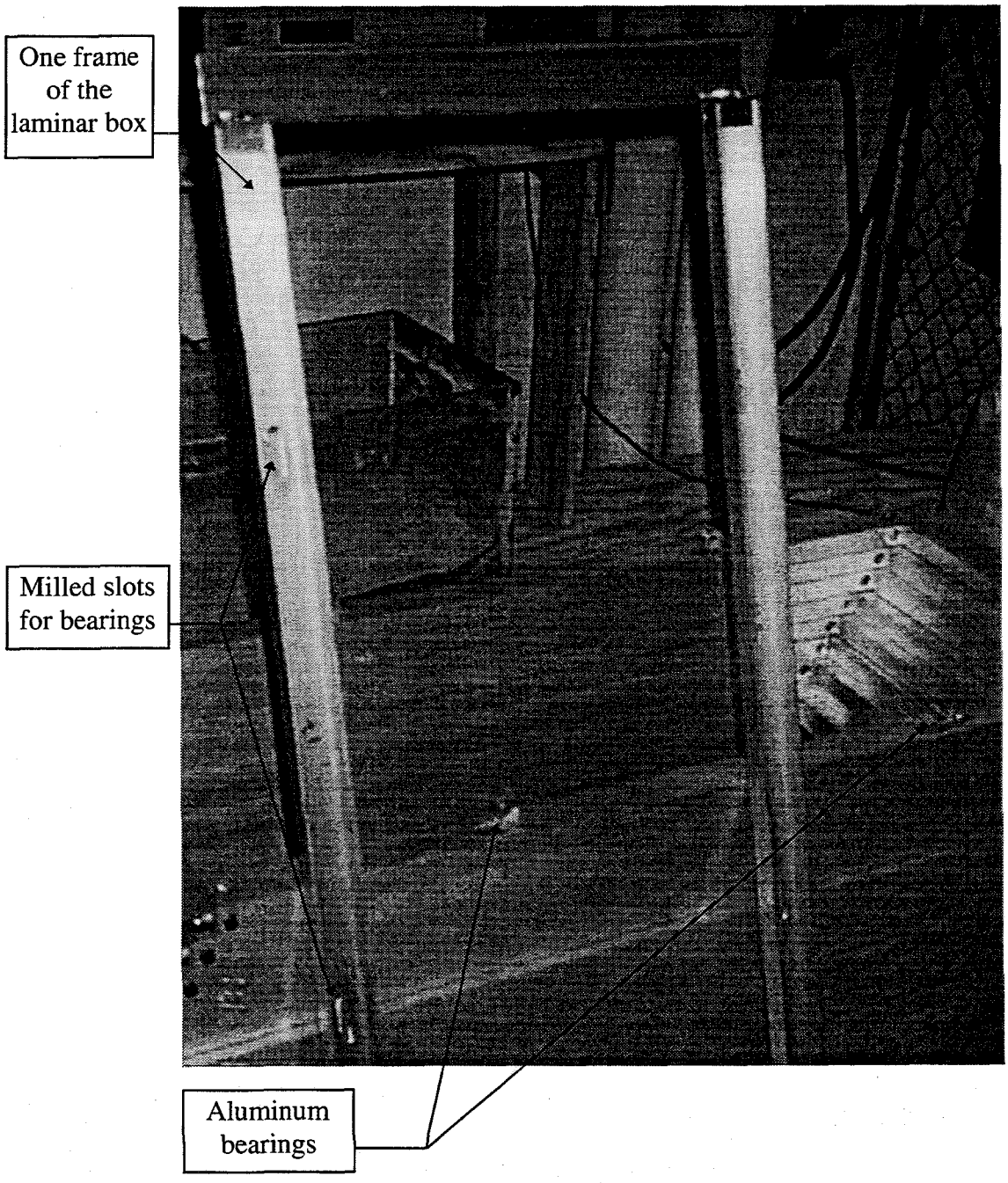

Figure 4-9: Details of the laminar box frames and bearings.

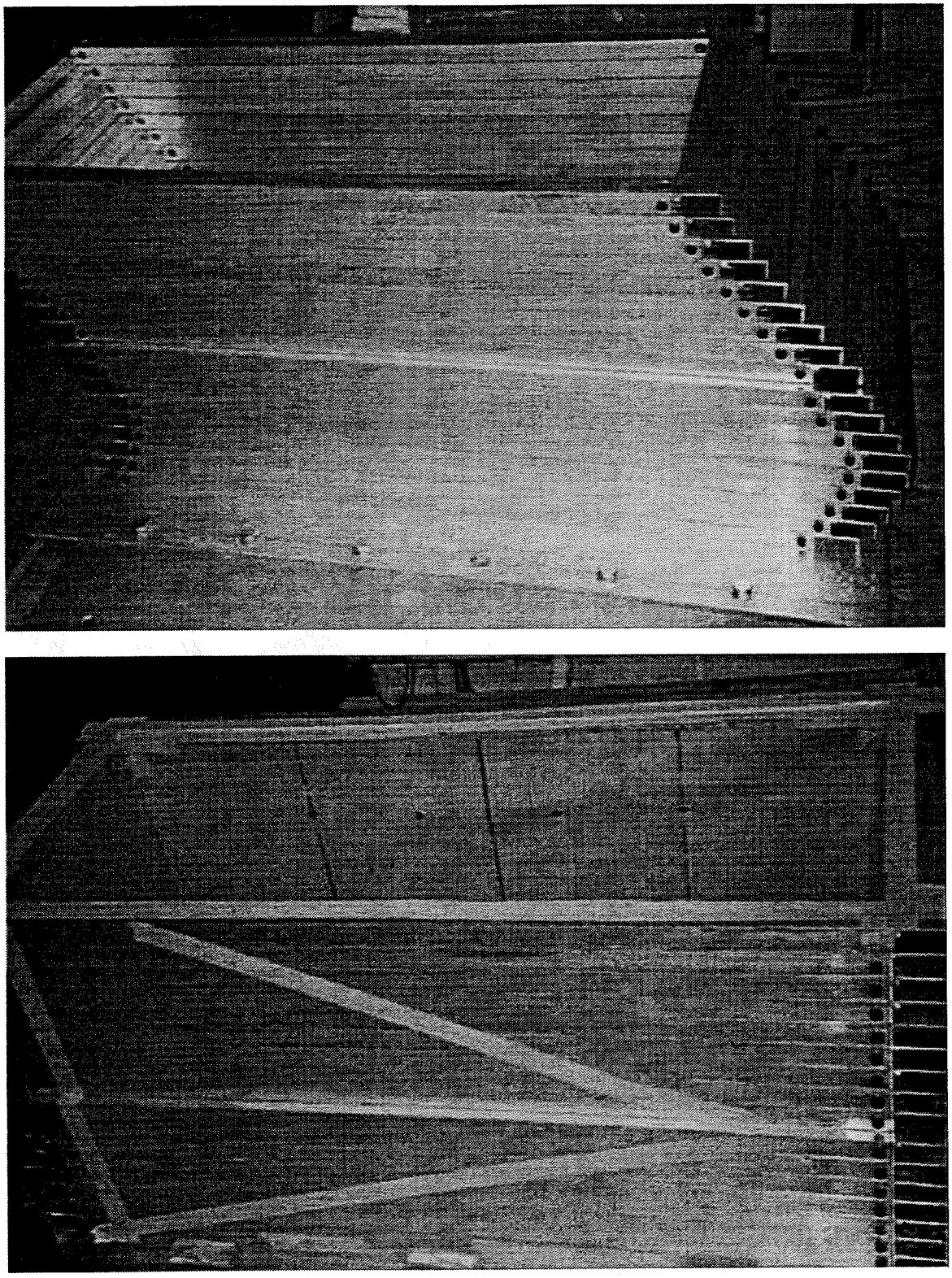

Figure 4-10: The laminar box in a deformed shape, and the laminar box prepared for model construction with the latex rubber liner in place.

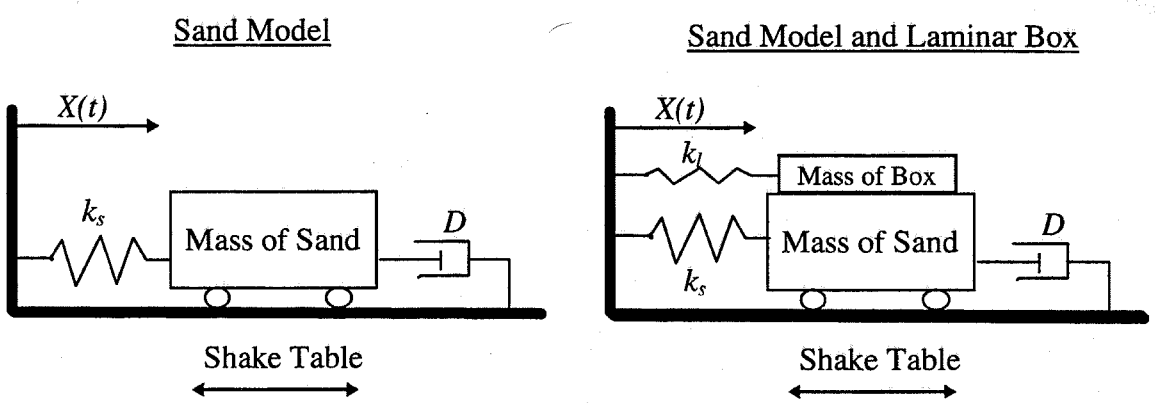

(a)

Comparison of the magnitude of the steady state response for the idealizations above, normalized with respect to the static displacment.

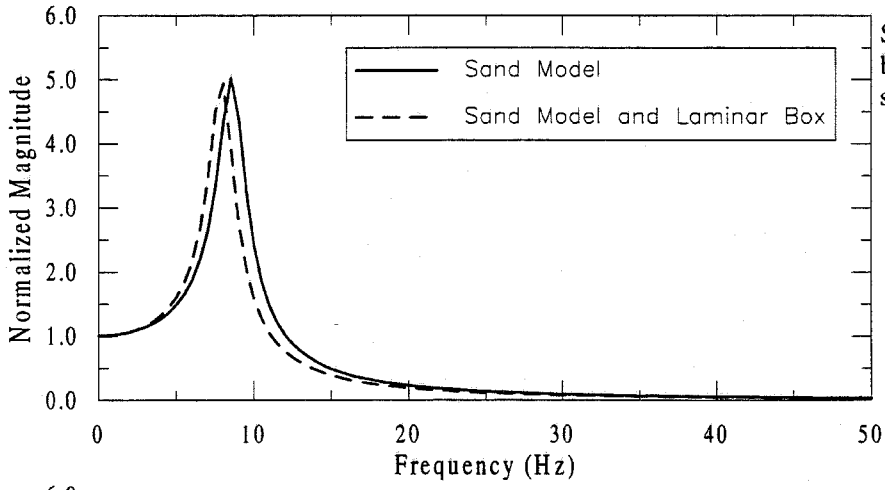

Solutions for the lower bound of expected shear moduli

(b)

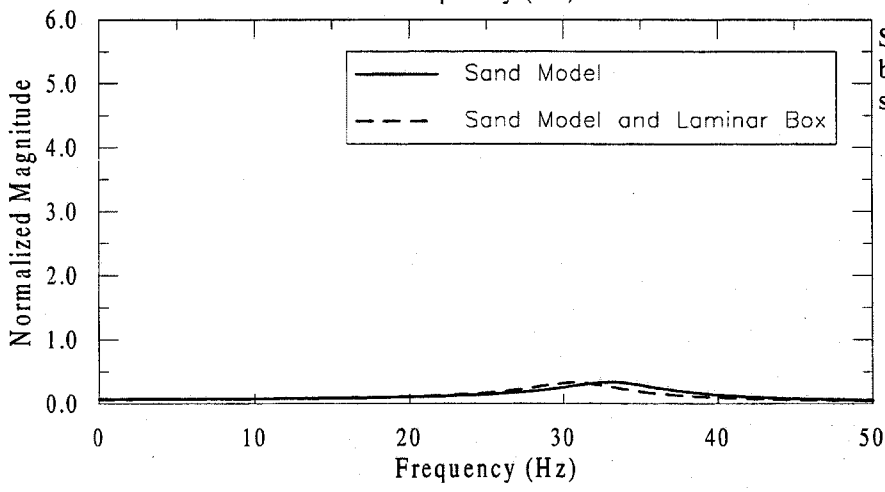

Solutions for the upper bound of expected shear moduli

(c)

Figure 4-11: Simple idealization of sand model and laminar box for the steady state response over the expected range of shear moduli for a sinusoidal excitation.

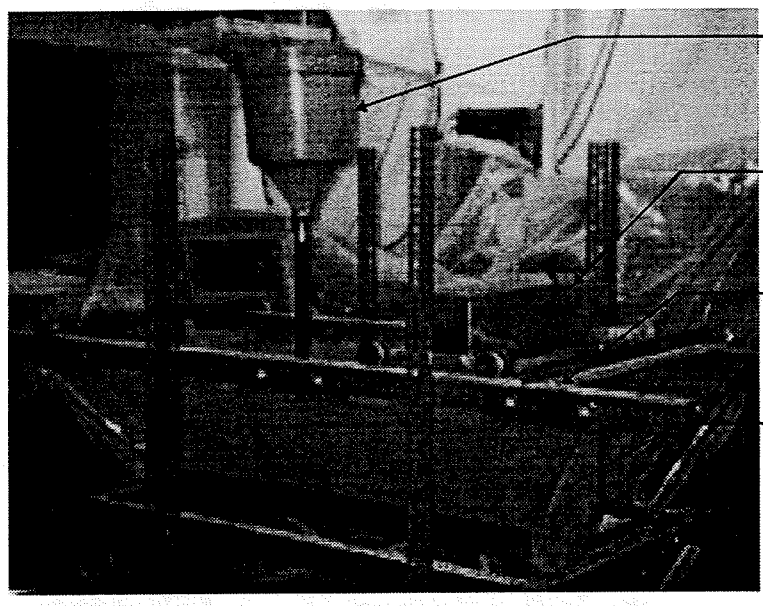

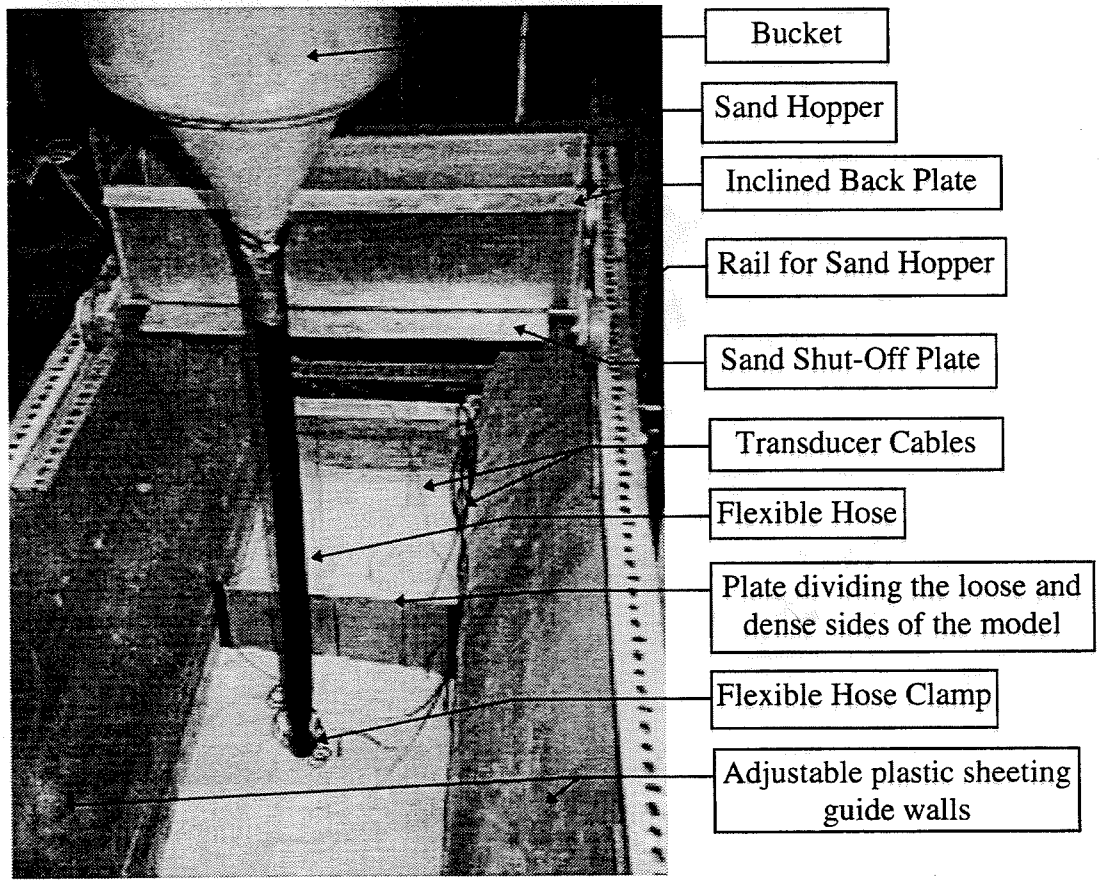

Figure 4-12: Photographs of the sand hopper and the bucket with a flexible hose, which were used to place the sand in the models.

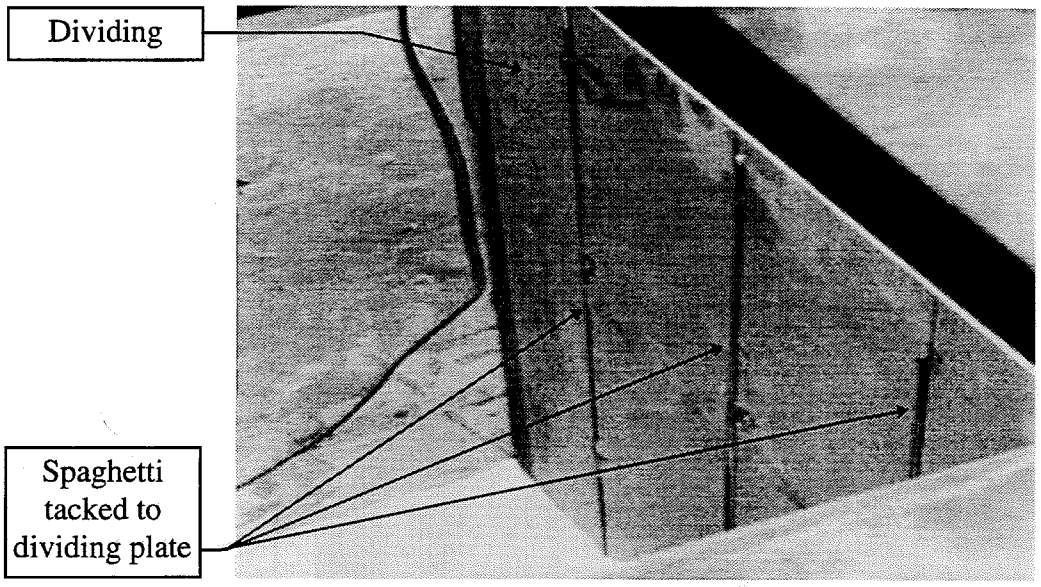

(a)

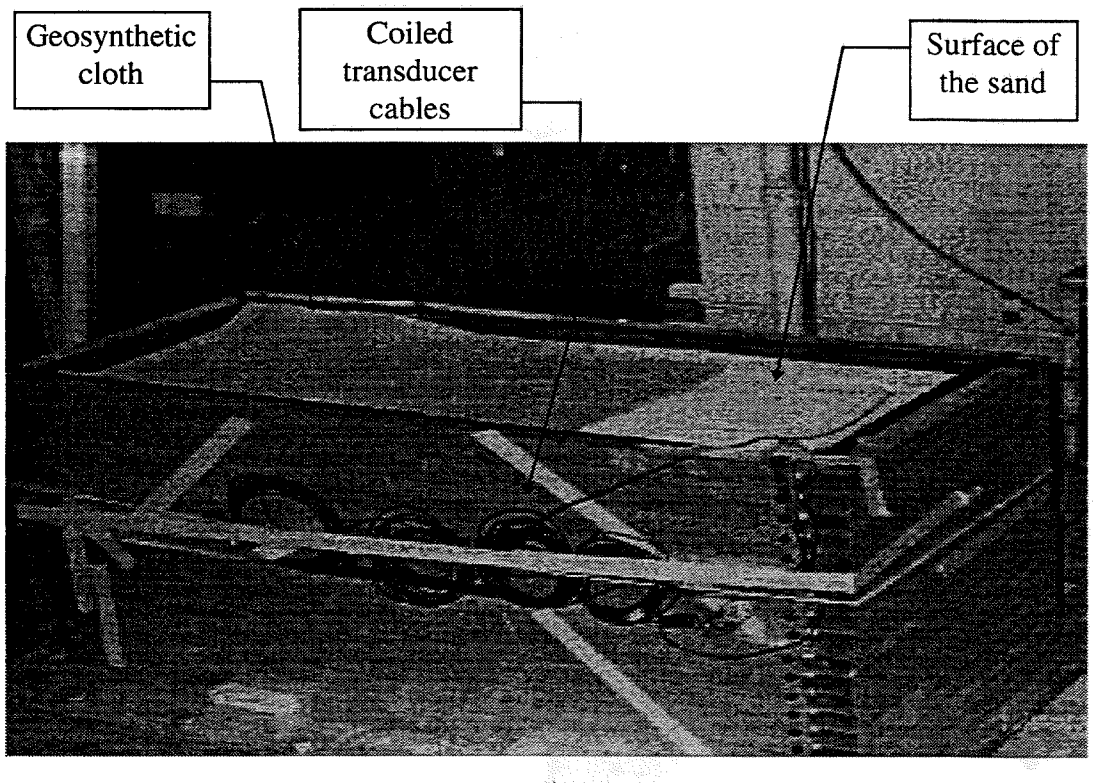

(b)

Figure 4-13: (a) Model divider plate and, (b), completed model ready for saturation.

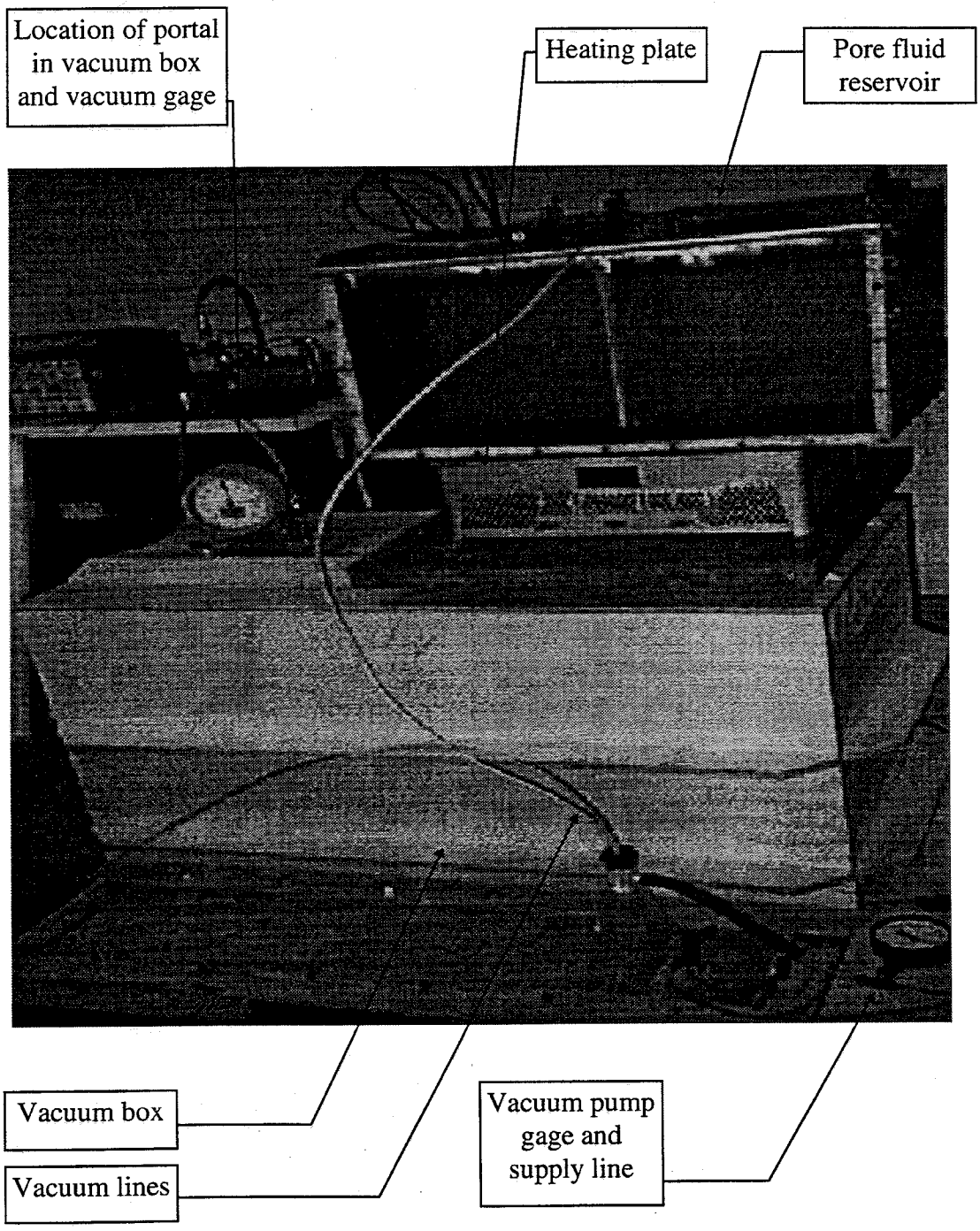

Figure 4-14: De-airing and saturation of model.

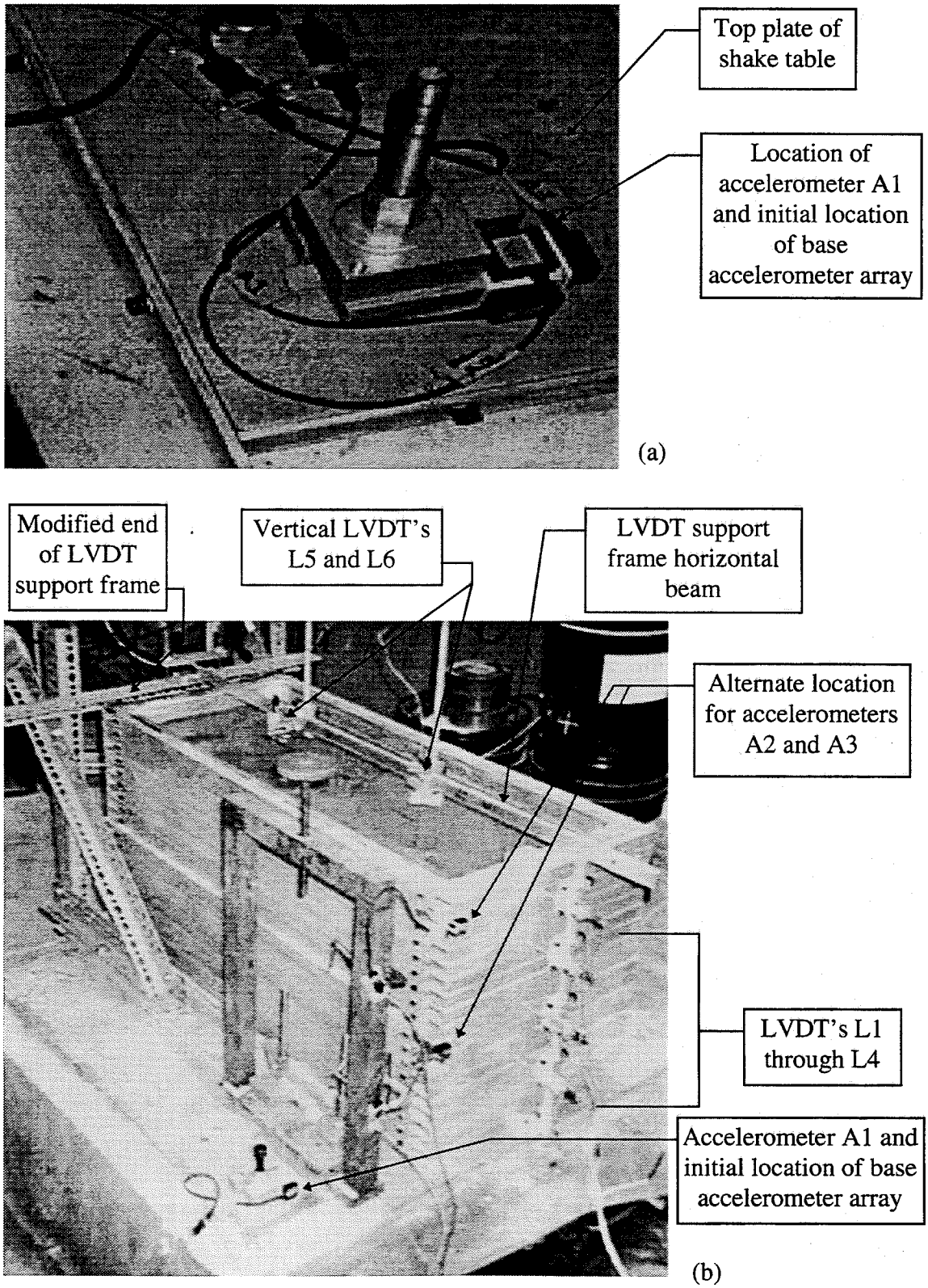

Figure 15: Instrumentation locations and setup.

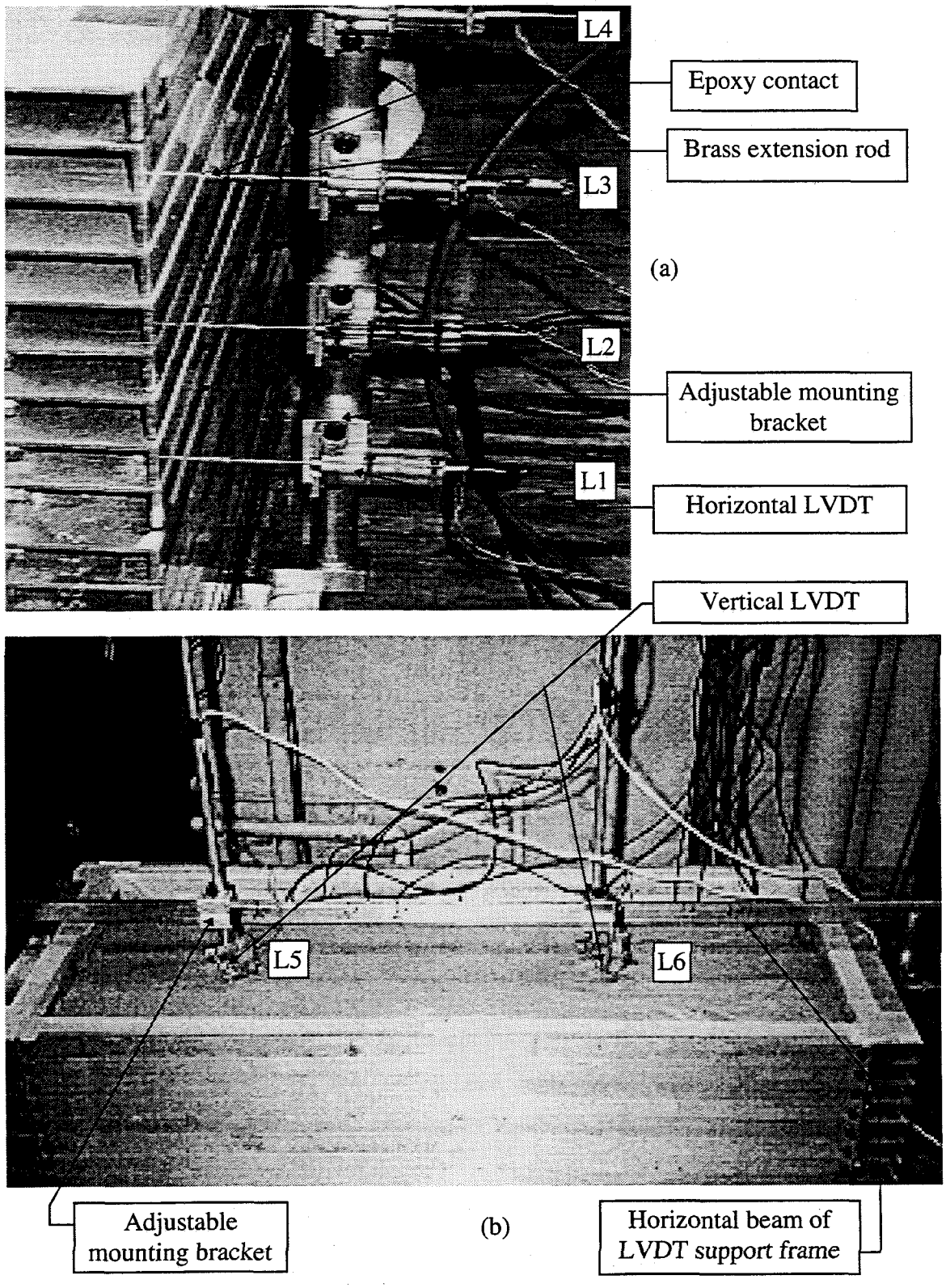

Figure 4-16: Setup of LVDT's L1 through L6.

Chapter 5

RESULTS OF MODEL TESTING

5.1 Introduction

The results of the centrifuge Model 3 test and the results of shake table one-g models are presented in this chapter. The centrifuge and one-g models are compared and discussed. A number of comparisons are also made between the various one-g models in order to explore the validity or otherwise of the scaling techniques presented in Chapter 2. The comparisons can be summarized as follows:

1) Centrifuge Model 3 compared to one-g models prepared at similar densities.

2) Centrifuge Model 3 compared to one-g models prepared at scaled densities in accordance with the scaling techniques described in Chapter 2.

3) One-g models constructed of different materials (Nevada sand and Blend 6-1 sand) at similar densities.

4) One-g models constructed with different pore fluids.

In addition the results also provide some insight into the behavior of a saturated sand subjected to an earthquake. The general behavior of saturated sands under dynamic loads was discussed in Chapter 2. The particular aspects of the behavior exhibited in the model tests can be summarized as follows:

1) The behavior of dry versus saturated sand.

2) The behavior of saturated loose and dense sands, adjacent to each other subjected to an earthquake.

3) The magnitude and rate of surface settlement and the dissipation of excess pore pressures.

Finally, the results and experience gained from the testing raise some issues about physical modeling methods (one-g and centrifuge) used to model the behavior of a saturated sand. The potential issues of concern are summarized as follows:

1) Repeatability of testing.

2) Effect of saturation.

3) Appropriate scaling of time.

All of the above items are discussed in more detail below.

5.2 Test Results from the Centrifuge and One-g Models

A description of the centrifuge Model 3 test (Hushmand et al., 1994) and a detailed description of the one-g models prepared as part of this research were given in Chapter 4. Ten one-g models were constructed with an initial configuration as summarized in Table 5-1. Each model was subjected to a series of model earthquakes created on the shake table, and a total of 73 tests were performed on the ten models.

The one-g models were tested at a range of densities, with the sand placed in a loose and dense state emulating the Model 3 configuration in some tests, and also in a uniform state throughout the laminar box in others. An alternative sand and pore fluid were also used in some of the models. In this discussion it is not possible to present the results for each of these tests, instead 20 representative tests have been selected for presentation and these are listed in Table 5-1.

The data are presented in Appendix B in a series of eight standard plots for each model test. The results are all given in terms of prototype values which were obtained by scaling the model test results using the scaling relations. The time is presented in terms of the dynamic time scale. The corresponding page numbers in Appendix B for each test are given in Table 5-1. Table 5-2 gives a generic description of the standard plots and identifies the transducer signals presented in each. The locations of the transducers are shown in the schematic cross section below Table 5-2.

To assist in making some general comparisons between the test results of the centrifuge and the one-g models, Table 5-3 presents some basic indexes of the observed behavior. In Table 5-3, the

one-g models have been grouped into their basic categories of model type. The indexes of observed behavior include:

- The initial relative density of the model prior to being subjected to the model earthquake.
- The maximum longitudinal acceleration recorded in the model at accelerometer A4.
- The maximum peak to peak average shear strains recorded at the end of the laminar box at LVDT's L1 and L4.
- The maximum excess pore pressure and pore pressure ratio, R_u , at the base transducers P1 and P2 (where R_u is the ratio of excess pore water pressure to the initial vertical effective stress). The estimated initial vertical effective stress at the pore pressure transducer locations in the models is given in Table 5-4.
- An approximate estimate of the time taken to fully dissipate the pore pressures at transducers P1 using the plotted data (note that the time scale is dynamic). It should be noted that the time at P2 was always approximately equal to that at P1.
- The settlements recorded at the surface of the model at LVDT's L5 and L6.

Unless otherwise noted all of the results presented in this chapter, as in Appendix B, have been scaled to prototype values. The scale factors used for each model are listed in Table 5-5, which were derived using the initial conditions of each model in accordance with the theory outlined in Chapter 2, Section 2.3. For the time scaling the dynamic time scale factor, t_d^*, was used. It should be noted that the scale factors, n, σ^* and t_d^* , for the subsequent tests of the same one-g model, for example SM3F8 and SM3J8, change slightly due to the settlement of the model surface created in prior tests of the model. The greatest variation calculated in these scaling factors was about +4% from the initial values presented in Table 5-5. For the sake of ease in processing the data, the initial scale factors were used to process the data for all subsequent tests completed on a single model. The remaining scale factors presented in Table 5-5, c_v^* and t_c^* , which are far more dependent on the density of the sand, change significantly under repeated testing; however, they are not directly used in the scaling of the test results.

The following general comments are made regarding the post test excavation to locate transducers and the final position of the softened spaghetti placed at the interface of the loose and dense columns of sand:

- The excavation was made after a model had been subjected to several tests; therefore, the measurements are indicative of trends in deformation only for the particular set of model tests.

- The transducers indicated that vertical downward movement occurred by an amount proportional to the settlement observed at the surface of the model immediately above the transducer. It appeared that, as expected, the transducers followed the deformations occurring in the sand.

- The softened spaghetti generally indicated that the dense column of sand penetrated the loose column. The amount of lateral movement was most pronounced at the surface of the model, decreasing with depth to a point one-half to two-thirds down in the model where no deformation was observed. In some cases the measurements indicated that below this depth some lateral movement may have occurred in the opposite direction, that is from loose to dense. However, the resolution of the measurements was inadequate to be conclusive.

- The final locations of the pore pressure transducers near the interface of the loose and dense columns of sand did indicate lateral movements consistent with that observed in the softened spaghetti.

The following sections describe the results from the model testing and make some qualitative comparisons. A more detailed analysis of the results is presented in Chapter 6.

5.2.1 Centrifuge Model 3

The data recorded at the transducers of the centrifuge Model 3 test (Hushmand et al., 1994) are reproduced in eight figures in Appendix B, pages B-4 through B-11, as indicated on Table 5-1.

The first two figures, pages B-4 and B-5, were previously presented in Chapter 4 and present the accelerations in the three components recorded at the base of the centrifuge model in terms of a time history and the Fast Fourier Transforms (FFT's), respectively.

The third figure, page B-6, shows the data recorded by the accelerometers A4 through A7 which were located below the surface of the model within the sand to record the longitudinal and vertical components of acceleration in the loose and dense halves of the model. A comparison of the accelerations indicates the response of the loose and dense halves of the box were very similar to each other. The magnitude of the longitudinal accelerations was about 60% of the

longitudinal base accelerations indicating that some attenuation of the longitudinal motions occurred as they propagated up through the model. The vertical component was similar in magnitude to the base vertical acceleration. These observations are also supported by the FFT data presented in the fourth figure, page B-7.

The transfer function of the centrifuge Model 3 is presented in Figure 5-1, and was computed from the ratio of the FFT's of the accelerations at A4 and A6 to the FFT of the base acceleration A1. The transfer function shows attenuation in the frequency range of about 1.5 to 4 Hz, which corresponds to the frequency range of greatest energy of the input earthquake (see page B-5, FFT of A1). This is consistent with the lower magnitude of accelerations observed at accelerometers A4 and A6. Outside of this frequency range, the transfer function in Figure 5-1 indicates amplification of the base motion occurred. This amplification generally occurred over the frequency range where lower energies were observed in the input earthquake.

The displacements recorded at the end of the model laminar box are presented in the fifth figure, page B-8. The data indicates that the displacement increased approximately linearly with height which implies the deformation was dominated by the first shear mode. The maximum peak to peak shear strains generated during the test were on the order of 1.5% as indicated in Table 5-3. After the shaking had ceased, there was residual displacement recorded by all the transverse LVDT's, with a maximum on the order of 40 mm at LVDT L4.

The excess pore pressures recorded in Model 3 are presented in the final three figures, pages B-9 through B-11. Each of these figures follows a vertical section (A, B, C, or D on Table 5-2) through the model at the location of the four vertical lines of pore pressure transducers. The initial vertical stresses at each of the transducer locations are given in Table 5-4. The results indicate that excess pore pressures were generated for about 12 seconds (starting at 6 seconds and continuing to 18 seconds) which corresponds to the time in which the base accelerations generally equaled or exceeded an input acceleration of about 0.15g and the level of peak to peak shear strains were on the order of 0.8%. The maximum excess pore pressures that were generated were generally well below the initial vertical effective stresses except in the upper portions of the model. The estimated maximum ratio, R_u , of excess pore water pressure to the initial effective stress was as follows:

Transducer	R_u	Transducer	R_u
P7, P10	98%	P8, P10	72%
P3, P4	67%	P5, P6	57%
P1	44%	P2	36%

Noting that R_u = 100% implies liquefaction, these results indicate that the centrifuge model liquefied in the upper portion of the loose sand and possibly near the surface of the dense sand. After significant shaking had stopped, the excess pore water pressures began to dissipate, and were fully dissipated in about 130 seconds (Table 5-3). During the generation and dissipation of the excess pore water pressures, the magnitudes were very similar along horizontal sections through the model, that is through P1 to P2, P3 to P6, and P7 to P10. It appears that the patterns of pore pressure behavior were very similar for the loose and dense halves of the model.

The settlement recorded at the surface of Model 3, at LVDT L5 and L6, is presented above the plots of the excess pore water pressures (pages B-9 through B-11). The magnitude of the surface settlement in the loose sand was about 175 mm, and in the dense sand was about 250 mm (Table 5-3). The majority of the settlement occurred during the period of significant shaking, but a residual amount occurred as the pore pressure continued to dissipate after the shaking had ceased. The final settlement in the loose sand was significantly less than the dense sand which is contrary to expectations. If densification of the sand was the only factor, then the loose column should have settled more than the dense column of sand. Hushmand et al. (1994) hypothesize that this occurred because the dense sand column penetrated laterally into the loose sand which in the upper layers had liquefied. The penetration would inhibit settlement in the loose column of sand and increase it in the dense sand column. This hypothesis was supported by data collected in the UC Davis test, which indicated that the interface of the dense and loose halves of the box had deflected mostly toward the loose sand column.

A final point on the magnitude of the settlements observed in the centrifuge Model 3: no mention is made by Hushmand et al. (1994) regarding the final configuration of the surface of the model. It is well known that if the sand softens sufficiently in the centrifuge during a test, the surface will become curved due the radial field exerted on the model by the centripetal accelerations while the centrifuge is in flight. Two millimeters of vertical movement in the centrifuge equates to 100mm of prototype settlement. If such curvature did occur in Model 3, then the magnitude of the

settlements could have been affected, though the relative difference reported for LVDT's L5 and L6 should remain unaffected.

5.2.2 One-g Models

Of the 73 one-g model tests performed, 20 have been selected for inclusion in Appendix B as indicated on Table 5-1. In general the models were all subjected to very similar earthquake motions in each of the tests conducted, as described in Chapter 4, Section 4.4.1. The recorded input earthquake for each test is presented in the first and second figures of the standard plots presented in Appendix B, and unless specifically identified it is assumed in the following discussion that the slight variations in the earthquake motions from test to test were a minor factor contributing to the observed differences between model tests.

5.2.3 Comparison of Model Results

5.2.3.1 Centrifuge Model 3 and One-g Models at Prototype Densities

Two one-g models, SM3B and SM3C, were constructed with the initial configuration of the centrifuge Model 3. The models were constructed from Nevada sand which was placed at prototype values of density, and water was used as the pore fluid. The results of the first tests performed on each model, SM3B1 and SM3C1, are presented in Appendix B, pages B-12 through B-18, in accordance with the standard figures described in Table 5-2.

From Table 5-3, the initial densities in the loose half of the models SM3B and SM3C spanned the possible range of relative densities which existed in the centrifuge Model 3. In the dense half the relative densities were lower than the targeted value especially in SM3C1. From Table 5-3 the basic behavior of the SM3B1 and SM3C1 appeared to be quite similar. The acceleration response of the two models was very comparable to each other, as evidenced by the transfer functions plotted in Figure 5-2a. The pore pressure response in both models was almost identical. The one major difference between the tests was the surface settlement recorded in the loose sand, which was 60 mm in SM3B1 and 109 mm in SM3C1. This difference could have been a consequence of the lower initial density of the loose sand in SM3C1, creating the potential for greater densification of the sand column. As indicated on Table 5-3, the settlement on the dense sides of the two models was almost identical.

For the purposes of comparison with the centrifuge Model 3, test SM3C1 has been selected. Figure 5-2b compares the transfer functions of Model 3 and SM3C1. It is evident that above frequencies of about 1.5 Hz, the attenuation is far greater in SM3C1 than Model 3. The reason for this is apparent when the excess pore pressures are compared in Figures 5-3 and 5-4. The pore pressures from SM3C1 are significantly greater than in Model 3, and from Table 5-3 it is apparent that SM3C1 fully liquefied in the loose sand and in the majority of the dense sand. This is in contrast to the far lower excess pore pressures recorded in Model 3, which would consequently exhibit stiffer behavior because of the existence of higher effective stresses. Therefore, the acceleration recorded in Model 3 would be expected to be higher, as observed. At the low frequencies (long period) the effect would be less significant as apparent from Figure 5-2b for frequencies less than 1.5 Hz.

The observed higher pore pressures in the one-g models compared to the centrifuge Model 3 is in contrast to what would typically be expected from our understanding of saturated sand behavior. As discussed in Chapter 2, Section 2.2, if two sands are placed at the same density, but at different confining pressures, the sand at a higher confining pressure would generate higher pore pressures under similar earthquake excitations. Given that the centrifuge is subjecting the sand to far higher confining pressures than the one-g model (approximately 25 times greater), it should generate higher excess pore pressures. The opposite has been observed, and the reason for this lies in the basic incompatibility between the dynamic time scales and the dissipation time scales inherent in the modeling techniques as previously discussed in Chapter 2, Section 2.6. The effect of the incompatibility as it relates to the model tests performed is discussed in detail in Chapter 6.

The settlements observed in SM3B1 and SM3C1 differed from the centrifuge Model 3 in three general respects.

1) The magnitude of the settlements in the one-g models was significantly less than the centrifuge.

2) The settlement in the loose sand was greater than in the dense sand whereas the opposite was observed in the centrifuge.

3) About 50 to 60% of the final settlements in the one-g tests occurred during the earthquake, and the remainder occurred as the excess pore pressures dissipated after shaking ceased. In the centrifuge the majority of the settlement occurred during the earthquake.

The difference in the magnitudes of the settlement could be related to possible curvature occurring in the centrifuge model as discussed in Section 5.2.1 above, or the fact that the acceleration response of the centrifuge model was higher than the one-g model (by up to a factor of 2 or more) which may have induced greater densification of the sand columns. The opposite trend observed in settlements from the loose to dense halves of the model is more difficult to explain because of the influence of the pore pressures which were significantly different between the one-g and centrifuge models. The one-g models did exhibit similar deformation behavior at the interface of the loose and dense halves of the model as observed in the centrifuge model. However, the degree to which the dense sand penetrates the loose column and inhibits settlement is a delicate balance between the relative strengths of the sand columns which change as the model as the excess pore pressures develop. This is discussed further in Section 5.3.3 below, along with a discussion regarding the rate of settlements observed.

In summary, the one-g models constructed at similar densities to the centrifuge model behaved differently. There was a significant difference between the observed excess pore pressures in the centrifuge and one-g models and the trend was contrary to the expected behavior of saturated sands in general. However, the observed trend was consistent in light of the scaling factors which govern the respective modeling techniques. Given the differences in the modeling techniques and the behavior of the excess pore pressure, it appears that a valid identification between the one-g model results and the centrifuge model resuilts is not achievable.

5.2.3.2 Centrifuge Model 3 and One-g Models at Scaled Densities

The one-g models, SM3F and SM3J, were also constructed to represent the geometry of the centrifuge Model 3, but the sand was placed at densities which had been scaled using the constitutive scaling technique described in Chapter 2, Section 2.4. The models were constructed from Nevada sand, and water was used as the pore fluid. The results of SM3F1 are presented in Appendix B, pages B-40 through B-47, and SM3J1 are presented in Appendix B, pages B-133 through B-140, in accordance with the standard figures described in Table 5-2.

The initial values of the relative density and void ratios in these models have been scaled to prototype values in accordance with the constitutive scaling described in Chapter 2. The scaled values of the model densities are presented in Table 5-6. The initial void ratio of the loose and dense halves of the model (which were determined after the model was constructed) have been scaled using the two alternate steady state lines (SSL's) presented in Chapter 3, Section 3.6. The

values based on the Been et al. (1993) SSL result in lower scaled void ratios (or higher scaled relative densities) than the values based on the Fit 2 SSL.

For the test SM3F1 the scaled values for the relative density of the loose sand fall within the range of values of the prototype relative densities for the centrifuge Model 3, which from Table 5-1 is 42 to 48%. The scaled values for the dense sand are somewhat lower than the corresponding range in prototype densities which from Table 5-1 is 74 to 79%. For test SM3J the scaled values of relative density correlate very closely to the range of prototype relative densities.

From Table 5-3 the basic behavior of the SM3F1 and SM3J1 appeared to be quite similar with the exception of the settlements, which are discussed below in more detail. In comparison with SM3B1 and SM3C1, which were described in the previous section, the behavior is also similar, although in SM3F1 and SM3J1, in the dense sand the excess pore pressures were larger, and in the loose sand they were generated faster and remained at the maximum excess pressure for a longer period of time. For the purposes of comparison, selected results of SM3J1 are compared with SM3C1. The excess pore pressures are compared in Figures 5-5 and 5-6 confirming the above comments. The differences in the excess pore pressures should be expected because SM3F1 and SM3J1 were deliberately placed in a looser state on account of the constitutive scaling method. In terms of the acceleration response, the behavior of SM3J1 and SM3C1 were very similar as indicated in Figure 5-7 which compares the transfer functions for the two tests.

The surface settlements (Table 5-3) in SM3F1 and SM3J1 were of similar magnitude but the trend was opposite. The loose (L5) column settled more than the dense (L6) column in SM3J1, but the opposite was observed in SM3F. The tests SM3B1 and SM3C1 followed the same trend as SM3J1 but the loose settlement was 2 to 3 times that of the dense settlement. In Figure 5-5, it appears that the settlement at L5 in the test SM3J1 was impeded from about 16 to 22 seconds in comparison to SM3C1. This time frame corresponds to the development of full excess pore pressures in P1. In fact for SM3F1 the settlement observed at L5, at a similar stage in the record, indicated that heave actually occurred (Appendix B, page B-45) and explains why the loose sand settled less than the dense in that test. It is hypothesized that the lower relative density in the dense sand in SM3F1 in comparison to SM3J1 was enough to exaggerate the observed effect which is discussed further in Section 5.3.4. The presence of heaving in SM3J1 and SM3F1, and the absence of it in SM3B1 and SM3C1, adds credence to the discussion made in Section 5.2.3.1 above.

With regard to a comparison of the results of SM3F1 and SM3J1 with the centrifuge Model 3, the same conclusions drawn in Section 5.2.3.1 apply, except as noted above for observed settlements, which at least suggest a trend similar to that observed in the centrifuge. Finally, it is also possible to compare the shear strains (which were not available for SM3B and SM3C). From Table 5-3 the average shear strains, computed from the displacements at L1 and L4, are comparable between the centrifuge and the one g models, SM3F1 and SM3J1, except the shear strains in the upper portion of the one-g models are less and in the lower portions are perhaps greater. This indicates that in the one-g models, the lower portions were softer which is consistent with the development of higher excess pore pressures, and in the upper portions the response was lower which is consistent with the recorded accelerations indicated by Figure 5-7.

In summary, the one-g models SM3F and SM3J behaved similarly to the one-g models SM3B and SM3C. However, higher excess pore pressures were generated This should be expected because of the lower density of the sand placed in these models to conform to the constitutive scaling technique. The higher excess pore pressures and lower densities in SM3F and SM3J resulted in slightly "softer" behavior than SM3B and SM3C. The conclusions drawn in Section 5.2.3.1 apply to the one-g models SM3F1 and SM3J1 with regard to a comparison with the results of centrifuge Model 3.

5.2.3.3 One-g Models with Alternate Sand

Two one-g models, SM3D and SM3G, were constructed with the loose and dense columns of sand as in SM3J1 and SM3F1, except an alternative sand, the Blend 6-1 sand, was used. The pore fluid was water. As indicated on Table 5-1, SM3D was constructed with initial densities approximating the upper range of the prototype densities, and SM3G was constructed at lower densities. The initial void ratios achieved in SM3G were scaled to equivalent prototype values following the technique described in Chapter 2, Section 2.4 and using the SSL's presented in Chapter 3, Section 3.6. The prototype values of void ratio and relative densities of SM3G1 were in the range of the prototype densities as indicated on Table 5-6. The results of SM3D1 are presented in Appendix B, pages B-26 through B-32, and SM3G1 are presented in Appendix B, pages B-56 through B-63, in accordance with the standard figures described in Table 5-2.

In comparison to each other, SM3D1 behaved in a slightly stiffer manner than SM3G1, exhibiting a higher acceleration response in the upper part of the model. Also, the pore pressures generated in SM3D1 were slightly lower than SM3G1. These trends should be expected given the

contrast in the densities of the models. The behavior of the surface settlements is discussed below.

In a general comparison with the one-g models constructed of Nevada sand, Table 5-3 indicates that SM3D1 and SM3G1 performed in a similar fashion. The major exception was the time taken for the pore pressures to dissipate (R_u=0), which in SM3D1 and SM3G1 occurred about 5 to 10 times faster than in the Nevada sand models. This is a direct consequence of the higher permeability of the Blend 6-1 sand which is approximately eight times more permeable than Nevada sand (Chapter 3, Section 3.3).

SM3D1, which has similar densities to SM3B1 and SM3C1, showed slightly stiffer behavior reflecting its slightly higher densities. Its relative settlements in the loose and dense columns of sand exhibited a similar trend, but the magnitudes were slightly higher and the majority of the settlement occurred during the earthquake. The test SM3G1 has similar densities to SM3F1 and SM3J1, and for the purposes of comparison the results from SM3G1 are compared with SM3J1.

Figures 5-8 and 5-9 show the pore pressures and settlements recorded in SM3G1 and SM3J1. As noted above, the excess pore pressures generated during shaking are quite comparable, but the dissipation rates are different. The settlements of the two models follow a similar trend, but the settlement in SM3G1 is initiated as soon as shaking starts and occurs more rapidly, and apparently tracks the faster dissipation rate of the excess pore pressures. At L5, there is evidence of greater heave occurring in SM3G1 than SM3J1 during the period of maximum excess pore pressures. This heaving behavior resulted in the settlement in the loose column of sand (L5) being less than the dense column of sand (L6), which is the trend observed in SM3F1 and the centrifuge Model 3. The acceleration response of the SM3J1 and SM3G1 are compared in Figure 5-10, which shows a close correlation except that there appears to be a slight shift in the frequency content. Considering the very different composition of the two model sands, the match in Figure 5-10 is quite surprising. The shear deformation behavior of the two models was almost identical as indicated in Table 5-3, and evident from comparing the two standard figures included in Appendix B, pages B-137 and B-60.

In summary, the models constructed of the Blend 6-1 sand behaved in a very similar manner to their counterparts constructed of Nevada sand, except, the dissipation of the excess pore pressures and rate of settlement occurred 5 to 10 times faster, and the magnitudes of the settlements were slightly greater.

5.2.3.4 One-g Model with a Different Pore Fluid

A one-g model, SM3K, was constructed with an alternative pore fluid to explore the possibility of using the properties of the pore fluid to remedy the incompatibility that exists between the dynamic and dissipation time scales as discussed in Chapter 2, Section 2.6. There are two aspects that require resolution as follows:

1) Can the viscosity of the pore fluid be scaled to produce a targeted adjustment to the dissipation time scale, and will this produce the desired results in an actual test?

2) Given the modifications to the pore fluid, will other aspects of the test, such as the dynamic response and settlements, be affected?

To this end SM3K was constructed using the Blend 6-1 sand and a mixture of water and glycerin as the pore fluid. The results of SM3K1 are presented in Appendix B, pages B-149 through B-156, in accordance with the standard figures described in Table 5-2.

Two other one-g models were selected for comparison with SM3K, or perhaps more appropriately for the calibration of SM3K. The first of these models was SM3G, as described in Section 5.2.3.3 above. Essentially SM3K was a repeat of SM3G but the pore fluid was changed from water to a mixture of glycerin and water (glycerin/water). From Table 5-3 the relative densities achieved in the model SM3K were very close to those obtained in SM3G. The results of tests performed on these models are compared below in order to address item 2) above to ascertain the effect that the modified pore fluid might have on the model response.

In Section 5.2.3.3, SM3G1 was compared to the test SM3J1, which, as described in Section 5.2.3.2. was constructed from Nevada sand using water as a pore fluid. The comparison of the results from SM3J1 and SM3G1 found the behaviors to be quite similar, except the excess pore pressures dissipated far faster in SM3G1. Based on this observation, the dynamic viscosity of the glycerin/water pore fluid in model SM3K was increased in order to match the longer dissipation time observed in SM3J1. A subsequent comparison of the results from test SM3K1 with SM3J1 would address item 1) raised above.

The required dynamic viscosity for the glycerin/water pore fluid was estimated by equating the coefficient of consolidation, c_v, for SM3K1 to the computed value for SM3J1. Using the equations 2-16 and 2-17 (Chapter 2) and the properties for the permeability and compressibility presented in Chapter 3 which primarily determine c_v, it was determined that the viscosity should

be about 16 times greater than the water used in the other one-g models. Of this amount, the permeability contrast between SM3J and SM3K required a viscosity eight times greater, and the compressibility contrast required viscosity about two times greater, giving the total of 16. The actual dynamic viscosity of the final glycerin/water mixture at the model test temperature was 16.8 times greater than that of the water used in SM3J1, as reported in Chapter 4, Section 4.4.5.

The excess pore water pressure curves for SM3J1 and SM3K1 are compared in Figures 5-11 and 5-12. The generation and dissipation phases are quite similar, except the estimated time to dissipate the excess pore pressures is about 1.5 times longer in SM3K1 than that observed in SM3J1 (Table 5-3). This implies the viscosity of the glycerin/water pore fluid was too high. If the dissipation times of the two tests are equated using a simple one-dimensional consolidation approach (Equation 2-15), the actual coefficient of consolidation in SM3K1 was about two thirds that of SM3J1. If the test was repeated, presumably increasing the dynamic viscosity of the pore fluid by about 11 times instead of 16 times would account for the observed discrepancy in the dissipation times. The concept behind the scaling of the pore fluid is explored further in Chapter 6. It should be noted that the settlement behavior of SM3K1 also exhibited the heaving in the loose sand as observed in the tests SM3J1 and SM3F1. In comparison, it was more pronounced as indicated in Figure 5-11.

To assess the impact of the modified pore fluid on the dynamic response of the model, the results of SM3K1 can be compared with SM3G1 which was also constructed using the Blend 6-1 sand. The transfer functions for the two models are plotted together in Figure 5-13, and are very similar. The shear deformations are also almost identical as indicated on Table 5-3, and evident from comparing the two standard figures included in Appendix B, pages B-60 and B-153. The settlements recorded in SM3K1 showed the same trend in settlements in the loose and dense columns as observed in SM3G1, including heaving in the loose sand, but the magnitude of the settlements was less in SM3K1. This lower final settlement could be related to the longer dissipation time in SM3K1 which appears to control the rate of settlement.

In addition to SM3K1 and SM3G1, a comparison can also be made between the subsequent tests, SM3G2 and SM3K8. From Table 5-3, the initial relative densities were quite close, and a comparison of the results from these tests indicates that the dynamic response was also very similar at a higher model density. For a comparison of results from these two tests, the reader is referred to Appendix B.

In summary, the alternate pore fluid did not appear to adversely effect the dynamic response of the model SM3K when compared to its counterpart SM3G1, which used water as a the pore fluid. The scaling of the dynamic viscosity using conventional consolidation theory over-predicted the required dynamic viscosity by a factor of one third for these tests. Considering the simplifications inherent in the method used to estimate the initial viscosity of the glycerin/water pore fluid, the scaling worked quite well. It should be noted that if the scaling had been completed using only the contrast in permeabilities, the dynamic viscosity would have been two thirds of that required to match the dissipation behavior.

5.3 Behavior of Saturated Sand in the Models

While it is not the focus of the research described in this thesis, the model tests performed do provide some insights into the behavior of saturated sands subjected to earthquake-like motions.

The observed excess pore pressures in each of the model tests typically show a phase in which pressures accumulate or are generated, followed by a phase of decay or dissipation of the excess pore pressures. The generation phase occurs while the model earthquake is exciting the model, and the dissipation phase commences after significant shaking has ceased. It should be noted that during the generation phase, numerous spikes are observed in the records usually not exceeding about 10 to 15% of the excess pore pressure corresponding to a liquefied condition. These spikes are not an artifact of the instrumentation or data acquisition system, but are a real phenomenon occurring in the experiment and are also exhibited in records obtained in the field, for example at Lotung (Shen, 1989). Possible mechanisms creating these spikes could be as follows:

1) P-waves or dilatational waves propagating through the soil and pore fluid create dynamic transient pressures.

2) Local changes in the structure of the soil matrix create dynamic transient pressures as voids collapse or expand suddenly.

For mechanism (1), P-waves in the real prototype come from the earthquake source which is three-dimensional. For the model tests performed, the input motion from the shake table is one-dimensional and therefore only S-waves were generated. However, the interaction of the boundaries of the test box with the soil and pore fluid would create P-waves. The work of Westergaard (1933) can be used to predict the order of magnitude of the maximum dynamic transient pressures generated at the boundary. In a rigid water filled container (with the

configuration of the model tests), the transient pressure developed by the peak base accelerations would be equivalent to about 10% of the excess pore pressures of the liquefied condition in the soil and pore fluid models. It should be noted that the actual model container is a laminar box and therefore is not a rigid container as assumed in Westergaard's analysis and therefore the pore pressure increase can be expected to be less than 10%. It is interesting to note that this estimate is on the order of the spikes observed in the actual model test records. Whether mechanism (1) or (2) creates the spikes remains unresolved and is not the focus of this research.

The following sections describe some general observations regarding the model test results.

5.3.1 Behavior of a Dry Model

The one-g model SM3H was constructed from Nevada sand with the general configuration of the centrifuge Model 3. Unlike the other one-g models, no pore liquid was added to the sand, and the pore fluid was air. A series of tests was performed on the model, and of these SM3H1, SM3H2, and SM3H4 are presented in Appendix B, pages B-80 through B-100.

The basic test indexes are presented in Table 5-3. From the relative densities the initial state of the model was looser than any of the previous one-g model tests, which can be attributed to the absence of additional densification created when a pore liquid is added as discussed in Chapter 4, Section 4.4.3. Correspondingly, it is not surprising that SM3H1 had the largest surface settlements of any of the Nevada one-g models. The settlement in the loose column was consistently about 50% larger than that observed in the dense column for all the SM3H tests. All of the settlement occurred within the period of shaking, and it appears that settlements were solely caused by densification created during shaking. There was no apparent movement of the dense columns towards the loose columns in any of SM3H tests, contrary to that observed in the models with a pore liquid. From the sequence of tests, the magnitude of settlements decreased and also the duration of the time in which settlement occurred decreased. Given that the earthquake was essentially identical for each test, this latter observation indicates that progressively higher accelerations are required to create densification as the density of the sand increases. A similar trend is observed with the magnitude of excess pore pressures generated in a saturated sand (as discussed in Section 5.3.2), and suggests that the two behaviors are linked.

With regard to making direct comparisons between the settlements observed in the dry model versus the saturated models, the following must be considered:

- The dry model had a higher acceleration response in its upper layers implying that these layers were subjected to a greater intensity of shaking which could induce larger amounts of densification.
- The role that the pore fluid plays in the redistribution and densification of the sand grains is uncertain, and may enhance or inhibit the process.

Based on the above, comparisons of the magnitude of settlements in the dry model and models with pore fluid have not made for the set of test data presented in this thesis. However, it is probably safe to assume that the settlements observed in SM3H1 represent an upper bound.

Some small pore pressures were recorded throughout the model depth (for example see Appendix B, page B-85 and B-86). These pore pressures were of course air pressure created when densification of the sand occurred. In comparison to a saturated model, it rapidly dissipated due to the very low viscosity of the air. The lack of any real excess pore pressures meant that the SM3H model responded far more stiffly than any of the models containing pore fluid with the sand at similar densities. The series of SM3H tests provide a useful history of the response of a sand deposit as it progressively increases in density. From Table 5-3 the acceleration response is seen to gradually increase as the model stiffens. Consistent with this the shear deformations in the lower portions of the model decrease, while in contrast the shear deformations in the upper parts of the model increase, presumably caused by the stronger acceleration response.

5.3.2 Behavior of a Uniform Model

Two models, SM3E and SM3I, were constructed using the Nevada sand placed at a uniform density throughout the laminar box. The pore fluid was water. These tests were performed to investigate the following:

1) To compare the behavior of a uniform deposit of Nevada sand with the behavior in the one-g models which had loose and dense columns of sand.
2) To confirm the performance of the laminar box, which should exhibit the same behavior at any vertical section along its length when a sand is placed in it at a uniform density.

The results for SM3E1 are presented in Appendix B, pages B-33 through B-39. The results for SM3I1, SM3I3, SM3I4, and SM3I5, are presented in Appendix B, pages B-101 through B-132.

The basic test indexes for the test series SM3I and SM3E1 are provided in Table 5-3. The relative densities of the four SM3I tests correspond with the range of relative densities employed in the one-g model tests which were constructed to represent the centrifuge Model 3. The correlation's with these models and pertinent indexes of pore pressures and settlements taken from Table 5-3 are as follows:

Range of results from SM3I based on measurements from each side of the model.			Range of results from the one-g tests representing with loose and dense columns of sand.		
Test No.	Maximum Excess Pore Pressure (kPa)	Settlement (mm)	Correlation with One-g Model Test	Maximum Excess Pore Pressure (kPa)	Settlement (mm)
SM3I1	107-110	90-92	SM3J1, SM3F1 Loose column	105-105	59-86
SM3I4	40-45	10-25	SM3J1, SM3F1 Dense column	100	57-83
SM3I3	105-105	52-55	SM3B1, SM3C1 Loose column	100-105	60-109
SM3I5	20-22	31-32	SM3B1, SM3C1 Loose column	90-90	28-30

The above results indicate that the excess pore pressures in tests of SM3H1 and SM3I3 correlate well with the values observed in the loose columns of sand in the one-g tests which had adjacent columns loose and dense sand. However, a similar correlation in the dense columns indicates that far lower excess pore pressures were observed in SM3I4 and SM3I5. This implies that in the one-g tests performed with adjacent loose and dense columns of sand, the pore pressures in the dense column of sand appear to have been boosted.

With regard to the performance of the laminar box, the results in Appendix B and the table above confirms that the behavior of the laminar box was consistent at any vertical section along its length. The one test which showed some difference was SM3I4, which as indicated in the table above, showed a wide range in the surface settlements although the rest of its behavior was consistent. In addition to this wide range in settlements, SM3I4 also had less settlement than the subsequent test SM3I5. This suggests that perhaps SM3I4 was a poor test.

As for the test series SM3H discussed in Section 5.2.1, the test series SM3I exhibits the same trends as the density of the model increases from test to test. The acceleration response increases, as indicated by the transfer functions shown in Figure 5-14, and the shear strains decrease in the

lower portion of the model while increasing in the upper portion. In addition, the magnitude and rate at which excess pore pressures are generated decrease as the density of the sand increases. From Figure 5-14, there is a dramatic increase in the transfer function from SM3I3 to SM3I4 indicating that the response became significantly stiffer in the latter model. This is also observed in the excess pore pressures, which were significantly less in SM3I4. This sudden change in behavior corresponds to the different relative densities in the models of 42% in SM3I3 and 57% in SM3I4. From these results and others presented herein, it appears that in the range of 40% to 60% the sand behavior changes dramatically as it shifts from a "loose" state to a "dense" state.

5.3.3 Behavior of a Model with Adjacent Loose and Dense Sands

The observations of the one-g models SM3B, SM3C, SM3F, SM3G, SM3J, and SM3K, which were all constructed with adjacent loose and dense columns of sand, have been described in detail in Section 5.2. The behavior of the adjacent loose and dense sand columns was also compared with the behavior of a uniform deposit of sand in Section 6.3.2 (test series SM3I). In all the observations and comparisons made previously, it is apparent that the excess pore pressures generated during the earthquake primarily control the response of the models and the observed settlements and deformations.

To explore the behavior of the trends in the excess pore pressures, the results of the test SM3G1 have been converted into contour plots as presented in Figures 5-15 through 5-18. This test was selected because it exhibited behavior common to the other model tests, and because the excess pore pressures were dissipated relatively quickly. The Figures 5-15 through 5-18 correspond to the cross-section shown below Table 5-2, with the loose sand located in the left half of the box, and the dense sand in the right half. Each plot presents a snapshot of the contours of the pore water pressure ratio, R_u, at times 4, 6, 8, 12, 16, 24, 30, and 40 seconds into the test. The earthquake shaking, recorded up until the time of the snapshot, is shown below each contour plot. It should be noted that the traces of excess pore pressures recorded at the pore pressure transducers are presented in Appendix B, pages B-61 through B-63.

SM3G1 was constructed from the Blend 6-1 sand and therefore the dissipation of pore pressures occurred faster than the Nevada sand models. However, this should not affect any conclusions drawn about the behavior of the loose and dense columns of sand. In all other respects the

behavior observed in SM3G1 typified the behavior observed in other one-g models, including exhibiting heave in the loose column of sand.

Referring to Figures 5-15 through 5-18, it can be seen that in the first 12 seconds the location of maximum R_u occurs in the lower part of the loose sand, and it appears that the contours radiate out through the section from this location. In the first 8 seconds the values of R_u in the dense sand significantly lag behind those in the loose sand, but by 12 seconds the distribution of R_u becomes more uniform through the loose and dense halves of the section. At 16 seconds the intensity of shaking has dropped and it appears that generation of the excess pore pressures has stopped as indicated by the contour of R_u=100% which is moving toward the surface of the loose sand. This trend strengthens in the remaining contour plots, and it appears that in the loose sand the dissipation is predominantly occurring in the vertical direction only (one-dimensional). In the dense half of the section, a similar trend is also observed, but there appears to be a greater two-dimensional effect near the interface of the loose and dense halves, and the rate of the dissipation there appears to be greater.

In summary, the Figures 5-15 through 5-18 indicate that the excess pore pressures generated in the lower portion of the loose column propagate into the upper layers of loose sand and into the adjacent dense sand. When combined with the test results of other one-g models, it appears that the pore pressures in the upper layers and dense layer remain at higher excess pore pressures than would be the case in the absence of the lower loose layer. This appears to be dominated primarily by the diffusion process and supports the observation made in Section 5.3.2 that the presence of the loose sand boosts the excess pore pressures generated in the dense sand. After significant shaking ceases, the dissipation of pore pressures appears to be more rapid in the dense sand, which is consistent with the relative difference between the loose and dense coefficients of consolidation. The stronger dissipation in the dense sand appears to accelerate the dissipation in the loose sand, and it is evident that a two-dimensional process occurs.

In all of the one-g models and the centrifuge test, the observed surface settlements and lateral deformation at the interface of the dense and loose sands indicates that the dense sand moves toward the loose sand. This indicates there is an interaction between the two adjacent columns of sand. However, the relative surface settlements vary and appear to be dependent on a subtle interplay of the excess pore pressures and the relative strengths of the two sand columns. There are a number of possible mechanisms which could explain the observed surface settlements, but

the resolution of the correct one is beyond the scope of this thesis. The hypothesis of Hushmand et al. (1994), that the dense sand column penetrated laterally into the loose sand and impeded the surface settlement in the loose column while increasing it in the dense sand column, is not contradicted by any of the data collected during these experiments.

With regard to the dynamic performance of the adjacent loose and dense columns of sand, it is important to note that the acceleration response behavior of the two sand columns appears to follow the behavior of the loose sand column. This conclusion can be drawn by comparing Figure 5-7 with Figure 5-14. Figure 5-7 shows the transfer functions for the test SM3J1, which had loose and dense columns of sand. This compares well with the transfer functions presented in Figure 5-14 for tests SM3I1 and SM3I3, which represent a loose uniform layer of sand. The transfer function for SM3I4, which represents a uniform dense layer of sand, is significantly greater. It should be noted that the transfer function for SM3I5 is even larger than for SM3I4.

Similarly, the shear deformation behavior appears to follow the behavior of loose sand column but with slightly lower magnitudes than expected for uniform loose layer. This behavior can be verified by comparing the relevant figures in Appendix B, for example the results for SM3J1 on page B-137 with the results for SM3I1 and SM3I4 on pages B-105 and B-121, respectively.

The primary reason for the above observations in the models with two sand columns is that higher excess pore pressures developed in the dense sand due to high excess pore pressures generated in the adjacent loose sand. Essentially the effective stresses in both materials become very small, and as indicated in Chapter 3, on Figure 3-11, the shear moduli of both sands also became small.

This behavior of the loose and dense columns, as discussed above, could be very important in evaluating seismic performance of geotechnical structures or sites which contain saturated sands. Current practice generally ignores dense materials in assessing the overall liquefaction potential of saturated sands. However, as evident from the results shown here the excess pore pressures which migrate into the dense material from adjacent loose materials and the consequent decrease in effective stresses may be significant. The dense sand may not fully liquefy *per se*, but the potential exists for significant cyclic mobility to develop. In practice, adjacent vertical columns of loose and dense sand are often found following a site remediation, in which portions of the loose sands on the site have been artificially densified.

While the model tests represent vertical columns of loose and dense sands, the same observations would be made for adjacent horizontal layers of loose and dense sands. In practice, adjacent layers of loose and dense sands occur naturally in many soil deposits.

5.4 Physical Model Testing

The results and experience gained from the testing described in this chapter raise some issues about physical modeling methods (one-g and centrifuge) used to represent the behavior of a saturated sand. These are briefly discussed in sections that follow.

5.4.1 Test Methodology

The procedures that were followed to prepare the models and test them were described in detail in Chapter 4, and in general they were quite successful. However, some comments are pertinent on a number of the difficulties encountered during testing.

Control of Sand Density: The methods used to place the sand in the models are described in Section 4.4.3 and it was reported that the sand densities achieved within the models were within 1.5% of the target values. Considering the potential variations in the pluviation of the sand, the additional densification of the sand which occurred as further layers were placed, and the additional densification which occurred when the pore fluid was added, the 1.5% variation is considered quite good. However, this converts to a potential error of 5 to 7% in terms of the relative density of the sand, which in terms of controlling the potential model sand behavior is significant. In practice, several trials are required for each model to obtain the target relative density.

Laminar Box and Liner: The laminar box appears to have performed its function. After each test it should be disassembled and cleaned to ensure that any sand particles do not inhibit the bearings. For the dimensions of laminar box used in these experiments, the clearance between adjacent laminae should be at least 1.0 to 1.5 mm. For the tests performed, the liner easily accommodated this amount of clearance. Regarding the liner, which was made from latex rubber, it survived the entire testing program without puncturing or tearing. However, it did shrink with time by about 2 to 3%. This shrinkage did not adversely affect the tests because the compliance of the liner was such that it stretched to meet the full volume of the box when the material was placed within it. The only problem areas were in the immediate vicinity of corners. Perhaps a

thinner liner would have reduced this shrinkage and increased the compliance without compromising the durability too significantly.

Vacuum Box and Saturation: As reported in Chapter 4, Table 4-5, the calculated saturation achieved in the models prior to testing ranged from 91.4% to 96.9%, with a mean of 94.9%, which is well below an acceptable target for saturation of 99% (as discussed in Chapter 2, Section 2.2).The potential error in the calculated value of the saturation is estimated to be ± 7.6% (Chapter 4, Section 4.5), which indicates that using the estimated density of the sand and the total volume of water added to the model is a poor method. In typical laboratory practice the saturation is determined by a B-value test. Unfortunately, it is not possible to perform this type of test on the completed one-g models, and at this stage it should be presumed that the consistently low estimates of the saturation are indicative of the true state of the model.

It is difficult to assess the impact of the low values of saturation on the behavior of the models during testing. The responses of the pore pressure transducers during the testing were not typical of a poorly saturated sample, and when the models were excavated, there was no evidence of small cavities or bubbles in the sand matrix which would be typical of a poorly prepared model. Also during the shaking of the model, no air bubbles were observed rising to the surface of the model when it liquefied.. These observations imply that any gases in the sand and pore fluid matrix were in solution and therefore the size of any air voids would be very small. For pure water the air content in solution is about 2% (Batchelor, 1973), which if present in the one-g models would account for only a 2% reduction in saturation.

The wooden vacuum box performed its function adequately throughout the test program. However, if a vacuum was applied to the box in excess of 45 kPa, the deflection of the sides and top of the box were sufficient to stress the joints of the box and create leakage. In hindsight a lightweight metal aluminum box would have been preferable, and perhaps the application of a higher vacuum to the models would have resulted in higher values of measured saturation.

5.4.2 Repeatability and Comparison of Test Results

Two aspects of the model testing are discussed below. Firstly, the repeatability of test results, and secondly, the limitations on making comparisons of test results.

One of the concerns with any testing method is that the results from one test be duplicated in another. This obviously provides some assurance that the experimental methodology is sound.

For the one-g tests completed as part of this research, several duplicate tests were performed. In these tests, the same model sand was used, which was placed at similar densities. The pore fluid was identical and earthquake motions were very comparable. Of the model tests, there were two basic categories: initial tests, which were the first test performed on a model, and sequential tests, which were one of a series of tests performed on a model after the initial test.

Of the initial tests, SM3B1 and SM3C1 were duplicate tests and as described in Section 5.2.3.1, the results were very comparable. Similarly, SM3F1 and SM3J1 were also duplicate tests and, as described in Section 5.2.3.1, the results were very comparable. Of the sequential tests, SM3F8 and SM3J8 have been included in Appendix B as an example of duplicate tests. From Table 5-1 the initial densities of these tests were very similar. A comparison of the results indicates that the behavior of these tests was very similar.

The similarity in the results of the duplicate tests cited above tends to confirm that the model tests could be repeated with some assurance of uniformity.

In comparing test results from different model tests, some limitations exist. For example, from Table 5-1, the initial densities of SM3B1 (an initial test) and SM3J8 (a sequential test) are quite similar. However, the results of these tests are significantly different, even though they were subjected to comparable earthquakes. As shown on Table 5-3, SM3J8 had lower excess pore pressures and consequently behaved in a far stiffer manner than SM3B1. The reason probably lies in the fact that the estimate of the initial density in the loose sand column in SM3J8 is incorrect, and is in fact greater. As discussed previously, the models with dense and loose columns of sand showed evidence of lateral movement toward the loose material. This was not accounted for in the estimate of initial density of the model, which for the sequential tests is calculated based on the total surface settlement which has occurred at L5 in all prior tests of the model. The effect of the lateral movement on the density could be as high as 1%, which equates to about a 5% shift in relative densities. This may not have as much influence at lower relative densities, which will fully liquefy anyway, but could have a significant effect in the tests where the loose sand column is in the range of, say, 40 to 60% relative density.

Contrary to the above observations, the test SM3I3 is a sequential test that was performed on a model with the Nevada sand uniformly distributed throughout it. This can be compared to the initial test SM3E1 which was a model with the same configuration and density as SM3I3. As indicated on Table 5-3 and from the results in Appendix B, these two tests exhibited quite similar

behavior. This suggests that the hypothesis above regarding the density of the loose sand in SM3J8 may be valid.

Regardless of the above, caution should be exercised in making comparisons between the sequential tests and initial tests because, presumably, once a model sand has been shaken and liquefied, its fabric will be different from that of an initial test which was pluviated into place. There is a considerable amount of experimental data which confirms that sample preparation methods do affect test results, at least in small samples.

5.4.3 Time Scaling

As discussed in Chapter 2, Section 2.6, there are two time scales which potentially govern the model behavior, the dynamic time scale and the dissipation time scale. With reference to Table 5-5, the difference between the two time scales in the centrifuge model is a factor of 50, which implies that the pore pressures are dissipating 50 times faster than they should be in comparison to the generation of the excess pore pressures created by the earthquake. In the one-g models, SM3B1 and SM3C1, the difference in the time scales is considerably less. It ranges from about 9 to 12 times depending on whether the loose or dense sand dominates the behavior as the effective stresses increase and the sand experiences an increase in load. Obviously this difference is much closer to the real prototype which has identical dynamic and dissipation time scales.

The results of the model tests appear to confirm the above factors because the pore pressures in the centrifuge Model 3 test were far lower at all times than in comparable one-g tests, as described in Section 5.2.3.1 and 5.2.3.2. This assumes that the sand in both models had the potential to generate the same amount of excess pore pressure, which seems reasonable because the sand was placed at similar states and subjected to virtually the same earthquake.

The above effects are discussed in detail in Chapter 6, and analyses are presented to support the statements above.

5.5 References

Batchelor, G. K., 1973, "An Introduction to Fluid Dynamics," Cambridge University Press, Cambridge, UK.

Been, K., M. G. Jefferies, J. E. Hachey, and L. Rothenburg, 1993, "Numerical prediction for Model No. 2," in Verification of Numerical Procedures for the Analysis of Soil Liquefaction Problems, Vol. 1, pp. 331-341, Arulanandan, K. and R. F. Scott, eds., Balkema, Rotterdam.

Hushmand, B., R. F. Scott, and H. Rashidi, 1994, "VELACS Model No. 3: Liquefaction in dense and loose sand columns," in Verification of Numerical Procedures for the Analysis of Soil Liquefaction Problems, Vol. 2, pp. 1415-1442, Arulanandan, K. and R. F. Scott, eds., Balkema, Rotterdam.

Jafarzadeh, F., and E. Yanagisawa, 1995, "Settlement of sand models under unidirectional shaking," in First Int. Conf. on Earthquake Geotech. Eng., Volume 2, pp. 693-698, K. Ishihara, ed., Balkema, Rotterdam.

Shen, C. K., et al. 1989, "Pore water pressure response measurements at Lotung site." Proc., EPRI/NRC/TPC Workshop on Seismic Soil Structure Interaction Analysis Techniques Using Data from Lotung, Taiwan, EPRI NP-6154, 2, 25-1-25-20.

Westergaard, H. M., 1933, "Water Pressures on Dams During Earthquakes," Transaction ASCE, Volume 98, pp. 418-433.

Table 5-1: Summary of model tests selected for analysis and discussion.

Test Method	Model Name	Model Sand	Pore Fluid	Test No.	Sand Column(1)	Init. Relative Density (%)	Void Ratio	App. B(3) Page No.'s
Centrifuge	Model 3	Nevada	Water	Caltech	Loose	42-48(2)	0.7305	B4-11
					Dense	74-79(2)	0.6102	
One-g	SM3B	Nevada	Water	SM3B1	Loose	49	0.7041	B12-18
					Dense	73	0.6137	
	SM3C	Nevada	Water	SM3C1	Loose	41	0.7336	B19-25
					Dense	64	0.6484	
	SM3D	Blend 6-1	Water	SM3D1	Loose	51	0.7203	B26-32
					Dense	79	0.6349	
	SM3E	Nevada	Water	SM3E1	Loose only	41	0.7317	B33-39
	SM3F	Nevada	Water	SM3F1	Scaled loose	33	0.7632	B40-47
					Scaled dense	51	0.6971	
				SM3F8	Scaled loose	47	0.7101	B48-55
					Scaled dense	67	0.6360	
	SM3G	Blend 6-1	Water	SM3G1	Scaled loose	32	0.7787	B56-63
					Scaled dense	63	0.6818	
				SM3G2	Scaled loose	37	0.7639	B64-71
					Scaled dense	69	0.6647	
				SM3G7	Scaled loose	55	0.7079	B72-79
					Scaled dense	81	0.6289	
	SM3H	Nevada	Dry	SM3H1	Scaled loose	19	0.8089	B80-86
					Scaled dense	53	0.6819	
				SM3H2	Scaled loose	25	0.7922	B87-93
					Scaled dense	57	0.6749	
				SM3H4	Scaled loose	30	0.7754	B94-100
					Scaled dense	59	0.6652	
	SM3I	Nevada	Water	SM3I1	Scaled loose	35	0.7558	B101-108
				SM3I3	Scaled loose	42	0.7305	B109-116
				SM3I4	Scaled loose	57	0.6379	B117-124
				SM3I5	Scaled loose	70	0.6254	B125-132
	SM3J	Nevada	Water	SM3J1	Scaled loose	29	0.7772	B133-140
					Scaled dense	62	0.6559	
				SM3J8	Scaled loose	47	0.7127	B141-148
					Scaled dense	70	0.6230	
	SM3K	Blend 6-1	Water& Glycerin	SM3K1	Scaled loose	28	0.7813	B149-156
					Scaled dense	57	0.6747	
				SM3K8	Scaled loose	46	0.7404	B157-164
					Scaled dense	85	0.6205	

Notes:

(1) Loose and dense refer to the left and right-hand sides of the model respectively. "Prototype" implies that no scaling of the initial state of the sand was performed, whereas "Scaled" implies that scaling was completed consistent with the proposed modeling method.

(2) Possible range in values as discussed in Chapter 4, Section 4.2.

(3) Results of tests are presented in Appendix B, in a series of eight standard plots for each test. See Table 5-2 for description.

Table 5-2: Summary of standard plots presented in Appendix B.

Standard Plot	Description of data presented.	Transducer signals presented(1).
Figure 1	Acceleration histories recorded at the base of the model.	A1, A2, and A3(2).
Figure 2	FFT's of acceleration recorded at the base of the model.	A1, A2, and A3(2).
Figure 3	Acceleration histories recorded in both halves of the model. Longitudinal and vertical components at prototype depth of about 2.2 m.	A4, A5, A6, and A7.
Figure 4	FFT's of acceleration recorded in each half of the model. Longitudinal and vertical components at prototype depth of about 2.2 m.	A4, A5, A6, and A7.
Figure 5	Longitudinal displacements recorded at the end of the laminar box, and, for the one-g models, at the shake table top.	L1, L2, L3, L4, and Table LVDT(3).
Figure 6	Surface settlement and excess pore pressures recorded in the left half of the model. Pore pressure transducers along the vertical section A.	L5. P1, P3, and P7.
Figure 7	Surface settlement and excess pore pressures from both halves of the model. Pore pressure transducers along the vertical sections B and C.	L5, and L6. P4, P5, P8, and P9.
Figure 8	Surface settlement and excess pore pressures recorded in the right half of the model. Pore pressure transducers along the vertical section D.	L6. P2, P6, and P10.

Notes:
(1) For the exact position of the transducers, see Chapter 4, Table 4-4.
(2) Accelerometers A2 and A3 were moved to the end of the laminar box for models SM3F through SM3K.
(3) For models SM3B through SM3E, Figure 5 is not included due to errors in the LVDT readings (see Chapter 4, Section 4.4.7).

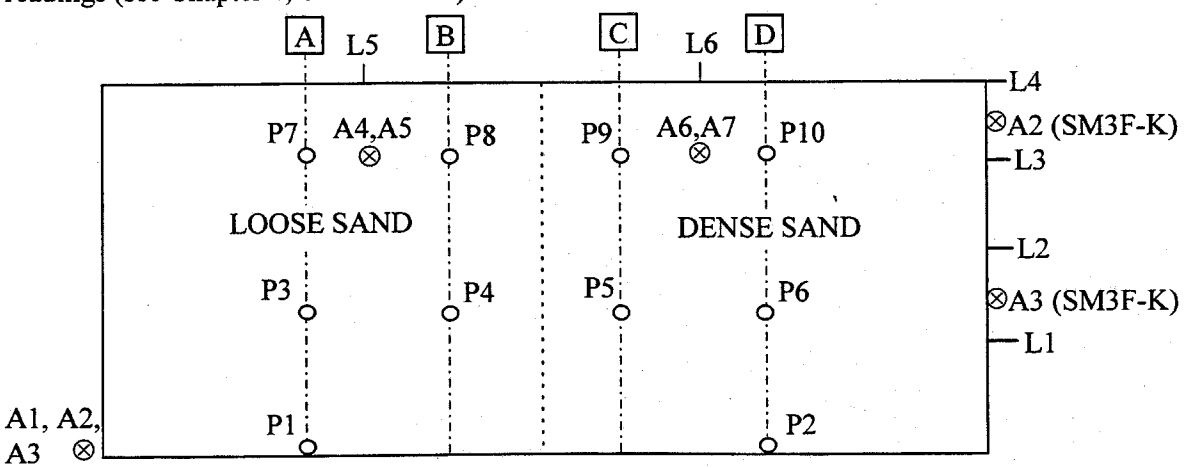

⊗ Accelerometers, "A"
O Pore Pressure Transducers, "P"
⊥ Displacement Transducer LVDT, "L"

Table 5-3: Summary of model test results presented in scaled prototype values.

Model Name and Test No.	Initial Relative Density (%)		Peak Accel. at A4(1) (g)	Peak to Peak Shear Strain (%) at LVDT's(3)		Peak excess pore pressure (kPa) at base		Excess pore pressure ratio, R_u (%) at base		Time for R_u =0(4) (secs)	Surface Settlement (mm)	
	Loose	Dense		L1	L4	P1	P2	P1	P2	P1	Loose L5	Dense L6
Centrifuge model (Nevada sand and water).												
Model 3	42 to 48(2)	74 to 79(2)	0.20	1.2	1.5	45	40	44	36	130	175	250
One-g models at prototype densities with loose and dense sides (Nevada sand and water).												
SM3B1	49	73	0.10	-	-	105	90	100	82	230	60	30
SM3C1	41	64	0.10	-	-	100	90	97	82	220	109	28
One-g models at scaled densities with loose and dense sides (Nevada sand and water).												
SM3F1	33	51	-	1.9	0.9	105	-	100	-	260	59	83
SM3F8(5)	47	67	-	0.7	1.0	85	-	83	-	180	35	40
SM3J1	29	62	0.07	1.2	0.8	105	100	100	91	220	86	57
SM3J8(5)	47	70	+0.40	0.5	1.0	65	40	63	36	170	32	18
One-g models at scaled densities with loose and dense sides (Blend 6-1 sand and water).												
SM3D1	51	79	0.20	-	-	90	90	87	82	28	102	41
SM3G1	32	63	0.10	1.3	0.7	105	110	100	100	50	90	115
SM3G2(5)	37	69	0.10	1.0	0.7	105	105	100	95	35	78	85
SM3G7(5)	55	81	+0.40	0.6	1.4	35	28	33	25	15	30	13
One-g model using with loose and dense sides (Blend 6-1 sand and water/glycerin mixture).												
SM3K1	28	57	0.07	1.2	0.9	100	100	97	95	330	41	81
SM3K8(5)	46	85	+0.15	0.9	0.9	95	75	92	68	230	24	34
One-g models with sand at a uniform density on both sides (Nevada sand with water).												
SM3E1	41	41	0.06	-	-	-	105	-	95	240	56	64
SM3I1	35	35	0.06	1.5	1.0	110	107	100	97	270	90	92
SM3I3(5)	42	42	0.07	1.9	1.0	105	105	100	95	210	52	55
SM3I4(5)	57	57	+0.40	0.6	1.4	45	40	44	36	110	10	25
SM3I5(5)	70	70	+0.70	0.3	1.5	20	22	19	20	95	31	32
One-g model using dry sand with loose and dense sides (Nevada sand, no pore fluid).												
SM3H1	19	53	0.20	1.0	0.9	25	22	-	-	10	144	90
SM3H2(5)	25	57	0.22	0.9	1.1	20	12	-	-	10	59	37
SM3H4(5)	30	59	0.23	0.9	1.3	10	8	-	-	6	31	22

Notes:

1) The use of "+" indicates there were isolated spikes in excess of the reported value. Note that the peak base acceleration at A1 was on the order of 0.35 to 0.40 g.

2) Possible range in values as discussed in Chapter 4, Section 4.2.

3) Shear strains were calculated using the maximum peak to peak displacement recorded at LVDT L1 and L4 divided by the height of the transducer. Therefore, the values represent an average value of maximum shear strain over depth.

4) At P1, the value of R_u=0 (the ratio of excess pore pressure to the initial vertical effective stress) occurs when the excess pore pressures have dissipated. The times are in terms of the prototype dynamic time scale and are an approximate estimate since the generation of pore pressures ceased. Similar times were also observed at P2.

5) Model had been subjected to previous earthquake(s) in prior test.

Table 5-4: Initial prototype effective stresses at the pore pressure transducer locations in the centrifuge and one-g models for the Nevada and Blend 6-1 sands.

Side of model with "Loose" sand			Side of model with "Dense Sand"		
Transducer Number	Vertical Effective Stress (kN/m^2)		Transducer Number	Vertical Effective Stress (kN/m^2)	
	Centrifuge	One-g		Centrifuge	One-g
P7, P8	20.5	21.7	P9, P10	22.0	23.4
P3, P4	62.3	62.9	P5, P6	67.0	67.7
P1	102.6	102.7	P2	110.2	110.4

Table 5-5: Scaling factors for the centrifuge model and each of the one-g models based on properties calculated at mid depth in the model.

Model Name	Sand column	Depth of model (m)	Dry Density (kN/m^3)	Scale factors for each model						
				Length x^* or n	Stress σ^*	Consolidation(1) c_v^*		Time Dynamic t_d^*	Time Dissipation(1) t_c^*	
						Unload	Load		Unload	Load
Centrifuge	Loose	0.220	15.13	50	1	1	1	50	2500	2500
Model 3	Dense		16.26	50	1	1	1	50	2500	2500
SM3B	Loose	0.424	15.36	25.9	25.6	9.8	12.9	5.1	68	52
	Dense	0.432	16.22	25.5	25.5	8.2	14.0	5.0	80	46
SM3C	Loose	0.432	15.10	25.5	25.5	8.3	10.9	5.0	78	59
	Dense	0.432	15.88	25.5	26.1	6.0	10.2	5.0	109	64
SM3D	Loose	0.432	15.16	25.5	25.5	0.5	0.6	5.0	1281	1115
	Dense	0.432	16.95	25.5	26.0	0.3	0.6	5.0	2146	1018
SM3E	Loose	0.432	15.12	25.5	25.5	8.4	11.0	5.0	77	59
SM3F	Loose	0.431	14.85	25.5	26.0	7.3	9.5	5.1	89	68
	Dense	0.428	15.43	25.7	27.1	4.3	7.4	5.1	153	89
SM3G	Loose	0.432	14.66	25.5	26.3	0.4	0.5	5.0	1547	1344
	Dense	0.432	15.51	25.5	26.8	0.3	0.5	5.0	2621	1242
SM3H	Loose	0.432	14.42	25.5	26.7	6.0	5.5	5.0	-	-
	Dense	0.432	15.51	25.5	26.7	4.5	7.7	5.0	-	-
SM3I	Loose	0.431	14.91	25.5	25.9	7.6	7.0	5.1	86	93
SM3J	Loose	0.430	14.73	25.6	26.3	6.9	9.0	5.1	95	73
	Dense	0.432	15.81	25.5	26.2	5.6	9.6	5.0	115	68
SM3K	Loose	0.431	14.70	25.5	29.5	7.5	8.6	5.1	87	76
	Dense	0.433	15.63	25.4	29.6	4.6	9.7	5.0	140	67

Notes:

1) The values corresponding to "Unload" or "Load" relate to the alternate values of the coefficient of compressibility, a_v (Chapter 3, Section 3.4) which is used in the calculation of c_v (Equation 2-16, Chapter 2).

Table 5-6: Scaled values of void ratio and relative density for models SM3F through SM3K[1].

Model Name	Sand Column	Initial Relative Density (%)	Initial Void Ratio	Scaled values based on Been et al. SSL[1]		Scaled values based on Fit 2 SSL[1]	
				Relative Density (%)	Void Ratio	Relative Density (%)	Void Ratio
SM3F1	Loose	33	0.7632	50	0.6992	44	0.7214
	Dense	51	0.6971	68	0.6329	62	0.6552
SM3F8	Loose	47	0.7101	64	0.6454	58	0.6679
	Dense	67	0.6360	84	0.5710	78	0.5936
SM3G1[2]	Loose	32	0.7787	46	0.7146	40	0.7369
	Dense	63	0.6818	72	0.6177	66	0.6400
SM3G2[2]	Loose	37	0.7639	50	0.6996	44	0.7220
	Dense	69	0.6647	76	0.6003	70	0.6227
SM3G7[2]	Loose	55	0.7079	65	0.6430	59	0.6655
	Dense	81	0.6289	86	0.5641	80	0.5866
SM3H1	Loose	19	0.8089	36	0.7518	30	0.7740
	Dense	53	0.6819	70	0.6242	64	0.6464
SM3H2	Loose	25	0.7922	42	0.7280	37	0.7503
	Dense	57	0.6749	74	0.6107	68	0.6330
SM3H4	Loose	30	0.7754	47	0.7110	41	0.7333
	Dense	59	0.6652	76	0.6008	70	0.6232
SM3I1	Loose	35	0.7558	52	0.6917	46	0.7140
SM3I3	Loose	42	0.7305	59	0.6662	53	0.6885
SM3I4	Loose	57	0.6379	74	0.6089	68	0.6315
SM3I5	Loose	70	0.6254	87	0.5598	81	0.5826
SM3J1	Loose	29	0.7772	46	0.7131	41	0.7353
	Dense	62	0.6559	79	0.5919	73	0.6142
SM3J8	Loose	47	0.7127	64	0.6478	58	0.6704
	Dense	70	0.6230	87	0.5565	82	0.5809
SM3K1[2]	Loose	28	0.7813	48	0.7083	42	0.7313
	Dense	57	0.6747	76	0.6021	70	0.6251
SM3K8[2]	Loose	46	0.7404	59	0.6719	52	0.6957
	Dense	85	0.6205	90	0.5522	84	0.5759

Notes:

1) Scaling of density or void ratio follows procedure described in Chapter 2, Section 2.4, using the steady state lines (SSL's) presented in Chapter 3, Section 3.6. For scaling purposes the mean vertical effective stress in the model and the prototype has been used.

2) These models used the Blend 6-1 sand as the model material. The scaling can be completed as described in Note (1) above, or the SSL's can be recast in terms of the relative density (Chapter 2, Section 2.4). If the latter is performed, the scaled values of void ratio fall within the range of values arrived at using the former method (Note (1)).

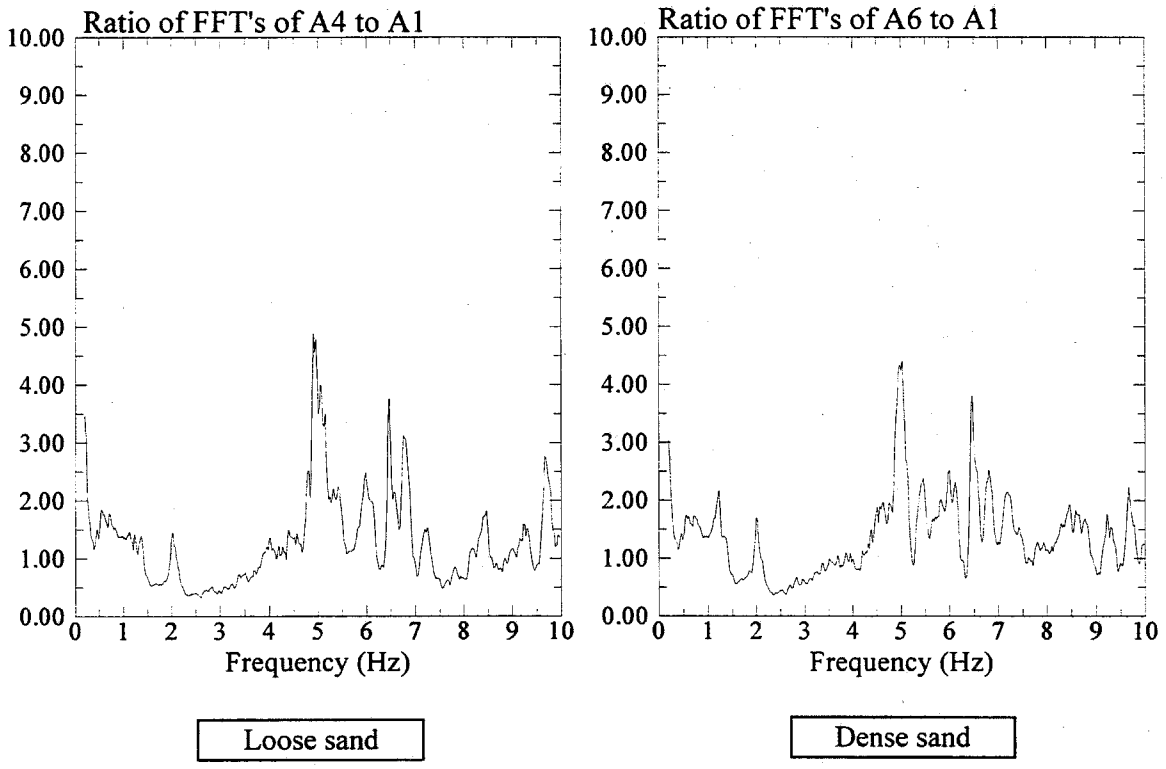

Figure 5-1: Transfer functions for the centrifuge Model 3 test.

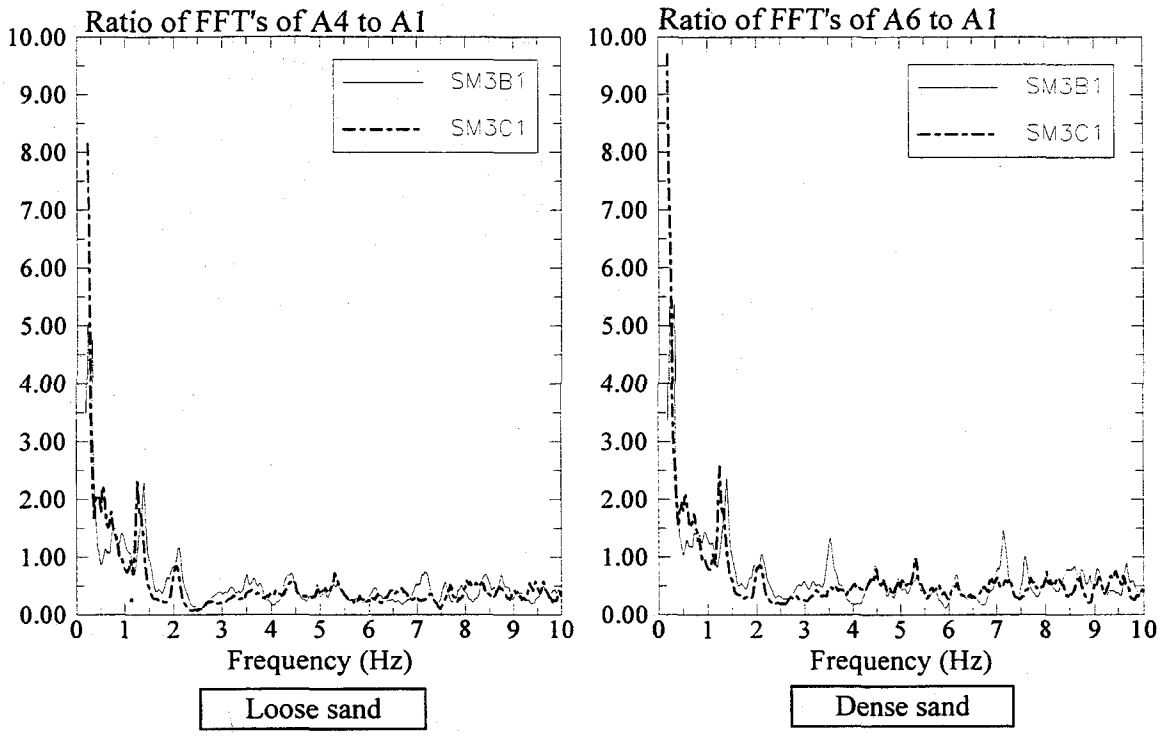

Figure 5-2a: Transfer functions for the one-g model tests, SM3B1 and SM3C1.

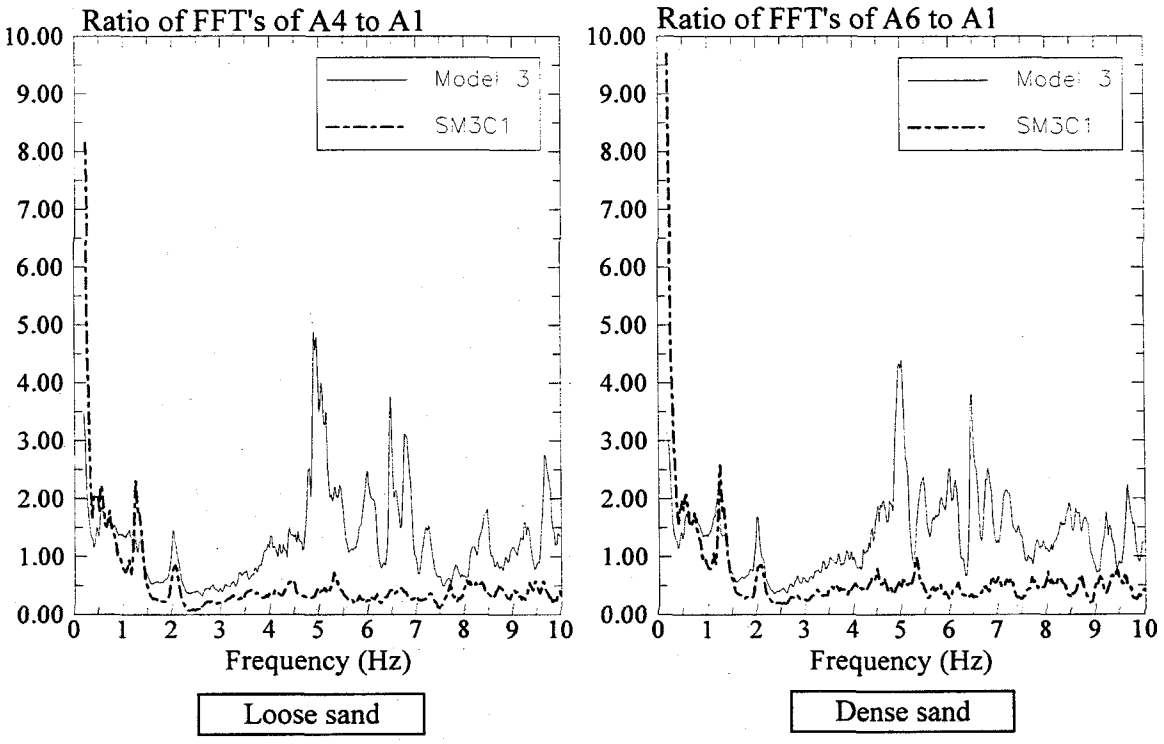

Figure 5-2b: Transfer functions for the test SM3C1 compared with the Model 3 test.

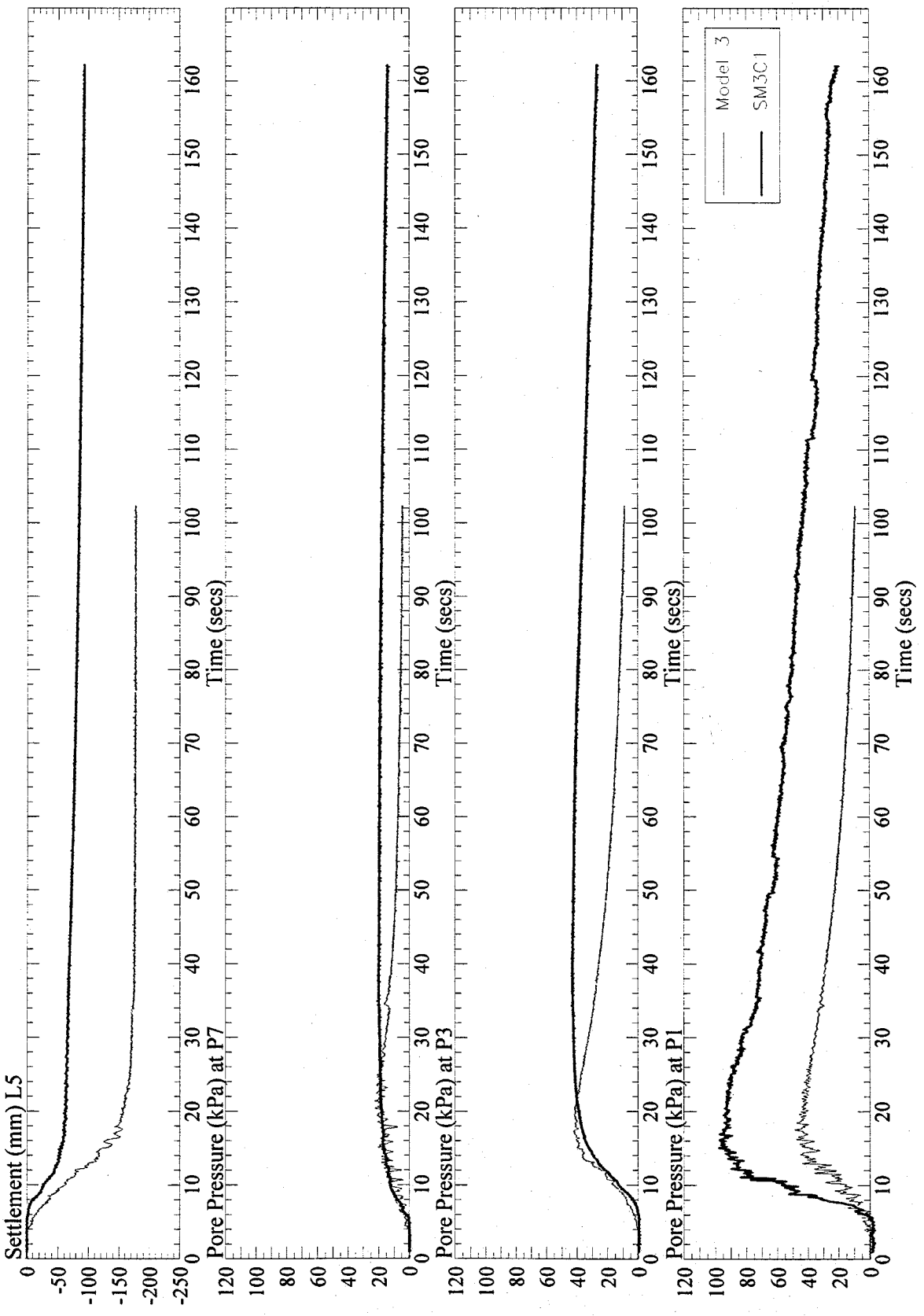

Figure 5-3: Excess pore water pressures for the tests SM3C1 and Model 3 in loose sand.

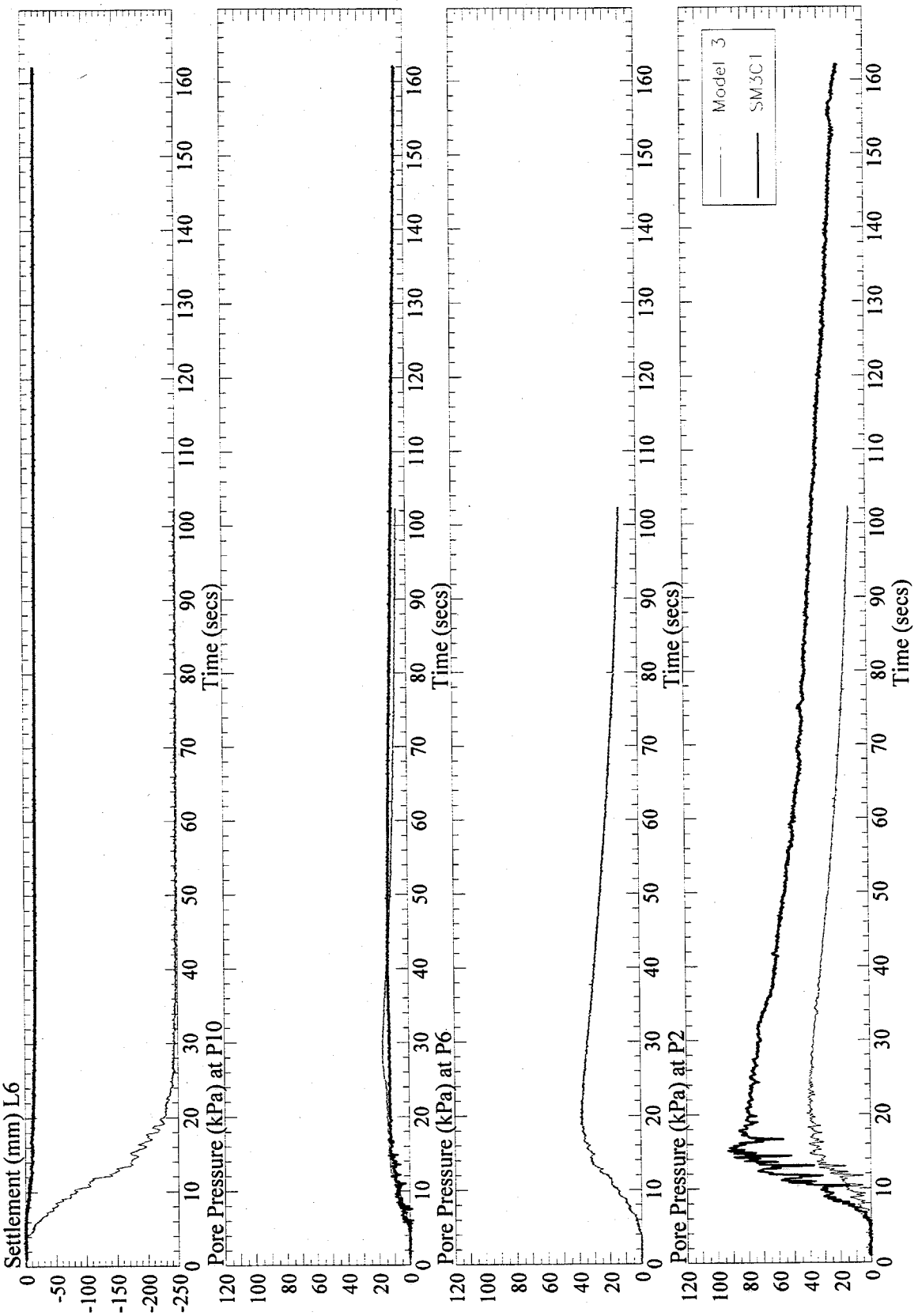

Figure 5-4: Excess pore water pressures for the tests SM3C1 and Model 3 in dense sand.

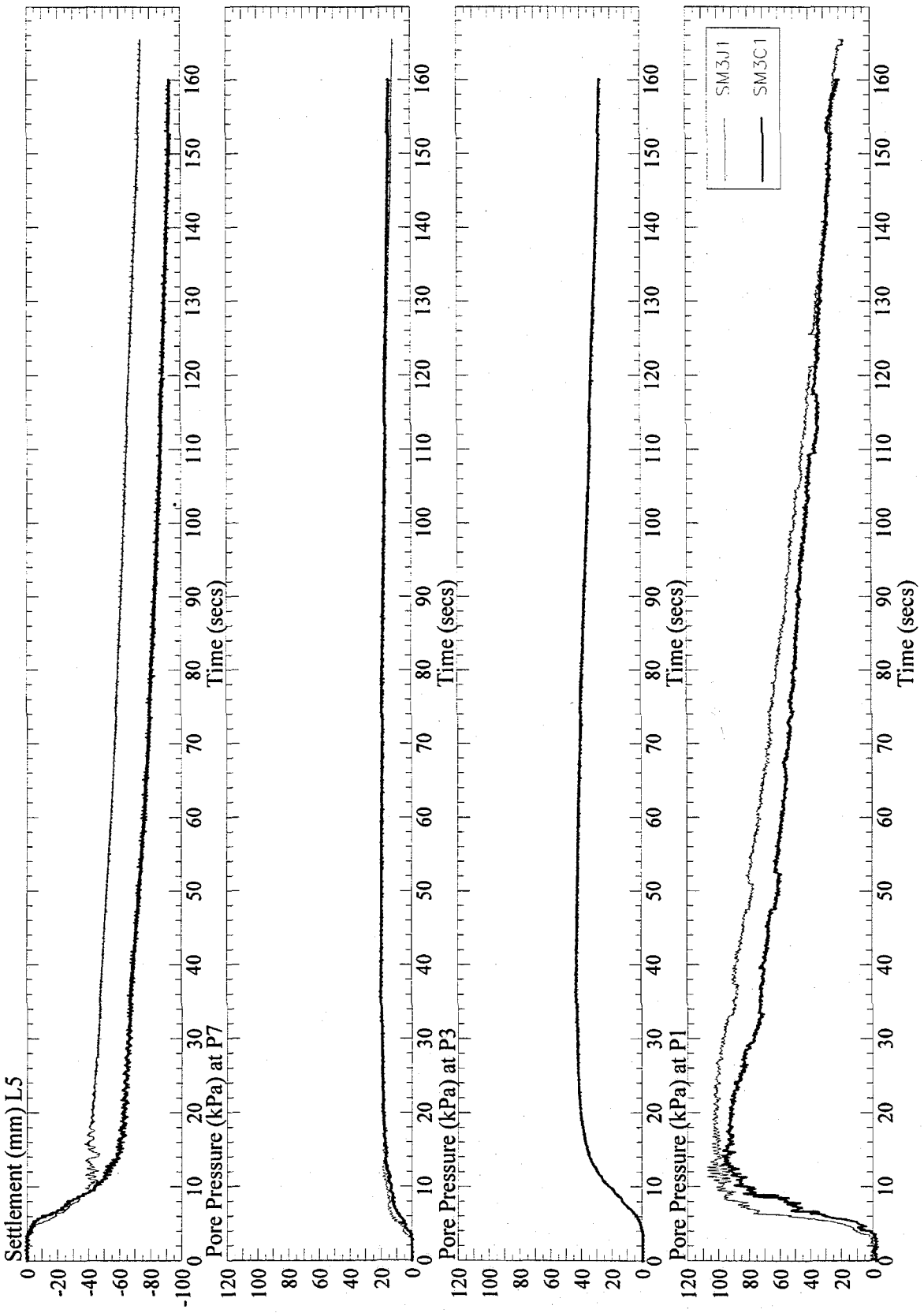

Figure 5-5: Excess pore water pressures for the tests SM3C1 and SM3J1 in loose sand.

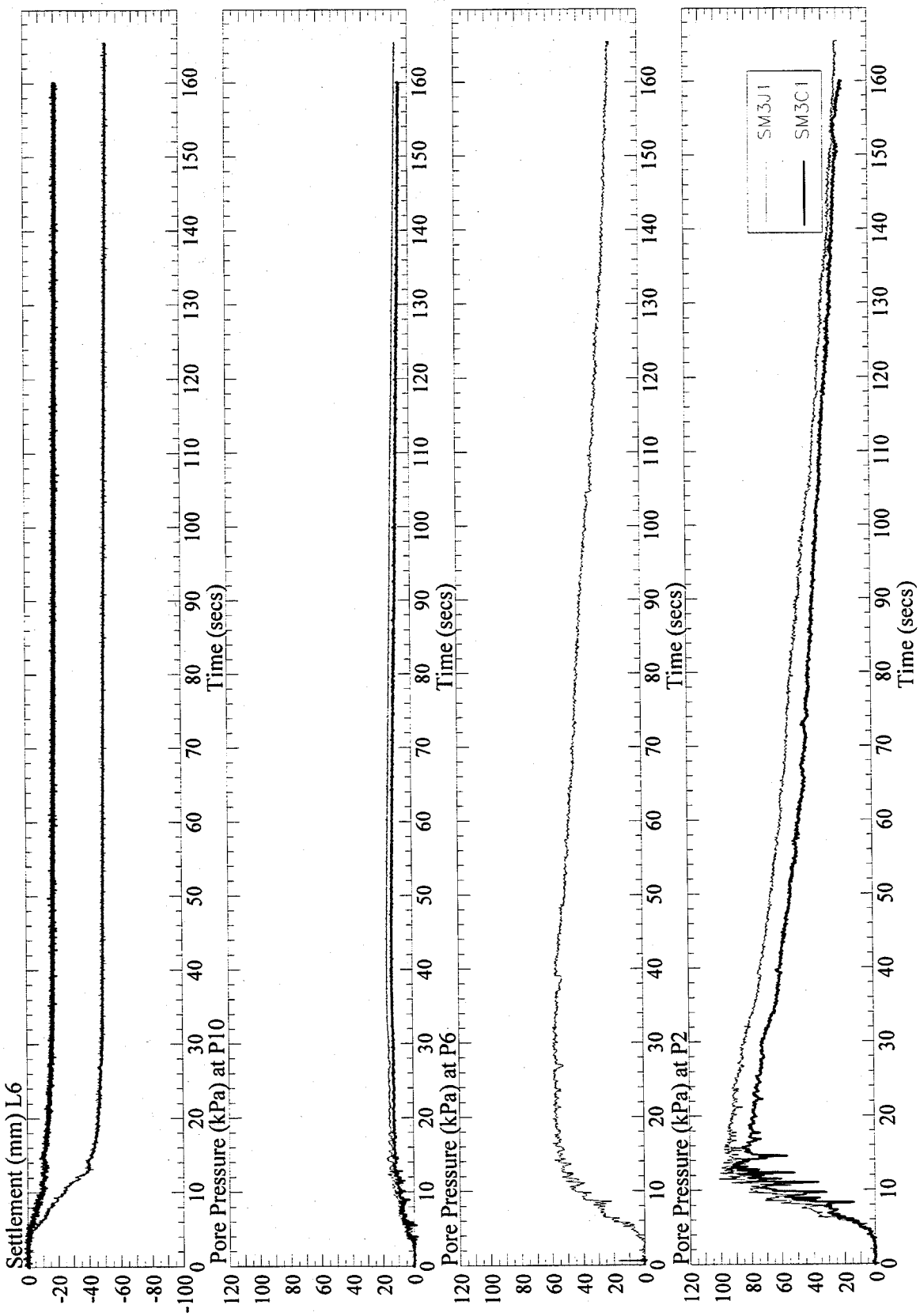

Figure 5-6: Excess pore water pressures for the tests SM3C1 and SM3J1 in dense sand.

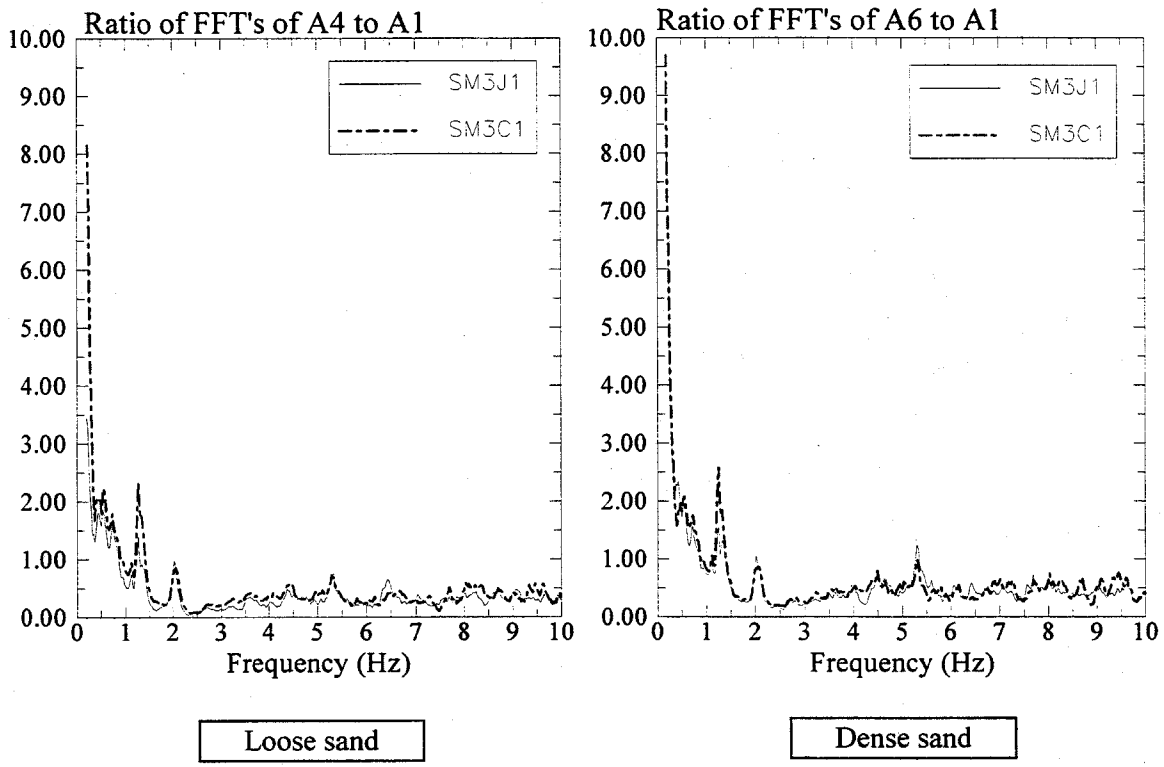

Figure 5-7: Transfer functions for tests SM3C1 and SM3J1.

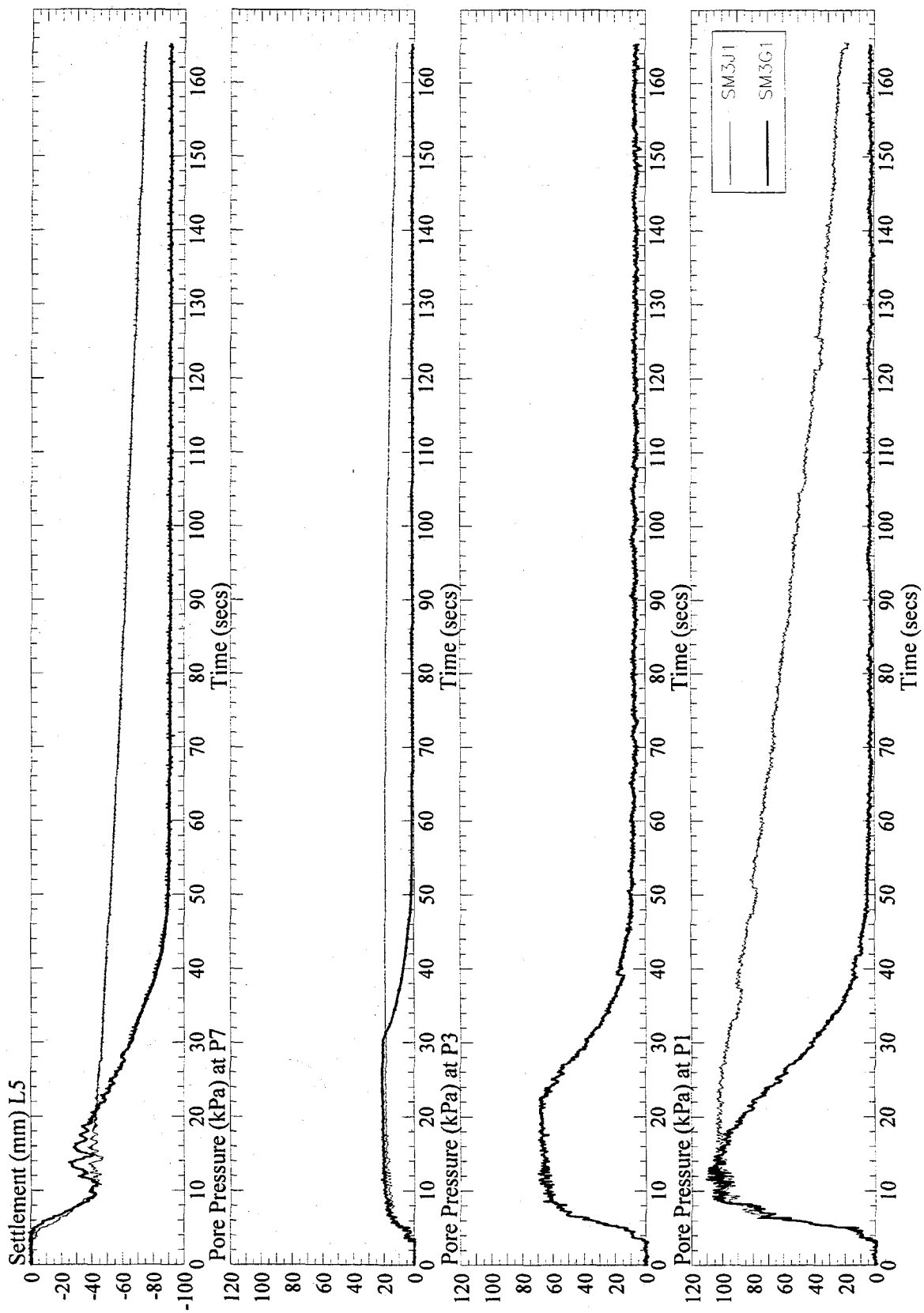

Figure 5-8: Excess pore water pressures for the tests SM3J1 and SM3G1 in loose sand.

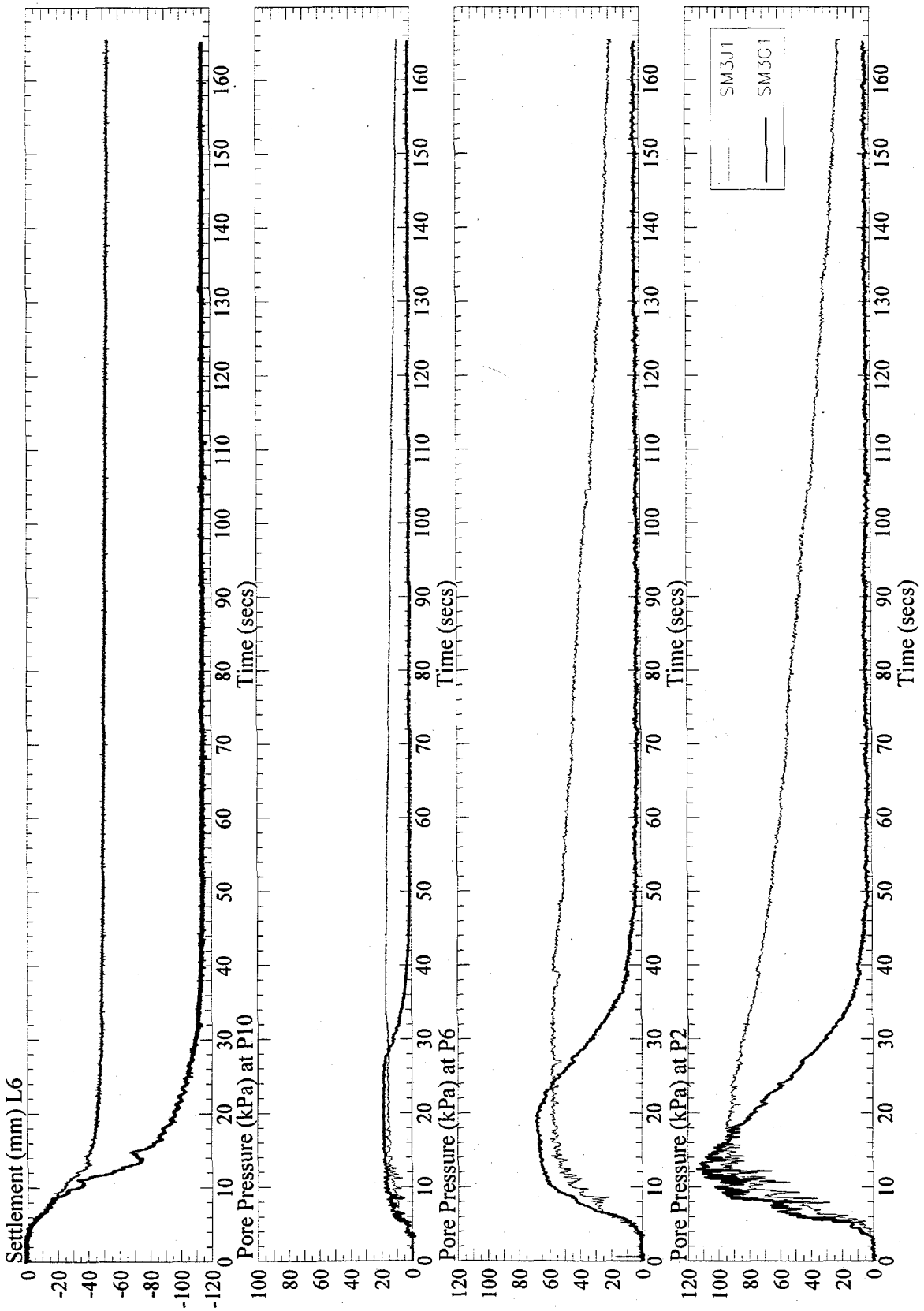

Figure 5-9: Excess porewater pressures for the tests SM3J1 AND SM3G1 in dense sand.

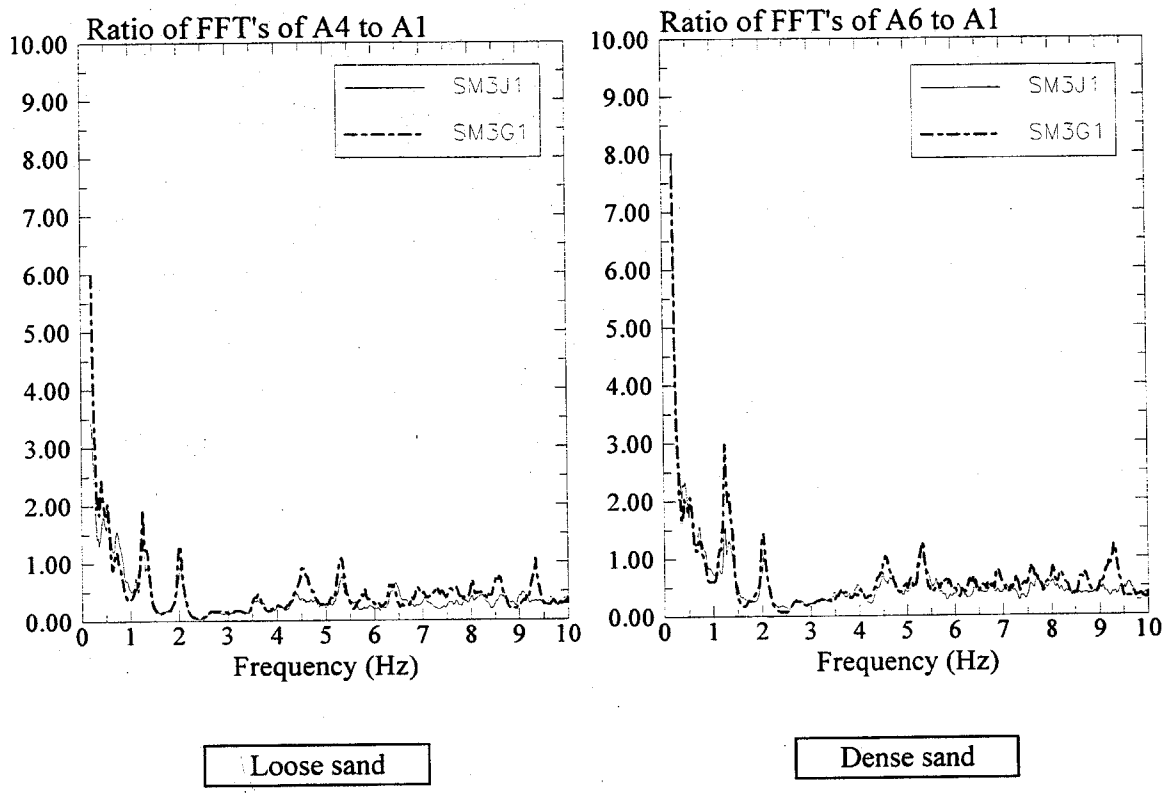

Figure 5-10: Transfer functions for the tests SM3J1 and SM3G1.

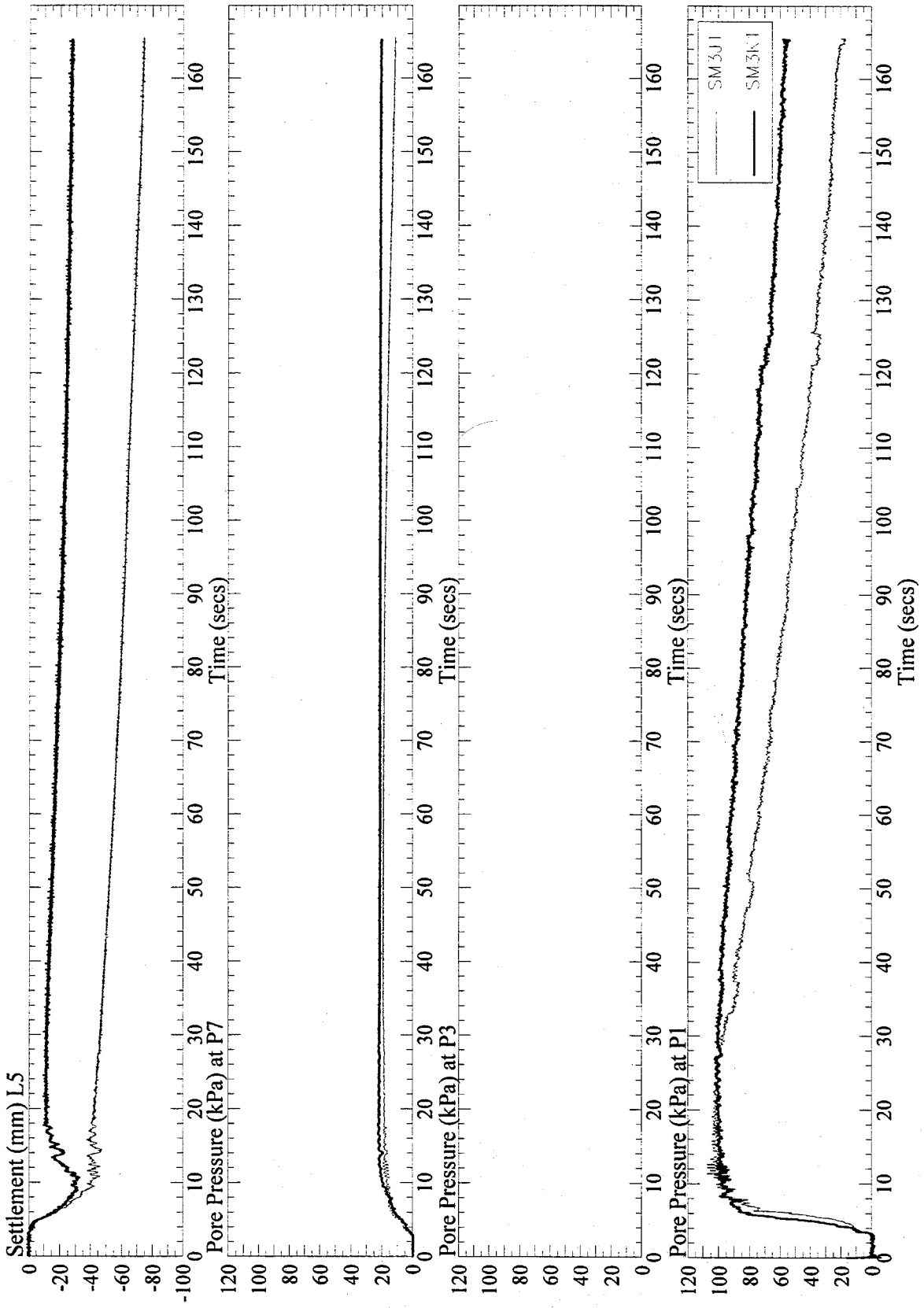

Figure 5-11: Excess porewater pressures for the tests SM3J1 and SM3K1 in loose sand.

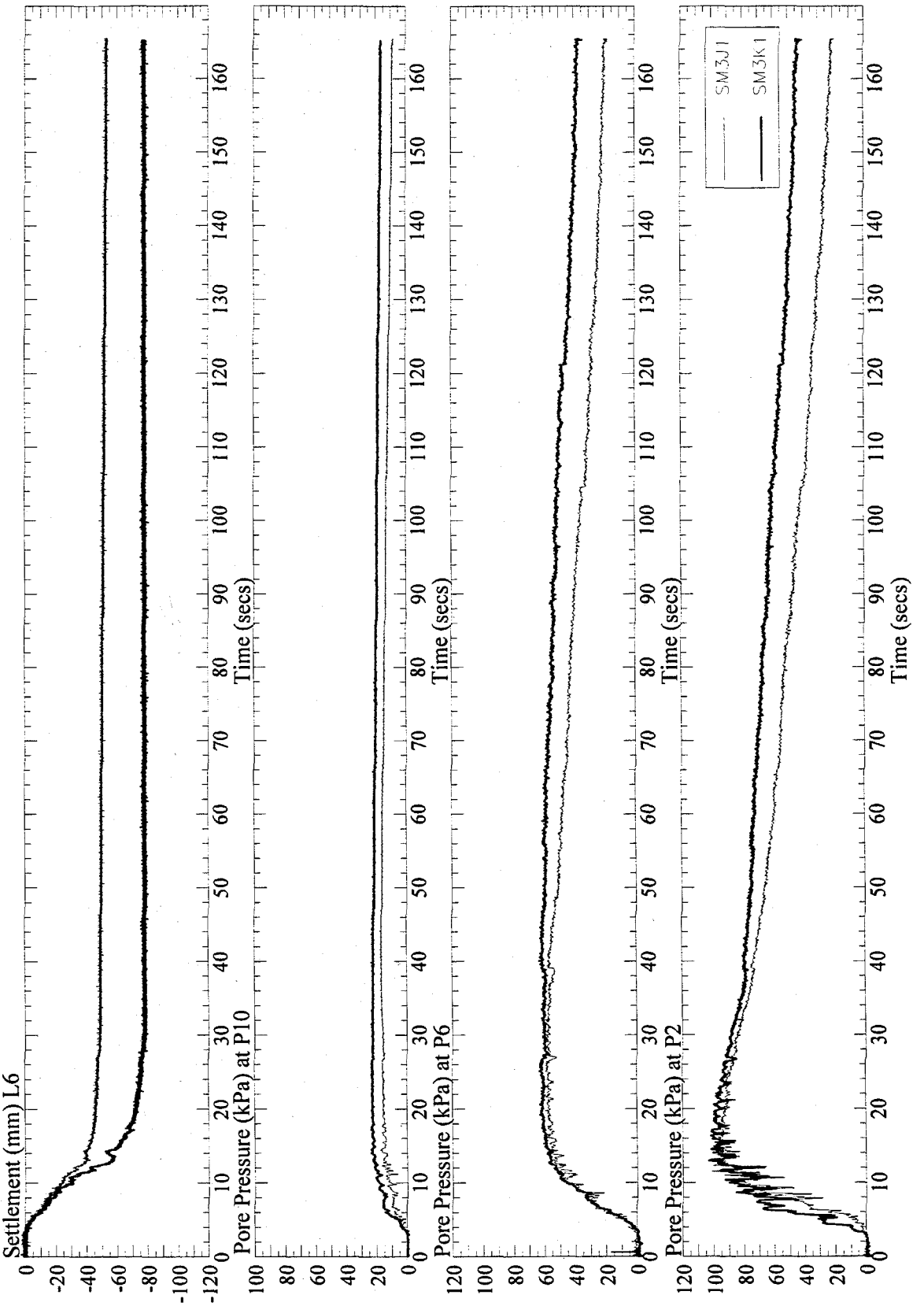

Figure 5-12: Excess porewater pressures for the tests SM3J1 AND SM3K1 dense sand.

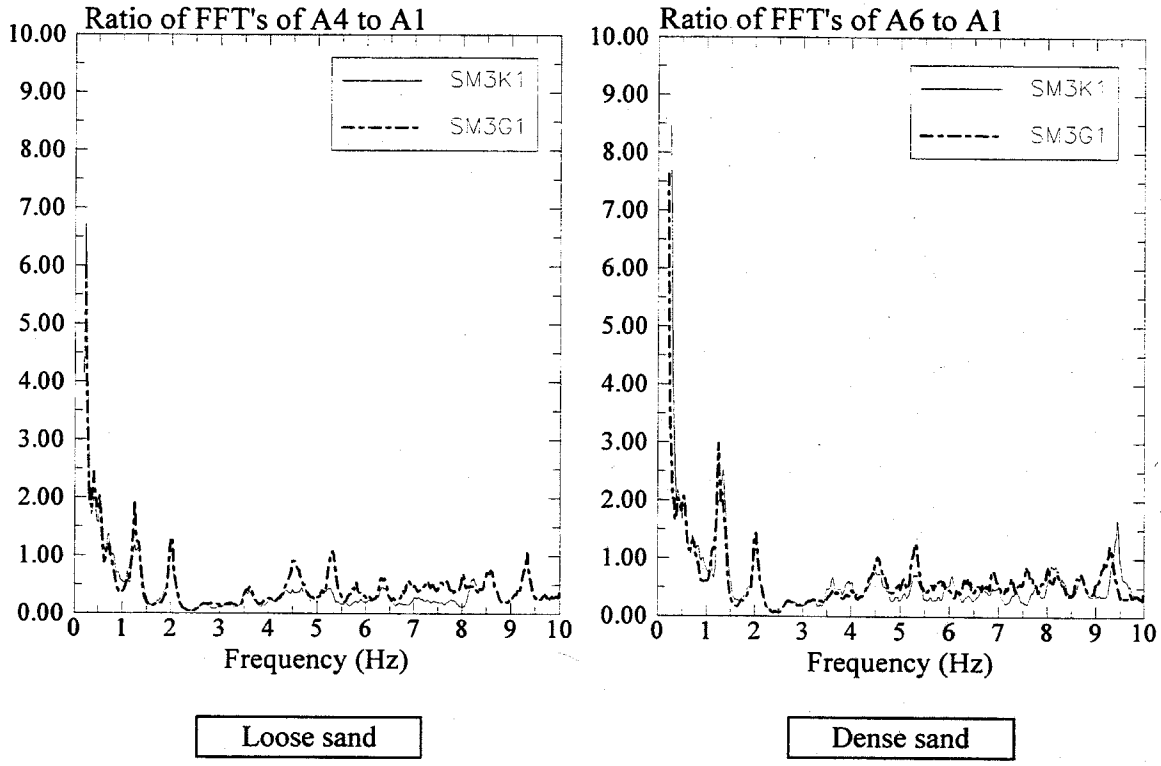

Figure 5-13: Transfer functions for the tests SM3K1 and SM3G1.

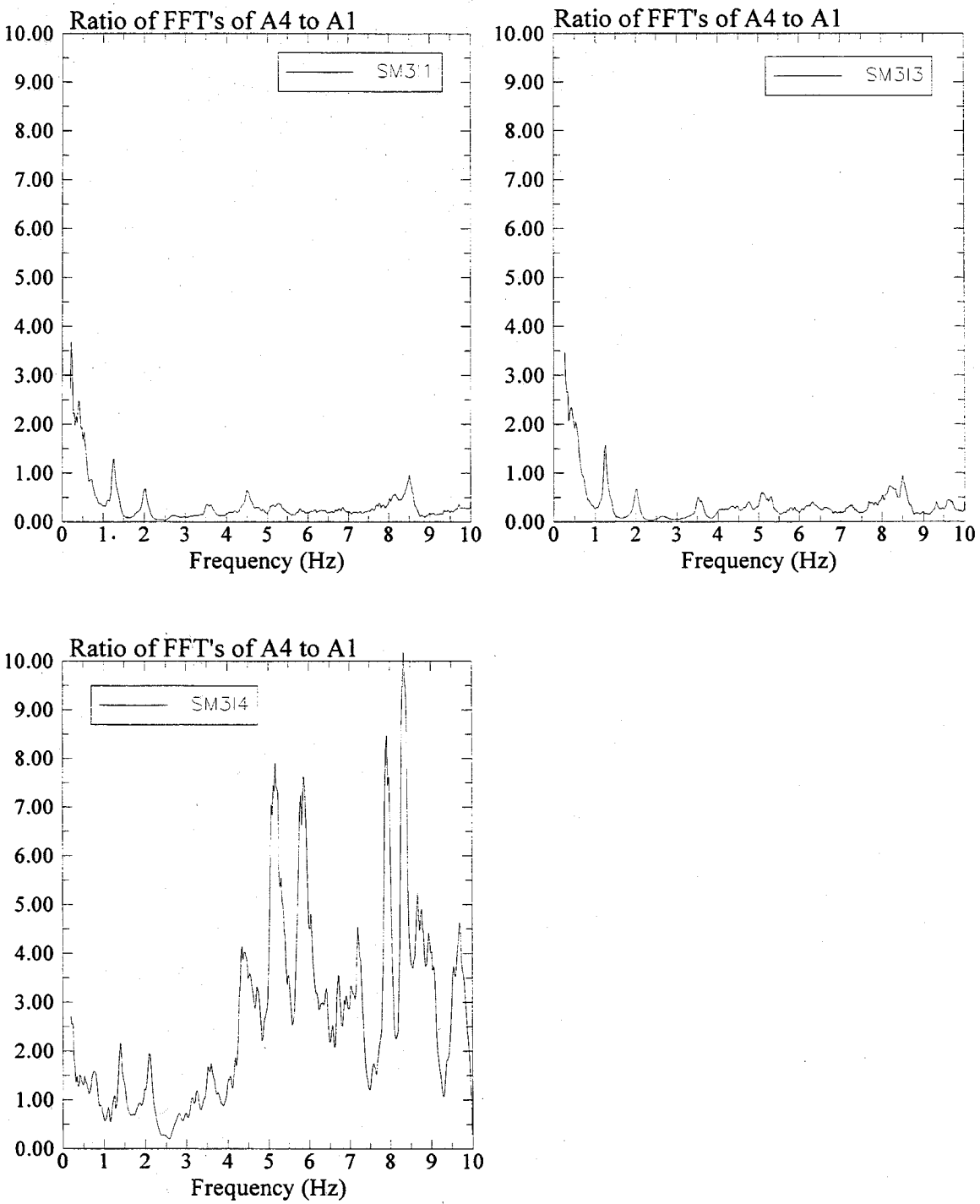

Figure 5-14: Transfer functions for the tests SM3I1, SM3I3, and SM3I4 which had uniform sand densities throughout the model.

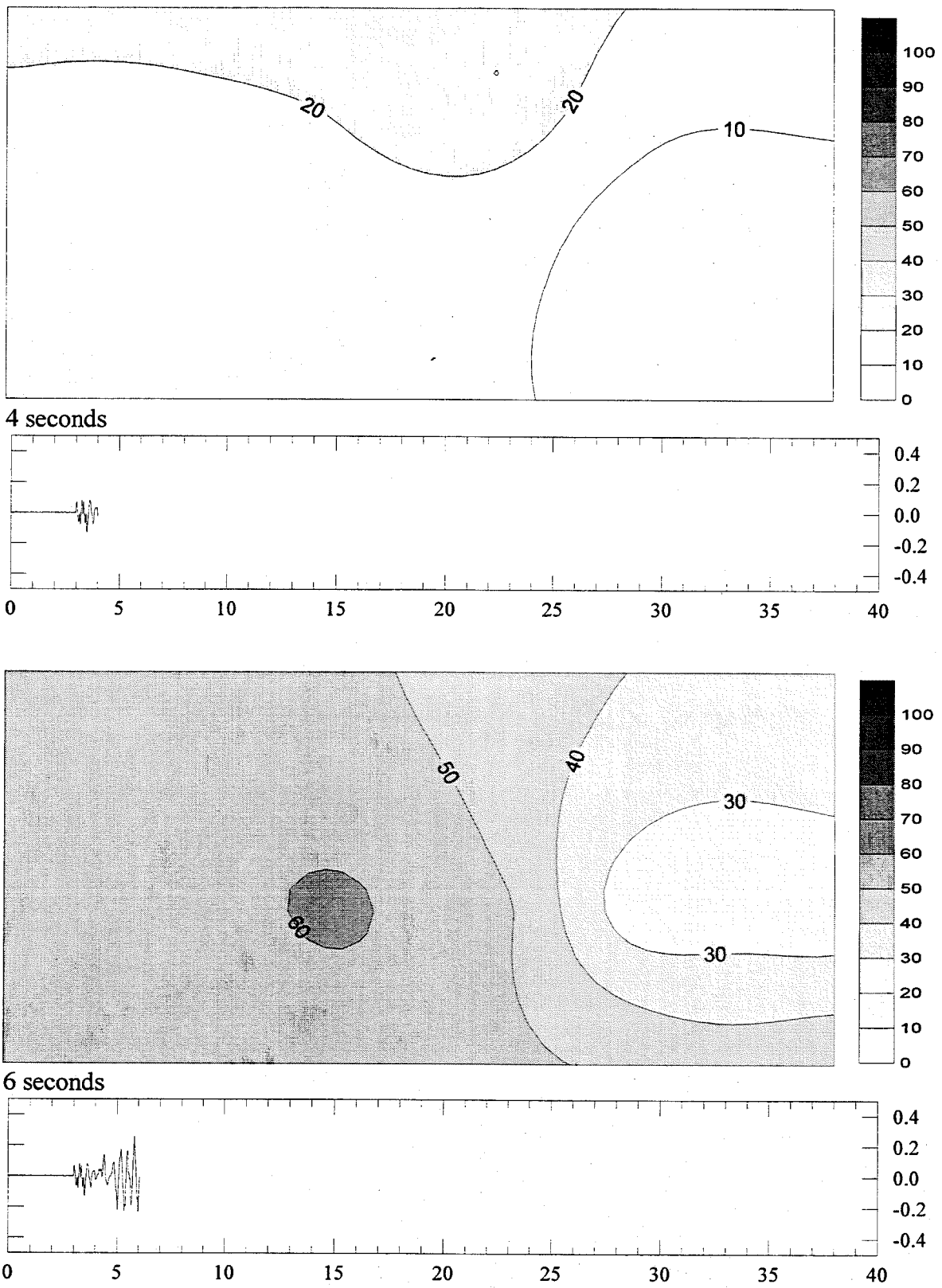

Figure 5-15: Contours of the pore pressure ratio, R_u(%), in the model test SM3G1 at times equal to 4 seconds, and 6 seconds (prototype scale).

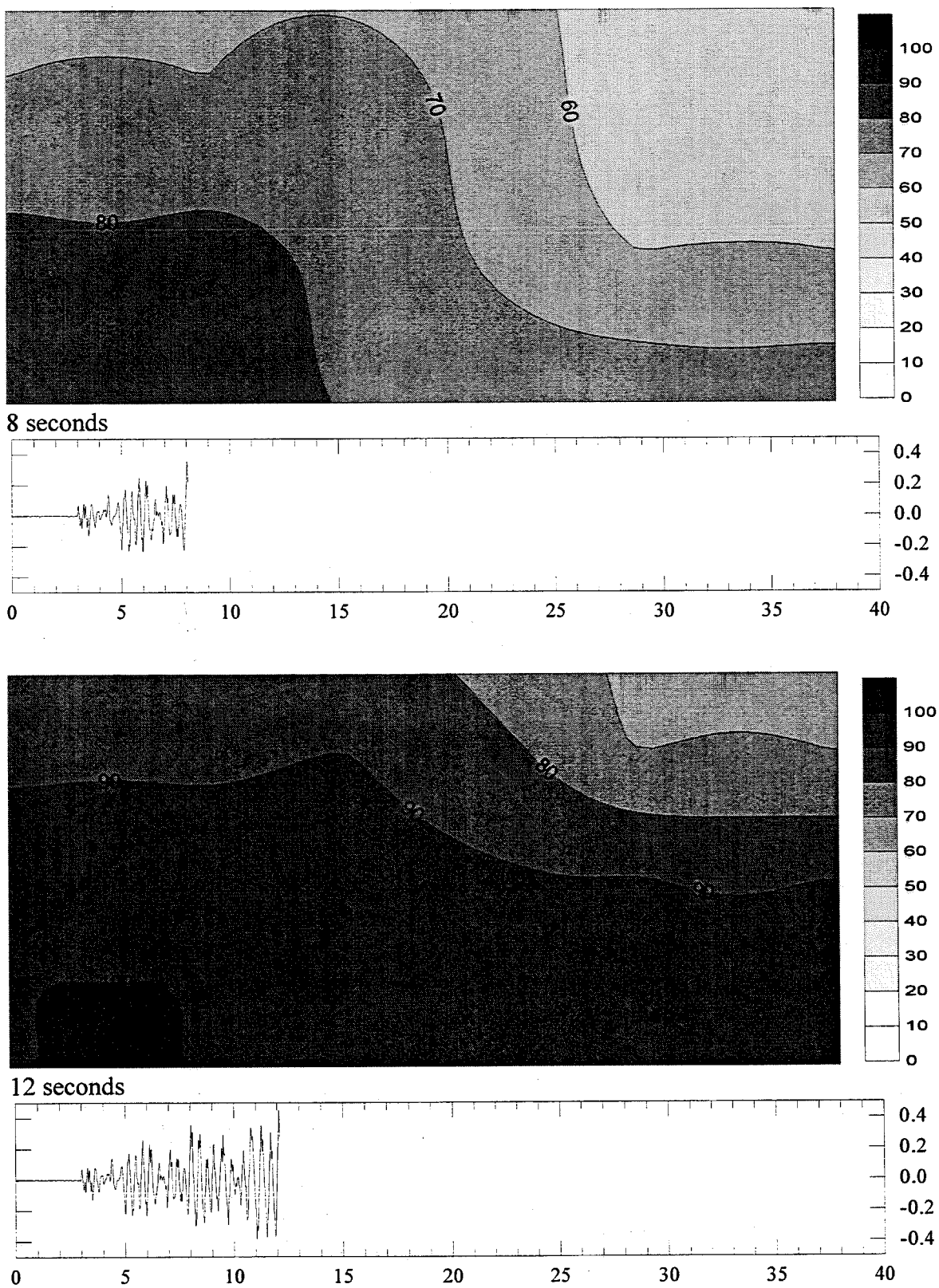

Figure 5-16: Contours of the pore pressure ratio, R_u(%), in the model test SM3G1 at times equal to 8 seconds, and 12 seconds (prototype scale).

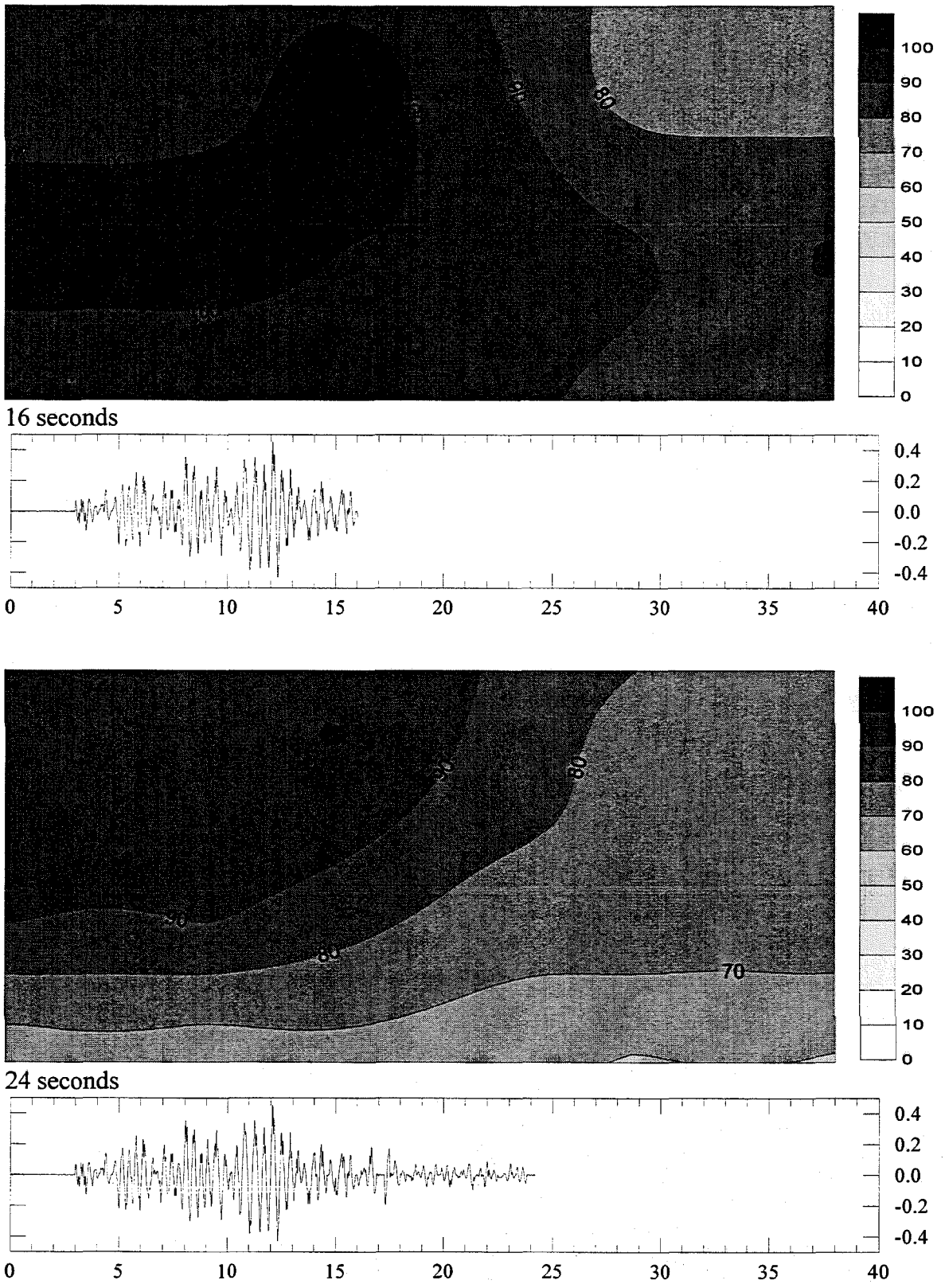

Figure 5-17: Contours of the pore pressure ratio, R_u(%), in the model test SM3G1 at times equal to 16 seconds, and 24 seconds (prototype scale).

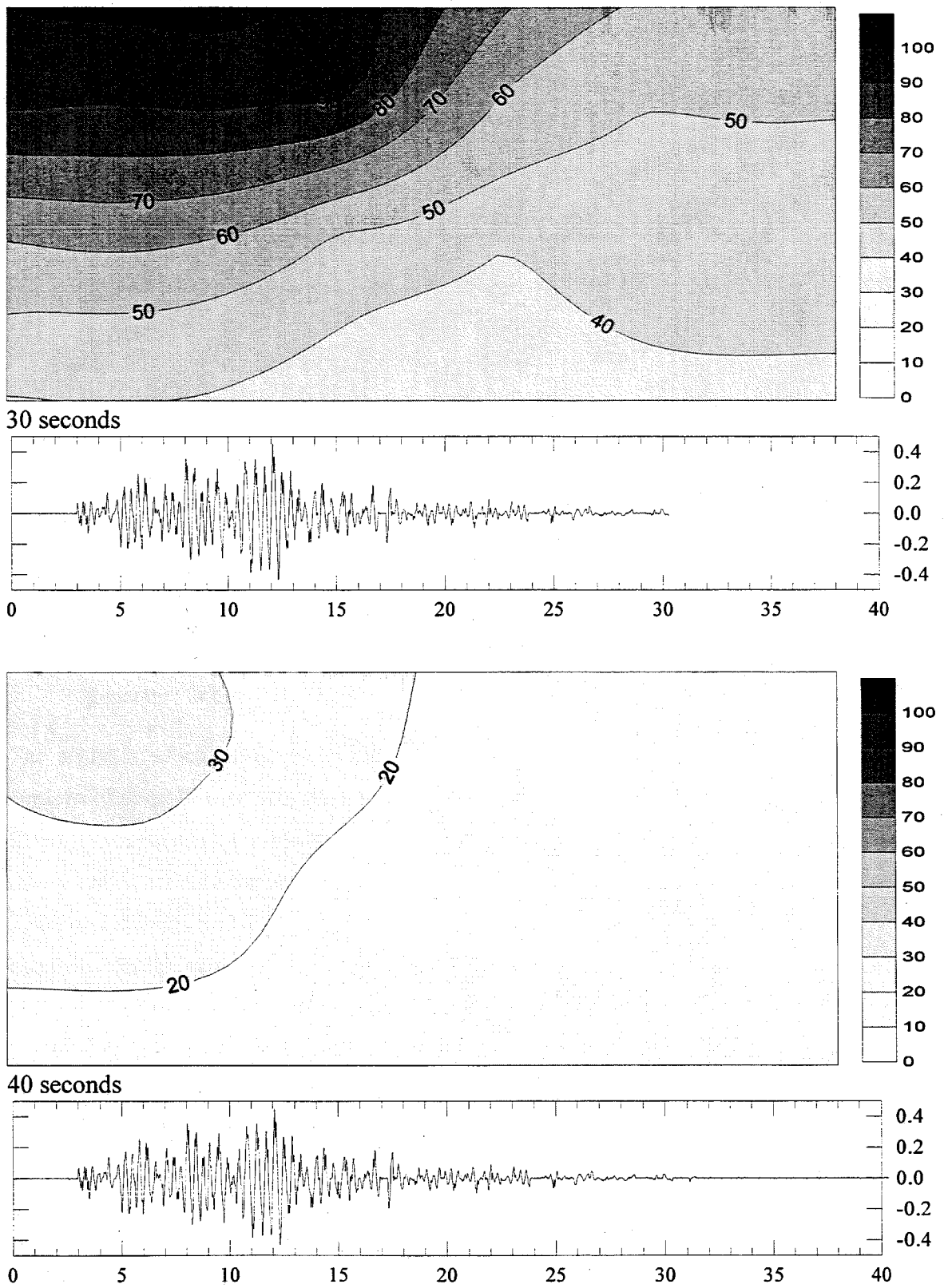

Figure 5-18: Contours of the pore pressure ratio, R_u(%), in the model test SM3G1 at times equal to 30 seconds, and 40 seconds (prototype scale).

Chapter 6

ANALYSIS OF TEST RESULTS

6.1 Introduction

The results of the one-g model testing and the centrifuge Model 3 test were presented and discussed in Chapter 5. In the following chapter some analyses are described to explain or clarify two important issues which were identified in Chapter 5. They are as follows:

1) The apparent conflict of the dynamic time and diffusion time scales.

2) The behavior of adjacent loose and dense sands in terms of the excess pore pressures generated in both.

The analyses which have been performed are based on Terzaghi's consolidation theory. The concept of consolidation was discussed in Chapter 2, Section 2.2, and the equations governing Terzaghi's theory were introduced in Chapter 2, Section 2.3, equations 2-14 through 2-17. The theory only considers the behavior of the excess pore pressure within a soil, and is based on a linear one-dimensional compressional model of soil behavior. In reality the pore pressure is coupled with the generally non-linear constitutive behavior of the soil. Therefore, the analyses presented herein make significant simplifications of the real behavior of the sand in the models. However, as will become evident, they prove to be quite useful in demonstrating factors which dominate the model excess pore pressure behavior, and in evaluating the issues (1) and (2) above.

6.2 One-Dimensional Consolidation Theory Applied to Results

In Chapter 5, Section 5.2.3, the results from the centrifuge Model 3 tests and equivalent one-g models were compared in terms of the prototype dynamic time. The magnitude and rate of generation of excess pore pressures in the one-g models were in general greater than those in the centrifuge Model 3, and the rate of excess pore pressure dissipation was, in general, less.

If the behavior at the base of the models is compared, the data (Chapter 5, Figures 5-3 through 5-6) indicates that the generation of pore pressures in the one-g models occurred at a rate about 3 to 5 times greater than in the centrifuge Model 3. From the same data, the rate of dissipation (after the earthquake shaking had ceased) at the base of the models was about the same in the one-g models and the centrifuge Model 3.

If, for the moment, the two-dimensional effects are ignored at the base of the model and it is assumed that the dissipation of the excess pore pressures is occurring principally in the vertical direction, then the model can be analyzed using one-dimensional consolidation theory. From equation 2-15 (Chapter 2) the following relationship is defined:

$$\text{Non-dimensional time } T = \frac{c_v \, t}{H^2} \quad \text{where}$$

(6-1) t = time

H = effective length of drainage, which for the models tested is the depth

c_v = coefficient of consolidation (equation 2-16)

Equation (6-1) can be used to make an assessment of the relative ability of the centrifuge model and one-g models to dissipate the excess pore pressures. The degree of consolidation is related to the non-dimensional time, T, from the solution of the non-dimensional form of the consolidation equation (Scott, 1963). The degree of consolidation at a point is simply the ratio of the excess pore pressure dissipated up to time t, to the initial excess pore pressure at the same point at time zero.

In equation (6-1) the coefficient of consolidation, c_v, is a function of the pore fluid unit weight, the void ratio, permeability, and compressibility of the sand. The pore fluid unit weight can be assumed to remain constant during a model test; however, the remaining parameters do change. In all of the tests, the void ratio decreased as the sand densified. The maximum amount of change observed in the models was about 3%; therefore, for the purposes of calculating c_v, it can be assumed to be constant. The permeability was defined in Chapter 3, Figure 3-2, as a function of the void ratio. Therefore, it is reasonable to assume that it also changes little during a test. The compressibility of the soil, a_v was defined in Chapter 3, Figure 3-7, based on the results of confined compression tests. The factors which determine a_v, were the vertical effective stress, relative density (D_r), and loading condition (unloading or loading). Whether these same factors control the sand behavior to the same degree in the model tests is a point of some conjecture. The

confined compression test externally loads the sand in a quasi-static way, which is very different from the model tests which were subjected to dynamic excitation. The stress path of the sand in the two tests is quite different. This will be discussed further in subsequent sections, but for the moment it is considered that the same factors directly affect the compressibility behavior in the model tests.

Of the variables defining a_v, the relative density changes with the void ratio, and therefore remains relatively constant in a test. However, the vertical effective stress and the loading-unloading condition can change dramatically during a test. For example, in the centrifuge Model 3, the initial effective stress at the base of the model was on the order of 100 kPa, and decreased as the generation of excess pore pressure occurred, to a minimum of about 60 kPa. In the upper part of the model, the initial effective stresses were lower due to the shallower depth and decreased to near zero values as these layers liquefied. Similarly, for the one-g models the confining stresses changed at the model base from about 4 kPa to 0 kPa as the sand liquefied in these tests. From Figure 3-7 in Chapter 3, the resulting change in the coefficients of compressibility (and consequently c_v) caused by the change in effective stress could be up to 300%. It should also be noted that the vertical effective stresses vary both with time and depth in a model test. Upper layers have significantly different values of a_v (and hence c_v) from lower layers. Given that the dissipation of the excess pore pressures occurs by upward drainage of the pore fluid through the sand, the conditions in the upper layers influence the drainage in the lower layers and *vice versa.*

The remaining parameter influencing the compressibility of the soil, a_v, is the loading condition which exists in the sand. As indicated in Chapter 3, Figure 3-7, loading or unloading conditions can be developed in a static confined compression test. The loading condition corresponds to virgin compression, which occurs when the vertical effective stresses in the sand increase above any previous magnitudes of stress. If the vertical effective stress decreases, unloading occurs and sand rebounds. It should be noted that for the test sands the coefficient of compressibility for the unloading condition is a factor of 5 to 10 times less than for the loading condition (Figure 3-7 and Figure 3-9). If the vertical effective stresses subsequently increase again, then the sand is reloaded, but the compressibility of the soil follows the unloading values until the magnitude of the stress exceeds any prior level. At this stage the sand returns to virgin loading behavior. In the

present tests the loading or unloading state is caused by the decrease or increase of pore pressures at constant total stress.

From the above discussion of the parameters influencing equation (6-1), it is obvious that the dissipation or diffusion of excess pore pressures is complex even in terms of Terzaghi's one-dimensional consolidation theory. Since the void ratio and permeabiltity are relatively constant, the compressibility influences the behavior most strongly. It should be noted that the dissipation processes occur after the earthquake shaking ceases, and but also during earthquake shaking at the same time as generation of excess pore pressures occurs. These aspects of the model tests are discussed further in the following sections, and will be termed the "generation" and "dissipation" phases.

6.2.1 Dissipation of Excess Pore Pressures After Shaking Ceases

During the generation phase in the model tests, the excess pore pressures increased and the vertical effective stress decreased. In terms of the discussion in the Section 6.2, the sand is experiencing unloading during this phase. After the earthquake shaking ceased, the generation of excess pore pressures also ceased and only dissipation continued. The magnitudes of the excess pore pressures decreased and the vertical effective stress in the model increased. It terms of the discussion in Section 6.2, the sand is presumably experiencing reloading during this dissipation phase. However, the sand was significantly disturbed by the earthquake during the generation phase, and in most cases actually liquefied. This is quite different from the conditions in the confined compression test as discussed in Section 1.2, and it is quite possible that the disturbance of the grain matrix was sufficient to create virgin loading behavior in the subsequent dissipation phase. As described in Section 6.2, there is a significant difference between the compressibility values for virgin loading and reloading.

To attempt to resolve which behavior best mimics the actual behavior of the models, equation 6-1 will be used to attempt to predict the observed time for the dissipation of excess pore pressures at the base of some of the model tests. The tests include the centrifuge Model 3 and the one-g tests SM3C1 and SM3G1. The Figures 5-4 and 5-5 can be referred to for Model 3 and SM3C1 (constructed from Nevada sand), and Figures 5-5 and 5-6 for SM3G1 (constructed from Blend 6-1 sand). The pore pressure histories at pore pressure transducers P1 and P2 at the base of the models have been selected for comparison.

From the plots, the drop in excess pore pressure has been measured from the time when the dissipation phase starts to some arbitrary time in the record. The duration of the dissipation time t, over which the drop in excess pore pressures occurs, is given in Table 6-1. The degree of consolidation is calculated at t, and the non-dimensional time T for the base of the models is determined (Scott, 1963) using a solution which assumes a triangular distribution of excess pore pressures throughout the depth of the model.

For each of the models, the coefficient of consolidation, c_v, has been calculated using the initial state of the models and the laboratory data (and relationships) reported in Chapter 3. It should be noted that the laboratory data was determined by tests completely independent of any model tests, and therefore the values derived from them provide an independent assessment of the properties of the sand in the model tests. A range of computed c_v values is presented in Table 6-1 which corresponds to a prototype vertical effective stress range of 5 to 100 kPa. The corresponding range in calculated times of dissipation (in terms of the prototype dynamic time scale) is also presented in Table 6-1.

A comparison of the values presented in Table 6-1 indicates that in both the loose and dense material, the measured time of dissipation, t, is bracketed by the range of calculated values which corresponds to the virgin loading condition. The calculated range of dissipation times corresponding to the reload (or unload) condition is significantly different from the measured values. Based on these results it appears that the use of the virgin loading condition, as defined by the one-dimensional confined compression tests, most reasonably represented the dissipation phase behavior.

As discussed previously the results presented in this thesis have all been presented in terms of the dynamic prototype time scaling to provide a uniform consistent reference. From Chapter 5, Table 5-5, the dynamic scale factor for the centrifuge model is 50, and all results of the Model 3 test were plotted in terms of prototype time (recorded model time multiplied by 50). On Table 5-5 the dissipation time scale factor is given as 2500, and if the primary interest is a dissipation process, this factor should be used to multiply the model times recorded in centrifuge Model 3 test. Certainly in this discussion of the dissipation phase (after the earthquake shaking ceased), it is appropriate to use the dissipation time scale the factor of 2500 for this phase of the Model 3 test. The results of the centrifuge Model 3 test presented in Appendix B are already in terms of prototype dynamic time; therefore, to convert this to a dissipation time scale it has to be stretched

by an additional factor of 50. A similar process should be followed for the one-g models, but as indicated in Table 5-5 the scaling factor for the dissipation time is significantly less. There is also a choice between a scaling factor corresponding to an unloading or loading value condition in the sand. Based on the earlier discussion, the loading value is appropriate, and implies the prototype dynamic time scale should be stretched by about 12 times.

To demonstrate the effect of these stretched time scales, Figure 5-3 (Chapter 5) has been re-plotted to the modified time scales in Figure 6-1. In this figure the time scale switches at 18 seconds from a prototype dynamic scaled value, to a prototype dissipation scaled value according to the values presented above. At 18 seconds, significant earthquake shaking ceases, and dissipation behavior subsequently dominates the model behavior. The results show that the dissipation rates of excess pore pressures in the centrifuge Model 3 and the one-g model SM3C1 match extremely well in this correctly scaled time frame. At P1 the magnitude of the excess at the pore pressure transducer in the centrifuge is significantly less, but as discussed in Section 6.2.2 below, this is due to the effect of the dynamic and dissipation time scaling incompatibility in the generation behavior.

In the one-g model SM3K, which was constructed with the Blend 6-1, the pore fluid was modified in an attempt to mimic the much slower dissipation times observed in one-g models constructed of Nevada sand. The results of that test are presented in Chapter 5, Section 5.2.3.4. The scaling of the pore fluid viscosity was arrived at by using the scaling relationships derived in Chapter 2, which utilize Terzaghi's one-dimensional consolidation theory. In that derivation the behavior of the sands during the dissipation phase was assumed to follow a loading behavior in terms of the discussion above. Considering the assumptions inherent in the methodology, the modification of the pore fluid viscosity worked quite well in achieving the targeted results.

In summary, the simplified analyses using the one-dimensional consolidation theory above indicate that the assumption of a virgin loading condition in the sand during the dissipation phase provides reasonable results. This is supported by:

1) The comparison of calculated times of dissipation with measured values.

2) The favorable comparison of the dissipation behavior in the centrifuge Model 3 and one-g model SM3C1 when the time scale was modified assuming a loading condition in the sands.

3) The results of the one-g model SM3K, in which the properties of the alternate pore fluid were arrived at by assuming a loading condition.

It is emphasized that underlying the above conclusion is that the loading and unloading behavior of the sand in the model is represented by the confined compression tests. As discussed previously in Section 6.2, the conditions which exist in the models and the confined compression test are significantly different. Therefore, while the assumption of a virgin loading condition during the dissipation phase appears to give reasonable results when the one-dimesional consolidation theory is employed, it probably does not reflect the true behavior of the sand in the models, which, as discussed before is very complex.

6.2.2 Generation of Excess Pore Pressures

During the earthquake shaking, the generation of excess pore pressures occurred in the models. In the generation phase there is essentially a competition between the ability of the earthquake to create excess pore pressure and the ability of the sand to dissipate the excess pore pressures, which was discussed conceptually in Chapter 2, Section 2.2. In idealized terms, the earthquake can be viewed as a long series of spikes or increments in excess pore pressure. As soon as the spike or increment occurs, the dissipation of that spike begins. If the full dissipation of the excess pore pressure has not occurred before the next spike or increment, then the excess pore pressures begin to accumulate and grow as observed in the generation phase of the model tests.

Some of the factors which determine the ability of the earthquake to generate excess pore pressures are the initial state or density of the sand, the intensity of shaking which affects the cyclic stresses and strains imposed on the sand, and the effective confining pressures within the sand. For the one-g models and the centrifuge models, the earthquake motions were quite similar and the sand densities were of the same order. However, the effective confining stresses were quite different. Given the similar densities and earthquake motions, the higher confining stresses in the centrifuge Model 3 should result in greater generation of excess pore pressures as discussed in Chapter 2, Section 2.2. However, contrary to this expectation, the centrifuge model generated excess pore pressures at a lower rate than the one-g models, as discussed in Chapter 5, Section 5.2.3.1. A comparison of the rates at the base of the centrifuge Model and the one-g model SM3C1 indicates that the generation in the one-g model SM3C1 was about 3 times greater than in Model 3 (Chapter 5, Figures 5-3 and 5-4).

To investigate this observation, a simplified analysis can be performed using one-dimensional consolidation theory. In effect the relative ability of the test sands to dissipate the increments in excess pore pressure while they are being generated is analyzed. If identical increments of pore pressure are applied to each model, the time, t, for the pore pressures to dissipate to some equal value can be calculated. This is equivalent to making the non-dimensional time, T, equal in both models. Given this, equation (6-1) can be recast as follows:

$$\frac{t_g}{t_c} = \frac{c_{vc}}{c_{vg}}\left[\frac{H_g}{H_c}\right]^2 \qquad (6\text{-}2)$$

where the subscript, c, denotes the centrifuge model
and the subscript, g, denotes the one - g model

If the value of the ratio $\frac{t_g}{t_c}$, was equal to the ratio of the dynamic time scales of the two models, then the generation rate when the data are plotted to the appropriate time scale should be similar. For the model tests above, the ratio of the dynamic time scales is approximately 10 (Chapter 5, Table 5-5).

During the earthquake shaking, the excess pore pressures increase and the vertical effective stresses decrease. Therefore, it seems appropriate to use values of c_v which correspond to an unloading or reloading condition. This assumption becomes questionable as the excess pore pressures approach higher levels because the fabric of the sand becomes significantly disturbed; however, for the moment it will be assumed to be a reasonable approximation. Using equation (6-2) and the values of the coefficients of consolidation in Table 6-1, corresponding to a load or reload condition, the ratio of the time of dissipation in SM3C1, t_g, to the time of dissipation in Model 3, t_c , during the generation of the excess pore pressures pore was calculated to range from 22 to 31.

In comparison to the ratio of the dynamic time scales of 10, the above ratio implies that in the one-g model SM3C1, during the shaking, the pore pressures are dissipating about 2 to 3 times slower than the centrifuge model. This implies that the rate of generation of excess pore pressures would be significantly greater in the one-g model SM3C1. They were, in fact, observed to be about 3 times greater as described previously.

It is important to note that in the centrifuge Model 3, the maximum excess pore pressures generated at the base were significantly less than in the one-g model SM3C1 which actually liquefied. From the above analysis it seems apparent that the lower generation of excess pore pressures in the centrifuge Model 3 is an artifact of the modeling technique and not necessarily the behavior of the sand.

The above results compare the behavior of centrifuge and one-g models; however, similar comparisons can also be made between the models and a real prototype. The values of c_v for the prototype are the same as reported for the centrifuge Model 3 in Table 6-1, but the depth of the prototype is 50 times greater than the centrifuge Model 3. Following the same analysis procedure as above indicates that the dissipation rate in the centrifuge model during the earthquake will be 50 times greater than in the prototype. For the one-g model SM3C1, the dissipation rate during the earthquake will be 16 to 21 times greater. Both of these results indicate that the rate of generation of excess pore pressures in the models will be lower than what would occur in the real prototype. It is not possible to say that the rate of generation in the prototype would be 50 times greater than observed in the centrifuge model, or 16 to 21 times greater than the one-g model, because two-dimensional effects have been ignored and the variation of properties with time has been ignored. The change in properties is potentially a very significant issue because the dynamic behavior of the sand is strongly coupled to the excess pore pressures, which are being dissipated during the shaking. This highlights the problem of the incompatibility that exists between the dynamic time scale and dissipation time scale during the generation of pore pressures.

Unlike the dissipation phase after the earthquake shaking ceases (as discussed in Section 6.2.1), it is not possible to simply adjust the time scales of the results to correct for the incompatibility as was done in Section 6.2.1 for the centrifuge Model 3 and the one-g model SM3C1 (Figure 6-1). This is because during the generation of pore pressures both dynamic and dissipation processes are occurring; therefore, both dynamic and dissipation time scaling effects are inherently present in the model behavior. The dynamic processes are created by the excitation of the earthquake, and the dissipation processes occur as soon the pore pressures begin to rise. As a best guess, the generation behavior in the prototype lies somewhere between the dynamic time scale (as plotted) and the dissipation time scale values which require the dynamic time scale to be compressed by factor of 50 for the centrifuge results, and a factor of 16 to 21 for the one-g model test SM3C1 results.

The significance of the above is apparent in the results of the centrifuge Model 3, which as discussed previously did not liquefy at the base. However, the one-g model SM3C1 did liquefy, and based on the factors given above, this implies that the prototype would certainly liquefy. This error, inherent in the modeling technique, is significant if the prediction of liquefaction in the prototype is an important element of the model testing. If the results of the centrifuge Model 3 were used directly, the inference for the prototype behavior would be wrong. If the one-g model results were used, the divergence from the true prototype behavior is less for the particular set of conditions modeled in this thesis. However, if the intensity of the earthquake was progressively reduced in the one-g model test, presumably there would be a point when the excess pore pressures did not reach liquefaction levels. Yet if the same reduced earthquake was applied to the prototype, it would exhibit full liquefaction. Given this scenario, the one-g model technique also has the potential to give misleading indications of the maximum excess pore pressures in the prototype.

In summary, Terzaghi's one-dimensional consolidation theory was applied to assessing the relative behavior of the centrifuge Model 3 and the one-g model SM3C1 (as an example) during the earthquake shaking and generation of excess pore pressures. It was assumed that during this phase the sand would exhibit an unloading or reloading type behavior as defined by the confined compression tests. The results of the analysis correlated with the observed behavior in the actual model tests. In addition to this, the simplified analysis above indicates that the generation of pore pressures in the real prototype could be significantly under-predicted by the models, because of the incompatibility between the dynamic and dissipation behaviors in the models.

6.3 Two-Dimensional Consolidation and Varying Properties

From the discussion of the results in Chapter 5, and above in Section 6.2, there are two issues which should not be ignored in the analysis of the model behaviors, namely the two-dimensional effects and the variation of properties with time.

In Chapter 5, Section 5.3.3, the distribution of excess pore pressures across the section of the model SM3G1 at various times indicated that the generation and dissipation of the pore pressures were influenced by the two-dimensional properties of the model. This was most evident near the interface of the loose and dense columns of sand. In Section 6.2, Terzaghi's one-dimensional consolidation theory was applied to the model test results with some success. At the suggestion of

Dr. R. F. Scott, the theory was extended to two dimensions (as described in Section 6.3.1.1) to attempt to address the true behavior of the models.

Regarding the variation of properties with time, Table 6-1 indicates that the coefficient of consolidation c_v could vary by a factor of about 10 in the centrifuge model depending on whether the excess pore pressures are high or low. The variation in c_v is primarily caused by the compressibility behavior of the test sands which changes significantly with the effective stresses and loading conditions as discussed in Section 6.2.2. The change in c_v potentially plays a significant role in the observed behavior of the models and, therefore, in the analyses presented in this section a provision was added to allow for its variation.

The extended two-dimensional analysis method described above has been used to perform numerical simulations of the centrifuge Model 3, some of the one-g models, and also the prototype.

6.3.1 Methodology of Analysis

The two-dimensional form of Terzaghi's consolidation theory is put into a finite difference formulation as explained in Section 6.3.1.1 below. In this formulation, the coefficient of consolidation, c_v , is a function of the vertical effective stress at any point in the analysis cross-section at any given time. If the model is in the generation phase then the values of c_v are based on unloading (or reloading) behavior, and if in the dissipation phase the values of c_v are based on loading behavior. Other properties required to compute c_v, namely the void ratio and permeability, are given an initial distribution across the analysis cross-section and are held constant throughout the analysis. The basis for this above treatment of c_v was discussed at length in Section 6.2 when Terzaghi's one-dimensional consolidation theory was introduced. It is emphasized that this theory does not account for the two-dimensional constitutive behavior of the granular structure, but is used here only as a reference against which the pore pressure behavior in the tests can be compared.

The finite difference formulation which incorporates the above features was coded to permit numerical analysis. A copy of the code is contained in Appendix A. References used in the development of the algorithm are Scott (1963) and Salvadori and Baron (1959).

6.3.1.1 Two-Dimensional Formulation

The two-dimensional form of Terzaghi's consolidation theory can be written as follows:

$$\frac{k}{\gamma_f}\nabla^2(u) = -\frac{\partial e}{\partial t}\frac{1}{(1+e_0)} = \text{Rate of Volume Strain} \tag{6.3}$$

where

k = coefficient of permeability.

γ_f = unit weight of the pore fluid.

u = excess pore fluid pressure.

t = time.

e = void ratio.

e_0 = intial void ratio.

In addition to this, some definitions are presented below. These have been presented in this thesis previously but are repeated for convenience.

$$\text{Coefficient of Consolidation, } c_v = \frac{k(1+e_0)}{\gamma_f a_v}$$

$$\text{Coefficient of Compressibility, } a_v = \frac{\partial e}{\partial \sigma_v'} \tag{6-4}$$

where

σ_v' = Vertical Effective Stress = $\sigma_v - u$

σ_v = Total Vertical Stress

Now, if the total vertical effective stress remains constant at any point, which is a reasonable assertion for the model tests performed, the following can be derived.

$$\frac{\partial \sigma_v'}{\partial t} = -\frac{\partial u}{\partial t} \tag{6-5}$$

Using equations (6-4) and (6-5), equation (6-3) can be developed as follows;

From (6-4) and (6-5), $\frac{\partial e}{\partial t} = \frac{\partial e}{\partial \sigma_v'} \frac{\partial \sigma_v'}{\partial t} = -a_v \frac{\partial u}{\partial t}$

(6-6) Substituting into (6-3), $-\frac{k}{\gamma_f} \nabla^2(u) = \frac{\partial e}{\partial t} \frac{1}{(1+e_0)} = -a_v \frac{\partial u}{\partial t} \frac{1}{(1+e_0)}$

$$\Leftrightarrow \quad \frac{k(1+e_0)}{\gamma_f} \nabla^2(u) = a_v \frac{\partial u}{\partial t}$$

where $a_v = f(\sigma_v') = f(\sigma_v - u)$

The finite difference form of this equation can be formulated, where it is assumed that the analysis section has been divided into a grid of nodes with equal dimensions between nodes. The equations governing a single node at a given time are as shown in (6-7) below, where the convention for the numbering of the nodes is as indicated;

$$\text{Equation (6-6)} \Rightarrow \frac{k(1+e_0)}{\gamma_w} \left[\frac{u_1 + u_2 + u_3 + u_4 - 4u_0}{\Delta x^2} \right] = f(\sigma_v - u_0) \left[\frac{\Delta u_0}{\Delta t} \right]$$

$$\Rightarrow \frac{k(1+e_0)}{\gamma_w \, f(\sigma_v - u_0)} \left[\frac{u_1 + u_2 + u_3 + u_4 - 4u_0}{\Delta x^2} \right] \Delta t = \Delta u_0$$

(6-7)
$$\Rightarrow c_{vo} \left[\frac{u_1 + u_2 + u_3 + u_4 - 4u_0}{\Delta x^2} \right] \Delta t = \Delta u_0$$

where, $c_{vo} = \frac{k(1+e_0)}{\gamma_w \, f(\sigma_v - u_0)}$, and $\Delta x = \Delta y$

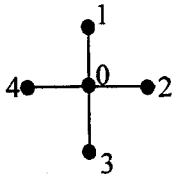

Using the final form of equation (6-7), the excess pore pressure at the center node at some small increment in time, Δt, can be found as follows;

(6-8) $$(u_o)_{t+\Delta t} = (u_o)_t + (c_{vo})_t \left[u_1 + u_2 + u_3 + u_4 - 4u_0 \right]_t \frac{\Delta t}{\Delta x^2}$$

Using equation (6-8), a code was written to perform the analyses numerically. The boundary conditions for the models analyzed consist of a no-flow condition across the bottom and side boundaries of the laminar box, and zero excess pore pressures at the surface for all time. In addition to the above, the interface at the loose and dense halves of the model requires some averaging of the material properties. The treatment of these various conditions, and the constraints put on the time step to ensure stability and accuracy, are given in the source code in Appendix A.

In the formulation above, there is no provision to generate any excess pore pressures as the earthquake shaking progresses. Terzaghi's theory of consolidation is limited to the dissipation of excess pore pressures and, as stated before, is based on a limited constitutive behavior of the sand itself. It would be appropriate to prescribe that the initial conditions in the numerical analyses are taken to be equal the conditions of model tests at the conclusion of the generation phase when earthquake shaking ceases. As noted before, this is when subsequent behavior is dominated by dissipation (or consolidation) processes. However, in Section 6.2.2, it was postulated that during the earthquake shaking, the generation of excess pore pressures was a competition between the ability of the earthquake to create excess pore pressures and the sands' ability to diffuse those same pressures. The application of Terzaghi's one-dimensional consolidation theory during the generation phase appeared to give a reasonable assessment of observation in the model tests. Based on this, it was decided to attempt to include a generation phase in the formulation derived above.

To do this, the earthquake generation of excess pore pressures was treated as a series of continuous increments which accumulated throughout the duration of significant shaking. At each time step in the numerical calculations, an increment was added to the excess pore pressures which were computed using the algorithm in equation (6-8). The magnitude of the increment was based on a rate of generation selected for the soil density and the depth of the soil within the model. The details of the actual procedure used to select the values of the increments are described in Section 6.3.2.1. It is emphasized that in this analysis dynamic effects from the earthquake shaking are accounted for by artificial generation of excess pore pressure.

6.3.1.2 Selection of Properties

The properties used in the analyses have been based on the values and relationships reported in Chapter 3. The properties were measured in laboratory tests which were completed independently

of the model tests. The laboratory data has been used directly, and no modifications were made to improve the results of the analyses.

The mean void ratio and density of the analysis cross sections matches the mean void ratio and density that was measured in the actual models. However, the void ratio in the analysis cross-section is distributed based on the variation of vertical effective stress while maintaining the target mean value. The permeability is distributed throughout the analysis cross section based on the void ratio calculated at the various nodes in the analysis section. The coefficient of consolidation has been calculated for the analysis cross-section using the above values of void ratio and permeability, and the relationships for the coefficient of compressibility,a_v, as defined by the confined compression tests in Chapter 3. The values of a_v were distributed as a function of the vertical effective stress throughout the analysis section, and were updated as the analysis proceeded to account for the change in the vertical effective stress. During the generation phase of excess pore pressures, the unload (or reload) relationship was used for a_v. During the dissipation phase (after the generation phase), the loading (virgin) relationship was used for a_v.

6.3.2 Analysis of Models and Prototype

The analysis method was first used to match the excess pore pressure behavior observed in the centrifuge and one-g models using the model dimensions at model time. In this matching process, only the duration of shaking and rate of excess pore pressure generation were varied to improve the fit of analysis results to the model test results. The analysis sections represent the true scale of the models actually tested, and just like the physical model tests described in Chapter 5, the results of the analyses have been scaled to prototype values to permit comparisons to be made.

The analysis was also applied to assess the potential behavior of the excess pore pressures in an equivalent prototype structure of the models. The duration and rate of generation which gave a satisfactory match of the analysis results for the particular model tests were used in the analysis of the prototype. The only change made in the analysis was to increase the dimensions of the analysis cross-section in accordance to the prototype dimensions, and scale the rate of generation and duration in accordance with the scaling factors reported in Chapter 5, Table 5-5.

The initial matching between the analysis results with the model tests provided some confidence that even with the assumptions made, the analysis could be extended to the prototype. It is

emphasized that these analyses are not intended to capture or 'model' the full behavior of the sand in the model tests or prototype which, as stated previously, is very complex.

6.3.2.1 Generation of Pore Pressures

The generation of pore pressures in the analysis has been idealized as a series of constant increments in excess pore pressure applied at the nodes in the cross section during the period of excess pore pressure generation, which is termed the generation phase of the analysis. Several assumptions have been made with regard to the generation of excess pore pressures as follows:

- The duration of the generation phase was selected based on the one-g model test results for the uniform deposits of sand (Model SM3I) as described below. It was observed that in the uniform model tests (SM3I) the generation of pore pressures ceased when the earthquake accelerations fell below about a level of about 0.10g, and this point was selected as the cessation of significant shaking and generation of excess pore pressures. The duration for the generation phase was observed to decrease as the density (or relative density) of the sand increased.

- The rate of generation, which determines the size of the increment of excess pore pressure applied in the analysis, was selected based on the one-g model test results for the uniform deposits of sand (Model SM3I) as described below. The rate of generation was observed to decrease as the density (or relative density) of the sand increased.

- The increments of excess pore pressure at a given point in the model were constant for the duration of significant shaking, and no provision was made to vary the increment based on the intensity of shaking.

- The magnitude of the increment increased linearly with depth.

- The increment was always zero at the surface of the model.

- The rate of generation, or increment, was applied for the duration of the generation phase regardless of whether the excess pore pressures had reached the maximum values (or liquefaction value).

The above assumptions provide a simplistic approach to the generation of excess pore pressures created during earthquake shaking. In particular, the linear distribution of the magnitude of the

excess pore pressure increments with depth was entirely based on judgment considering the following factors:

- It was observed in the model tests that the dynamic response was significantly lower in the upper portions of the model when compared to the earthquake which was input at the base. This implies that the level of cyclic stresses imposed on the sand increased as with depth, and therefore the potential for excess pore pressure generation could be expected to increase also.

- The vertical effective stresses increase linearly with depth, and as stated previously, experimental evidence indicates the potential for excess pore pressures does increase with increasing confining stresses.

To obtain an estimate of appropriate duration of the generation phase and the rate of excess pore pressure generation, the results of the one-g model tests SM3I1, SM3I3, SM3I4, and SM3I5 were employed. These tests are described in detail in Chapter 5, Section 5.3.2. All of the tests were performed on the model SM3I which had a uniform deposit of Nevada sand with water as the pore fluid. The relative density of the sand in the model increased through the test series. Using the results of these tests (Appendix B, pages B-101 through B-132), the rate of excess pore pressure generation at the base of the models (transducers P1 and P2) was estimated for each test. Also an estimate was made of the duration of significant shaking which corresponds to the duration of generation of excess pore pressures. The estimated values are presented in Table 6-2, along with the initial relative density of the model when each test was performed. From the values the trend is that the duration of generation and the magnitude of rate of generation decrease as the relative density increases. This is consistent with the expected behavior as the sand becomes denser. It is interesting to note that a marked decrease in the rate of generation occurs at about 55 to 60% relative density. This relative density range is often used as a "rule of thumb" measure separating the liquefaction potential of saturated sands.

To represent the effect of the earthquake-generated excess pore pressures using the simplified approach described above, the observed generation rates (which include densification) need to be increased to obtain an appropriate "generation factor" for use in the analyses. In the formulation of the analysis, the dissipation of excess pore pressures occurs throughout the generation phase as occurs in the model tests (Section 6.2.2). Consequently, the rate of generation calculated by the analysis will always be less than the generation factor used in the analysis. To demonstrate this,

an analysis was performed of the model test SM3I1 using a generation factor of 45 kPa/sec which corresponds to the rate (in prototype scale) observed in the actual test (Table 6-2). This rate was converted to the appropriate one-g model value by dividing it by the stress scaling factor and multiplying it by the time scale factor (Chapter 5, Table 5-5). The results of the analysis for the generation phase are compared in Figure 6-2. The rate of generation from the analysis of SM3I1 was about 33 kPa/sec which is about 27% less than the 45 kPa/sec. To obtain a calculated rate of generation of 45 kPa/sec, it was found by some trial and error that the generation factor used in the analysis needed to be 58 kPa/sec as indicated in Table 6-2. A similar analysis was performed for each of the remaining SM3I tests and the modified generation factors are shown in Table 6-2.

The primary scaling effect is the conflict between the dynamic time and the diffusion times in the model as discussed in Section 6.2.2. The application of the consolidation theory (one-dimensional) indicated that the observed rate of generation of excess pore pressures in the one-g models would be less than what would be observed in the equivalent prototype. To assess this, an analysis was performed of the test SM3I1 at an equivalent prototype scale. The only change made to the analysis described above was to increase the dimensions of the analysis section by the scale factor of 25.5 as indicated in Chapter 5, Table 5-5. The generation factor of 45 kPa/sec was used, as was also used in the prior analysis described above. The results of the prototype analysis during the generation phase is shown on Figure 6-2, next to the generation factor actually used and the results of the one-g model analysis section of SM3I1. The rate of generation from the prototype analysis was about 43 kPa/sec, approximately 5% less than the initial generation rate of 45 kPa/sec. The rate of generation from the prototype analysis was approximately 30% greater than that calculated for the one-g model analysis section.

In Figure 6-3 the rates of generation observed in the tests and the associated generation factors are plotted versus the initial relative density of the tests. From this plot, a generation factor for the Nevada sand can be selected for use in an analysis for any initial relative density of the sand, and for any particular analysis cross-section. The generation factors will represent the effect of the same earthquake in analysis sections of a prototype or centrifuge model, in addition to the one-g models. This is because the back calculation of the generation factor has essentially removed the effects related to any scaling issue associated with the one-g models.

From this simple analysis for the one-g model test SM3I1, it can be inferred the observed rate of excess pore pressure generation in the model test is about 30% less than what would be observed

in the prototype. Further discussion and analysis results investigating this difference are presented in Section 6.3.2.4 below. With reference to the generation factors derived above for use in the analyses, it would appear that the majority of the difference between the observed rates in the SM3I test series and the back calculated generation factors (Figure 6-2) is caused by the conflict in time scales that exists in the one-g models.

6.3.2.2 Centrifuge Model 3

The results of the centrifuge Model 3 were presented and discussed in Chapter 5, Section 5.2.1. An analysis of the centrifuge Model 3 was performed using the dimensions of the centrifuge model and in terms of model time. The results of the analyses were subsequently converted to prototype values of stress and dynamic time to enable comparisons to be made. It was assumed that the initial relative densities of the sand in the model test were at the upper end of the ranges indicated in Chapter 5, Table 5-1. The relative density of the loose sand column was 48% and the dense sand column was 79%. From Figure 6-2, the appropriate generation factors for the analysis would be about 31 kPa/sec and 3 kPa/sec for the loose and dense sands, respectively. From Table 6-2, the duration of the generation phase can be inferred to be about 13 seconds and 10 seconds for the loose and dense sands, respectively.

Using these values, the excess pore pressures calculated in the analysis were significantly larger in the loose sand and lower in the dense sand than was actually observed in the test data. After some trial and error, it was found that the generation factor in the loose sand should be reduced and in the dense sand should be increased to obtain a satisfactory match with results. In addition, it was also found that the duration of generation in the dense sand should be increased to equal that in the loose sand. The final analysis results are compared with the test data in Figures 6-4 and 6-5. The change in the generation factor required to obtain the match is indicated in Figure 6-6a.

From Figure 6-4 and 6-5, the analysis results match the actual test results reasonably well. During the dissipation phase the analysis results apparently decrease at a slightly faster rate than the actual model test results, which implies that in the analysis the value of the coefficient of consolidation was over-predicted. However, considering that the properties of the sand in the analyses have been arbitrarily determined from the laboratory data in Chapter 3, the comparison of the analysis results with the actual test results is quite good.

However, to obtain this match the generation factors had to be modified from those originally prescribed using Figure 6-3. As described above and as indicated in Figure 6-6a, the generation

factor in the loose sand had to be decreased and in the dense sand had to be increased. Based on the shift in the generation factor in Figure 6-6a, the loose sand behaved as if it had a relative density of about 53% instead of 48%, and the dense sand behaved as if had relative density of about 69% instead of 79%. Effectively the loose column of sand had to be treated as more dense, and the dense column of sand had to be treated as more loose. This trend is consistent with what should be expected in the actual centrifuge Model 3 test which had two adjacent columns of loose and dense sand (Chapter 5, Section 5.2.1).

The presence of the loose sand column will induce the adjacent dense column to behave in a softer manner in comparison to the behavior that would occur if the entire model was a dense sand. In the tests this was compounded because the excess pore pressures in the dense sand were enhanced by the presence of the elevated excess pore pressures generated in the loose sand. The softer behavior of the dense column implies that the cyclic strains would be higher and this would increase the rate of generation of excess pore pressures. This is also a plausible explanation why the duration of excess pore pressure generation in the dense sand needed to be increased in the analysis to equal that prescribed for the loose sand.

In the loose column of sand the presence of the adjacent dense sand will have the opposite effect to that described above. The loose column will behave in a stiffer manner when compared to a model comprised only of loose sand. Consequently, the rate of generation of excess pore pressures will be less than those in a model comprised only of loose sand. This trend was required in the analysis to obtain a reasonable match with the centrifuge Model 3 test results.

In the above analyses the generation factor and duration were modified to obtain a better fit of the analysis results to the observed test results. To further explore whether the generation factor is a reasonable approximation of the pore pressure generation during the model earthquake, another analysis was completed with the same properties and values used in the analysis of the centrifuge Model 3, but it was assumed that one-g model conditions existed. The same duration's and generation factors were used, but in the new analysis it was assumed the test was performed in the one-g laminar box on the shake table rather than in the centrifuge. Of course the material properties were identical in both analyses, as these were pre-determined by the independent laboratory testing as discussed previously.

The actual experiment, which most closely represents the one-g analysis condition described above was the one-g model SM3B1, which had similar initial relative densities as that in the

centrifuge Model 3. The results of the analysis and the one-g model SM3B1 are compared in Figures 6-7 and 6-8. It appears the analysis of the one-g condition gives a reasonable approximation of the actual one-g model test SM3B1. The back-calculated values found from the analysis of the centrifuge Model 3 appear to hold for the one-g condition as well. This provides added confidence that the simplified analysis methodology using the generation factor is sufficient to capture the general excess pore pressure behavior observed in the physical models.

The actual numbers used in the analysis above are indicative only of the behavior of the sand in the actual model test. It is not possible to quantify the true change in behavior of the sands in the model tests using the above analysis method, because as stated previously (Section 6.3.1) the analysis cannot model any dynamic behavior of the sand itself, and only represents a simplistic interpretation of the behavior of the excess pore pressures. However, it would be valid to use the back-calculated values required in the analysis above, in an analysis of an equivalent prototype in order to assess the effects that the model scaling may have on the observed results. This is completed in Section 6.3.2.3 below.

6.3.2.3 One-g Models

Of the one-g models tests performed, SM3C1 was selected for analysis as an example. The model and the results of the test were presented in Chapter 5, Section 5.2.3.1. From Chapter 5, Table 5-5, the initial relative density of the loose and dense sands in SM3C1 was 41% and 64% respectively.

Similar to the analysis of the centrifuge Model 3 described in Section 6.3.2.2, it was found that the generation factors developed in Section 6.3.2.1 for a uniform sand needed to be adjusted. The initial values of the generation factors based on the initial relative densities of the sands and the final values used in the analysis to obtain a satisfactory match with the test results are indicated on Figure 6-6b. The duration of the generation phase in the analysis was 13 seconds in the loose sand, and 10 seconds in the dense sand. The results of the analysis are compared to the excess pore pressures observed in the one-g model SM3C1 in Figures 6-9 and 6-10.

The general discussion in Section 6.3.2.2, regarding the comparison of the analysis of the centrifuge Model 3 with the actual test results, also applies to the analysis results of the one-g model SM3C1. It should be noted that the rate of generation of excess pore pressures tends to have been over estimated in the upper portion of the loose sand column in the analysis of SM3C1. It should be noted that in this test it is possible that the pore pressure transducer at P3

did not respond well due to a malfunction of the transducer. This would contribute to the observed divergence of analysis results from the actual values recorded.

6.3.2.4 Prototype

The values used in the analyses of the centrifuge Model 3 and the one-g model SM3C1 have been substituted into analyses of a prototype section. This was completed to investigate the potential effect that the conflict between the dynamic and dissipation time scales in both modeling techniques may have on the behavior of excess pore pressures. In the prototype analysis there is no conflict between the time and dissipation scales. By using the parameters which resulted in a reasonable fit of the analysis results to the centrifuge Model 3 and one-g model SM3C1 results as described in Sections 6.3.2.3 and 6.3.2.3, it should be possible to assess the relative divergence of the excess pore pressure behavior in the respective models from the true prototype behavior.

Figures 6-11 and 6-12 compare the analysis results of the centrifuge Model 3 with the analysis results of an equivalent prototype. There is a significant divergence in the excess pore pressures in the prototype section relative to the centrifuge model. During the generation phase the rate of excess pore pressure growth is faster and the magnitudes are greater. During the dissipation phase, the rate at which the pore pressures drop are significantly lower in the prototype. These two observations can be attributed to the conflict in the time scaling in the centrifuge model, in which the dissipation processes occur 50 times faster than the dynamic processes (see Chapter 5, Table 5-5). The magnitude of the difference is due to the size of the centrifuge Model 3 and the scaling required for the centrifuge modeling technique.

Figures 6-13 and 6-14 compare the analysis results of the one-g model SM3C1 with the analysis results of an equivalent prototype. The divergence in the excess pore pressures in the prototype section relative to the one-g model follow the same trends as observed above for the centrifuge model. However, the divergence is not as great, and this can be primarily attributed to smaller discrepancy between the time scales in the one-g model. For SM3C1 the scaling factors (see Chapter 5, table 5-5) indicate that the dissipation processes occur about 16 to 22 times faster than the dynamic processes during the generation phase, and 12 to 13 times faster during the dissipation phase. The smaller difference between the time scales in the one-g model SM3C1 compared to the centrifuge Model 3 is primarily due to the larger size of the one-g model and the scaling required for the one-g modeling technique.

There is a difference between the calculated excess pore pressure behavior of the two prototype analyses. This is a direct result of the contrast in the densities of the sand represented in the two analyses. For the prototype analysis of the centrifuge Model 3 the initial relative density of the sand is 48% in the loose sand and 79% in the dense sand. In the prototype analysis of the one-g model SM3C1, the initial relative density of the sand is 41% in the loose sand and 64% in the dense sand. Therefore, it should be expected that the rate of generation and magnitude of excess pore pressures should be greater in the equivalent prototype of SM3C1. This is, in fact, what the analyses indicate.

It is of interest to note that for the one-g model SM3C1, the rate of generation of excess pore pressures in the prototype analysis were about 40% larger in the loose sand and 25% larger in the dense sand than observed in the actual model test results. With reference to the discussion in Section 6.2.2, this does quantify the relative effect of the time scaling conflicts during the generation phase.

As described in Chapter 5, Section 5.2.3.2, the one-g model tests SM3J1 and SM3F1 were placed at lower densities on account of the constitutive scaling method described in Chapter 2, Section 2.4. In part, the scaling of the initial density should compensate for the divergence of the excess pore pressure of the one-g model from the prototype as observed above for SM3C1. The test SM3J1, when scaled to prototype values (Chapter 5, Table 5-6), has similar initial densities to that used in the prototype analysis of the one-g model SM3C1. In effect, the one-g model test results from SM3J1 should represent the results from the above prototype analysis. Using the method that was introduced in Section 6.2.1 to stretch the time scale during the dissipation phase of the model test, the results of SM3J1 are compared with the prototype analysis results in Figures 6-15 and 6-16 for the loose and dense sands, respectively. From this comparison there is close match of the results of SM3J1 with the prototype, which indicates that the constitutive scaling method appears to produce the desired effect.

6.4 Implication of Analysis Results

In Section 6.2, Terzarghi's one-dimensional consolidation theory was applied to some of the results of the model tests. Within the limitations of the analysis method as stated in that section, it appears that the theory reasonably approximated the behavior and trends of the excess pore pressures observed in the model tests. This is important for two main reasons:

1) The theory was used in Chapter 2, Section 2.2, to develop the scaling relation for the dissipation time in the models to the prototype.

2) The theory can be used as a simple method to set particular parameters in the model tests and to interpret the results. For example, it was used to provide a target viscosity for the glycerin pore fluid in one-g model SM3K, and it was also used to perform the stretching of the time scale during the dissipation phase of the tests to remove from the results the time scale incompatibilities between the dissipation and dynamic processes.

In Section 6.3, Terzarghi's one-dimensional theory was extended to two dimensions, and was applied in an analysis of the centrifuge Model 3 test and the one-g model SM3C1 test. Both of these models had adjacent loose and dense columns of sand. The analyses indicated the following:

1) It appears that the generation of higher excess pore pressures in the loose column of sand increases the excess pore pressures in the adjacent dense sand, as observed in Chapter 5.

2) The use of the laminar box in the one-g tests and centrifuge tests affected the response of the loose and dense columns in comparison to a uniform deposit of dense or loose sand. The dense sand behaved in a softer manner and the loose sand behaved in a stiffer manner. This affected the excess pore pressure response and, based on the analyses, the generation of excess pore pressures in the dense sand was increased by up to 50% and in the loose sand was decreased by up to 30%. With the limitations of the analyses performed, it is not possible to define how much of this affect contributes to the observation made in item (1) in comparison to the process of diffusion raising the excess pore pressures in the dense sand.

3) From item (2) above it follows that the model tests of the two columns of sand are probably indicative of the excess pore pressure behavior near the interface of loose and dense sands.

4) If the results of the model tests are taken at face value as a prediction of prototype excess pore pressure behavior, the real prototype behavior could be seriously under-estimated. The rate of pore pressures generated in the model tests is lower and the dissipation of pore pressures is faster than in the prototype. This is a direct result of the conflict

between dissipation and dynamic time scales that exists in both the centrifuge and one-g modeling techniques.

5) With respect to item (4), the centrifuge modeling technique has a larger divergence from the prototype behavior than the one-g modeling technique. This is a consequence of the scaling relations governing the two techniques and also the fact that centrifuge models are typically constructed at smaller absolute sizes than one-g models.

6) The constitutive scaling method proposed in Chapter 2 does appear to appropriately compensate for the one-g model lower stress regime in the generation phase of excess pore pressures. If the results of the one-g tests with scaled densities are modified by stretching the time scale during the dissipation phase, they appear to match the behavior expected in the prototype. This conclusion can only be drawn for the particular configuration of the one-g models tested in this thesis, for the given conditions.

7) Despite its limitations and simplifications, the use ofTerzaghi's consolidation theory as applied in the analyses proved valuable. It indicated that the coefficient of consolidation can be used as an index of the diffusion behavior of a sand, and that the definition of it using independent laboratory tests provides reasonable results. In addition, the variation of the coefficient of consolidation with the effective stresses is a significant factor in the excess pore pressure behavior and is primarily caused by the changes in compressibility of the sand. The permeability of the sand appears to remain relatively constant throughout the process of excess pore pressure generation and dissipation.

In summary, a simplified analysis methodology was applied in a consistent manner to arrive at the conclusions cited above. Further analyses of a similar nature could be performed to arrive at some resolution of items (1) and (2) discussed in the inset immediately above.

6.5 References

Salvadori, M. G., and M. L. Baron, 1959, "Numerical Methods in Engineering," Prentice-Hall Inc., New Jersey.

Scott, R. F., 1963, "Principles of Soil Mechanics," Addison Wesley, Reading, Massachusetts.

Table 6-1: Comparison of measured times of dissipation with calculated values using one-dimensional consolidation theory.

Model test and sand condition.	Measured values			Range in calculated values corresponding to 5-100kpa range in prototype vertical effective stresses(2).			
	Time of Dissipation t (secs)	Degree of Consol. U	Non-dim. Time T(1)	Load (virgin) Condition		Reload or Unload Condition	
				c_v	t	c_v	t
Model 3							
P1 (loose)	82	0.78	0.567	0.0084-0.0993	163-14	0.0974-0.7044	14-2
P2 (dense)	82	0.70	0.403	0.0053-0.0740	184-13	0.0395-0.2849	25-3
SM3C1							
P1 (loose)	148	0.78	0.567	0.0031-0.0074	172-72	0.0119-0.0856	45-6
P2 (dense)	120	0.70	0.403	0.0020-0.0065	187-58	0.0068-0.0493	55-8
SM3G1							
P1 (loose)	22	0.95	1.125	0.0719-0.1679	15-7	0.4295-1.4558	2-1
P2 (dense)	19	0.95	1.125	0.0506-0.1180	21-9	0.3018-1.0230	3-1

Notes:

(1) From the analytical solution for U versus T at the base of a layer with an initial triangular excess pore pressure distribution.

(2) The lower c_v value corresponds to the lower stress of 5 kPa and the longer time t.

Table 6-2: Duration of generation phase and rate of excess pore pressure generation.

Test No.	Initial Relative Density, D_r (%).	Estimated from test results (in terms prototype values and dynamic time scale).		Modified value of generation factor based on analysis (kPa/sec)
		Duration of Generation (secs)	Average Rate of Generation (kPa/sec)	
SM3I1	35	15	45	58
SM3I3	42	14	34	31
SM3I4	57	10	8	12.5
SM3I5	70	10	2	3.5

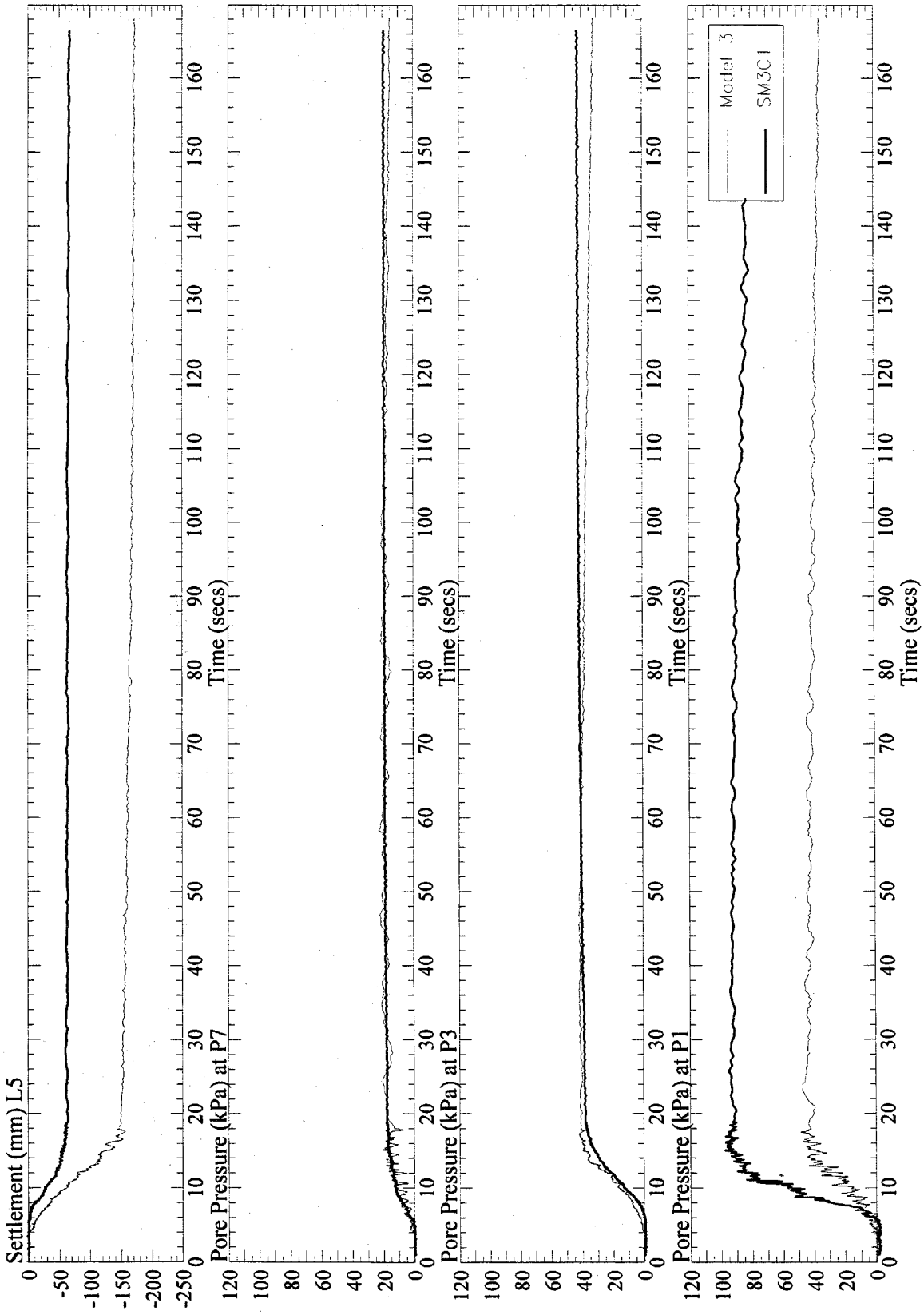

Figure 6-1: Comparison of excess pore pressures and surface settlements in the centrifuge Model 3 and the one-g model SM3C1using alternate time scales.

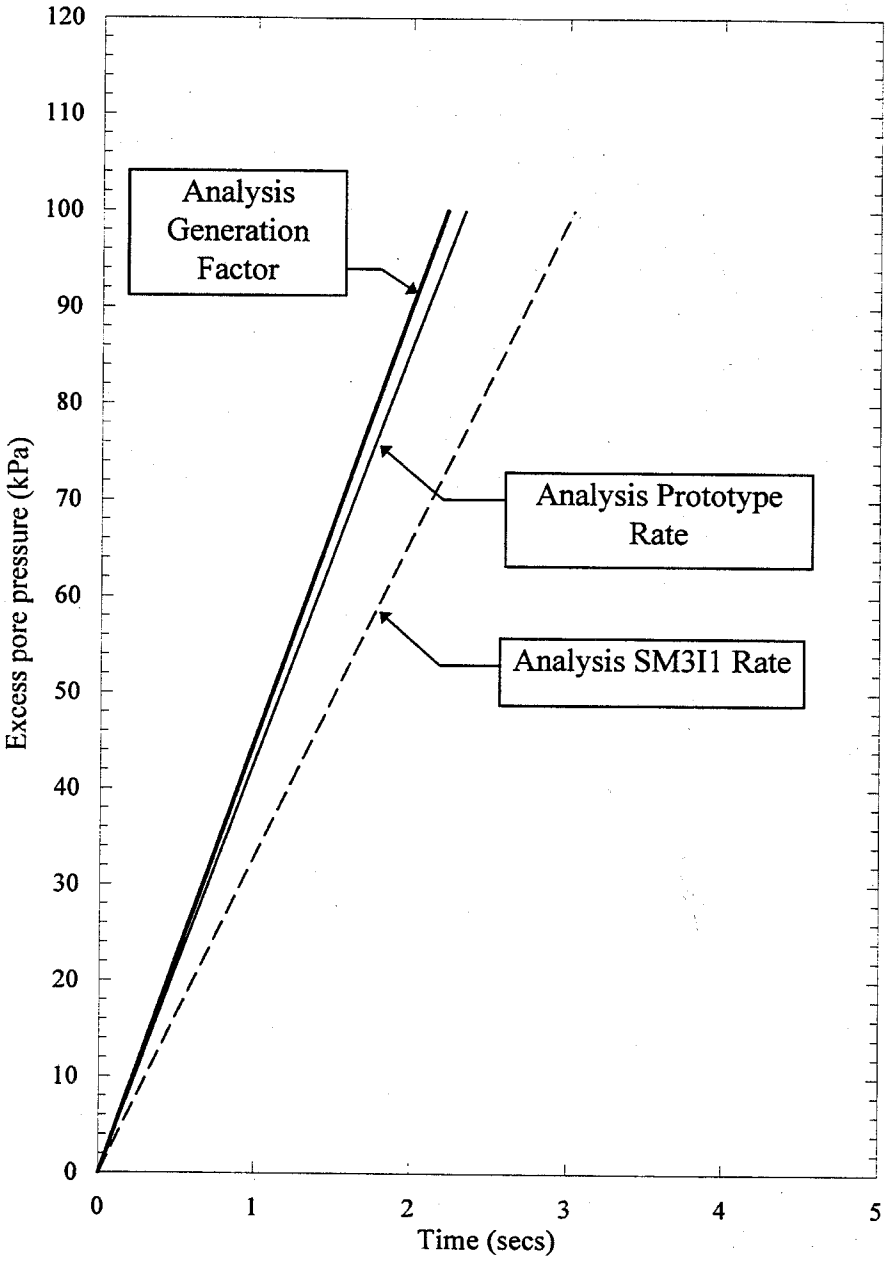

Figure 6-2: Comparison of rates of generation of pore pressure from analysis of SM3I1.

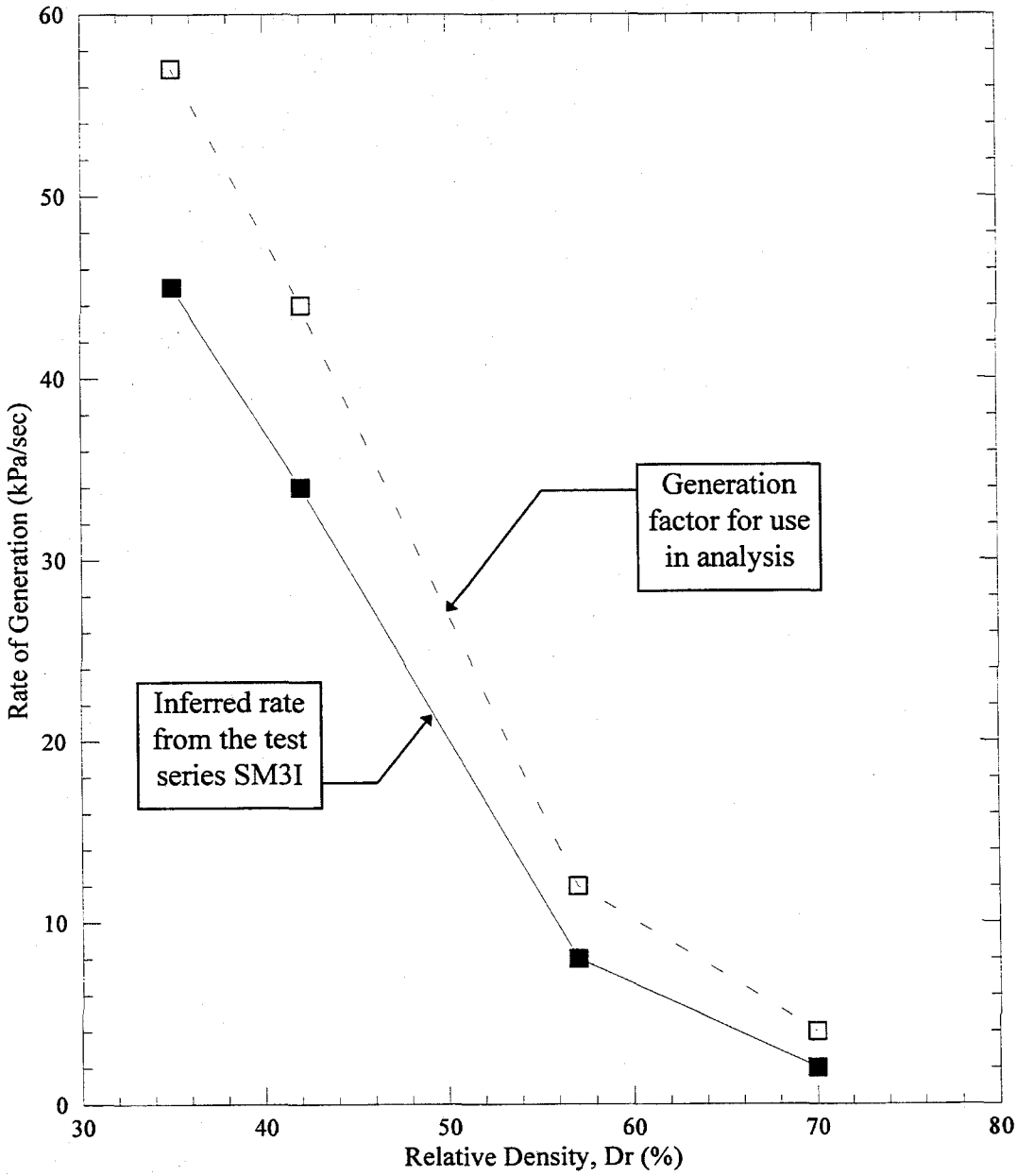

Figure 6-3: Rate of excess pore pressure generation from the one-g test series SM3I.

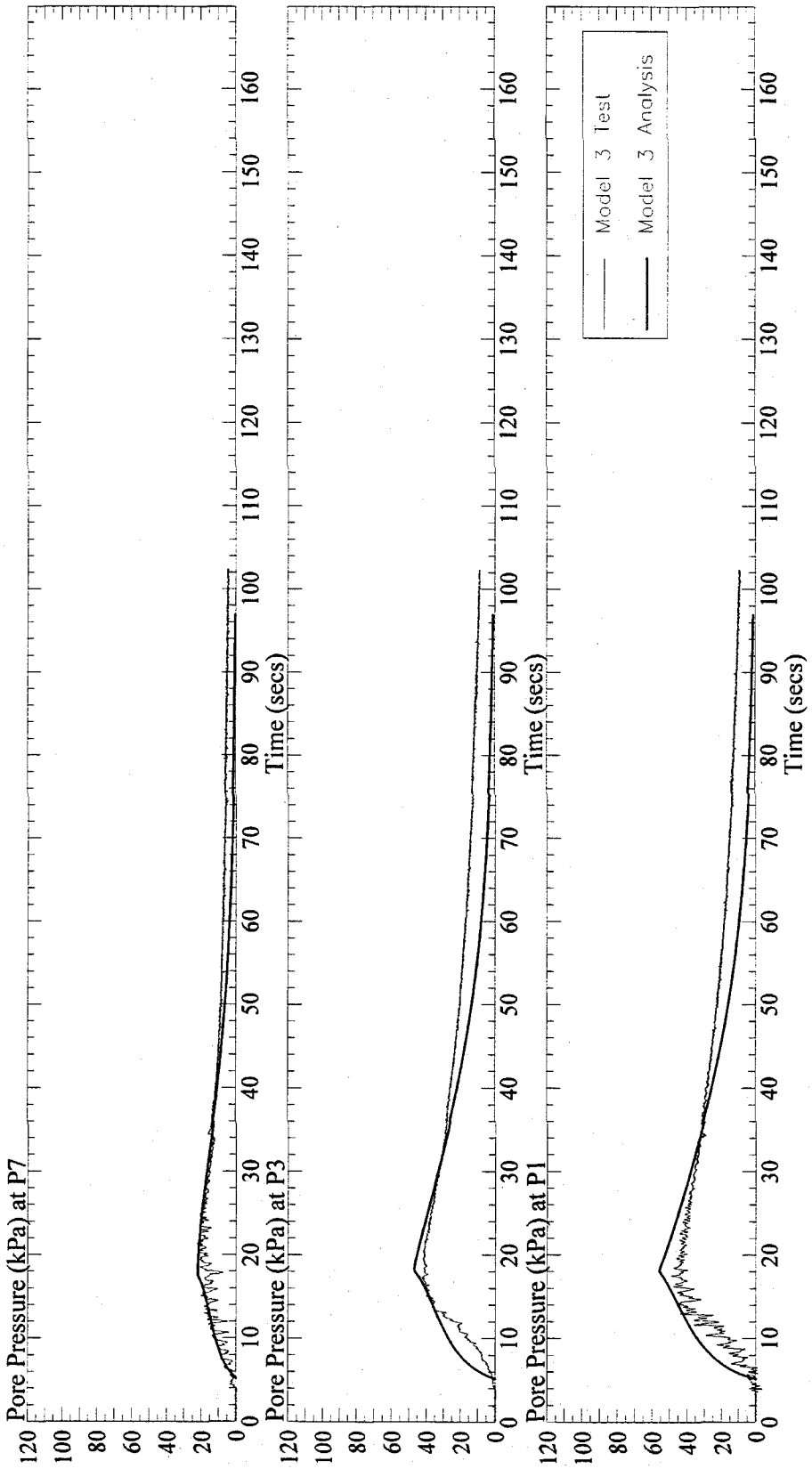

Figure 6-4: Comparison of the excess pore pressures in the loose sand of the centrifuge Model 3 test and the analysis of Model 3.

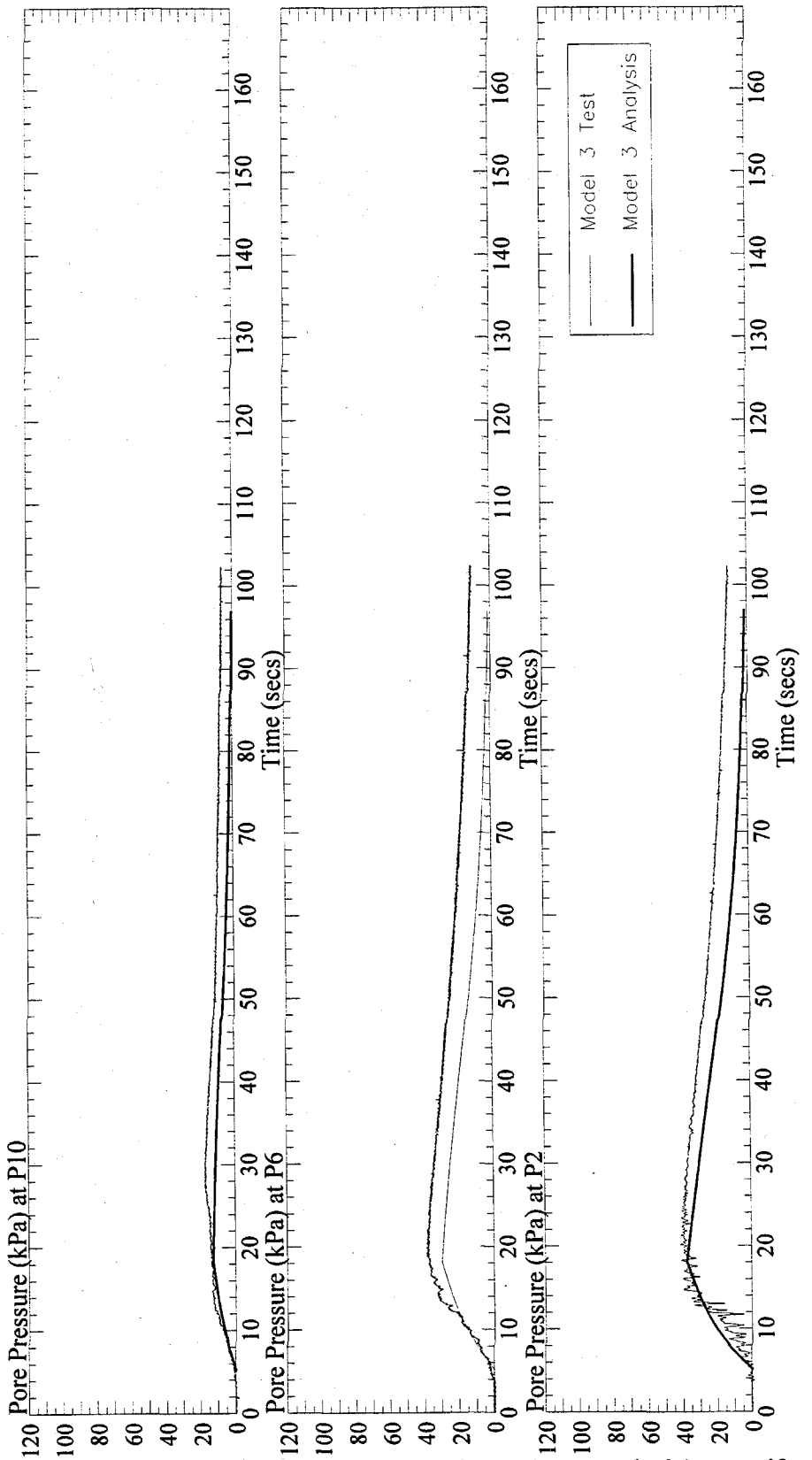

Figure 6-5: Comparison of the excess pore pressures in the dense sand of the centrifuge Model 3 test and the analysis of Model 3.

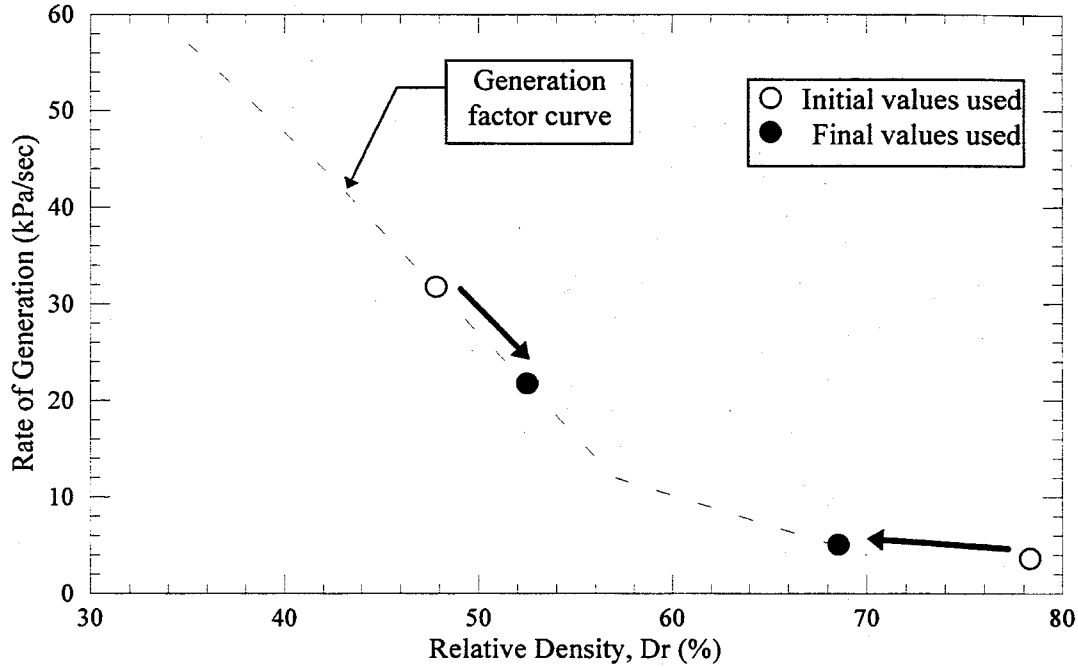

Figure 6-6a: Generation factors used in the analysis of the centrifuge Model 3.

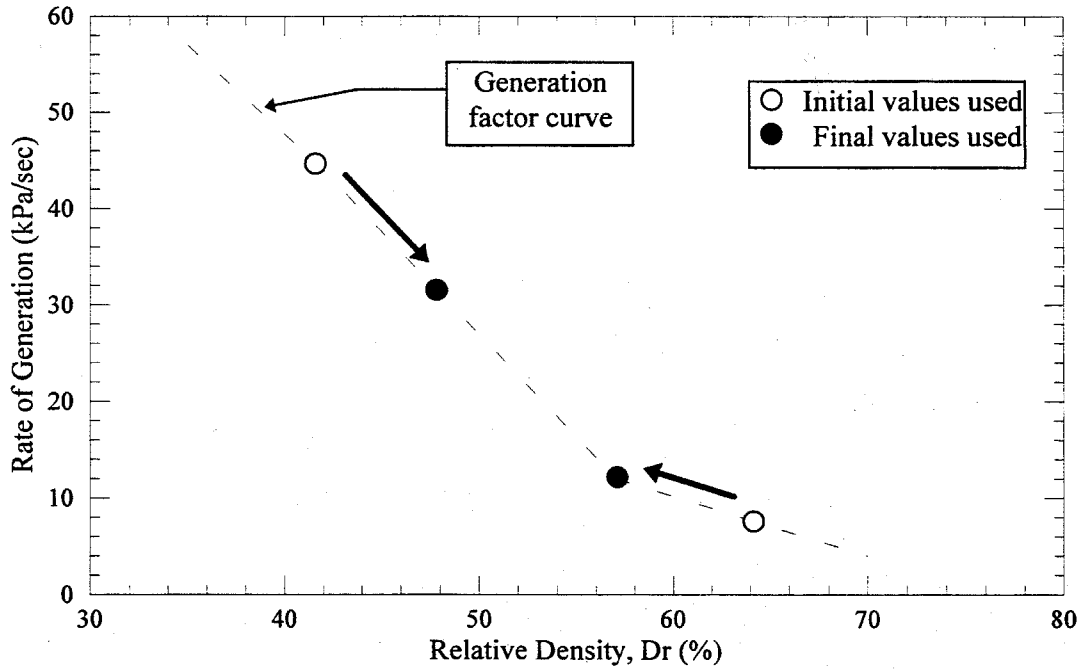

Figure 6-6b: Generation factors used in the analysis of the one-g model SM3C1.

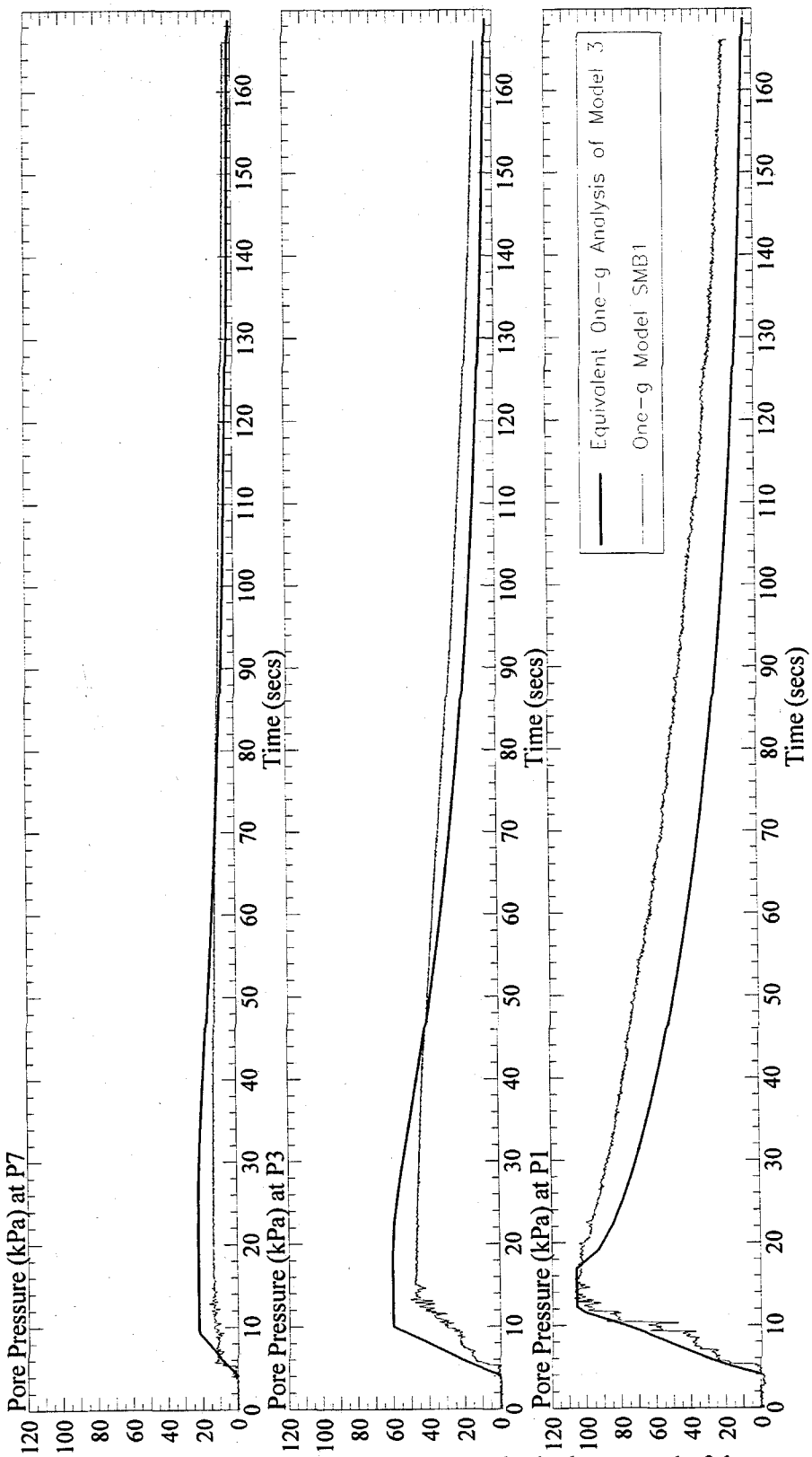

Figure 6-7: Comparison of the excess pore pressures in the loose sand of the one-g model SM3B1 and an analysis of an equivalent one-g model with the centrifuge Model 3 initial conditions.

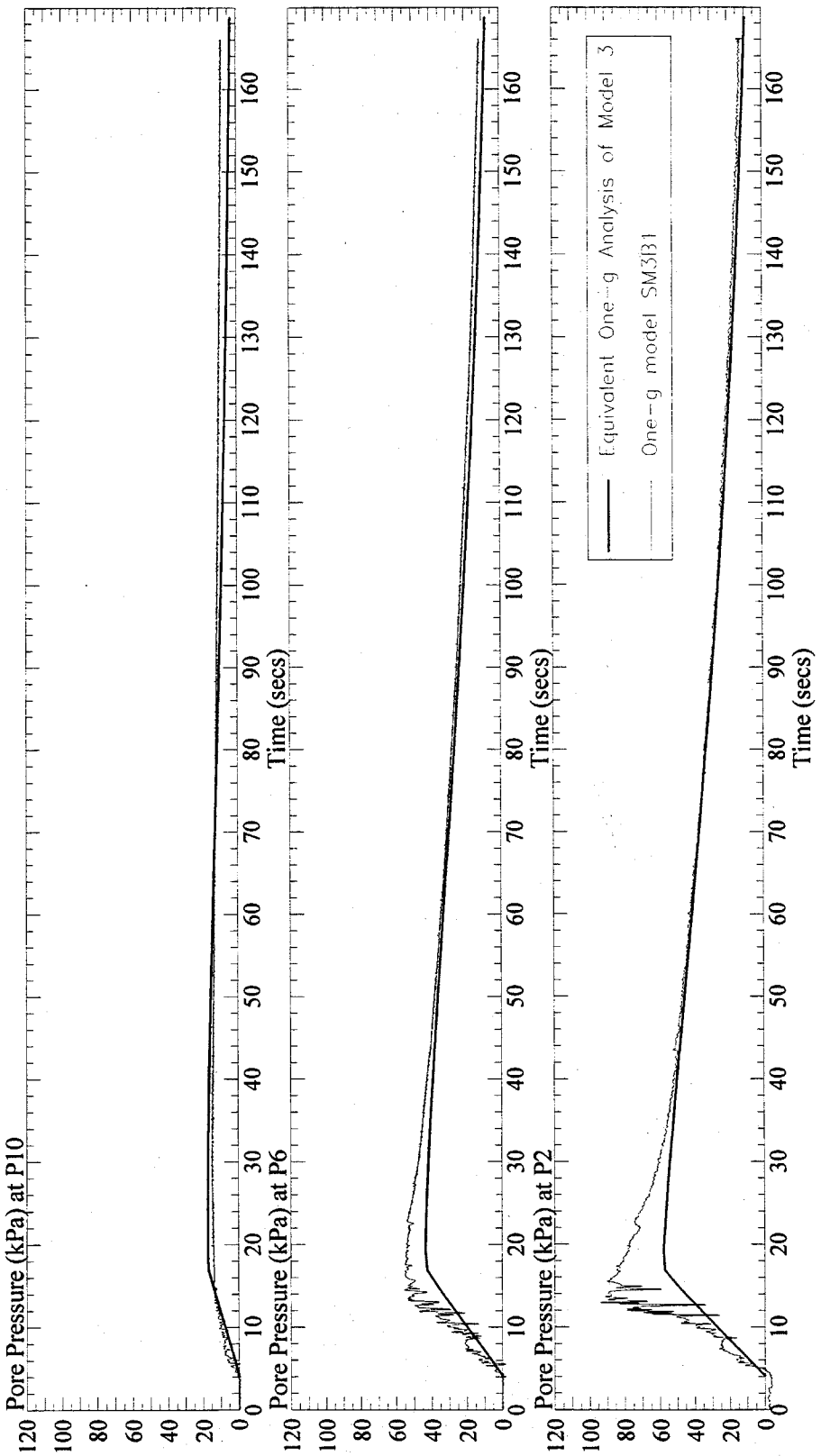

Figure 6-8: Comparison of the excess pore pressures in the dense sand of the one-g model SM3B1 and an analysis of an equivalent one-g model with the centrifuge Model 3 initial conditions

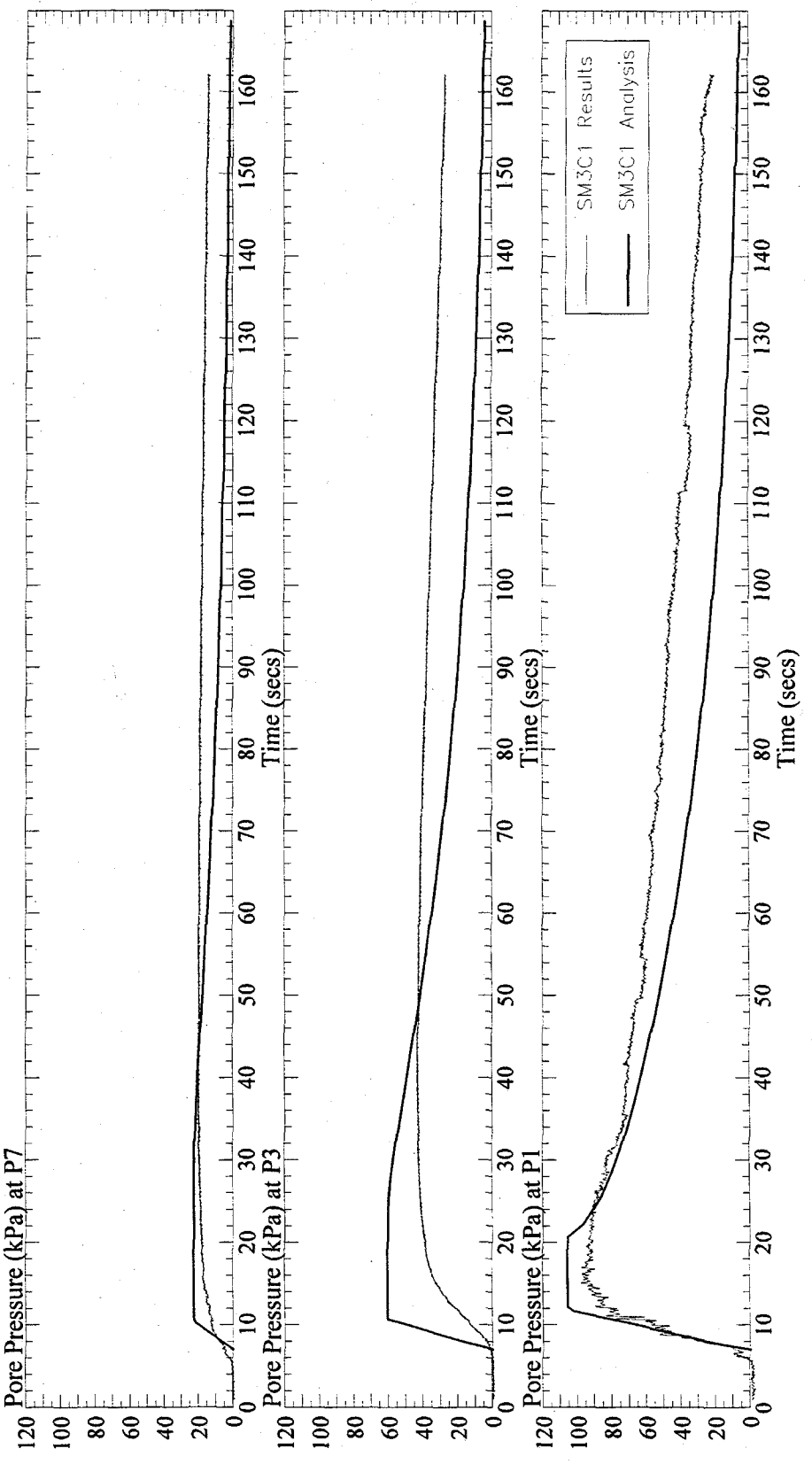

Figure 6-9: Comparison of the excess pore pressures in the loose sand of the one-g model SM3C1 test and the analysis of SM3C1.

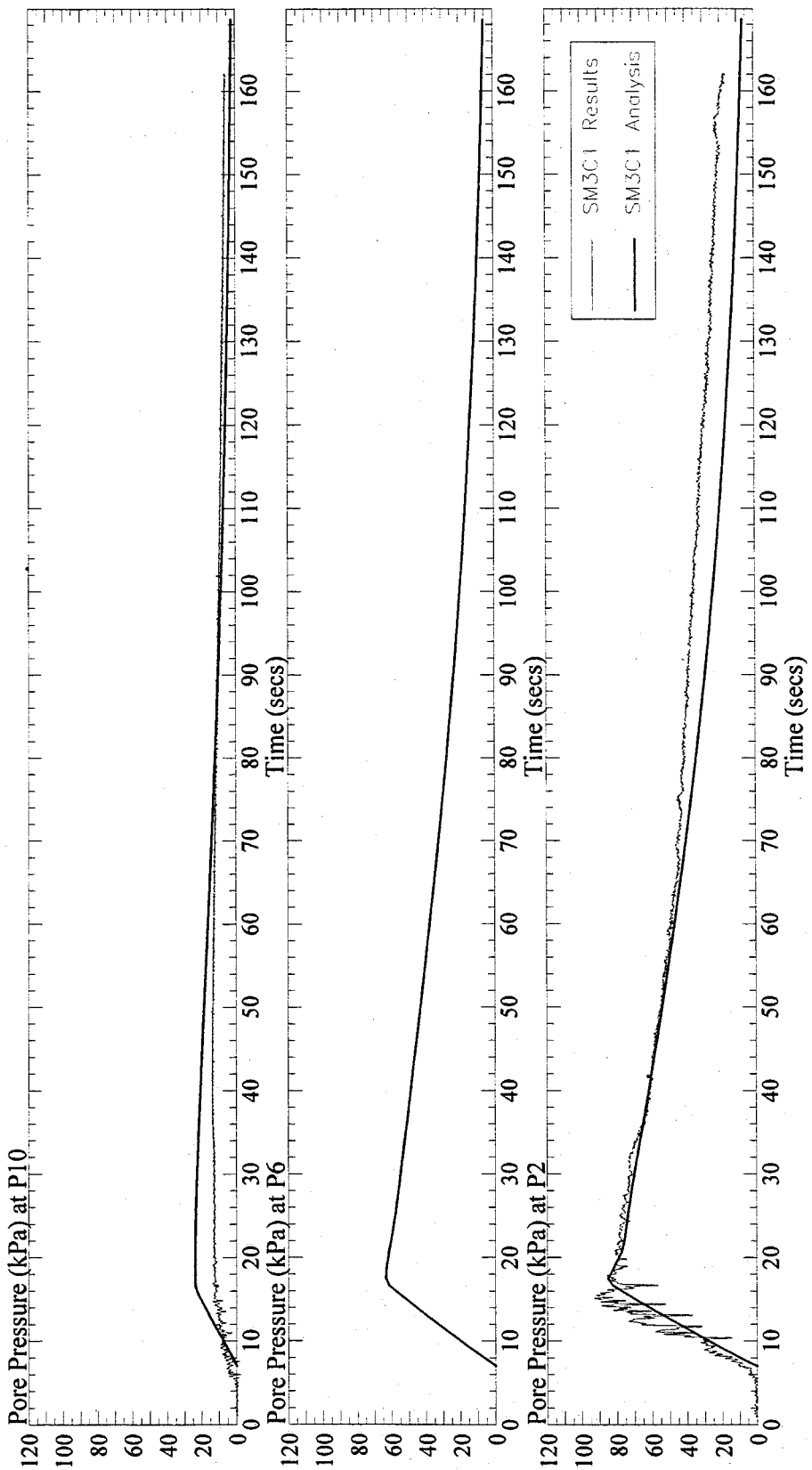

Figure 6-10: Comparison of the excess pore pressures in the dense sand of the one-g model SM3C1 test and the analysis of SM3C1.

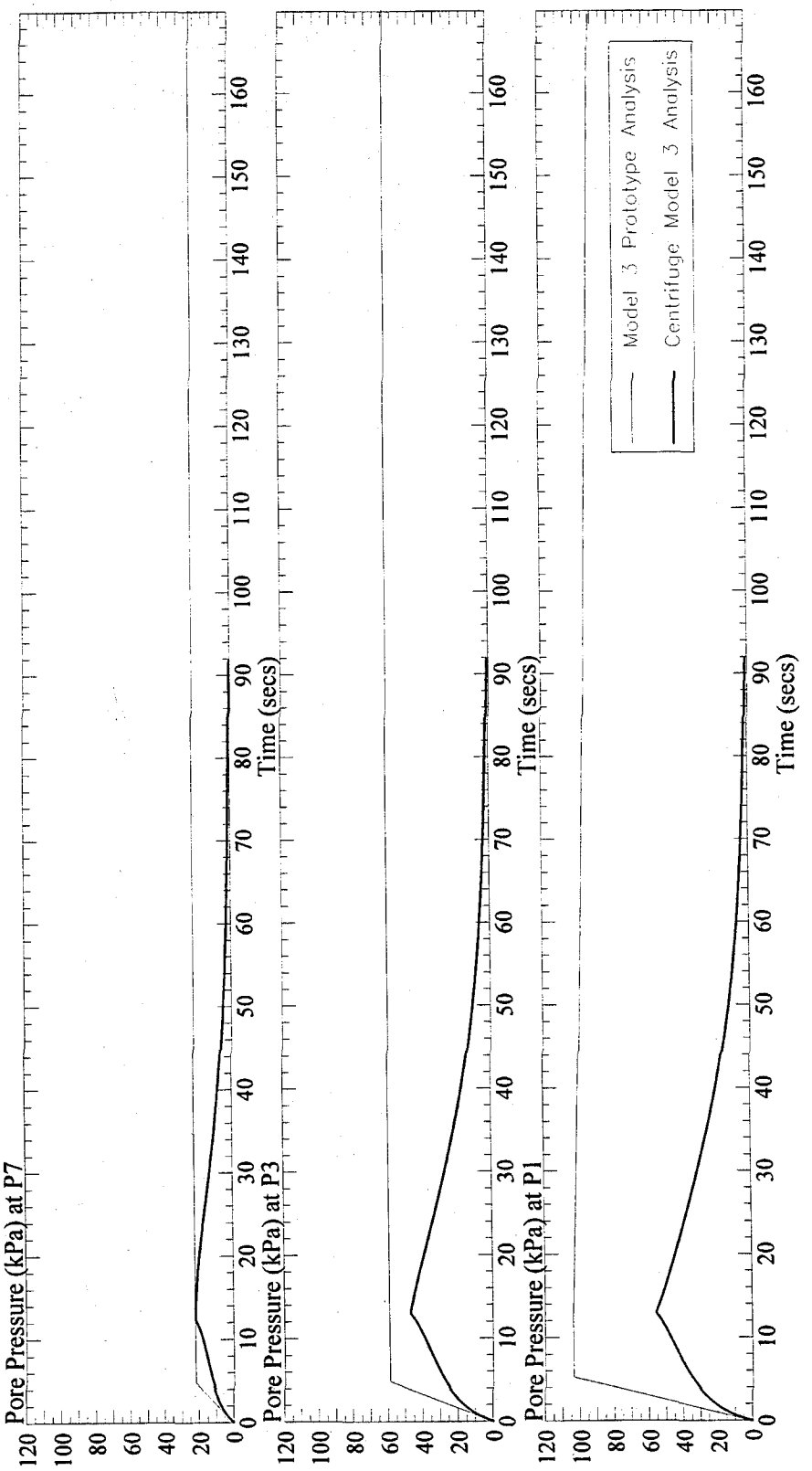

Figure 6-11: Comparison of the analyses of the centrifuge Model 3 test and an equivalent prototype in the loose sand.

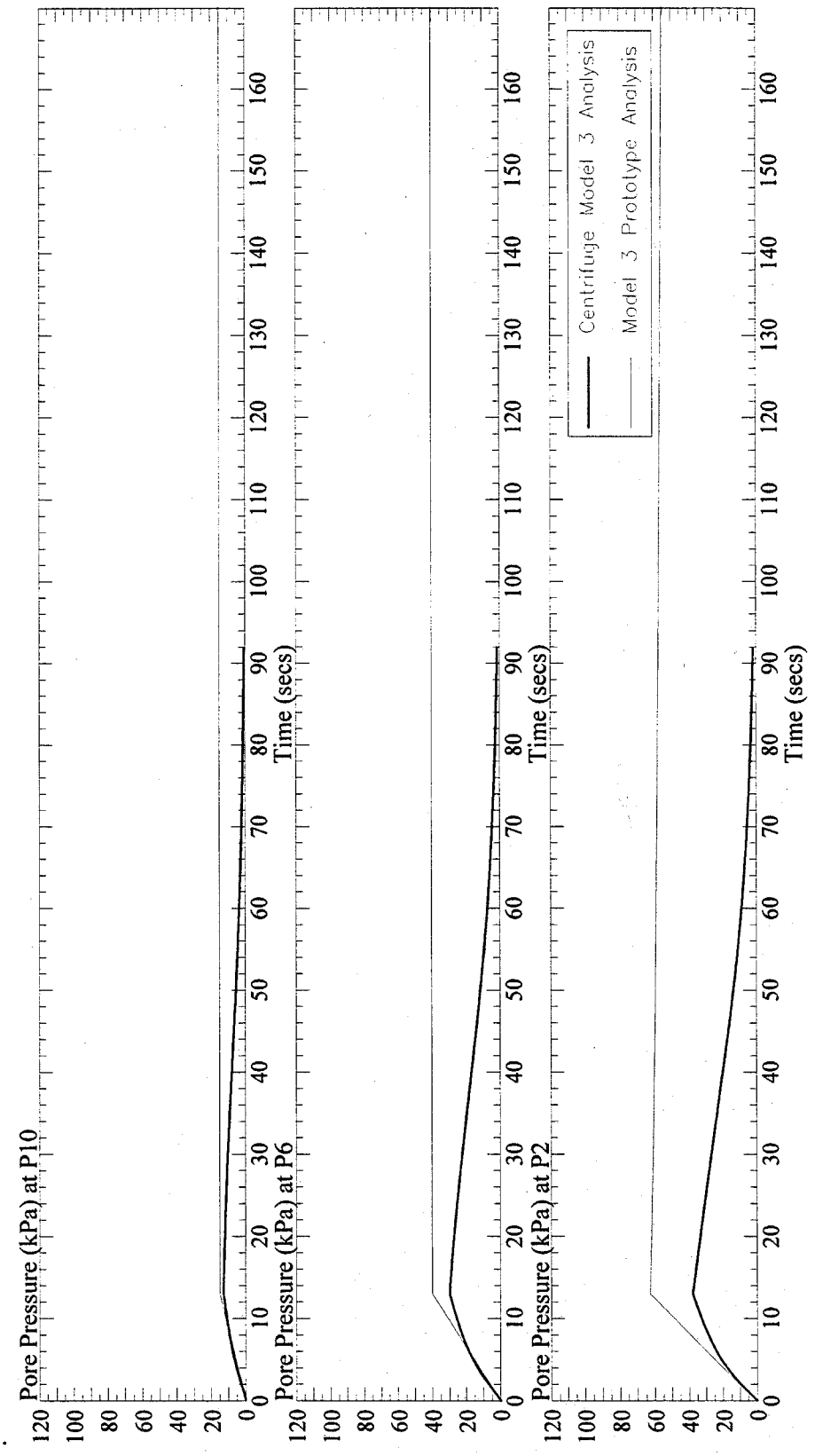

Figure 6-12: Comparison of the analyses of the centrifuge Model 3 test and an equivalent prototype in the dense sand.

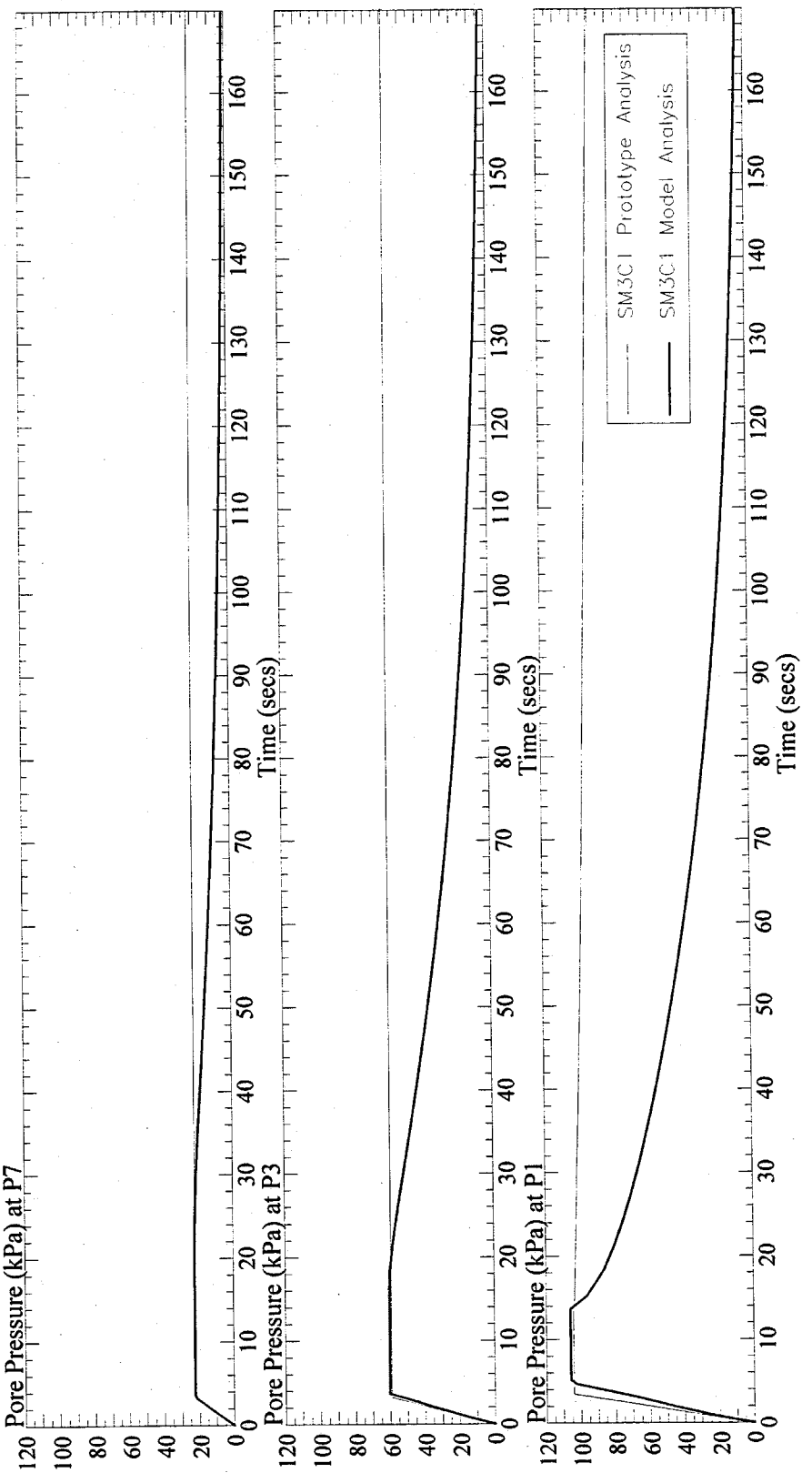

Figure 6-13: Comparison of the analyses of the one-g model SM3C1 and an equivalent prototype in the loose sand.

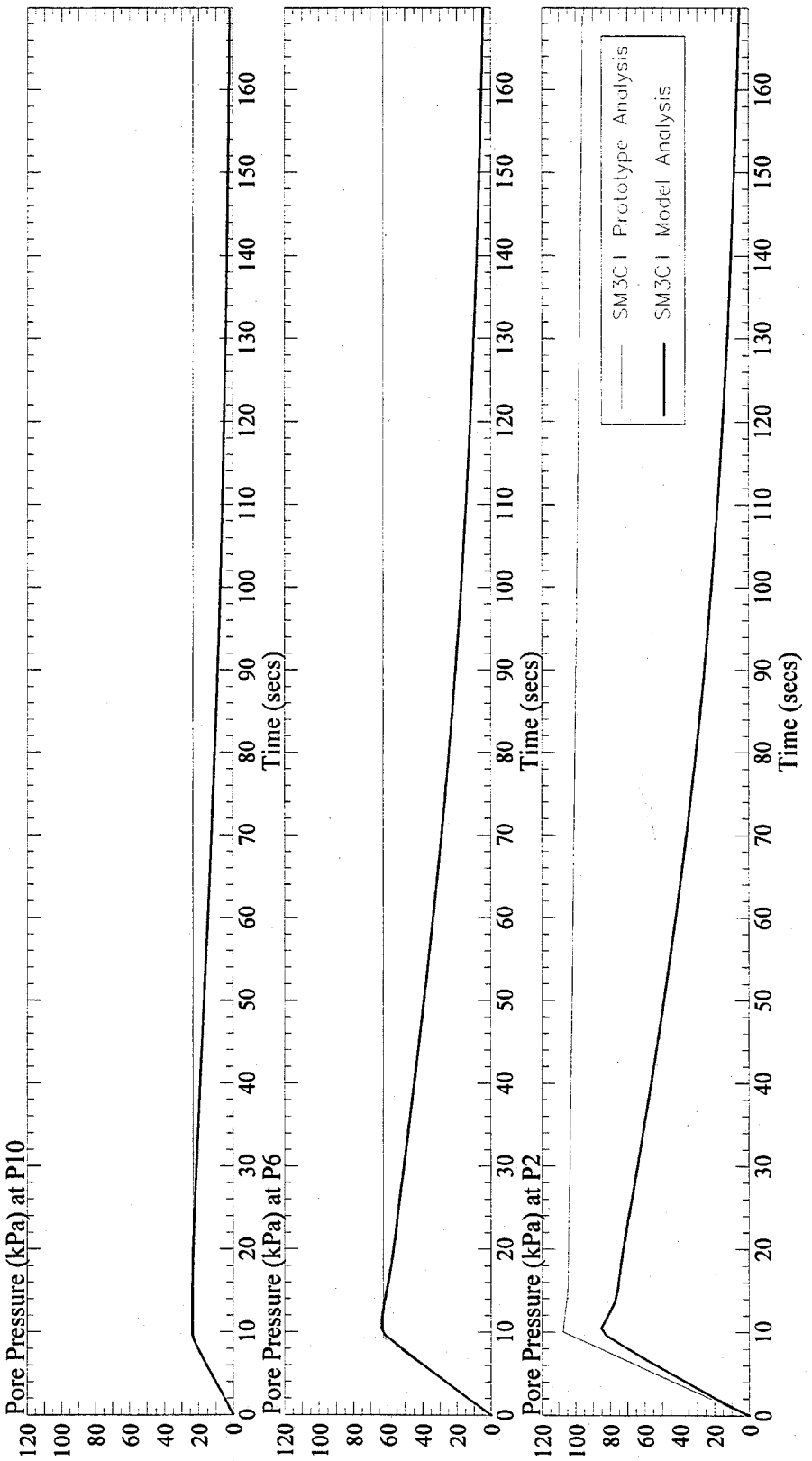

Figure 6-14: Comparison of the analyses of the one-g model SM3C1 and an equivalent prototype in the dense sand.

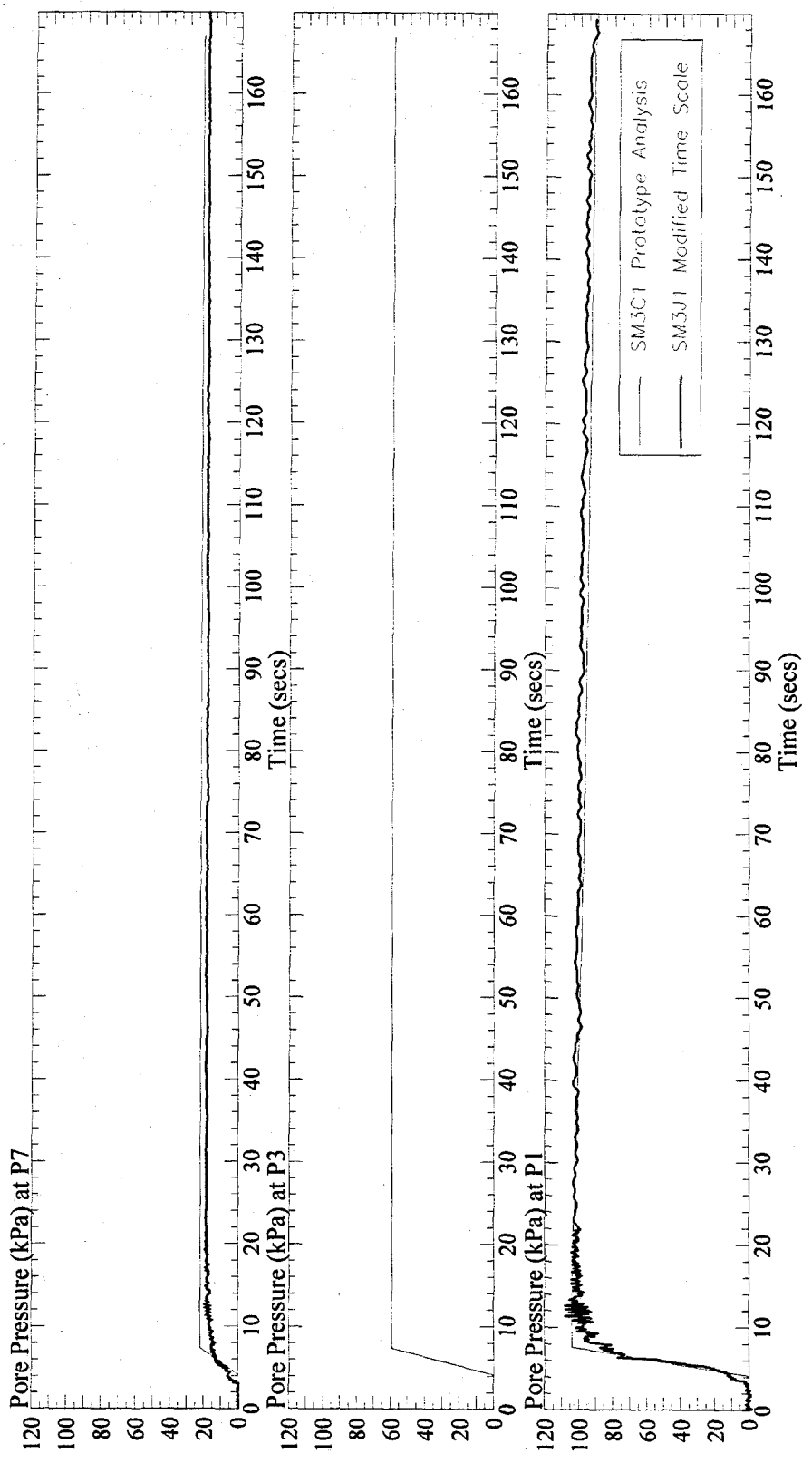

Figure 6-15: Comparison of the one-g model SM3J1 (modified time scale) with the analysis of the equivalent prototype for the one-g model SM3C1 in the loose sand.

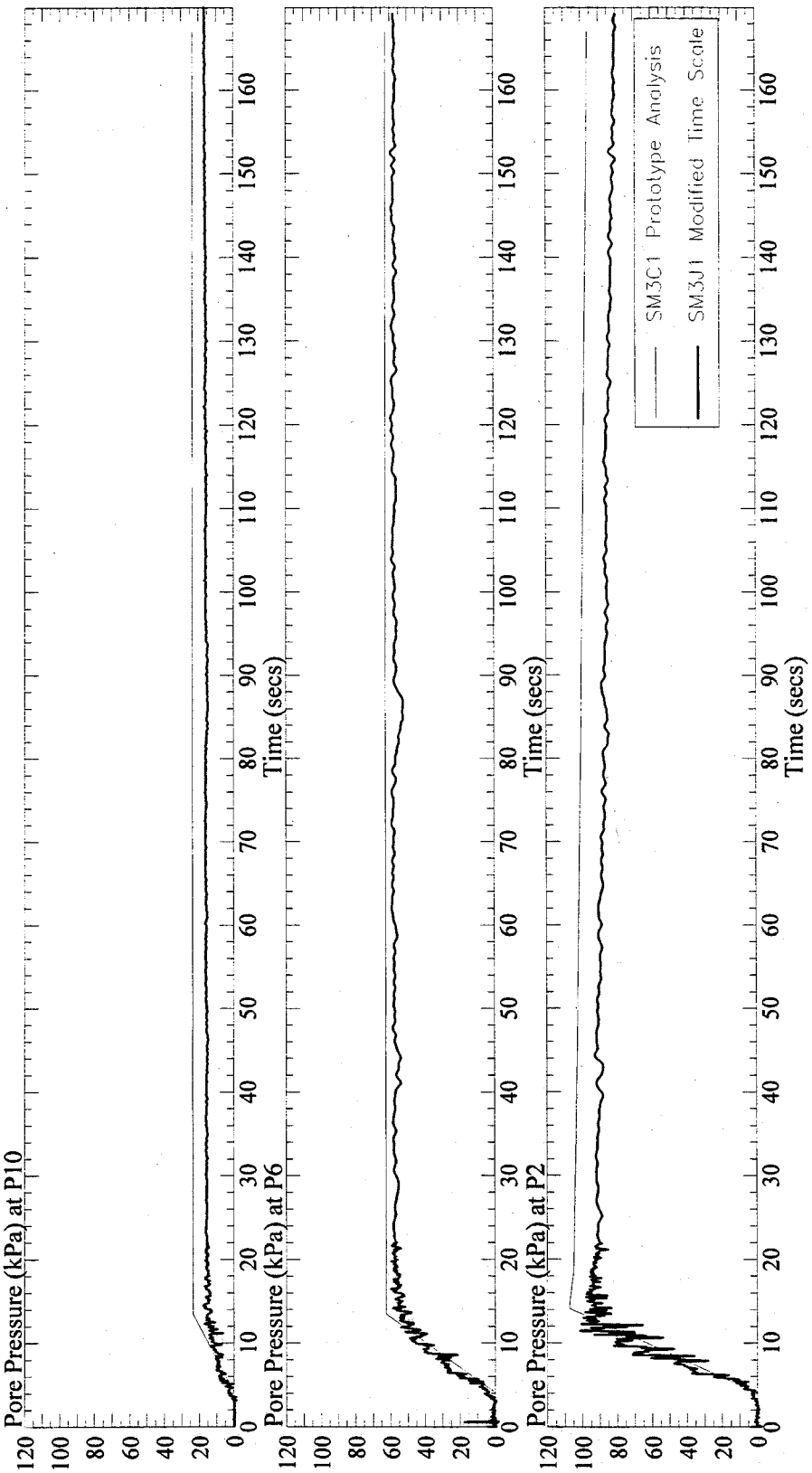

Figure 6-16: Comparison of the one-g model SM3J1 (modified time scale) with the analysis of the equivalent prototype for the one-g model SM3C1 in the dense sand.

Chapter 7

CONCLUSIONS AND RECOMMENDATIONS

7.1 Introduction

The initial focus of the research was to explore the scaling relations which convert the behavior of a physical model to the anticipated behavior of the equivalent prototype. The centrifuge modeling technique was compared with a one-g modeling technique as proposed by Scott (1989) with some additional minor modifications. The proposed one-g technique incorporated a method of constitutive scaling of the model soil properties using the steady state or critical state concept.

To achieve the above, an extensive set of experiments was performed on a shake table. A total of ten models was constructed of sand within a laminar box, and each was subjected to series of very similar model earthquakes. A total of 73 tests were performed on the ten models in this way, and all exhibited pore pressure rises or liquefaction behavior. The models were constructed with a range of initial conditions as follows:

1) Nevada sand was placed in a loose condition and a dense condition in two adjacent columns in the laminar box and water was used as a pore fluid in the model. The initial densities and configuration of the sand emulated the centrifuge Model 3 test as reported (Hushmand et al., 1993).

2) The model in item (1) was repeated, but the initial density of the Nevada sand was reduced in accordance with the constitutive scaling method.

3) The model in item (1) was repeated but no pore fluid was added and the model remained in a dry condition throughout subsequent testing.

4) Nevada sand was placed in a uniform state throughout the laminar box, and water was used as the pore fluid. The initial densities of subsequent testing matched the range of densities in the models described in items (1) and (2) above.

5) The model in item (1) was repeated but an alternative sand, Blend 6-1, was used.

6) The model in item (2) was repeated but an alternative sand, Blend 6-1, was used.

7) The model in item (6), using the Blend 6-1 sand, was repeated but a modified pore fluid of glycerin and water was used in the model.

The array of model tests performed did provide insight into the factors influencing the scaling relations in both the centrifuge modeling technique and the proposed one-g modeling technique. In addition, the model tests provided the following:

- A well-documented set of experimental date which can be used as a reference for future work related to model testing, and also for use in the verification of numerical codes.
- Insight into the behavior of adjacent loose and dense sands, which could have serious implications for seismic assessment of real geotechnical sites and structures.

To further investigate the behavior of the excess pore pressures which were generated in the models during testing, a set of simplified analyses were performed. The analysis methodology was based on Terzaghi's consolidation theory, and therefore did not represent any of the dynamic behavior of the models, but did reveal some important issues regarding the conflict of the dynamic and dissipation time scales that exist in both the one-g and centrifuge modeling techniques. Using the analysis method, it was also possible to make a reasonable prediction of the excess pore pressure behavior of an equivalent prototype of the models. This projected prototype behavior was compared with the actual behavior observed in the model tests.

Conclusions which are based on the model tests and the analyses performed are summarized in Section 7.2. The potential implications of the research are described in Section 7.3, and recommendations regarding future work are summarized in Section 7.4.

7.2 Conclusions

The following conclusions are based solely on the observations of the model tests performed as part of this research as described in Chapter 5, and the limited analyses described in Chapter 6. In

the discussion of the results the observed behavior of the model tests has been divided into two phases; a generation phase which occurs while earthquake shaking continues and excess pore pressures are increasing, and a dissipation phase which occurs after significant shaking has ceased and the excess pore pressures decrease. It should be noted that dissipation of excess pore pressures occurs in both these phases.

Scaling Relations: The set of scaling relations for the centrifuge and one-g modeling techniques was derived in Chapter 2. Using these relations it was possible to relate the results of the centrifuge Model 3 test with comparable one-g models, and either match the results or explain the differences. Similarly, the relations were also used to compare various one-g models with one another. From these comparisons it appears that the scaling relations as derived provide a consistent reference and can explain the relative behaviors observed in the models.

In particular the identification of the incompatibility of the time scales for dynamic and dissipation processes appears to be accurately reflected in the scaling relations. The use of Terzaghi's consolidation theory in the derivation of the dissipation time scale provided relatively consistent results. The dissipation scaling relations were used to stretch the time scale of the results of the model tests in the dissipation phase of the testing with apparent success. This method of mixing time scales when the model tests are converted to prototype values is one possible method of correcting for the conflict between the dynamic and dissipation time scales, at least for the model configurations used in this research. This method could not be used if significant dynamic processes are expected to occur after the earthquake shaking has ceased. Examples of this would be flow failures, slope failures, or subsidence of a structure on liquefied ground.

To fully compensate for the incompatibility of the time scales, the use of an alternate pore fluid appears to be an acceptable solution. The properties of the pore fluid can be selected using the scaling relations to effectively match the time scales of the dissipation and dynamic processes. For the model test performed with an alternate pore fluid (which was 16 times more viscous than water), there appeared to be little effect on the dynamic response of the model when compared to a similar model which used water as a pore fluid. The modified viscosity of the pore fluid increased the rate of generation of excess pore pressures and slowed the rate at which the excess pore pressures declined after the earthquake shaking ceased. These modifications to the excess pore pressures are a direct result of the increased pore fluid viscosity increasing the time taken

for dissipation processes to occur. Based on the scaling relations these are the trends that would also be observed in the equivalent prototype to the models.

Constitutive Scaling Method: A part of the proposed one-g modeling technique involves modifying the density of the sand in the model to better represent the behavior of the sand in the prototype. This has been referred to as the constitutive scaling method and essentially it attempts to account for the effect of the stress difference between the model and prototype on the behavior of the sand. Unfortunately, it is not possible to directly compare the behavior of the model tests which incorporate this scaling with a prototype. This is simply because at this time there is not a suitable documented history of a prototype liquefaction event which has all the information necessary to make such a comparison. Instead, for this research effort, the excess pore pressure behavior of the prototype was simulated by an analysis. A comparison of the results of a model test, which incorporated the constitutive scaling method, compared extremely well with the projected prototype excess pore pressure behavior.

In addition to this the comparison of the model test results of the Nevada sand with its counterpart constructed of the Blend 6-1 sand indicated a good correlation in behavior. The relationship between the two models was determined by the constitutive scaling method. Based on this and the prior work completed by Scott (1989), it appears that the constitutive scaling does create appropriate corrections to the one-g model behavior.

As described briefly in Section 7.1, the constitutive scaling method requires the use of steady state theory, and in particular the use the steady state lines (SSL's) for given sands. For the sands used in the model tests, a considerable amount of data was collected to define the SSL's for the Nevada sand and the Blend 6-1 sand; however, it was not straightforward to select a single SSL. The actual SSL's selected for use in this research did appear to work satisfactorily, but the need for comprehensive and careful testing of a model sand was emphasized if the constitutive scaling method is to be employed. As in general the slope of the SSL is the controlling parameter in the method, issues related to the uniqueness of the SSL have less effect.

Excess Pore Pressures in the Models: Due to the incompatibility in the dynamic and dissipation time scales, both one-g and centrifuge techniques have the potential to seriously underestimate the excess pore pressure development that would actually occur in a prototype. This is extremely important because, as demonstrated in the model testing, the excess pore pressures are strongly coupled with the dynamic behavior of the models. If the results of the models tests are taken at

face value as a prediction of the prototype behavior, a significant error could result, and in general the error is likely to be unconservative. There are two main issues which are of concern as follows:

- During the generation phase (while earthquake shaking is occurring) the rate of excess pore pressure generation is underpredicted in the model. Therefore, a model will most likely develop less excess pore pressure than would occur in the actual prototype.
- During the dissipation phase (after shaking has ceased) the excess pore pressures decline more rapidly in the model. This means that the effective stresses and strength of the sand increase more rapidly in the model than in an equivalent prototype in terms of the dynamic time.

Performance of Model Tests: From the experience gained through the model testing, some of the more difficult aspects of actually creating accurate models and performing tests were highlighted. These are summarized as follows:

- Obtaining full saturation of the models prior to testing proved to be very difficult and further development of an appropriate technique would be desirable. However, it should be noted that the lower levels of saturation did not appear to adversely affect the test results.
- The placement of the model sand at a consistent target density required a great deal of effort and trial and error. Even with an accuracy of ± 1% in the density, the corresponding accuracy is about ± 5% in the relative density of the sand, and for certain model configurations this may not be accurate enough. The pluviation of dry sand from the hopper described in Chapter 4 proved the most reliable and consistent method for placing the sand.
- Obtaining a target earthquake motion for the model testing is an essential aspect of the model testing if the model results are to be compared or used for the prediction of prototype behavior. To achieve this a computer algorithm was developed to obtain the target model earthquake on the shake table.

Behavior of Adjacent Loose and Dense Sands: The results of the model tests indicate that the excess pore pressures generated in the dense sand are increased by the presence of high excess pore pressures in the adjacent loose sand. These higher pore pressures can be attributed to the

transmission of excess pore pressures from the loose sand to the dense sand via diffusion, and to the modified response of the dense sand. The response of dense sand approached that of the loose sand, and behaved in a "softer" manner due to the higher pore pressures and the presence of the adjacent loose sand. This modified response is in part caused by the finite length of the laminar box, and means that the cyclic strain behavior of the dense sand is greater than would occur in a uniform deposit of dense sand. Consequently, the generation of excess pore pressures will be accentuated in the dense sand. Presumably this effect would only be present in a real prototype in the vicinity of the interface of the loose and dense sands.

It is difficult to predict the contribution that the altered response of the dense sand makes to the elevated pore pressures observed in the dense sand when compared to the contribution that occurs from the diffusion of the high excess pore pressures in the loose sand. Further experimental work and analysis is required to resolve these effects.

A model of the adjacent loose and dense sands was also tested without any pore fluid. It is of interest to note that excess pore pressures were observed to develop in this model during the earthquake shaking. This was caused by air pressure. This raises the possibility that in very fine grained materials, such as very fine sands or silts, liquefaction could occur even though the material is not saturated with a pore fluid.

Also observed in the model tests of loose and dense columns of sand were the varying trends in the surface settlements. In some models the settlement in the loose sand was greater than the dense sand, yet in other models the opposite was observed. This appeared to be a consequence of a subtle interplay between the excess pore pressures developed in the dense and loose sands, and the initial relative densities of the sands. It should be noted that in the centrifuge test Model 3, the magnitude of the surface settlements were significantly greater than those observed in the one-g models. It is possible that greater densification occurred in the centrifuge Model 3, or that curvature occurred in the surface of the model due to the radial acceleration gradient imposed by the centrifuge. If this latter effect occurred, then the surface settlements recorded in the centrifuge Model 3 would be overpredicted and require correction.

7.3 Implications of Research

The results and conclusions of the research have some important implications as described below.

Interpretation of Model Test Results: As discussed in Section 7.2, the excess pore pressures observed in a centrifuge model and a one-g model could be significantly less than what would occur in a real prototype. There exists the potential to seriously underpredict the behavior of the prototype in terms of: dynamic behavior during shaking; liquefaction potential; and post-seismic behavior. Therefore, the results of the model tests should not be taken at face value as a prediction of the real prototype behavior.

With careful interpretation the model test results can be modified to better represent the actual prototype behavior, as for example can be done by stretching the time scales during the dissipation phase. However, this method could not be used if significant dynamic processes (for example flow failures, slope failures, or subsidence of a structure on liquefied ground) are expected to occur after the earthquake shaking has ceased.

The only way to fully compensate for the potential errors is to use a modified pore fluid or perhaps use a finer-grained sand to reduce the diffusivity of the model sand. This can be used to eliminate the conflict between the dissipation and dynamic time scaling of the model methods.

Constitutive Scaling Method: As stated in Section 7.2 the constitutive scaling method appears to provide correction in the one-g model for the effect of the stress difference between prototype and model. For the particular set of conditions in the model tests reported it appeared to work well. This opens the possibility of obtaining *quantitative* results from a one-g model which previously could only be obtained from a centrifuge model. This has distinct advantages because, in general, larger models can be constructed at one-g than in the centrifuge which reduces the scaling divergence of the model from the prototype. A number of aspects of usual testing procedures are simplified at one-g. The instrumentation and construction of the one-g model is significantly easier than for the centrifuge technique, and as a consequence should be cheaper. There is also the possibility of using the constitutive scaling method in the centrifuge to make models of a model. This would potentially increase the capacity of the centrifuge.

Behavior of Adjacent Loose and Dense Sands: As discussed in Section 7.2 the behavior of the adjacent loose and dense sands is different from the behavior of a uniform loose sand or uniform dense sand. The current practice in industry regarding the evaluation of dense and loose deposits of sand is to treat them as separate uniform deposits. For example, in the liquefaction evaluation of a site it is common to rule out high excess pore pressure generation in a dense sand simply because in a uniform deposit it could not generate such pressures. However, the research above

indicates that the presence of an adjacent loose layer could induce high excess pore pressure in the dense sand. This in turn would significantly lower the strength of the dense sand and soften its dynamic response. This has serious implications for the assessment of the seismic performance of geotechnical sites or structures constructed above mixed layers or zones of saturated loose and dense material.

7.4 Further Research

Areas that are recommended for further research are briefly cited below.

Constitutive Scaling Method: From the conclusions in section 7.2 it appears that the proposed constitutive scaling method (Scott, 1989) shows promise. To positively assess the veracity of the proposed method, it is necessary to obtain the behavior of a prototype with which a model test can be compared. The original intent in this research effort was to use the centrifuge Model 3 as a prototype; however, as stated, the scaling incompatibility discounted the use of the Model 3 test as a true prototype. Therefore, it remains to find an appropriate prototype.

Pore Fluid Modification: Of the methods employed in the research to correct for the difference between the dynamic and dissipation time scales, the modified pore fluid provided the most complete solution. The modified pore fluid did not appear to adversely affect the dynamic response of the model tested. Further work is warranted to investigate the use of a scaled pore fluid. In addition to this the constitutive scaling method permits the use of a model sand which is different from that in the prototype. Therefore, instead of modifying the pore fluid it should be possible to modify the grain size of the sand to make the dissipation and dynamic time scales equal. This potential method was not explored in the current research effort but is suggested as a possibility for further research. In both the pore fluid or grainsize modification, it must be ensured that the dynamic response of the model is not adversely affected.

Behavior of Adjacent Loose and Dense Sands: Given the potential implications for the behavior of adjacent loose and dense sands, further research is recommended. This could involve additional model testing or analysis. The use of a more sophisticated analysis technique which incorporates the dynamic behavior of the sand would be desirable.

Steady State Line: The steady state line (SSL), or more importantly the slope of the steady state line, is an important element of the constitutive scaling methods. There remains a number of issues regarding the uniqueness of the SSL that remain unresolved, for example the effect of the

test method used to estimate it. From a review of the literature it appears that most of these concerns do not significantly change the slope of the SSL, and therefore this should not affect the constitutive scaling method when the same sand is used in the model as exists in the prototype. However, if an alternate sand is used in the model, then the uniqueness of the SSL becomes an issue. If it is assumed that the SSL's of the prototype sand and the alternate model sand are determined using identical test methodologies, then the relative difference between them should remain relatively constant regardless of which particular test method is selected, and therefore the constitutive theory would hold. Further research is required to verify that this is a reasonable assumption.

7.5 References

Hushmand, B., R. F. Scott, and H. Rashidi, 1994, "VELACS model No. 3: Liquefaction in dense and loose sand columns," in Verification of Numerical Procedures for the Analysis of Soil Liquefaction Problems, Vol. 2, pp. 1415-1442, Arulanandan, K. and R. F. Scott, eds., Balkema, Rotterdam.

Scott, R. F., 1989, "Centrifuge and Modeling Technology: A Survey," Rev. Franc. Geotech., No. 48, pp. 15-34, July.

Appendix A

SOURCE CODE FOR CITED PROGRAMS

A.1 Introduction

This Appendix A presents the source code for two programs written and used for the research described within the main text.

A.2 Program to Compute Input Motion for the Shake Table.

The following source code computes the necessary functions described in Chapter 4, Section 4.4.1. The code was prepared using QuickBasic. The code used to compute the Fast Fourier Transforms and inverse FFT's is based on a code included in "Numerical Recipes, Routines and Examples in Basic" Julien C. Sprott, Cambridge University Press, 1991.

```
'Program takes three time history signals for a shake table, an input (INP)
'an output (OUT), and a target motion (TARG).  The program finds the transfer
'function for the table (1 dof) in the frequency domain and then derives a
'new input (INPN) fft so that a better match can be obtained to the target fft.
'The new input fft is inverted to a time history which can then be post
'processed as new input for the shake table.  This process can be repeated
'until the output signal and fft matches the target signal and fft adequately.
'Note that the three signals must all have the same time increment.


'open a file which contains the basic input parameters
'file containing input data of input signal (INP), file containing
'output signal(OUT), and target signal (TARG), timestep of the time histories
'(should be same). Also note that the number of data points of each signal
'can be different but each must be within the same interval of powers of 2
'(eg, between 2048 and 4096)
'a smoothing factor SSTEP is also required to smooth the fft's prior to
'computing the transfer function, SSTEP must be an even number (0 will bypass
'smoothing subroutine).
```

```
'a maximum frequency value MFREQ for a low pass filter on the new fft
'so that aberrant higher frequencies can be eliminated prior to the inverse
'transform to obtain the new input signal (MFREQ=0 will bypass filter)
'filename and of new input signal (INPN) with time in first column
'(*.DAT), and without time signal (*.SIG); and filename (INPNF) for fft data
'with frequency in first column (*.DAT), and complex values only (*.FFT)
'further processing ie: inverse fft.
'eg:
' FILEINP.DAT, FILEOUT.DAT, FILETARG.DAT, TSTEP, SSTEP, MFREQ
' FILENEWSIG, FILENEWFFT

REM $DYNAMIC
OPEN "I", #1, "BATCH"
IF EOF(1) = -1 THEN 200
INPUT #1, INP$, OUT$, TARG$, TSTEP, SSTEP, MFREQ, INPN$, INPNF$
CLOSE #1
'time history timestep is TSTEP
'smoothing factor is SSTEP
'Compute the forward fft for each signal, smooth the fft by SSTEP
'and create an array to store the complex values in.
'Limit the number of data points that can be processed for each signal to 8192.
LIMIT = 8192
DIM DATQ(LIMIT)
OPEN "I", #2, INP$
 ISIGN = 1
 PRINT "INP$"
 DIM DAT(LIMIT)
 GOSUB 500
 ERASE DAT
 IF SSTEP = 0 GOTO 20
 DIM SIZE(N)
 GOSUB 4000
 ERASE SIZE
20  DIM DATI(NP)
   FOR I = 1 TO NP
   DATI(I) = DATQ(I)
   NEXT I
CLOSE #2
OPEN "I", #2, OUT$
 ISIGN = 1
 PRINT "OUT$"
 DIM DAT(LIMIT)
 GOSUB 500
 ERASE DAT
 IF SSTEP = 0 GOTO 40
 DIM SIZE(N)
 GOSUB 4000
 ERASE SIZE
40  DIM DATO(NP)
```

```
   FOR I = 1 TO NP
   DATO(I) = DATQ(I)
   NEXT I
CLOSE #2
OPEN "I", #2, TARG$
 ISIGN = 1
 PRINT "TARG$"
 DIM DAT(LIMIT)
 GOSUB 500
 ERASE DAT
 IF SSTEP = 0 GOTO 60
 DIM SIZE(N)
 GOSUB 4000
 ERASE SIZE
60  DIM DATT(NP)
   FOR I = 1 TO NP
   DATT(I) = DATQ(I)
   NEXT I
CLOSE #2

'Create new data file names for new input files,
INPNST$ = INPN$ + ".DAT"
INPNS$ = INPN$ + ".SIG"
INPNFTF$ = INPNF$ + ".DAT"
INPNFFT$ = INPNF$ + ".FFT"

'Erase the arrays which are no longer necessary to create memory space
ERASE DATQ

'goto subroutine which calculates the transfer function and generates a
'new input fft.
DIM DATN(NP)
GOSUB 3000

'Erase the arrays which are no longer necessary to create memory space
ERASE DATI, DATO, DATT

'Compute the inverse fft of the new signal and output to files FILENEWSIG.DAT
'and FILENEW.SIG
ISIGN = -1
DIM DATQ(NP)
PRINT "Generating new input signal"
FOR I = 1 TO NP
  DATQ(I) = DATN(I)
NEXT I
GOSUB 1000
'open file INPNS for output of array with time column and signal
OPEN "O", #3, INPNST$
'open file INPNS for output of signal without time data
```

```
OPEN "O", #4, INPNS$
FOR I = 1 TO NP
  W1 = (I - 1) * TSTEP
  PRINT #3, USING "####.####"; W1;
  W2 = DATQ(I) / N
  PRINT #3, USING "######.##"; W2
  WRITE #4, W2
NEXT I
CLOSE #3, #4

200
END

500
'Program to drive the  subroutines FOUR1 and REALFT to perform forward
'and inverse fourier transforms.
'the subroutines are based on "Numerical Recipes" W Press et el, Cambridge
'Press 1986.
'input from a one dimensional array of length NP with the leading data point
'ISIGN=1 gives forward fft, ISIGN= -1 will give inverse fft
'open input file containing the array of either real numbers for the fft
'or complex numbers for the inverse fft
ND = 0
'input to array DAT the input file which has a single column of data
FOR I = 1 TO LOF(2)
   INPUT #2, DAT(I)
   'counter to check number of data points in file
   ND = ND + 1
   IF EOF(2) = -1 THEN GOTO 520
NEXT I
520
PRINT "Number of data points in data  file is  ";
PRINT ND
IF ND < 256 THEN GOTO 700
IF ND = 256 THEN GOTO 550
IF ND > 256 AND ND <= 512 THEN FILL = 512
IF ND > 512 AND ND <= 1024 THEN FILL = 1024
IF ND > 1024 AND ND <= 2048 THEN FILL = 2048
IF ND > 2048 AND ND <= 4096 THEN FILL = 4096
IF ND > 4096 AND ND <= 8192 THEN FILL = 8192
IF ND > 8192 AND ND <= 16384 THEN FILL = 16384
IF ND > 16384 THEN GOTO 701
NP = INT(FILL)
N = INT(NP / 2)
TFILL = 2 * FILL - 1
PRINT "NP =  "; NP
'read from DAT the data into DATQ for fft processing
550 FOR I = 1 TO ND
   DATQ(I) = DAT(I)
```

```
   '*PRINT #5, USING "#####.###"; DATQ(I)
   NEXT I
'subroutine adds data points to end of file with value 0.0 to get power of 2
   FOR I = ND + 1 TO FILL
   DATQ(I) = 0!
   '* PRINT #5, USING "#####.###"; DATQ(I)
   NEXT I
'*CLOSE #5
'ISIGN = 1 will generate the forward transform
IF ISIGN = -1 THEN GOTO 600
GOSUB 1000
GOTO 702
600
'start of the inverse fft
GOSUB 1000
GOTO 702
END
700 PRINT "Number of data points less than 128, modify program"
END
701 PRINT "Number of data points greater than 8192, modify program"
END
702
705
RETURN

'SUBROUTINE CALL FOR FFT CALCULATION
1000
THETA# = 3.141592653589793# / CDBL(NP / 2)
C1 = .5
IF ISIGN = 1 THEN
 C2 = -.5
 GOSUB 2000
ELSE
 C2 = .5
 THETA# = -THETA#
END IF
WPR# = -2# * SIN(.5# * THETA#) ^ 2
WPI# = SIN(THETA#)
WR# = 1# + WPR#
WI# = WPI#
N2P3 = NP + 3
FOR I = 2 TO INT(NP / 4)
 I1 = 2 * I - 1
 I2 = I1 + 1
 I3 = N2P3 - I2
 I4 = I3 + 1
 WRS# = CSNG(WR#)
 WIS# = CSNG(WI#)
 H1R = C1 * (DATQ(I1) + DATQ(I3))
```

```
  H1I = C1 * (DATQ(I2) - DATQ(I4))
  H2R = -C2 * (DATQ(I2) + DATQ(I4))
  H2I = C2 * (DATQ(I1) - DATQ(I3))
  DATQ(I1) = H1R + WRS# * H2R - WIS# * H2I
  DATQ(I2) = H1I + WRS# * H2I + WIS# * H2R
  DATQ(I3) = H1R - WRS# * H2R + WIS# * H2I
  DATQ(I4) = -H1I + WRS# * H2I + WIS# * H2R
  WTEMP# = WR#
  WR# = WR# * WPR# - WI# * WPI# + WR#
  WI# = WI# * WPR# + WTEMP# * WPI# + WI#
NEXT I
IF ISIGN = 1 THEN
  H1R = DATQ(1)
  DATQ(1) = H1R + DATQ(2)
  DATQ(2) = H1R - DATQ(2)
ELSE
  H1R = DATQ(1)
  DATQ(1) = C1 * (H1R + DATQ(2))
  DATQ(2) = C1 * (H1R - DATQ(2))
  GOSUB 2000
END IF
RETURN

'SUBROUTINE CALL FOR FFT
2000
'replaces DATQ by its discrete F Transform if ISIGN =1; or replaces DATQ
'by NN times it inverse discrete F Transform if ISIGN = -1.  DATQ is a real
'array of length 2*NN.  NN must be an integer power of 2
NN = N
N = 2 * NN
J = 1
FOR I = 1 TO N STEP 2
      IF J > I THEN
       TEMPR = DATQ(J)
       TEMPI = DATQ(J + 1)
       DATQ(J) = DATQ(I)
       DATQ(J + 1) = DATQ(I + 1)
       DATQ(I) = TEMPR
       DATQ(I + 1) = TEMPI
      END IF
      M = INT(N / 2)
      WHILE M >= 2 AND J > M
       J = J - M
       M = INT(M / 2)
      WEND
      J = J + M
NEXT I
MMAX = 2
WHILE N > MMAX
```

```
      ISTEP = 2 * MMAX
      THETA# = 6.28318530717959# / (ISIGN * MMAX)
      WPR# = -2# * SIN(.5# * THETA#) ^ 2
      WPI# = SIN(THETA#)
      WR# = 1#
      WI# = 0#
      FOR M = 1 TO MMAX STEP 2
       FOR I = M TO N STEP ISTEP
        J = I + MMAX
        TEMPR = CSNG(WR#) * DATQ(J) - CSNG(WI#) * DATQ(J + 1)
        TEMPI = CSNG(WR#) * DATQ(J + 1) + CSNG(WI#) * DATQ(J)
        DATQ(J) = DATQ(I) - TEMPR
        DATQ(J + 1) = DATQ(I + 1) - TEMPI
        DATQ(I) = DATQ(I) + TEMPR
        DATQ(I + 1) = DATQ(I + 1) + TEMPI
       NEXT I
       WTEMP# = WR#
       WR# = WR# * WPR# - WI# * WPI# + WR#
       WI# = WI# * WPR# + WTEMP# * WPI# + WI#
      NEXT M
      MMAX = ISTEP
WEND
N = NN
RETURN


3000
'Subroutine Program takes three FFT input in the form of an array (1,NP) long where
'the components alternate from real to imaginary respectively.  The exception
'is the first two elements of the array (note the convention followed is
' the same as "Numerical Recipes").
' The three arrays are an input fft (INP), a recorded output fft (OUT) and
' a target fft (TARG)
'The program finds a new input fft (INPN) so that eventually the target
'fft can be obtained via iteration.
'Let INP=input signal fft
'   OUT=output signal fft
'   TARG=target signal
'therefore the transfer function fft TRN=OUT/INP
'Now a new input fft (INPN), will give a new output fft (OUTN)
'but INPN*TRN=OUTN  where TRN is determined from the prior INP and OUT as
'above, and OUTN => TARG
'so INPN*[OUT/INP] = TARG
'or
'  INPN = TARG * INP
'        ~~~~~~~~~~
'          OUT
'
'open file for output of INPN array with fft magnitude
```

```
OPEN "O", #3, INPNFTF$
'open file for output of fft array with complex data for use
'in later processing.
OPEN "O", #4, INPNFFT$
'define variables for program
'increment in frequency of fft
DFO = 1 / TSTEP / NP
'maximum frequency of original fft
MAXF = 1 / TSTEP / 2
'find resultant magnitude of input FFT arrays
N = CINT(NP / 2)
PRINT "Computing Transfer function"
DIM SIZEI(N)
DIM SIZEO(N)
DIM SIZET(N)
DIM SIZEN(N)
SIZEI(1) = ABS(DATI(1))
SIZEO(1) = ABS(DATO(1))
SIZET(1) = ABS(DATT(1))
FOR I = 2 TO N
  SIZEI(I) = SQR(DATI(2 * I - 1) ^ 2 + DATI(2 * I) ^ 2)
  SIZEO(I) = SQR(DATO(2 * I - 1) ^ 2 + DATO(2 * I) ^ 2)
  SIZET(I) = SQR(DATT(2 * I - 1) ^ 2 + DATT(2 * I) ^ 2)
  IF SIZEO(I) = 0! THEN PRINT I
NEXT I
'start algorithm to find INPN in terms of fft magnitude
FOR I = 1 TO N
  SIZEN = SIZET(I) * SIZEI(I) / SIZEO(I)
'find factor to scale input complex fft by
  SCALE = SIZEN / SIZEI(I)
'create new array for scaled complex values of new fft
  DATN(2 * I - 1) = SCALE * DATI(2 * I - 1)
  DATN(2 * I) = SCALE * DATI(2 * I)
NEXT I
'Pass the new fft through a low pass filter setting complex values to zero
'above frequency assigned (Note : Frequency = I/TSTEP/NP for I= 1 to N)
'Bypass lowpass filter if MFREQ=0
IF MFREQ = 0 GOTO 3500
PRINT "Low Pass Filter (Hz)=", MFREQ
LP = INT(MFREQ * TSTEP * NP) + 1
PRINT "LP=", LP
FOR I = LP TO N
  DATN(2 * I - 1) = O!
  DATN(2 * I) = O!
NEXT I
3500
'write to a file the complex fft values as a single column of data for later
'processing.
FOR I = 1 TO N
```

```
  WRITE #4, DATN(2 * I - 1)
  WRITE #4, DATN(2 * I)
'print to file the frequency and the scaled magnitude of fft (multiply by TSTEP)
  PRINT #3, USING "####.####"; I * DFO;
  PRINT #3, USING "#######.##"; SQR(DATN(2 * I - 1) ^ 2 + DATN(2 * I) ^ 2) * TSTEP
NEXT I
CLOSE #4
CLOSE #3
RETURN

4000
'Subroutine smooths fft spectrum prior to finding the transfer
'function and generating a new signal.  This is done to avoid
'gross amplification caused by division of near zero values which
'often occur in  random spectrum.
'Note that the smoothing factor applied to the resultant amplitude
'of the FFT will be applied to the real and imaginary parts of the
'fft (take the sqrt first).  In this way the FFT can be preserved
'so that the inverse FFT of the smoothed FFT can be found.
'integer range over which average will be taken for smoothing, must be
'an even number
'input from a one dimensional array of fft complex numbers of length NP
PRINT "Smoothing FFT"
N = CINT(NP / 2)
'start smoothing routine which is just an averaging routine.  Let SSTEP+1
'equal number of data points over which the averaging is performed. Let SSTEP
'be an even number
SIZE(1) = ABS(DATQ(1))
FOR I = 2 TO N
  SIZE(I) = SQR(DATQ(2 * I - 1) ^ 2 + DATQ(2 * I) ^ 2)
NEXT I
NSSTEP = INT(SSTEP / 2)
FOR I = 1 TO N
SUM = 0!
'first, average ends of array correctly
   IF I > NSSTEP AND I < (N - NSSTEP) THEN 4100
   IF I > NSSTEP THEN GOTO 4080
   FOR J = 1 TO (I + NSSTEP)
     SUM = SUM + SIZE(J)
   NEXT J
   GOTO 4150
4080 FOR J = (I - NSSTEP) TO N
     SUM = SUM + SIZE(J)
   NEXT J
   GOTO 4150
'now average the main bulk of the data
4100 FOR J = (I - NSSTEP) TO (I + NSSTEP)
      SUM = SUM + SIZE(J)
    NEXT J
```

```
4150
 AV = SUM / (SSTEP + 1)
 SCALE = AV / SIZE(I)
'smoothed complex values of original fft array
 C1 = SCALE * DATQ(2 * I - 1)
 C2 = SCALE * DATQ(2 * I)
 DATQ(2 * I - 1) = C1
 DATQ(2 * I) = C2
NEXT I
RETURN
```

A.3 Program to Compute Two Dimensional Consolidation.

The following source code computes the two-dimensional consolidation problem using a finite difference formulation of Terzaghi's theory of consolidation as explained in Chapter 6. The code presented specifically models the case of a centrifuge model as defined in the initial specifications of parameters. The code includes a provision to apply linearly increasing pore water pressure increments at each node at each time step to approximate the generation of excess pore water pressures in saturated sands during an earthquake. The coefficient of consolidation varies with time as s function of the effective stress. The code was written using QuickBasic.

```
'Program computes 2D diffusion
'Provides incremental pwp to left and right hand side of cross-section
'at different specified rates to simulate earthquake generation
'Loose and dense columns in centrifuge MODEL3
'Transforms from Cv unload to Cv load at the completion of earthquake generation.
'Computes Cv as a function of the vertical effective stress computed with time.
' 15 horizontal layers, and with 31 vertical node sections

'Property constants (SI):
'Initial void ratio distribution
'Mean Void Ratio MVR, and Mean Vertical Effective Stress MVES (kPa)
'Void ratio equation constants for Nevada sand (shift based on MVR)
'e=[2*ey0-(-eaa^2+2*eff*ey0-2*ex0*ey0)/(2*eff-ex0)]-[EMVES-MVR]
'where EMVES is the void ratio computed at MVES
'For side 1 (loose)
EY01 = .71
EX01 = -50
EAA1 = -2.21
```

```
MVES1 = 2
MVR1 = .7305
'For side 2 (dense)
EY02 = .608
EX02 = -26
EAA2 = -1.23
MVES2 = 2
MVR2 = .6102

'permeability distribution (m/s)
'Nevada sand eqn constants, k=[k01*e-k02]/100
K01 = .0328939
K02 = .0170283

'compressibility coefficient equation constants Nevada Sand loading
'Av=(2*y0-(-aa^2+2*eff*y0-2*x0*y0)/(2*(eff-x0))
'load for side 1 (loose)
Y01 = .000018
X01 = -5!
AA1 = .148
'load for side 2 (dense)
Y02 = .000008
X02 = -3!
AA2 = .11

'compressibility coefficient equation constants Nevada Sand unloading
'Av=(eff^bb)*cc
'unload same for side 1 and 2
BB = -.659981
CC = .000366252#

'total unit weight of sand (kN/m3)
G1 = 19.26
G2 = 19.99

'unit weight of water (kN/m3)
GW = 9.81

'Depth of model
Depth = .22

'Total pore pressure LDU (kPa) to be added at base of left half, and RDU (kPa)
'to be added at base of right half of box at time TU(model).
'The program automatically distributes the pore pressure
'to be linear with depth, and incremented uniformly per timestep.
'Note that the centerline is taken to be part of the left side.
LDU = 350
RDU = 32
LTU = .26
```

```
RTU = .2
'specify value of Ru at which properties for Cv change from unload to load
'RU = .95


'Effective body force acting on model in g's
NG = 50
'Length scaling of prototype/model
NL = 50
'Scale factor for time prototype/model
NT = 50
'Scale factor for stress prototype/model
NS = 1

'Total number model time to run program
TTOT = 3.2

'name output file for full cross section information
OUT$ = "OUTCEN5.DAT"
'Number of timesteps (INTERVAL) between each dump of all data for the
'cross-section
INTERVAL = 2000

'name output file to monitor properties at selected nodes
MON$ = "MONCEN5.DAT"

'name output file for history of information at single nodes
OUTN$ = "OUTNCEN5.DAT"
'Number of timesteps (TRIG) between each dump of data for histories at
'specified nodes
TRIG = 100
'input node numbers, allow for six only
I1 = 15
J1 = 5
I2 = 15
J2 = 19
I3 = 9
J3 = 5
I4 = 9
J4 = 19
I5 = 4
J5 = 5
I6 = 4
J6 = 19

'define the size of the mesh, no. of rows ITOT, number of columns JTOT
'note that JTOT must be odd must be proportioned so that the horizontal
'distance between nodes is the same as the vertical.
ITOT = 15
```

```
JTOT = 23

'#########################################################################
'start calculation
OPEN OUT$ FOR OUTPUT AS #1
OPEN OUTN$ FOR OUTPUT AS #2
OPEN MON$ FOR OUTPUT AS #3

'Compute constant
DZ = Depth / (ITOT - 1)

'divide columns into loose (left half), center, and dense (right half).
JTOTL = INT(JTOT / 2 - .5)
JTOTC = JTOTL + 1
JTOTR = JTOTL + 2

'Dimension various arrays for calculations
'dimension an array for the initial vertical effective stress
DIM VEFFI(ITOT, JTOT)
'dimension an array for the initial void ratio
DIM EI(ITOT, JTOT)
'dimension an array for the initial permeability
DIM KI(ITOT, JTOT)
'dimension an array for the vertical effective stress
DIM VEFF(ITOT, JTOT)
'dimension an array for initial values excess pwp
DIM INI(ITOT, JTOT)
'dimension an array for new values of excess pwp
DIM NEW(ITOT, JTOT)
'dimension an array for the increment of pore pressure applied
DIM DDU(ITOT, JTOT)
'dimension an array for values of Ru
DIM RRU(ITOT, JTOT)
'dimension an array which tracks unload or load value of Av based on Ru
DIM AZZ(ITOT, JTOT)
'dimension an array for values of Av
DIM AAV(ITOT, JTOT)
'dimension an array for values of Cv
DIM CCV(ITOT, JTOT)
'dimension an array for values of M
DIM MM(ITOT, JTOT)
'dimension an array for values of DD
DIM DD(ITOT)


'initialize a counter for printing purposes
COUNTERB = 0
COUNTERH = 0
```

```
'calculate the initial vertical effective stress at each node
GOSUB 2500
'calculate the initial void ratio distribution
GOSUB 2600
'calculate initial permeability distribution
GOSUB 2700

'apply pore pressure until LTU OR RTU (model secs),
100
IF 1 = LTZ AND RTZ THEN GOTO 200
TIME = TIME + DT
IF TIME > LTU THEN LTZ = 1
IF TIME > RTU THEN RTZ = 1
IF LTZ = 1 THEN LDU = 0
IF RTZ = 1 THEN RDU = 0
'compute vertical eff. stress
GOSUB 3000
'compute unload or load factor for Av
GOSUB 9000
'compute Av
GOSUB 8000
'compute Cv
GOSUB 4000
'compute time increment for next step
GOSUB 5000
'compute constants M and DD
GOSUB 6000
'compute distribution of applied pore pressure
GOSUB 7000
'compute next increment of excess pwp.
GOSUB 1000
'repeat until TU is reached
GOTO 100

200 TIME = TIME - DT
PRINT "TIME AT WHICH PWP GENERATION CEASED =  ";
PRINT TIME

250
IF TIME > TTOT THEN GOTO 300
'compute vertical eff. stress
GOSUB 3000
'compute unload or load factor for Av
GOSUB 9000
'compute Av
GOSUB 8000
'compute Cv
GOSUB 4000
```

```
'compute time increment for next step
GOSUB 5000
TIME = TIME + DT
'compute constants M and DD
GOSUB 6000
'compute next increment of excess pwp.
GOSUB 1000
GOTO 250
300
CLOSE #1
CLOSE #2
CLOSE #3
END

1000
  FOR I = 2 TO (ITOT - 1)
    'Left hand boundary
    J = 1
      NEW(I, J) = MM(I, J) * (2 * INI(I, J + 1) + INI(I - 1, J) + INI(I + 1, J) - 4 * INI(I, J)) +
INI(I, J) + (I - 1) * DDU(I, J)
    'Left half of box
    FOR J = 2 TO JTOTL
      NEW(I, J) = MM(I, J) * (INI(I, J - 1) + INI(I, J + 1) + INI(I - 1, J) + INI(I + 1, J) - 4 * INI(I,
J)) + INI(I, J) + (I - 1) * DDU(I, J)
    NEXT J
    'Compute for centerline of box
    J = JTOTC
      EE = (2 * KI(I, J - 1) / (KI(I, J + 1) + KI(I, J - 1)))
      FF = (2 * KI(I, J + 1) / (KI(I, J + 1) + KI(I, J - 1)))
      NEW(I, J) = DD(I) * MM(I, J + 1) * (EE * INI(I, J - 1) + FF * INI(I, J + 1) + INI(I - 1, J) +
INI(I + 1, J) - 4 * INI(I, J)) + INI(I, J) + (I - 1) * DDU(I, J)
    'compute right half of the box
    FOR J = JTOTR TO (JTOT - 1)
      NEW(I, J) = MM(I, J) * (INI(I, J - 1) + INI(I, J + 1) + INI(I - 1, J) + INI(I + 1, J) - 4 * INI(I,
J)) + INI(I, J) + (I - 1) * DDU(I, J)
    NEXT J
    'at the right boundary
    J = JTOT
      NEW(I, J) = MM(I, J) * (2 * INI(I, J - 1) + INI(I - 1, J) + INI(I + 1, J) - 4 * INI(I, J)) + INI(I,
J) + (I - 1) * DDU(I, J)
  NEXT I
    'compute lower boundary
    'Left hand boundary
    I = ITOT
    'Left half of box
    J = 1
      NEW(I, J) = MM(I, J) * (2 * INI(I, J + 1) + 2 * INI(I - 1, J) - 4 * INI(I, J)) + INI(I, J) + (I -
1) * DDU(I, J)
    FOR J = 2 TO JTOTL
```

```
    NEW(I, J) = MM(I, J) * (INI(I, J - 1) + INI(I, J + 1) + 2 * INI(I - 1, J) - 4 * INI(I, J)) + INI(I,
J) + (I - 1) * DDU(I, J)
   NEXT J
   'Compute for centerline of box
   J = JTOTC
    EE = (2 * KI(I, J - 1) / (KI(I, J + 1) + KI(I, J - 1)))
    FF = (2 * KI(I, J + 1) / (KI(I, J + 1) + KI(I, J - 1)))
    NEW(I, J) = DD(I) * MM(I, J + 1) * (EE * INI(I, J - 1) + FF * INI(I, J + 1) + 2 * INI(I - 1, J)
- 4 * INI(I, J)) + INI(I, J) + (I - 1) * DDU(I, J)
   'compute right half of the box
   FOR J = JTOTR TO (JTOT - 1)
    NEW(I, J) = MM(I, J) * (INI(I, J - 1) + INI(I, J + 1) + 2 * INI(I - 1, J) - 4 * INI(I, J)) + INI(I,
J) + (I - 1) * DDU(I, J)
   NEXT J
   'at the right boundary
   J = JTOT
    NEW(I, J) = MM(I, J) * (2 * INI(I, J - 1) + 2 * INI(I - 1, J) - 4 * INI(I, J)) + INI(I, J) + (I - 1)
* DDU(I, J)
'Print results of cross-section at intervals to a file
 IF COUNTERB = 0 THEN GOSUB 2000
 IF COUNTERB = INTERVAL THEN GOSUB 2000
 COUNTERB = COUNTERB + 1
'Print results of history at prescribed nodes at intervals
 IF COUNTERH = 0 THEN GOSUB 1500
 IF COUNTERH = TRIG THEN GOSUB 1500
 COUNTERH = COUNTERH + 1
'reset NEW values to INIitial values for next timestep
  FOR I = 1 TO ITOT
  FOR J = 1 TO (JTOT)
  INI(I, J) = NEW(I, J)
  NEXT J
  NEXT I
RETURN

'Print selected nodes as a history of data
1500
 PRINT DT;
 PRINT TIME * NT;
 PRINT INI(I1, J1) * NS;
 PRINT CCV(I1, J1);
 PRINT INI(I2, J2) * NS;
 PRINT CCV(I2, J2)
 PRINT #3, USING "###.#####"; DT;
 PRINT #3, ",";
 PRINT #3, USING "####.#####"; TIME;
 PRINT #3, ",";
 PRINT #3, USING "####.#####"; NT * TIME;
 PRINT #3, ",";
 PRINT #3, USING "####.#####"; VEFF(I1, J1) * NS;
```

```
PRINT #3, ",";
PRINT #3, USING "####.#####"; KI(I1, J1);
PRINT #3, ",";
PRINT #3, USING "####.#####"; EI(I1, J1);
PRINT #3, ",";
PRINT #3, USING "##.#######"; AAV(I1, J1);
PRINT #3, ",";
PRINT #3, USING "####.#####"; CCV(I1, J1);
PRINT #3, ",";
PRINT #3, USING "####.#####"; MM(I1, J1);
PRINT #3, ",";
PRINT #3, USING "####.#####"; DD(I1);
PRINT #3, ",";
PRINT #3, USING "####.#####"; DDU(I1, J1) * NS;
PRINT #3, ",";
PRINT #3, USING "####.#####"; INI(I1, J1) * NS
PRINT #3, USING "###.#####"; DT;
PRINT #3, ",";
PRINT #3, USING "####.#####"; TIME;
PRINT #3, ",";
PRINT #3, USING "####.#####"; NT * TIME;
PRINT #3, ",";
PRINT #3, USING "####.#####"; VEFF(I2, J2) * NS;
PRINT #3, ",";
PRINT #3, USING "####.#####"; KI(I2, J2);
PRINT #3, ",";
PRINT #3, USING "####.#####"; EI(I2, J2);
PRINT #3, ",";
PRINT #3, USING "##.#######"; AAV(I2, J2);
PRINT #3, ",";
PRINT #3, USING "####.#####"; CCV(I2, J2);
PRINT #3, ",";
PRINT #3, USING "####.#####"; MM(I2, J2);
PRINT #3, ",";
PRINT #3, USING "####.#####"; DD(I2);
PRINT #3, ",";
PRINT #3, USING "####.#####"; DDU(I2, J2) * NS;
PRINT #3, ",";
PRINT #3, USING "####.#####"; INI(I2, J2) * NS


PRINT #2, USING "###.#####"; TIME;
PRINT #2, ",";
PRINT #2, USING "###.#####"; NT * TIME;
PRINT #2, ",";
PRINT #2, USING "####.#####"; INI(I1, J1) * NS;
PRINT #2, ",";
PRINT #2, USING "####.#####"; INI(I2, J2) * NS;
PRINT #2, ",";
```

```
 PRINT #2, USING "####.#####"; INI(I3, J3) * NS;
 PRINT #2, ",";
 PRINT #2, USING "####.#####"; INI(I4, J4) * NS;
 PRINT #2, ",";
 PRINT #2, USING "####.#####"; INI(I5, J5) * NS;
 PRINT #2, ",";
 PRINT #2, USING "####.#####"; INI(I6, J6) * NS
COUNTERH = 0
RETURN

'Print subroutine for blocks of data at prescribed intervals
2000
PRINT TIME
PRINT #1, USING "###.#####"; TIME;
PRINT #1, ",";
PRINT #1, USING "###.#####"; NT * TIME
 FOR I = 1 TO ITOT
  FOR J = 1 TO (JTOT - 1)
  PRINT #1, USING "####.#####"; INI(I, J) * NS;
  PRINT #1, ",";
  NEXT J
  J = JTOT
  PRINT #1, USING "####.#####"; INI(I, J) * NS;
  PRINT #1, ","
 NEXT I
 COUNTERB = 0
RETURN

'subroutine to calculate the initial vertical effective stress at each node
2500
FOR I = 2 TO ITOT
  'left half of box
  FOR J = 1 TO JTOTL
  VEFFI(I, J) = (I - 1) * DZ * (G1 - GW) * NG
  NEXT J
  'right half of box
  FOR J = JTOTR TO JTOT
  VEFFI(I, J) = (I - 1) * DZ * (G2 - GW) * NG
  NEXT J
  'at centerline (use average)
  J = JTOTC
  VEFFI(I, J) = (I - 1) * DZ * ((G1 + G2) / 2 - GW) * NG
NEXT I
RETURN

'subroutine to calculate the initial distribution of void ratio
2600
'compute EMVES
```

```
 EMVES1 = 2 * EY01 - (-EAA1 ^ 2 + 2 * MVES1 * EY01 - 2 * EX01 * EY01) / (2 * (MVES1 -
EX01))
 EMVES2 = 2 * EY02 - (-EAA2 ^ 2 + 2 * MVES2 * EY02 - 2 * EX02 * EY02) / (2 * (MVES2 -
EX02))
 PRINT #3, USING "####.#####"; EMVES1;
 PRINT #3, ",";
 PRINT #3, USING "##.#######"; EMVES2

 FOR I = 2 TO ITOT
  'left half of box
  FOR J = 1 TO JTOTL
  EI(I, J) = 2 * EY01 - (-EAA1 ^ 2 + 2 * VEFFI(I, J) * EY01 - 2 * EX01 * EY01) / (2 *
(VEFFI(I, J) - EX01)) - (EMVES1 - MVR1)
  NEXT J
  'right half of box
  FOR J = JTOTR TO JTOT
  EI(I, J) = 2 * EY02 - (-EAA2 ^ 2 + 2 * VEFFI(I, J) * EY02 - 2 * EX02 * EY02) / (2 *
(VEFFI(I, J) - EX02)) - (EMVES2 - MVR2)
  NEXT J
  'at centerline (use average)
  J = JTOTC
  EI(I, J) = (EI(I, J - 1) + EI(I, J + 1)) / 2
NEXT I
RETURN

'subroutine to calculate the initial permeability at each node
2700
FOR I = 2 TO ITOT
  FOR J = 1 TO JTOT
  KI(I, J) = (K01 * EI(I, J) - K02) / 100 * NG
  NEXT J
NEXT I
RETURN

'subroutine to calculate the vertical effective stress at each node
'and ratio of pore pressure Ru. Limit excess pore pressure to be less
'than vertical effective stress
3000
FOR I = 2 TO ITOT
  FOR J = 1 TO JTOT
  VEFF(I, J) = VEFFI(I, J) - INI(I, J)
  IF VEFF(I, J) <= 0 THEN VEFF(I, J) = .01
  RRU(I, J) = INI(I, J) / VEFFI(I, J)
  IF RRU(I, J) > 1 THEN INI(I, J) = VEFFI(I, J)
  NEXT J
NEXT I
RETURN

'subroutine calculates the value of Cv and various constants at each node point
```

```
'Compute Cv
4000
FOR I = 2 TO ITOT
 'compute left half of the box
 FOR J = 1 TO JTOTL
 CCV(I, J) = KI(I, J) * (1 + EI(I, J)) / AAV(I, J) / (GW * NG)
 NEXT J
 'compute right half of the box
 FOR J = JTOTR TO JTOT
 CCV(I, J) = KI(I, J) * (1 + EI(I, J)) / AAV(I, J) / (GW * NG)
 NEXT J
NEXT I
RETURN

'Compute time step
5000
'Cv values along base of model will always be the largest due to higher
'vertical effective stress. M = CV * DT / (DZ)^2. For calculation of DT
'fix M = 1/24 for stability and compute minimum DT and use for next increment.
I = ITOT
 'left side
 DT = 1 / 24 * (DZ) ^ 2 / CCV(I, JTOT)
 FOR J = 1 TO JTOTL
 DT1 = 1 / 24 * (DZ) ^ 2 / CCV(I, J)
 IF DT1 < DT THEN DT = DT1
 NEXT J
 'right side
 FOR J = JTOTR TO JTOT
 DT1 = 1 / 24 * (DZ) ^ 2 / CCV(I, J)
 IF DT1 < DT THEN DT = DT1
 NEXT J
RETURN


'compute values for constants M and DD.
6000
FOR I = 2 TO ITOT
 FOR J = 1 TO JTOT
 MM(I, J) = CCV(I, J) * DT / (DZ) ^ 2
 NEXT J
 J = JTOTC
 DD(I) = (1 + KI(I, J - 1) / KI(I, J + 1)) / (1 + CCV(I, J + 1) / CCV(I, J - 1)) * (KI(I, J - 1) / KI(I,
J + 1))
NEXT I
RETURN

'Compute values to  distribute DU across section
7000
FOR I = 1 TO ITOT
```

```
    FOR J = 1 TO (JTOTL + 1)
    DDU(I, J) = LDU / (ITOT - 1) / LTU * DT
    NEXT J
    FOR J = JTOTR TO JTOT
    DDU(I, J) = RDU / (ITOT - 1) / RTU * DT
    NEXT J
NEXT I
RETURN

'subroutine calculates the value of Av
'Compute Av
8000
FOR I = 2 TO ITOT
 'compute left half of the box
 FOR J = 1 TO JTOTL
 'check load or unload condition for Av
 IF AZZ(I, J) = 1 THEN GOTO 8100
 'unload condition
 AAV(I, J) = (VEFF(I, J)) ^ BB * CC
 GOTO 8200
8100
 'load condition
 AAV(I, J) = 2 * Y01 - (-AA1 ^ 2 + 2 * VEFF(I, J) * Y01 - 2 * X01 * Y01) / (2 * (VEFF(I, J) -
X01))
8200 NEXT J
 'compute right half of the box
 FOR J = JTOTR TO JTOT
 'check load or unload condition for Av
 IF AZZ(I, J) = 1 THEN GOTO 8300
 'unload condition
 AAV(I, J) = VEFF(I, J) ^ BB * CC
 GOTO 8400
8300
 'load condition
 AAV(I, J) = 2 * Y02 - (-AA2 ^ 2 + 2 * VEFF(I, J) * Y02 - 2 * X02 * Y02) / (2 * (VEFF(I, J) -
X02))
8400 NEXT J
NEXT I
RETURN

'subroutine calculates the factor ZZ based on Ru or pwp generation to change Av unload to
'Av load for each node point
9000
FOR I = 2 TO ITOT
 FOR J = 1 TO JTOTL
'  IF RRU(I, J) > RU THEN AZZ(I, J) = 1
 IF LTZ = 1 THEN AZZ(I, J) = 1
 NEXT J
 'compute right half of the box
```

```
  FOR J = JTOTR TO JTOT
' IF RRU(I, J) > RU THEN AZZ(I, J) = 1
  IF LTZ = 1 THEN AZZ(I, J) = 1
  NEXT J
NEXT I
RETURN
```

Appendix B

RESULTS OF MODEL TESTS

B.1 Introduction

This appendix presents results from the testing completed on the centrifuge MODEL3 (Hushmand et al., 1994)[1], and the one-g models described in the main body of the thesis. Table B-1 summarizes the model tests included in this appendix, along with a description of the initial configuration of each model.

All of the results have been scaled to prototype values (or units) in accordance with the scaling theory described in Chapter 2. For each model test, eight figures, named "Figure 1" through "Figure 8", have been prepared to present the recordings of the signals from the various transducers placed in the models. The content of the figures is summarized in Table B-2. For the models SM3B through SM3E, Figure 5 is omitted because of errors in the data. For the model SM3H, Figure 7 is omitted because this data was not collected during the testing.

The initial prototype effective stresses at the pore pressure transducer locations in the centrifuge and one-g models were as follows:

Side of model with "Loose Sand"			Side of model with "Dense Sand"		
Transducer Number	Vertical Effective Stress (kN/m^2)		Transducer Number	Vertical Effective Stress (kN/m^2)	
	Centrifuge	One-g		Centrifuge	One-g
P7, P8	20.5	21.7	P9, P10	22.0	23.4
P3, P4	62.3	62.9	P5, P6	67.0	67.7
P1	102.6	102.7	P2	110.2	110.4

[1] Hushmand, B., R. F. Scott, and H. Rashidi, 1994, "VELACS model No. 3: Liquefaction in dense and loose sand columns," in Verification of Numerical Procedures for the Analysis of Soil Liquefaction Problems, Vol. 2, pp. 1415-1442, Arulanandan, K. and R. F. Scott, eds., Balkema, Rotterdam.

Table B-1: Summary of model tests included in Appendix B.

Test Method	Model Name	Model Sand	Pore Fluid	Test No.	Sand Column(1)	Init. Relative Density (%)	Void Ratio	App. B(3) Page No.'s
Centrifuge	Model 3	Nevada	Water	Caltech	Loose	42-48(2)	0.7305	B4-11
					Dense	74-79(2)	0.6102	
One-g	SM3B	Nevada	Water	SM3B1	Loose	49	0.7041	B12-18
					Dense	73	0.6137	
	SM3C	Nevada	Water	SM3C1	Loose	41	0.7336	B19-25
					Dense	64	0.6484	
	SM3D	Blend 6-1	Water	SM3D1	Loose	51	0.7203	B26-32
					Dense	79	0.6349	
	SM3E	Nevada	Water	SM3E1	Loose only	41	0.7317	B33-39
	SM3F	Nevada	Water	SM3F1	Scaled loose	33	0.7632	B40-47
					Scaled dense	51	0.6971	
				SM3F8	Scaled loose	47	0.7101	B48-55
					Scaled dense	67	0.6360	
	SM3G	Blend 6-1	Water	SM3G1	Scaled loose	32	0.7787	B56-63
					Scaled dense	63	0.6818	
				SM3G2	Scaled loose	37	0.7639	B64-71
					Scaled dense	69	0.6647	
				SM3G7	Scaled loose	55	0.7079	B72-79
					Scaled dense	81	0.6289	
	SM3H	Nevada	Dry	SM3H1	Scaled loose	19	0.8089	B80-86
					Scaled dense	53	0.6819	
				SM3H2	Scaled loose	25	0.7922	B87-93
					Scaled dense	57	0.6749	
				SM3H4	Scaled loose	30	0.7754	B94-100
					Scaled dense	59	0.6652	
	SM3I	Nevada	Water	SM3I1	Scaled loose	35	0.7558	B101-108
				SM3I3	Scaled loose	42	0.7305	B109-116
				SM3I4	Scaled loose	57	0.6379	B117-124
				SM3I5	Scaled loose	70	0.6254	B125-132
	SM3J	Nevada	Water	SM3J1	Scaled loose	29	0.7772	B133-140
					Scaled dense	62	0.6559	
				SM3J8	Scaled loose	47	0.7127	B141-148
					Scaled dense	70	0.6230	
	SM3K	Blend 6-1	Water & Glycerin	SM3K1	Scaled loose	28	0.7813	B149-156
					Scaled dense	57	0.6747	
				SM3K8	Scaled loose	46	0.7404	B157-164
					Scaled dense	85	0.6205	

Notes:

(1) Loose and dense refer to the left and right-hand sides of the model respectively. "Prototype" implies that no scaling of the initial state of the sand was performed, whereas "Scaled" implies that scaling was completed consistent with the proposed modeling method.

(2) Possible range in values as discussed in Chapter 4, Section 4.2.

(3) Results of tests are presented in Appendix B, in a series of eight standard plots for each test. See Table 5-2 for description.

Table B-2: Summary of standard plots presented in Appendix B.

Standard Plot	Description of data presented.	Transducer signals presented(1).
Figure 1	Acceleration histories recorded at the base of the model.	A1, A2, and A3(2).
Figure 2	FFT's of acceleration recorded at the base of the model.	A1, A2, and A3(2).
Figure 3	Acceleration histories recorded in both halves of the model. Longitudinal and vertical components at prototype depth of about 2.2 m.	A4, A5, A6, and A7.
Figure 4	FFT's of acceleration recorded in each half of the model. Longitudinal and vertical components at prototype depth of about 2.2 m.	A4, A5, A6, and A7.
Figure 5	Longitudinal displacements recorded at the end of the laminar box, and, for the one-g models, at the shake table top.	L1, L2, L3, L4, and Table LVDT(3).
Figure 6	Surface settlement and excess pore pressures recorded in the left half of the model. Pore pressure transducers along the vertical section A.	L5. P1, P3, and P7.
Figure 7	Surface settlement and excess pore pressures from both halves of the model. Pore pressure transducers along the vertical sections B and C.	L5, and L6. P4, P5, P8, and P9.
Figure 8	Surface settlement and excess pore pressures recorded in the right half of the model. Pore pressure transducers along the vertical section D.	L6. P2, P6, and P10.

Notes:
(1) For the exact position of the transducers, see Chapter 4, Table 4-4.
(2) Accelerometers A2 and A3 were moved to the end of the laminar box for models SM3F through SM3K.
(3) For models SM3B through SM3E, Figure 5 is not included due to errors in the LVDT readings (see Chapter 4, Section 4.4.7).

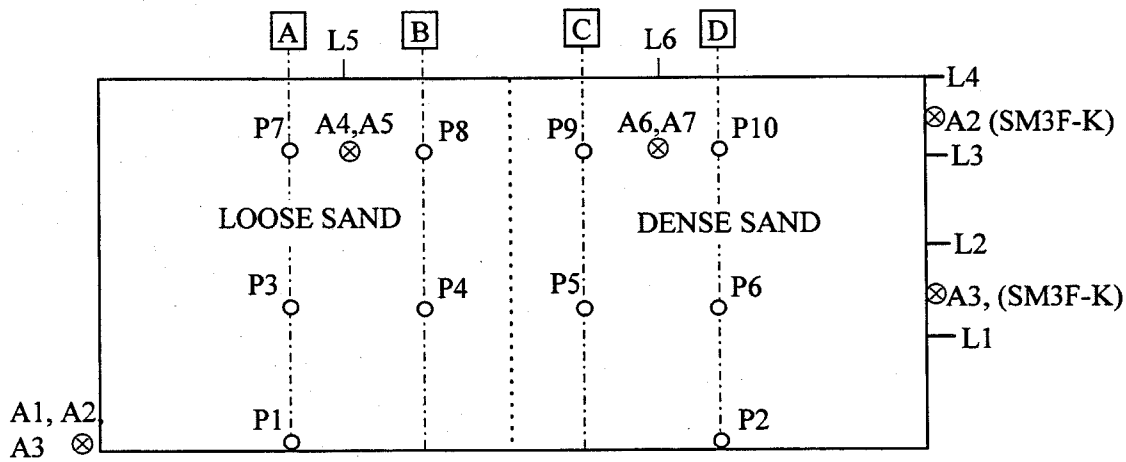

⊗ Accelerometers, "A"
O Pore Pressure Transducers, "P"
⊥ Displacement Transducer LVDT, "L"

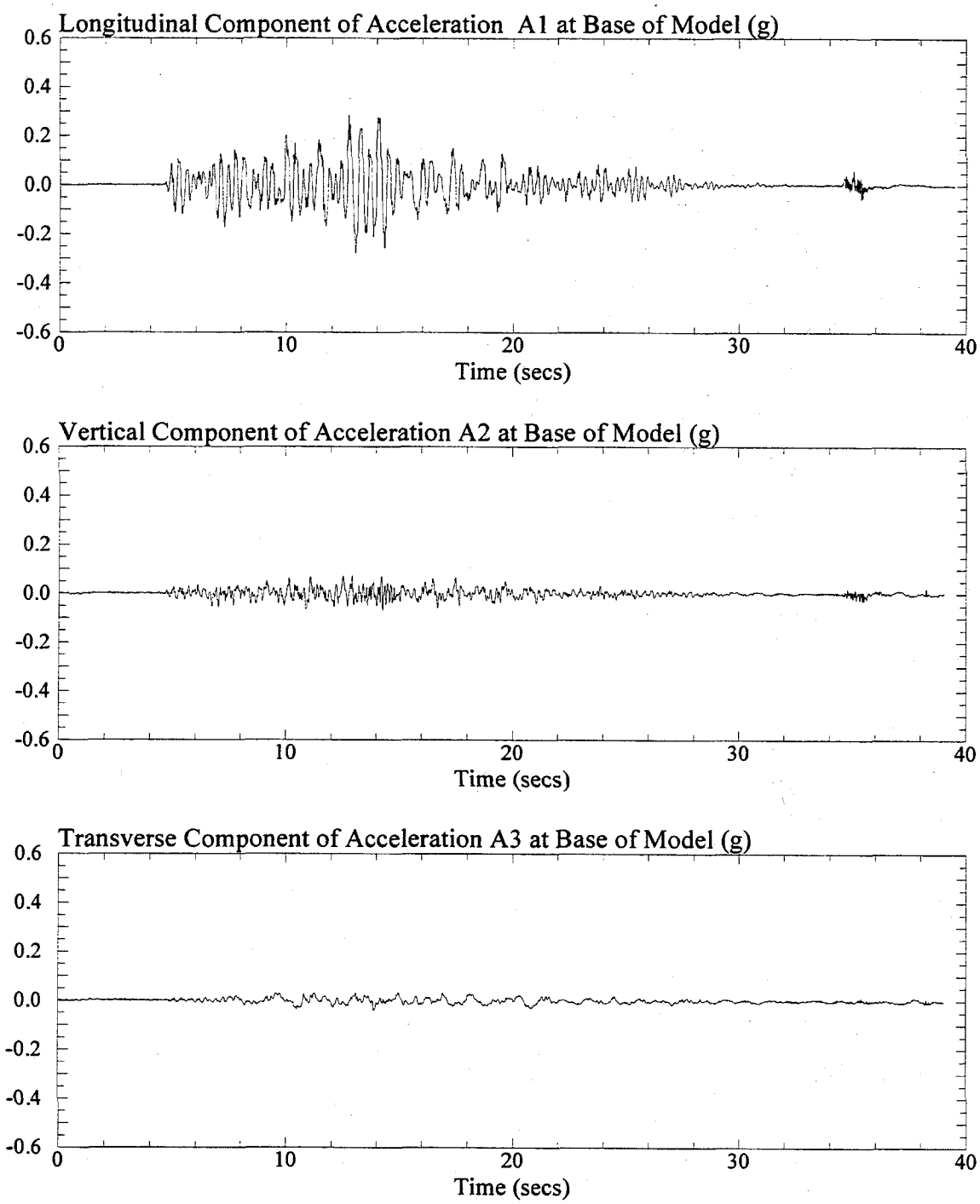

Figure 1: Longitudinal, vertical, and transverse components of recorded acceleration at base of the centrifuge MODEL3. Signals were post processed with a low pass filter of 20 Hz.

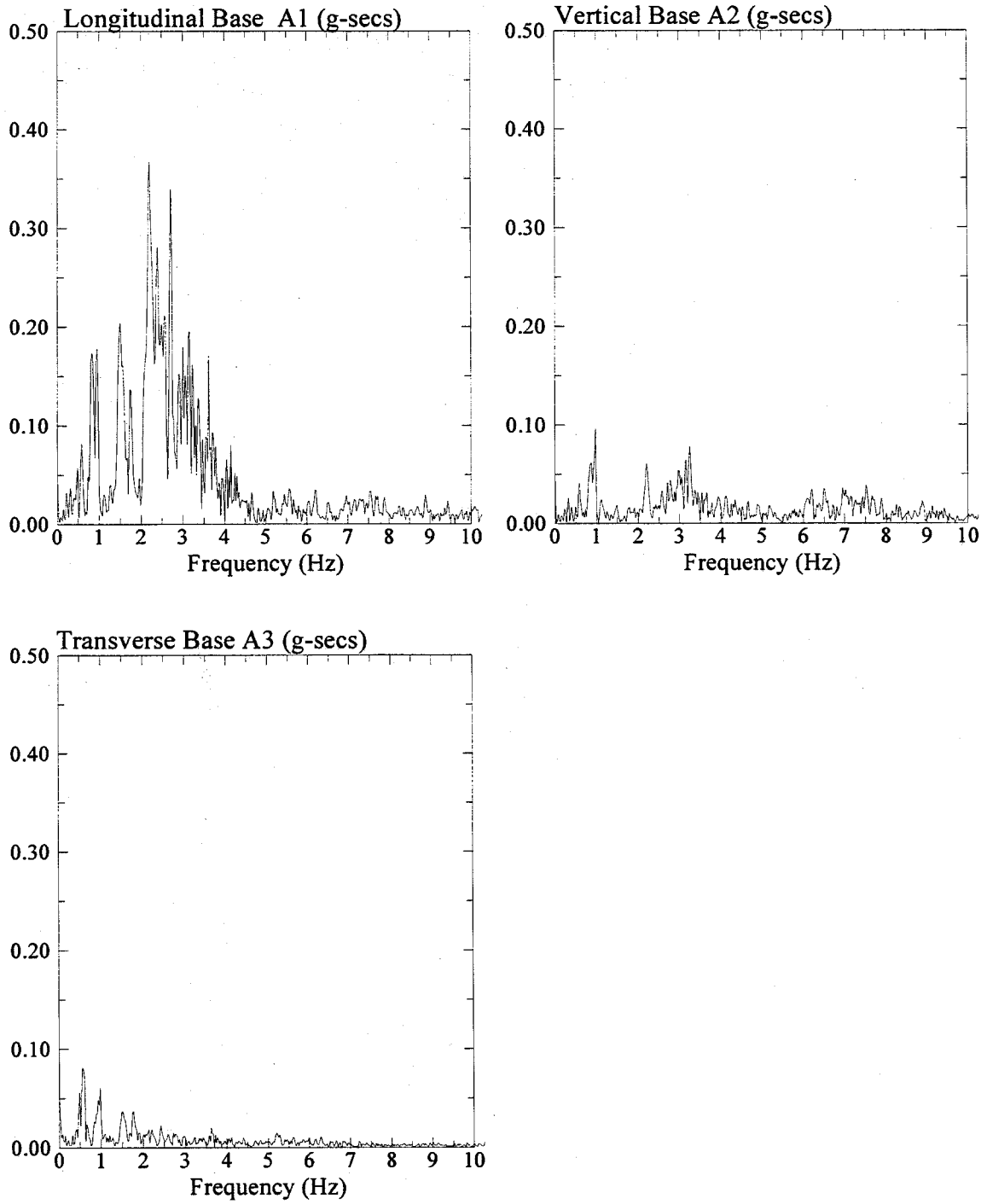

Figure 2: Fast Fourier Transform of longitudinal, vertical, and transverse components of recorded acceleration at base of the centrifuge MODEL3.

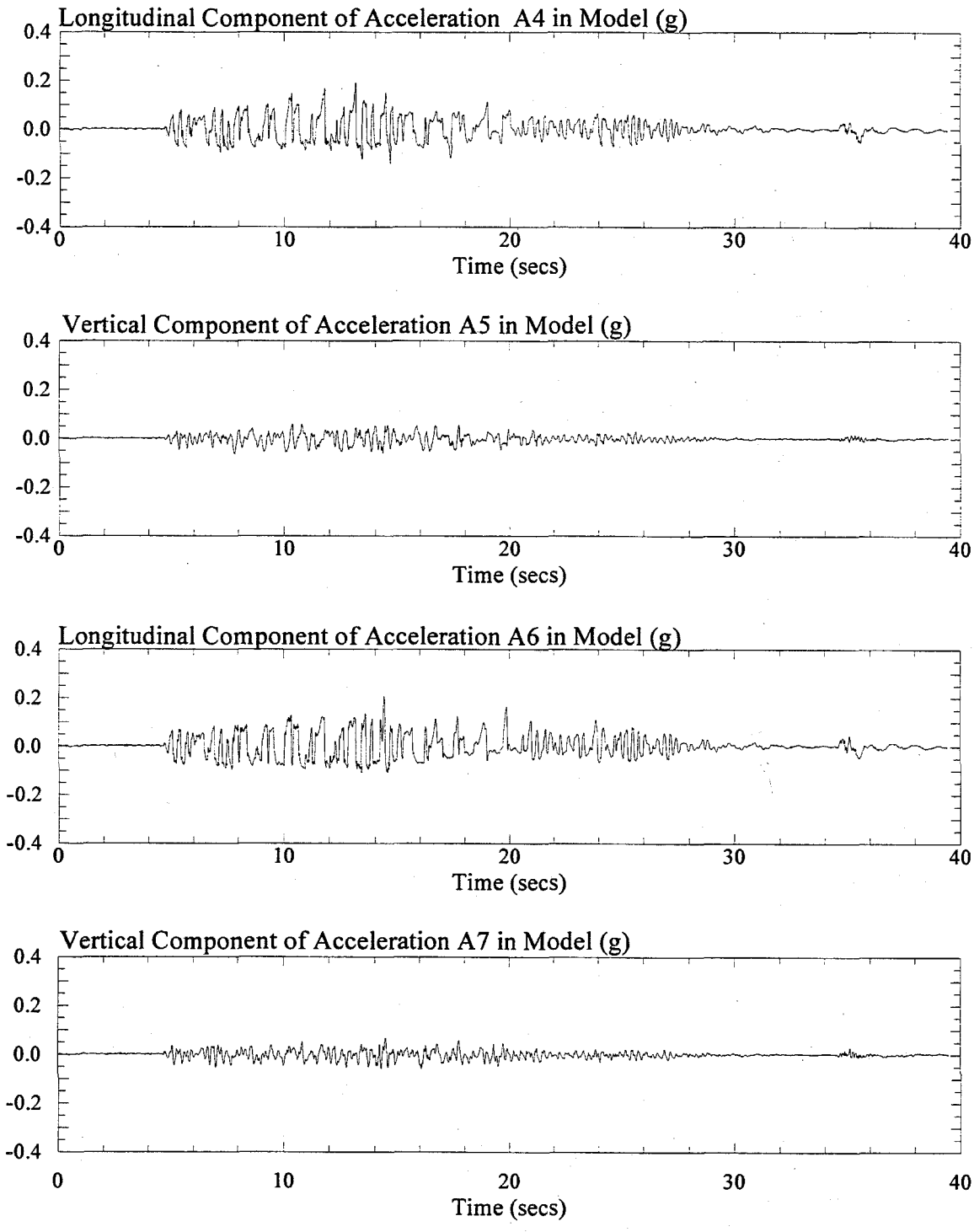

Figure 3: Longitudinal and vertical components of recorded acceleration in the centrifuge MODEL3. Signals were post processed with a low pass filter of 20 Hz.

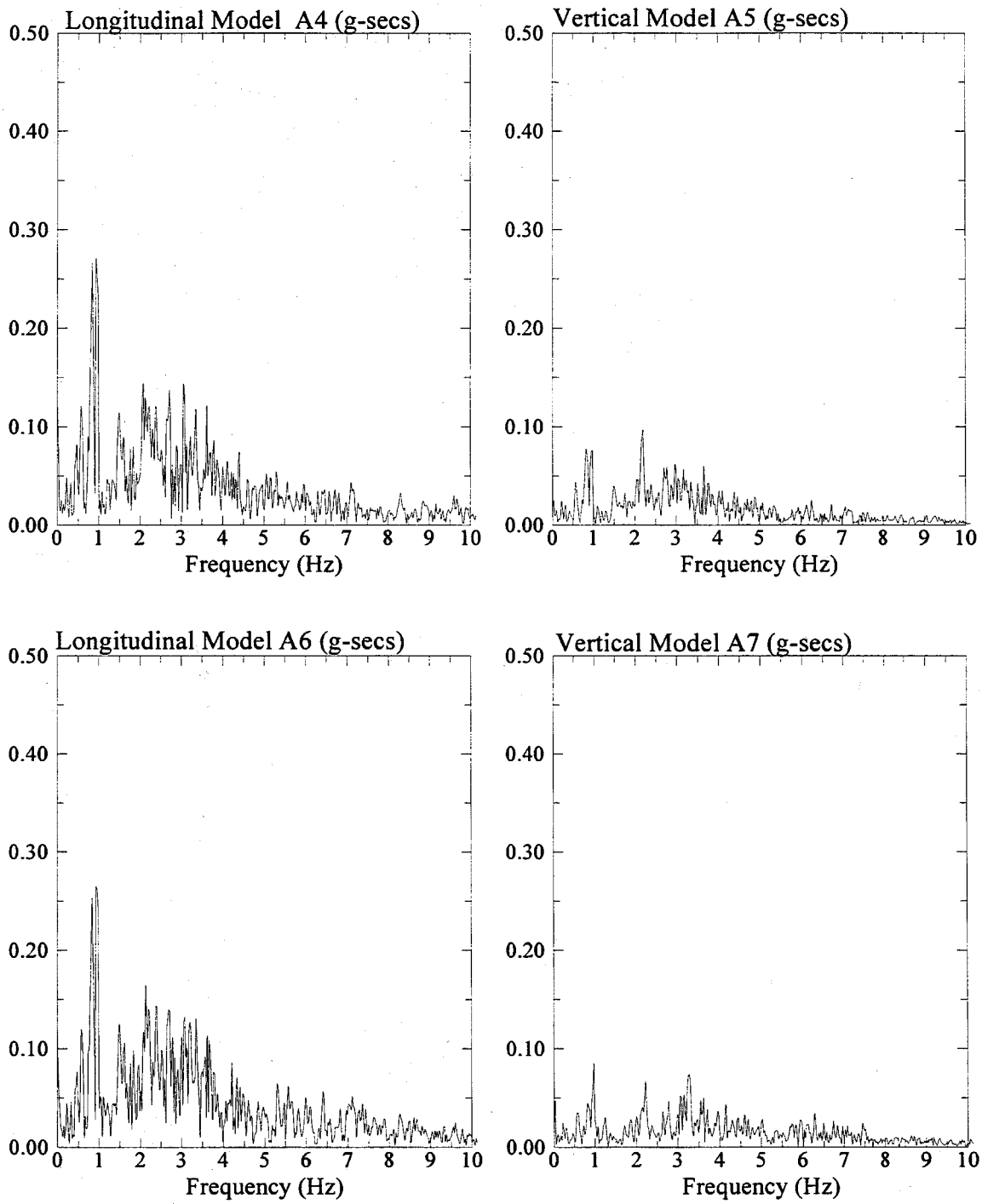

Figure 4: Fast Fourier Transform of longitudinal and vertical components of recorded acceleration in the centrifuge MODEL3.

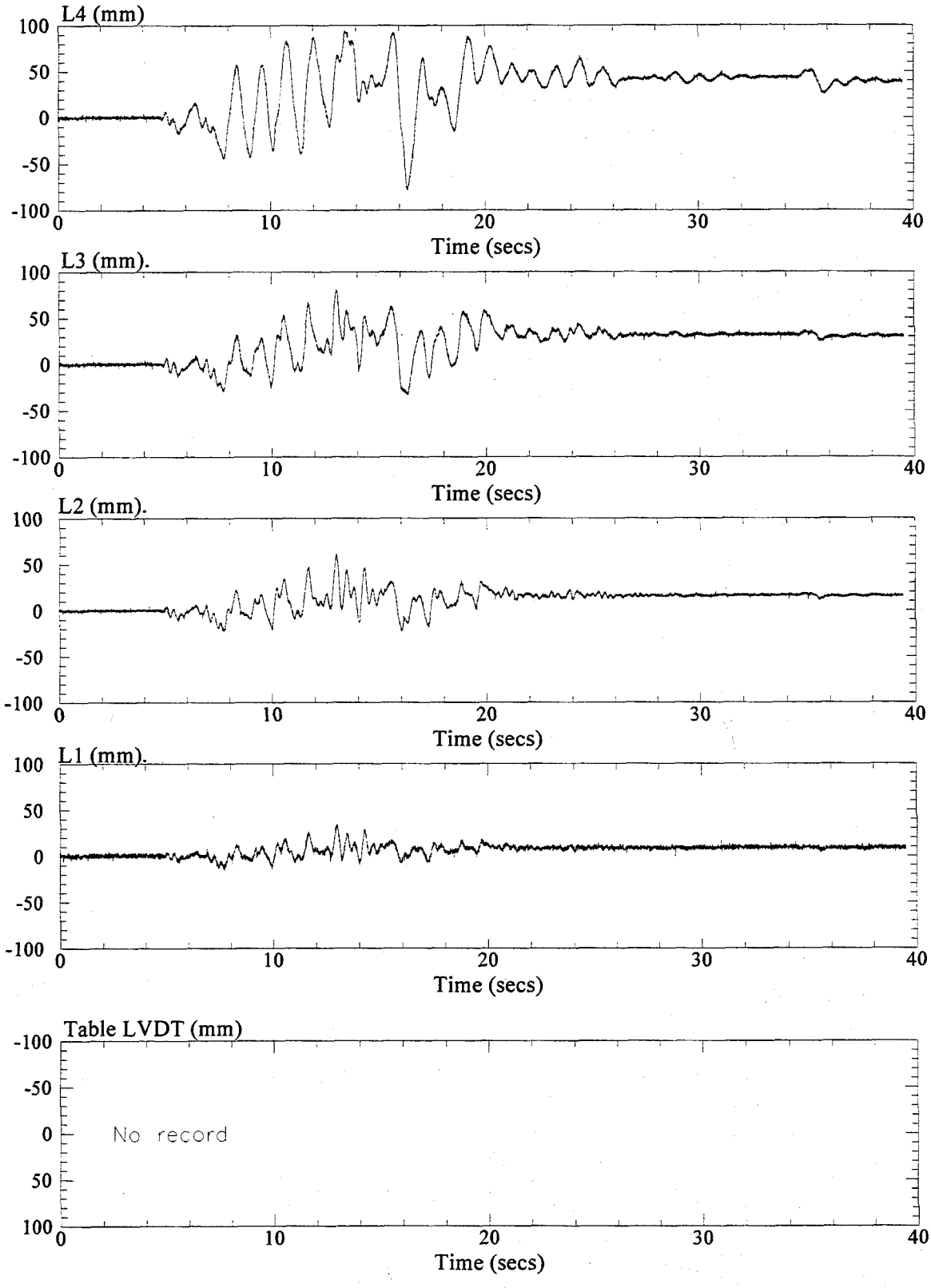

Figure 5: Longitudinal displacements recorded at LVDT's L1, L2, L3, and L4 in the centrifuge MODEL3.

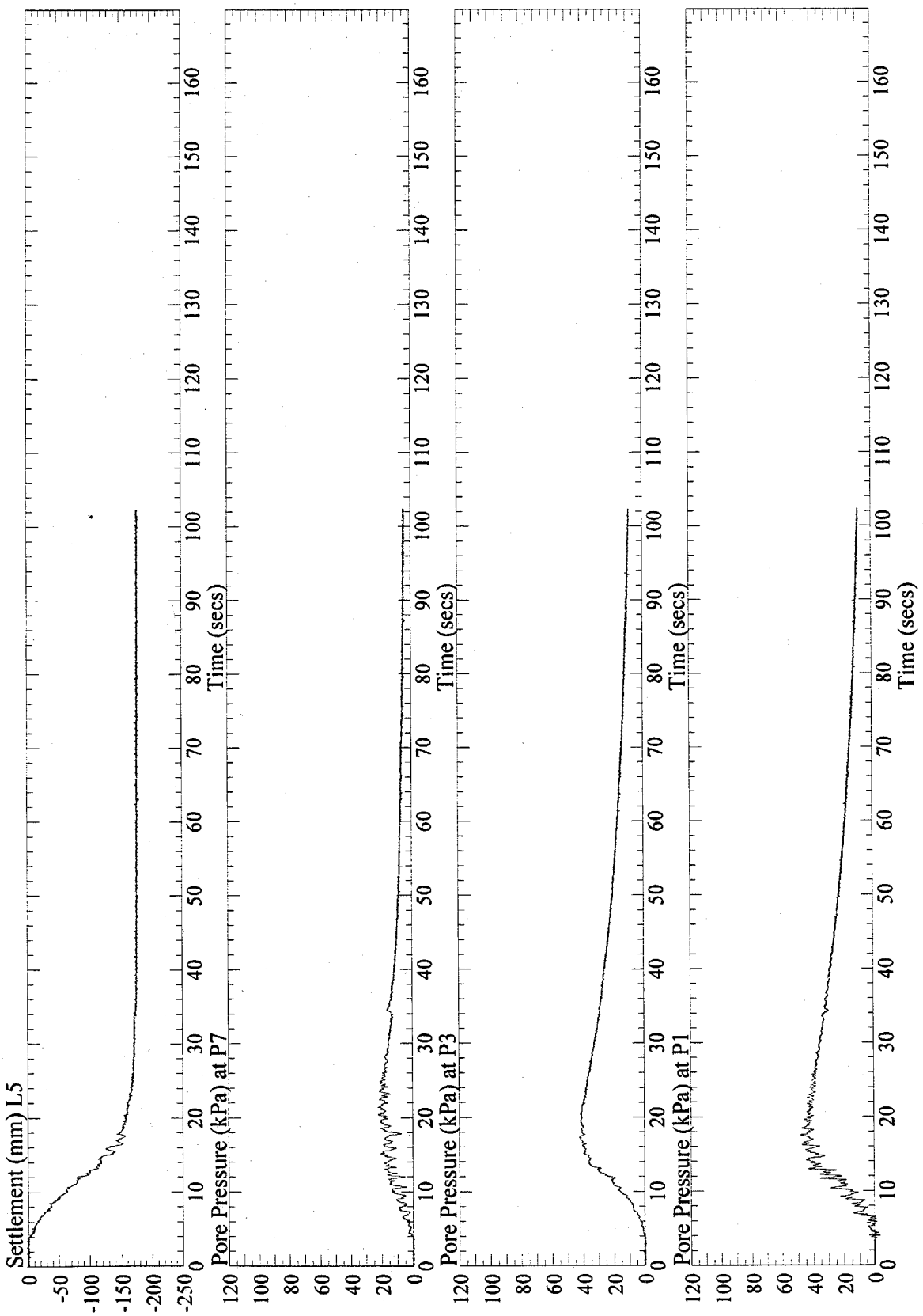

Figure 6: Vertical settlement at L5 and pore pressures at P1, P3, and P7, recorded in the centrifuge MODEL3.

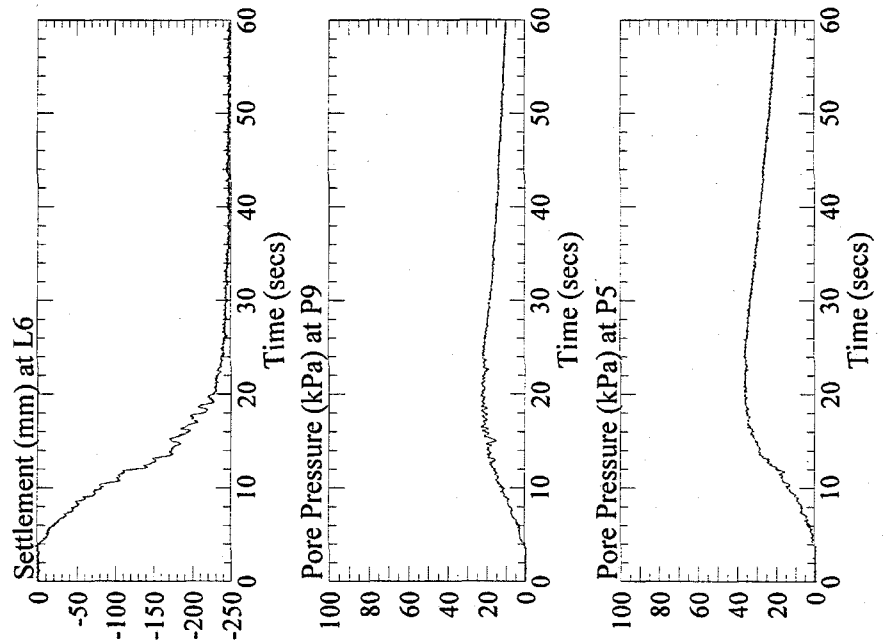

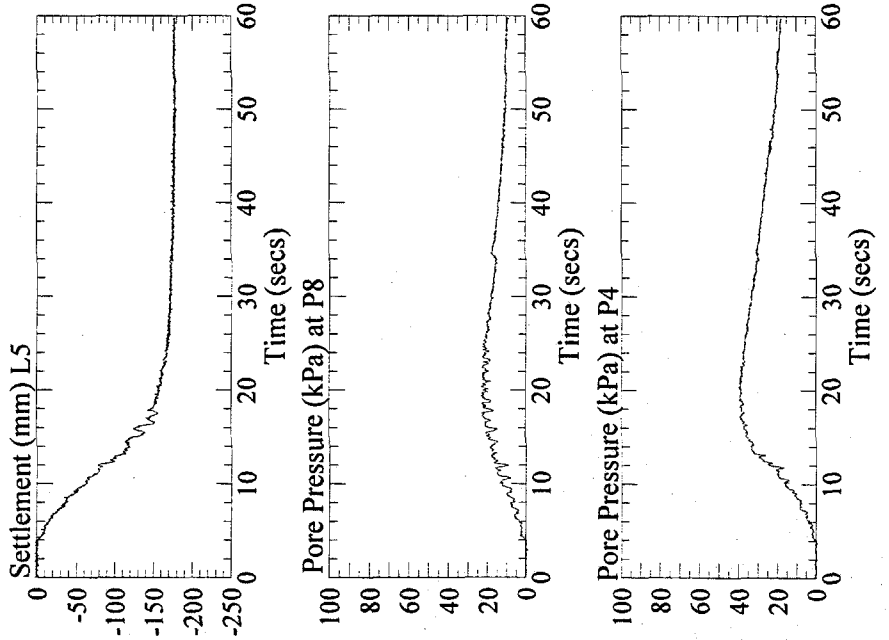

Figure 7: Vertical settlement at L5 and L6, and pore pressures at P4, P5, P8 and P9, recorded in the centrifuge MODEL3.

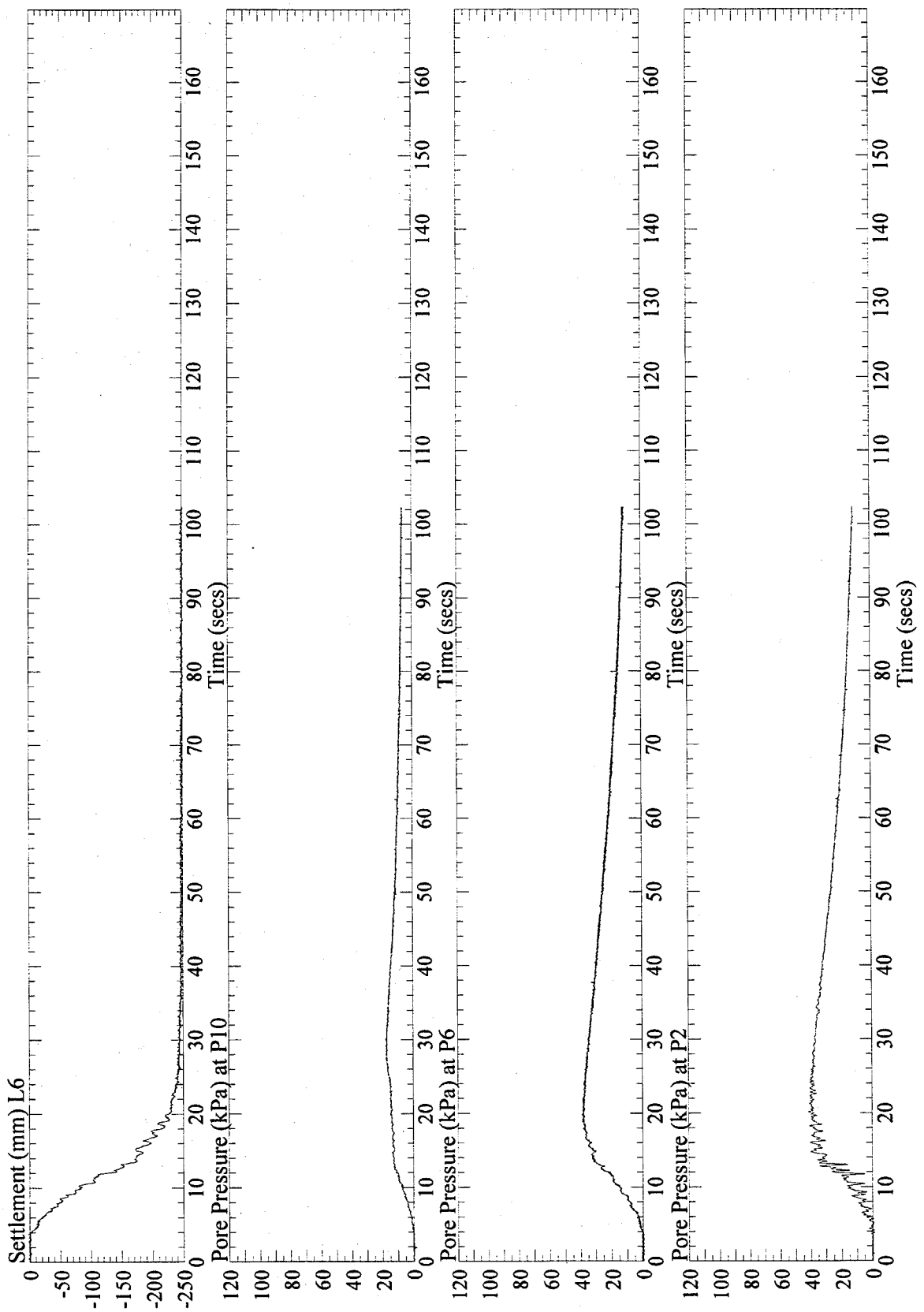

Figure 8: Vertical settlement at L6 and pore pressures at P2, P6, and P10, recorded in the centrifuge MODEL3.

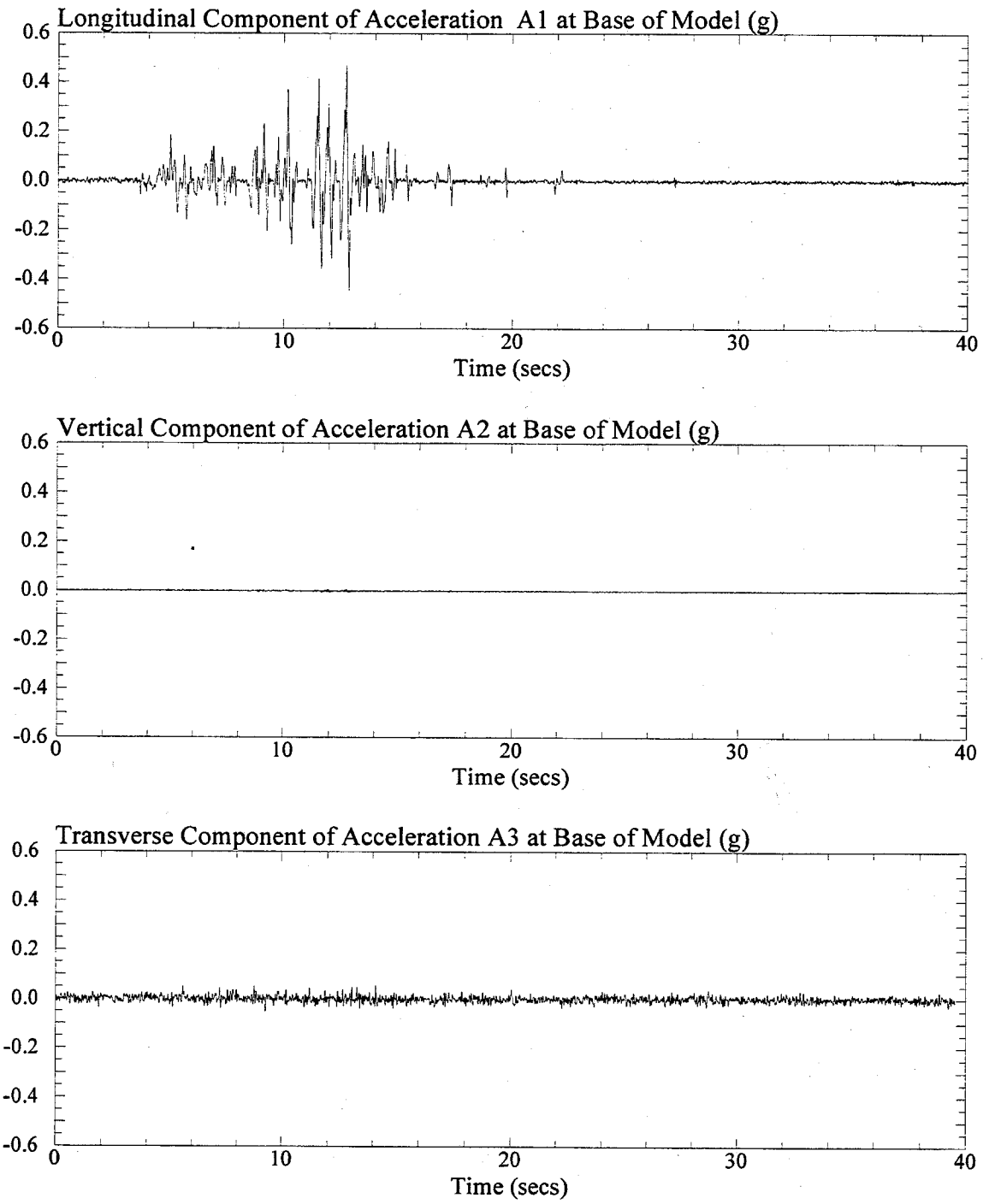

Figure 1: Longitudinal, vertical, and transverse components of recorded acceleration at base of the one-g model SM3B1. Signals were post processed with a low pass filter of 20 Hz.

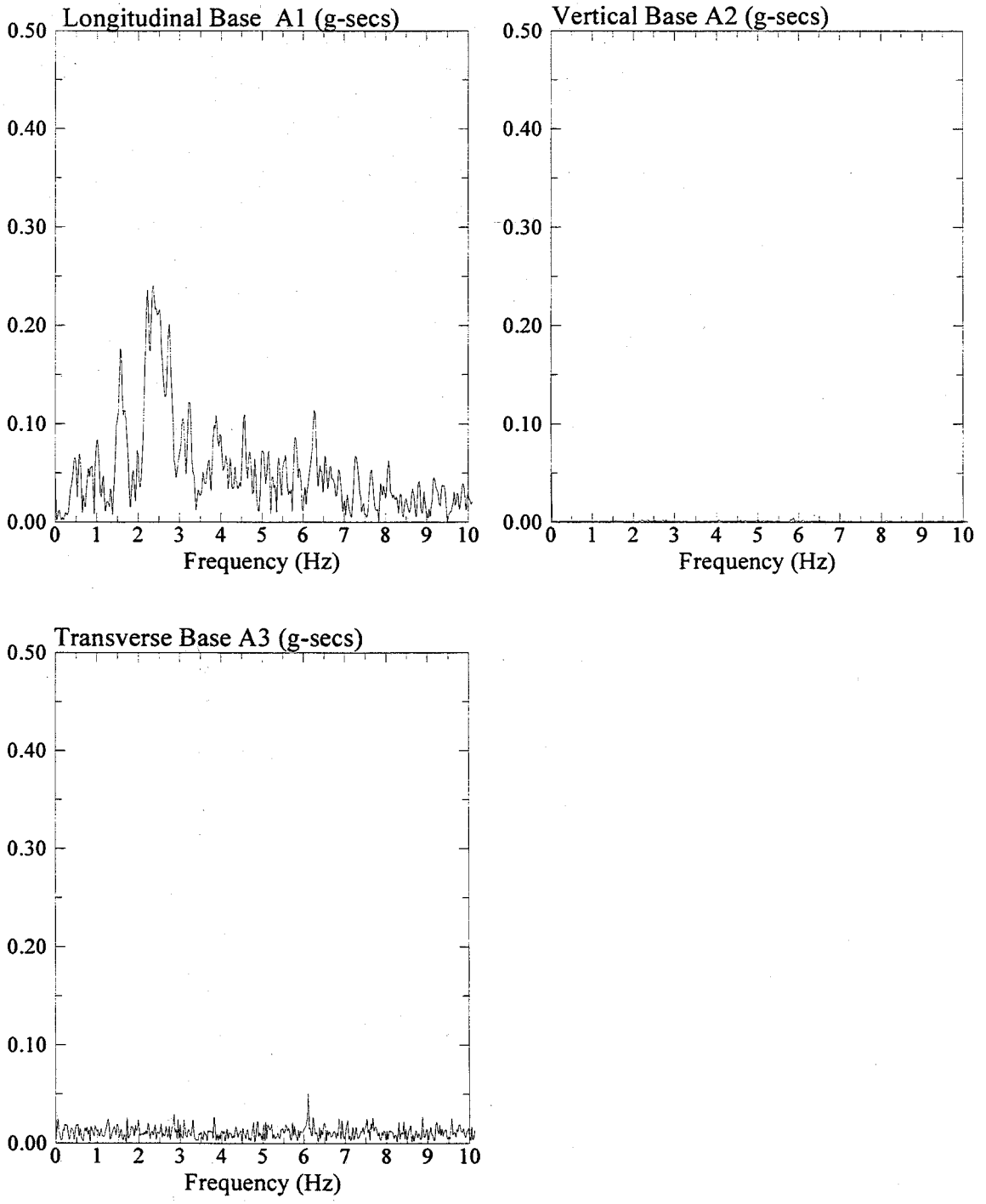

Figure 2: Fast Fourier Transform of longitudinal, vertical, and transverse components of recorded acceleration at base of the one-g model SM3B1.

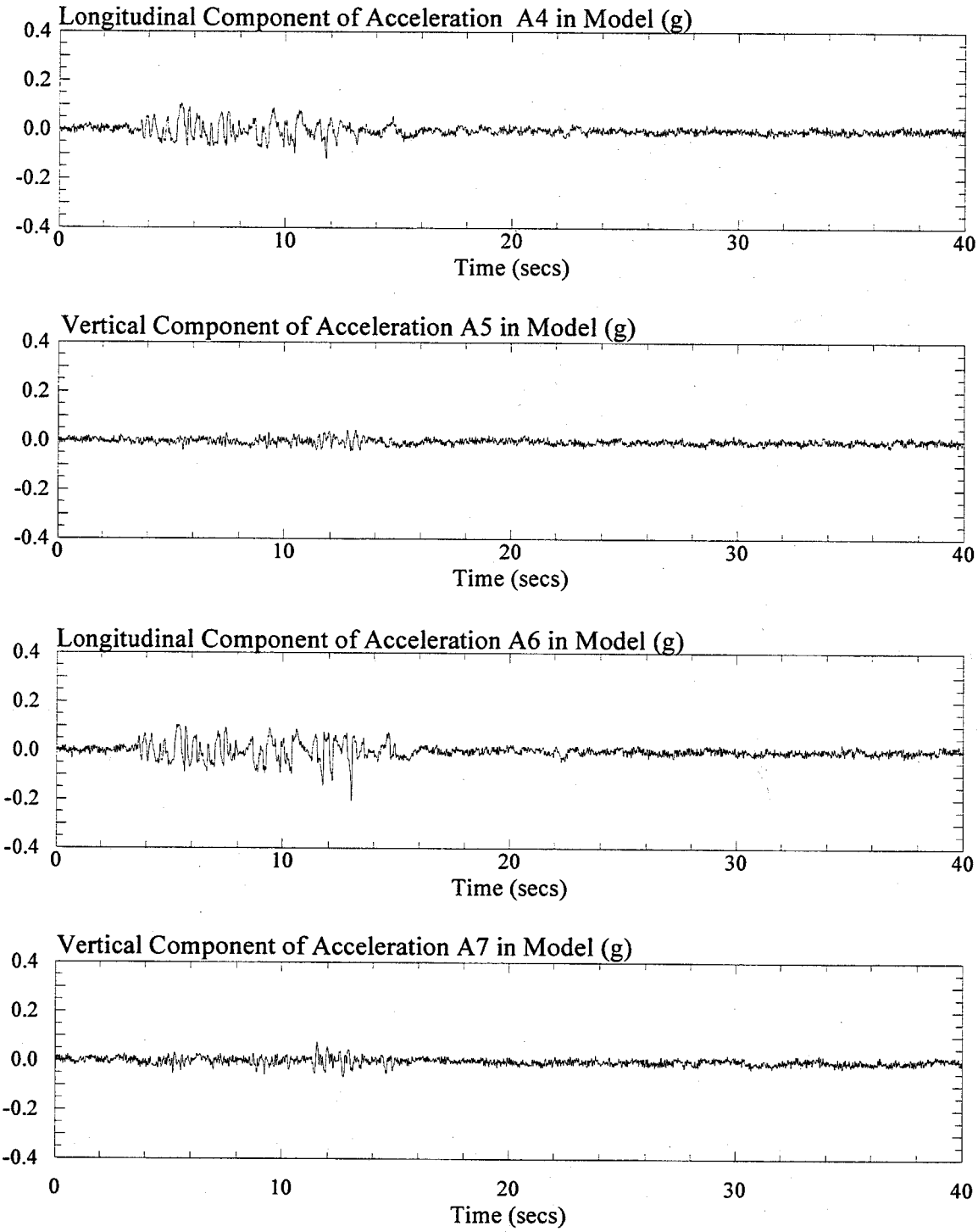

Figure 3: Longitudinal and vertical components of recorded acceleration in the one-g model SM3B1. Signals were post processed with a low pass filter of 20 Hz.

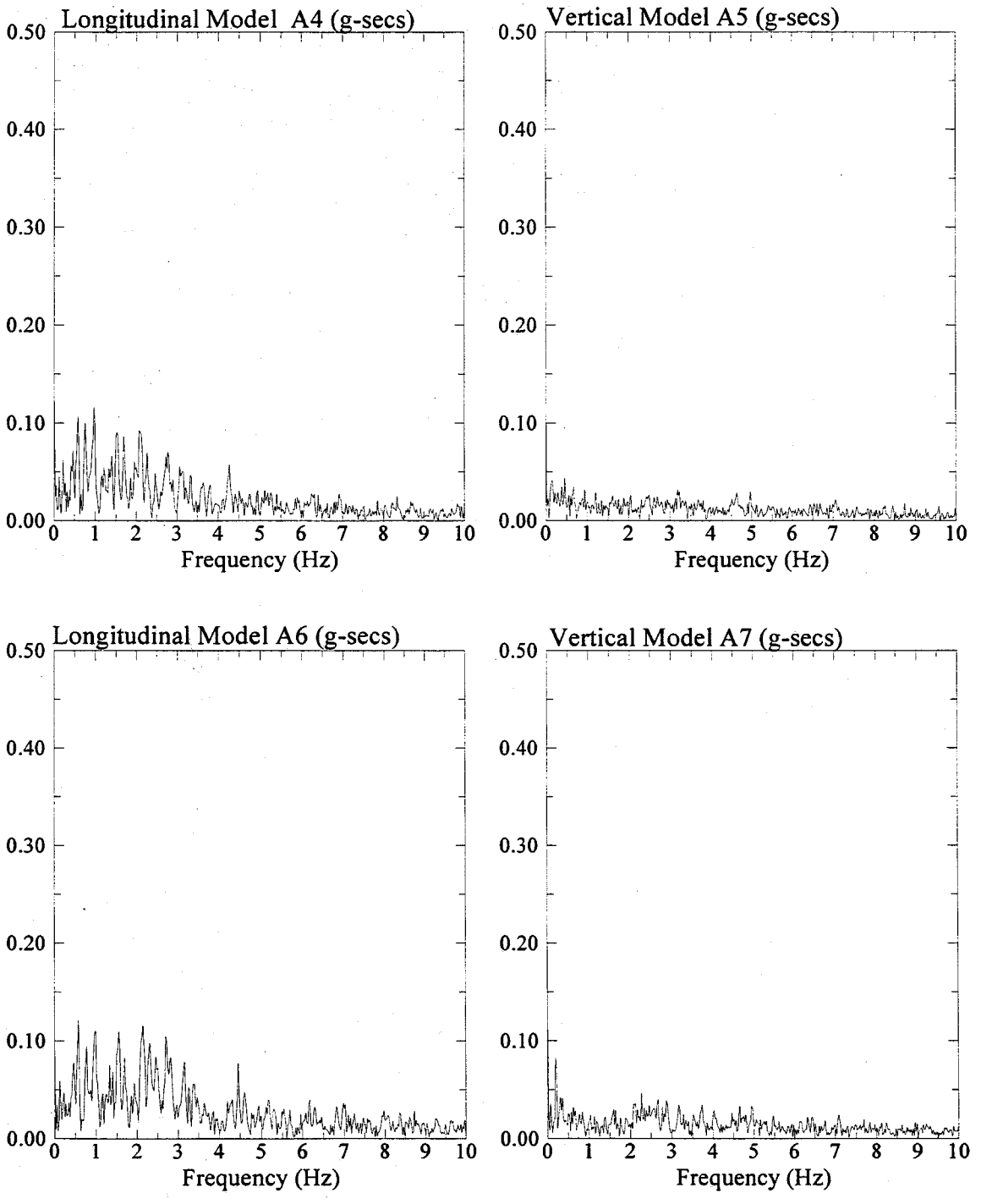

Figure 4: Fast Fourier Transform of longitudinal and vertical components of recorded acceleration in the one-g model SM3B1.

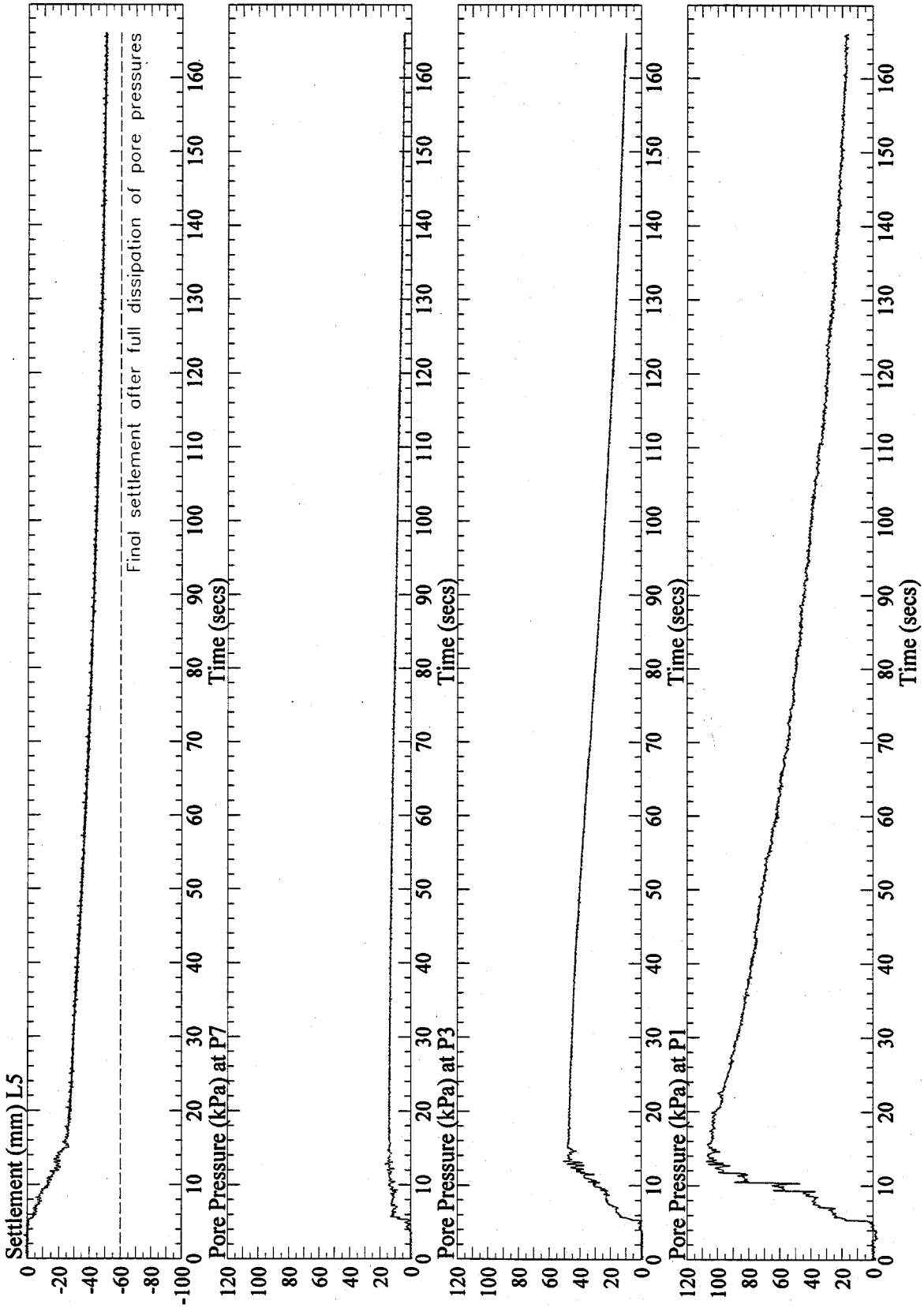

Figure 6: Vertical settlement at L5 and pore pressures at P1, P3, and P7, recorded in the one-g model SM3B1. Signal from P1 was post processed with a low pass filter of 10 Hz.

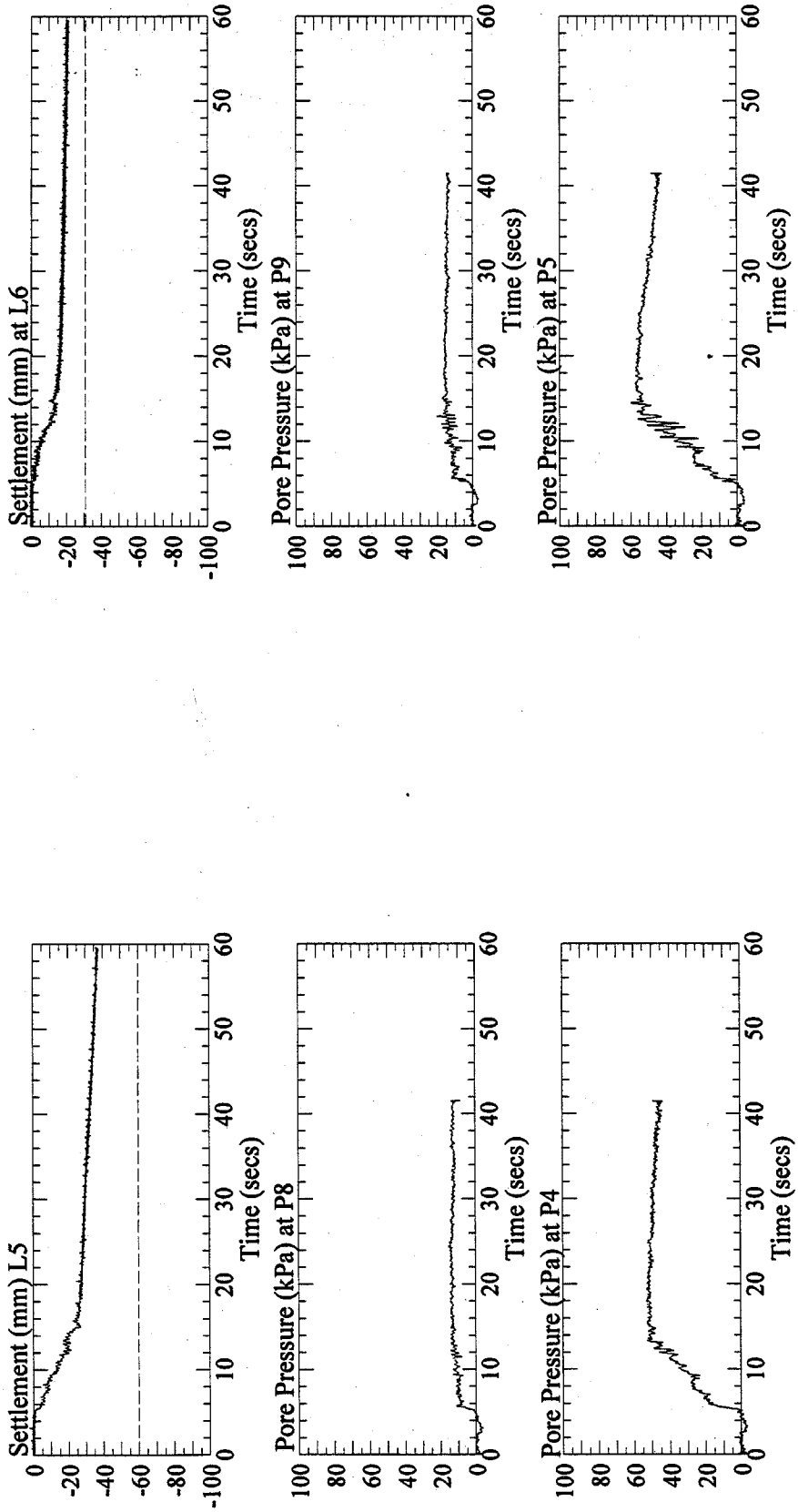

Figure 7: Vertical settlement at L5 and L6, and pore pressures at P4, P5, P8 and P9, recorded in the one-g model SM3B1. Pore pressure signals were post processed with a low pass filter of 10 Hz.

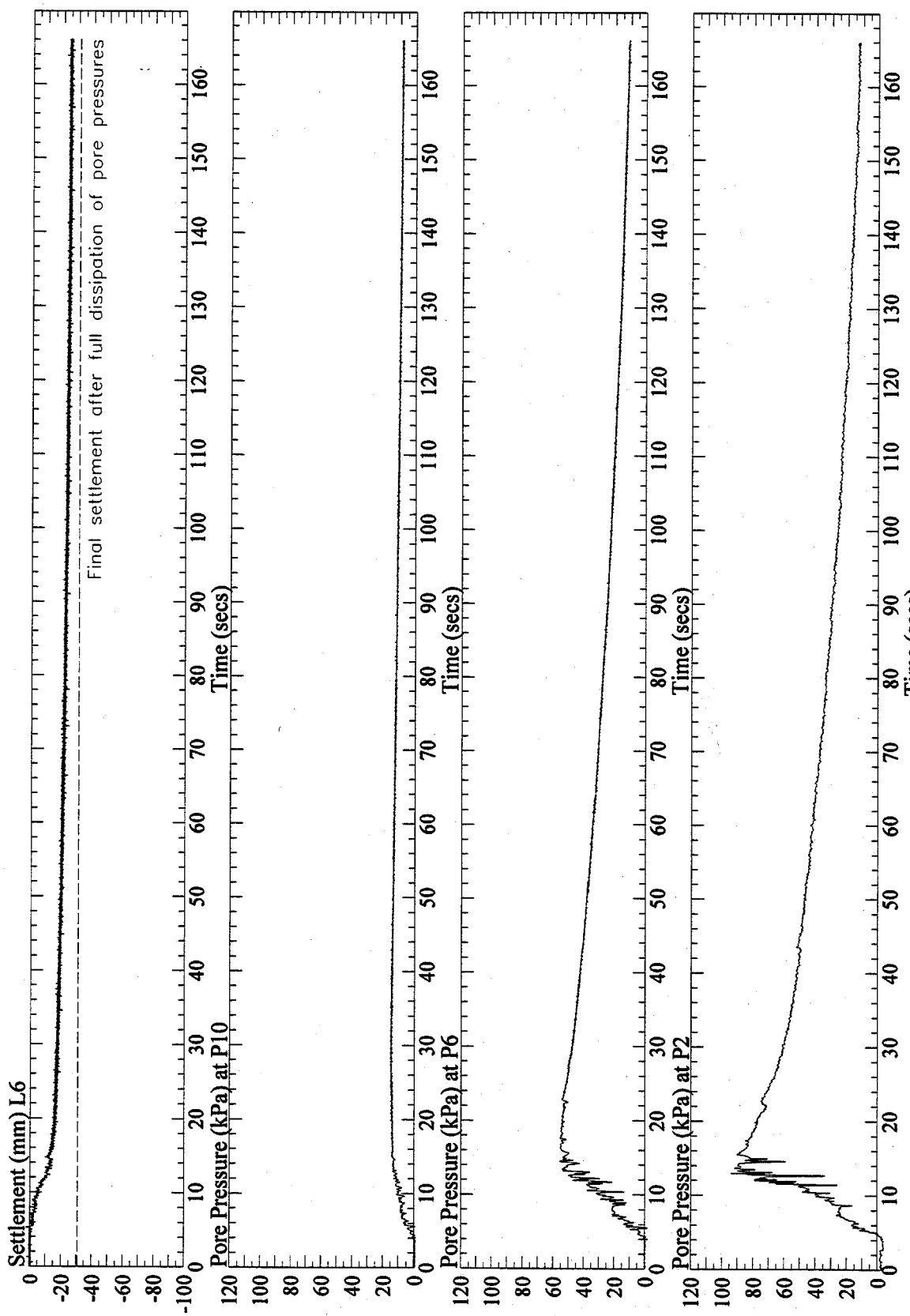

Figure 8: Vertical settlement at L6 and pore pressures at P2, P6, and P10, recorded in the one-g model SM3B1. Signal from P2 was post processed with a low pass filter of 10 Hz.

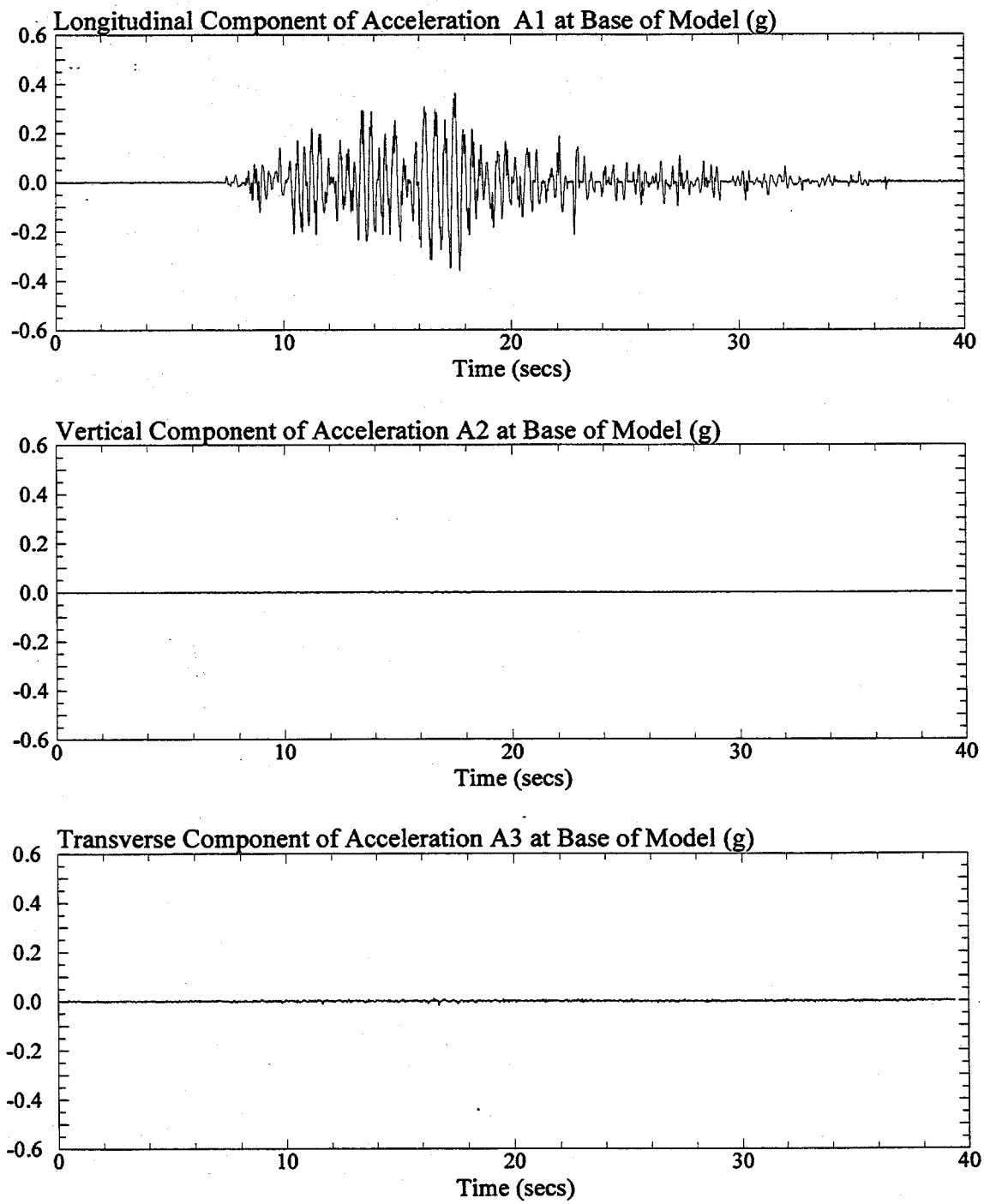

Figure 1: Longitudinal, vertical, and transverse components of recorded acceleration at base of the one-g model SM3C1. Signals were post processed with a low pass filter of 20 Hz.

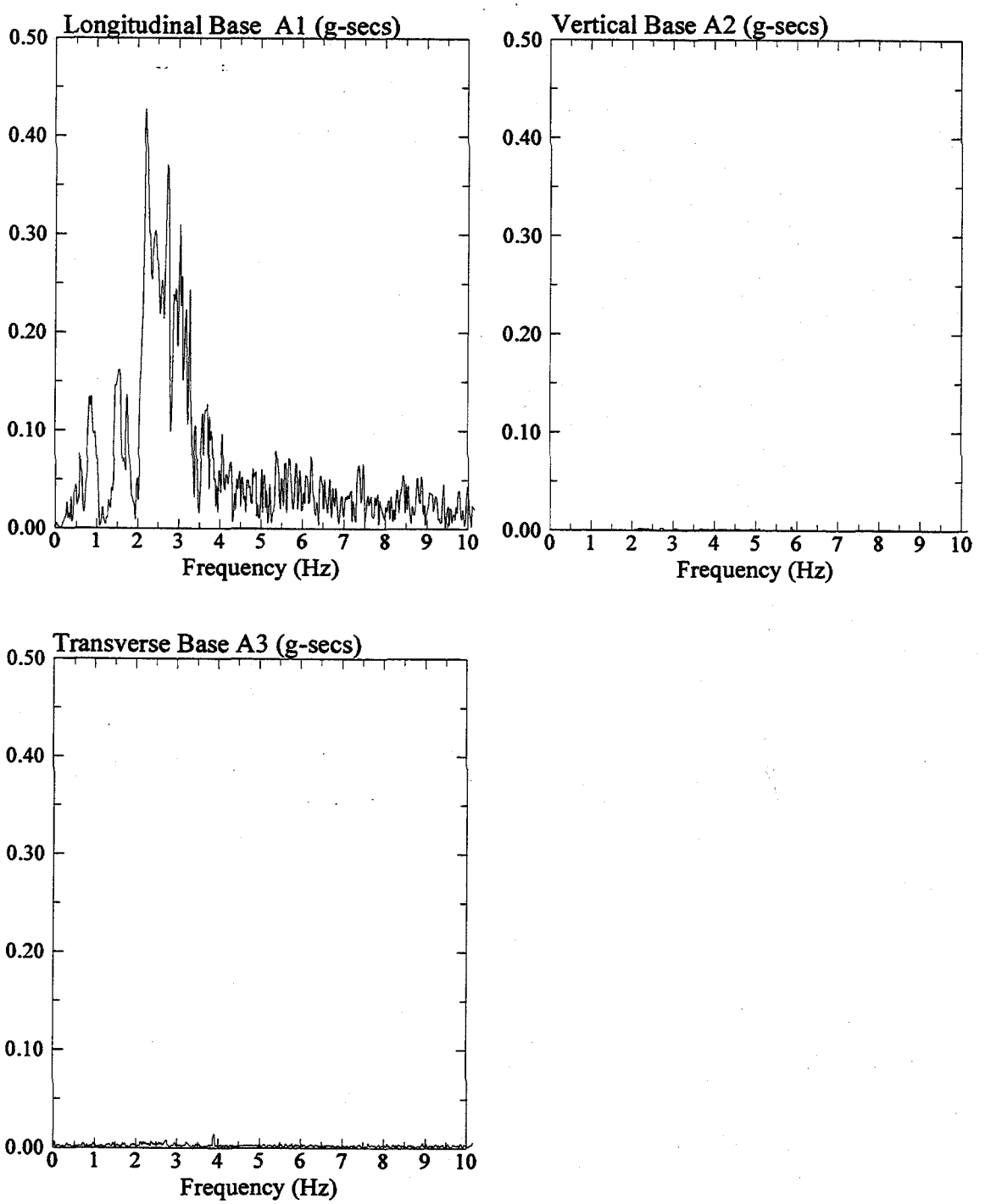

Figure 2: Fast Fourier Transform of longitudinal, vertical, and transverse components of recorded acceleration at base of the one-g model SM3C1.

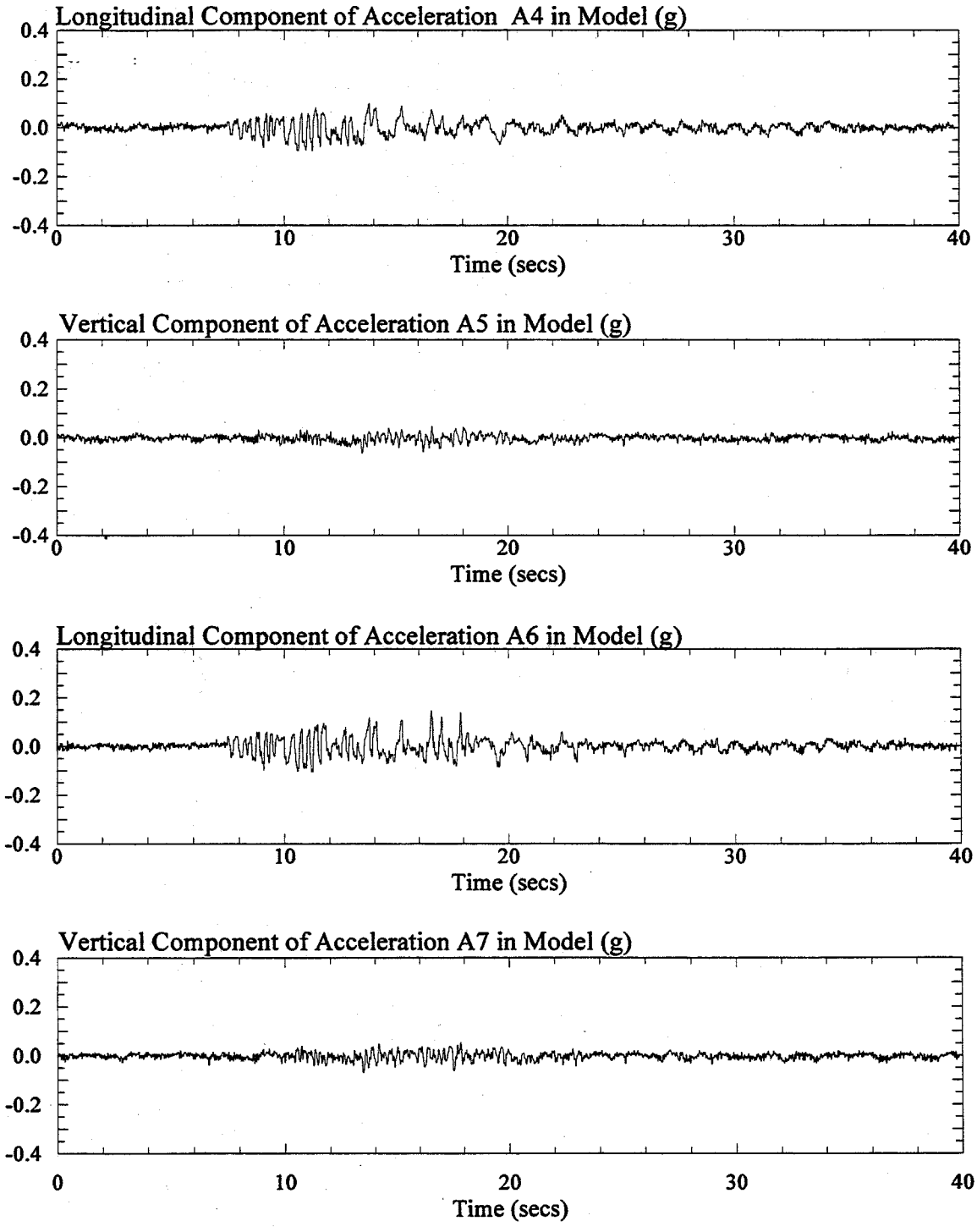

Figure 3: Longitudinal and vertical components of recorded acceleration in the one-g model SM3C1. Signals were post processed with a low pass filter of 20 Hz.

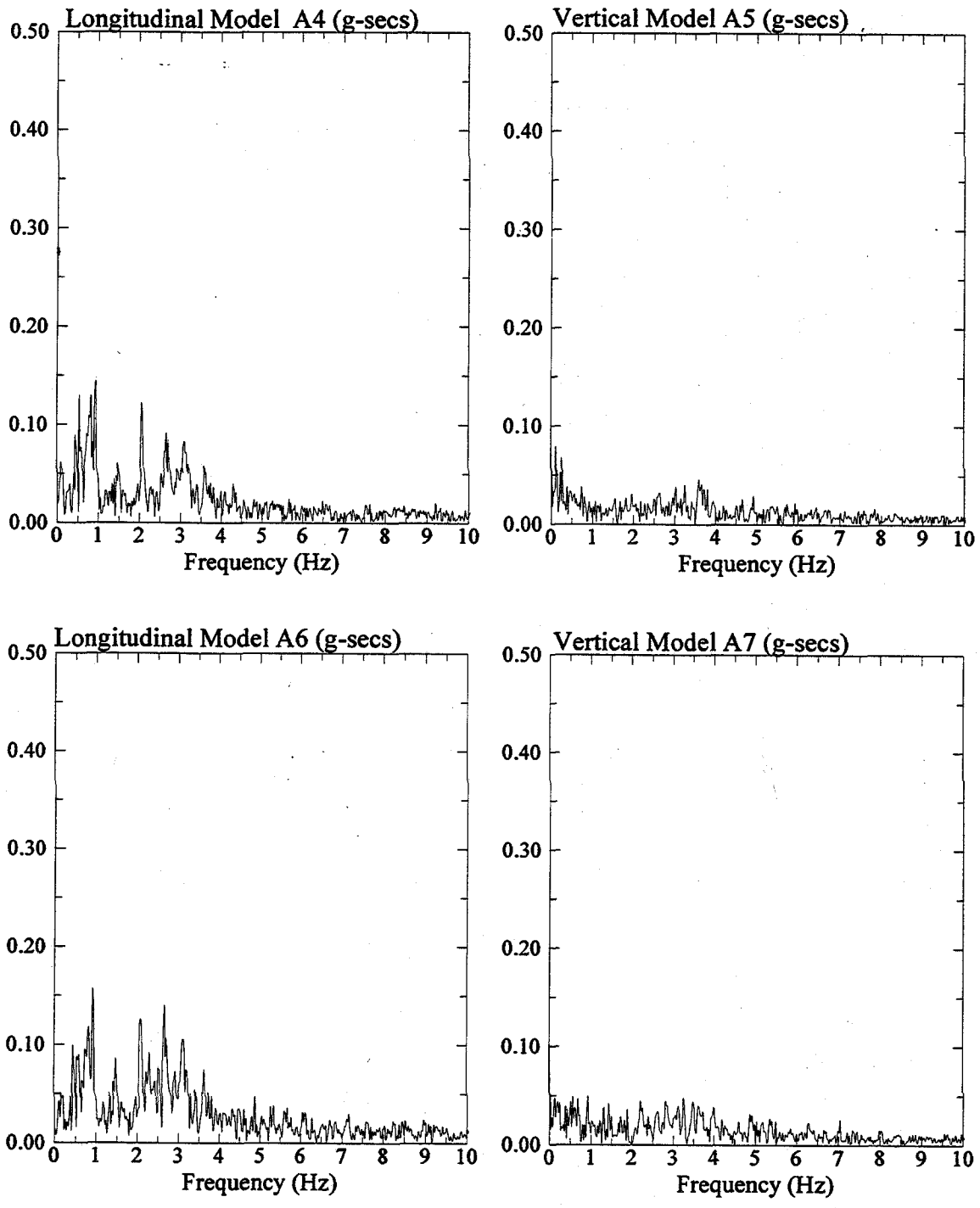

Figure 4: Fast Fourier Transform of longitudinal and vertical components of recorded acceleration in the one-g model SM3C1.

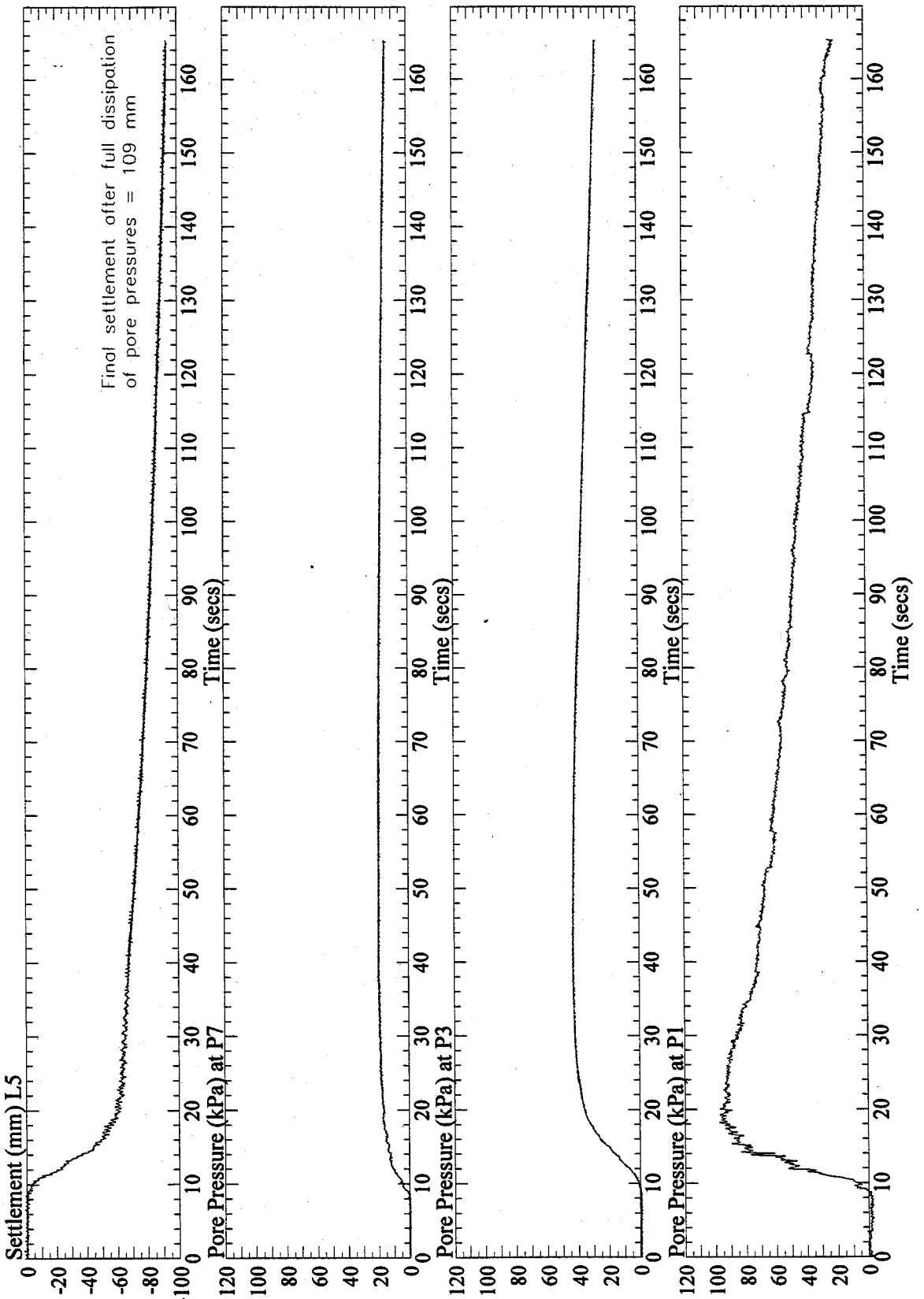

Figure 6: Vertical settlement at L5 and pore pressures at P1, P3, and P7, recorded in the one-g model SM3C1. Signal from P1 was post processed with a low pass filter of 10 Hz.

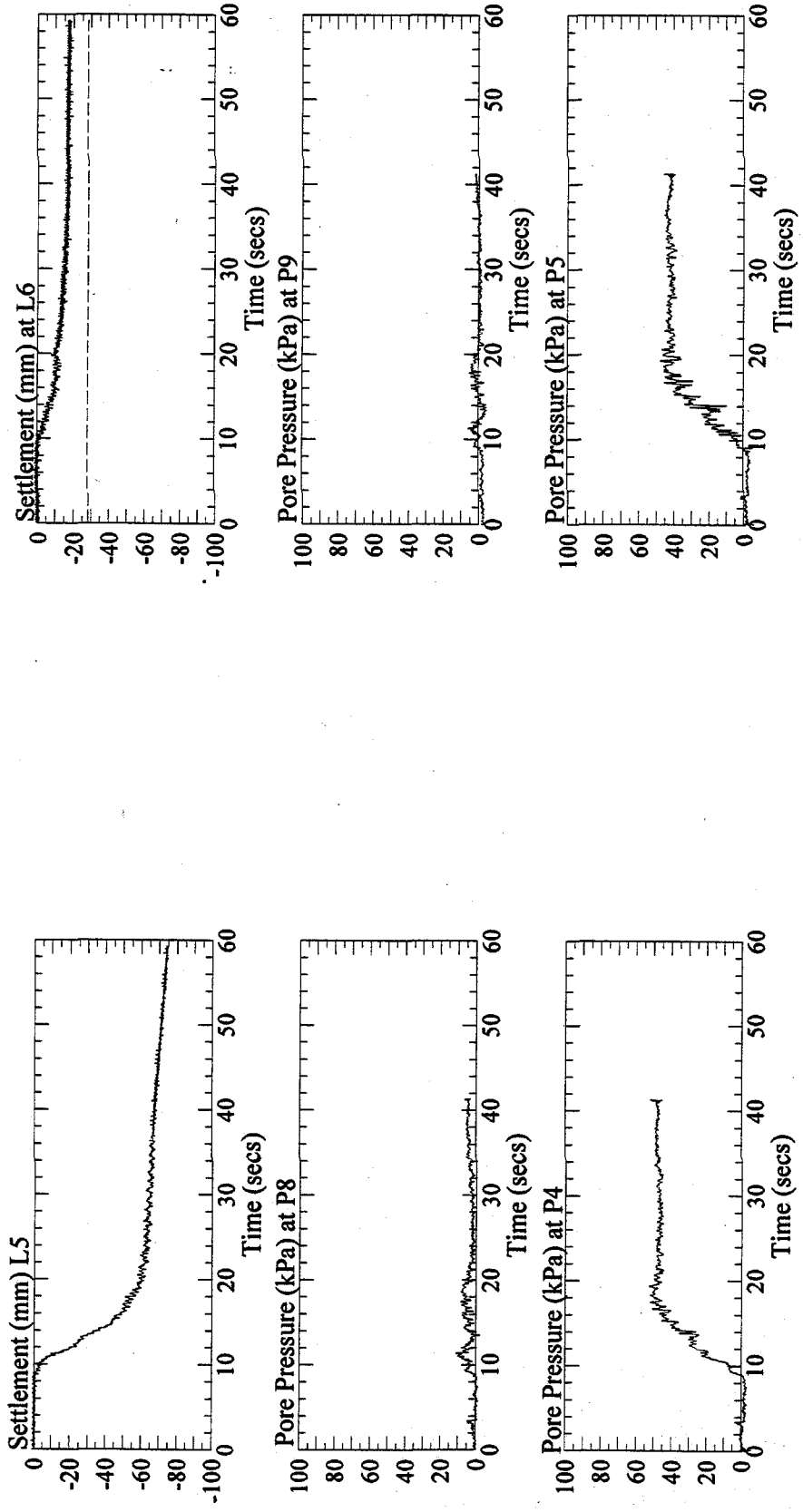

Figure 7: Vertical settlement at L5 and L6, and pore pressures at P4, P5, P8 and P9, recorded in the one-g model SM3C1. Pore pressure signals were post processed with a low pass filter of 10 Hz.

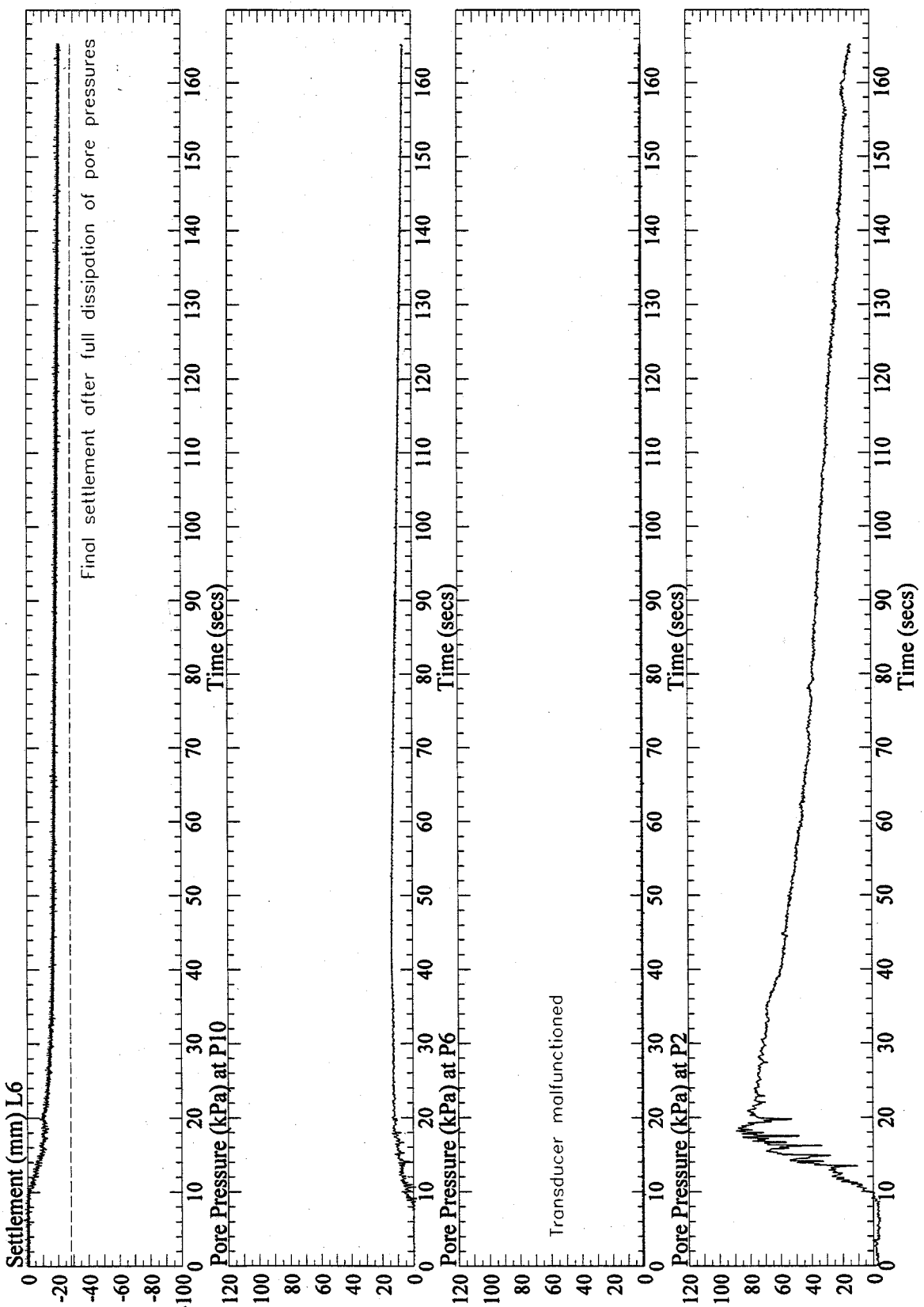

Figure 8: Vertical settlement at L6 and pore pressures at P2, P6, and P10, recorded in the one-g model SM3C1. Signal from P2 and P6 were post processed with a low pass filter of 10 Hz.

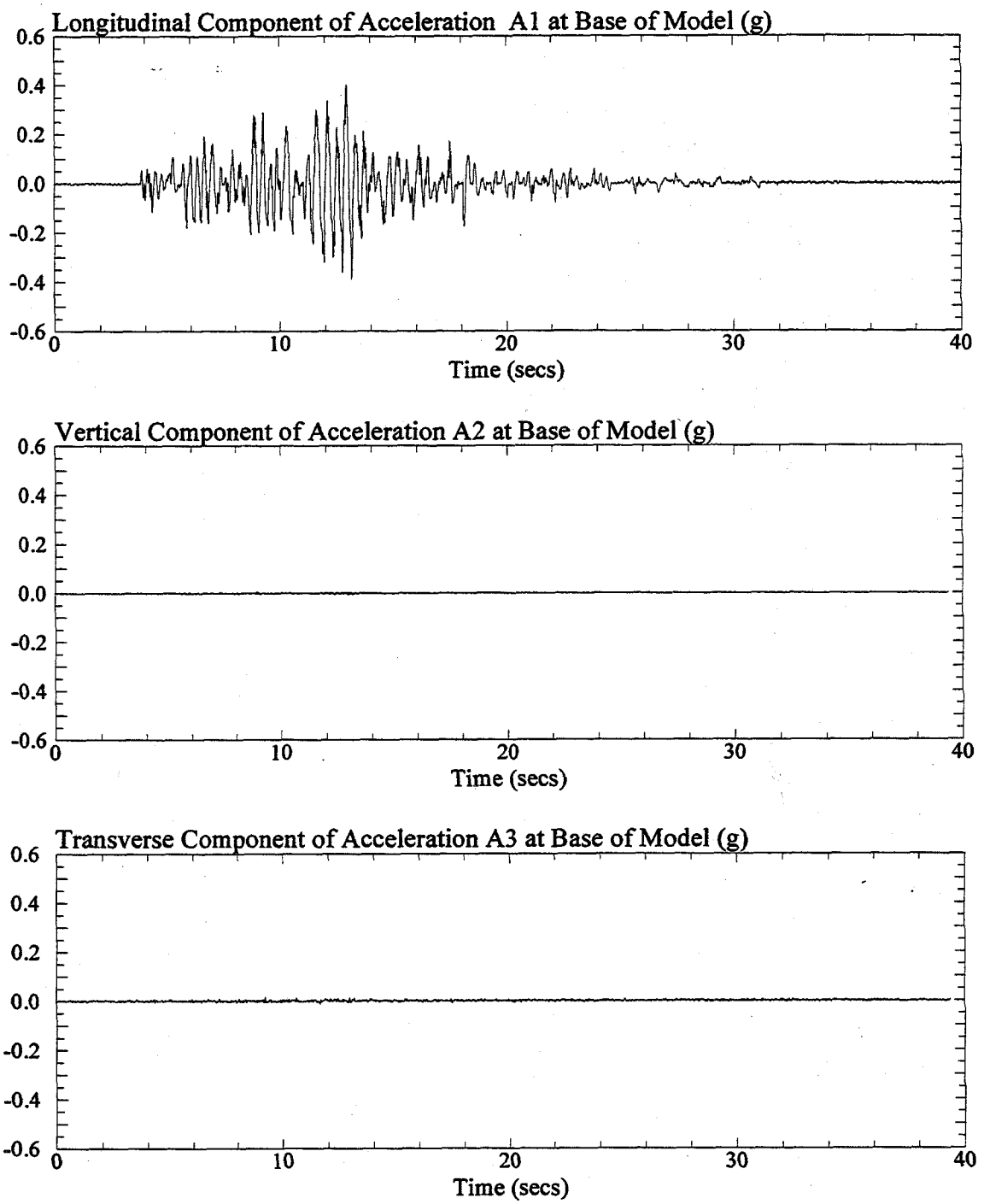

Figure 1: Longitudinal, vertical, and transverse components of recorded acceleration at base of the one-g model SM3D1. Signals were post processed with a low pass filter of 20 Hz.

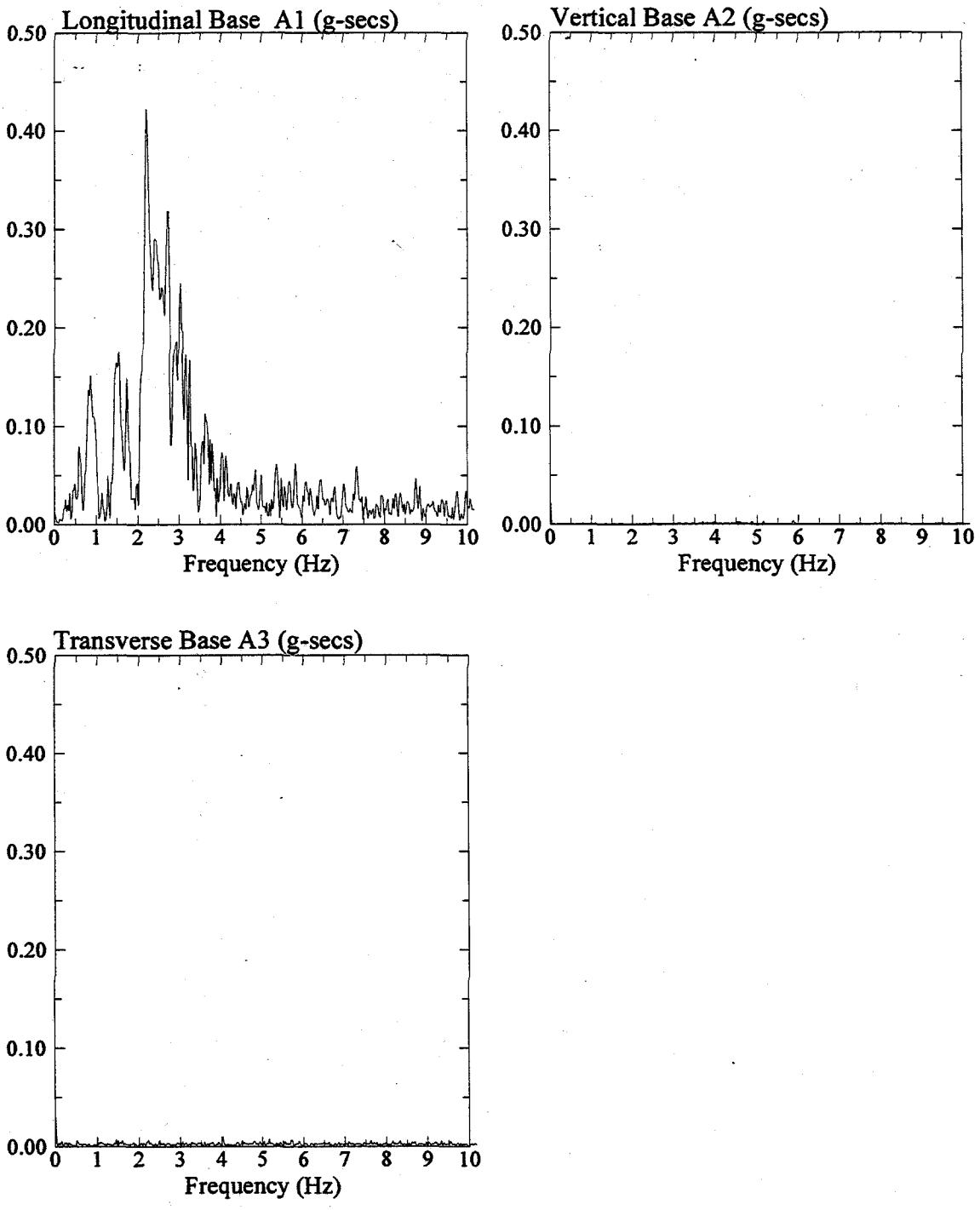

Figure 2: Fast Fourier Transform of longitudinal, vertical, and transverse components of recorded acceleration at base of the one-g model SM3D1.

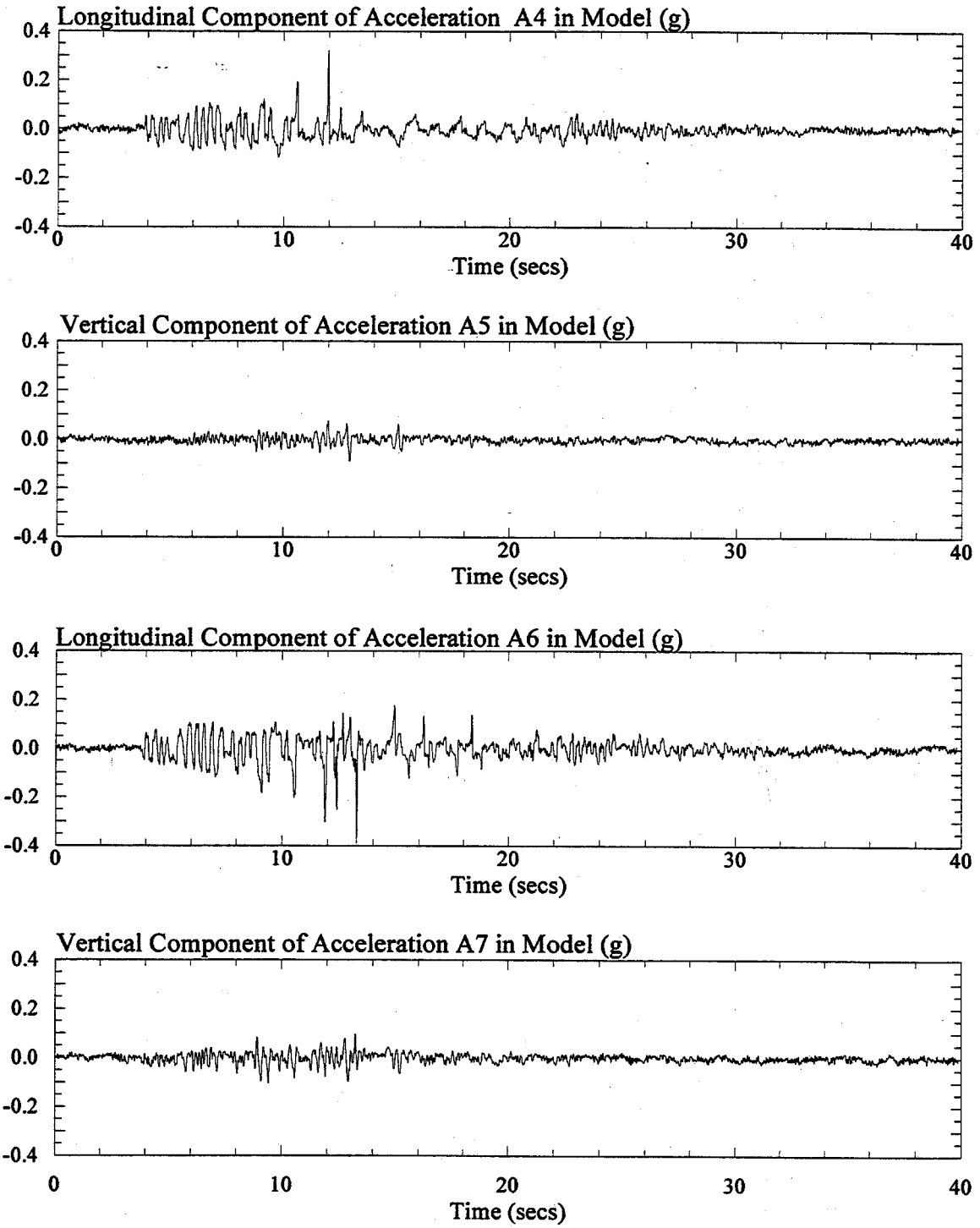

Figure 3: Longitudinal and vertical components of recorded acceleration in the one-g model SM3D1. Signals were post processed with a low pass filter of 20 Hz.

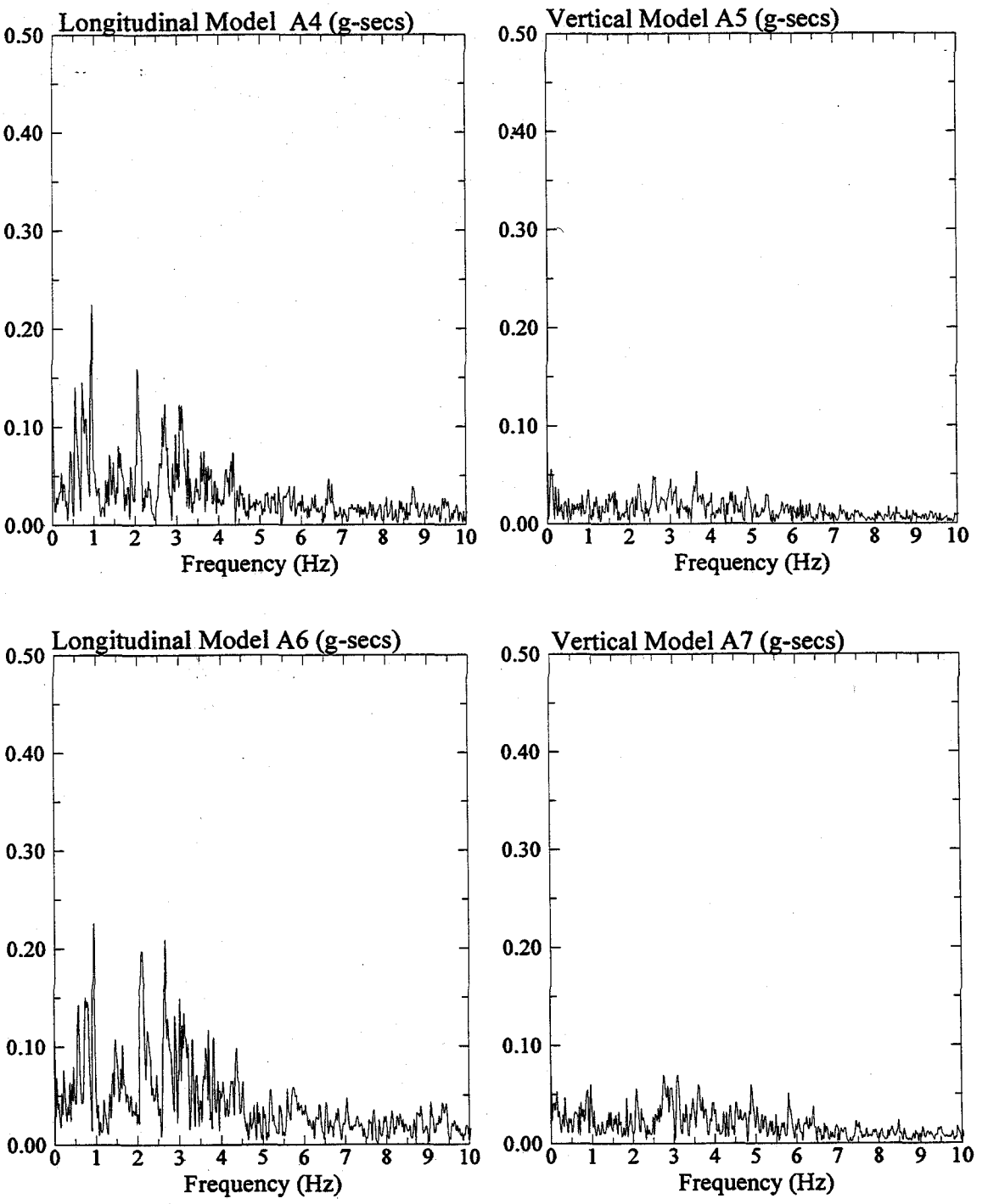

Figure 4: Fast Fourier Transform of longitudinal and vertical components of recorded acceleration in the one-g model SM3D1.

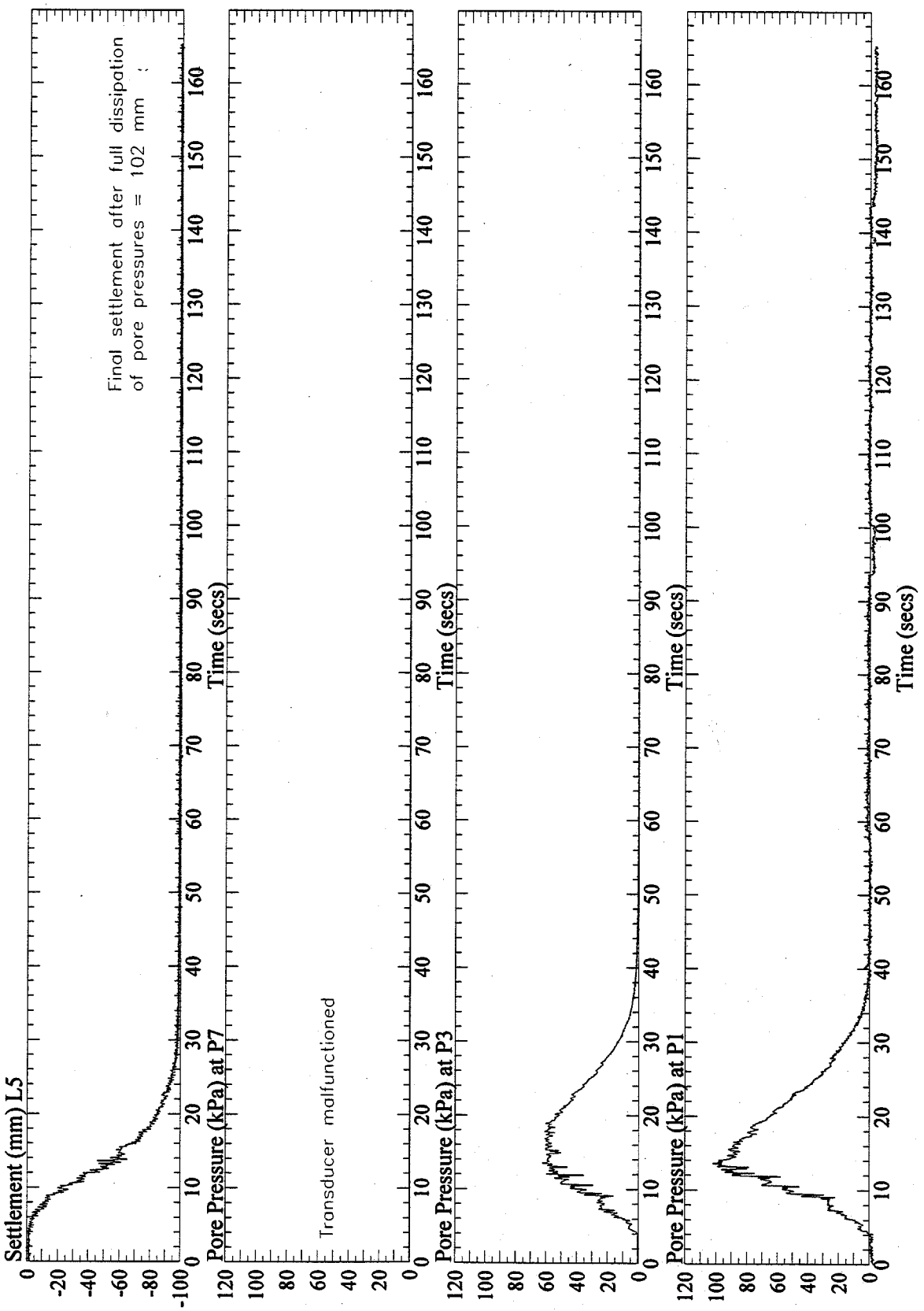

Figure 6: Vertical settlement at L5 and pore pressures at P1, P3, and P7, recorded in the one-g model SM3D1. Signal from P1 was post processed with a low pass filter of 10 Hz.

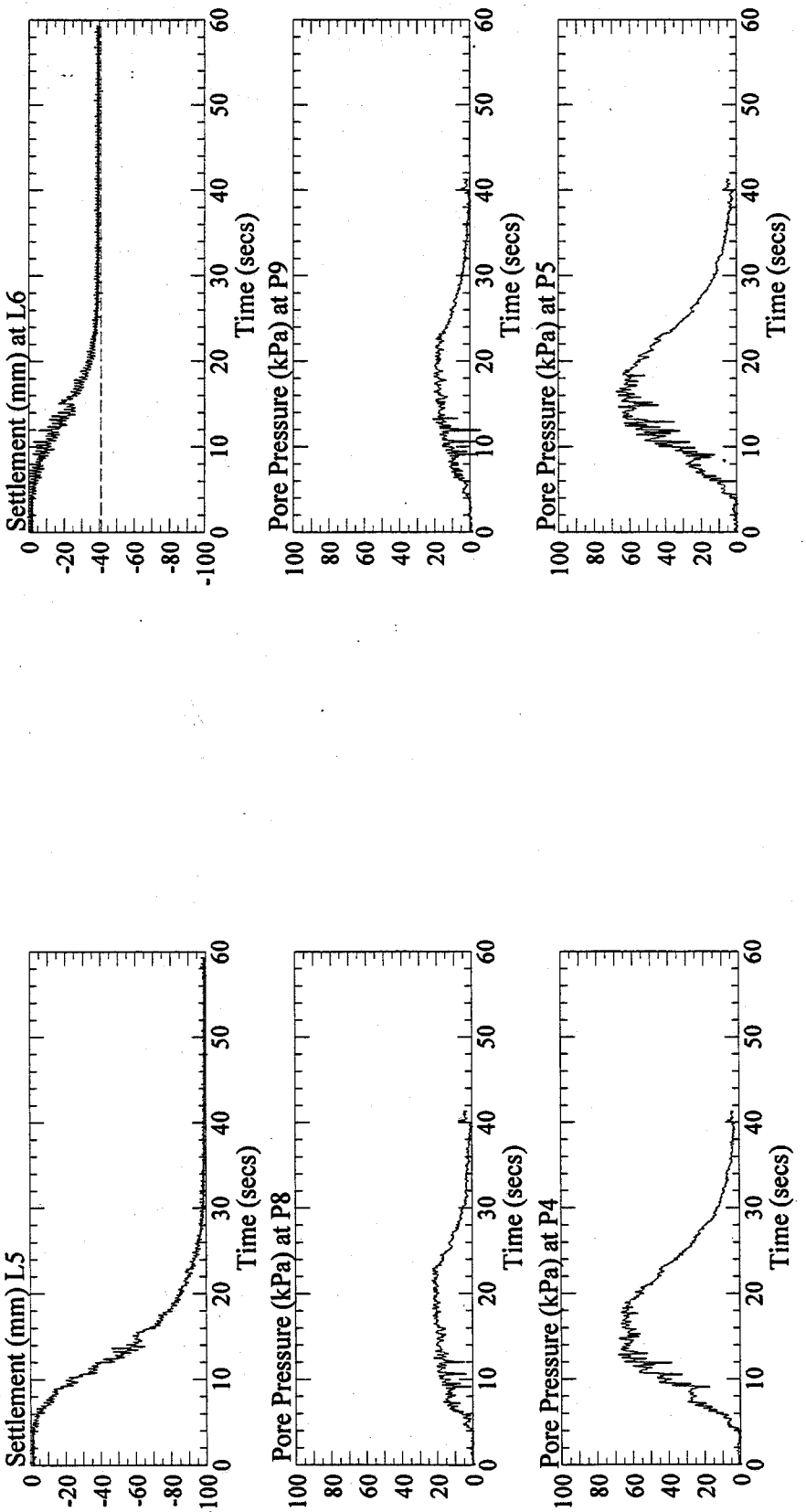

Figure 7: Vertical settlement at L5 and L6, and pore pressures at P4, P5, P8 and P9, recorded in the one-g model SM3D1. Pore pressure signals were post processed with a low pass filter of 10 Hz.

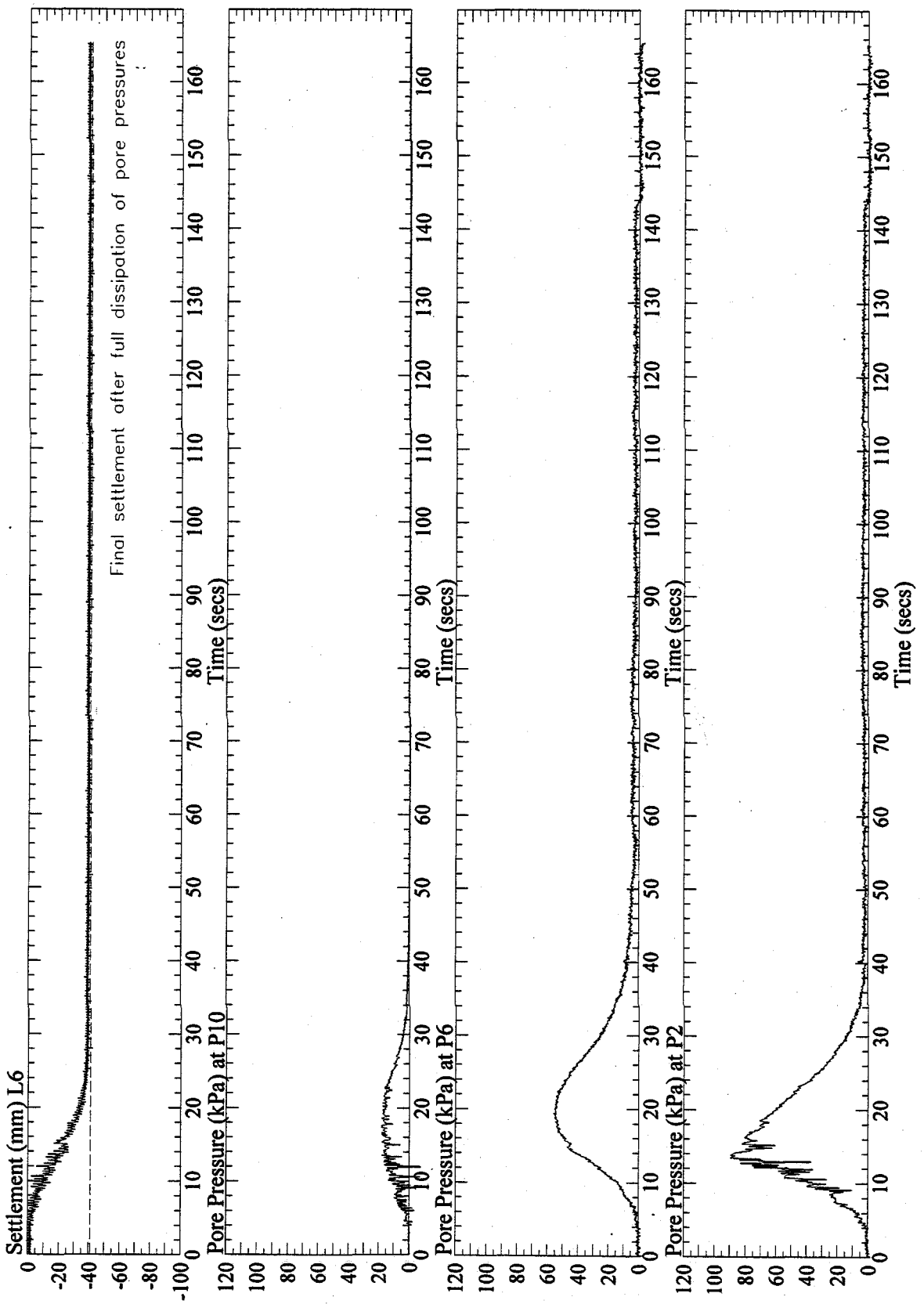

Figure 8: Vertical settlement at L6 and pore pressures at P2, P6, and P10, recorded in the one-g model SM3D1. Signal from P2 and P6 were post processed with a low pass filter of 10 Hz.

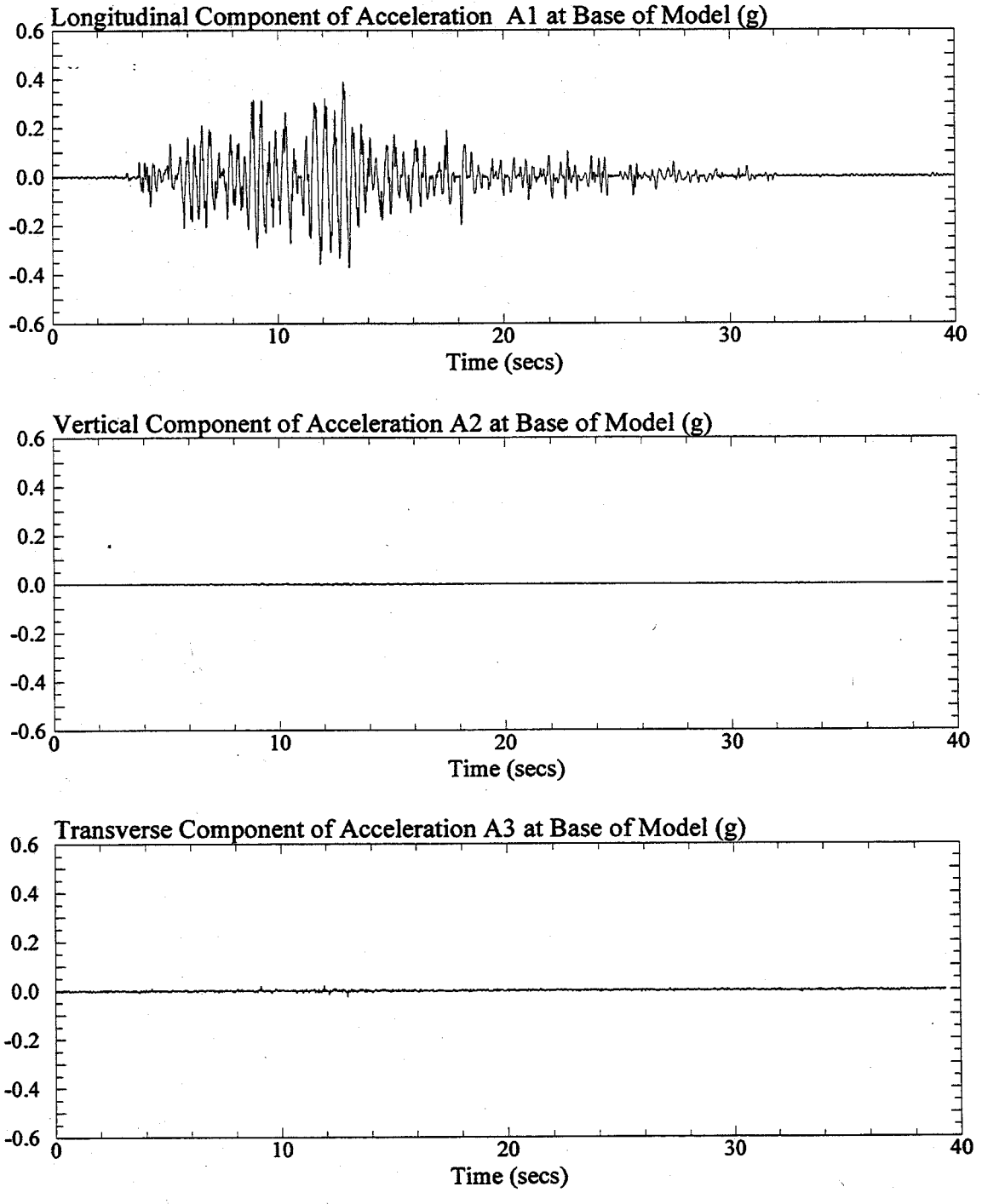

Figure 1: Longitudinal, vertical, and transverse components of recorded acceleration at base of the one-g model SM3E1. Signals were post processed with a low pass filter of 20 Hz.

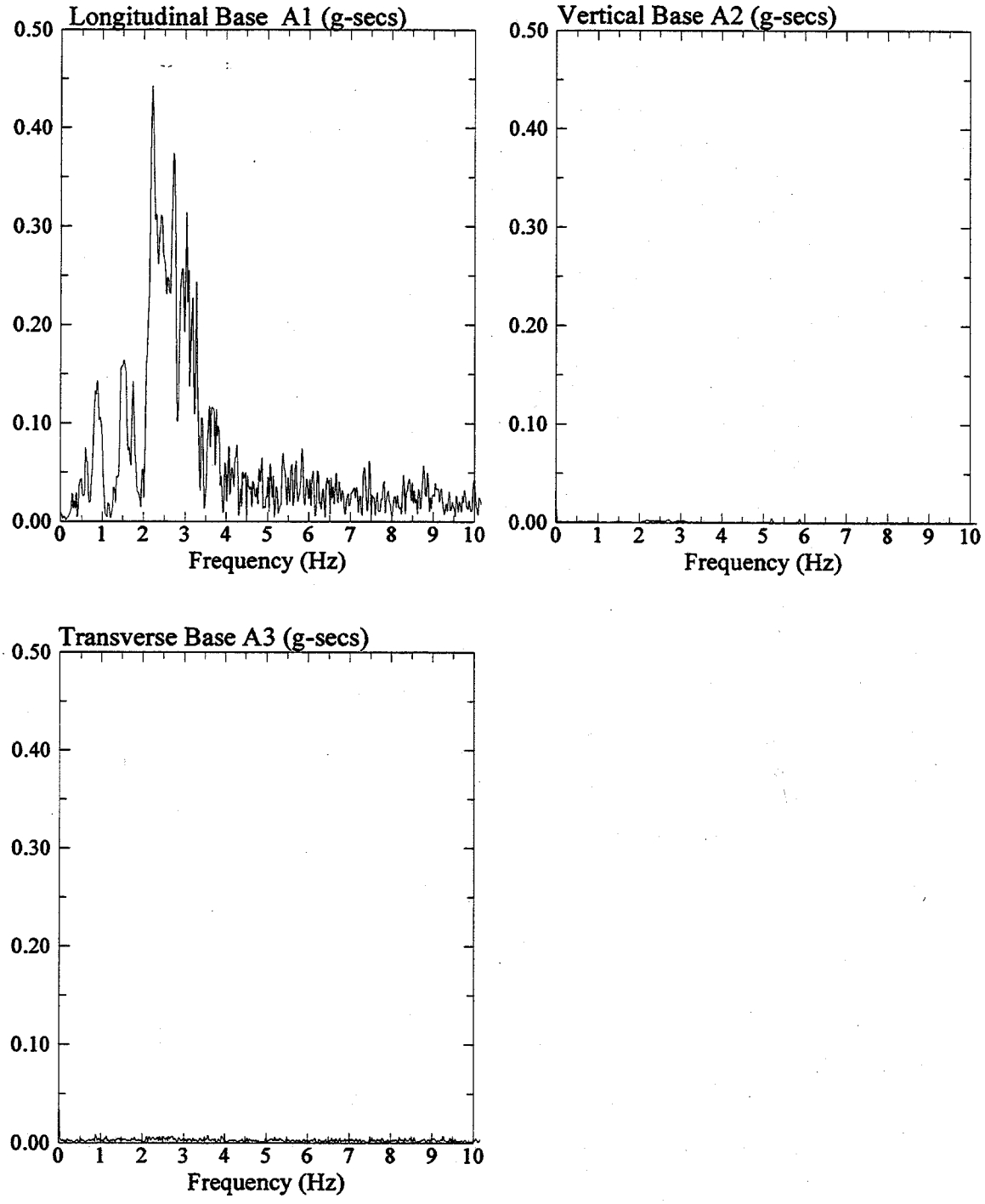

Figure 2: Fast Fourier Transform of longitudinal, vertical, and transverse components of recorded acceleration at base of the one-g model SM3E1.

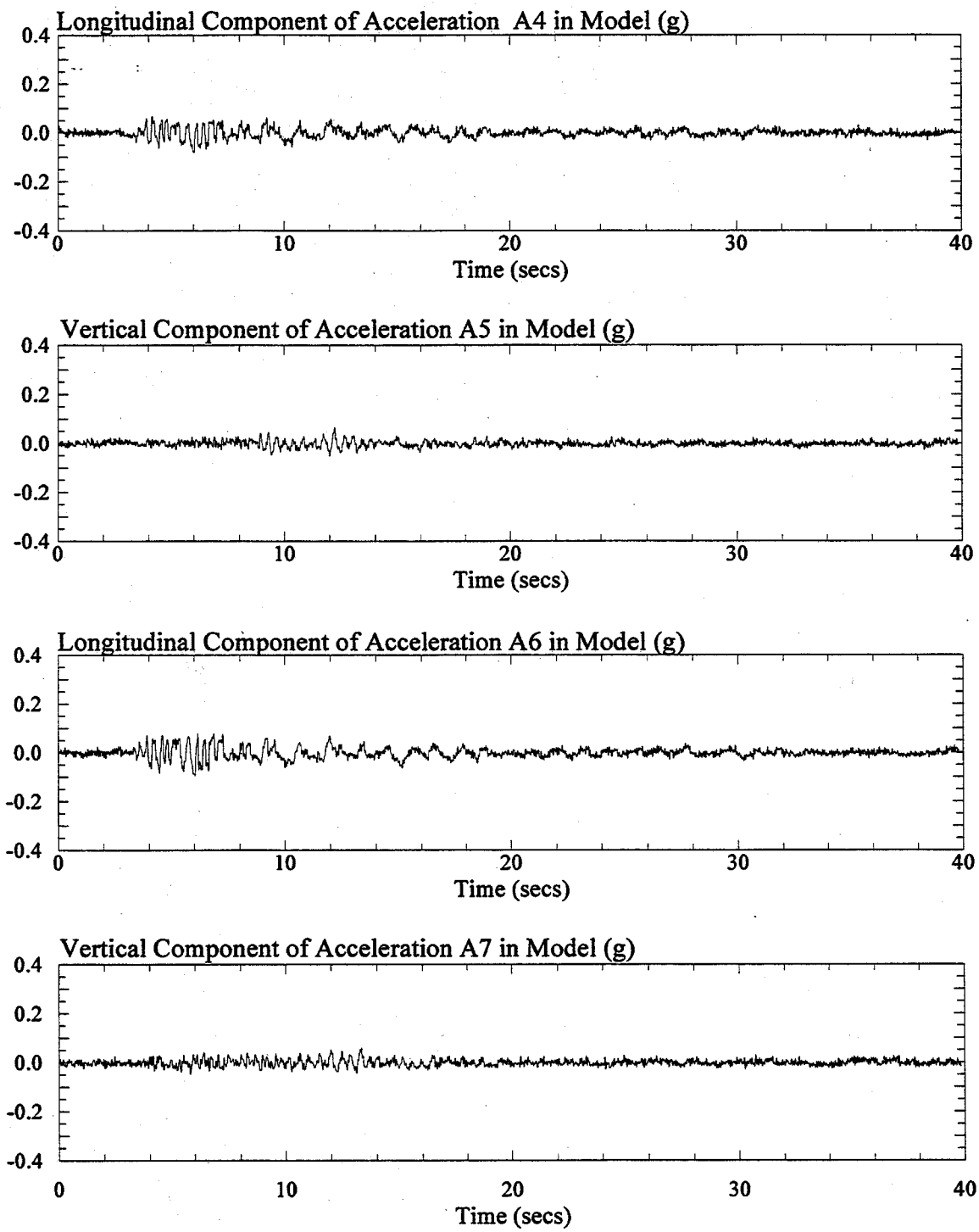

Figure 3: Longitudinal and vertical components of recorded acceleration in the one-g model SM3E1. Signals were post processed with a low pass filter of 20 Hz.

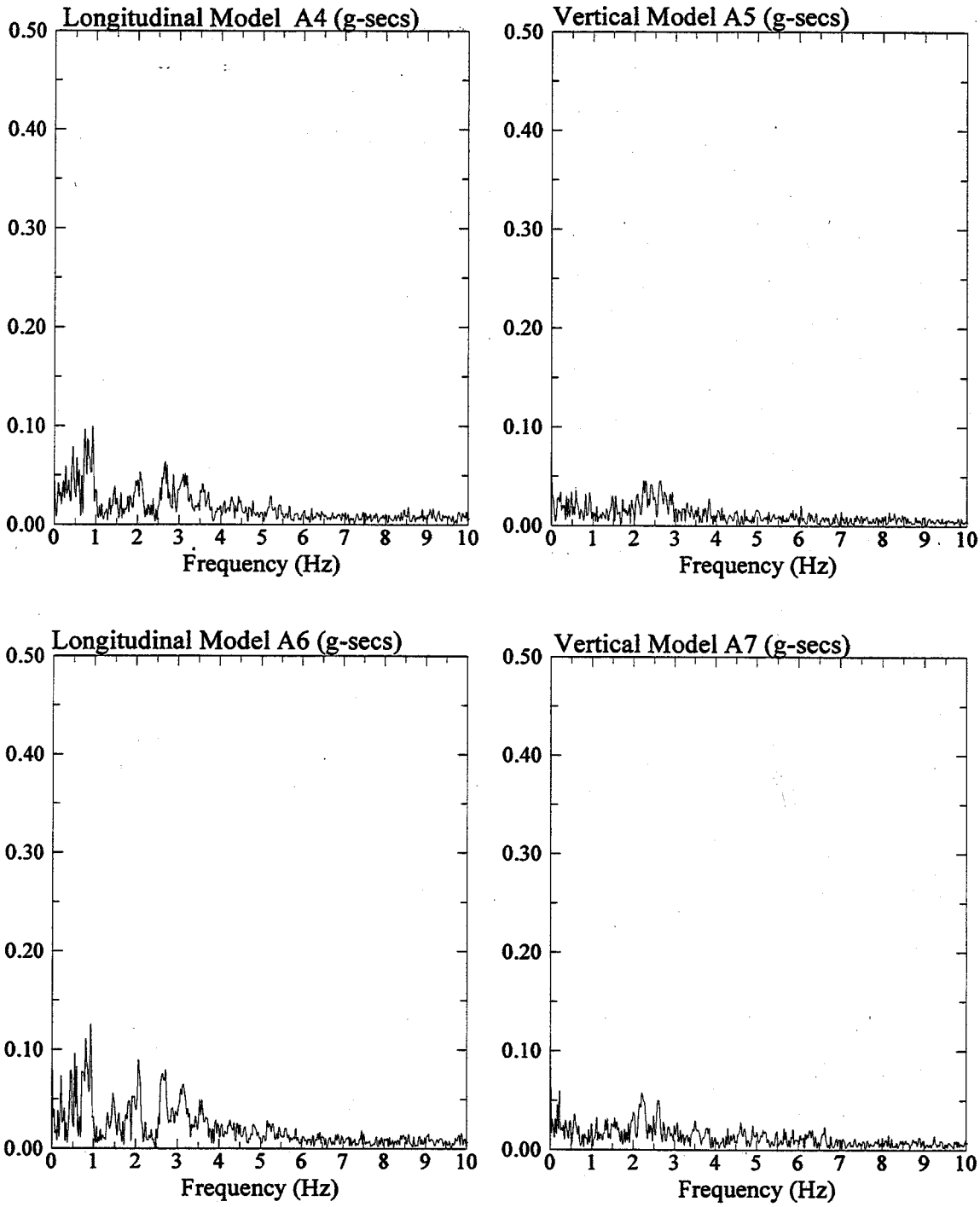

Figure 4: Fast Fourier Transform of longitudinal and vertical components of recorded acceleration in the one-g model SM3E1.

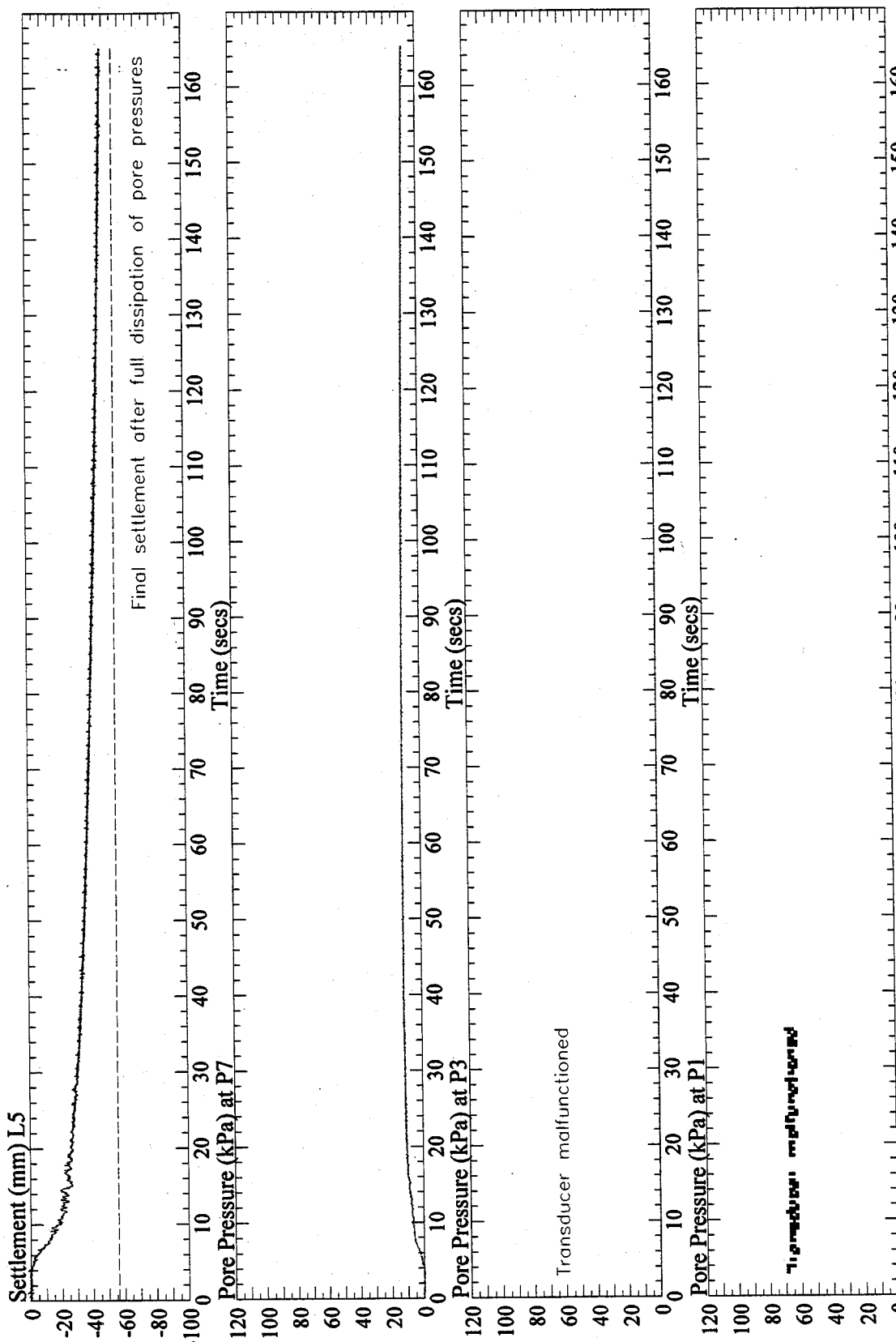

Figure 6: Vertical settlement at L5 and pore pressures at P1, P3, and P7, recorded in the one-g model SM3E1. Signal from P1 was post processed with a low pass filter of 10 Hz.

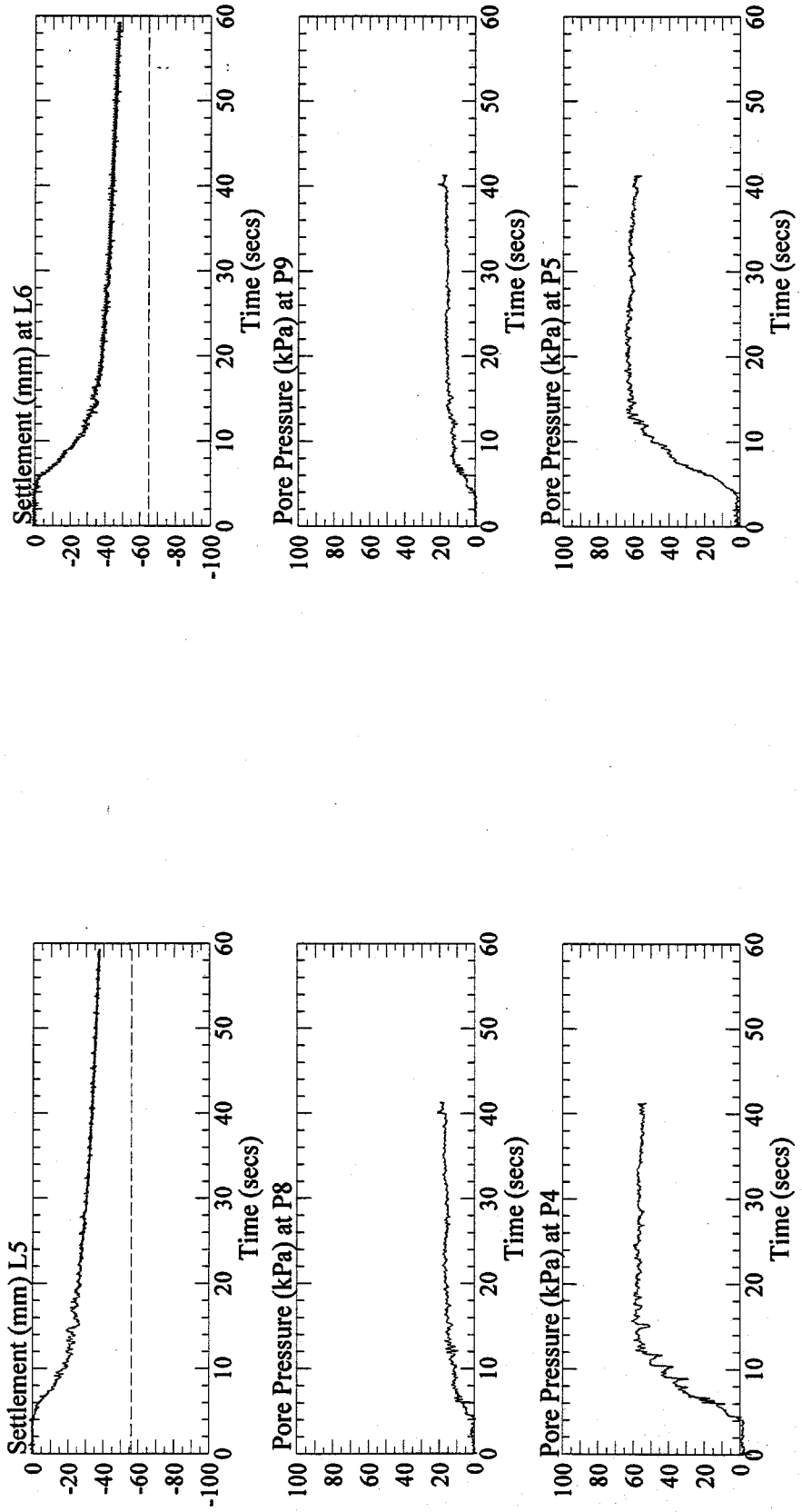

Figure 7: Vertical settlement at L5 and L6, and pore pressures at P4, P5, P8 and P9, recorded in the one-g model SM3E1. Pore pressure signals were post processed with a low pass filter of 10 Hz.

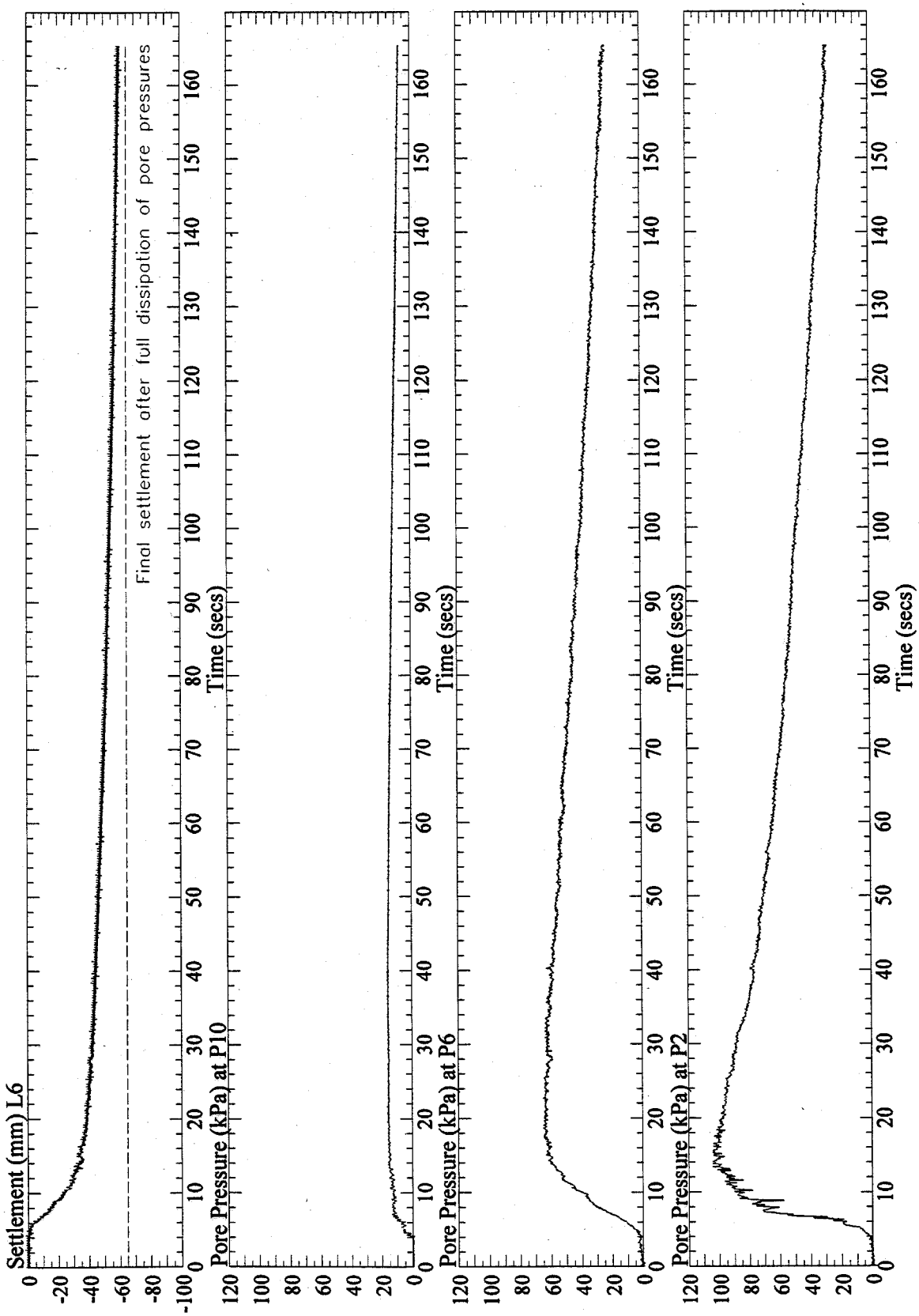

Figure 8: Vertical settlement at L6 and pore pressures at P2, P6, and P10, recorded in the one-g model SM3E1. Signal from P2 and P6 were post processed with a low pass filter of 10 Hz.

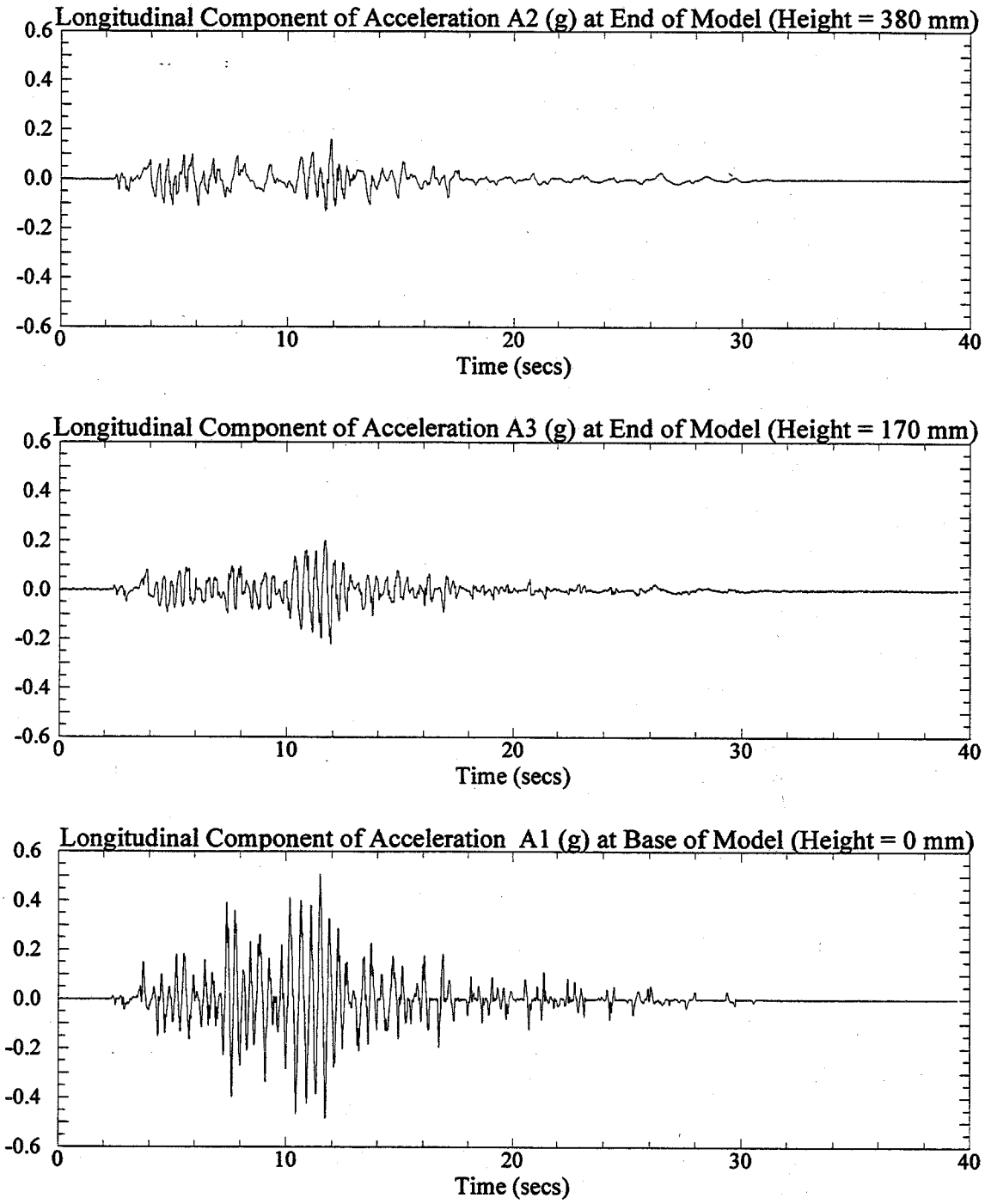

Figure 1: Longitudinal components of recorded acceleration at the base and end of the one-g model SM3F1. Signals were post processed with a low pass filter of 20 Hz.

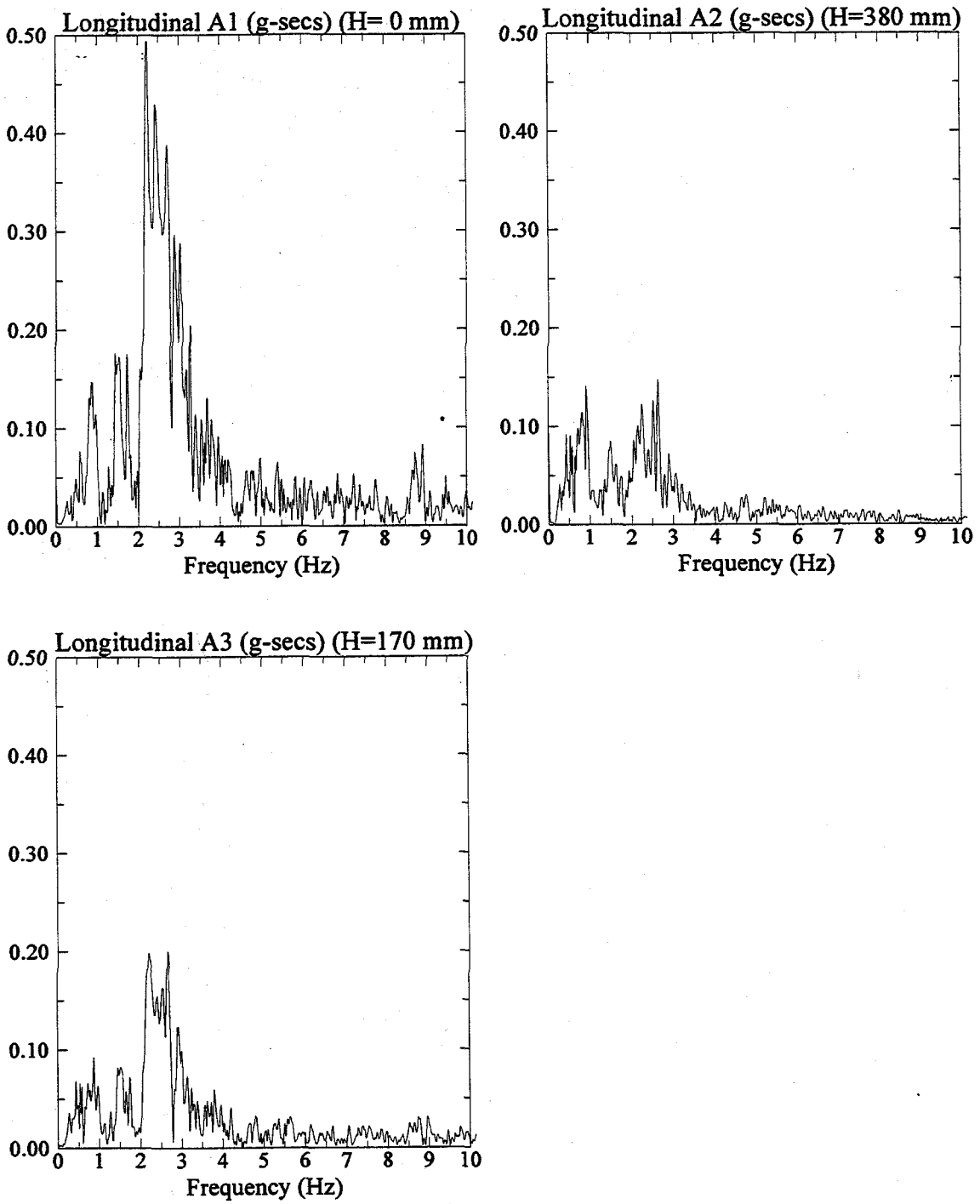

Figure 2: Fast Fourier Transform of longitudinal components of recorded acceleration at the base and end of the one-g model SM3F1.

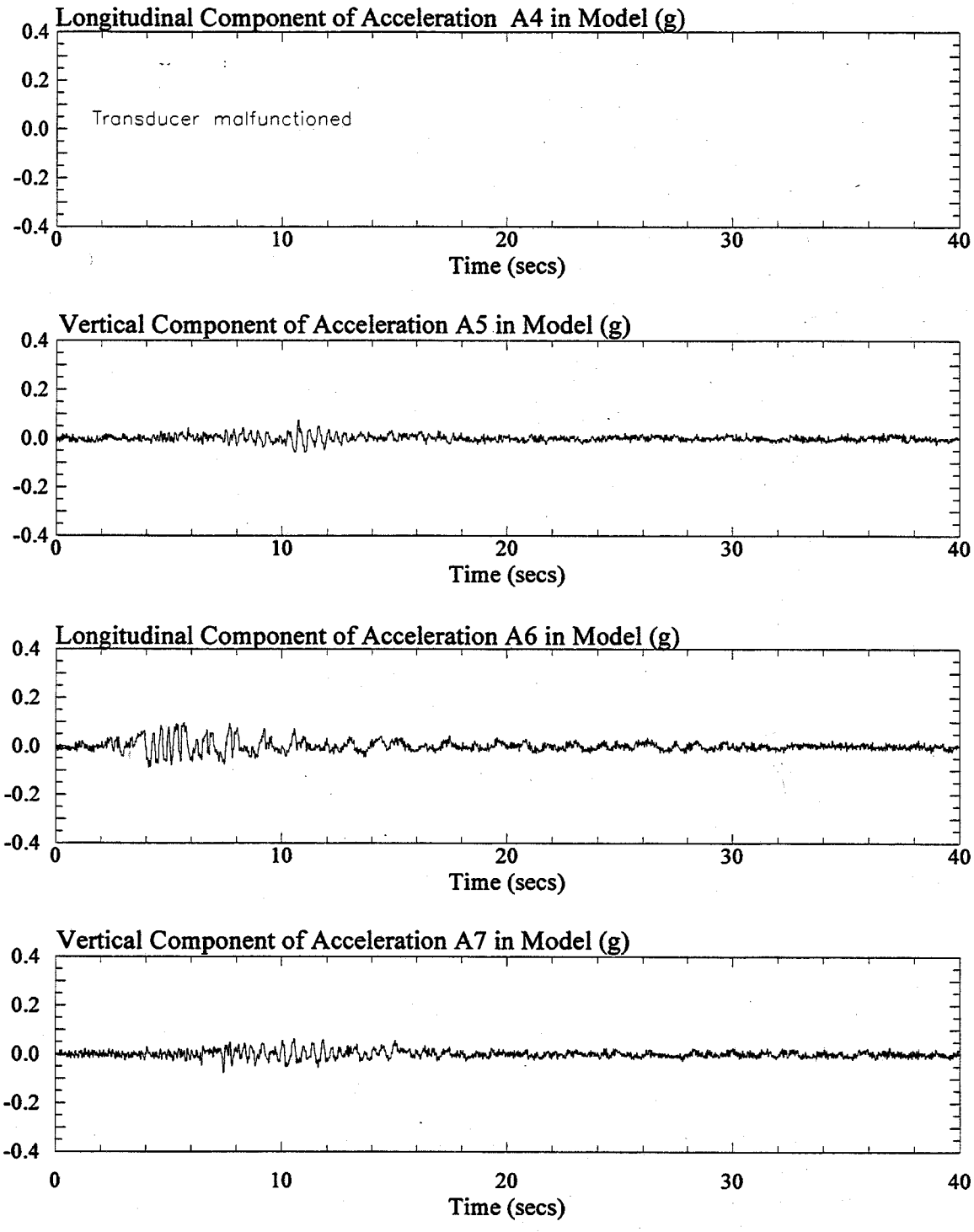

Figure 3: Longitudinal and vertical components of recorded acceleration in the one-g model SM3F1. Signals were post processed with a low pass filter of 20 Hz.

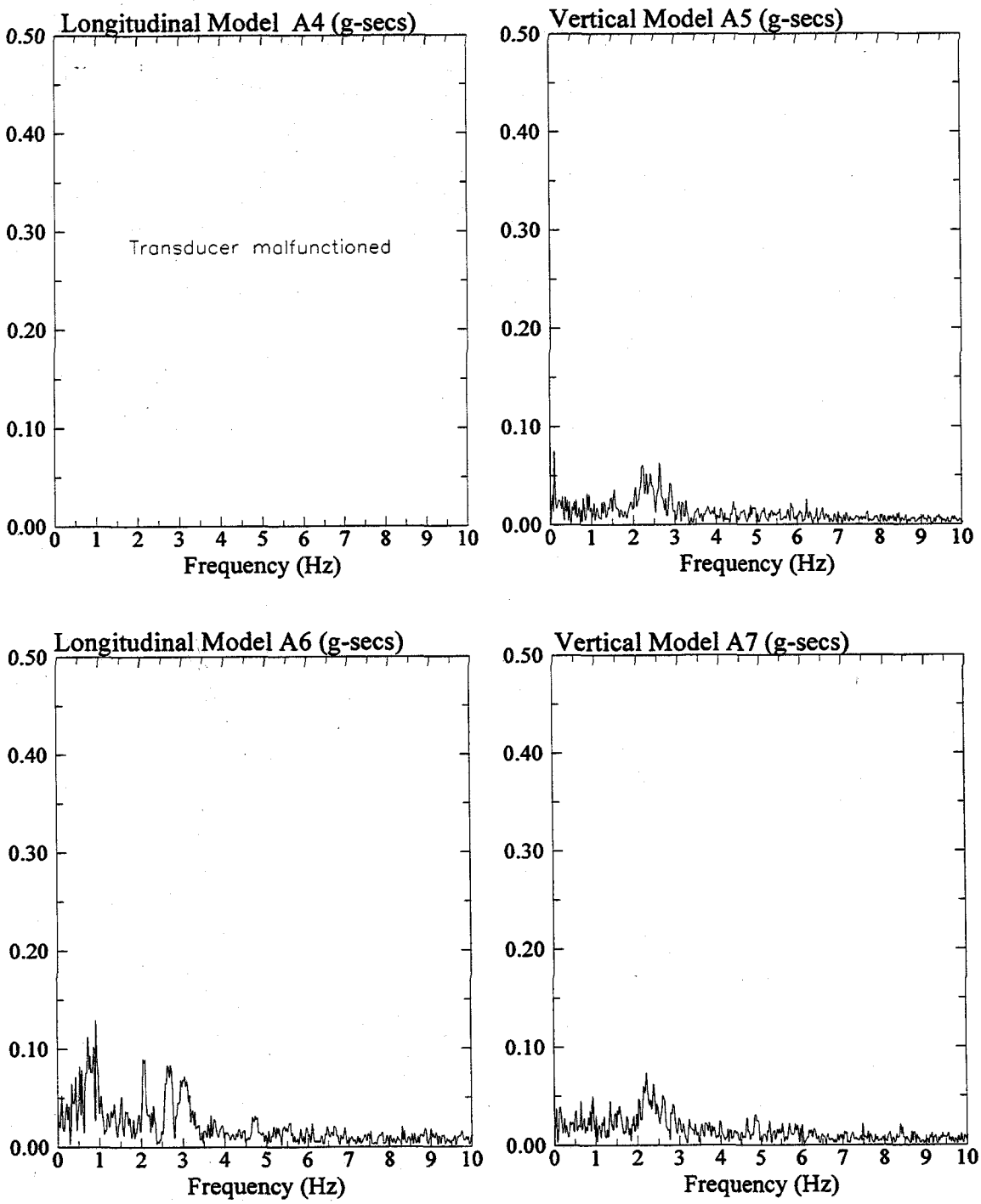

Figure 4: Fast Fourier Transform of longitudinal and vertical components of recorded acceleration in the one-g model SM3F1.

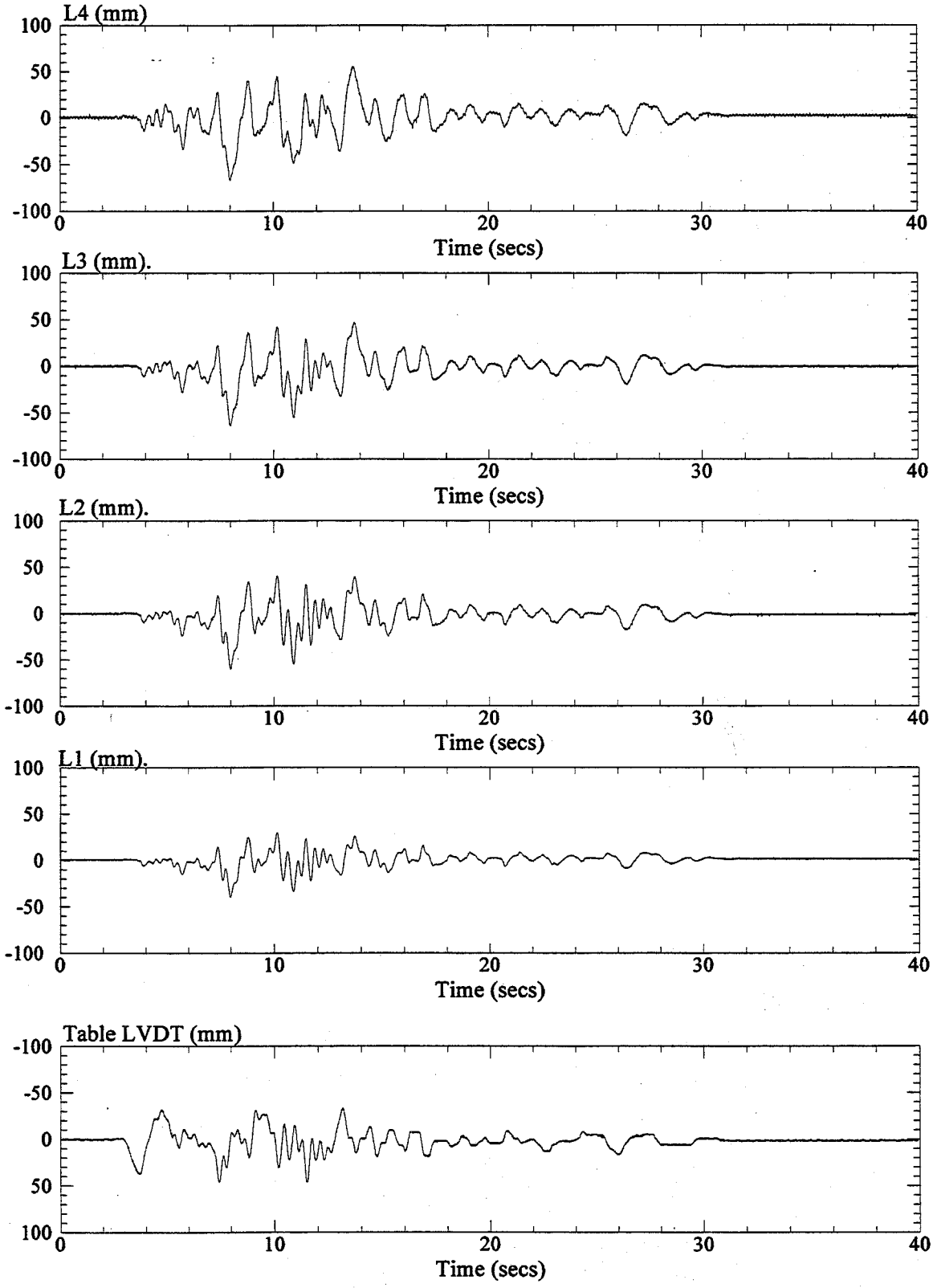

Figure 5: Longitudinal displacements recorded from the shake table LVDT and at LVDT's L1, L2, L3, and L4 in the one-g model SM3F1.

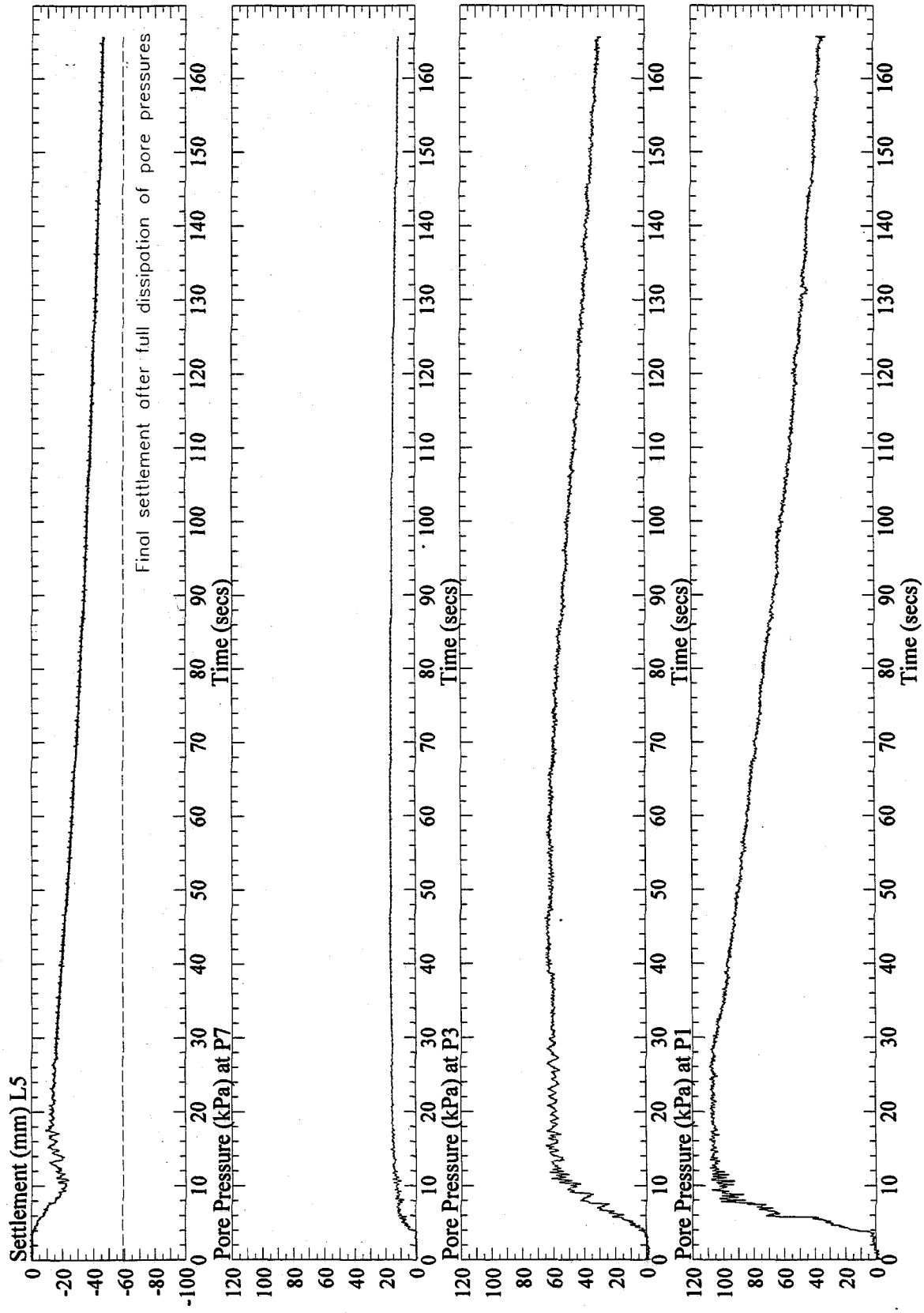

Figure 6: Vertical settlement at L5 and pore pressures at P1, P3, and P7, recorded in the one-g model SM3F1. Signals from P1 and P3 were post processed with a low pass filter of 10 Hz.

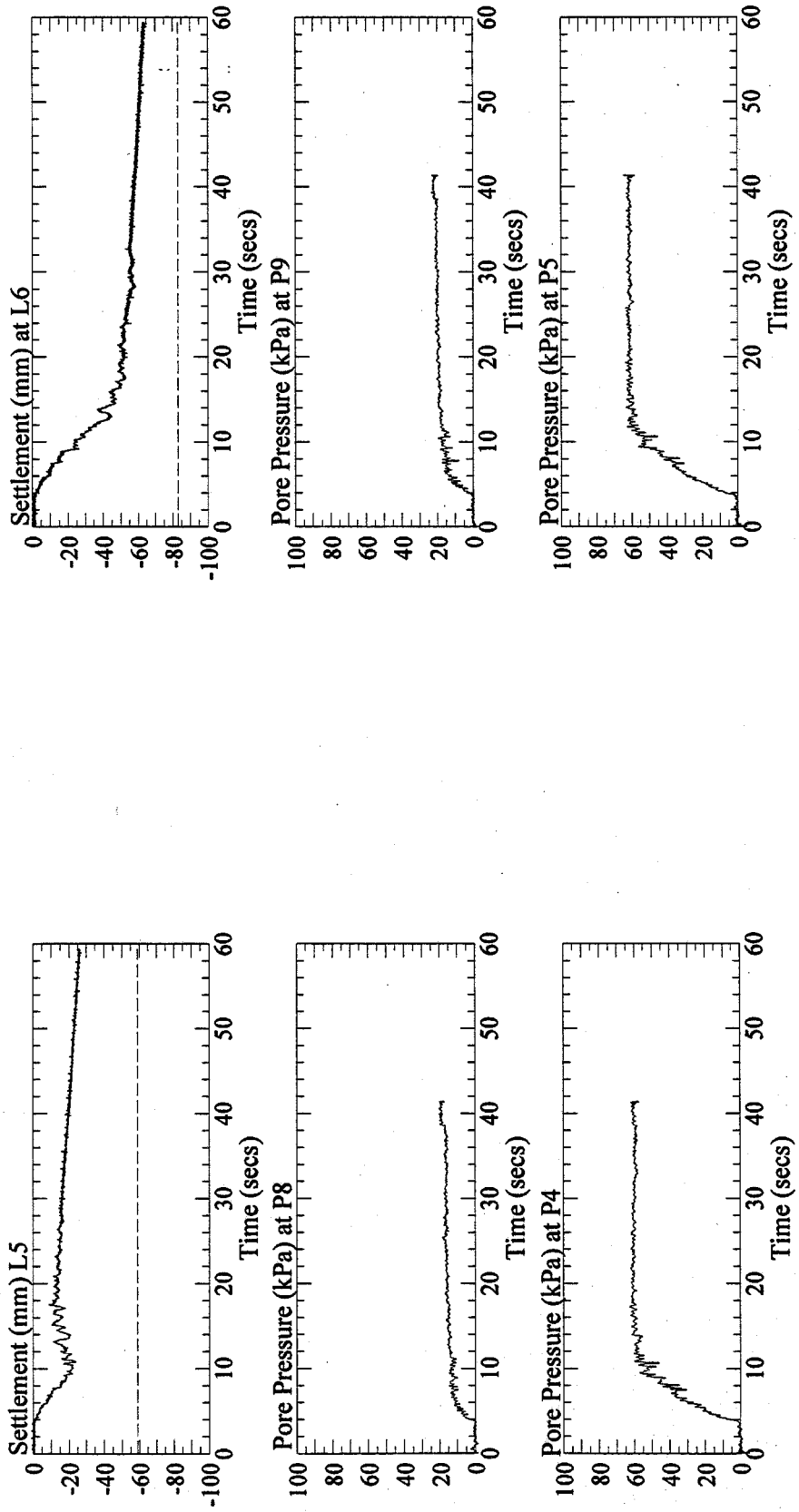

Figure 7: Vertical settlement at L5 and L6, and pore pressures at P4, P5, P8 and P9, recorded in the one-g model SM3F1. Pore pressure signals were post processed with a low pass filter of 10 Hz.

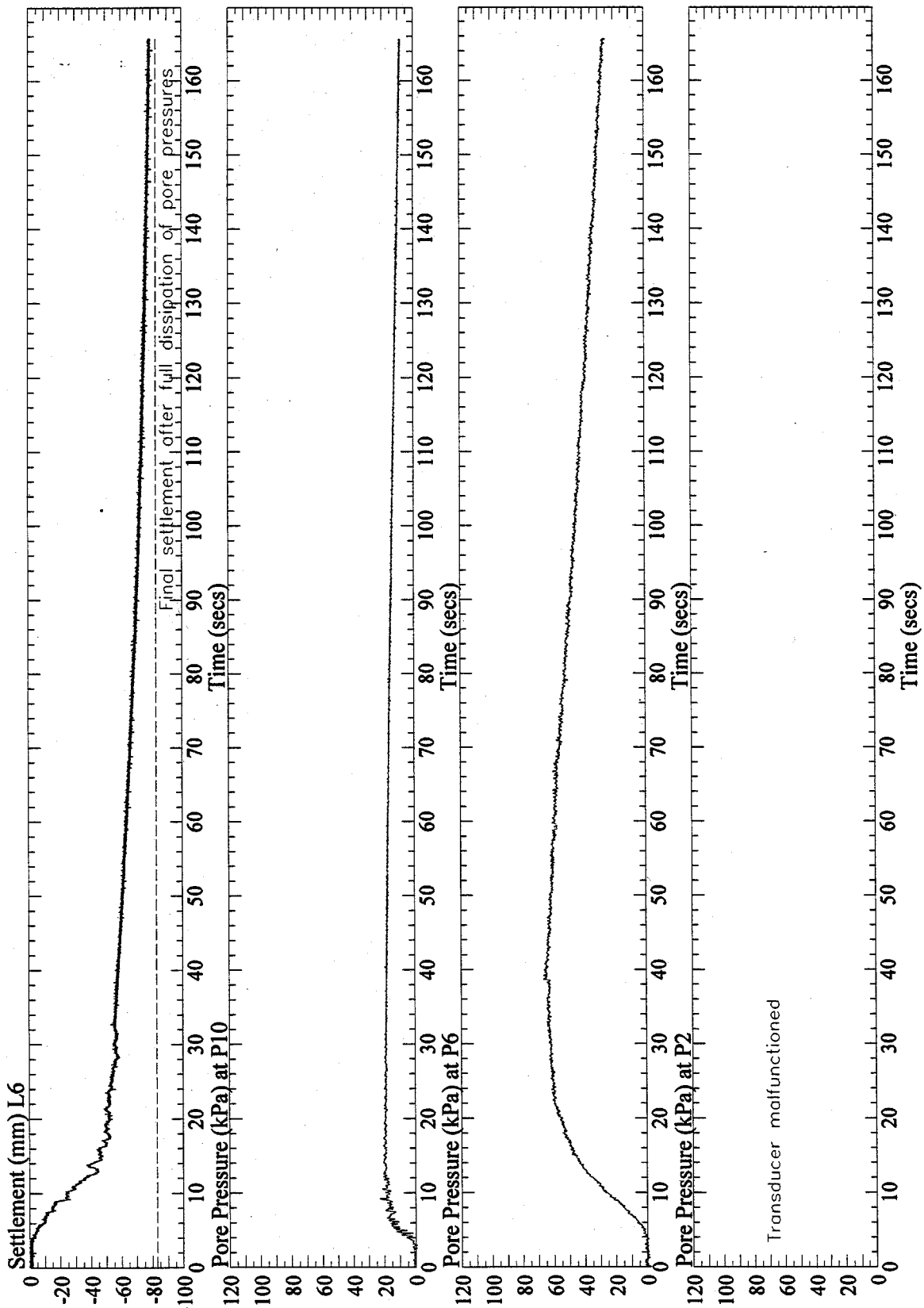

Figure 8: Vertical settlement at L6 and pore pressures at P2, P6, and P10, recorded in the one-g model SM3F1. Signal from P2 and P6 were post processed with a low pass filter of 10 Hz.

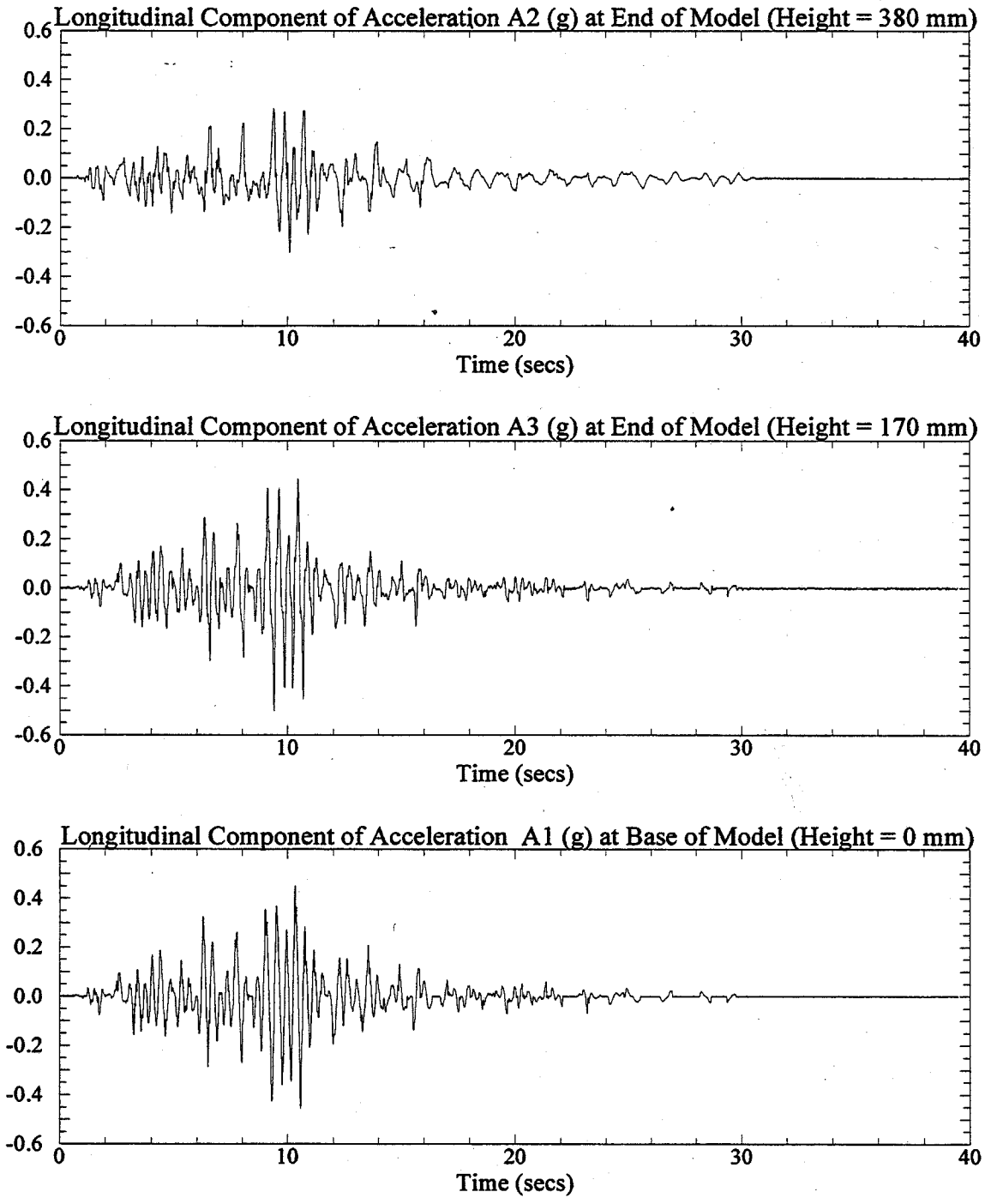

Figure 1: Longitudinal components of recorded acceleration at the base and end of the one-g model SM3F8. Signals were post processed with a low pass filter of 20 Hz.

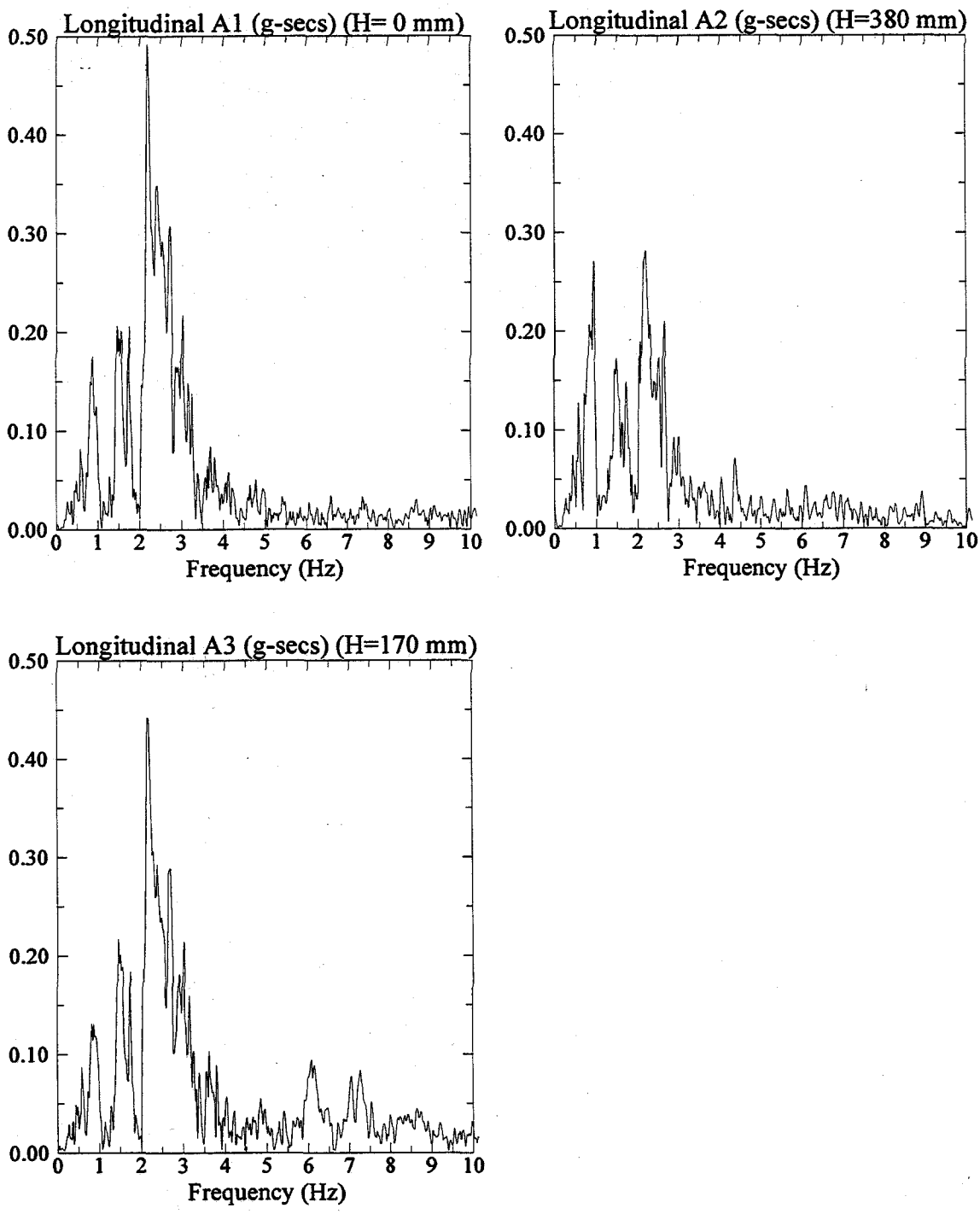

Figure 2: Fast Fourier Transform of longitudinal components of recorded acceleration at the base and end of the one-g model SM3F8.

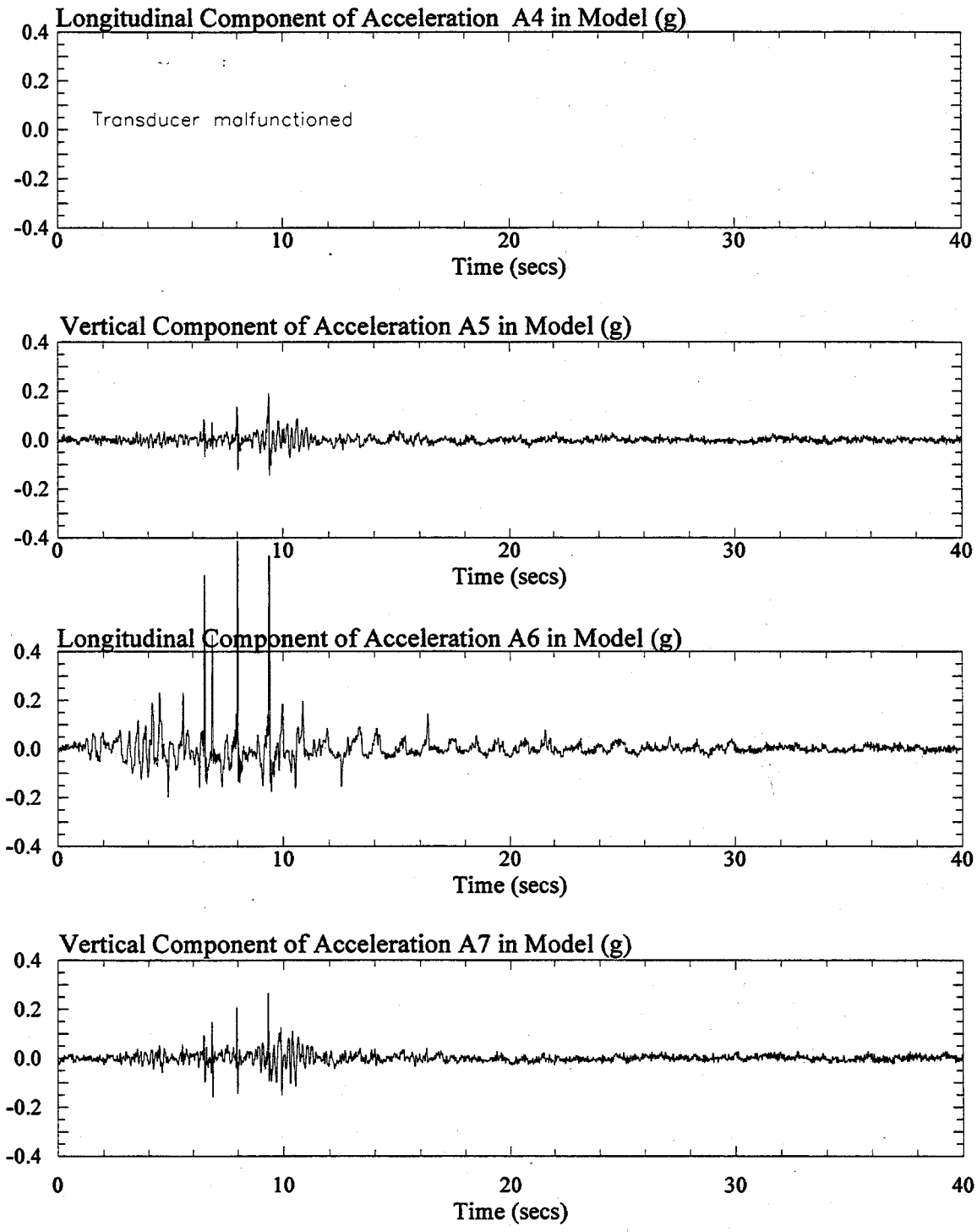

Figure 3: Longitudinal and vertical components of recorded acceleration in the one-g model SM3F8. Signals were post processed with a low pass filter of 20 Hz.

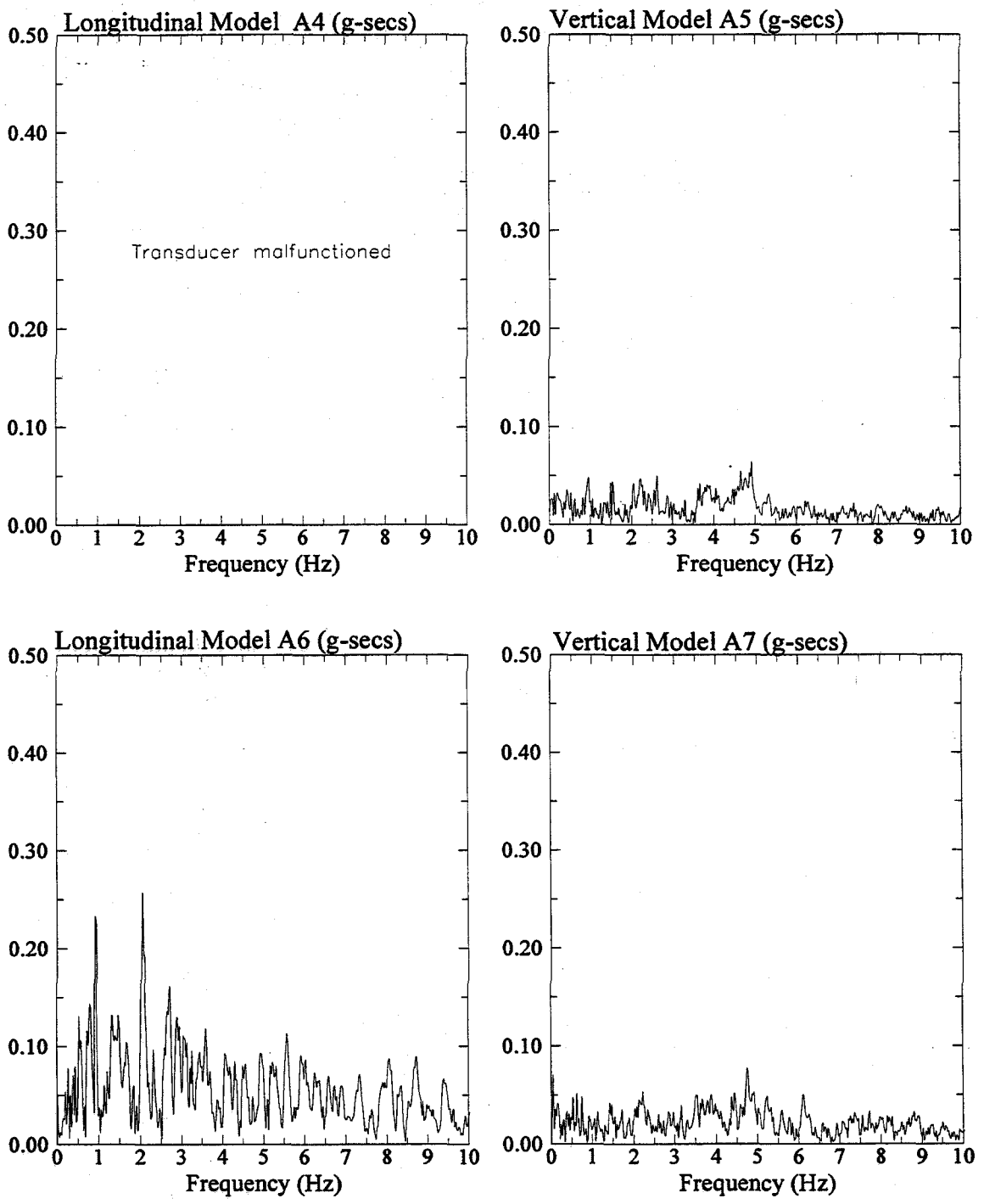

Figure 4: Fast Fourier Transform of longitudinal and vertical components of recorded acceleration in the one-g model SM3F8.

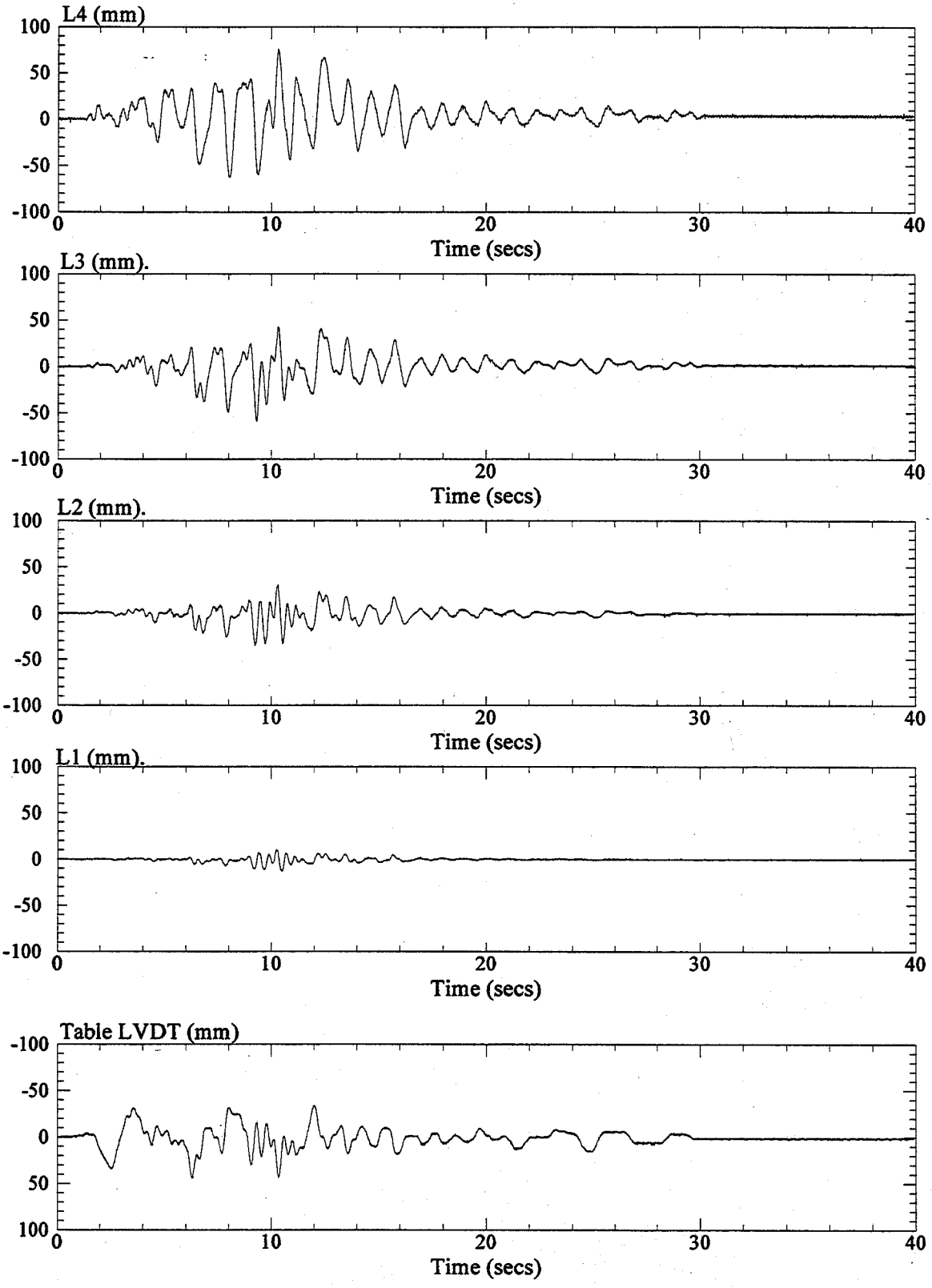

Figure 5: Longitudinal displacements recorded from the shake table LVDT and at LVDT's L1, L2, L3, and L4 in the one-g model SM3F8.

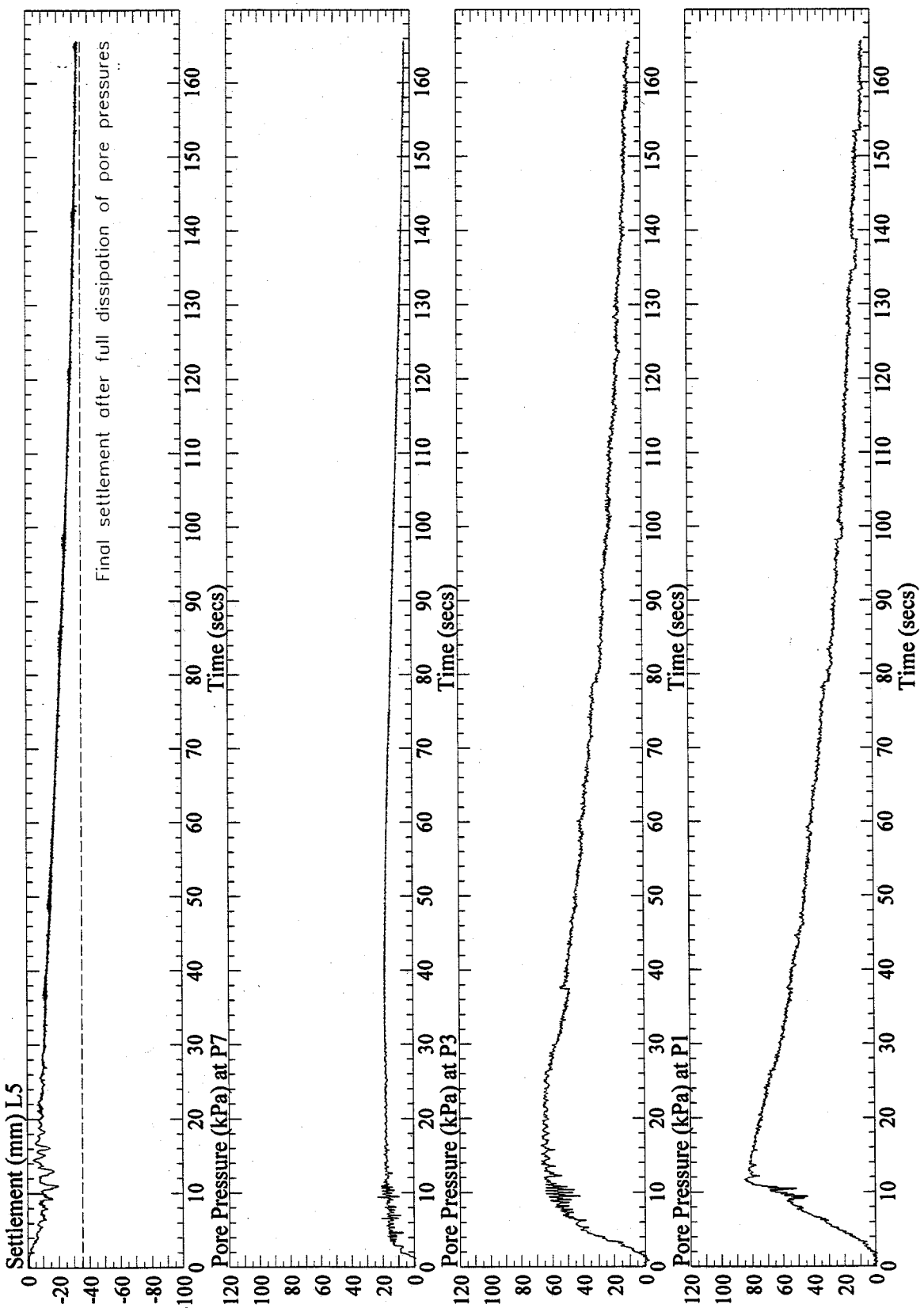

Figure 6: Vertical settlement at L5 and pore pressures at P1, P3, and P7, recorded in the one-g model SM3F8. Signals from P1 and P3 were post processed with a low pass filter of 10 Hz.

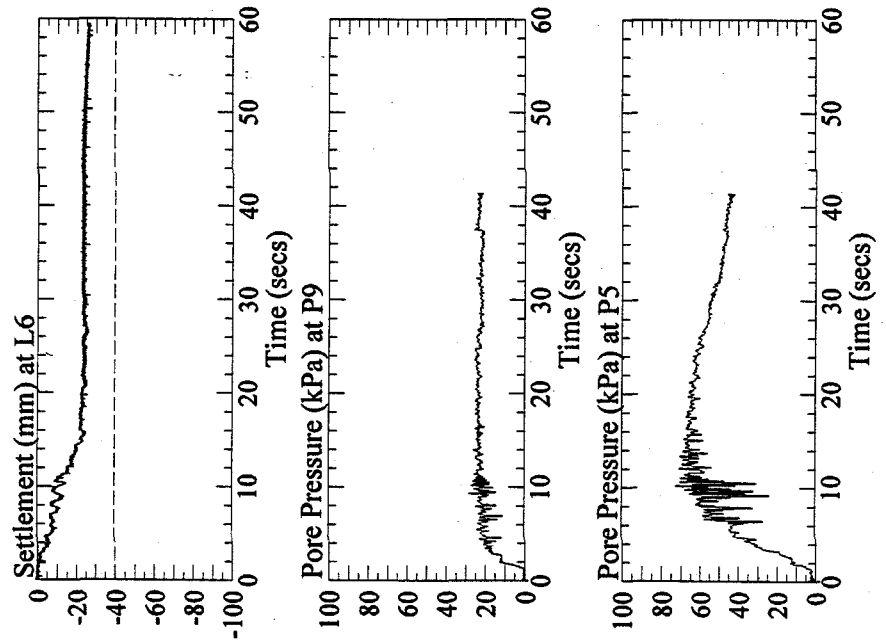

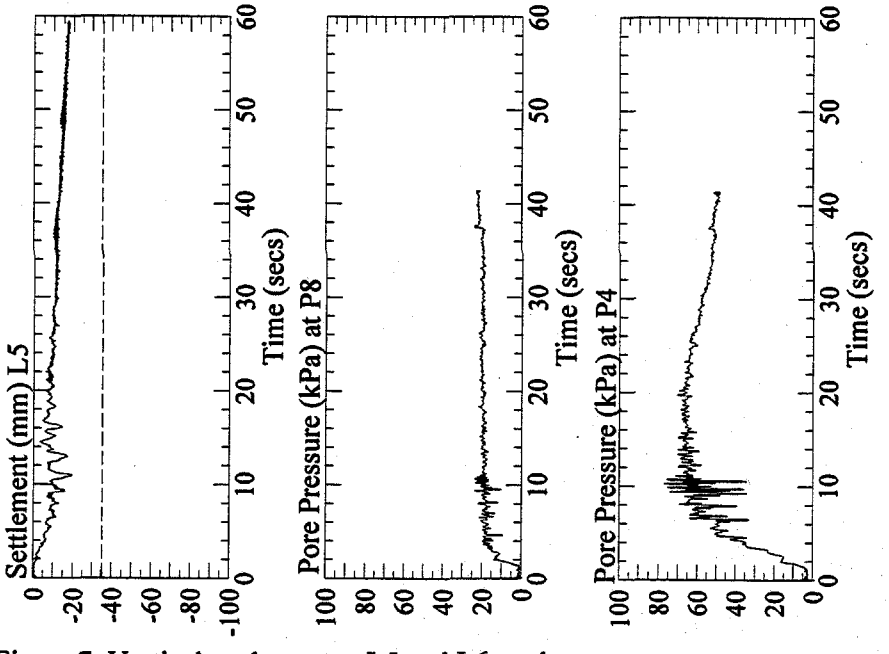

Figure 7: Vertical settlement at L5 and L6, and pore pressures at P4, P5, P8 and P9, recorded in the one-g model SM3F8. Pore pressure signals were post processed with a low pass filter of 10 Hz.

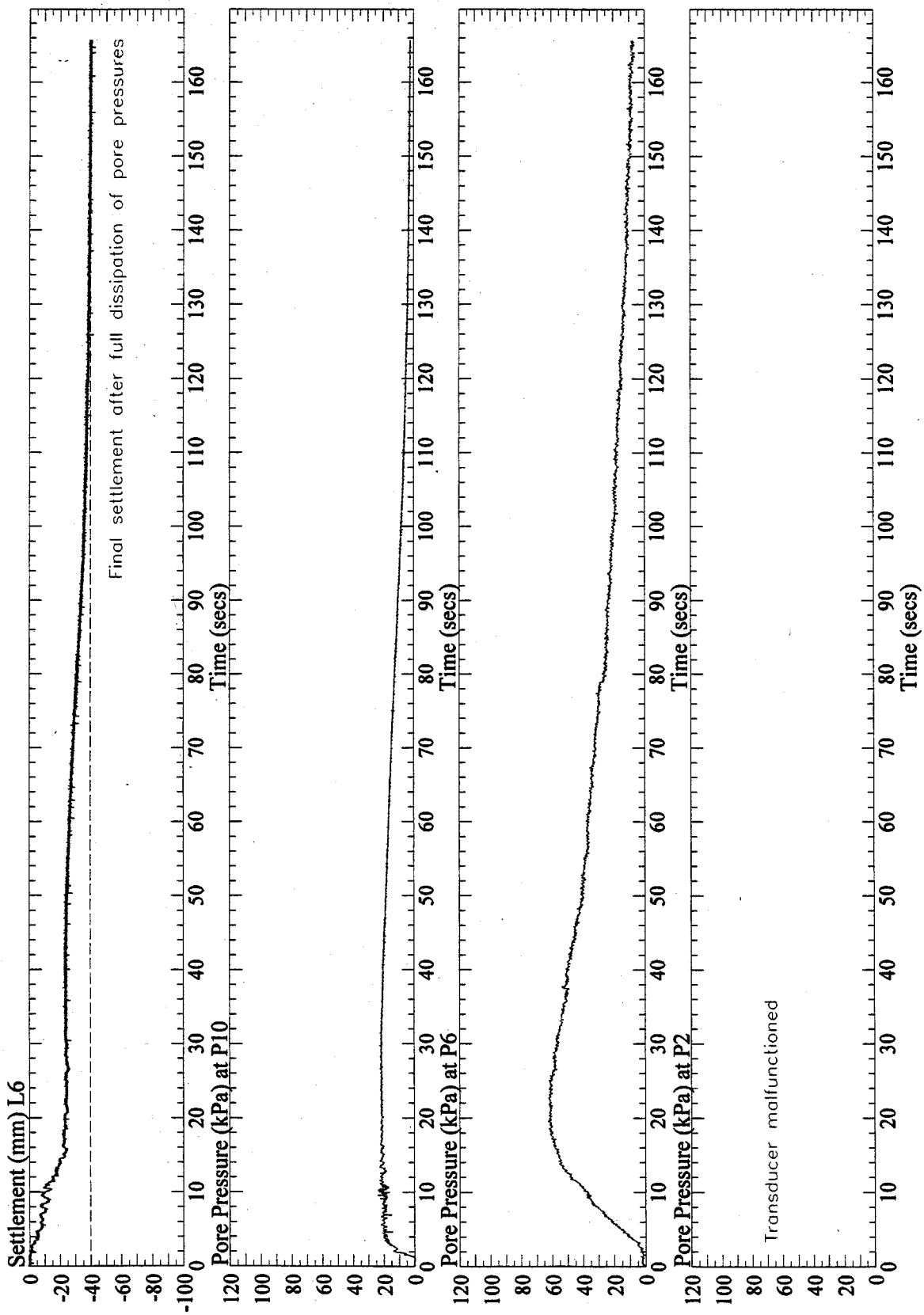

Figure 8: Vertical settlement at L6 and pore pressures at P2, P6, and P10, recorded in the one-g model SM3F8. Signal from P2 and P6 were post processed with a low pass filter of 10 Hz.

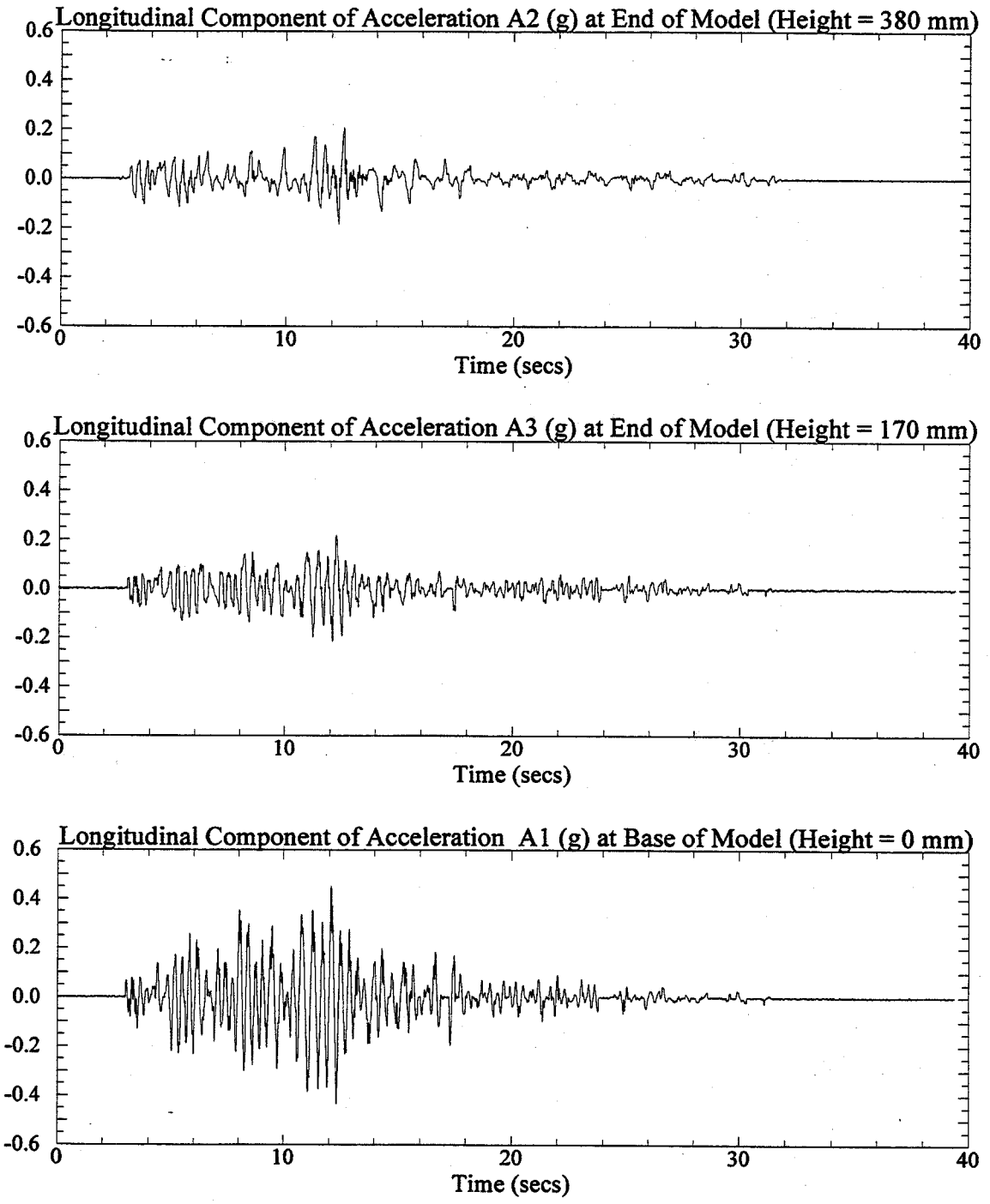

Figure 1: Longitudinal components of recorded acceleration at the base and end of the one-g model SM3G1. Signals were post processed with a low pass filter of 20 Hz.

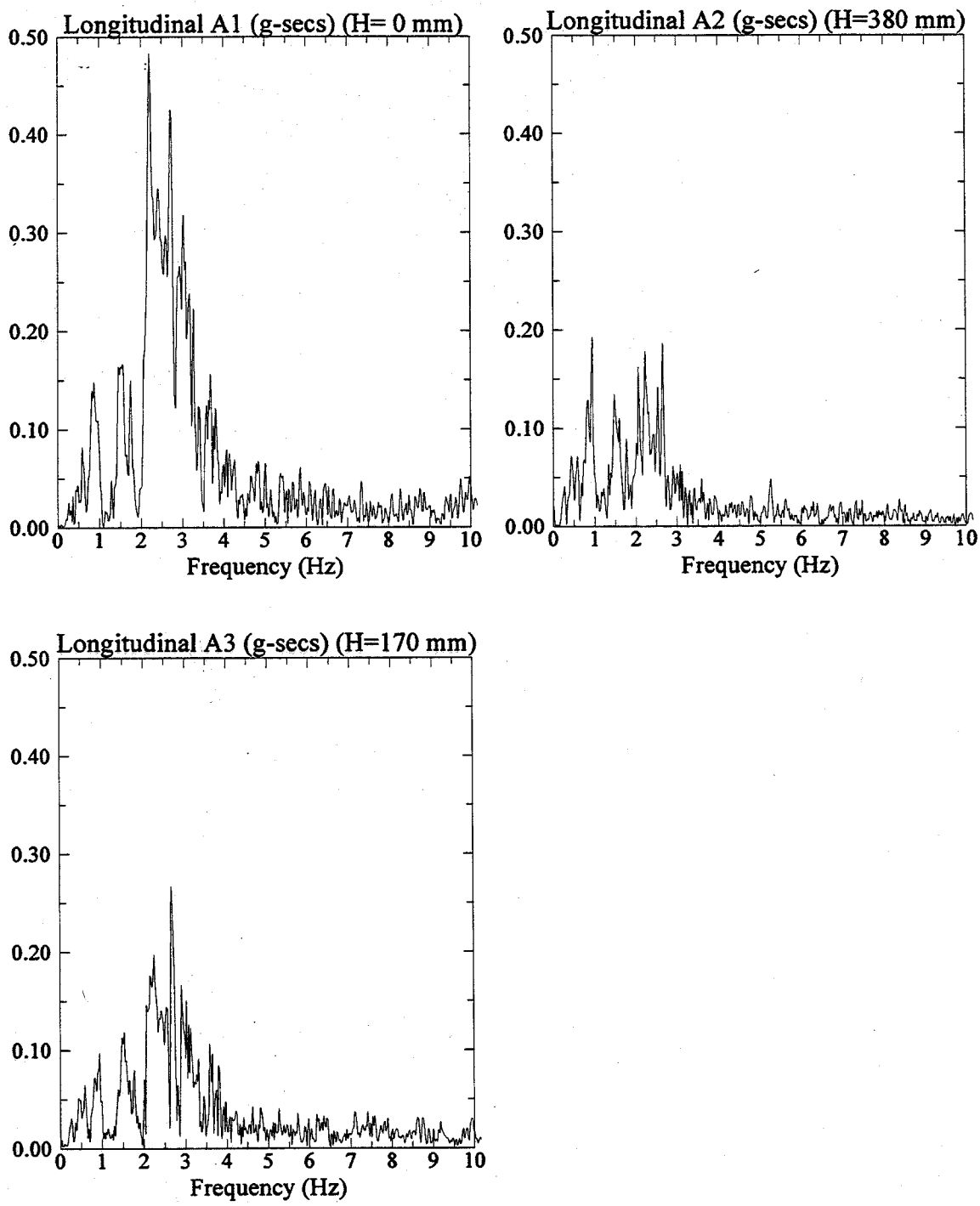

Figure 2: Fast Fourier Transform of longitudinal components of recorded acceleration at the base and end of the one-g model SM3G1.

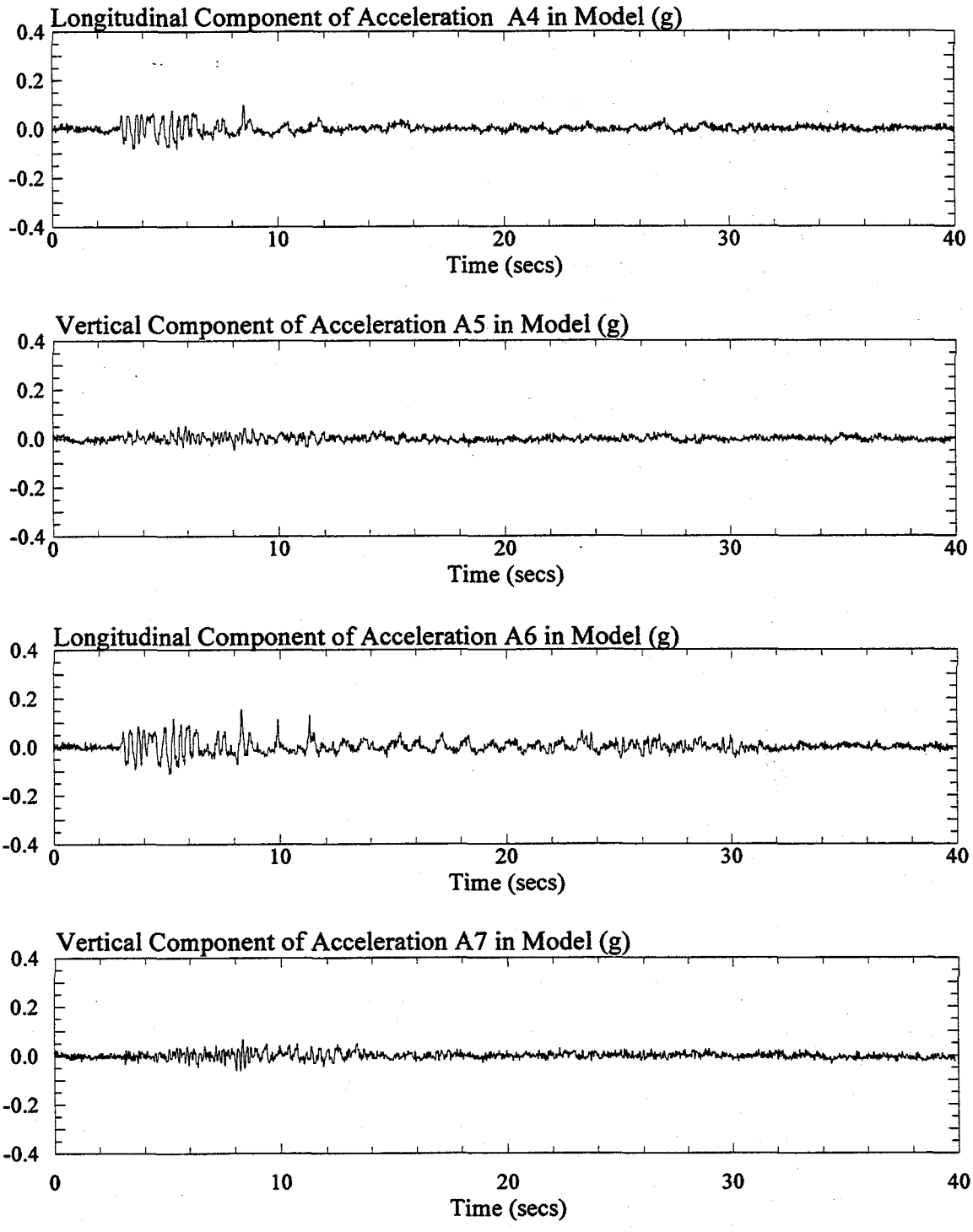

Figure 3: Longitudinal and vertical components of recorded acceleration in the one-g model SM3G1. Signals were post processed with a low pass filter of 20 Hz.

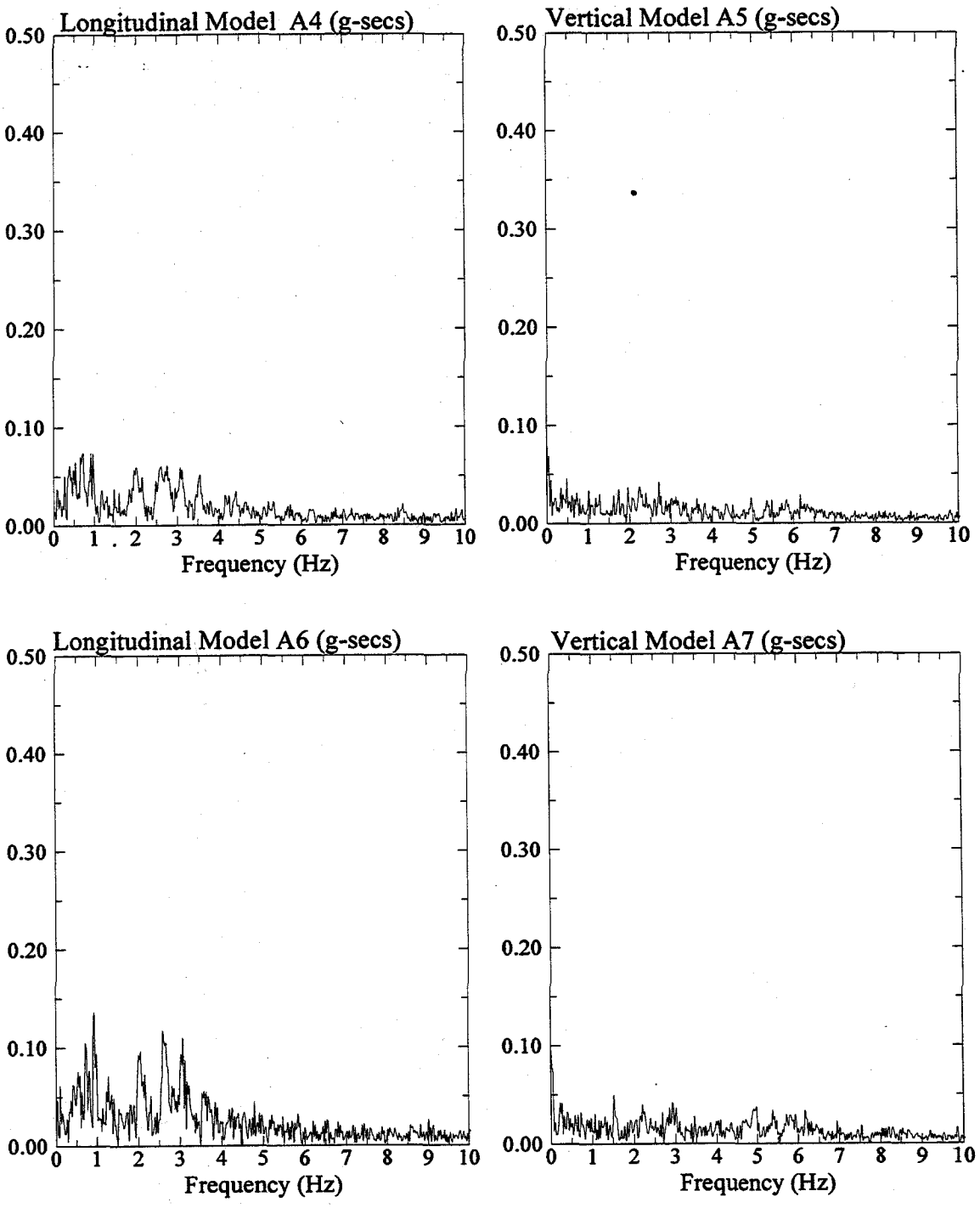

Figure 4: Fast Fourier Transform of longitudinal and vertical components of recorded acceleration in the one-g model SM3G1.

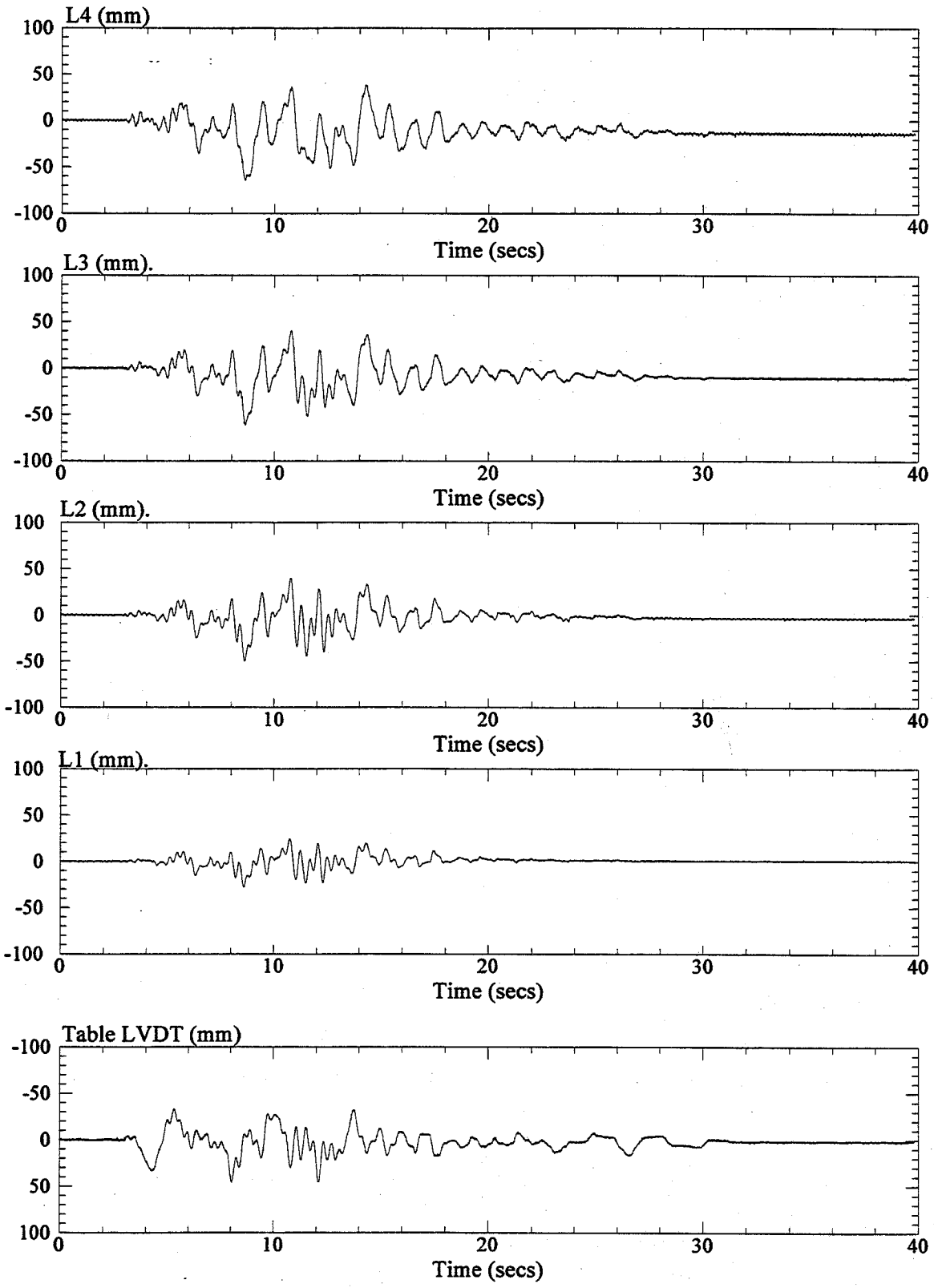

Figure 5: Longitudinal displacements recorded from the shake table LVDT and at LVDT's L1, L2, L3, and L4 in the one-g model SM3G1.

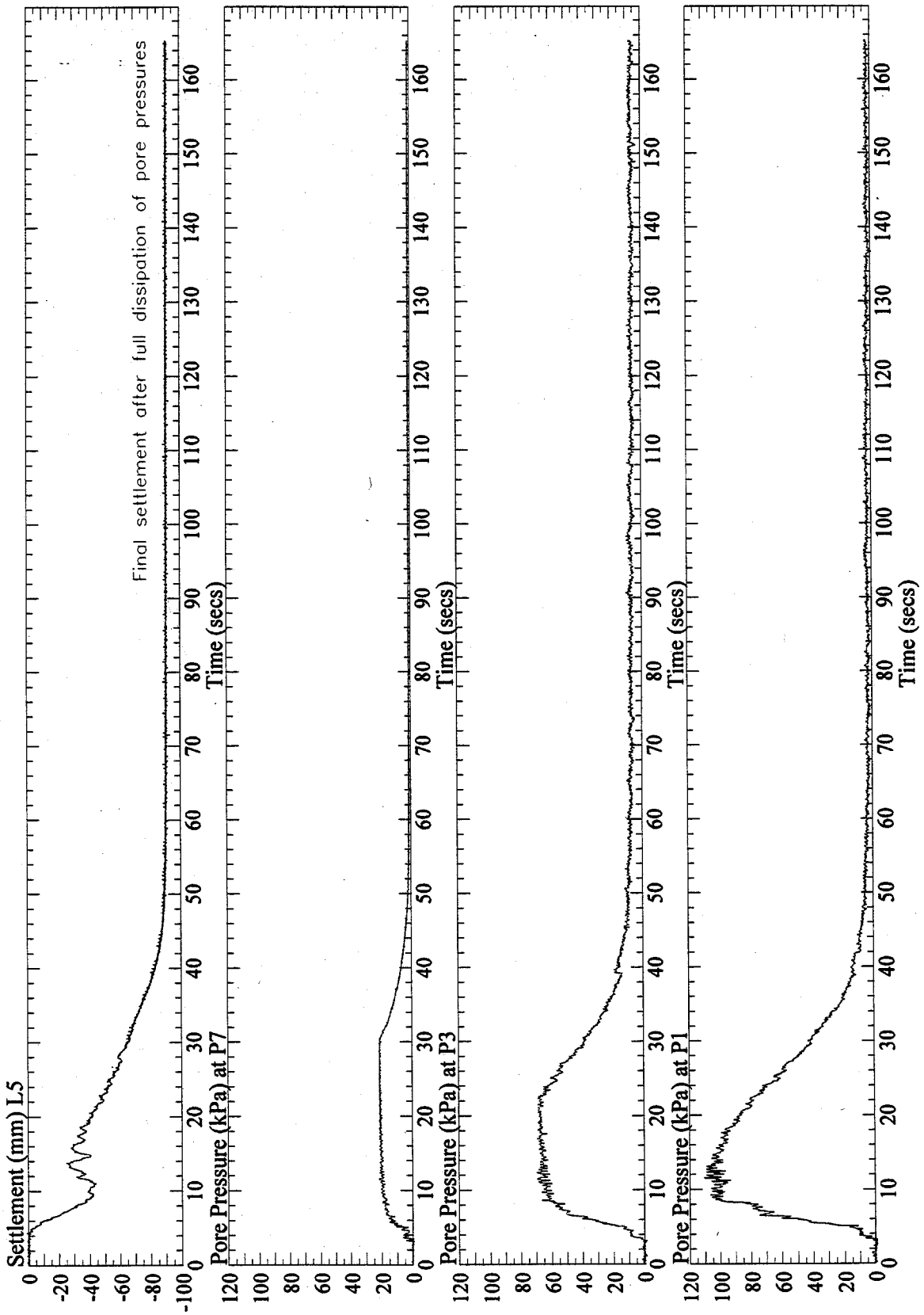

Figure 6: Vertical settlement at L5 and pore pressures at P1, P3, and P7, recorded in the one-g model SM3G1. Signals from P1 and P3 were post processed with a low pass filter of 10 Hz.

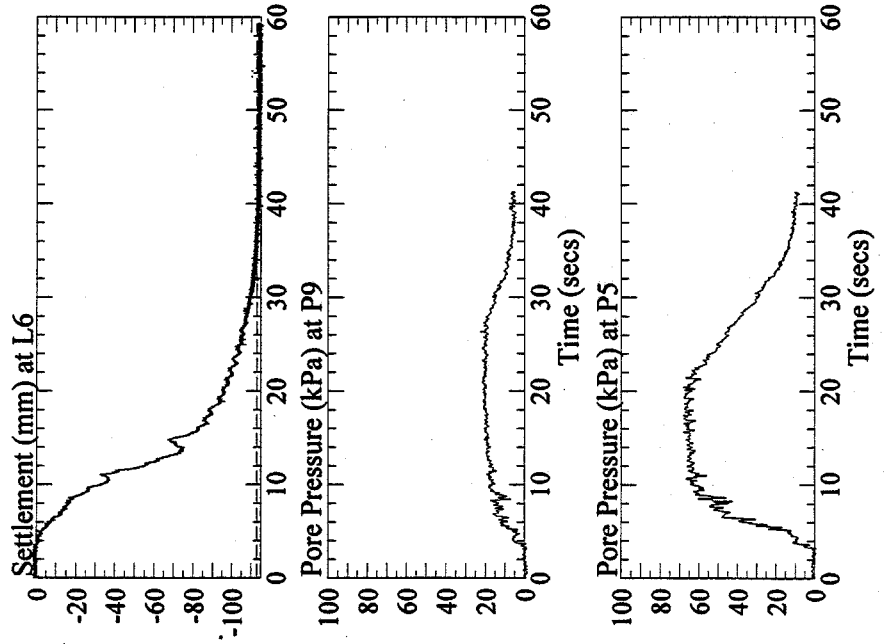

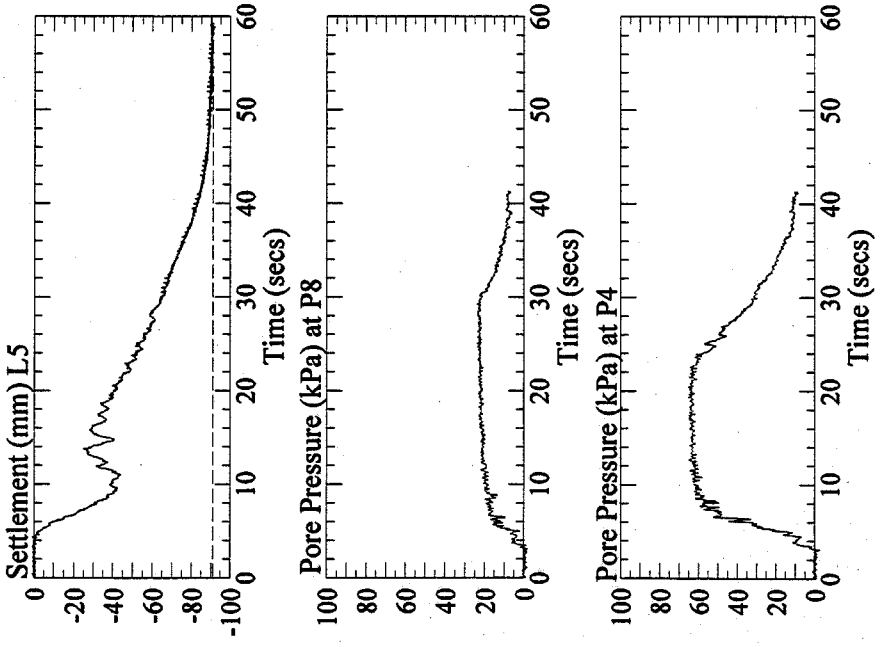

Figure 7: Vertical settlement at L5 and L6, and pore pressures at P4, P5, P8 and P9, recorded in the one-g model SM3G1. Pore pressure signals were post processed with a low pass filter of 10 Hz.

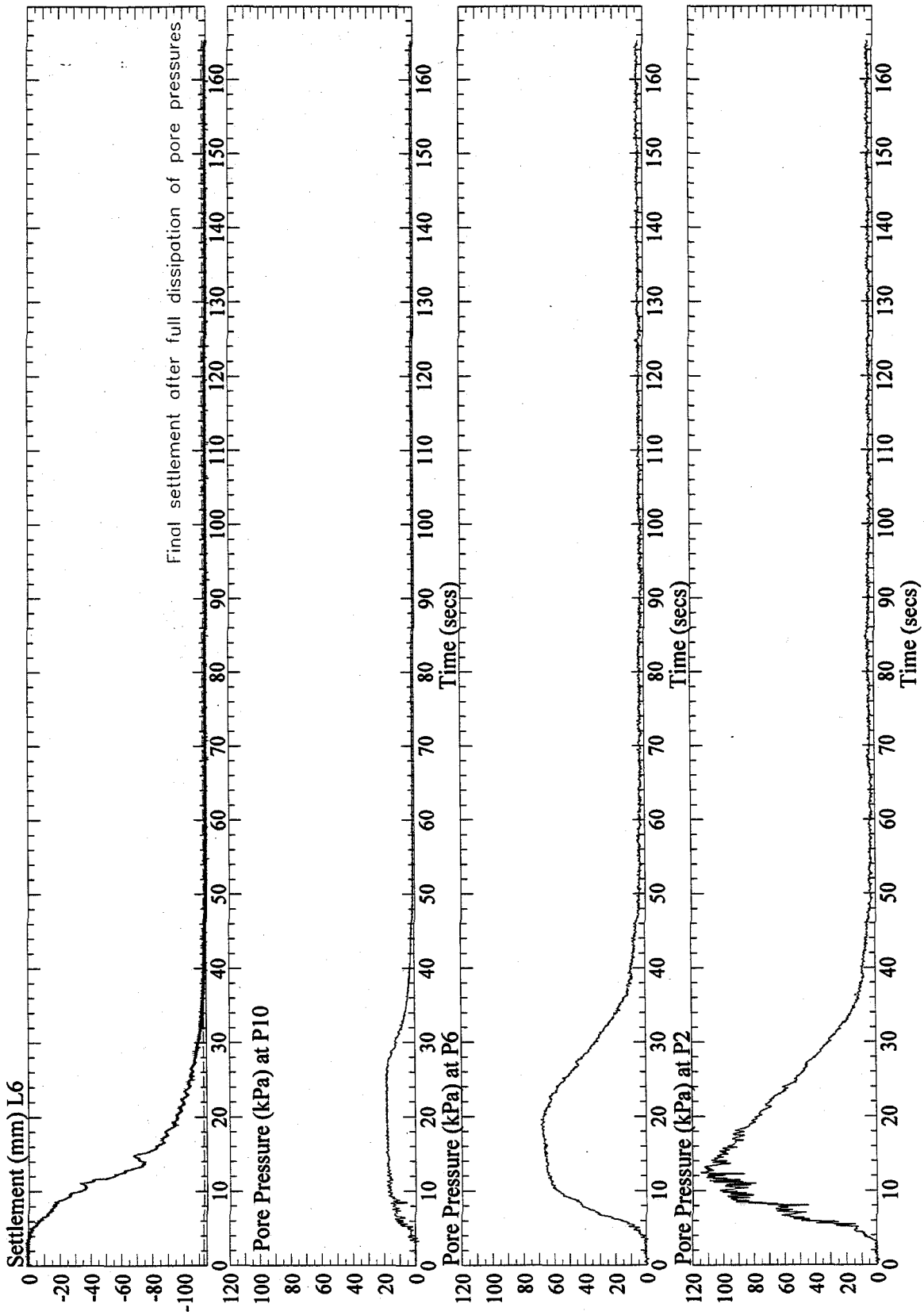

Figure 8: Vertical settlement at L6 and pore pressures at P2, P6, and P10, recorded in the one-g model SM3G1. Signal from P2 and P6 were post processed with a low pass filter of 10 Hz.

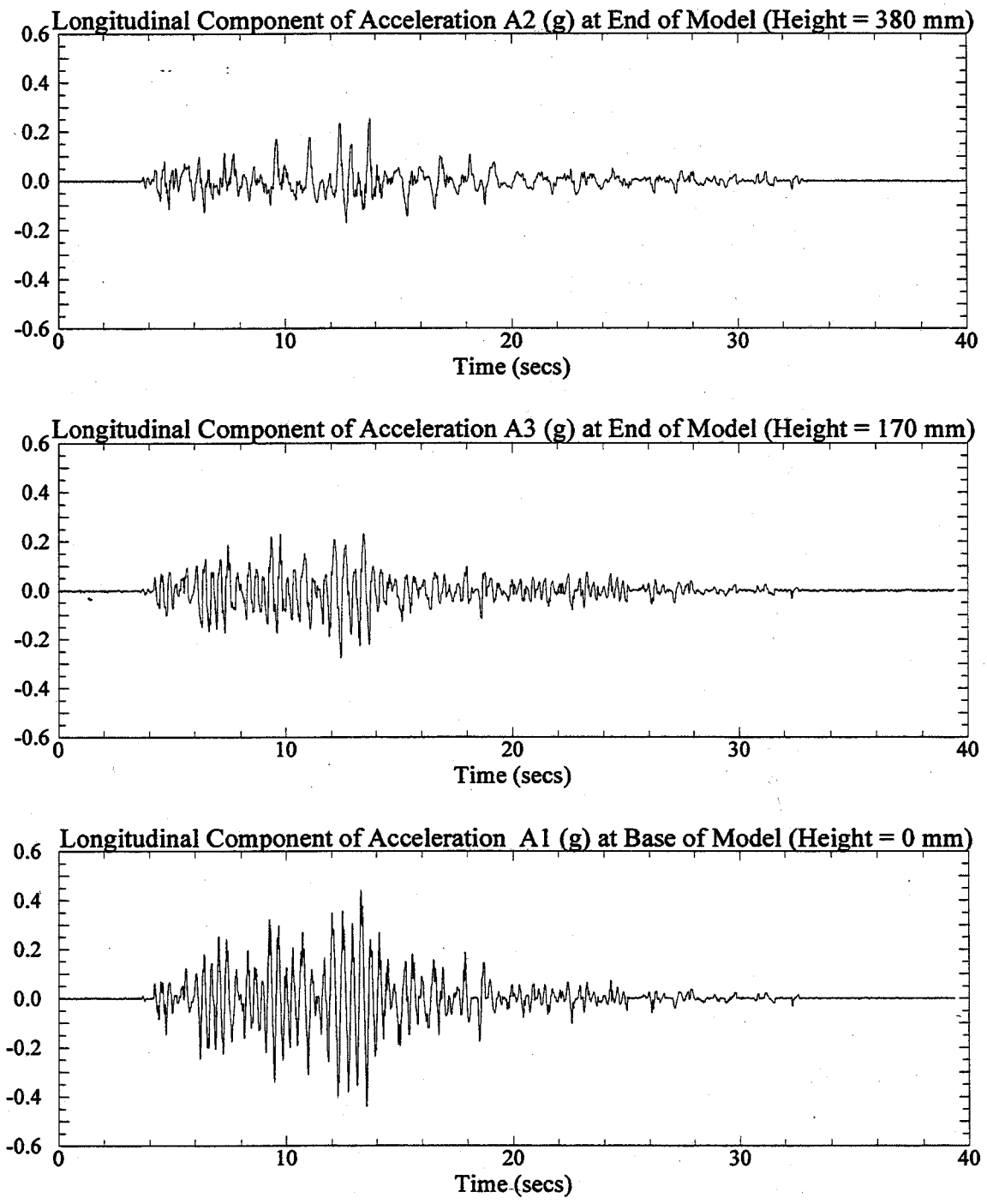

Figure 1: Longitudinal components of recorded acceleration at the base and end of the one-g model SM3G2. Signals were post processed with a low pass filter of 20 Hz.

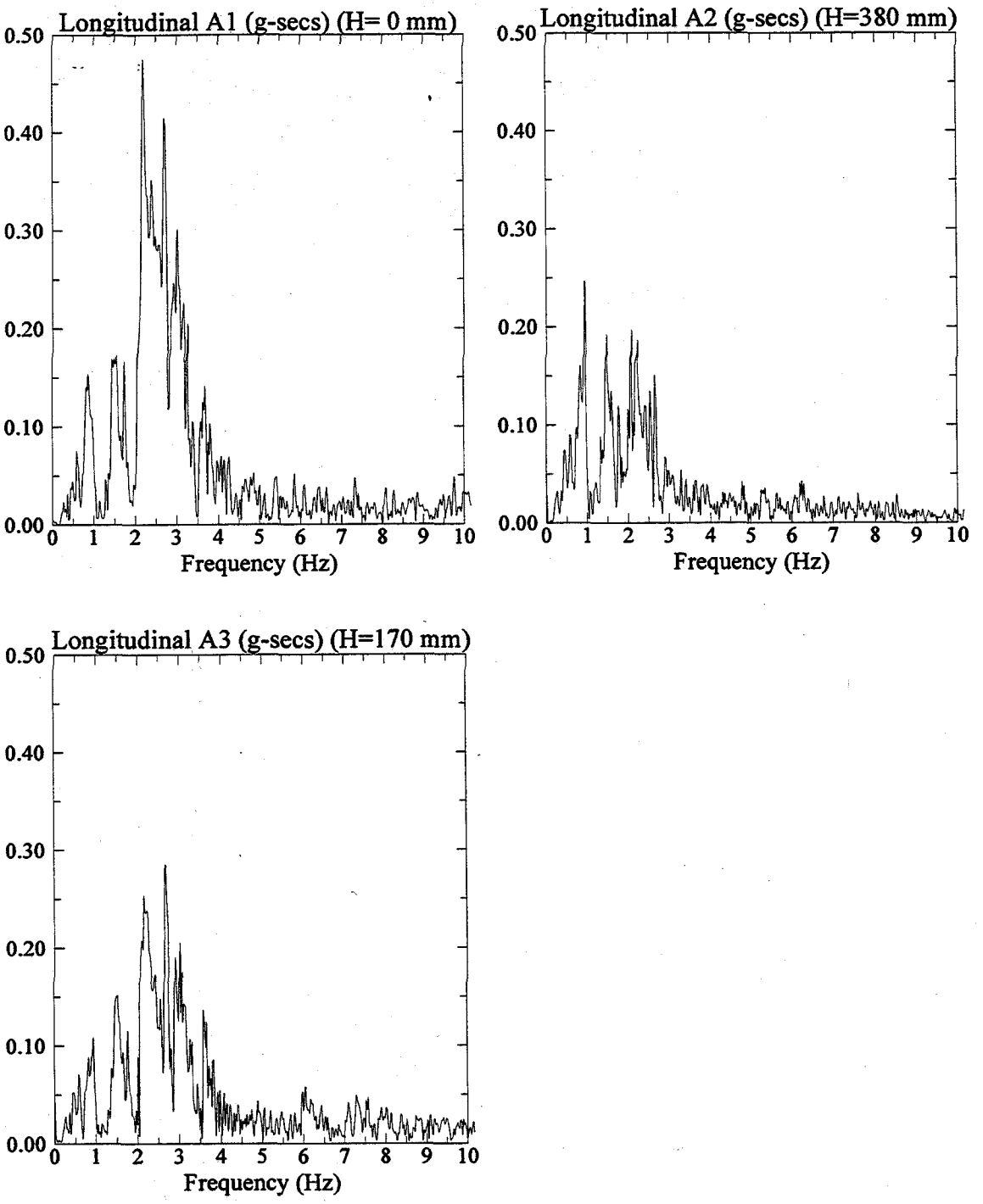

Figure 2: Fast Fourier Transform of longitudinal components of recorded acceleration at the base and end of the one-g model SM3G2.

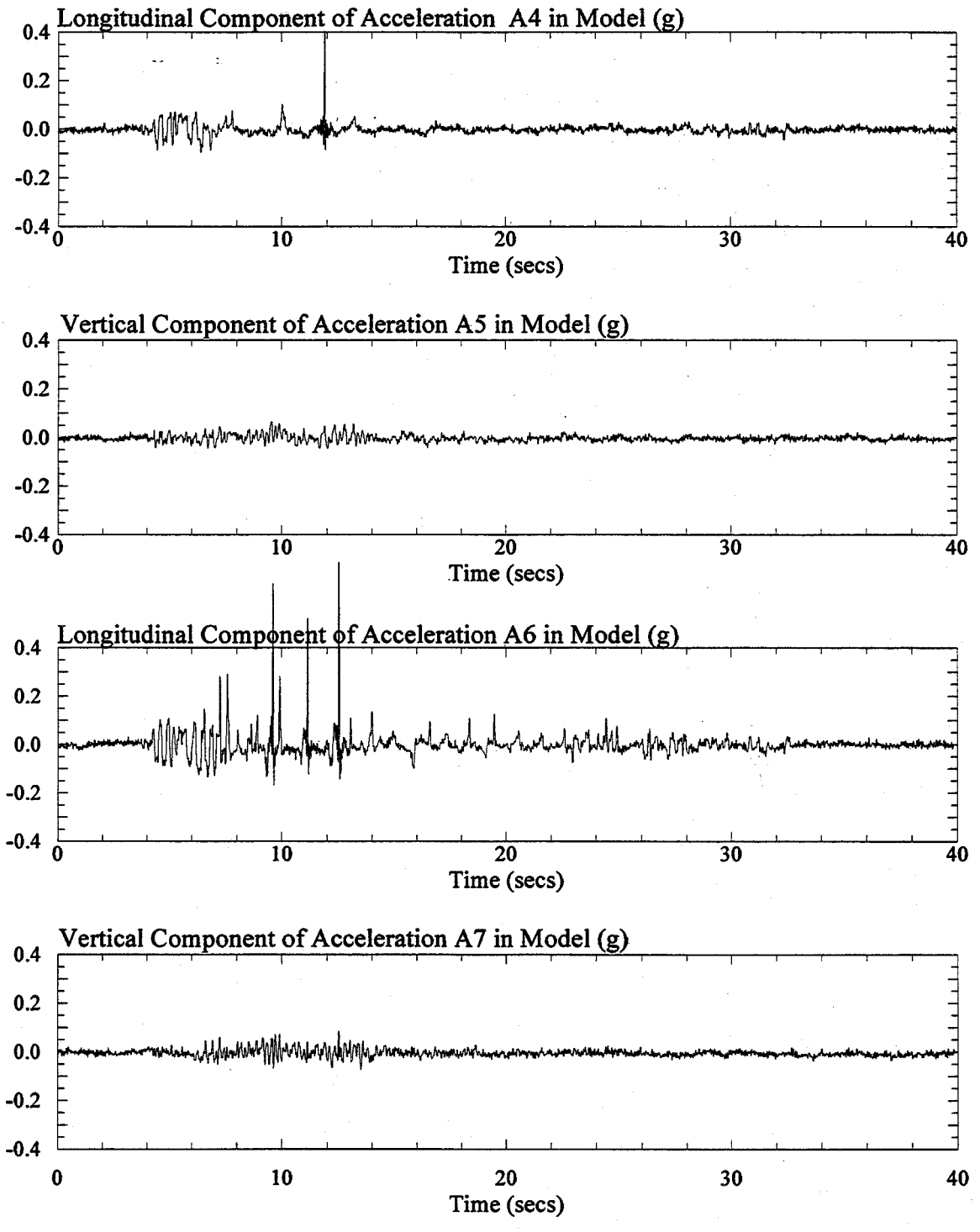

Figure 3: Longitudinal and vertical components of recorded acceleration in the one-g model SM3G2. Signals were post processed with a low pass filter of 20 Hz.

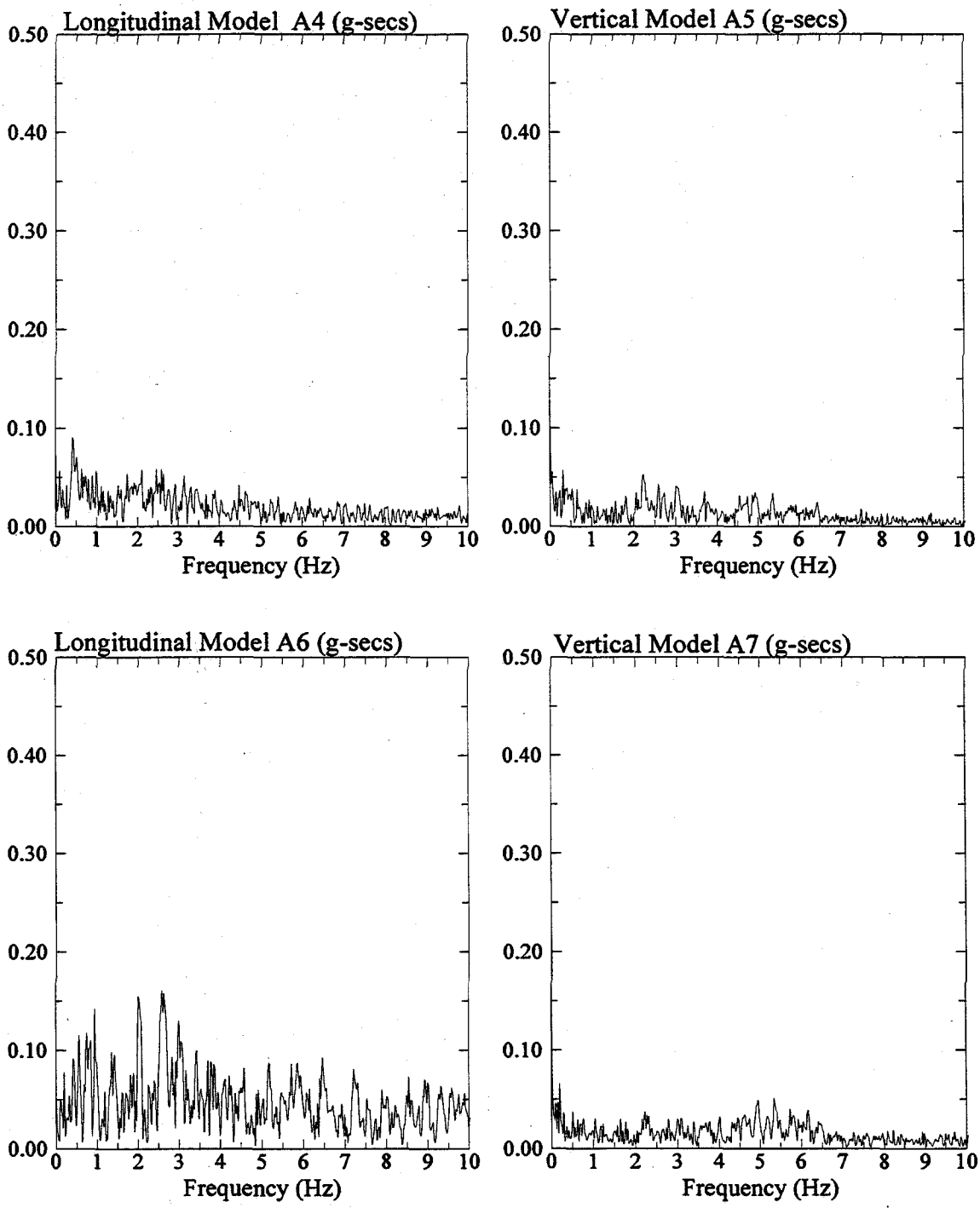

Figure 4: Fast Fourier Transform of longitudinal and vertical components of recorded acceleration in the one-g model SM3G2.

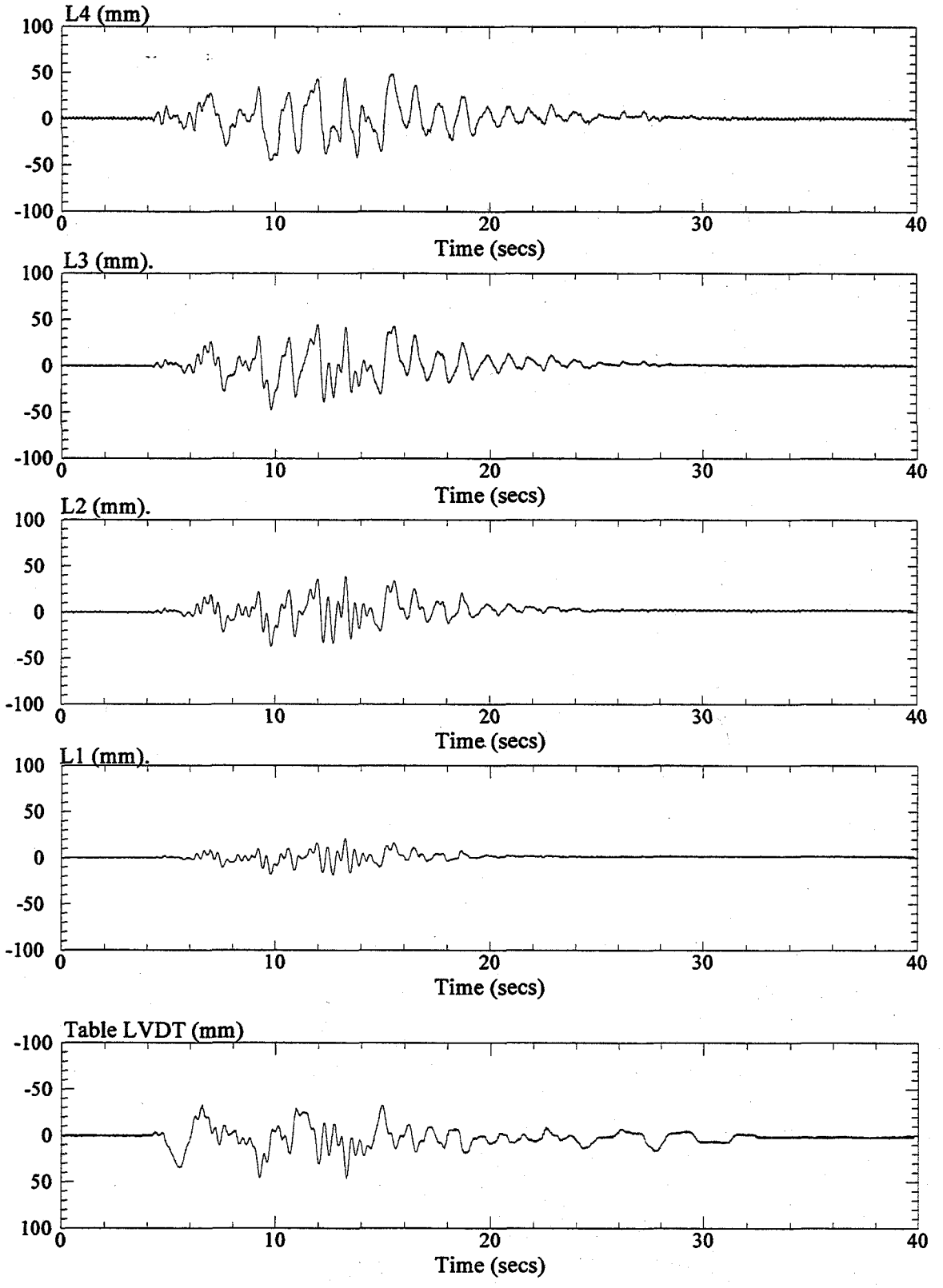

Figure 5: Longitudinal displacements recorded from the shake table LVDT and at LVDT's L1, L2, L3, and L4 in the one-g model SM3G2.

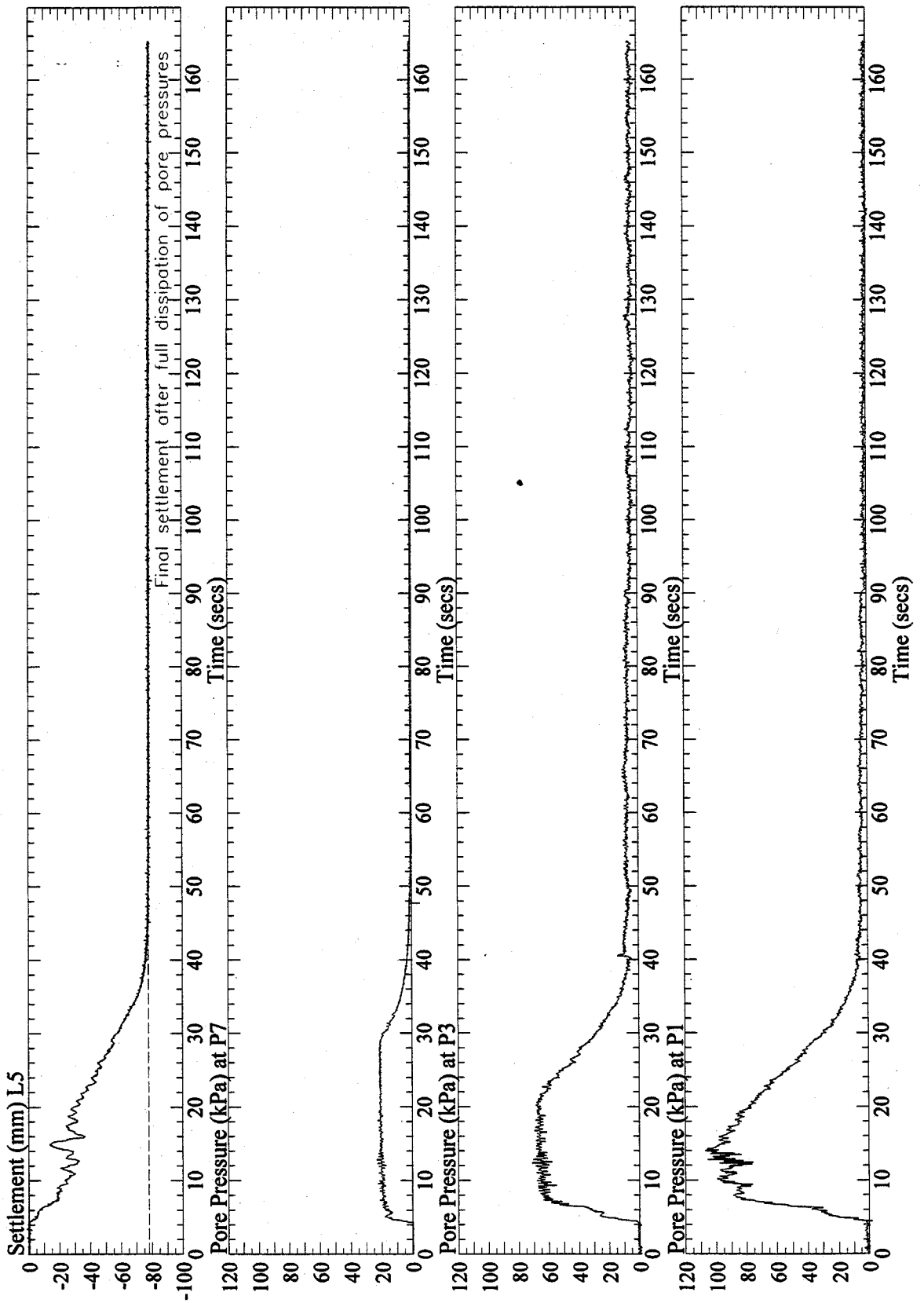

Figure 6: Vertical settlement at L5 and pore pressures at P1, P3, and P7, recorded in the one-g model SM3G2. Signals from P1 and P3 were post processed with a low pass filter of 10 Hz.

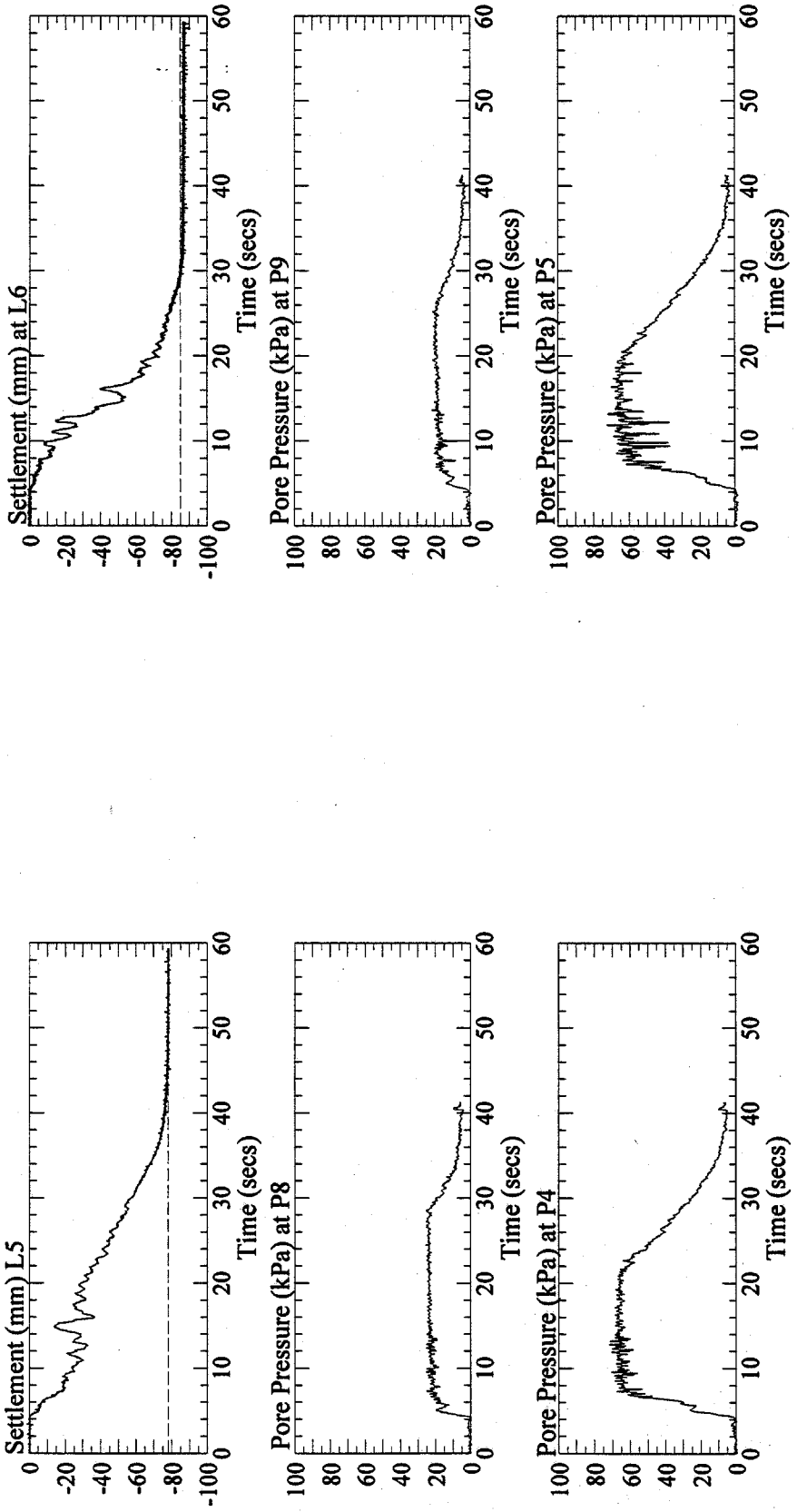

Figure 7: Vertical settlement at L5 and L6, and pore pressures at P4, P5, P8 and P9, recorded in the one-g model SM3G2. Pore pressure signals were post processed with a low pass filter of 10 Hz.

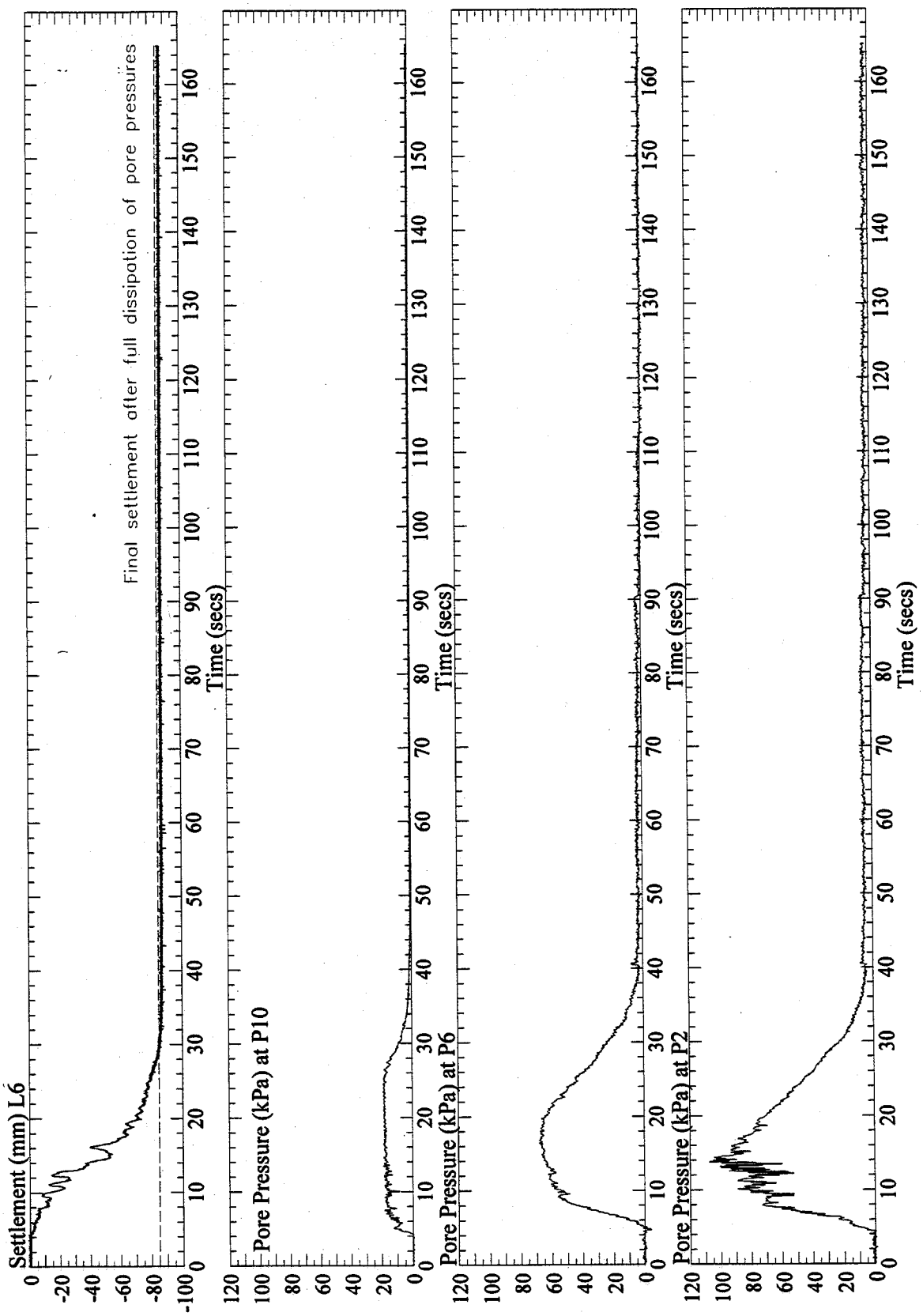

Figure 8: Vertical settlement at L6 and pore pressures at P2, P6, and P10, recorded in the one-g model SM3G2. Signal from P2 and P6 were post processed with a low pass filter of 10 Hz.

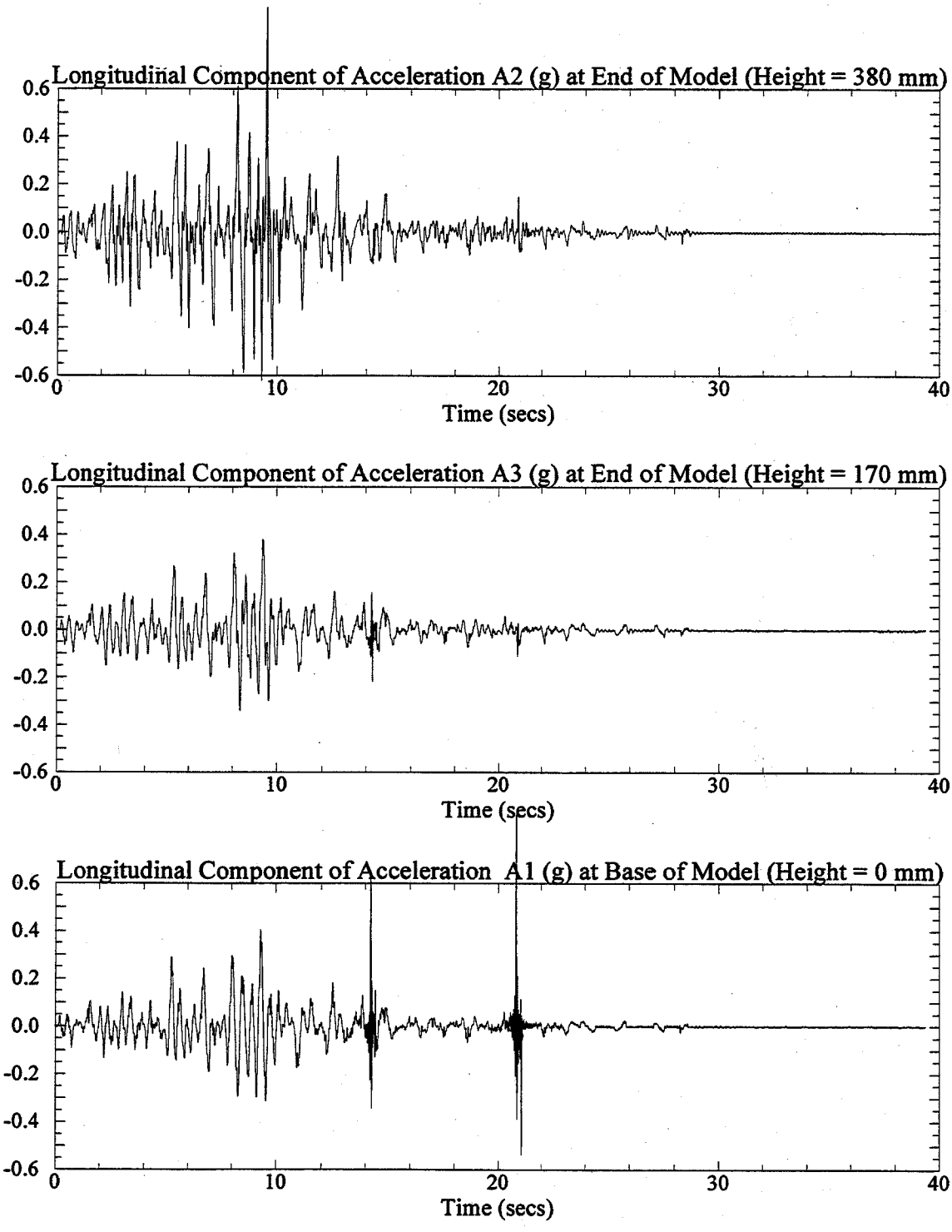

Figure 1: Longitudinal components of recorded acceleration at the base and end of the one-g model SM3G7. Signals were post processed with a low pass filter of 20 Hz.

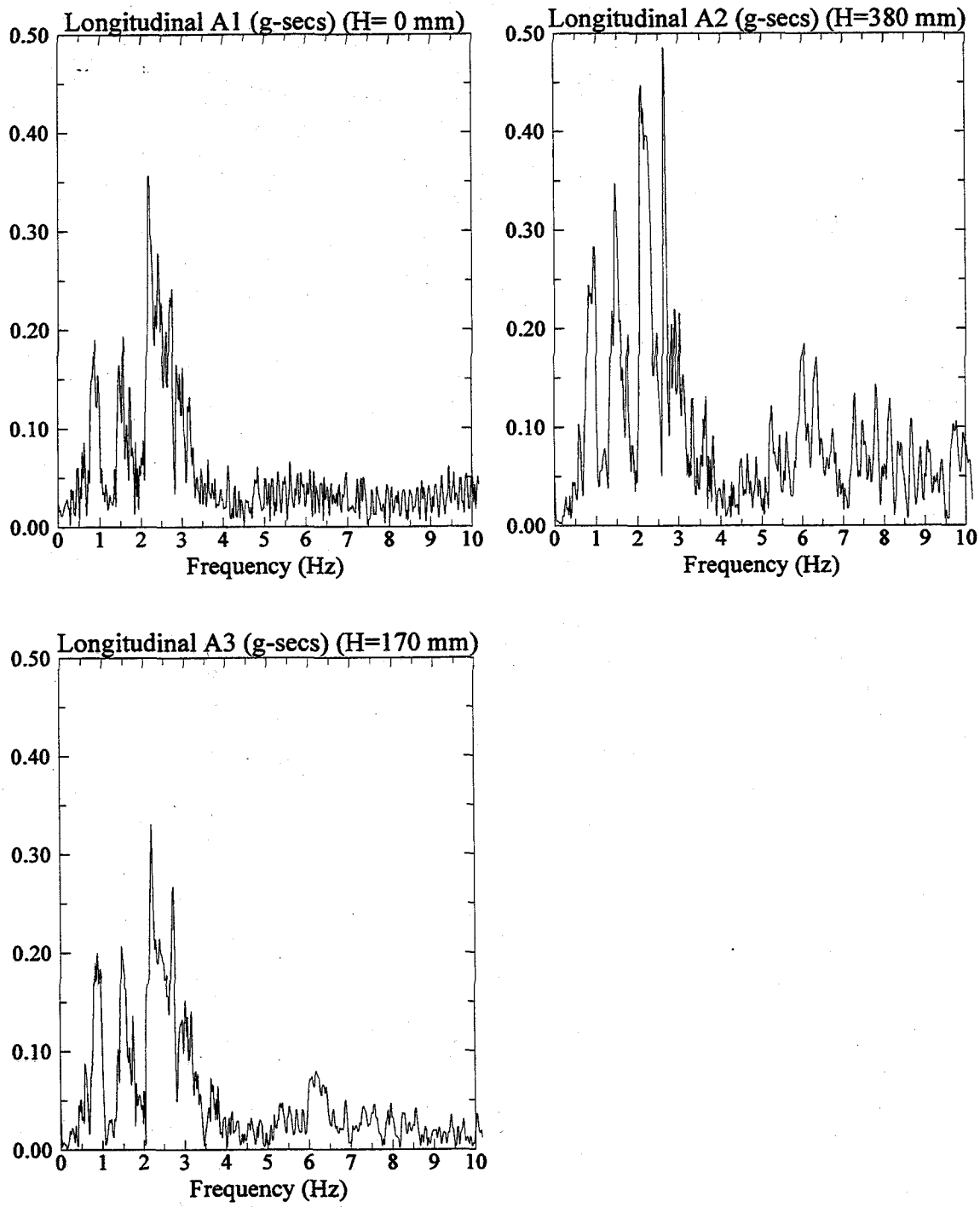

Figure 2: Fast Fourier Transform of longitudinal components of recorded acceleration at the base and end of the one-g model SM3G7.

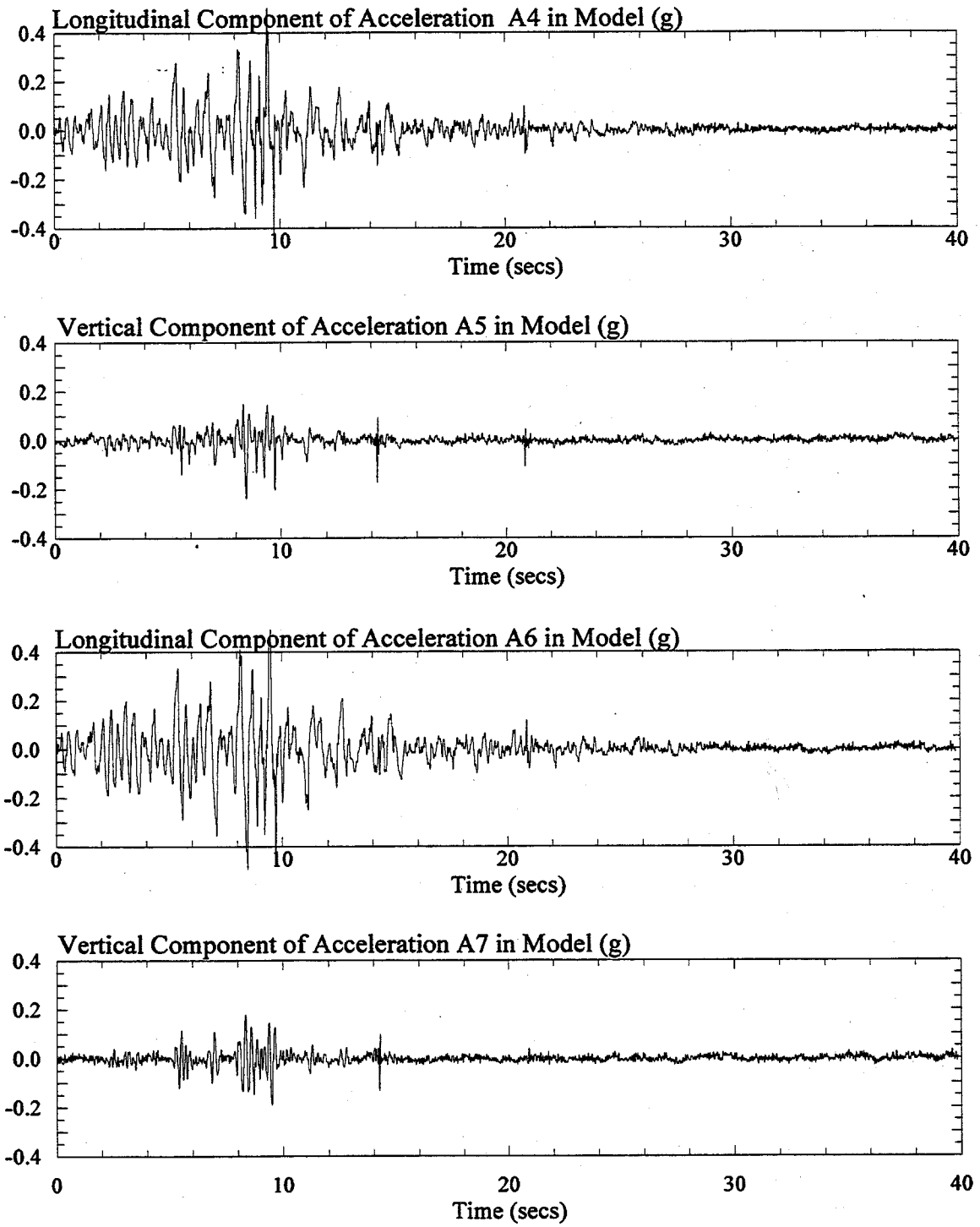

Figure 3: Longitudinal and vertical components of recorded acceleration in the one-g model SM3G7. Signals were post processed with a low pass filter of 20 Hz.

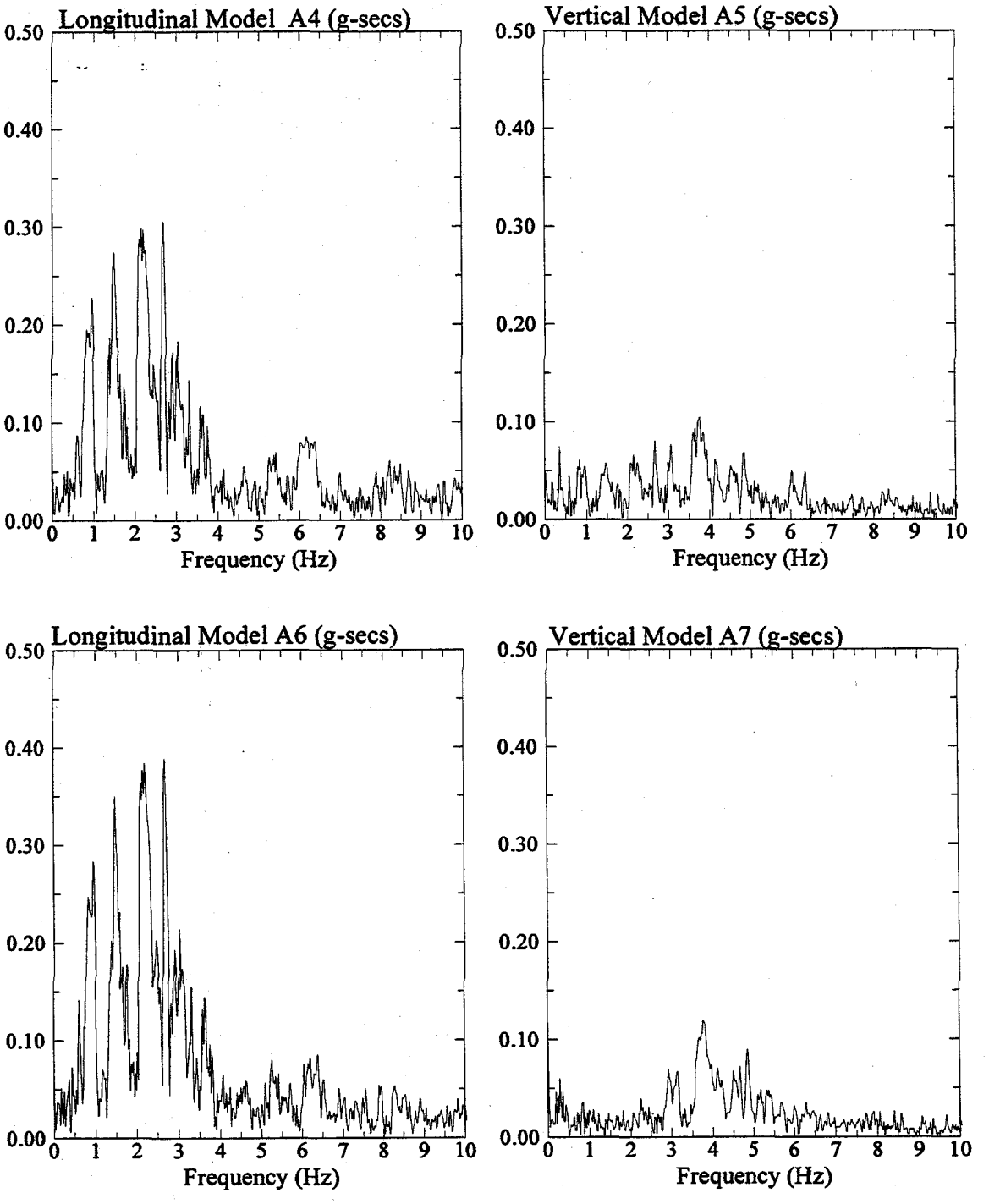

Figure 4: Fast Fourier Transform of longitudinal and vertical components of recorded acceleration in the one-g model SM3G7.

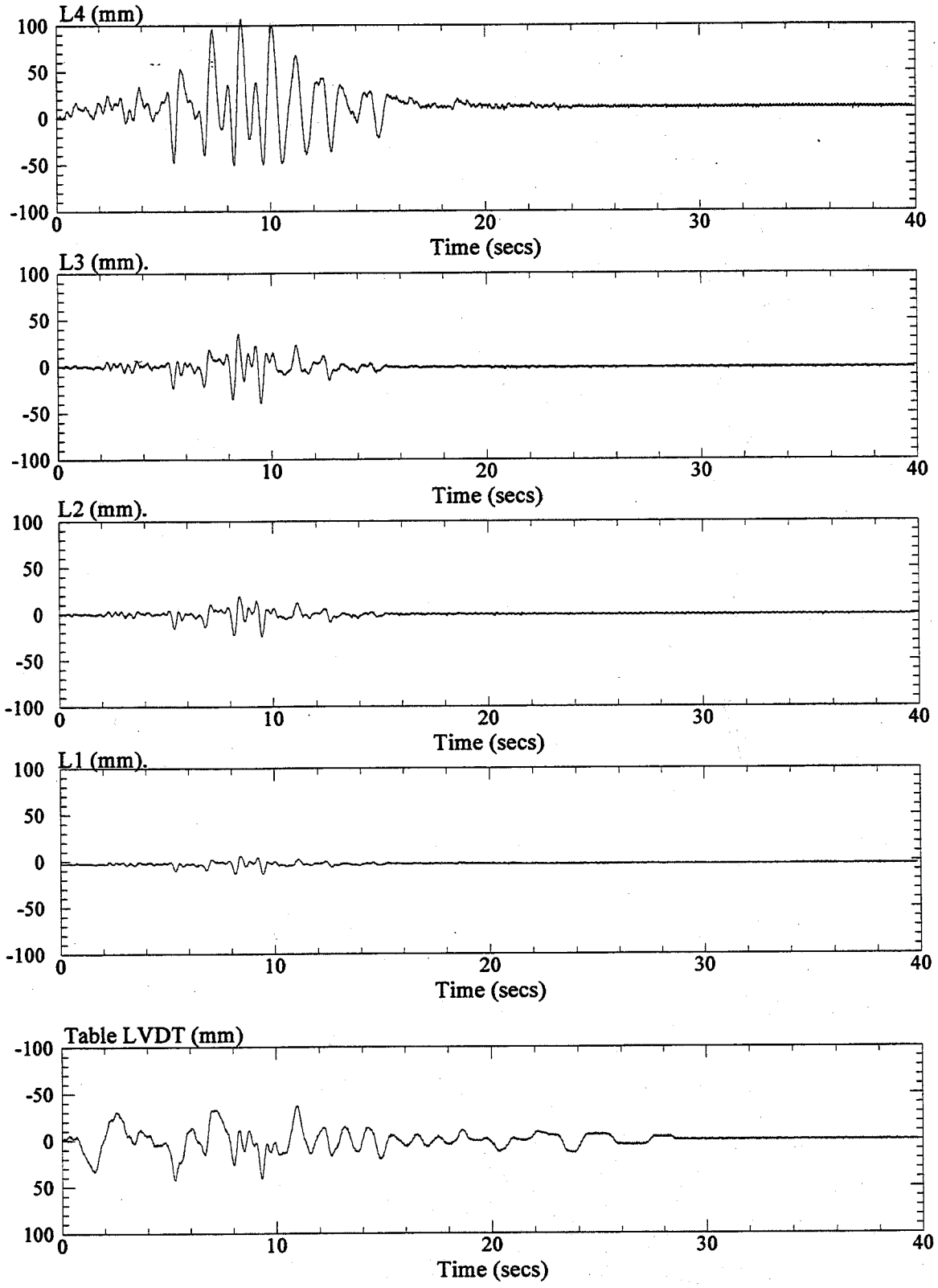

Figure 5: Longitudinal displacements recorded from the shake table LVDT and at LVDT's L1, L2, L3, and L4 in the one-g model SM3G7.

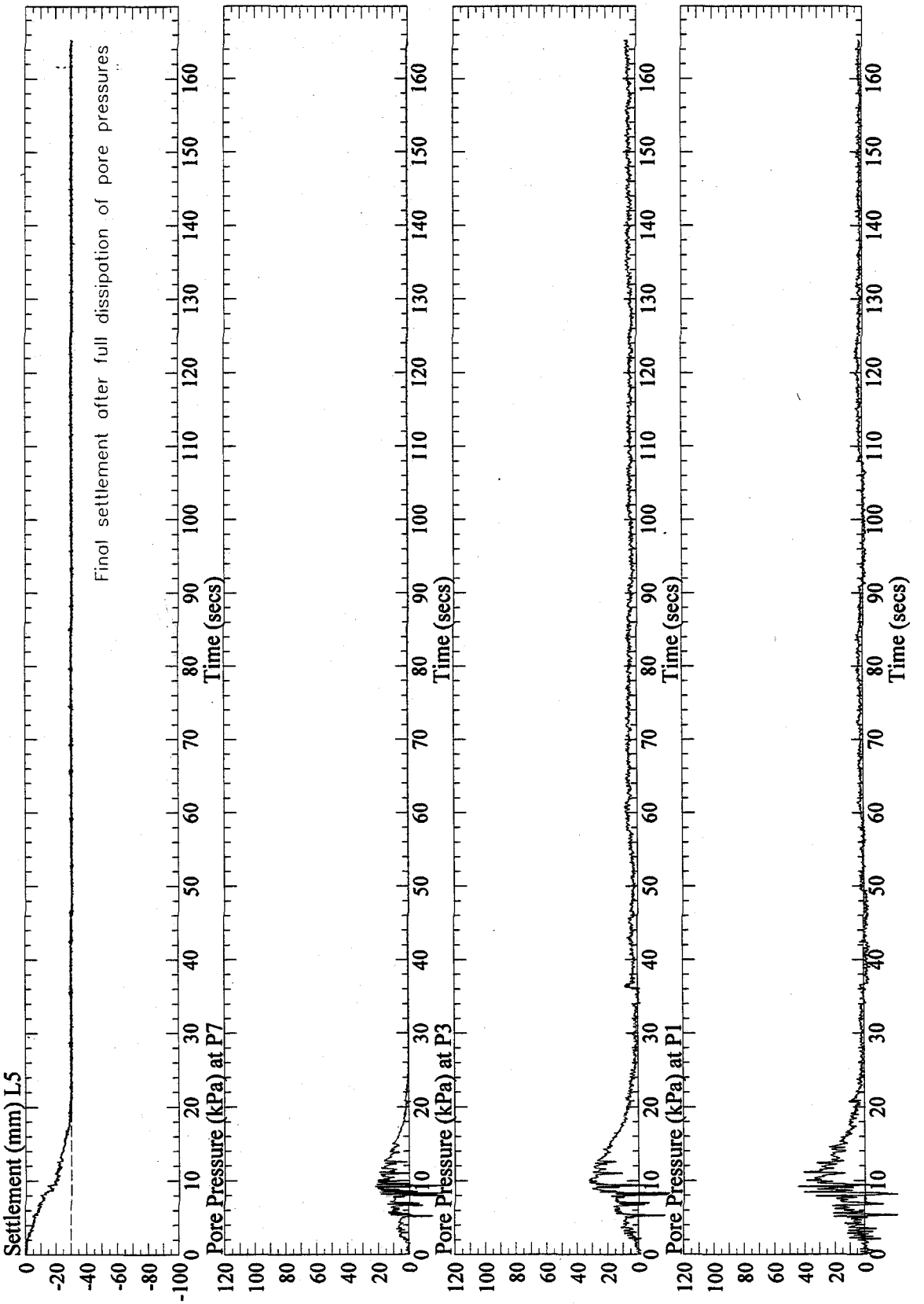

Figure 6: Vertical settlement at L5 and pore pressures at P1, P3, and P7, recorded in the one-g model SM3G7. Signals from P1 and P3 were post processed with a low pass filter of 10 Hz.

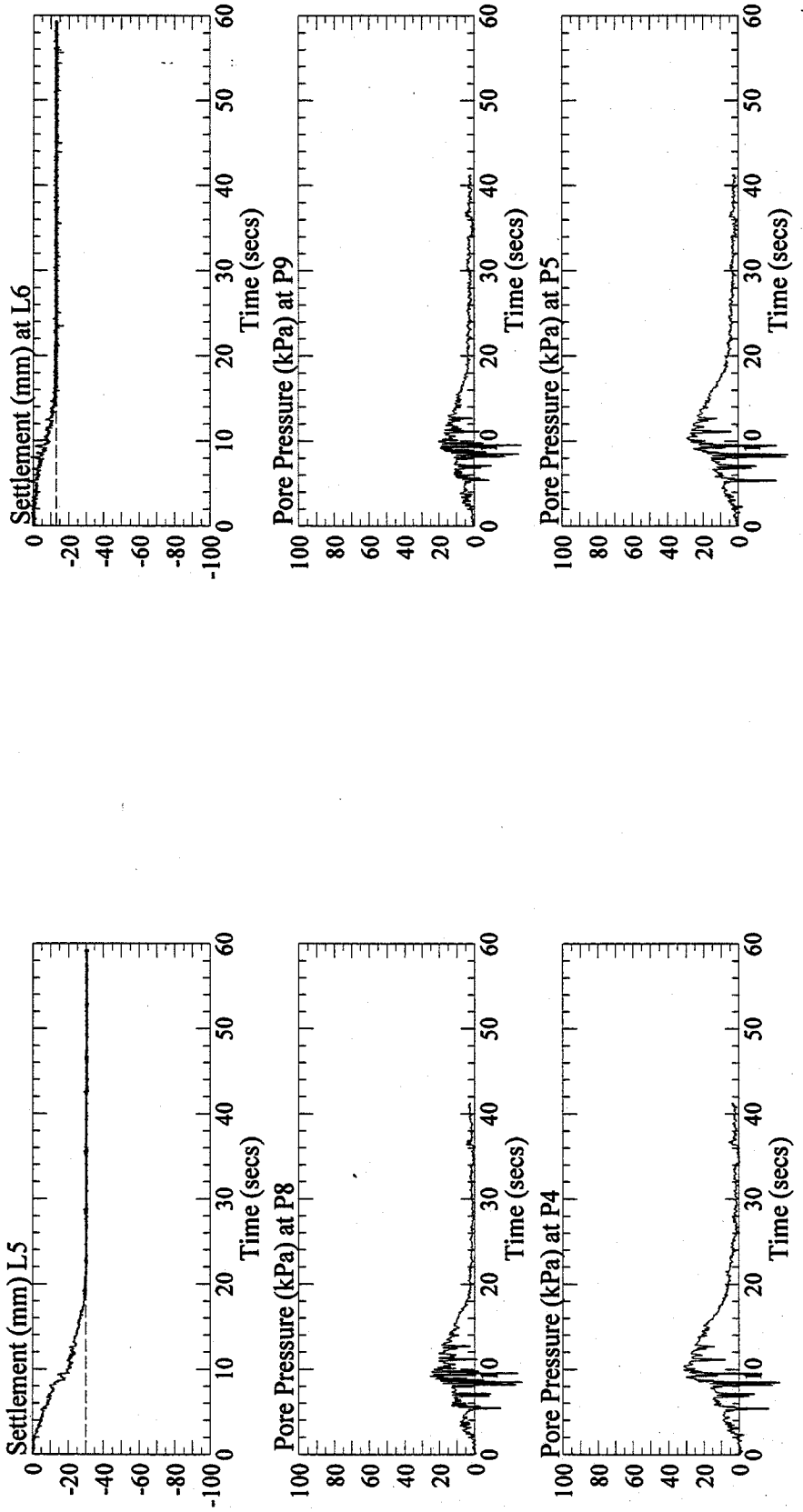

Figure 7: Vertical settlement at L5 and L6, and pore pressures at P4, P5, P8 and P9, recorded in the one-g model SM3G7. Pore pressure signals were post processed with a low pass filter of 10 Hz.

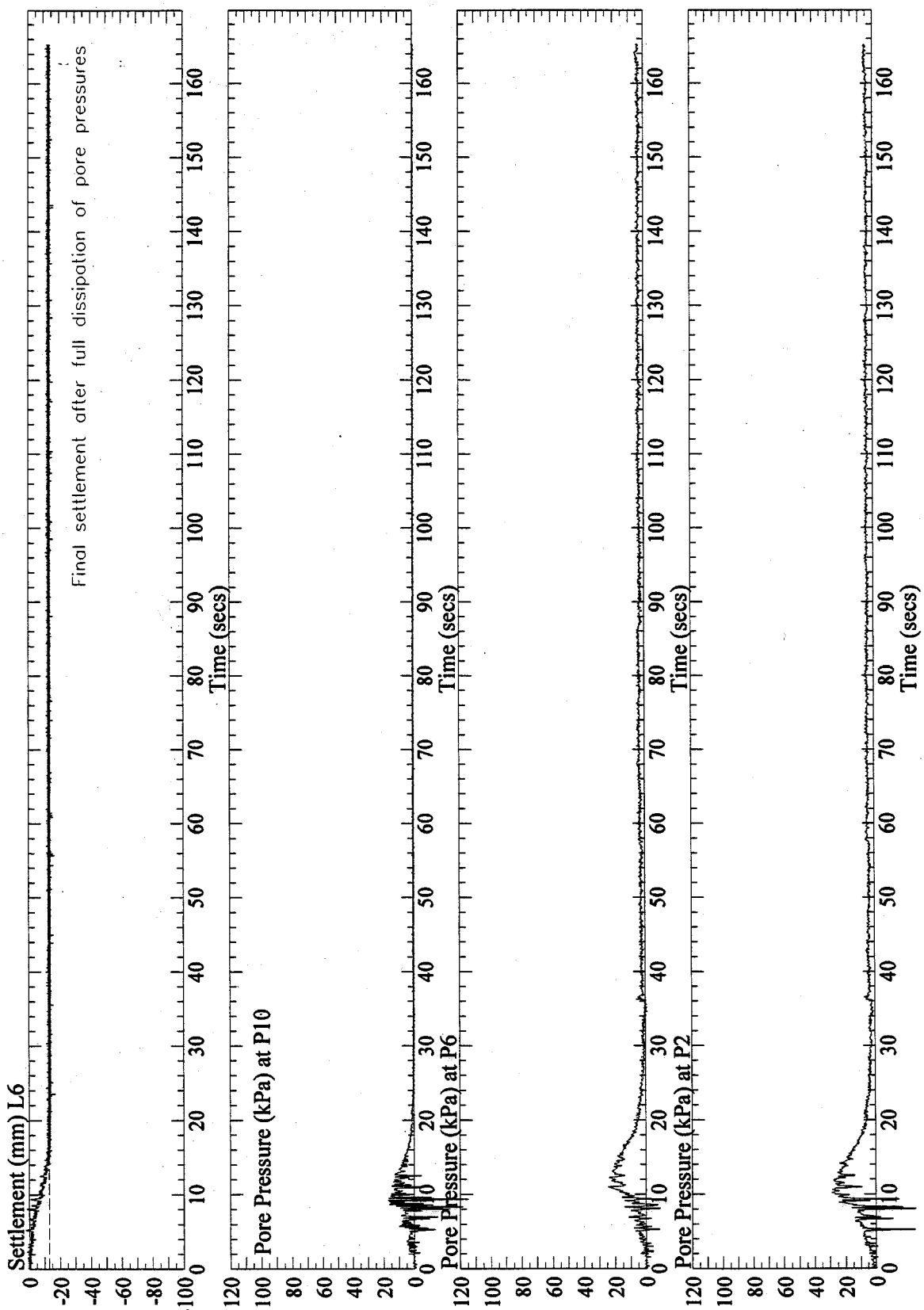

Figure 8: Vertical settlement at L6 and pore pressures at P2, P6, and P10, recorded in the one-g model SM3G7. Signal from P2 and P6 were post processed with a low pass filter of 10 Hz.

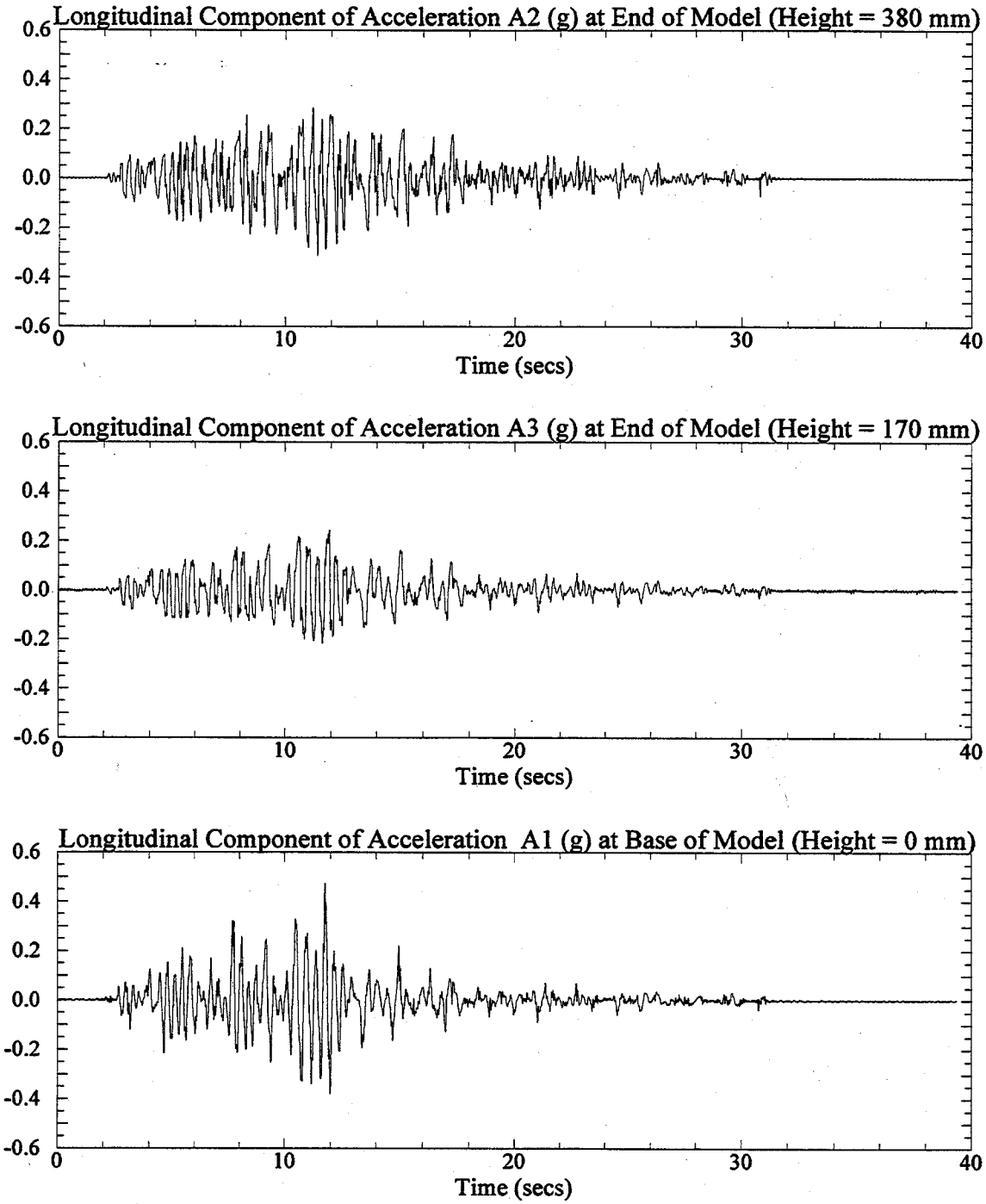

Figure 1: Longitudinal components of recorded acceleration at the base and end of the one-g model SM3H1. Signals were post processed with a low pass filter of 20 Hz.

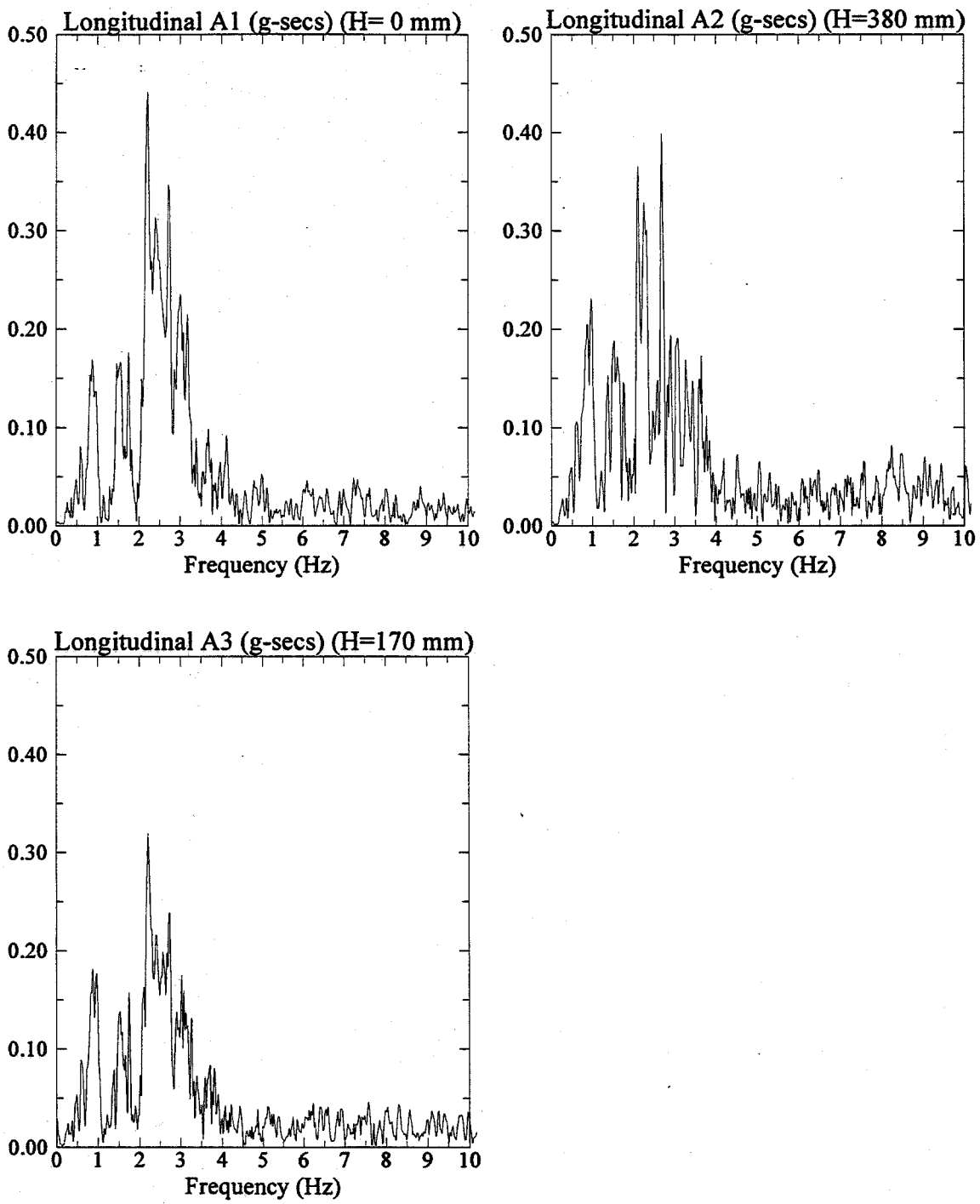

Figure 2: Fast Fourier Transform of longitudinal components of recorded acceleration at the base and end of the one-g model SM3H1.

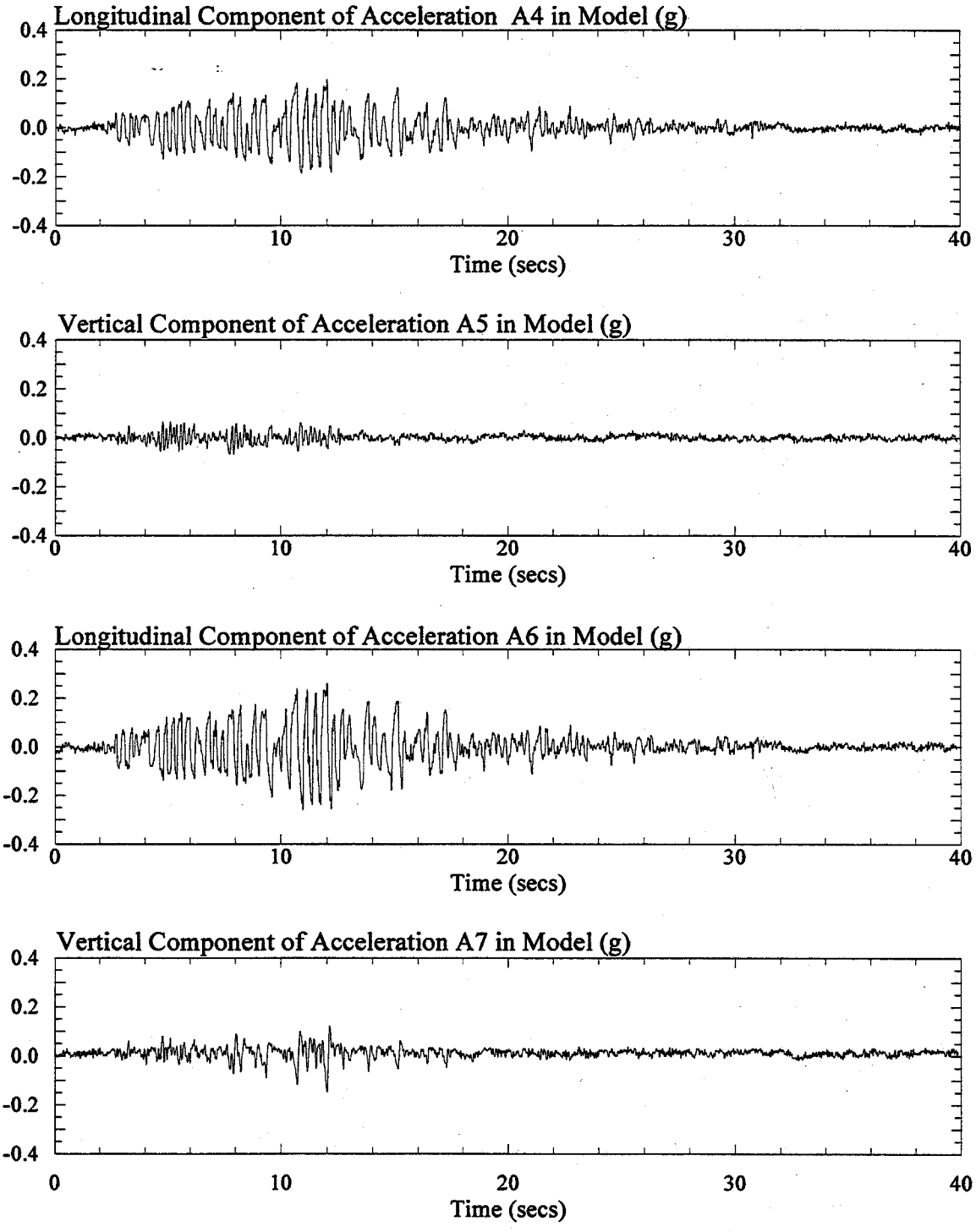

Figure 3: Longitudinal and vertical components of recorded acceleration in the one-g model SM3H1. Signals were post processed with a low pass filter of 20 Hz.

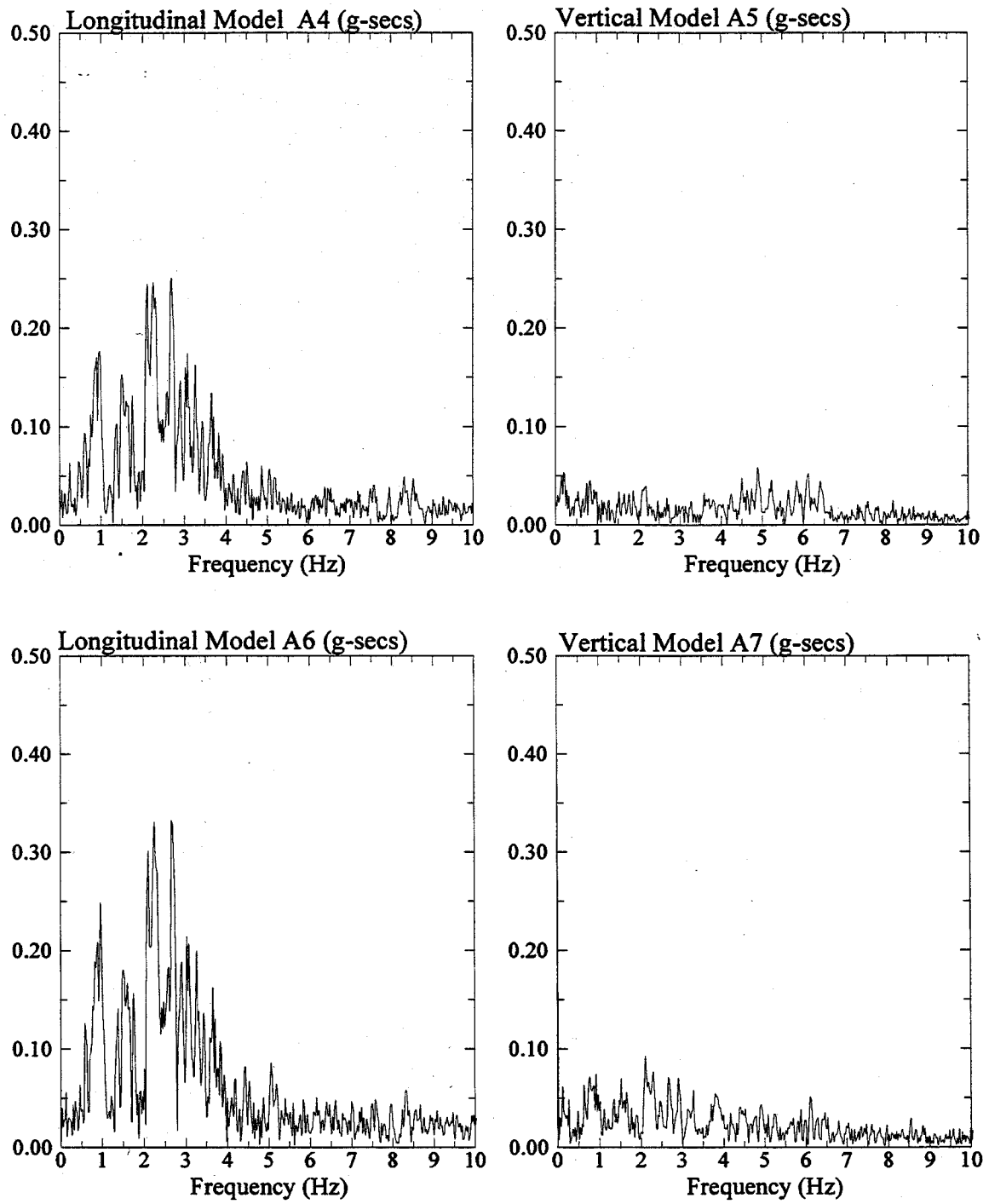

Figure 4: Fast Fourier Transform of longitudinal and vertical components of recorded acceleration in the one-g model SM3H1.

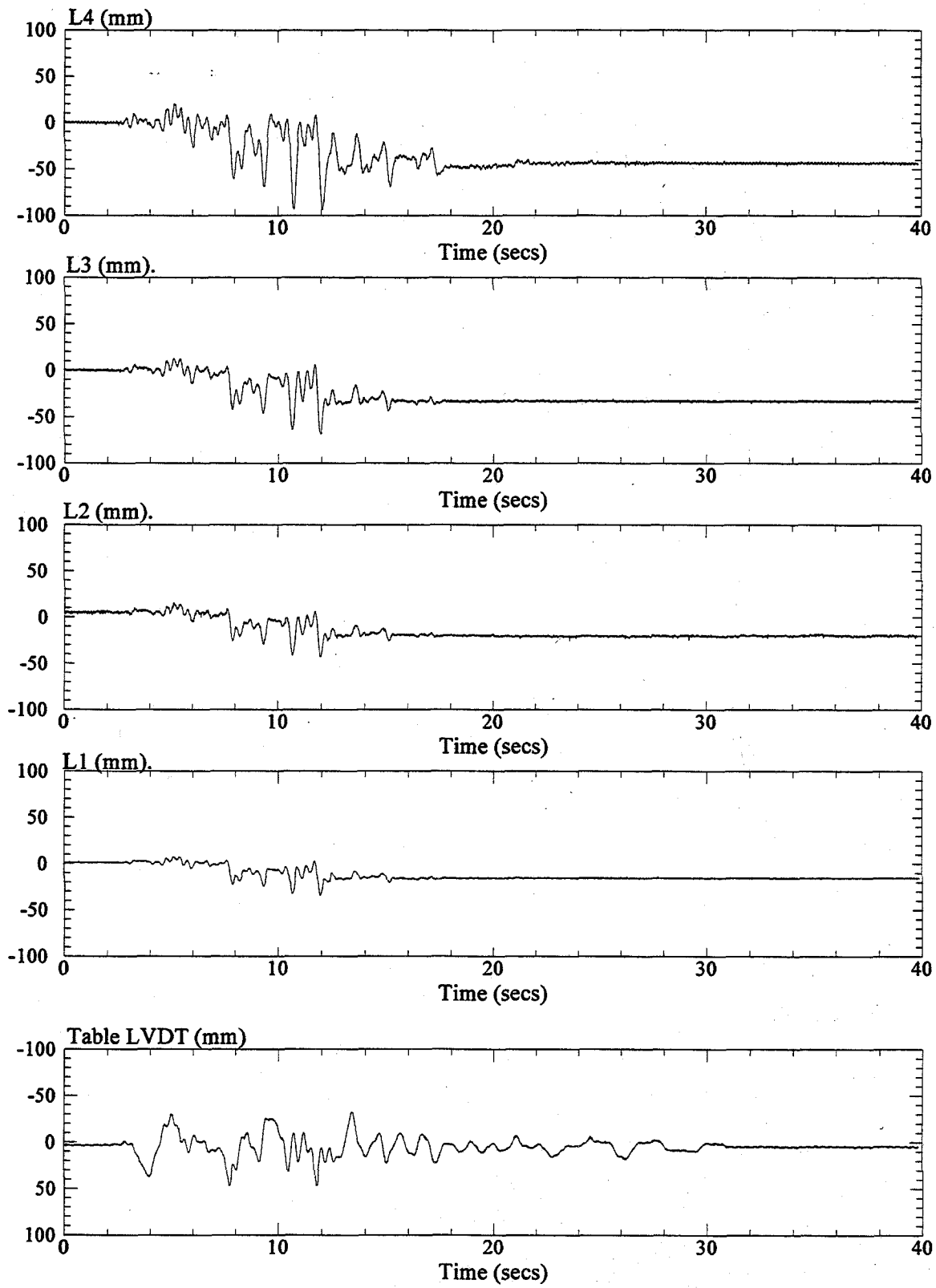

Figure 5: Longitudinal displacements recorded from the shake table LVDT and at LVDT's L1, L2, L3, and L4 in the one-g model SM3H1.

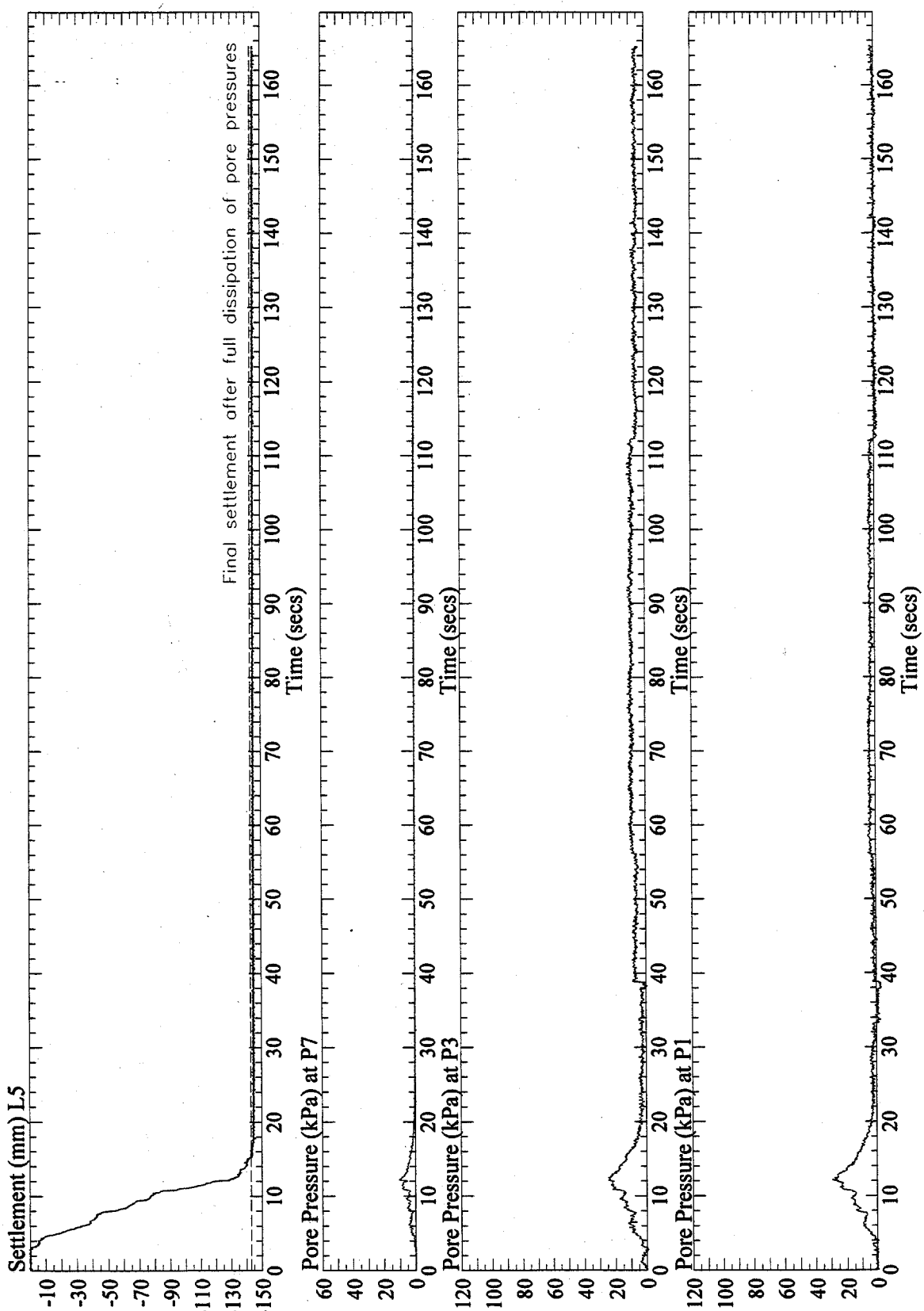

Figure 6: Vertical settlement at L5 and pore pressures at P1, P3, and P7, recorded in the one-g model SM3H1. Signals from P1 and P3 were post processed with a low pass filter of 10 Hz.

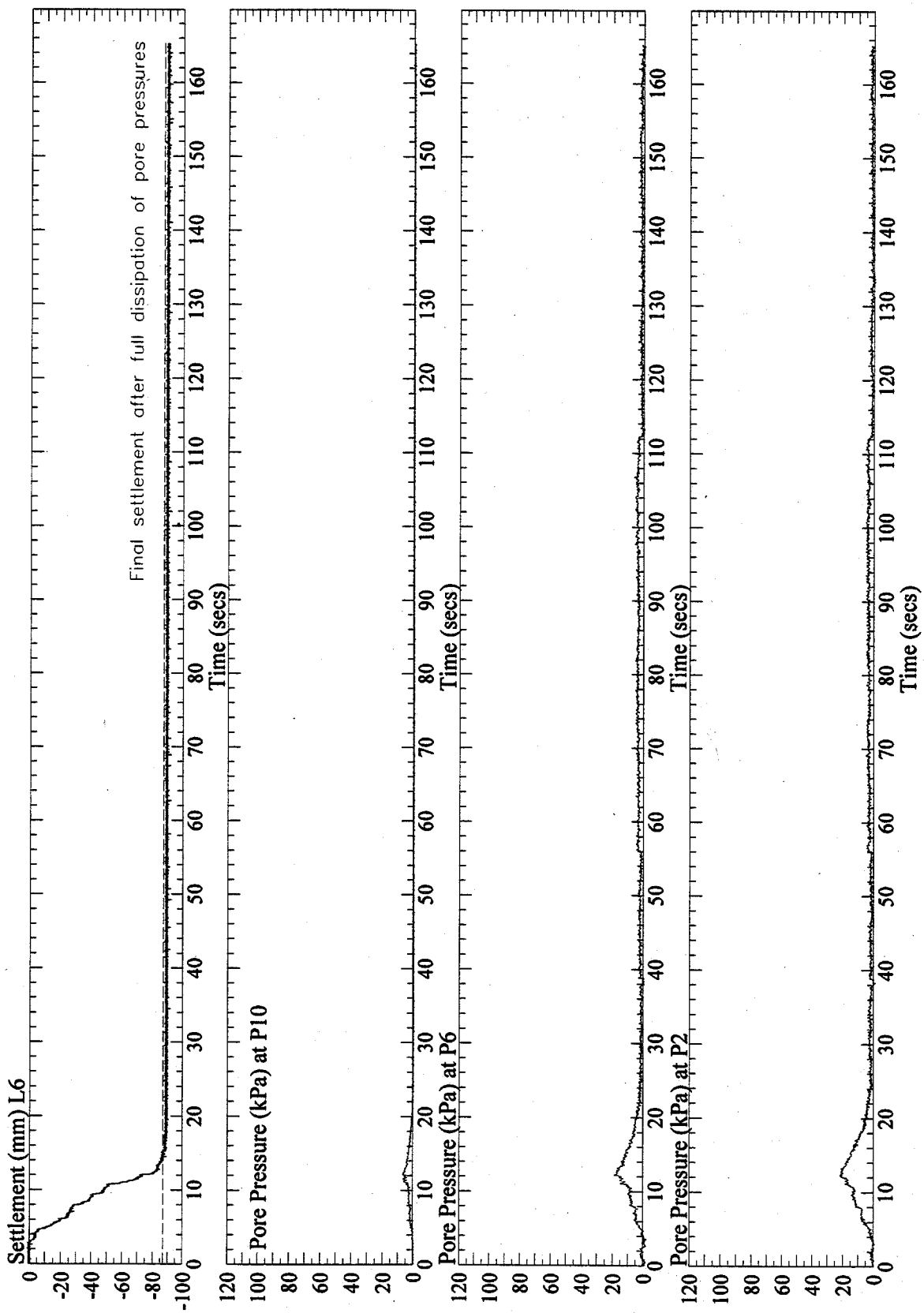

Figure 8: Vertical settlement at L6 and pore pressures at P2, P6, and P10, recorded in the one-g model SM3H1. Signal from P2 and P6 were post processed with a low pass filter of 10 Hz.

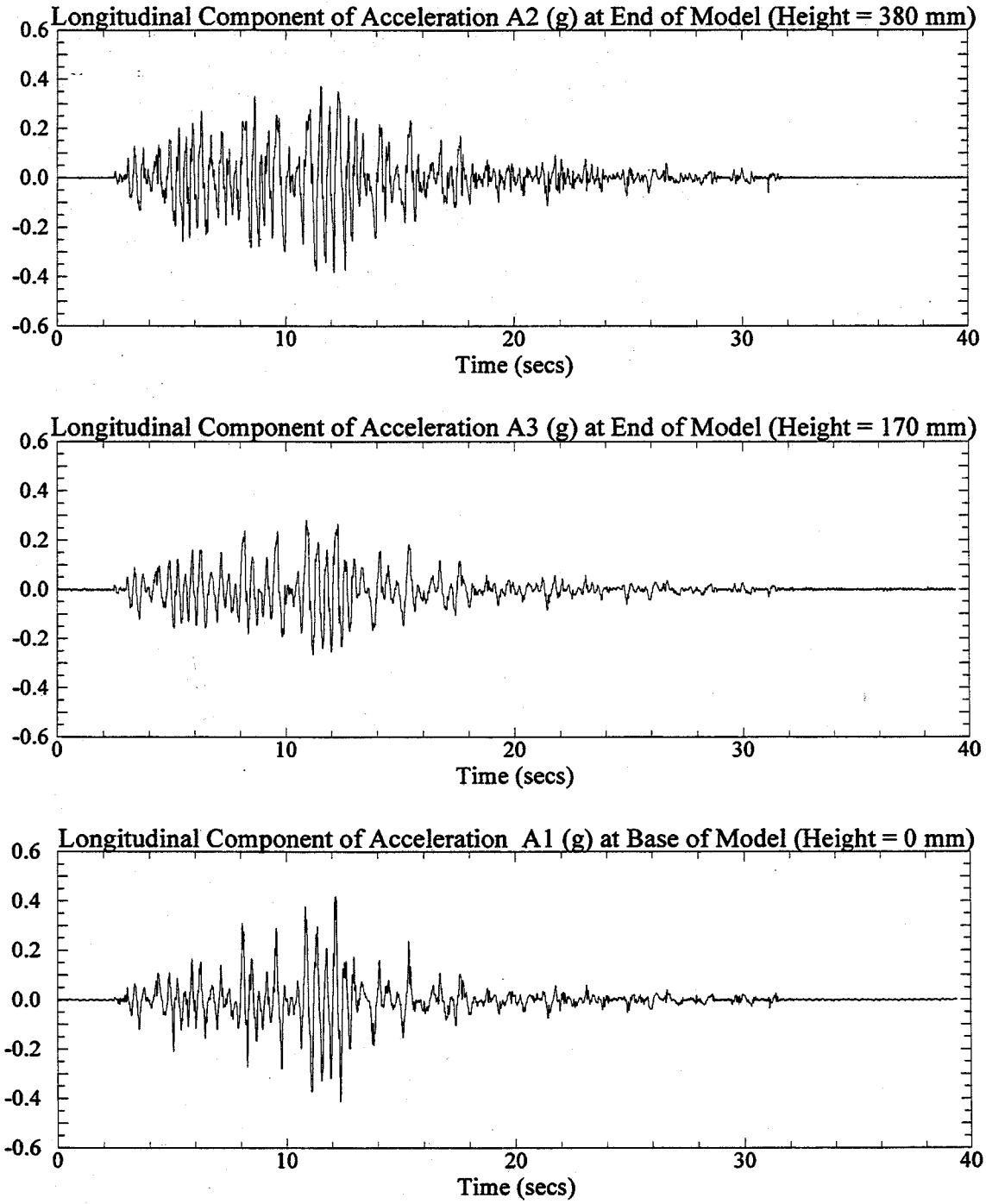

Figure 1: Longitudinal components of recorded acceleration at the base and end of the one-g model SM3H2. Signals were post processed with a low pass filter of 20 Hz.

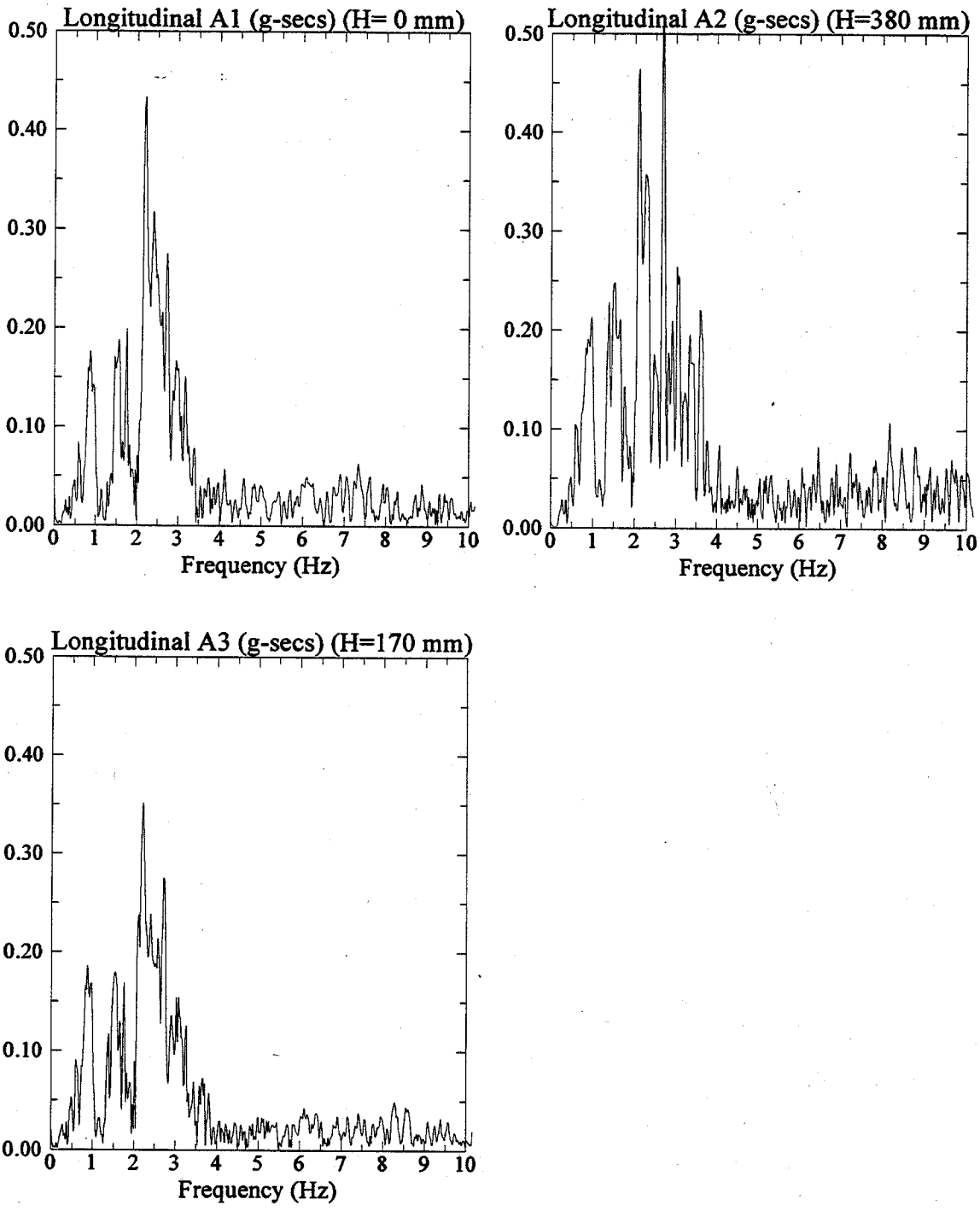

Figure 2: Fast Fourier Transform of longitudinal components of recorded acceleration at the base and end of the one-g model SM3H2.

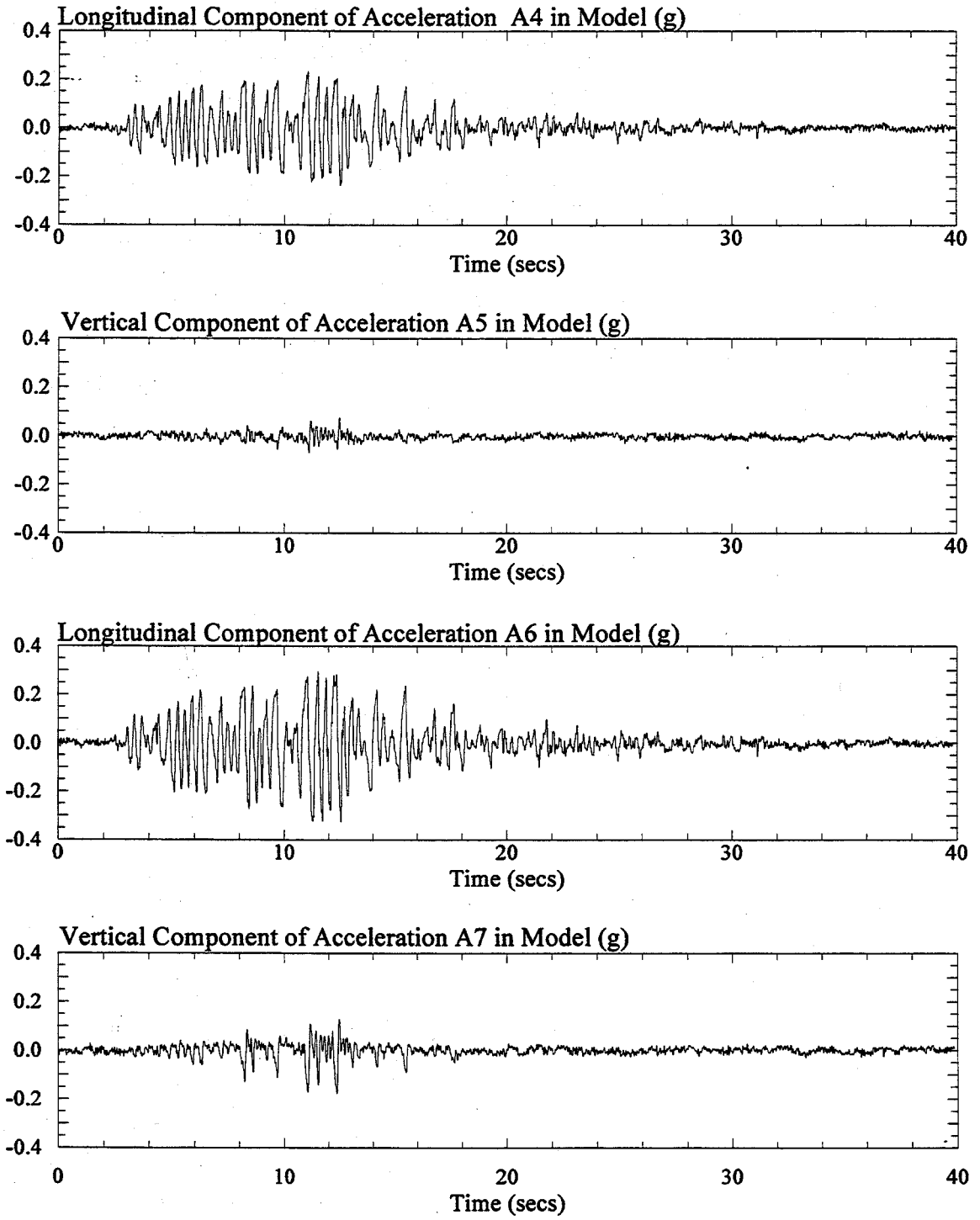

Figure 3: Longitudinal and vertical components of recorded acceleration in the one-g model SM3H2. Signals were post processed with a low pass filter of 20 Hz.

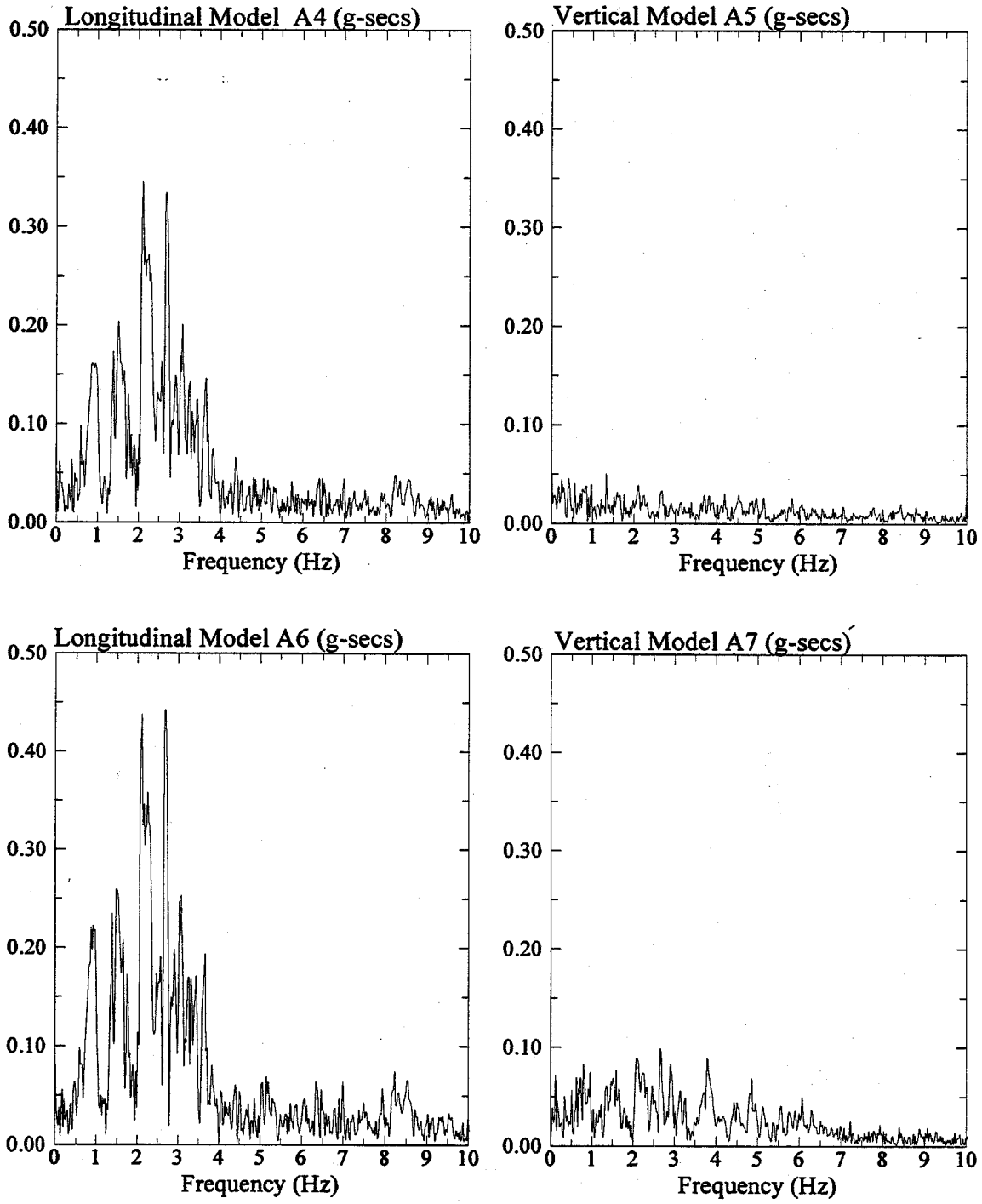

Figure 4: Fast Fourier Transform of longitudinal and vertical components of recorded acceleration in the one-g model SM3H2.

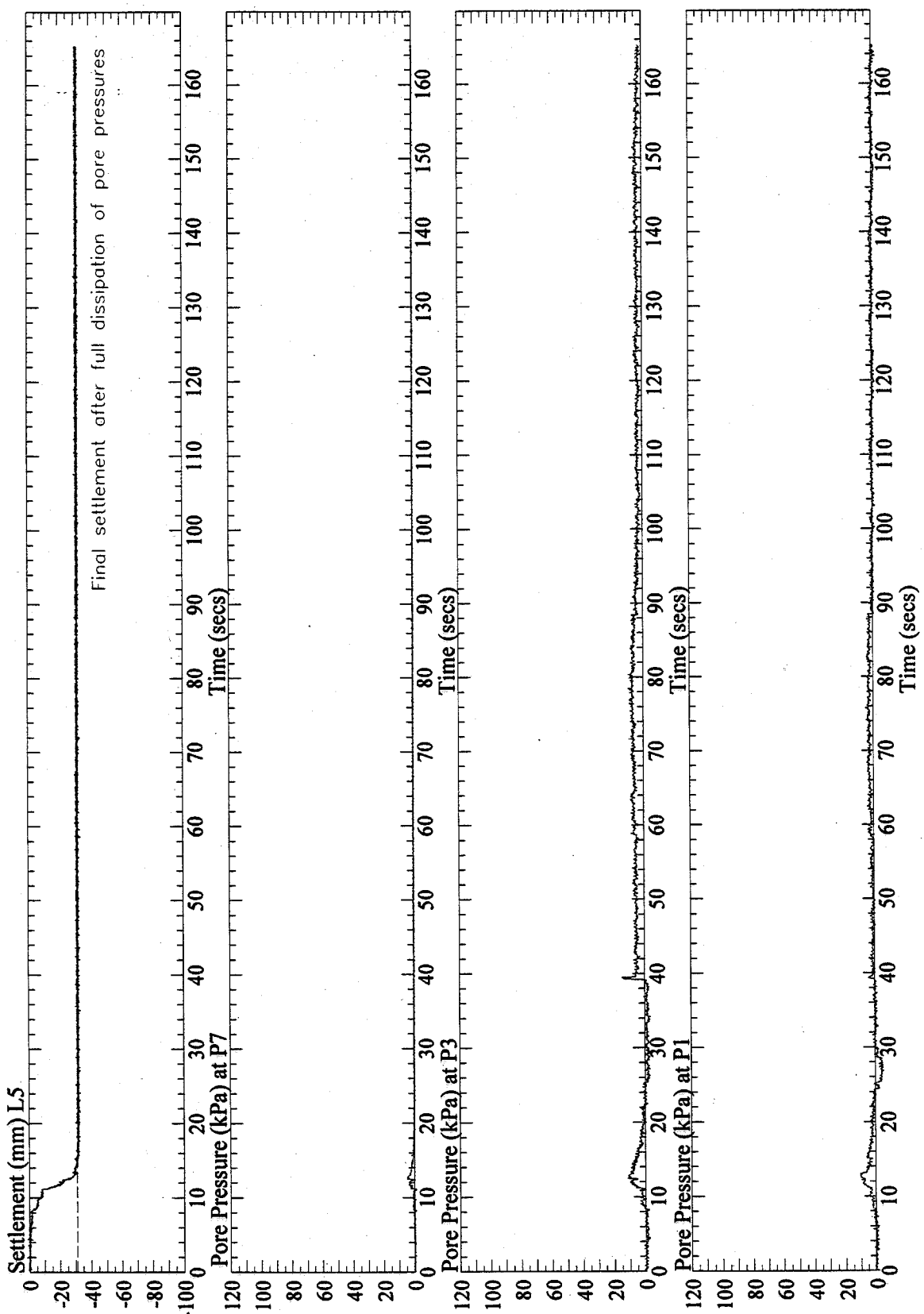

Figure 6: Vertical settlement at L5 and pore pressures at P1, P3, and P7, recorded in the one-g model SM3H4. Signals from P1 and P3 were post processed with a low pass filter of 10 Hz.

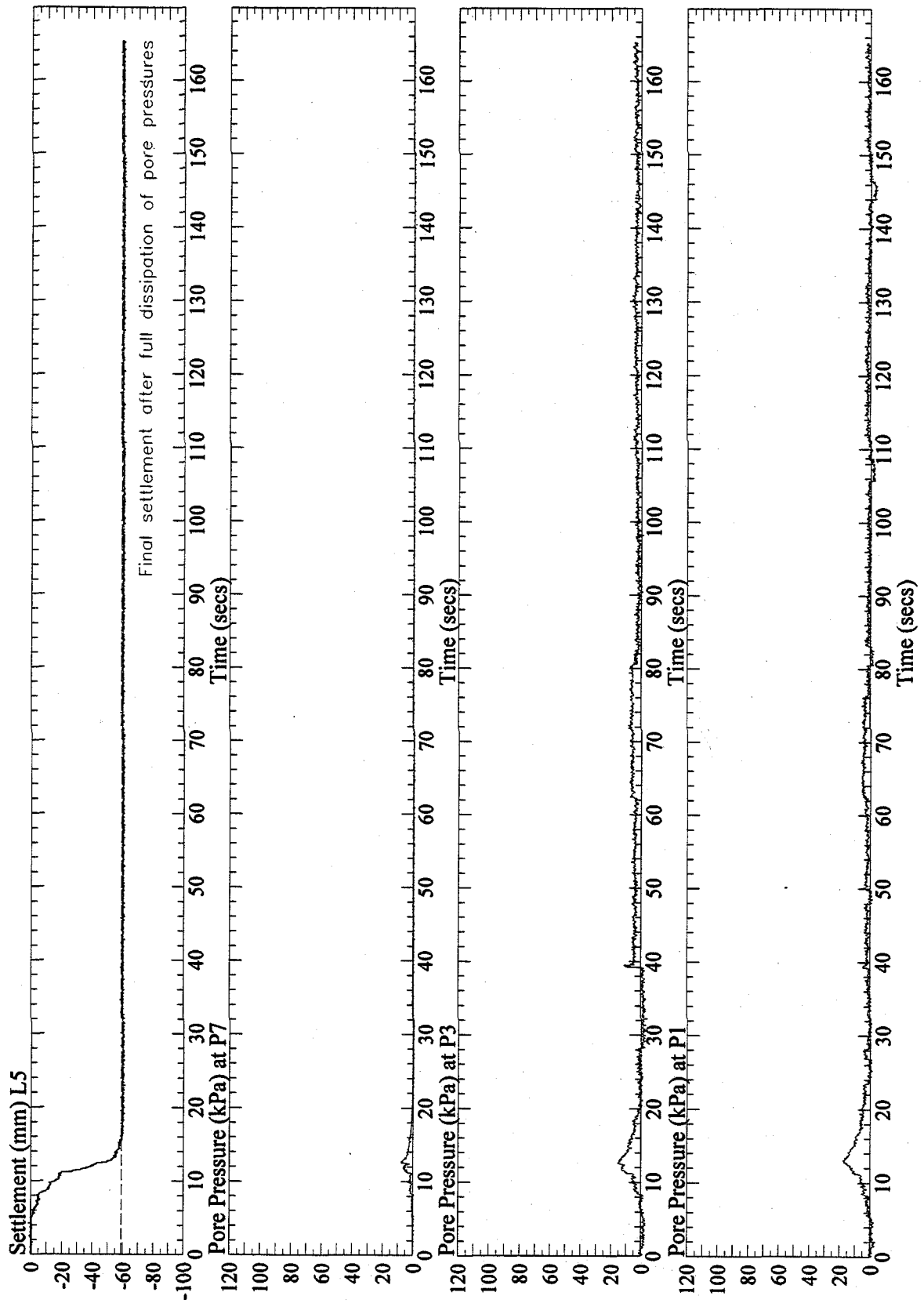

Figure 6: Vertical settlement at L5 and pore pressures at P1, P3, and P7, recorded in the one-g model SM3H2. Signals from P1 and P3 were post processed with a low pass filter of 10 Hz.

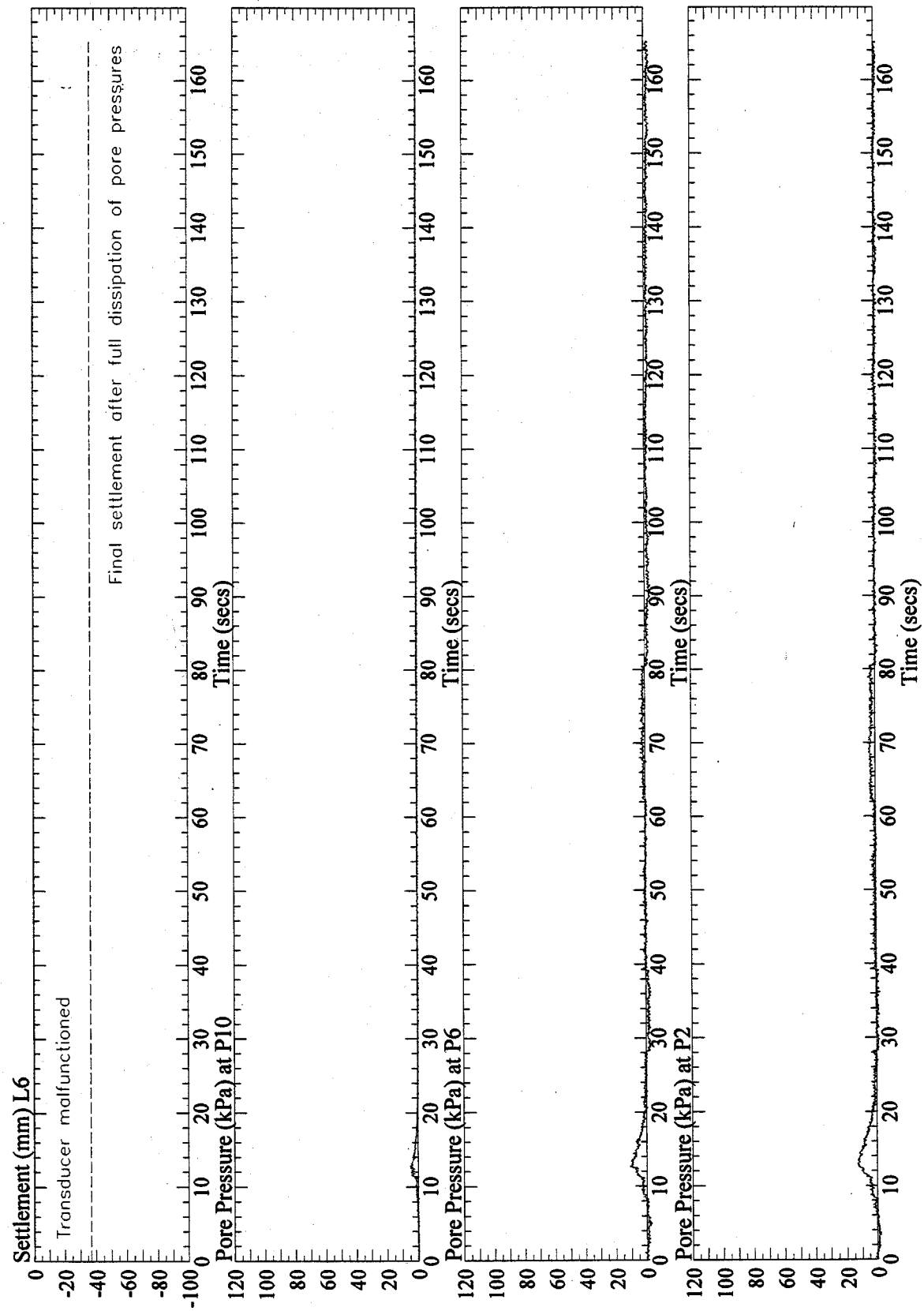

Figure 8: Vertical settlement at L6 and pore pressures at P2, P6, and P10, recorded in the one-g model SM3H2. Signal from P2 and P6 were post processed with a low pass filter of 10 Hz.

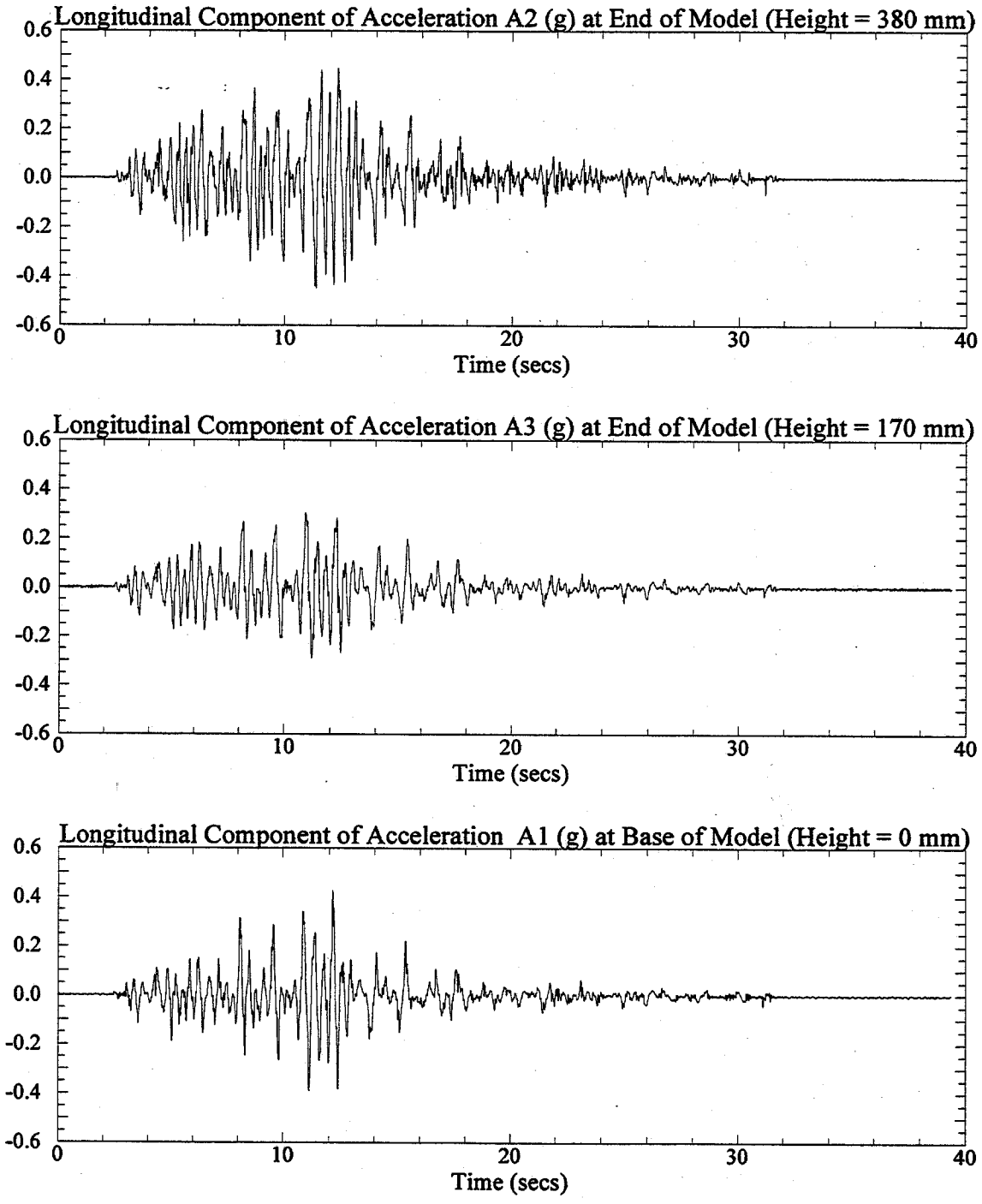

Figure 1: Longitudinal components of recorded acceleration at the base and end of the one-g model SM3H4. Signals were post processed with a low pass filter of 20 Hz.

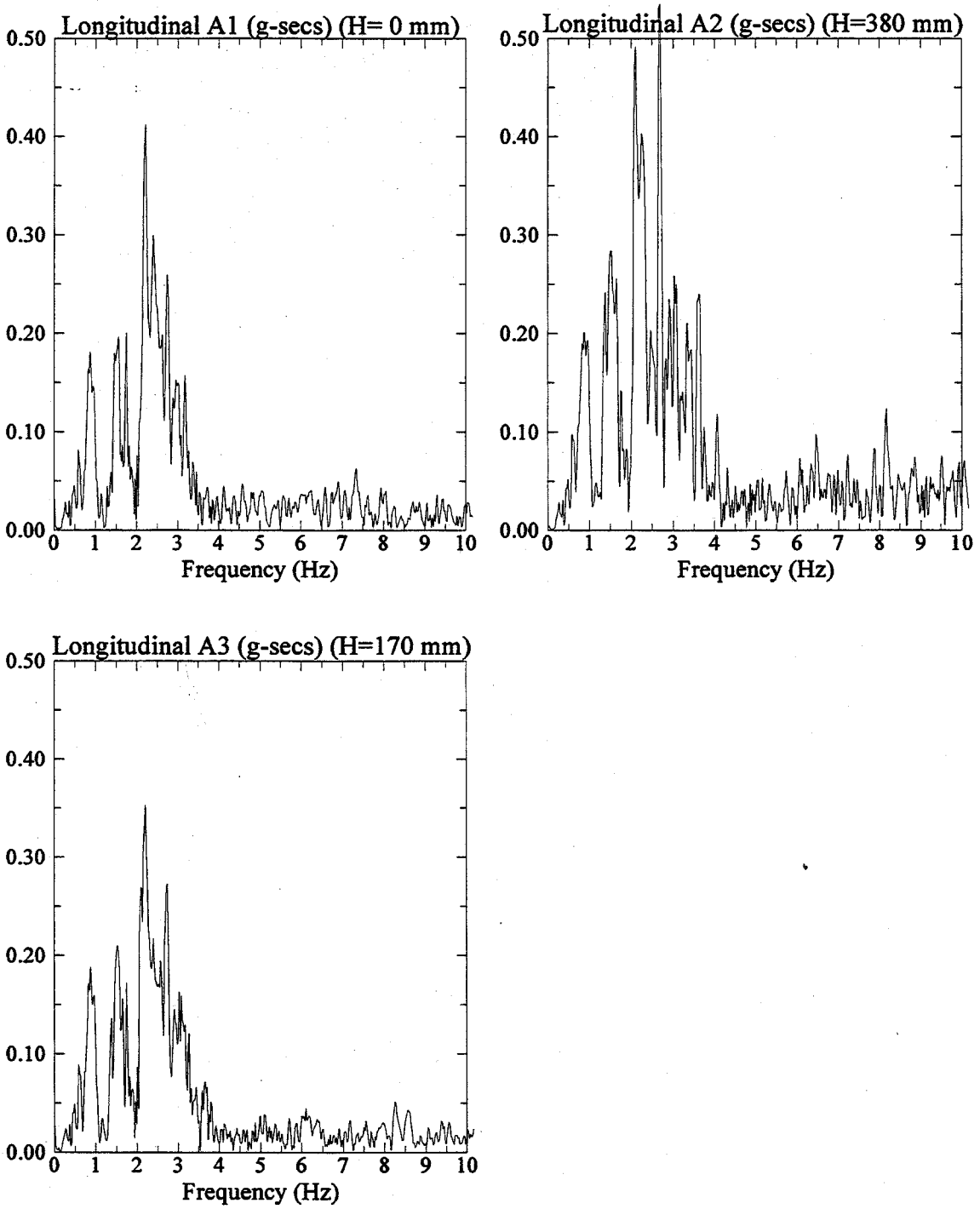

Figure 2: Fast Fourier Transform of longitudinal components of recorded acceleration at the base and end of the one-g model SM3H4.

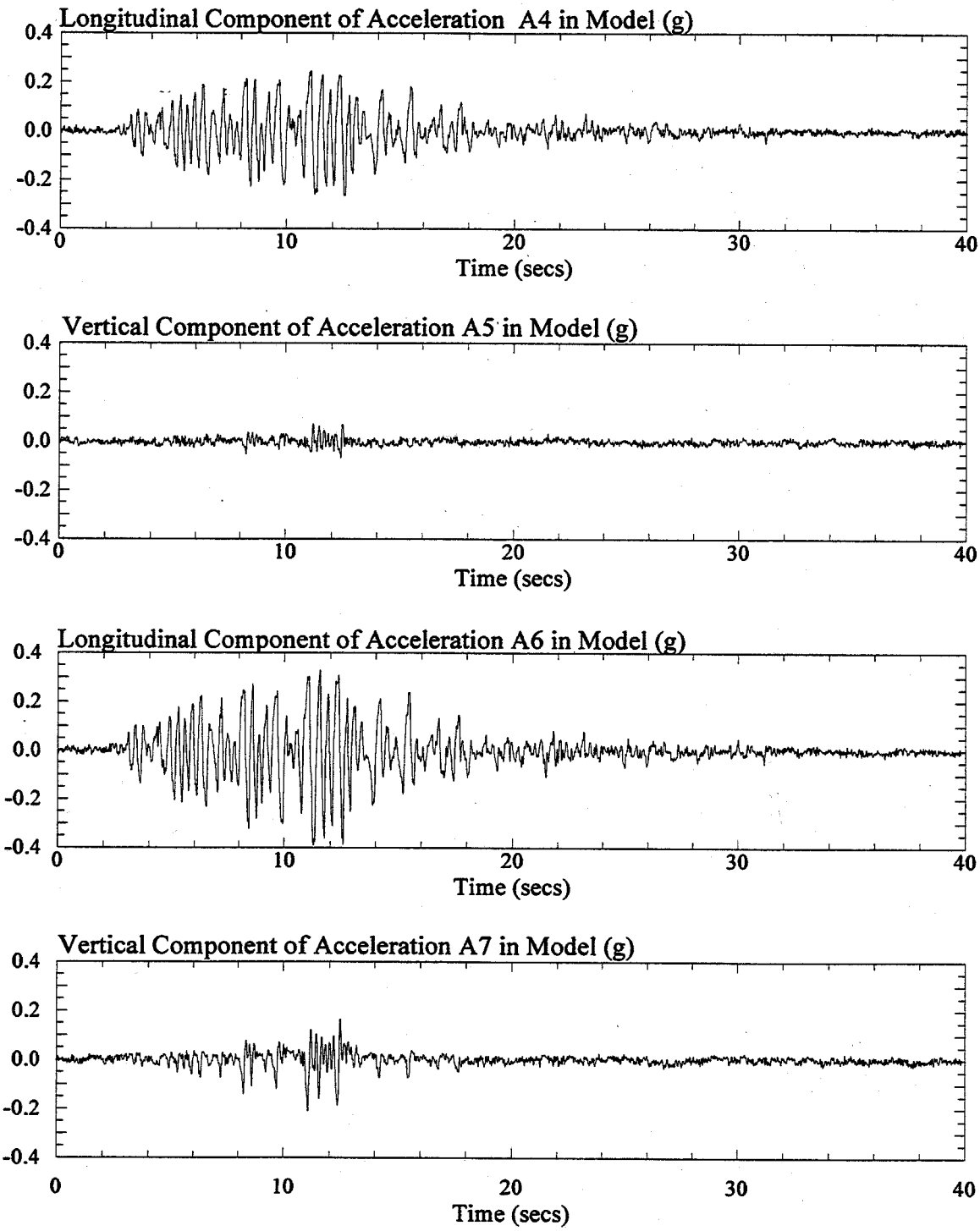

Figure 3: Longitudinal and vertical components of recorded acceleration in the one-g model SM3H4. Signals were post processed with a low pass filter of 20 Hz.

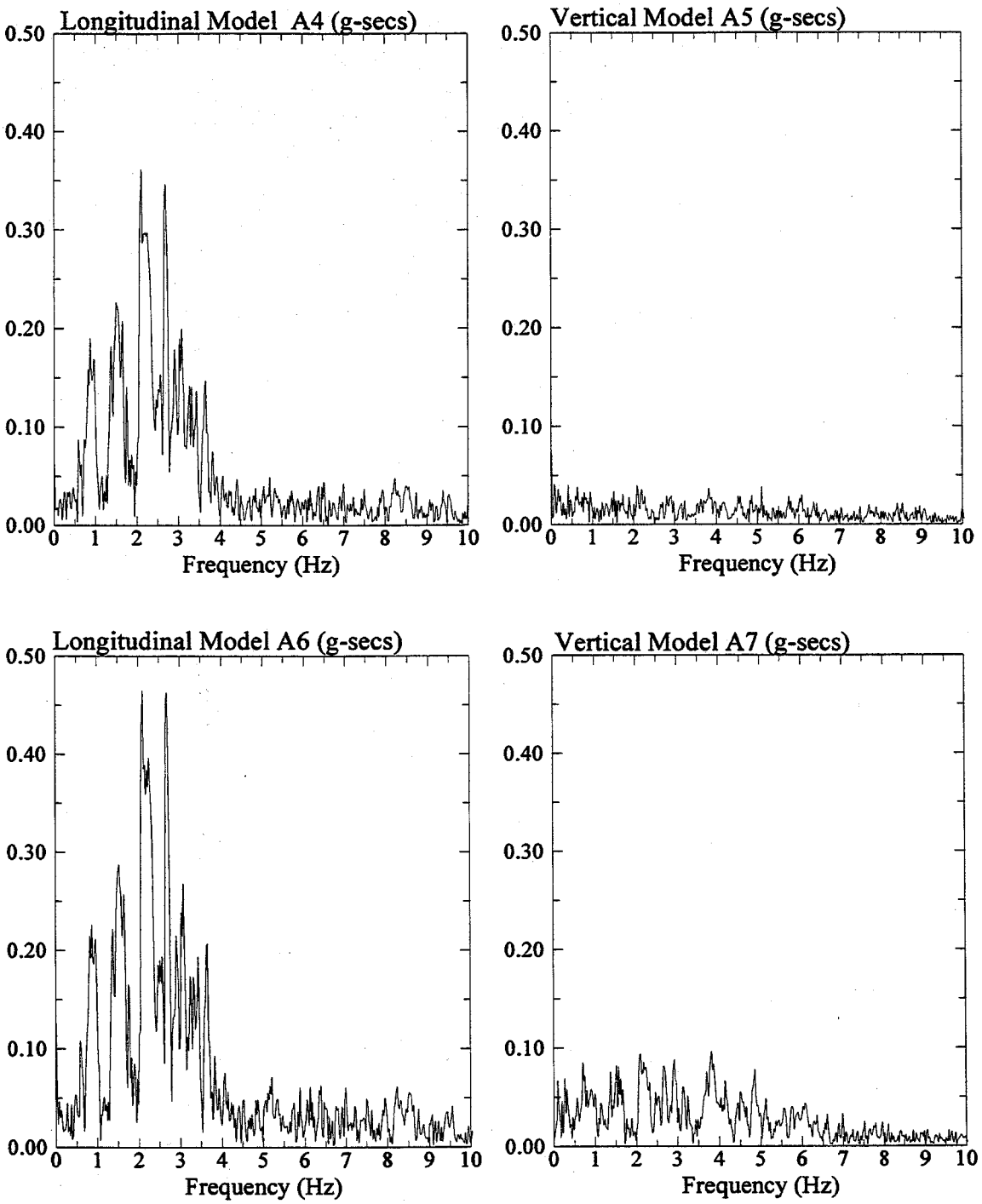

Figure 4: Fast Fourier Transform of longitudinal and vertical components of recorded acceleration in the one-g model SM3H4.

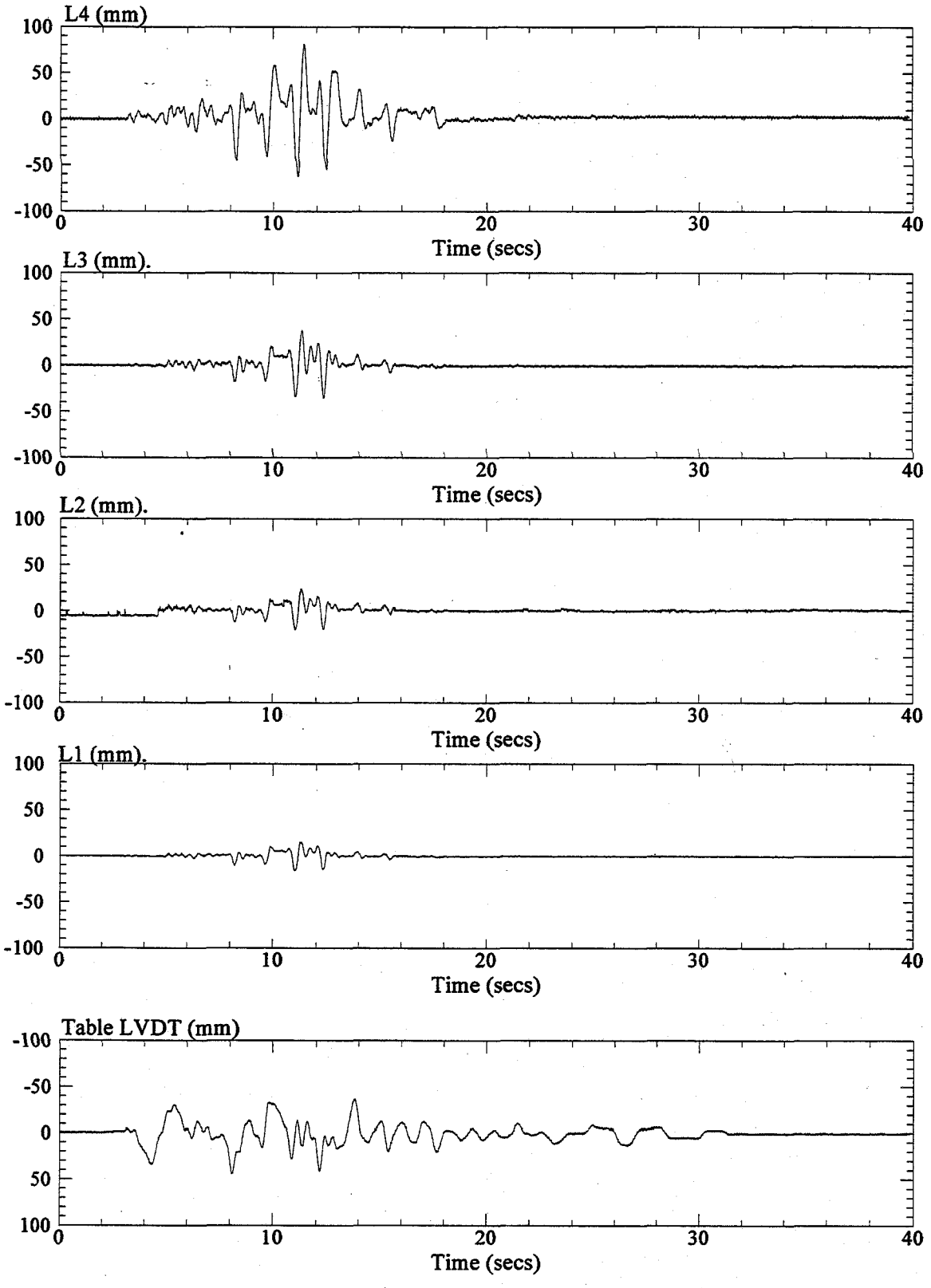

Figure 5: Longitudinal displacements recorded from the shake table LVDT and at LVDT's L1, L2, L3, and L4 in the one-g model SM3H4.

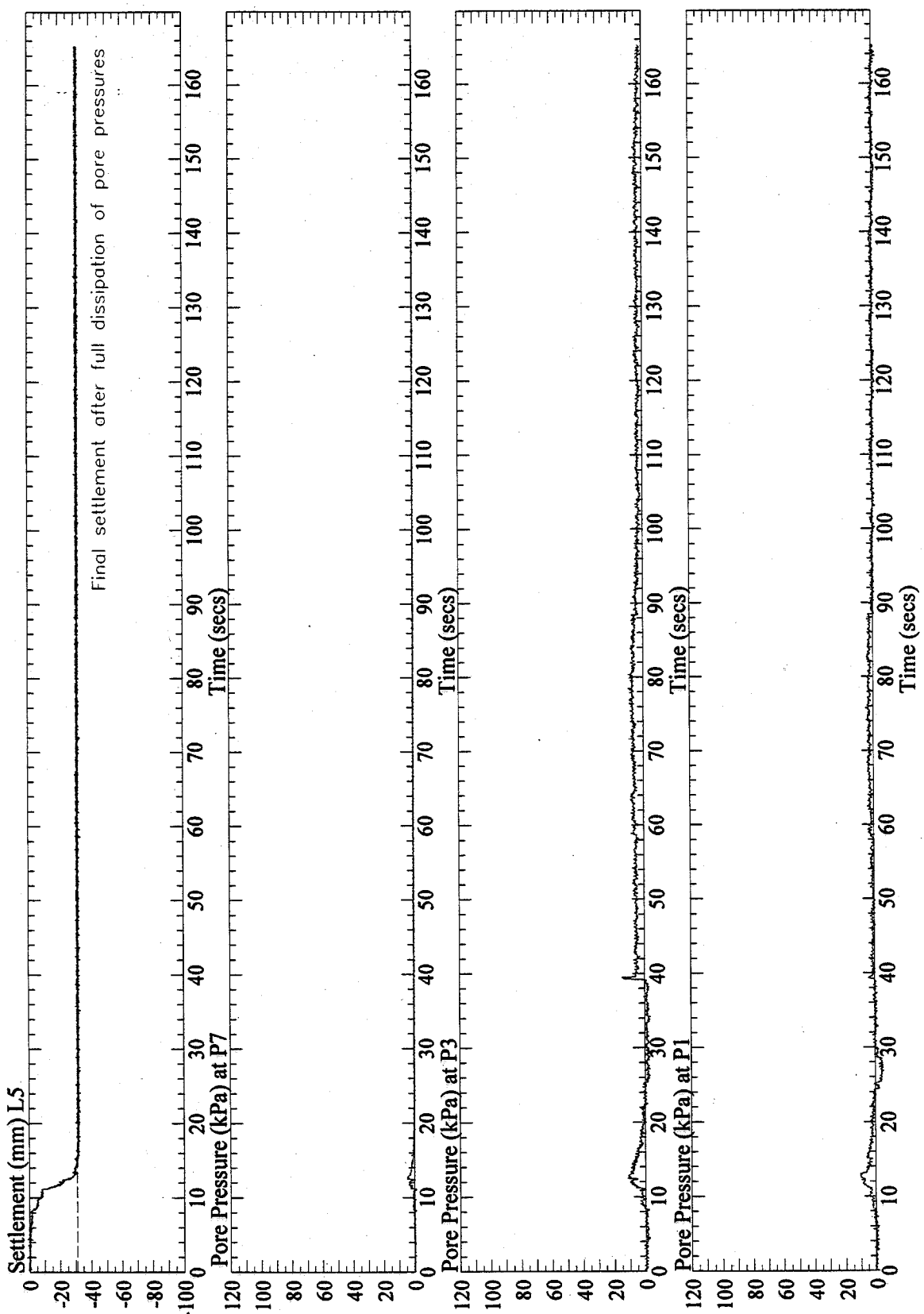

Figure 6: Vertical settlement at L5 and pore pressures at P1, P3, and P7, recorded in the one-g model SM3H4. Signals from P1 and P3 were post processed with a low pass filter of 10 Hz.

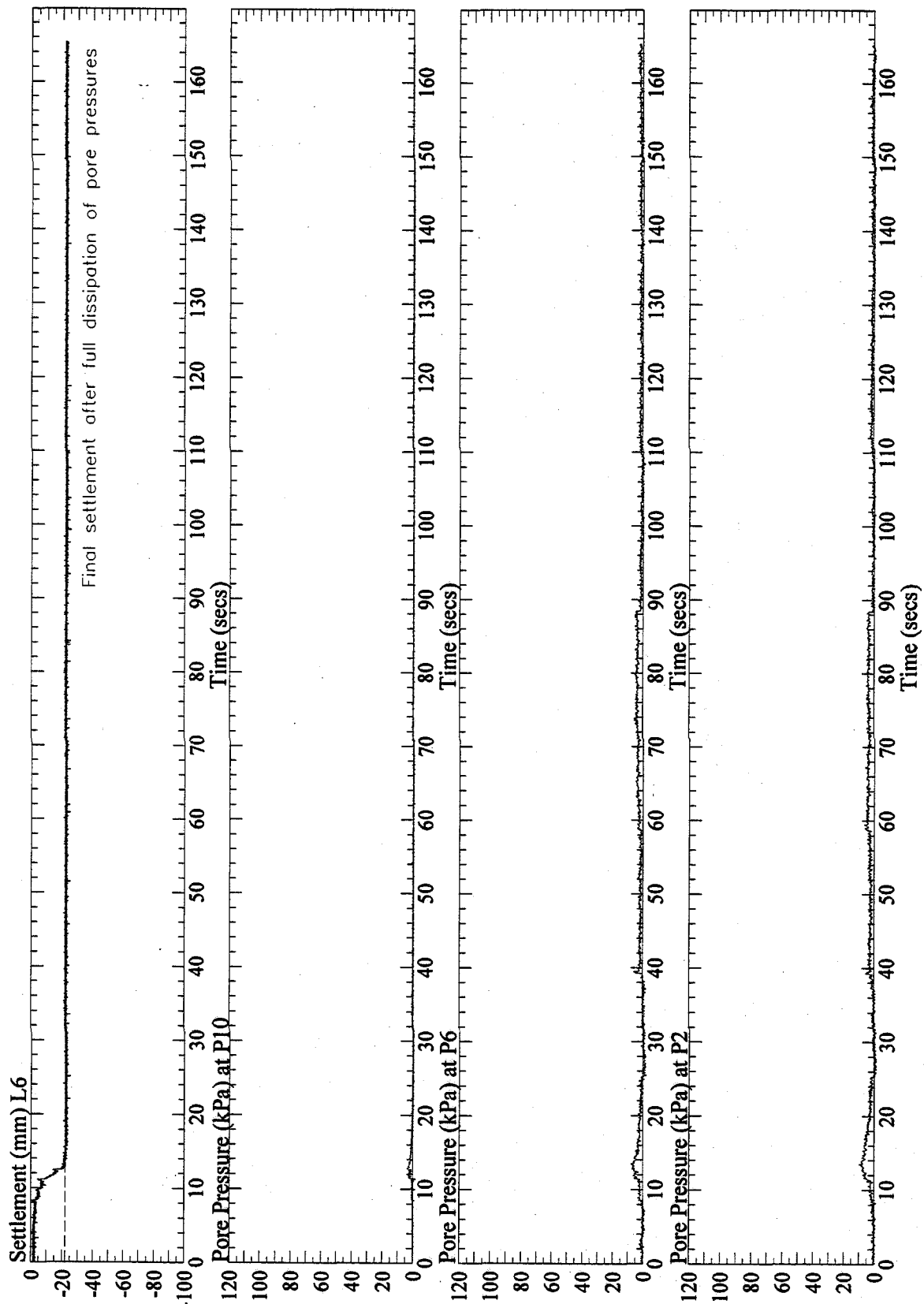

Figure 8: Vertical settlement at L6 and pore pressures at P2, P6, and P10, recorded in the one-g model SM3H4. Signal from P2 and P6 were post processed with a low pass filter of 10 Hz.

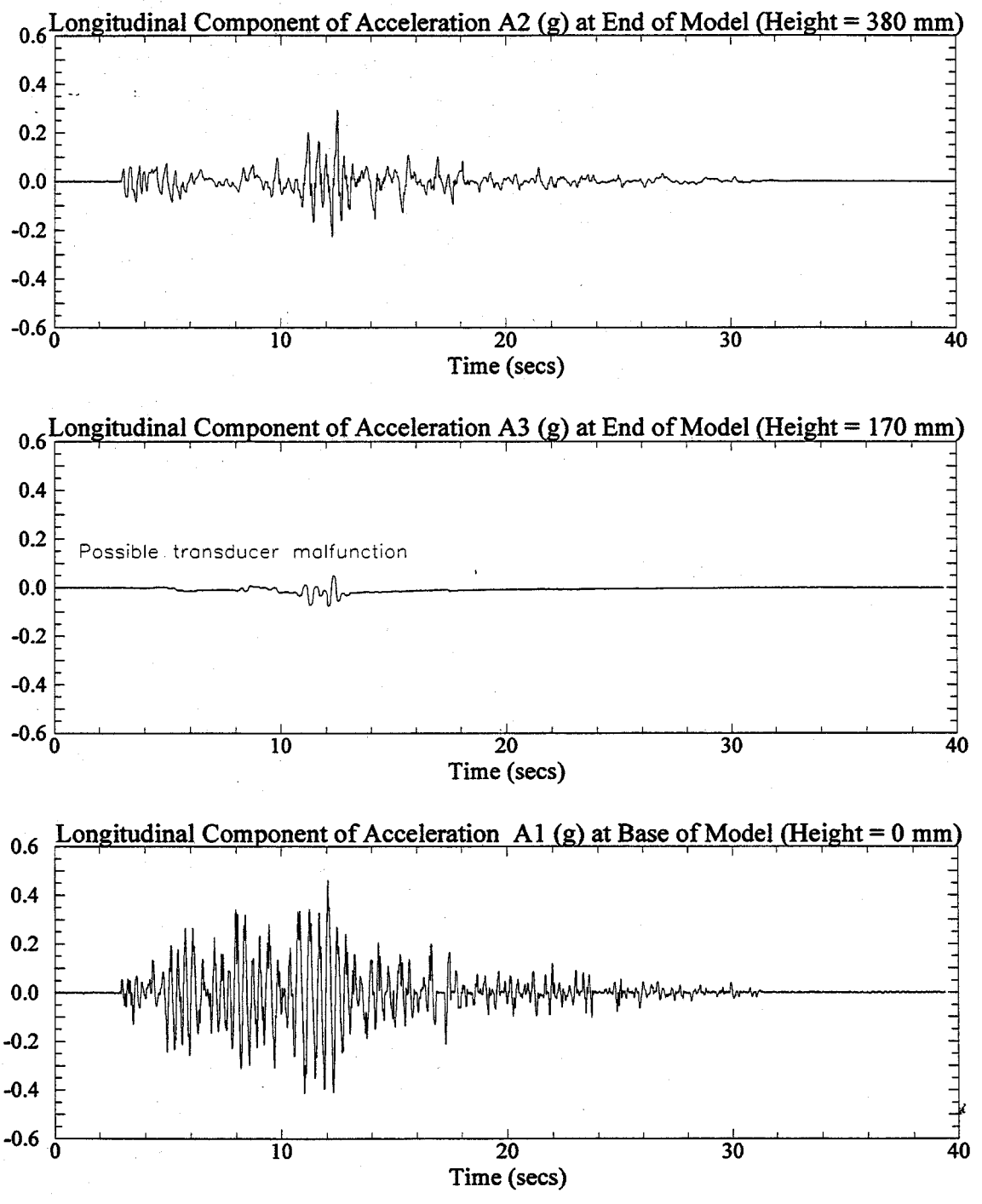

Figure 1: Longitudinal components of recorded acceleration at the base and end of the one-g model SM3I1. Signals were post processed with a low pass filter of 20 Hz.

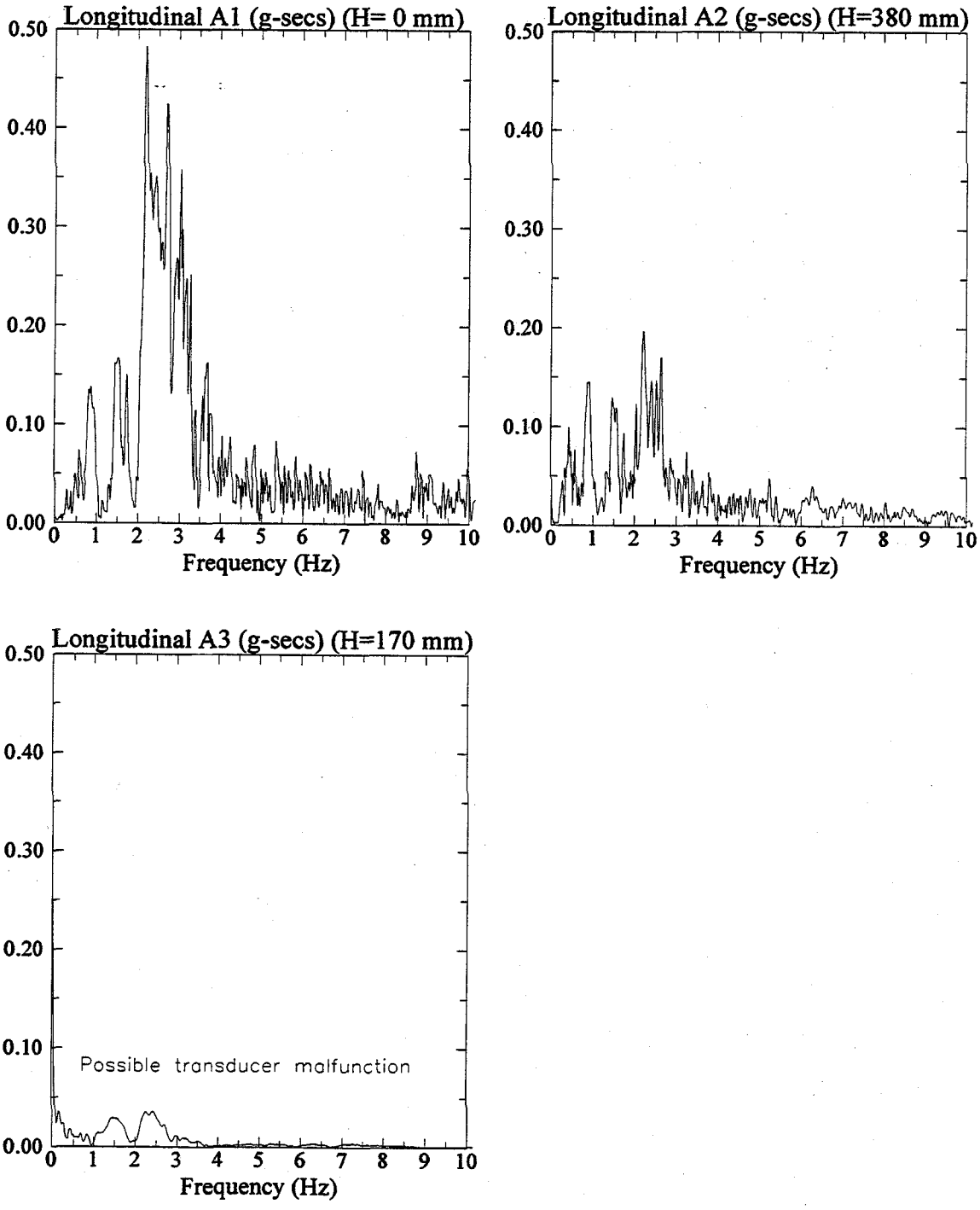

Figure 2: Fast Fourier Transform of longitudinal components of recorded acceleration at the base and end of the one-g model SM3I1.

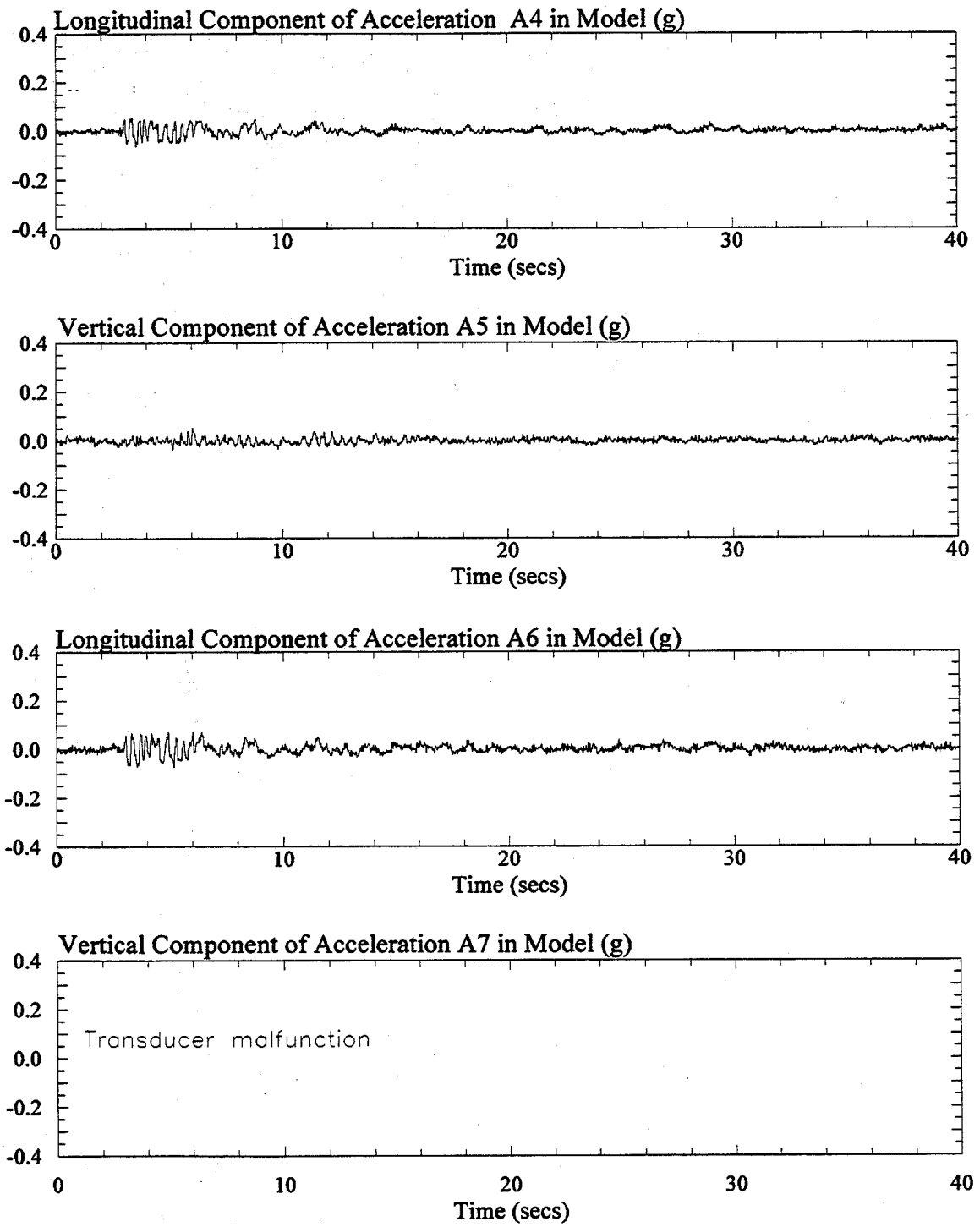

Figure 3: Longitudinal and vertical components of recorded acceleration in the one-g model SM3I1. Signals were post processed with a low pass filter of 20 Hz.

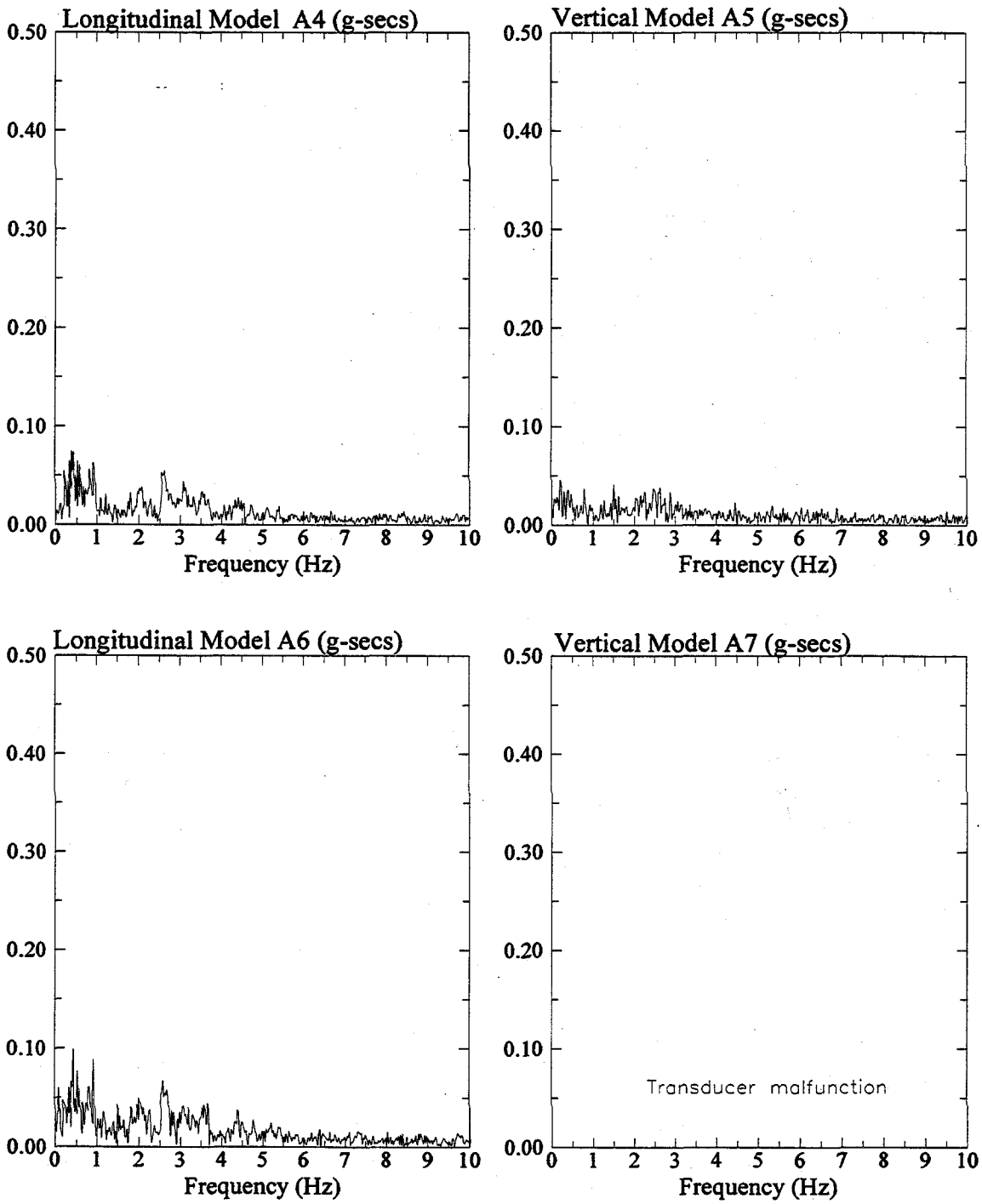

Figure 4: Fast Fourier Transform of longitudinal and vertical components of recorded acceleration in the one-g model SM3I1.

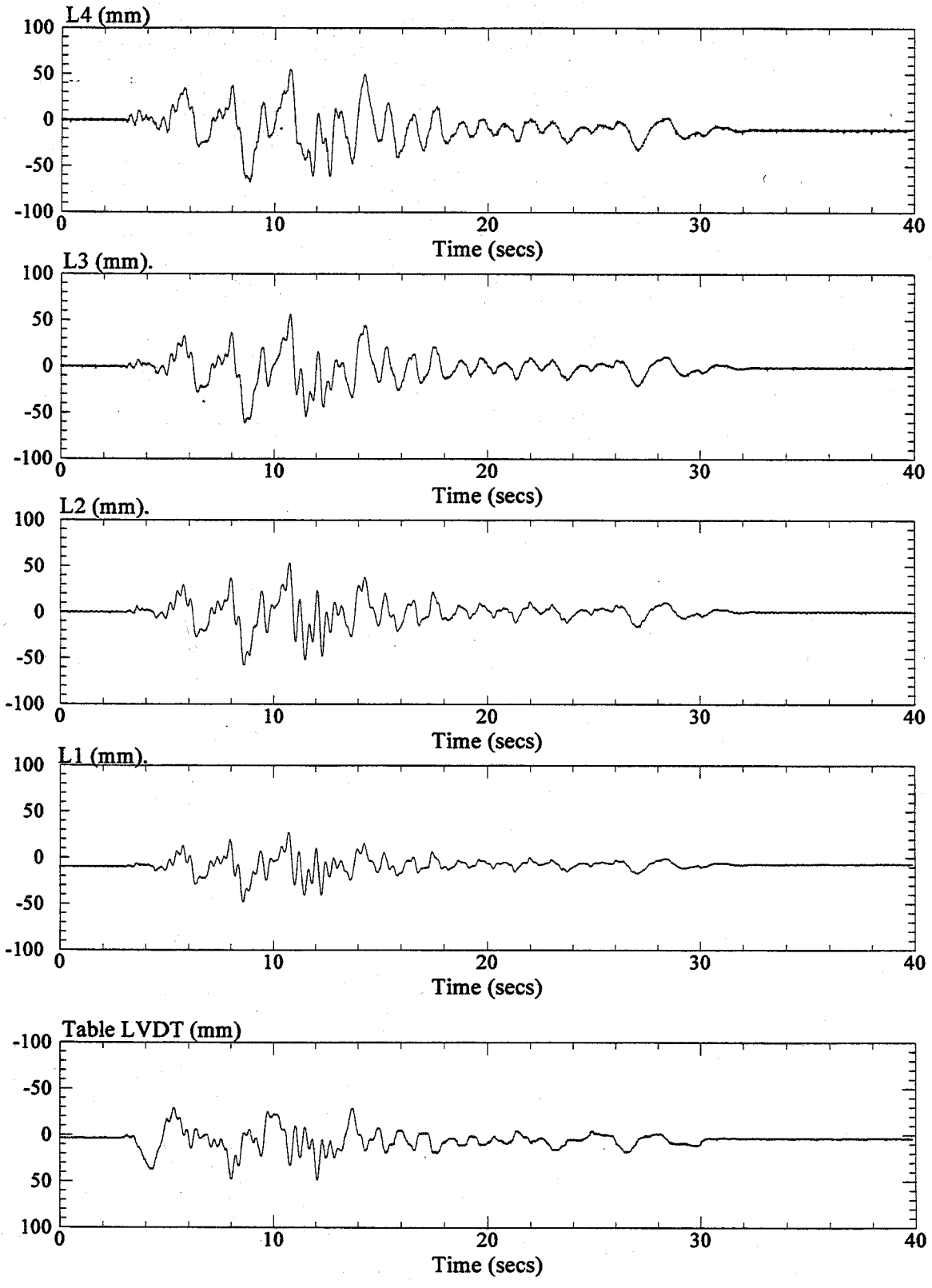

Figure 5: Longitudinal displacements recorded from the shake table LVDT and at LVDT's L1, L2, L3, and L4 in the one-g model SM3I1.

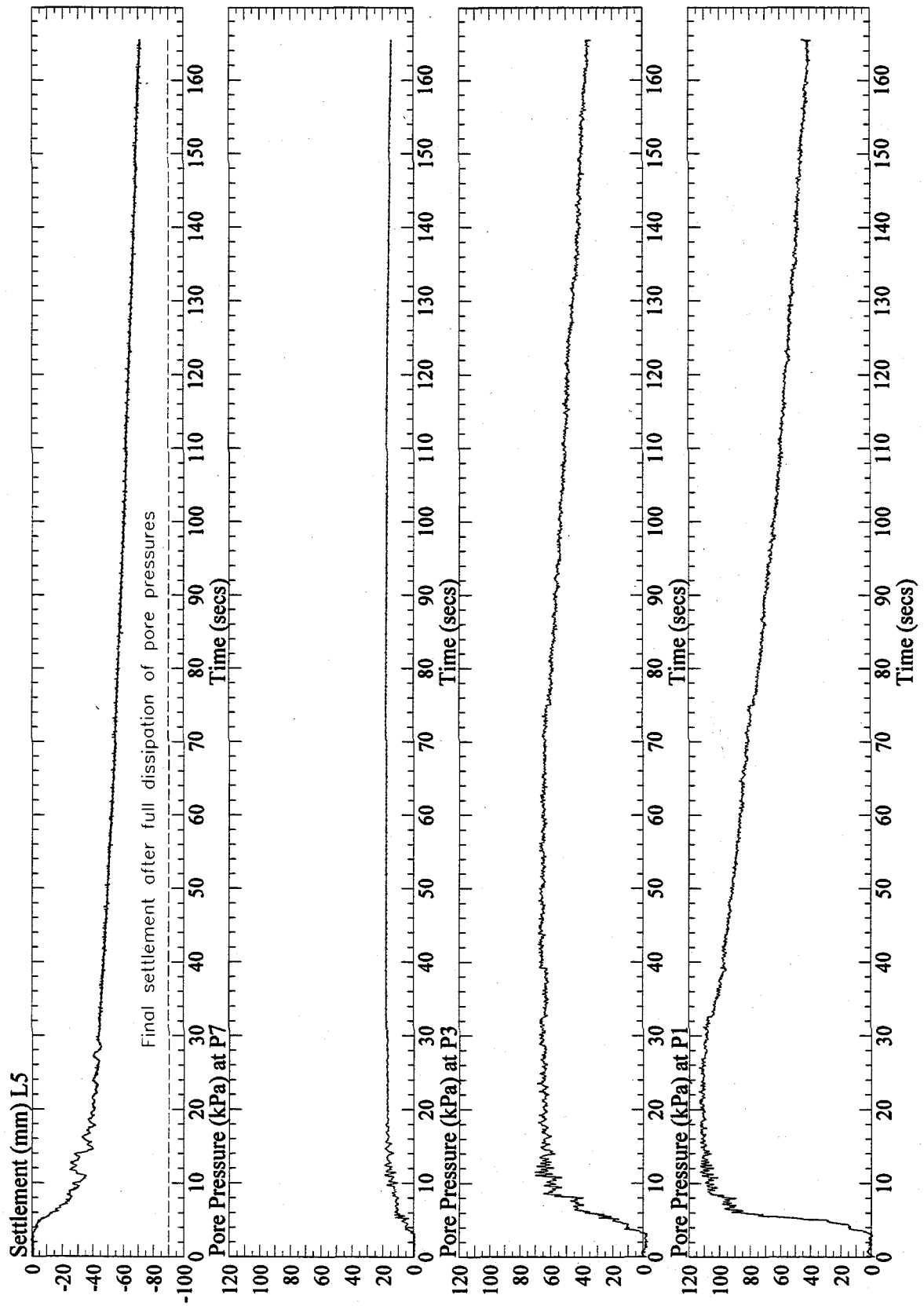

Figure 6: Vertical settlement at L5 and pore pressures at P1, P3, and P7, recorded in the one-g model SM3I1. Signals from P1 and P3 were post processed with a low pass filter of 10 Hz.

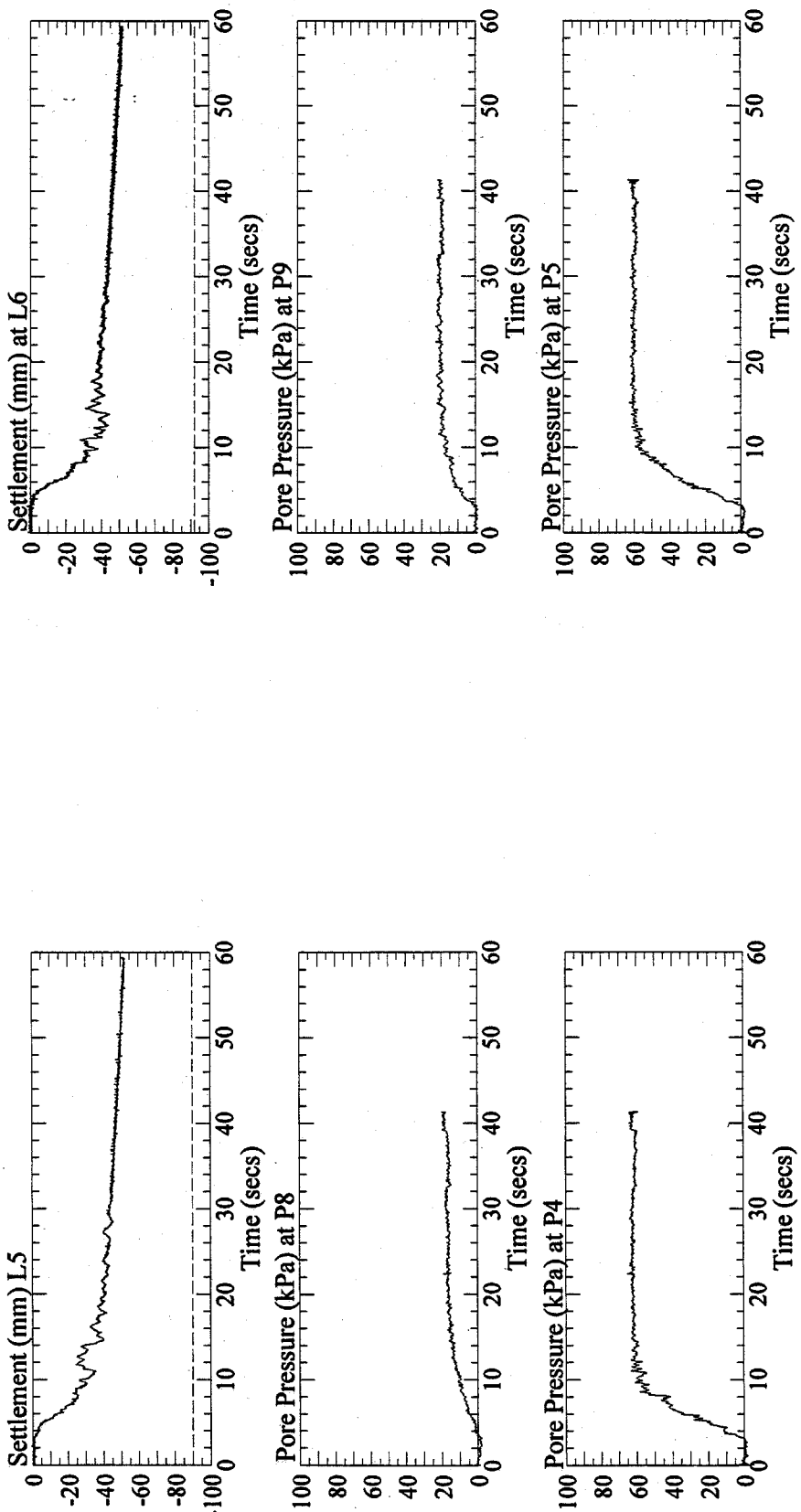

Figure 7: Vertical settlement at L5 and L6, and pore pressures at P4, P5, P8 and P9, recorded in the one-g model SM3I1. Pore pressure signals were post processed with a low pass filter of 10 Hz.

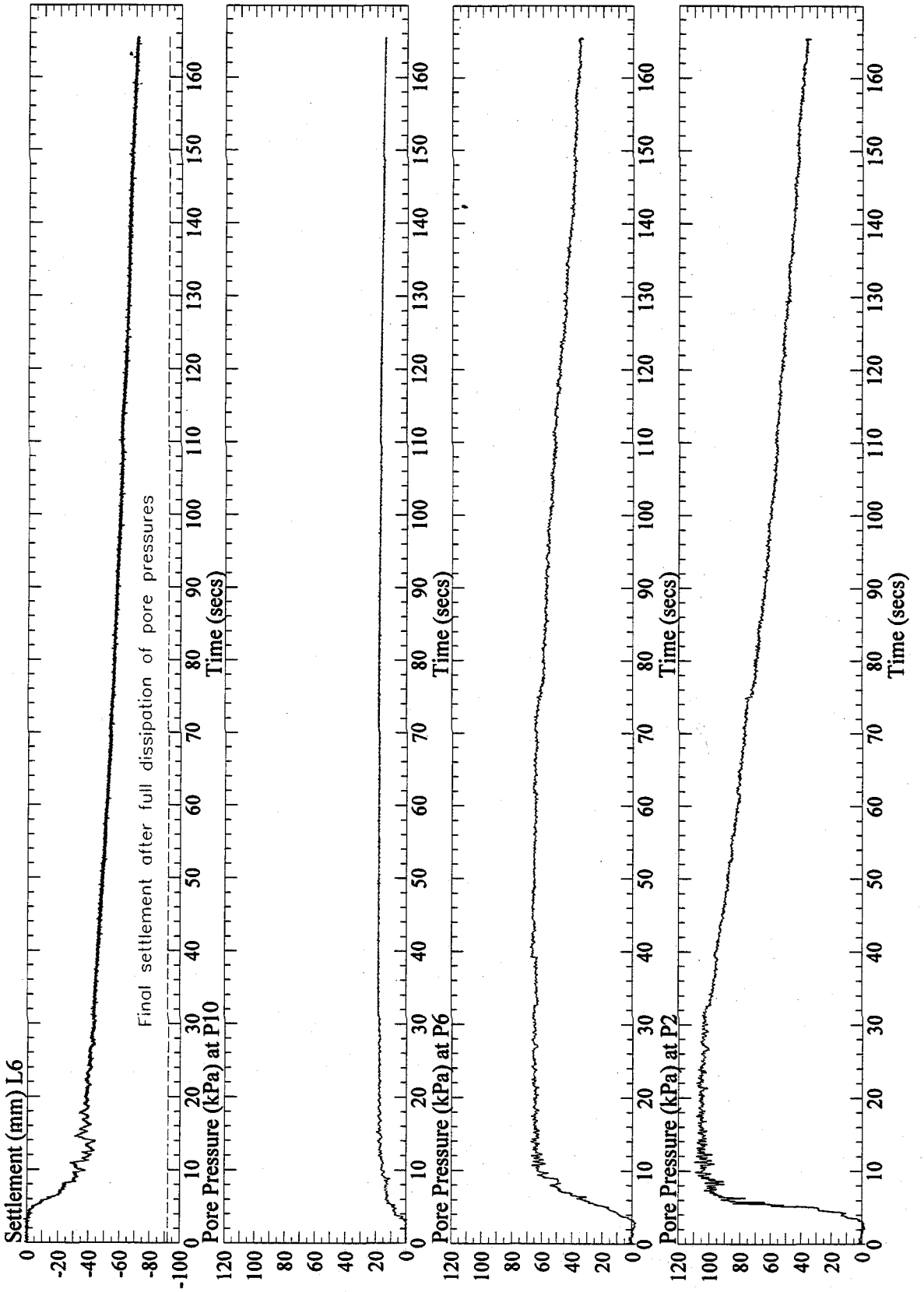

Figure 8: Vertical settlement at L6 and pore pressures at P2, P6, and P10, recorded in the one-g model SM3I1. Signal from P2 and P6 were post processed with a low pass filter of 10 Hz.

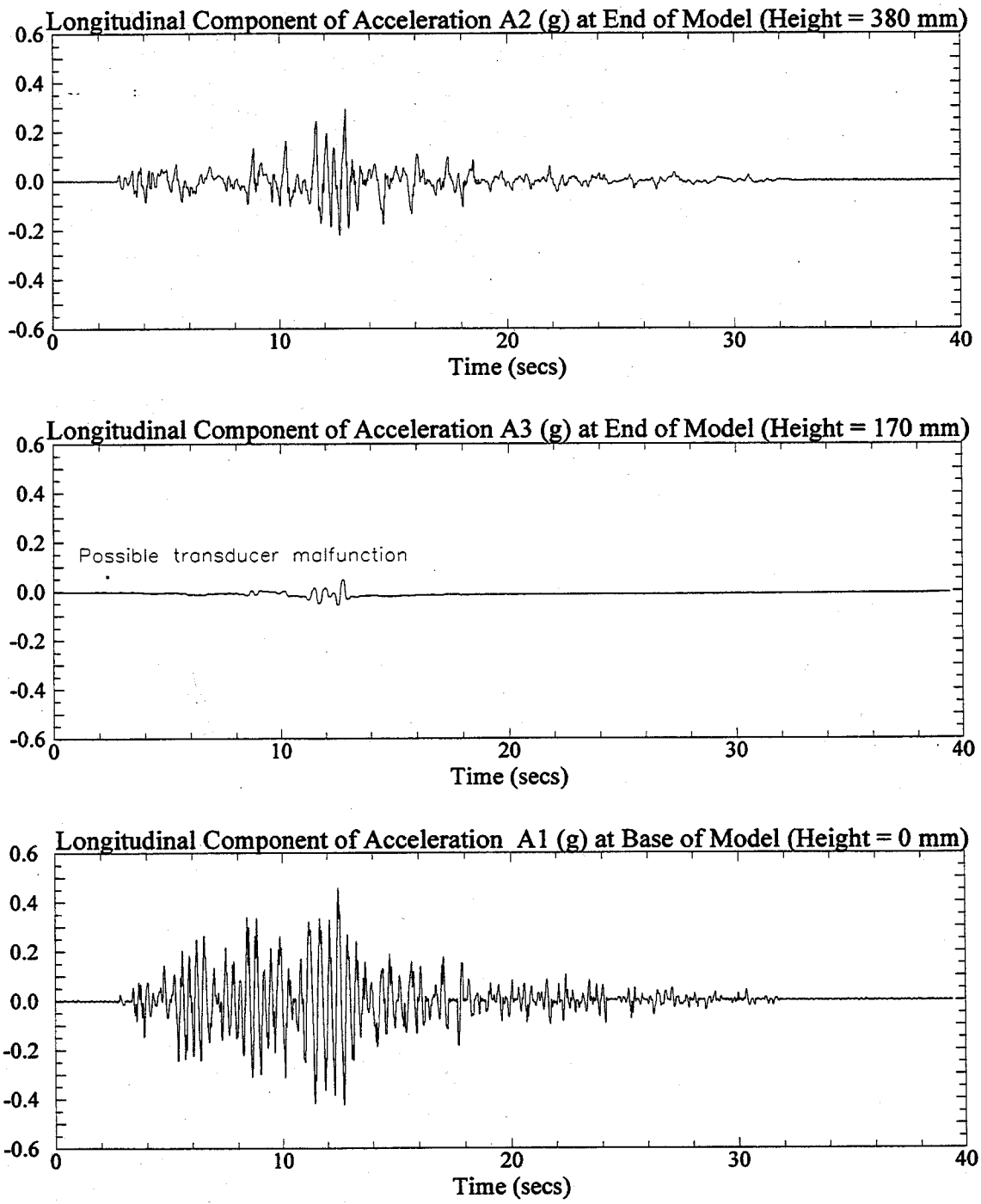

Figure 1: Longitudinal components of recorded acceleration at the base and end of the one-g model SM3I3. Signals were post processed with a low pass filter of 20 Hz.

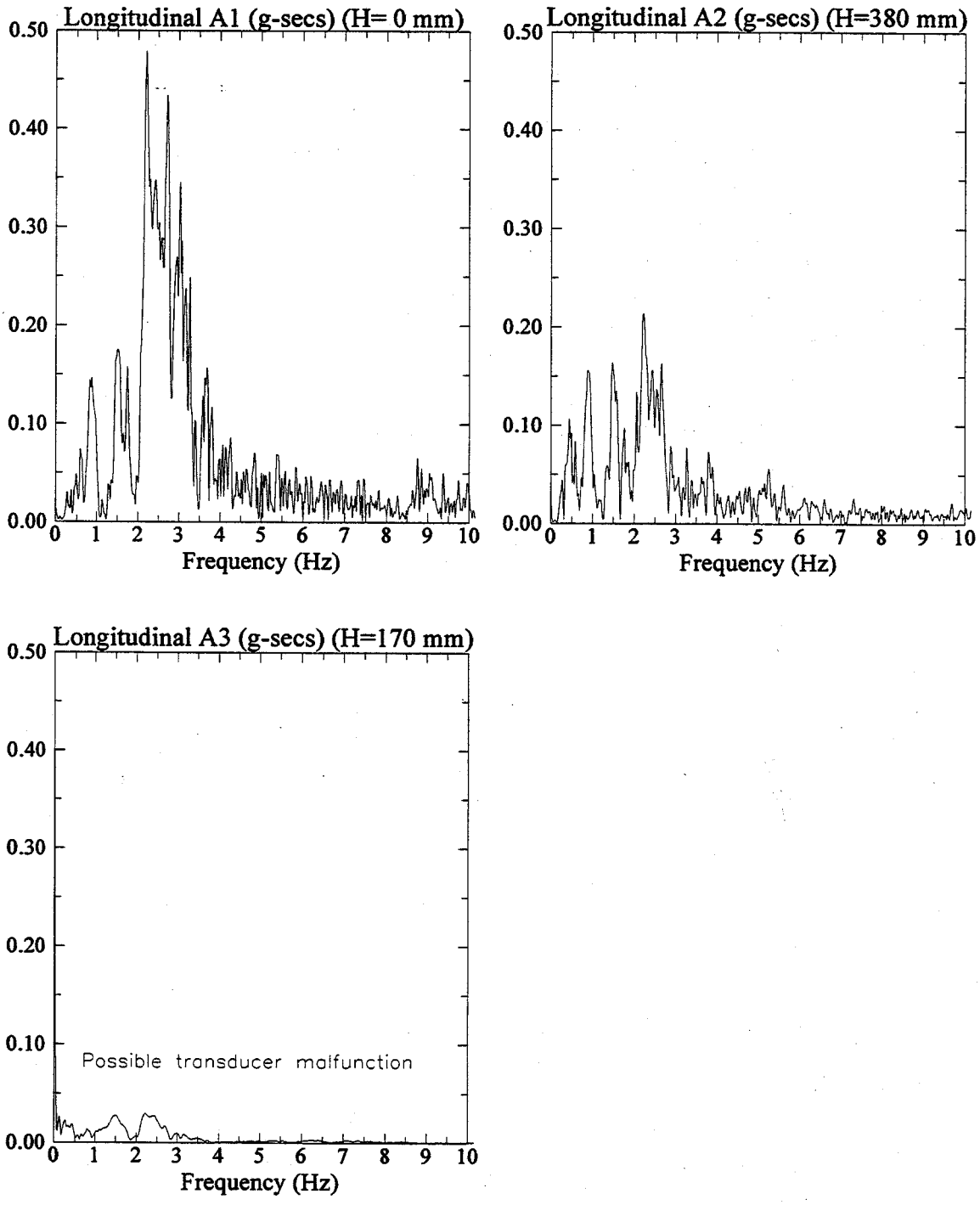

Figure 2: Fast Fourier Transform of longitudinal components of recorded acceleration at the base and end of the one-g model SM3I3.

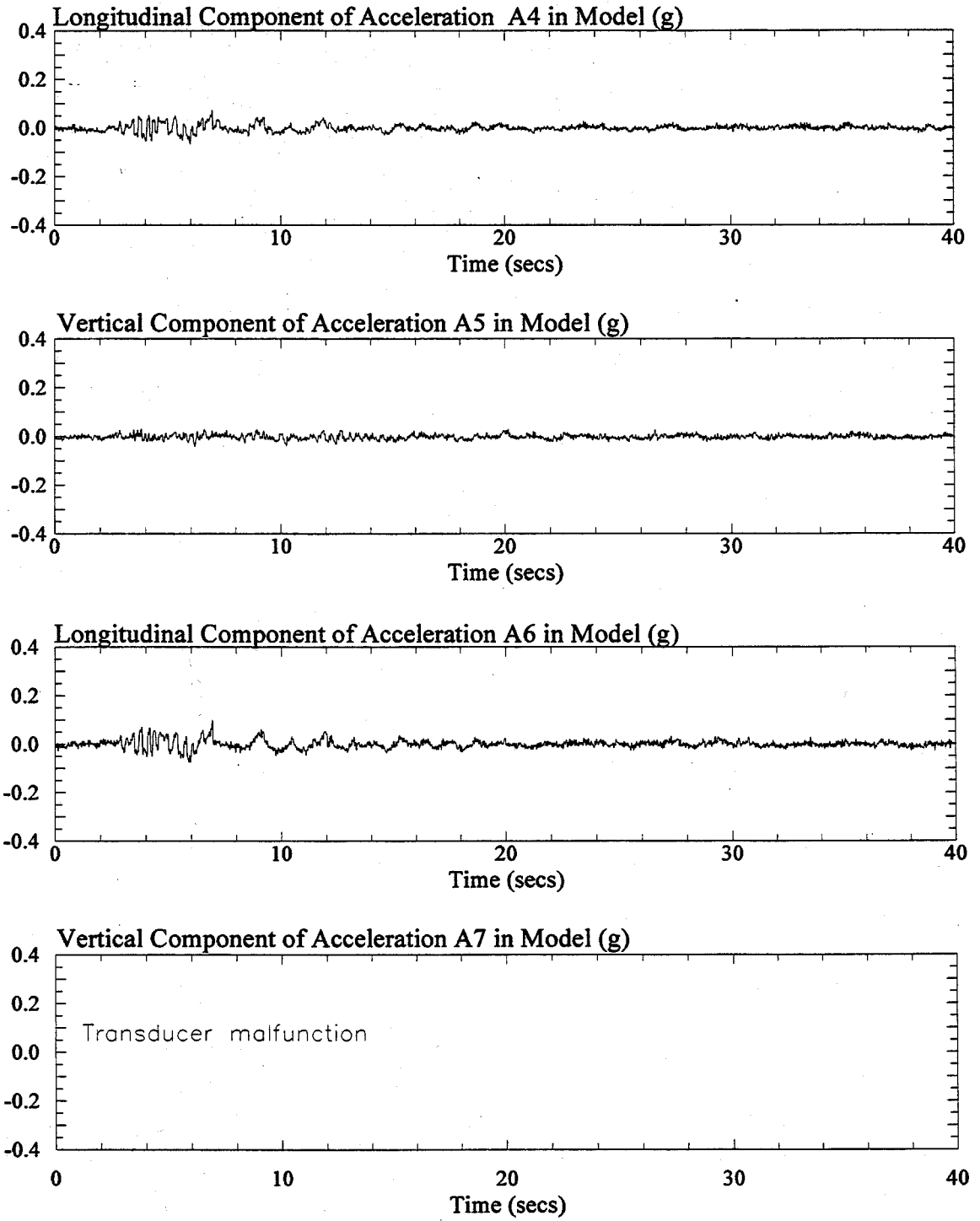

Figure 3: Longitudinal and vertical components of recorded acceleration in the one-g model SM3I3. Signals were post processed with a low pass filter of 20 Hz.

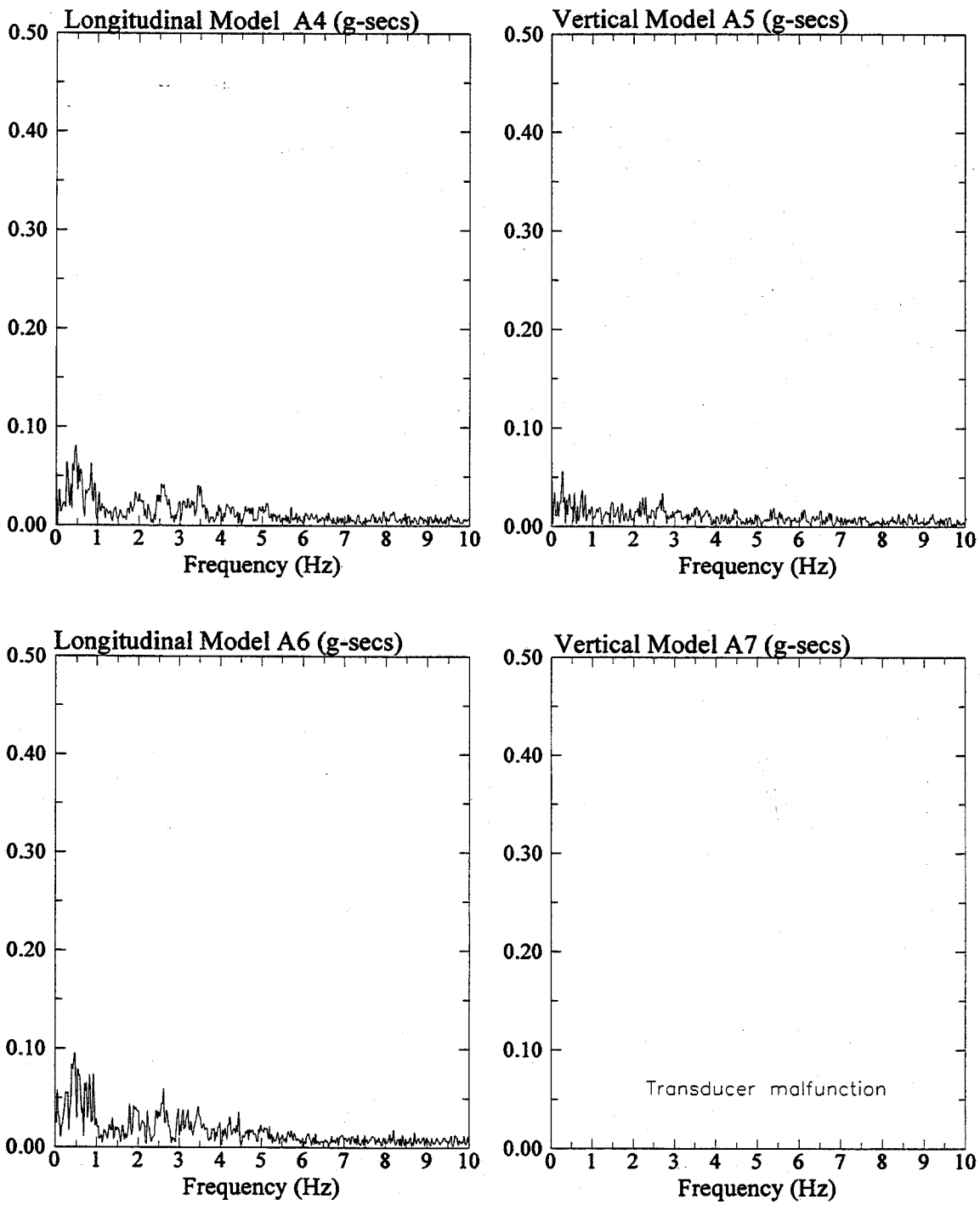

Figure 4: Fast Fourier Transform of longitudinal and vertical components of recorded acceleration in the one-g model SM3I3.

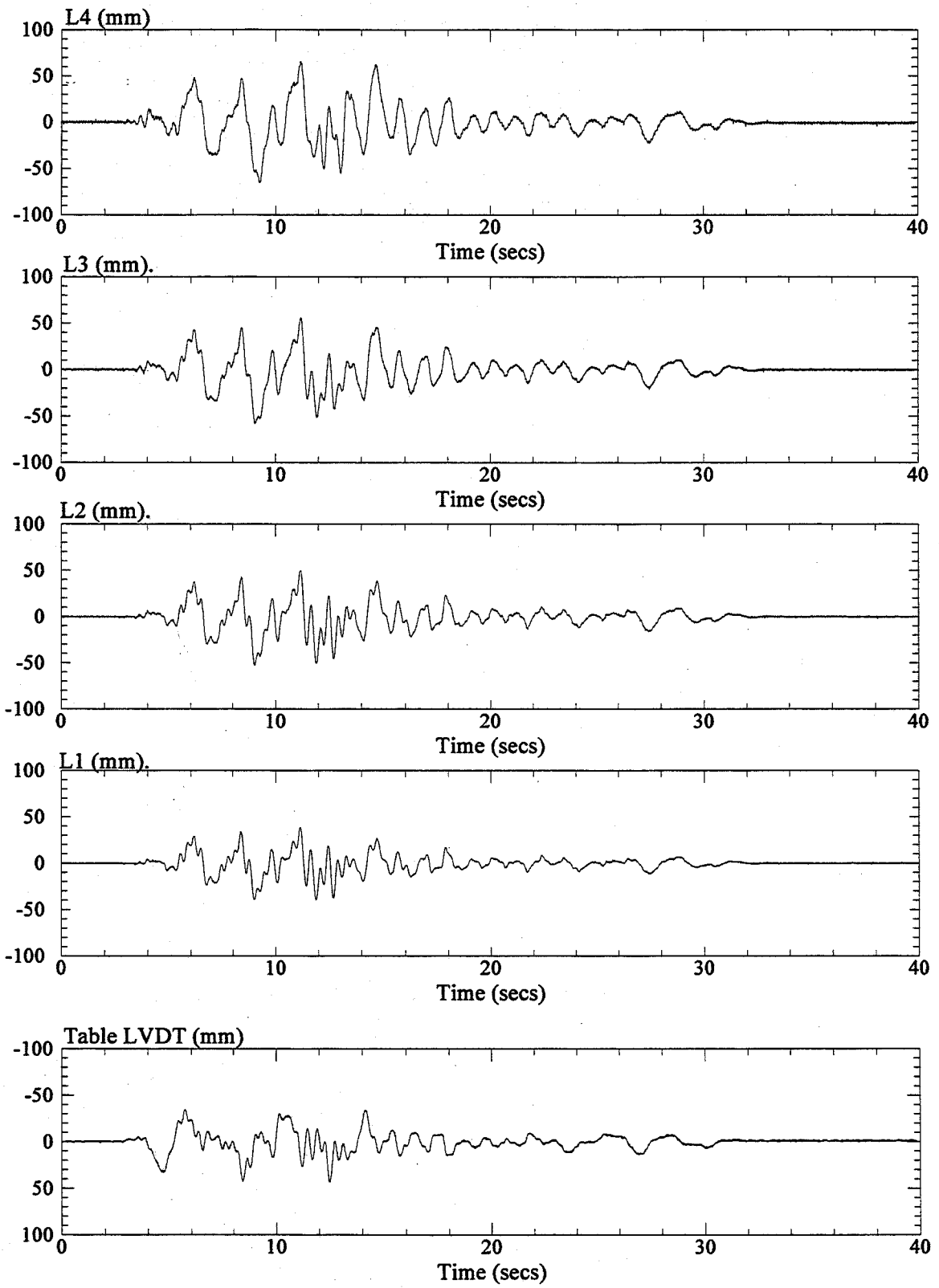

Figure 5: Longitudinal displacements recorded from the shake table LVDT and at LVDT's L1, L2, L3, and L4 in the one-g model SM3I3.

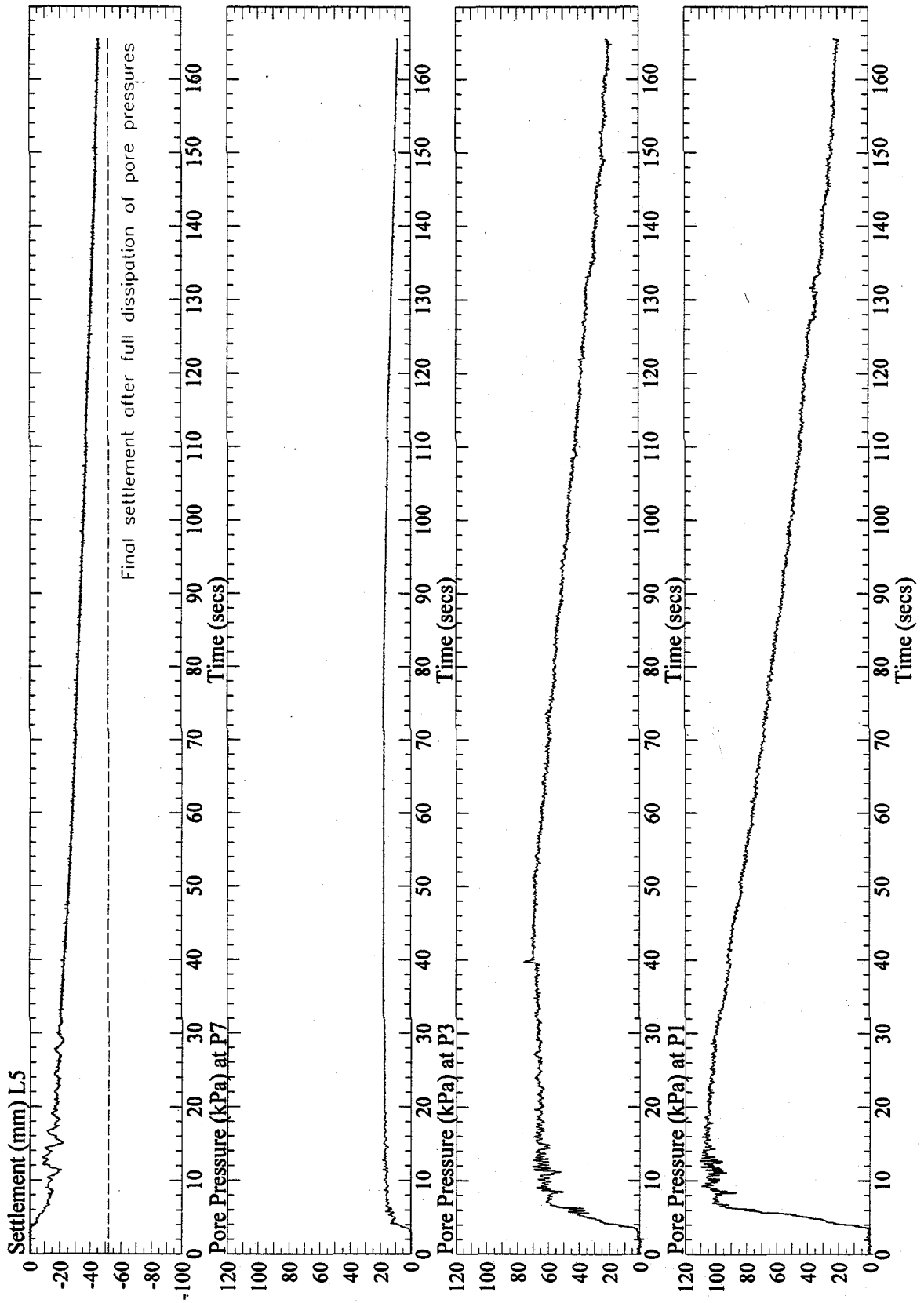

Figure 6: Vertical settlement at L5 and pore pressures at P1, P3, and P7, recorded in the one-g model SM3I3. Signals from P1 and P3 were post processed with a low pass filter of 10 Hz.

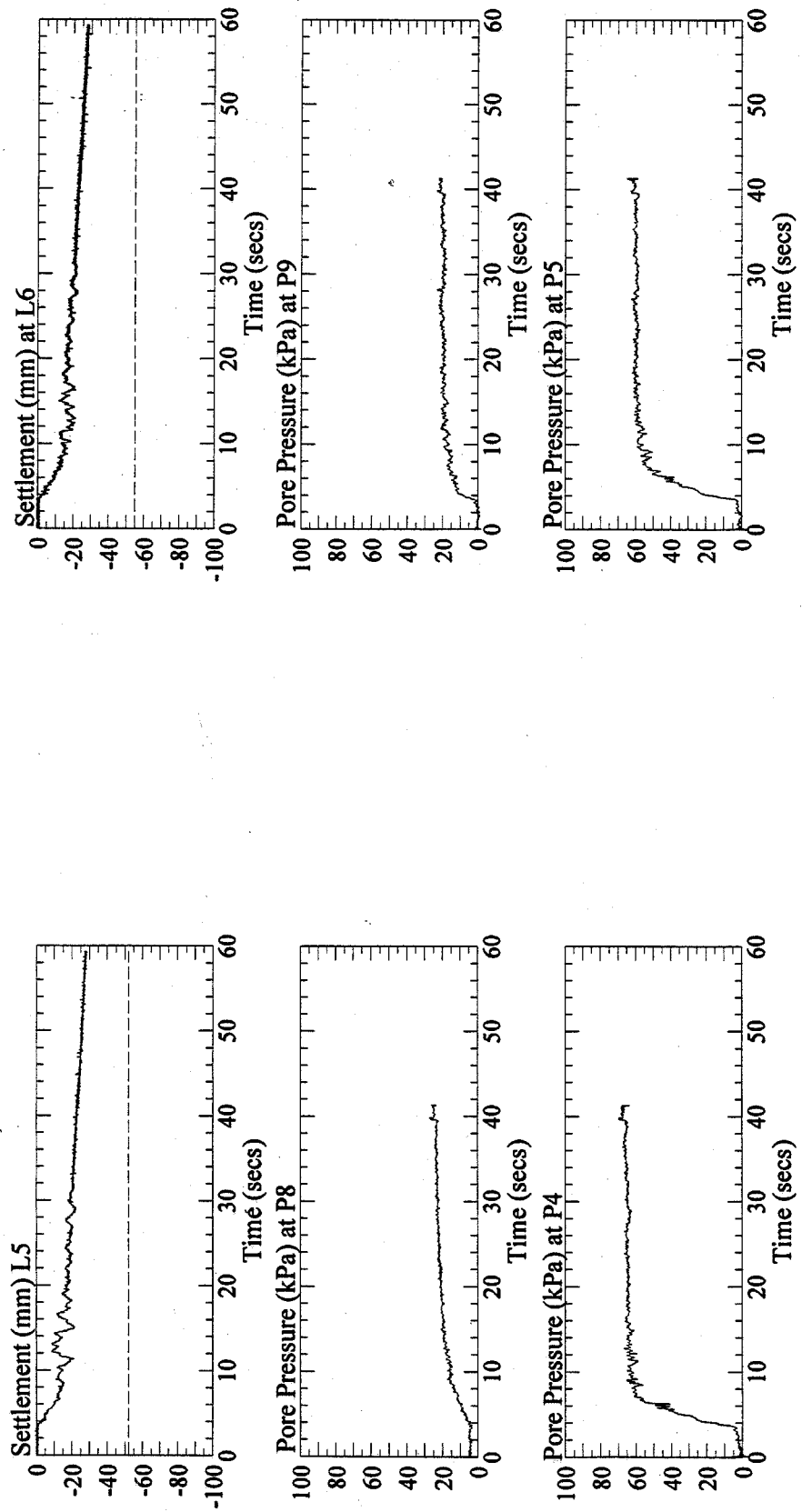

Figure 7: Vertical settlement at L5 and L6, and pore pressures at P4, P5, P8 and P9, recorded in the one-g model SM3I3. Pore pressure signals were post processed with a low pass filter of 10 Hz.

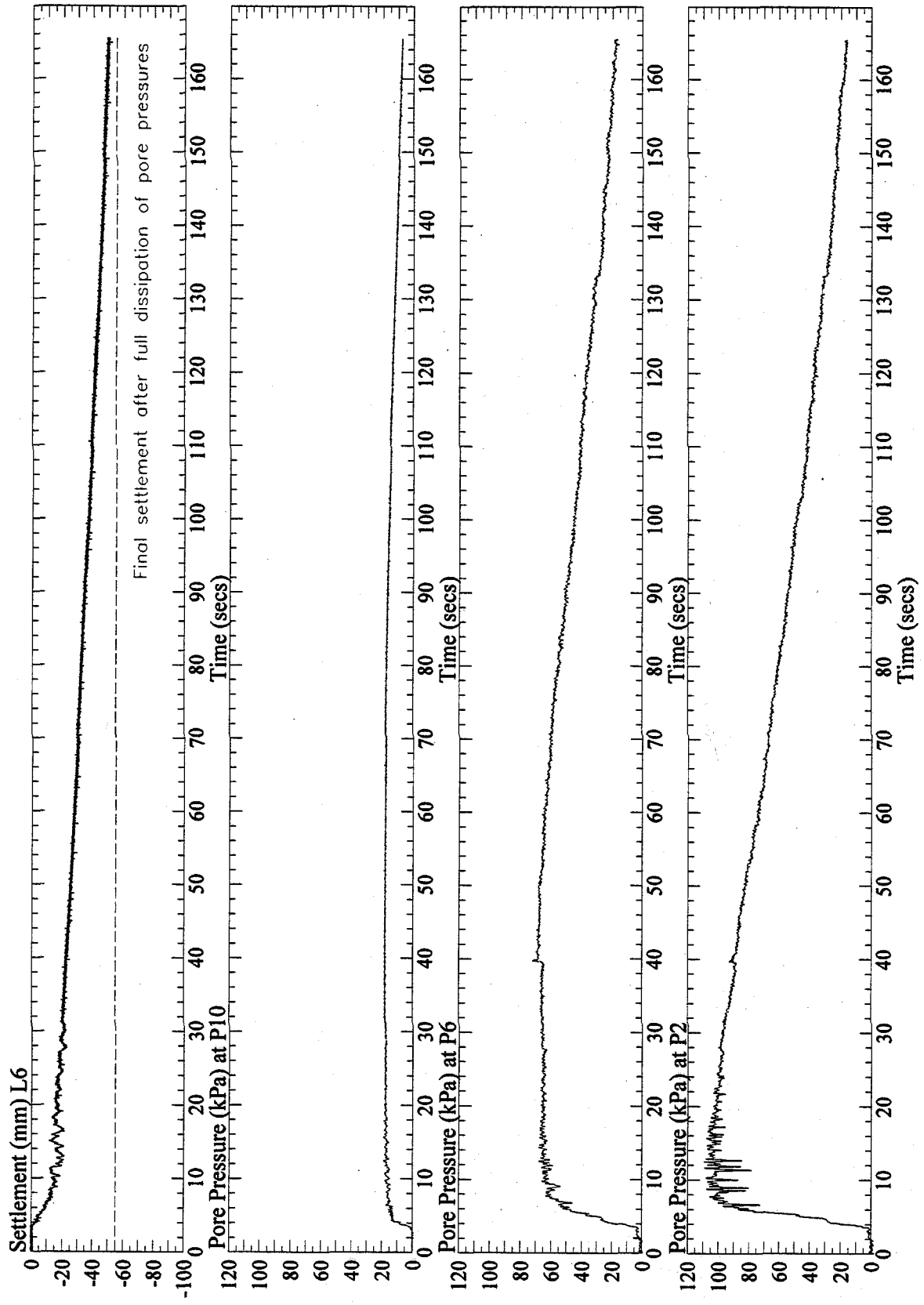

Figure 8: Vertical settlement at L6 and pore pressures at P2, P6, and P10, recorded in the one-g model SM3I3. Signal from P2 and P6 were post processed with a low pass filter of 10 Hz.

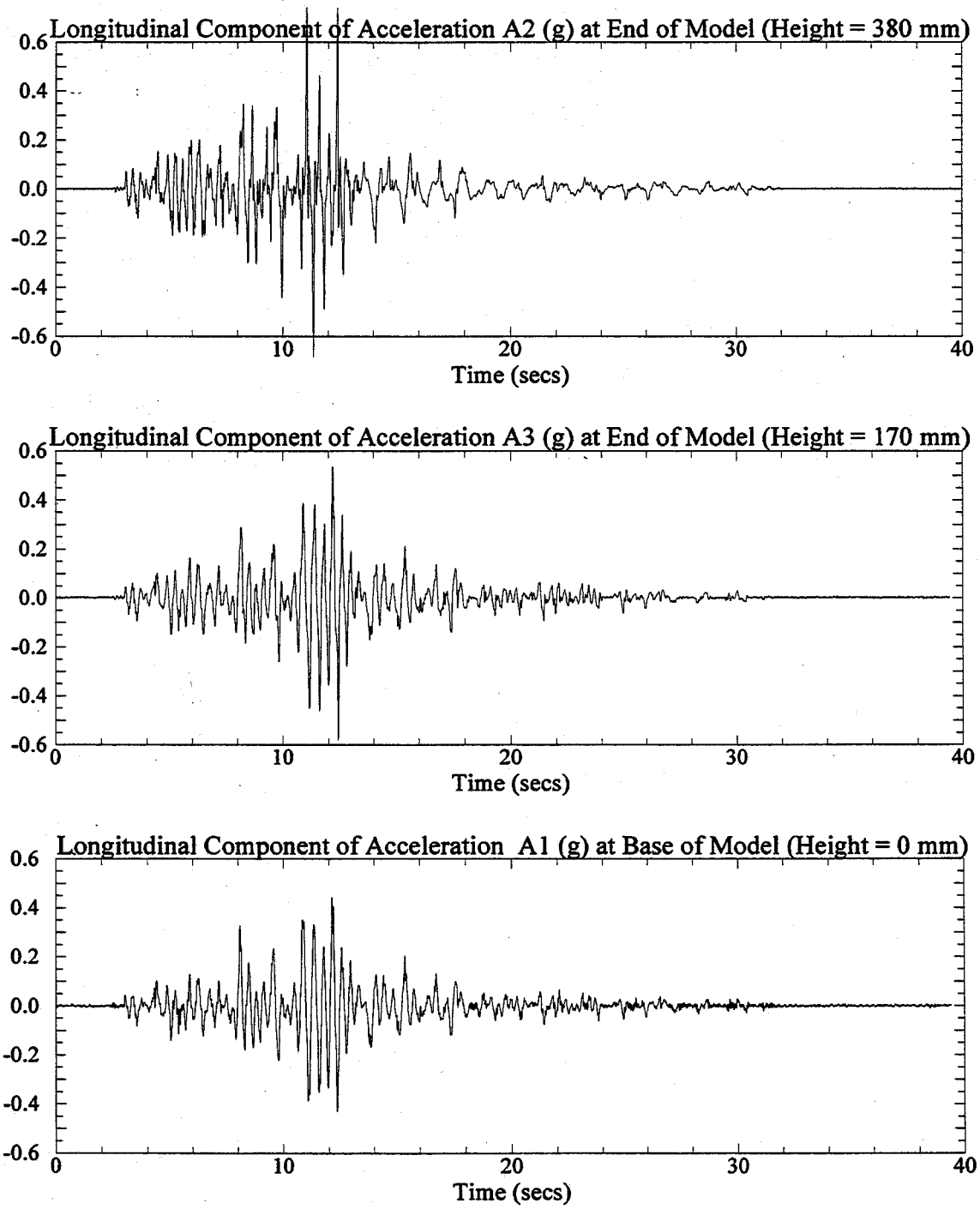

Figure 1: Longitudinal components of recorded acceleration at the base and end of the one-g model SM3I4. Signals were post processed with a low pass filter of 20 Hz.

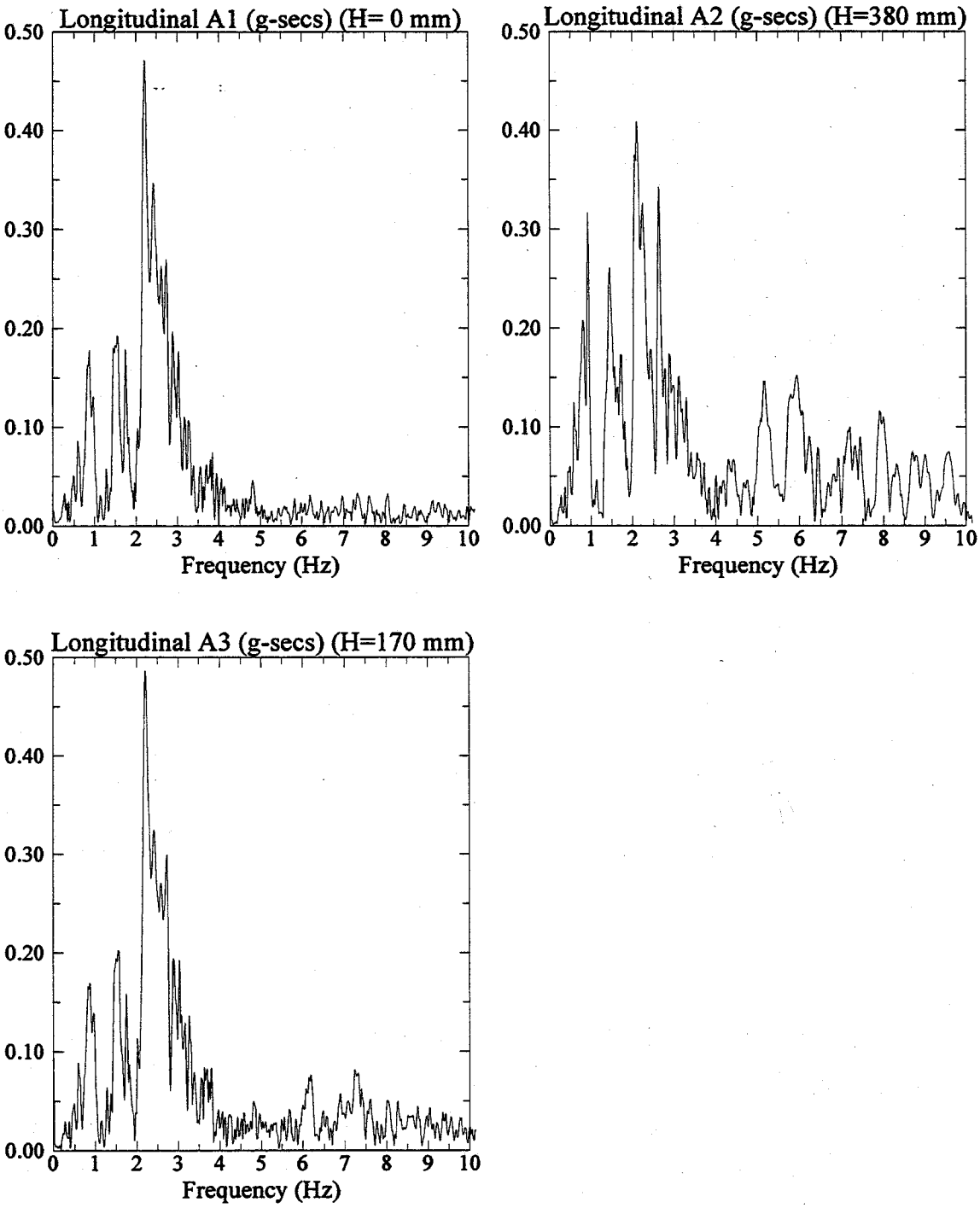

Figure 2: Fast Fourier Transform of longitudinal components of recorded acceleration at the base and end of the one-g model SM3I4.

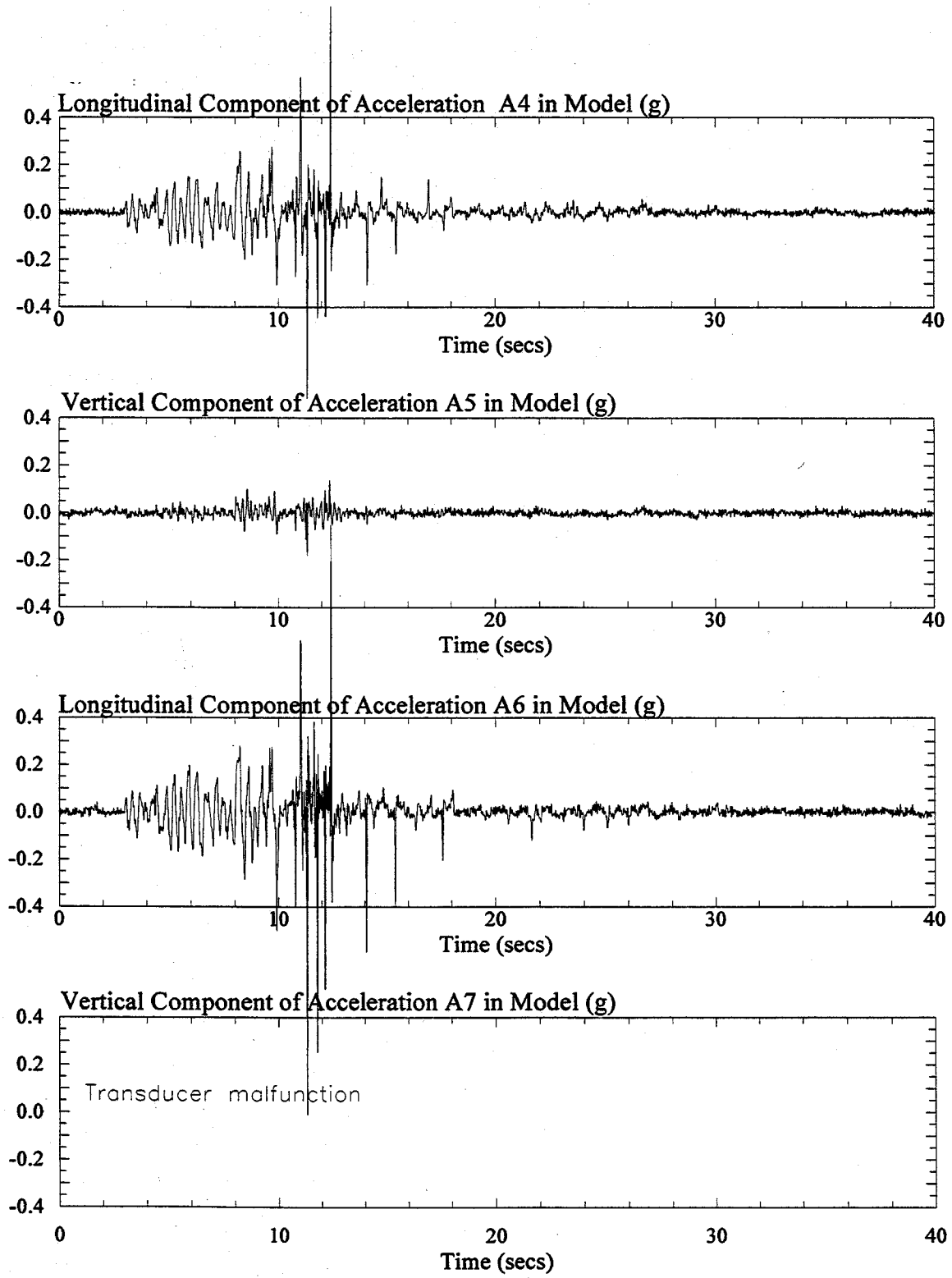

Figure 3: Longitudinal and vertical components of recorded acceleration in the one-g model SM3I4. Signals were post processed with a low pass filter of 20 Hz.

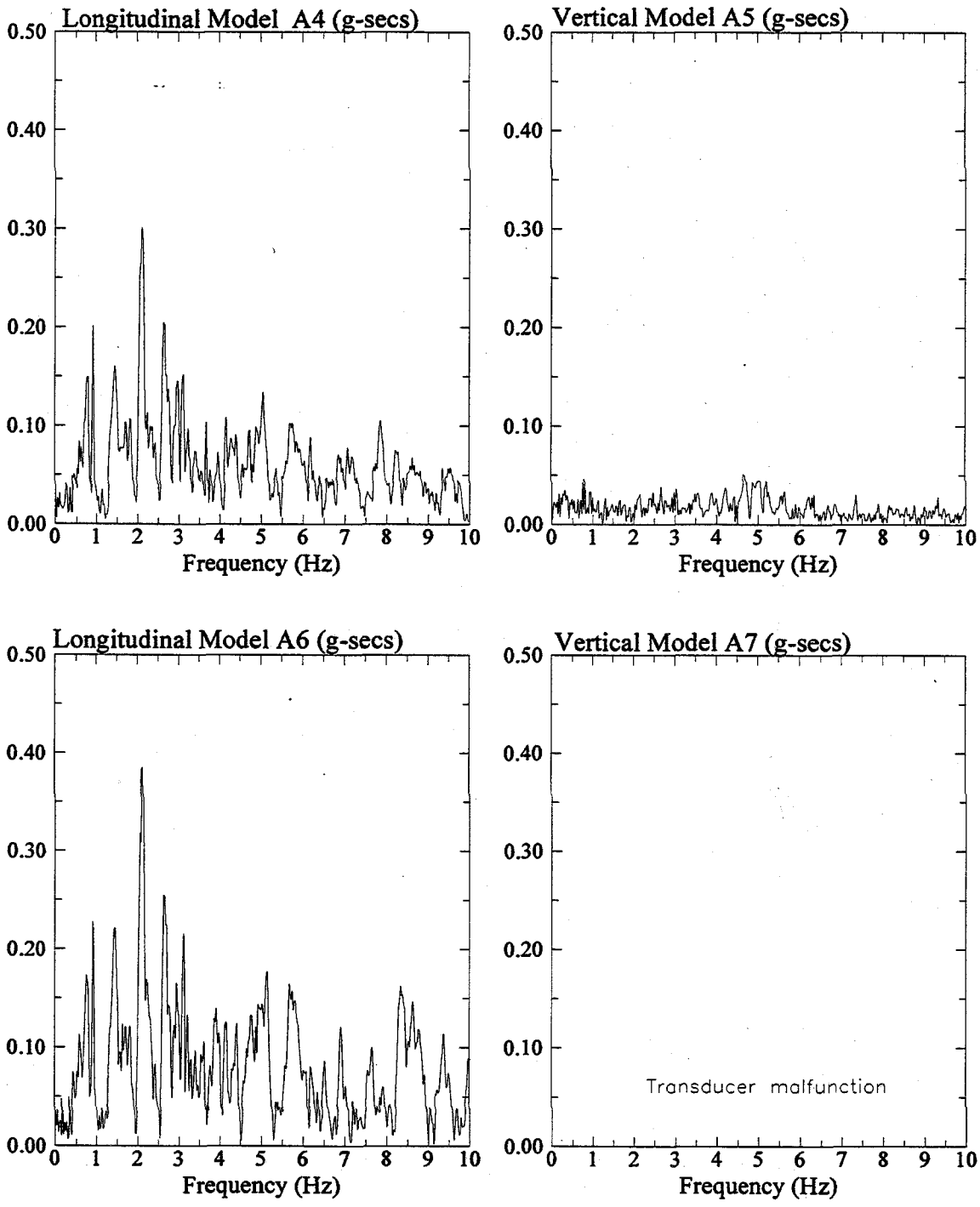

Figure 4: Fast Fourier Transform of longitudinal and vertical components of recorded acceleration in the one-g model SM3I4.

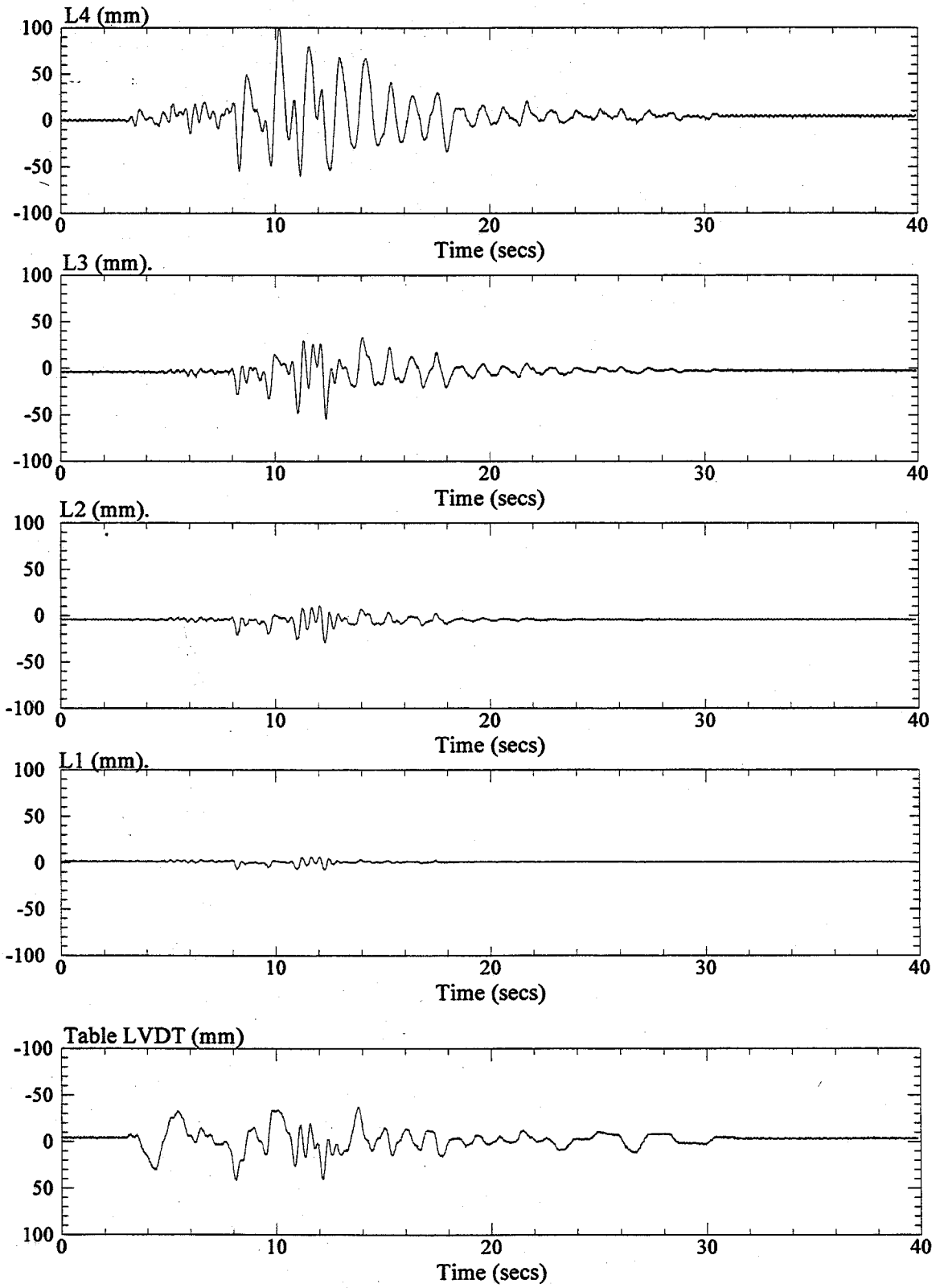

Figure 5: Longitudinal displacements recorded from the shake table LVDT and at LVDT's L1, L2, L3, and L4 in the one-g model SM3I4.

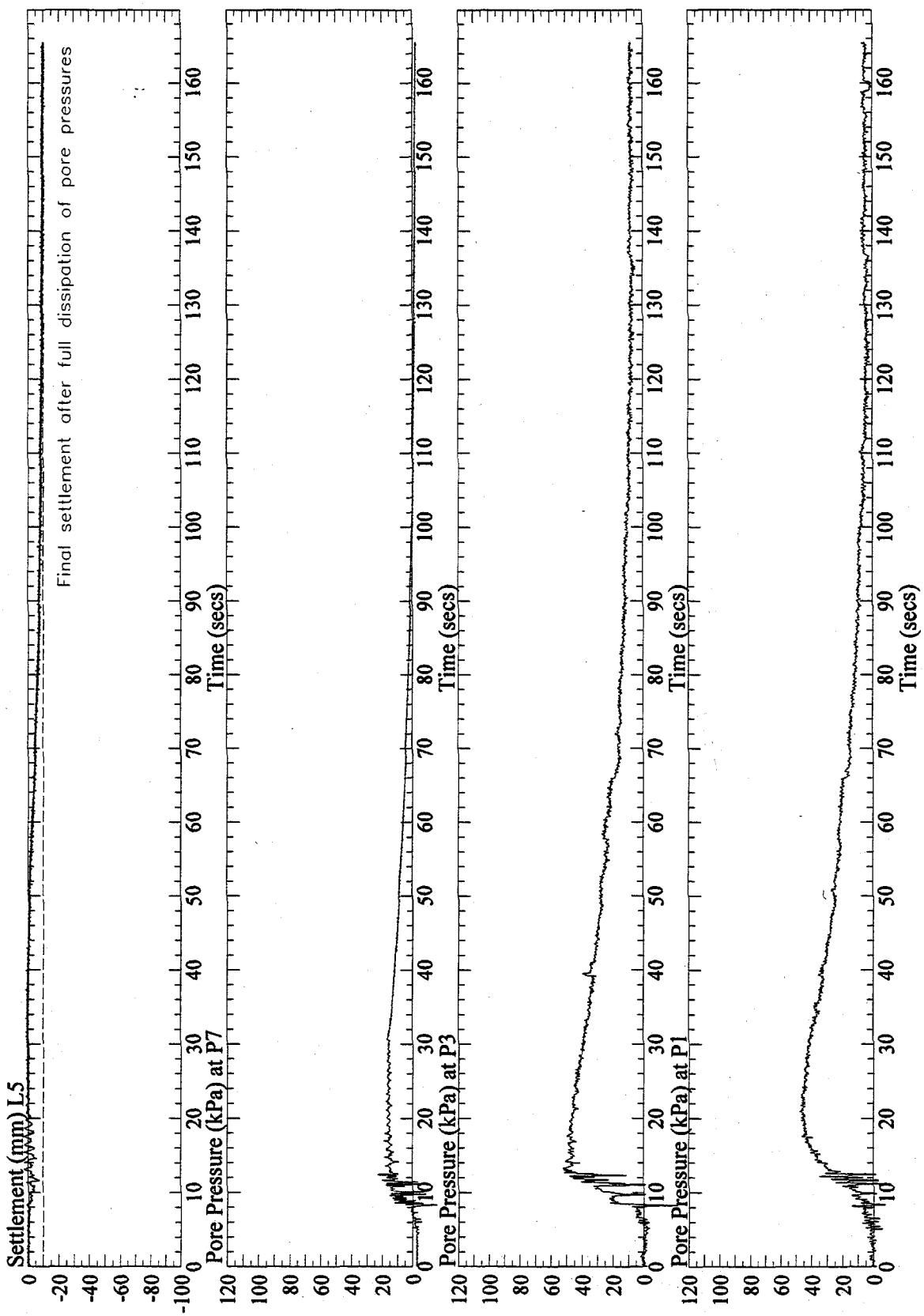

Figure 6: Vertical settlement at L5 and pore pressures at P1, P3, and P7, recorded in the one-g model SM3I4. Signals from P1 and P3 were post processed with a low pass filter of 10 Hz.

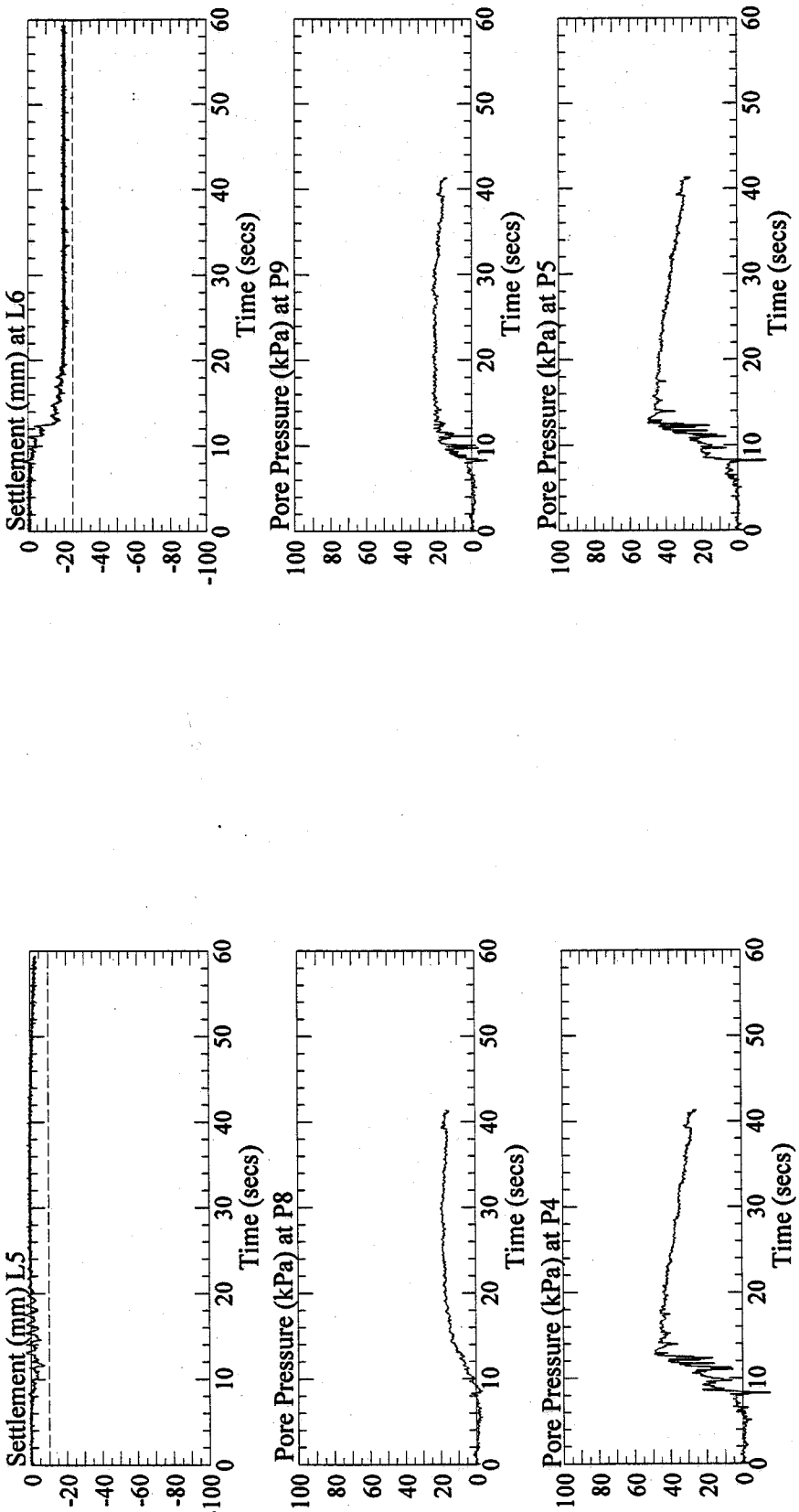

Figure 7: Vertical settlement at L5 and L6, and pore pressures at P4, P5, P8 and P9, recorded in the one-g model SM3I4. Pore pressure signals were post processed with a low pass filter of 10 Hz.

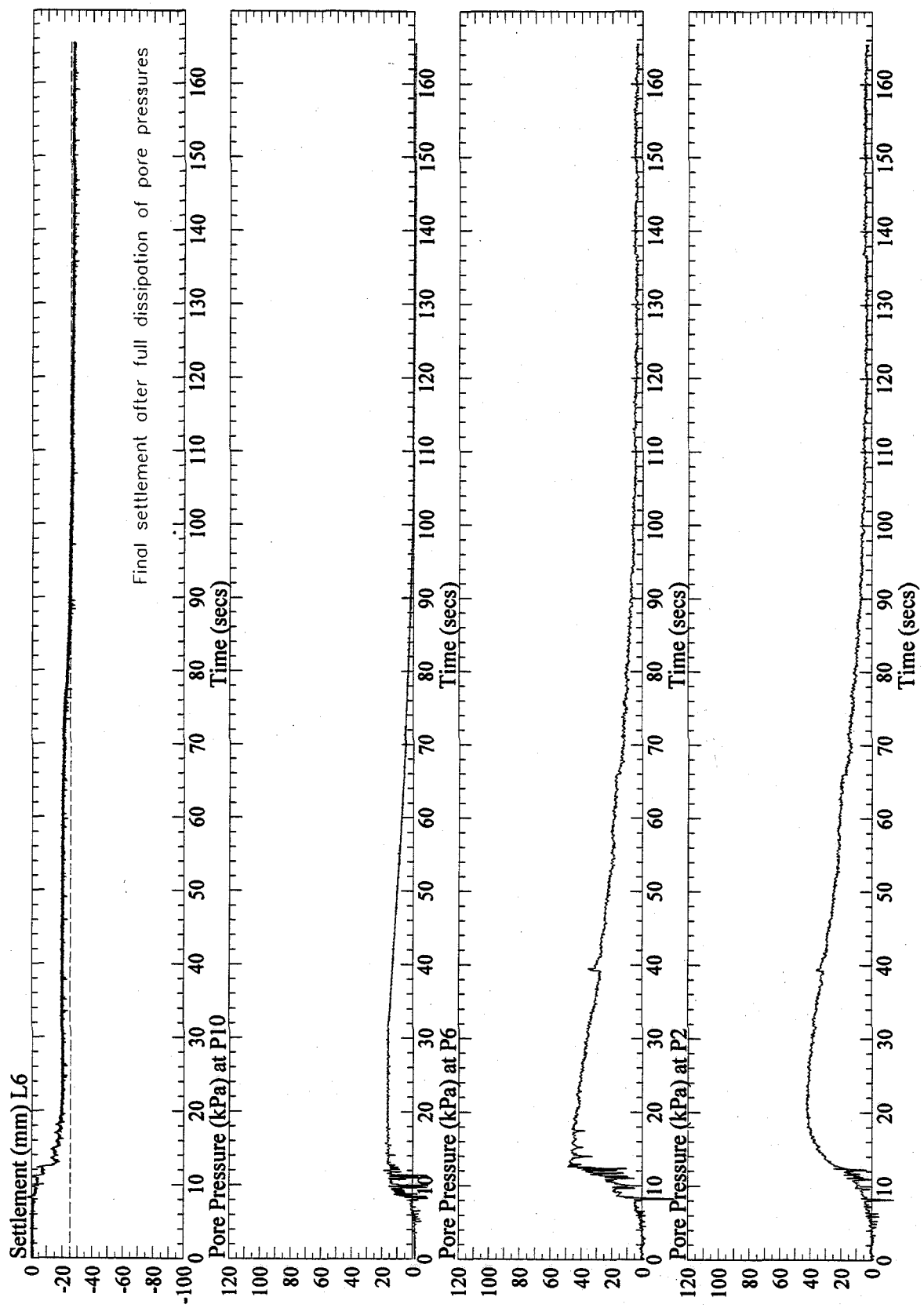

Figure 8: Vertical settlement at L6 and pore pressures at P2, P6, and P10, recorded in the one-g model SM3I4. Signal from P2 and P6 were post processed with a low pass filter of 10 Hz.

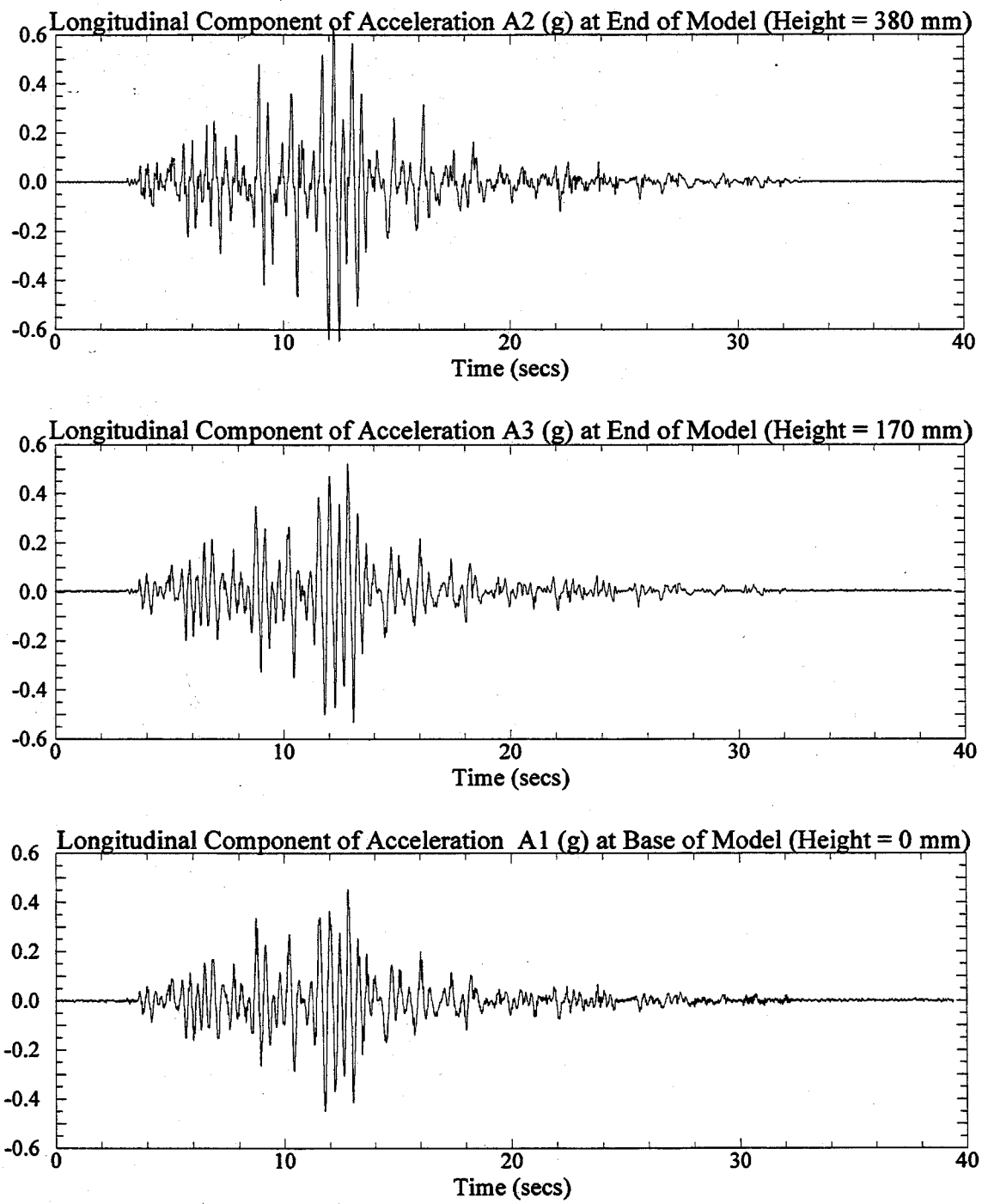

Figure 1: Longitudinal components of recorded acceleration at the base and end of the one-g model SM3I5. Signals were post processed with a low pass filter of 20 Hz.

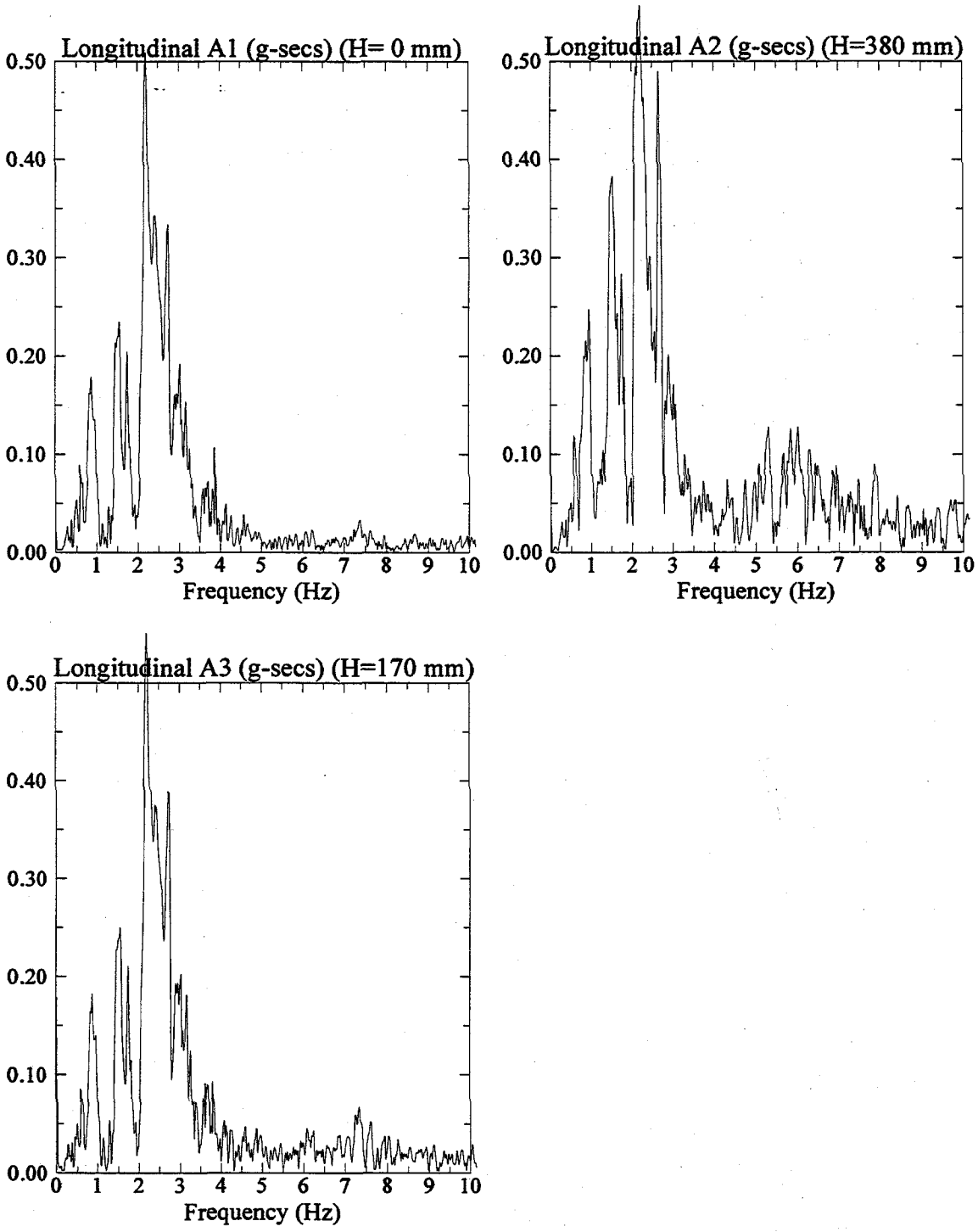

Figure 2: Fast Fourier Transform of longitudinal components of recorded acceleration at the base and end of the one-g model SM3I5.

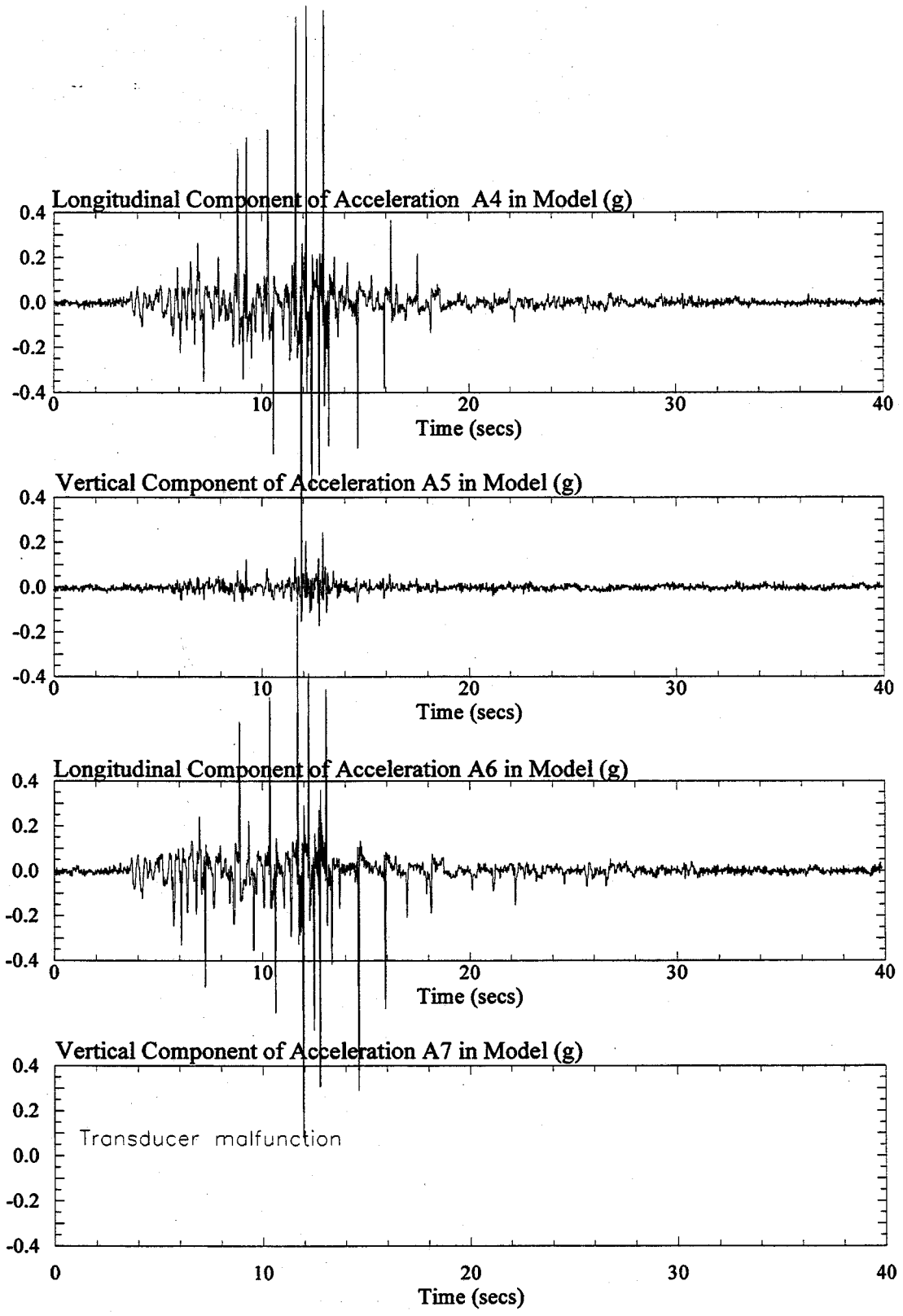

Figure 3: Longitudinal and vertical components of recorded acceleration in the one-g model SM3I5. Signals were post processed with a low pass filter of 20 Hz.

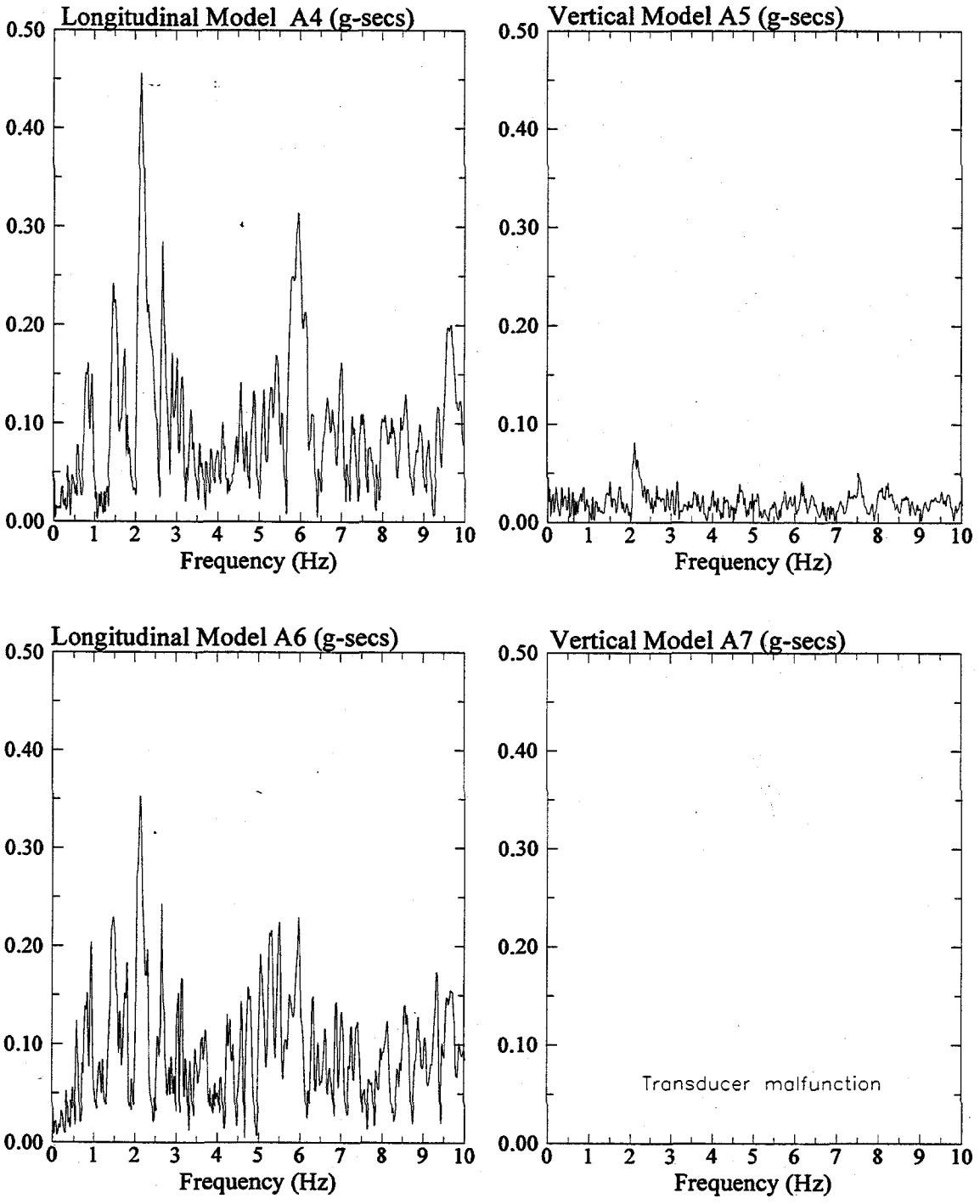

Figure 4: Fast Fourier Transform of longitudinal and vertical components of recorded acceleration in the one-g model SM3I5.

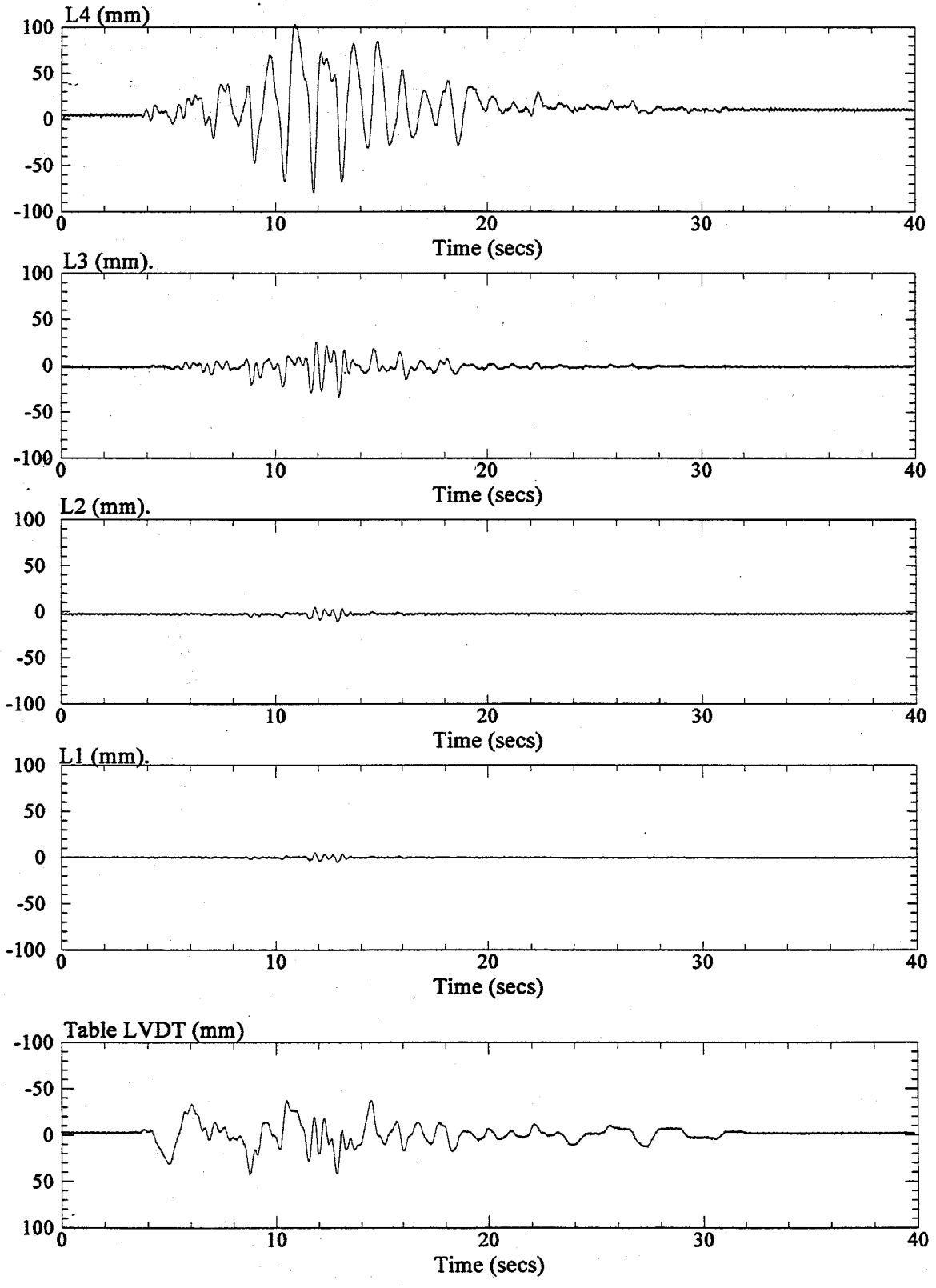

Figure 5: Longitudinal displacements recorded from the shake table LVDT and at LVDT's L1, L2, L3, and L4 in the one-g model SM3I5.

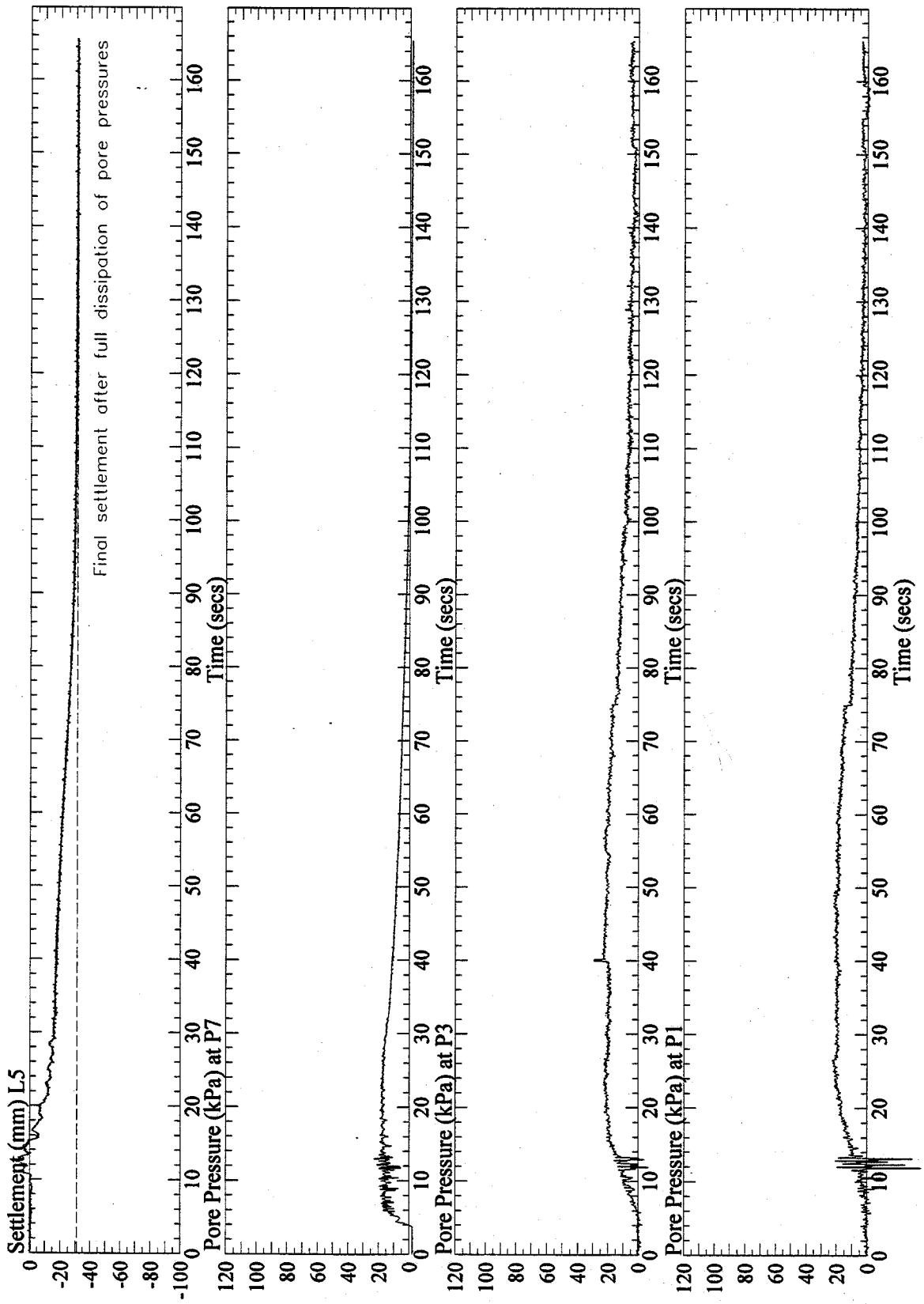

Figure 6: Vertical settlement at L5 and pore pressures at P1, P3, and P7, recorded in the one-g model SM3I5. Signals from P1 and P3 were post processed with a low pass filter of 10 Hz.

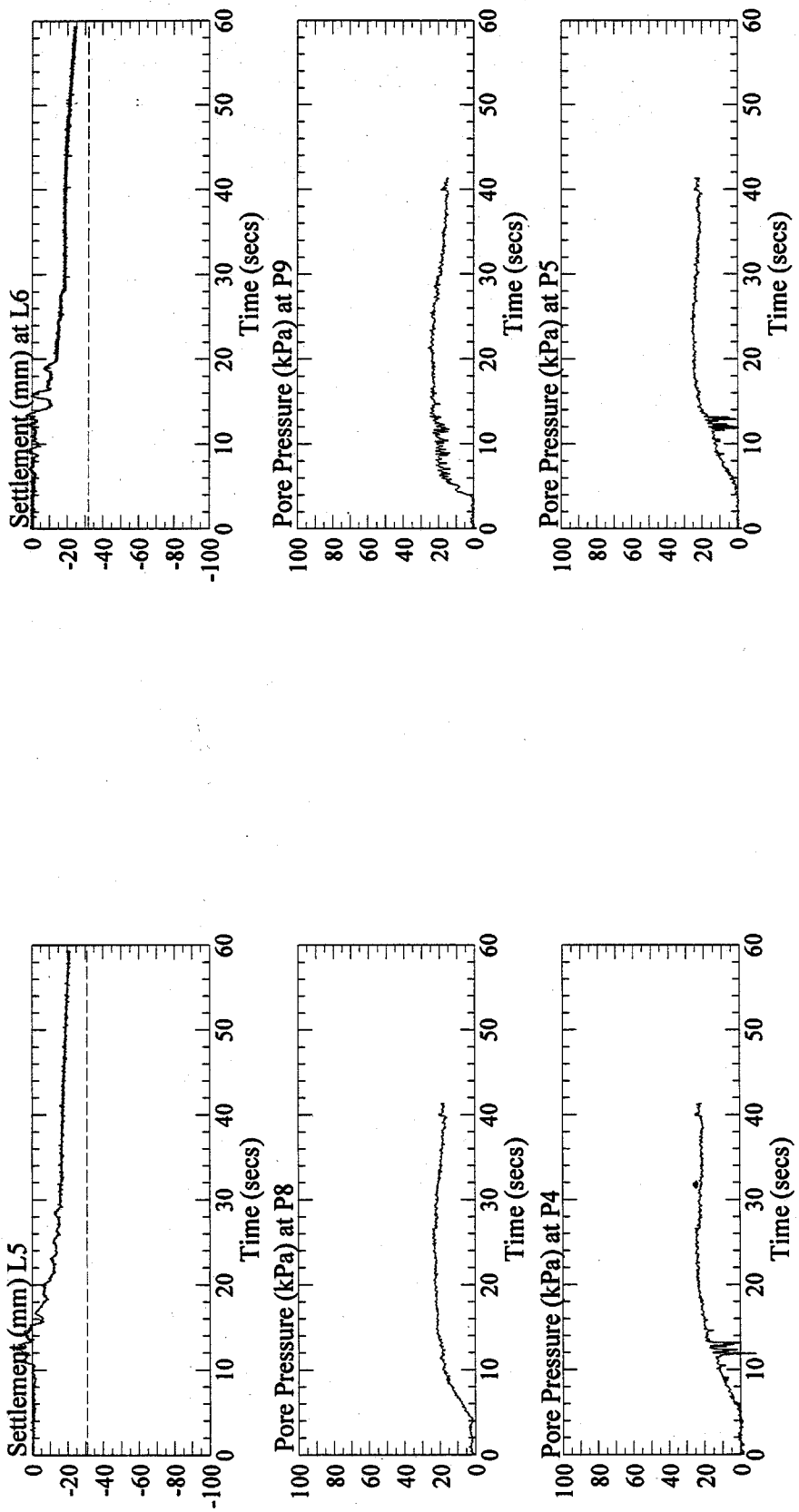

Figure 7: Vertical settlement at L5 and L6, and pore pressures at P4, P5, P8 and P9, recorded in the one-g model SM3I5. Pore pressure signals were post processed with a low pass filter of 10 Hz.

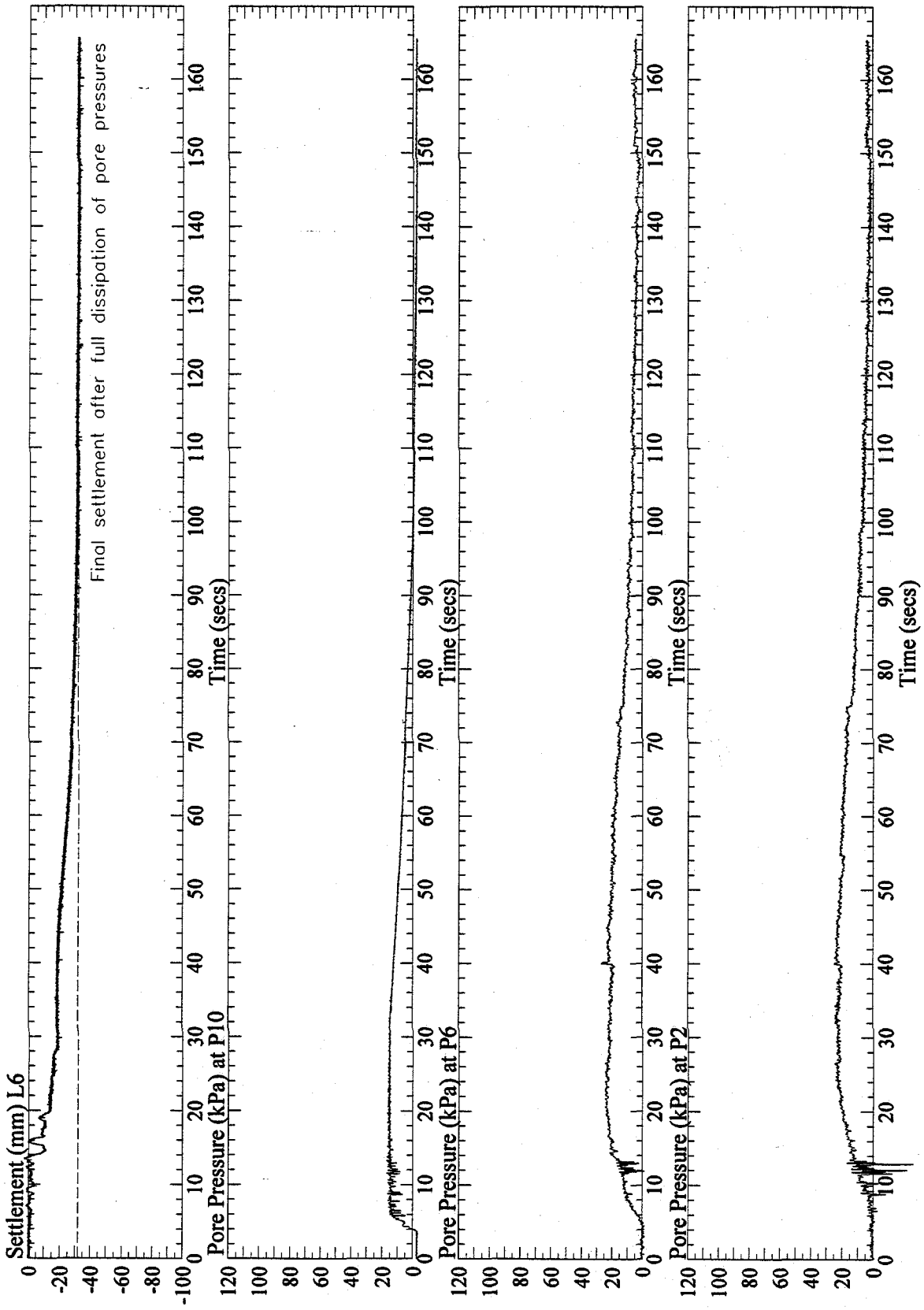

Figure 8: Vertical settlement at L6 and pore pressures at P2, P6, and P10, recorded in the one-g model SM3I5. Signal from P2 and P6 were post processed with a low pass filter of 10 Hz.

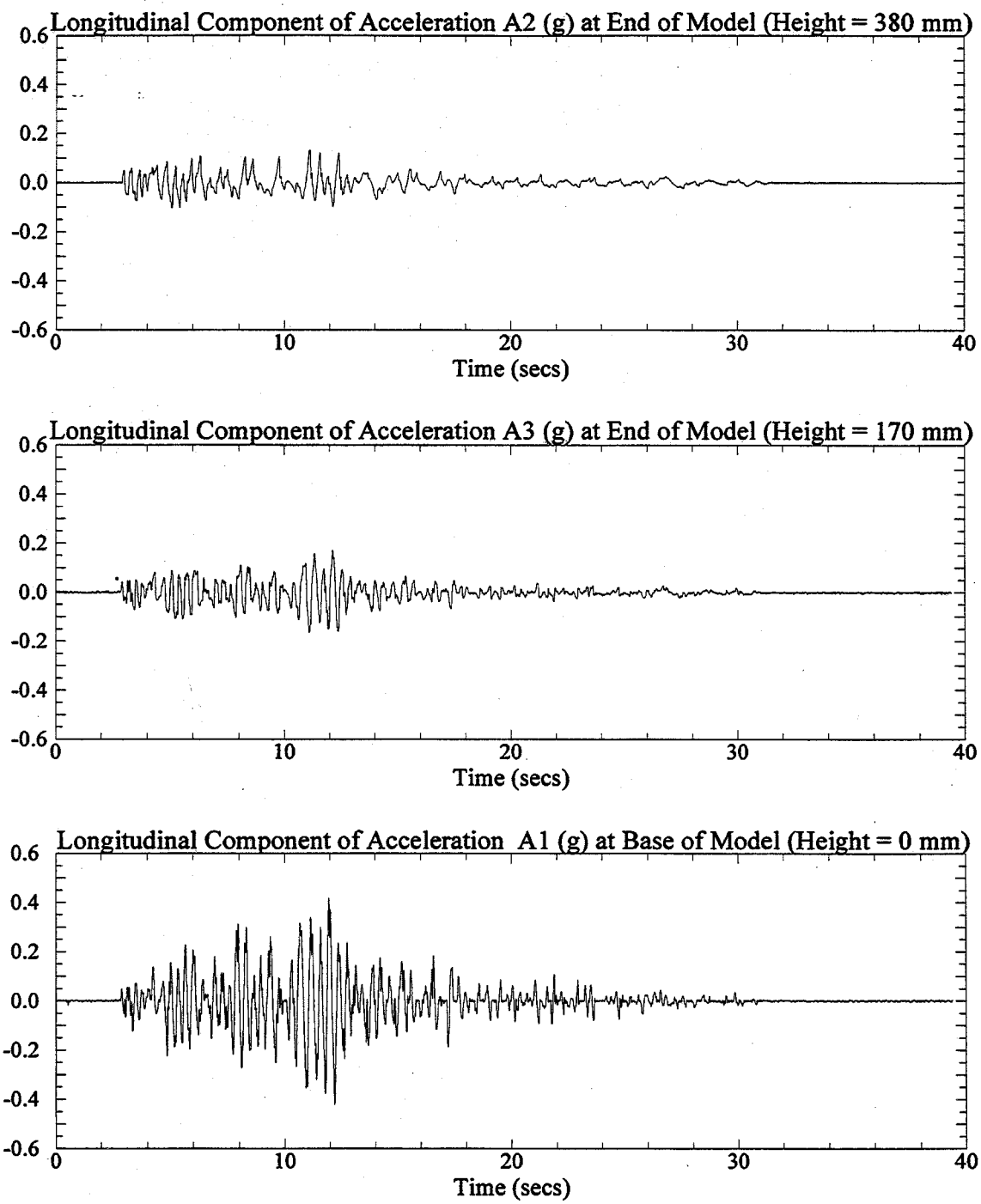

Figure 1: Longitudinal components of recorded acceleration at the base and end of the one-g model SM3J1. Signals were post processed with a low pass filter of 20 Hz.

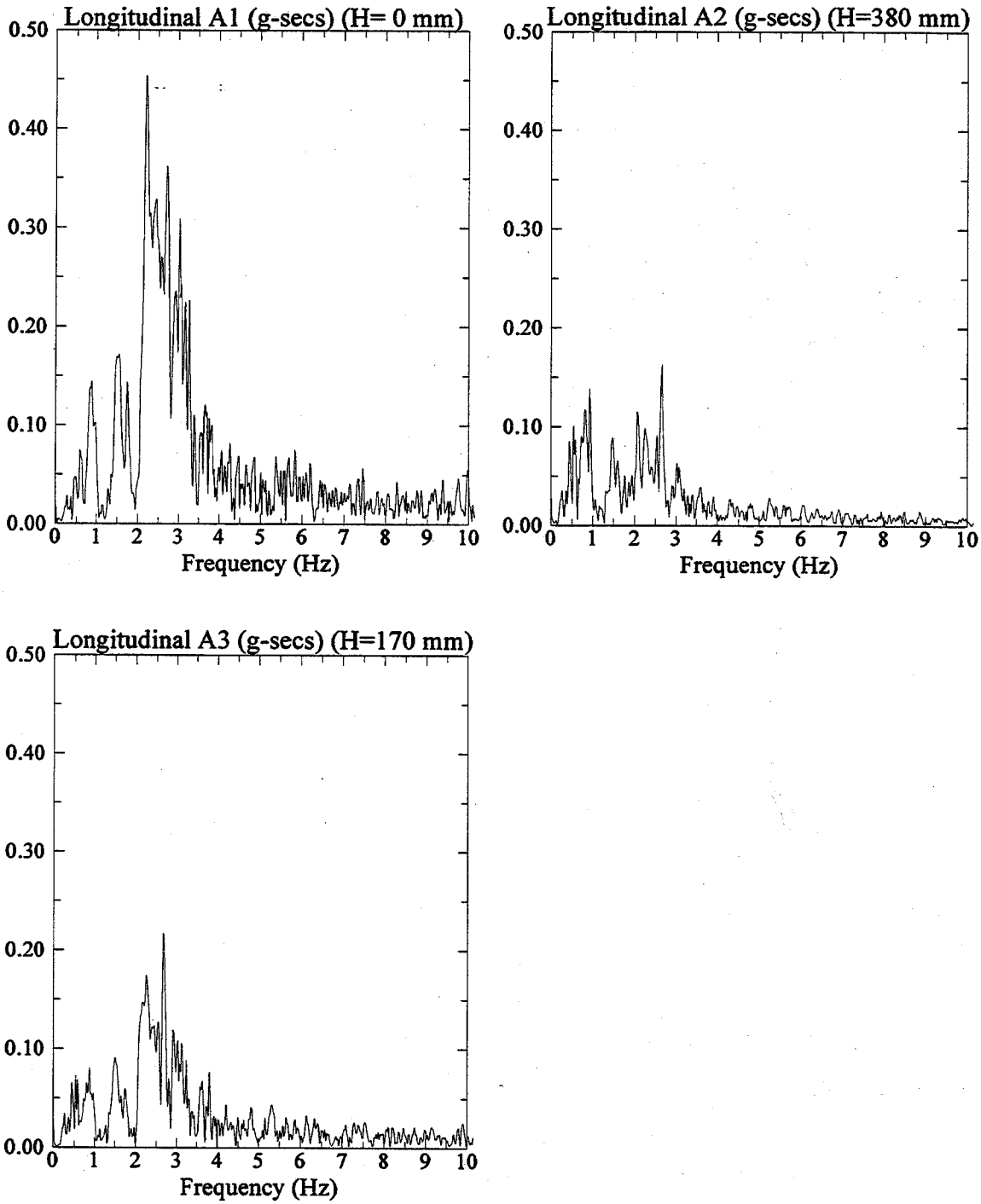

Figure 2: Fast Fourier Transform of longitudinal components of recorded acceleration at the base and end of the one-g model SM3J1.

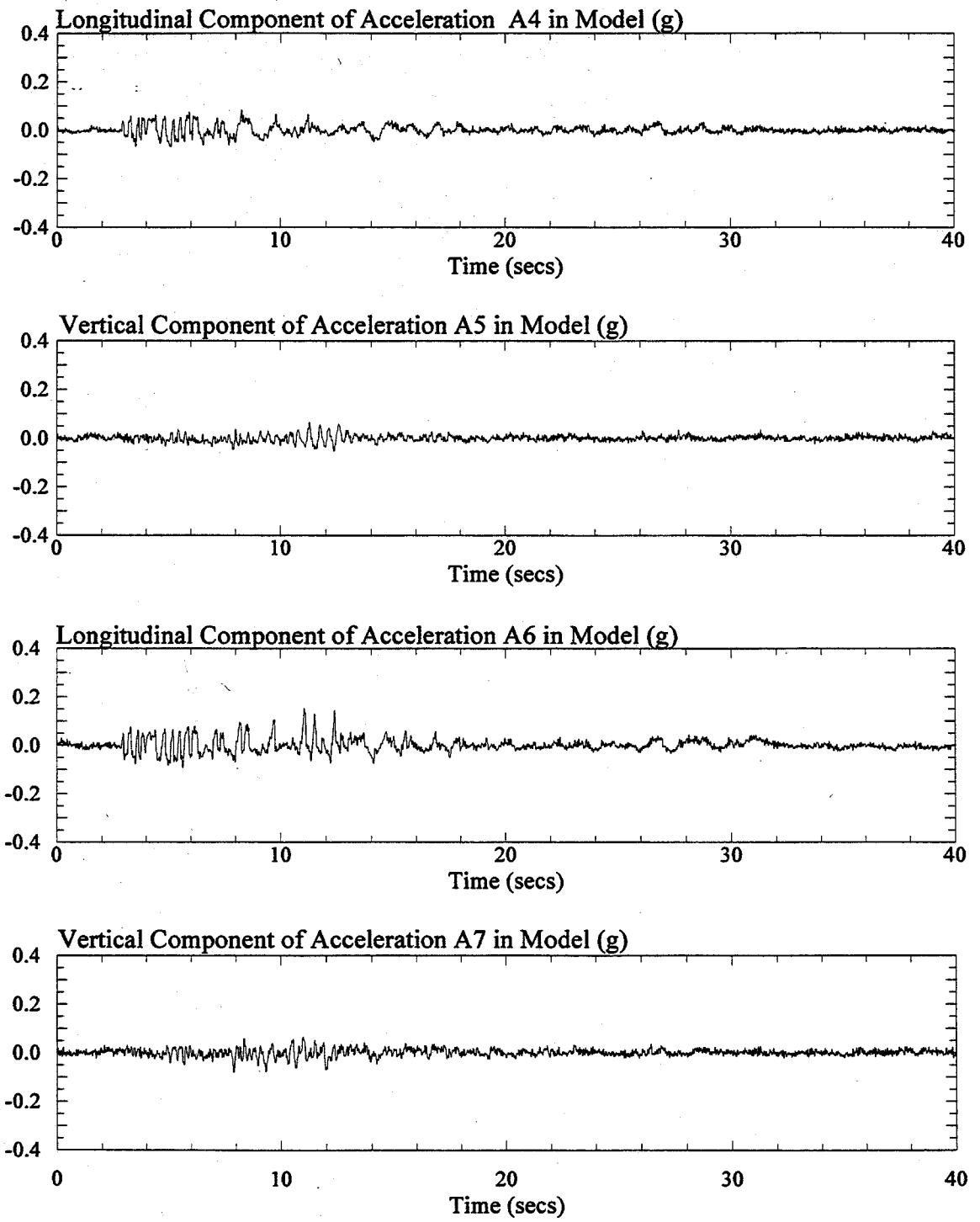

Figure 3: Longitudinal and vertical components of recorded acceleration in the one-g model SM3J1. Signals were post processed with a low pass filter of 20 Hz.

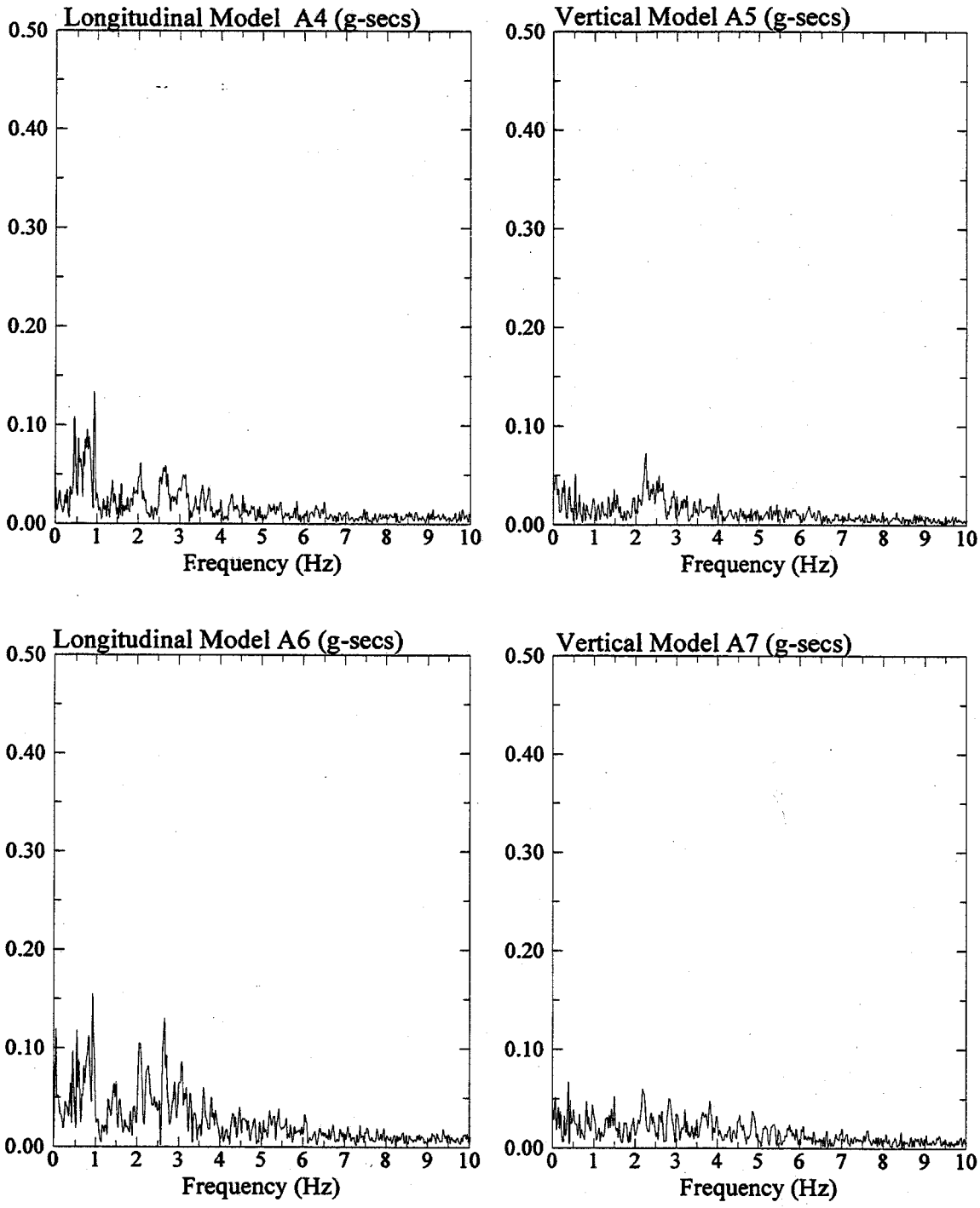

Figure 4: Fast Fourier Transform of longitudinal and vertical components of recorded acceleration in the one-g model SM3J1.

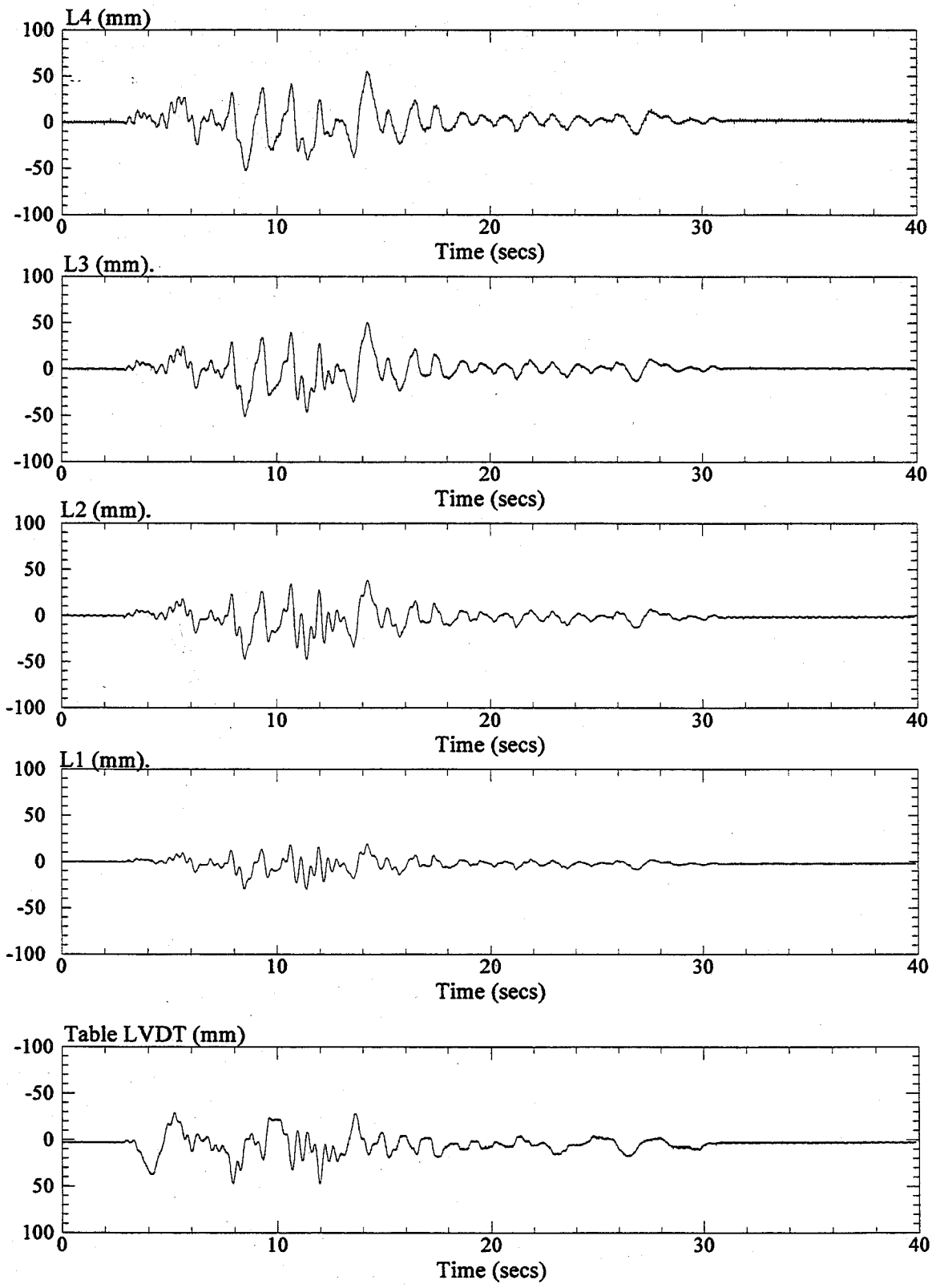

Figure 5: Longitudinal displacements recorded from the shake table LVDT and at LVDT's L1, L2, L3, and L4 in the one-g model SM3J1.

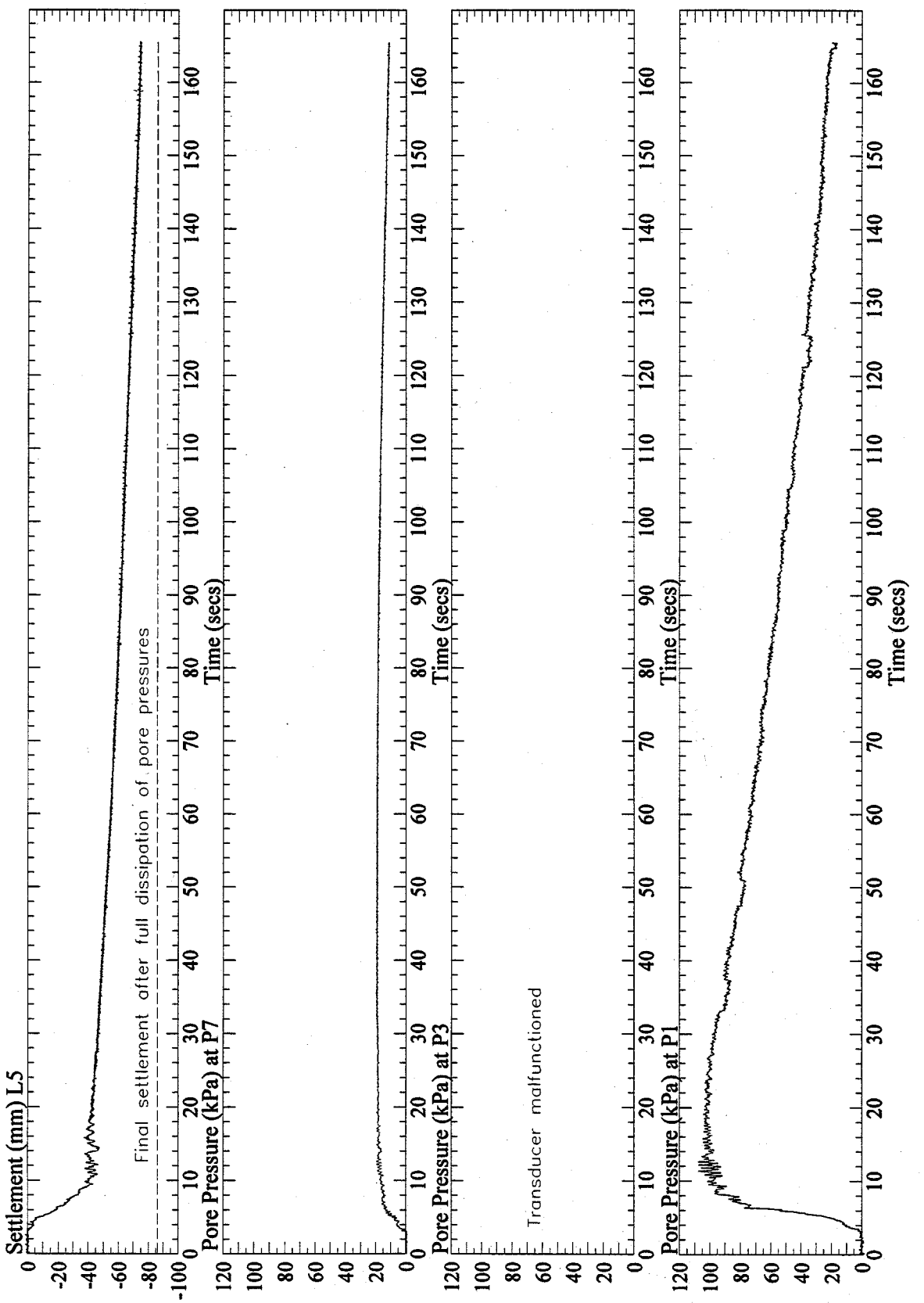

Figure 6: Vertical settlement at L5 and pore pressures at P1, P3, and P7, recorded in the one-g model SM3J1. Signals from P1 and P3 were post processed with a low pass filter of 10 Hz.

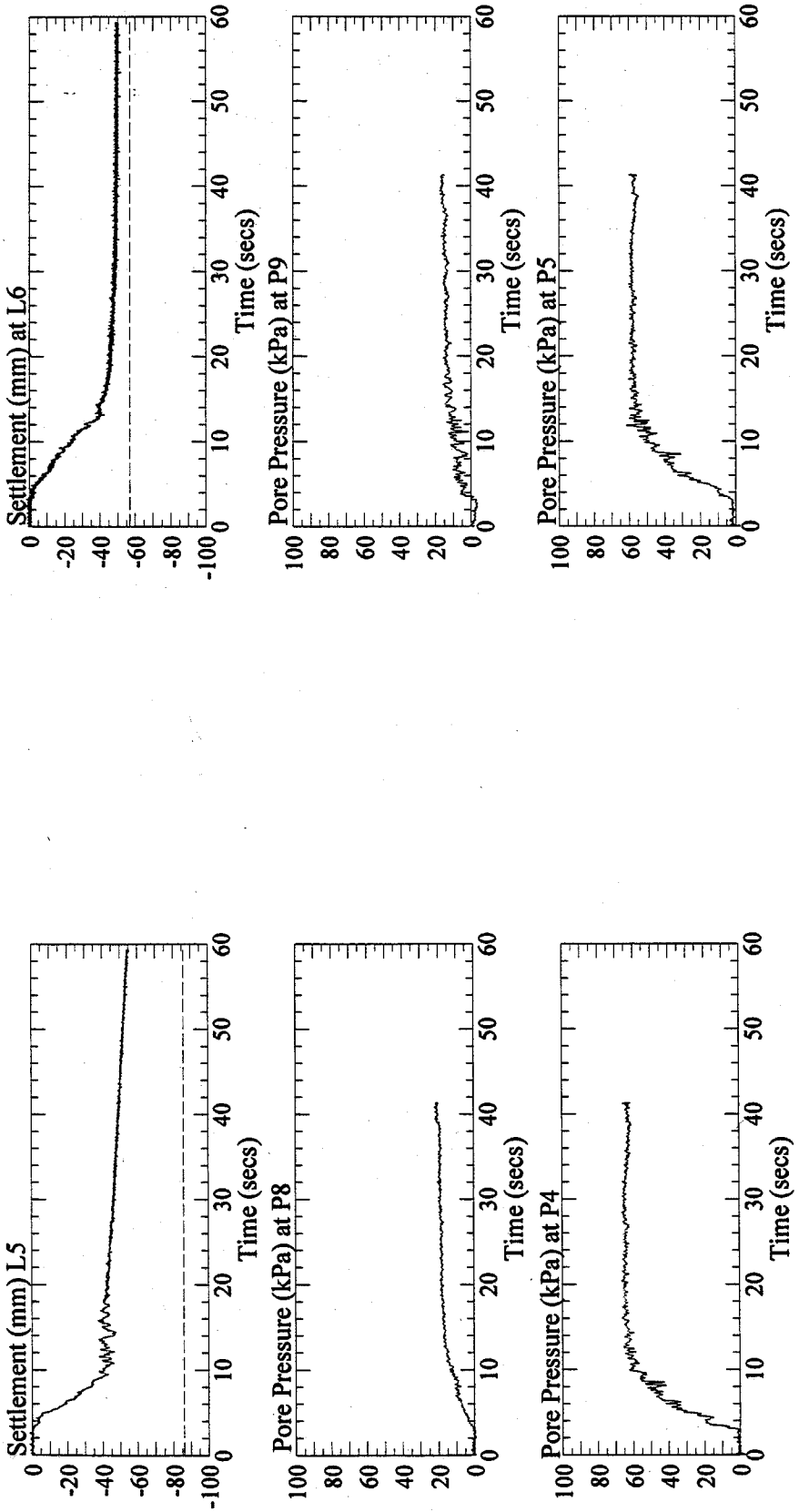

Figure 7: Vertical settlement at L5 and L6, and pore pressures at P4, P5, P8 and P9, recorded in the one-g model SM3J1. Pore pressure signals were post processed with a low pass filter of 10 Hz.

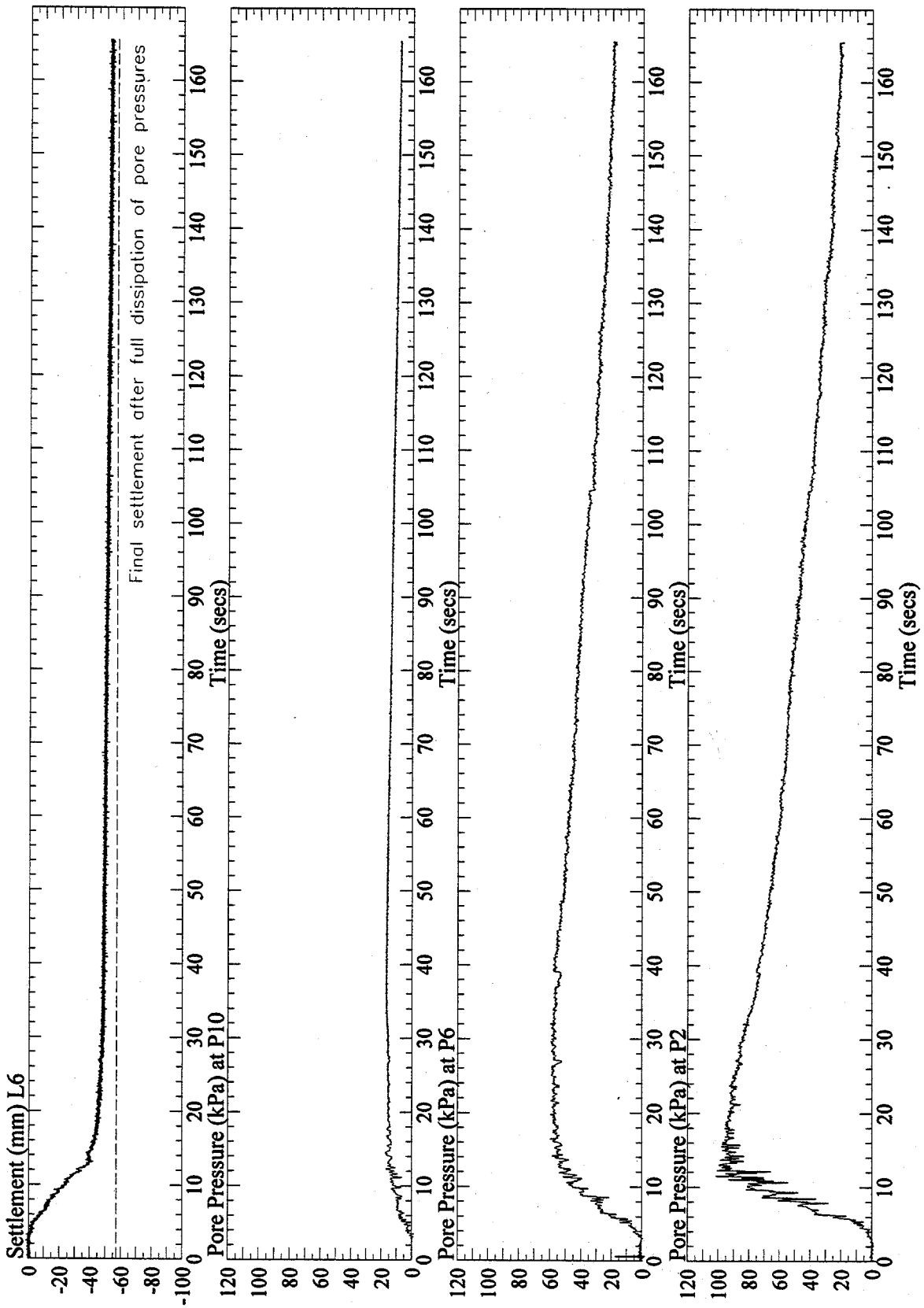

Figure 8: Vertical settlement at L6 and pore pressures at P2, P6, and P10, recorded in the one-g model SM3J1. Signal from P2 and P6 were post processed with a low pass filter of 10 Hz.

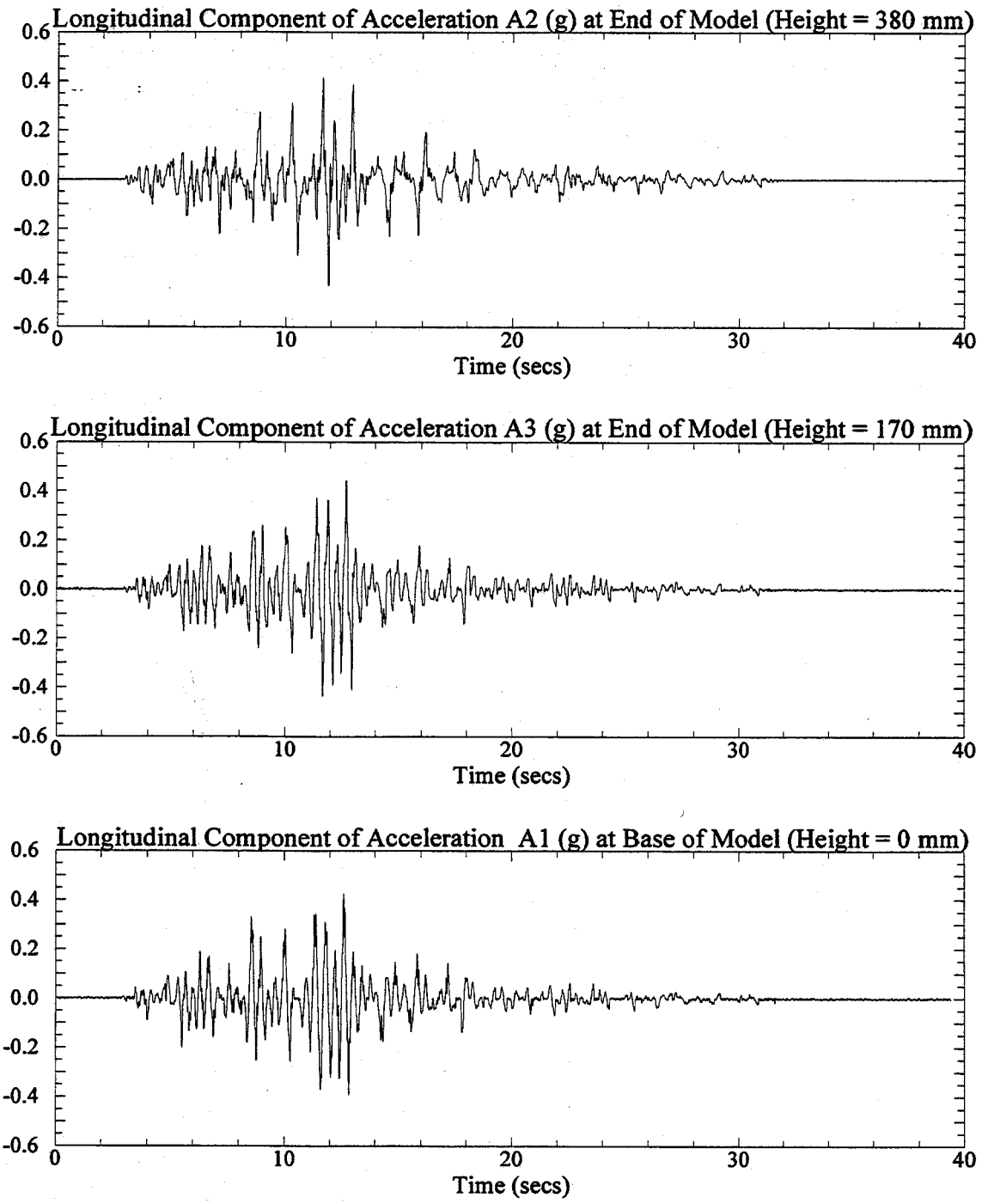

Figure 1: Longitudinal components of recorded acceleration at the base and end of the one-g model SM3J8. Signals were post processed with a low pass filter of 20 Hz.

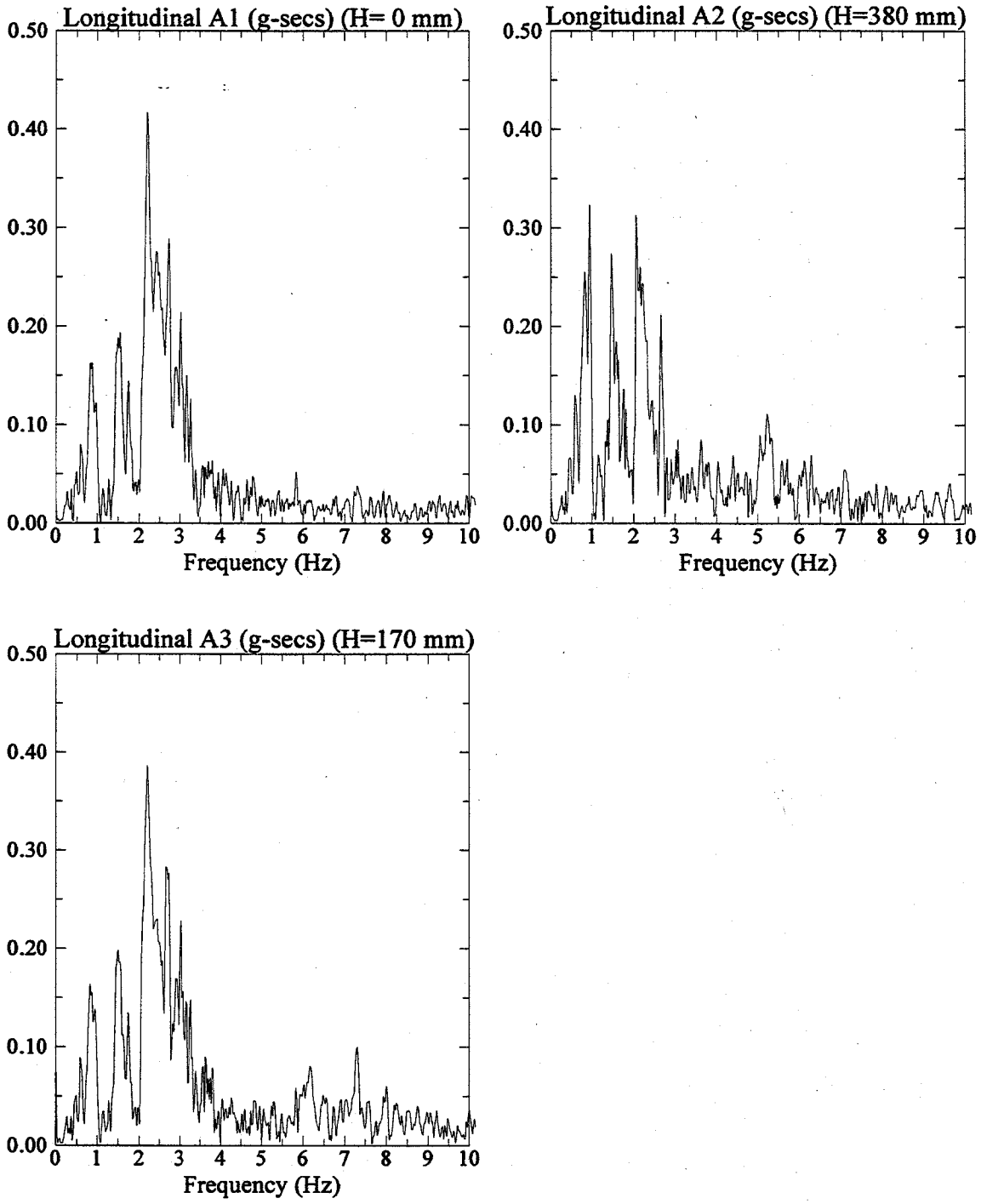

Figure 2: Fast Fourier Transform of longitudinal components of recorded acceleration at the base and end of the one-g model SM3J8.

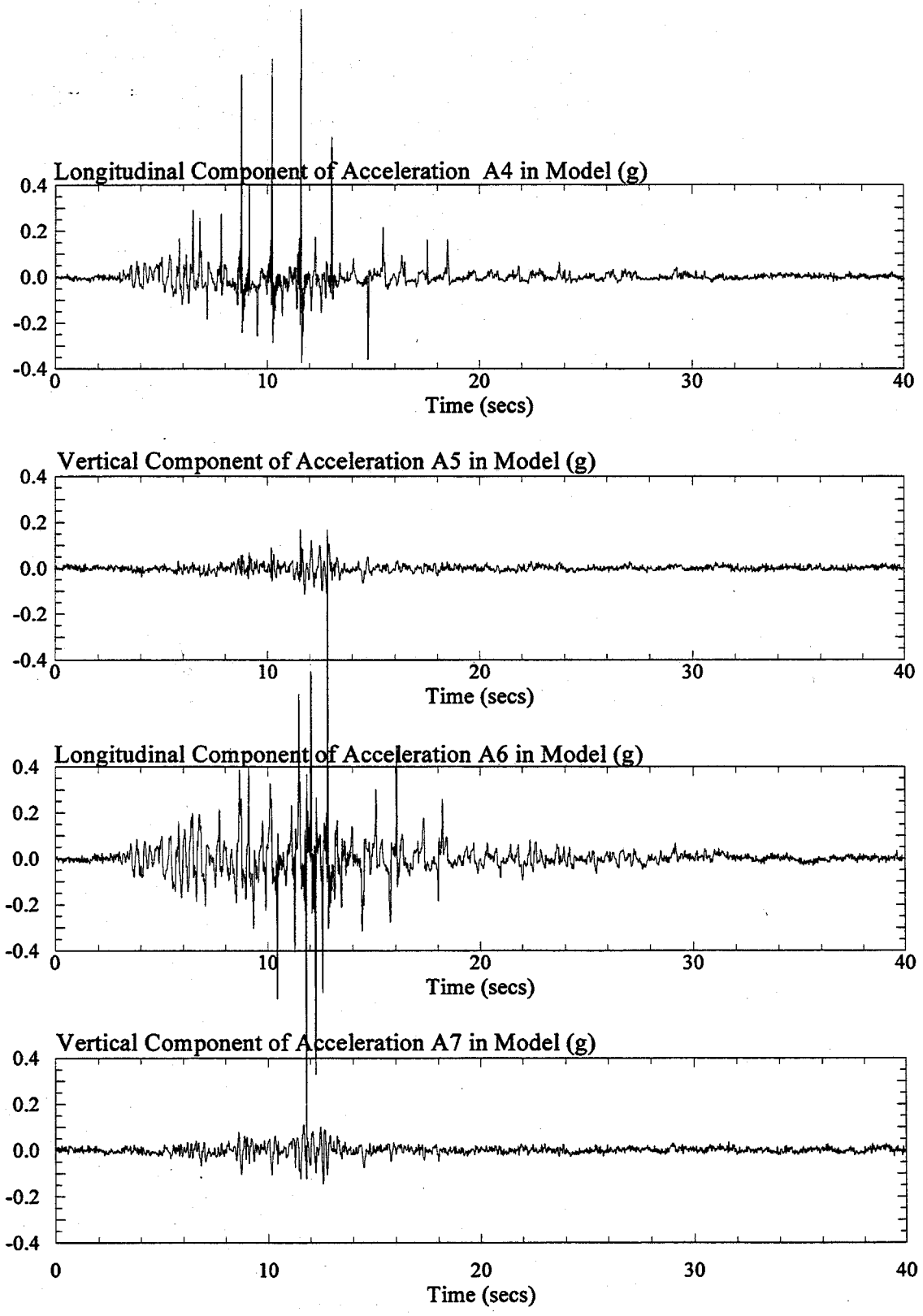

Figure 3: Longitudinal and vertical components of recorded acceleration in the one-g model SM3J8. Signals were post processed with a low pass filter of 20 Hz.

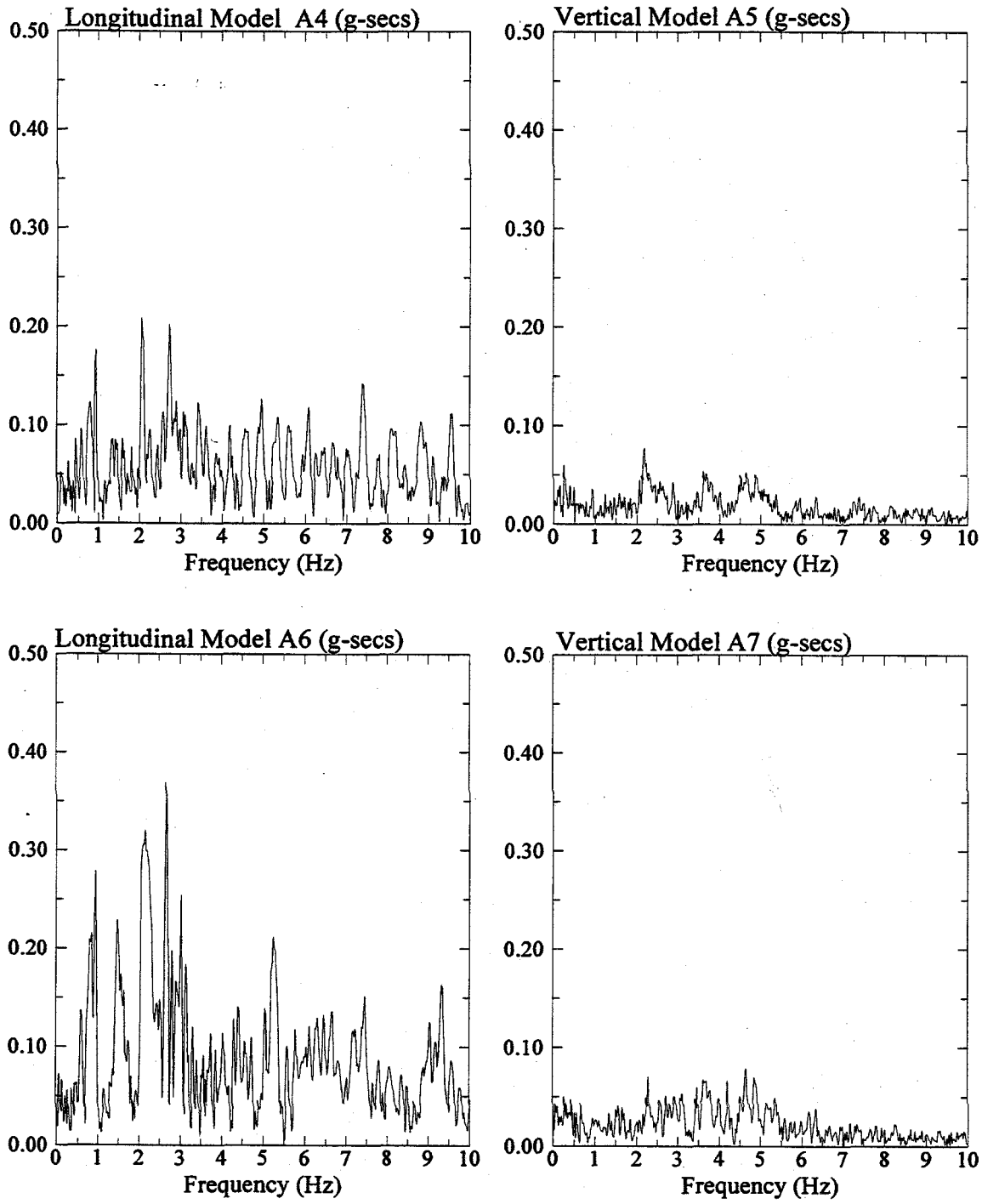

Figure 4: Fast Fourier Transform of longitudinal and vertical components of recorded acceleration in the one-g model SM3J8.

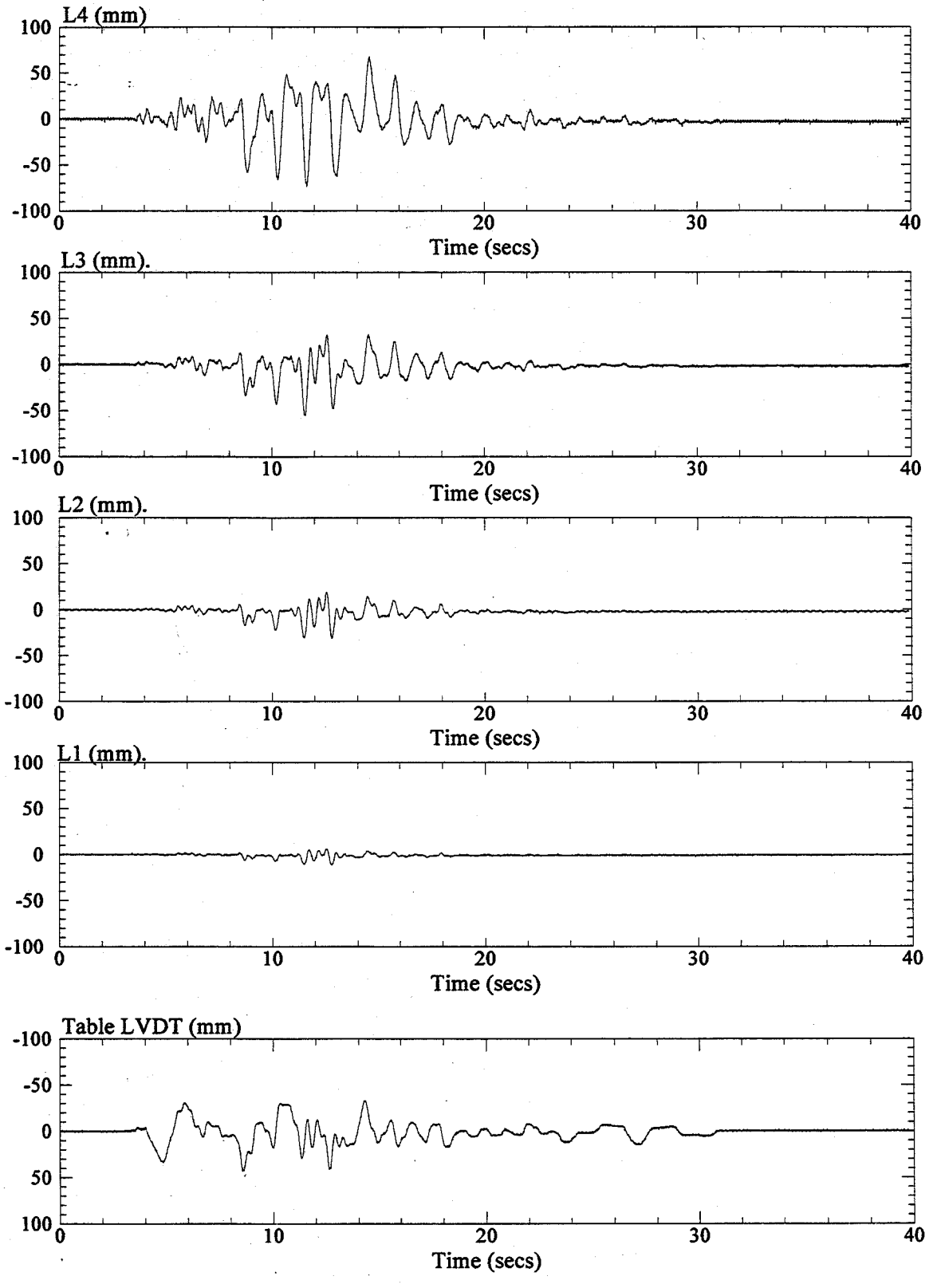

Figure 5: Longitudinal displacements recorded from the shake table LVDT and at LVDT's L1, L2, L3, and L4 in the one-g model SM3J8.

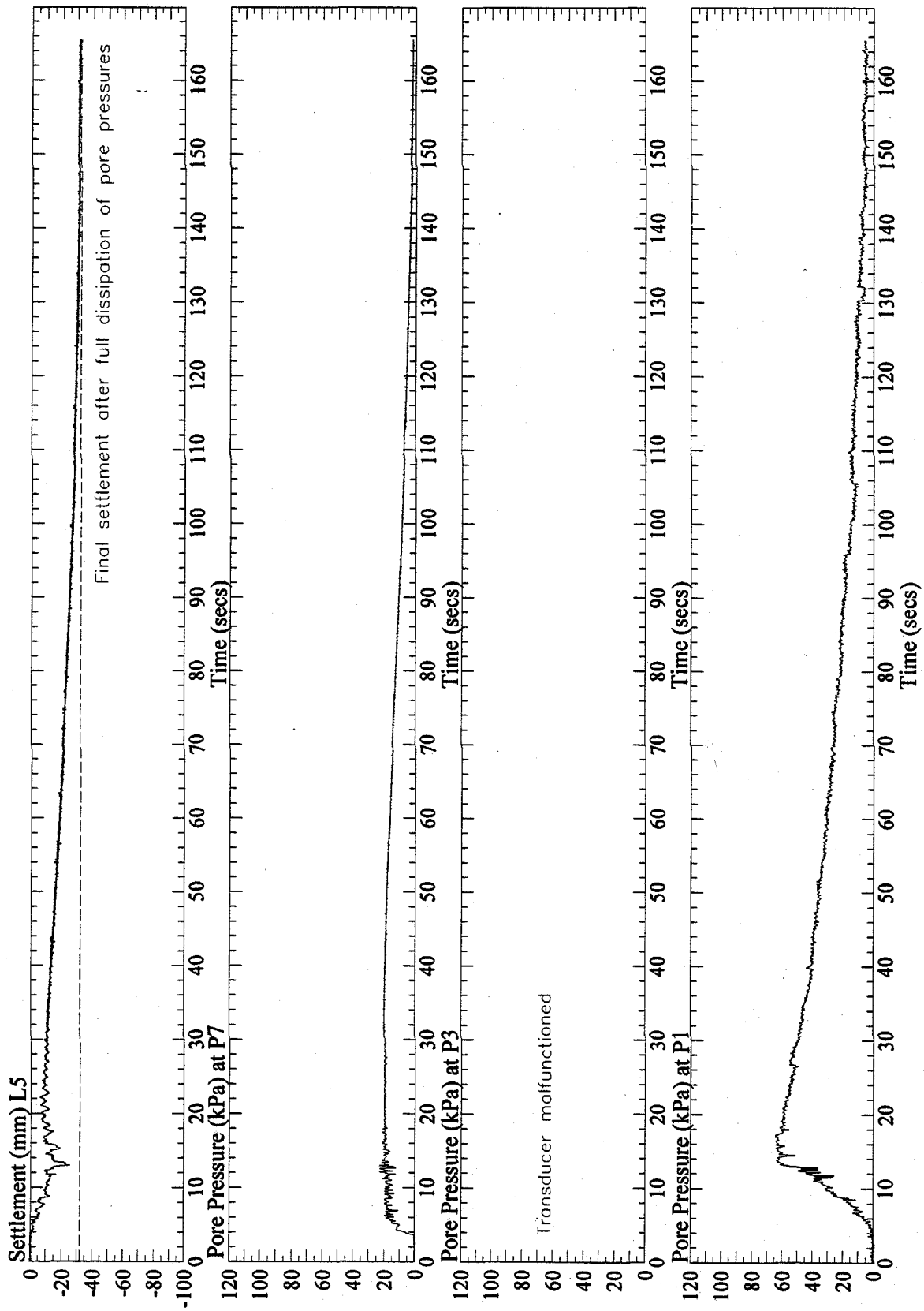

Figure 6: Vertical settlement at L5 and pore pressures at P1, P3, and P7, recorded in the one-g model SM3J8. Signals from P1 and P3 were post processed with a low pass filter of 10 Hz.

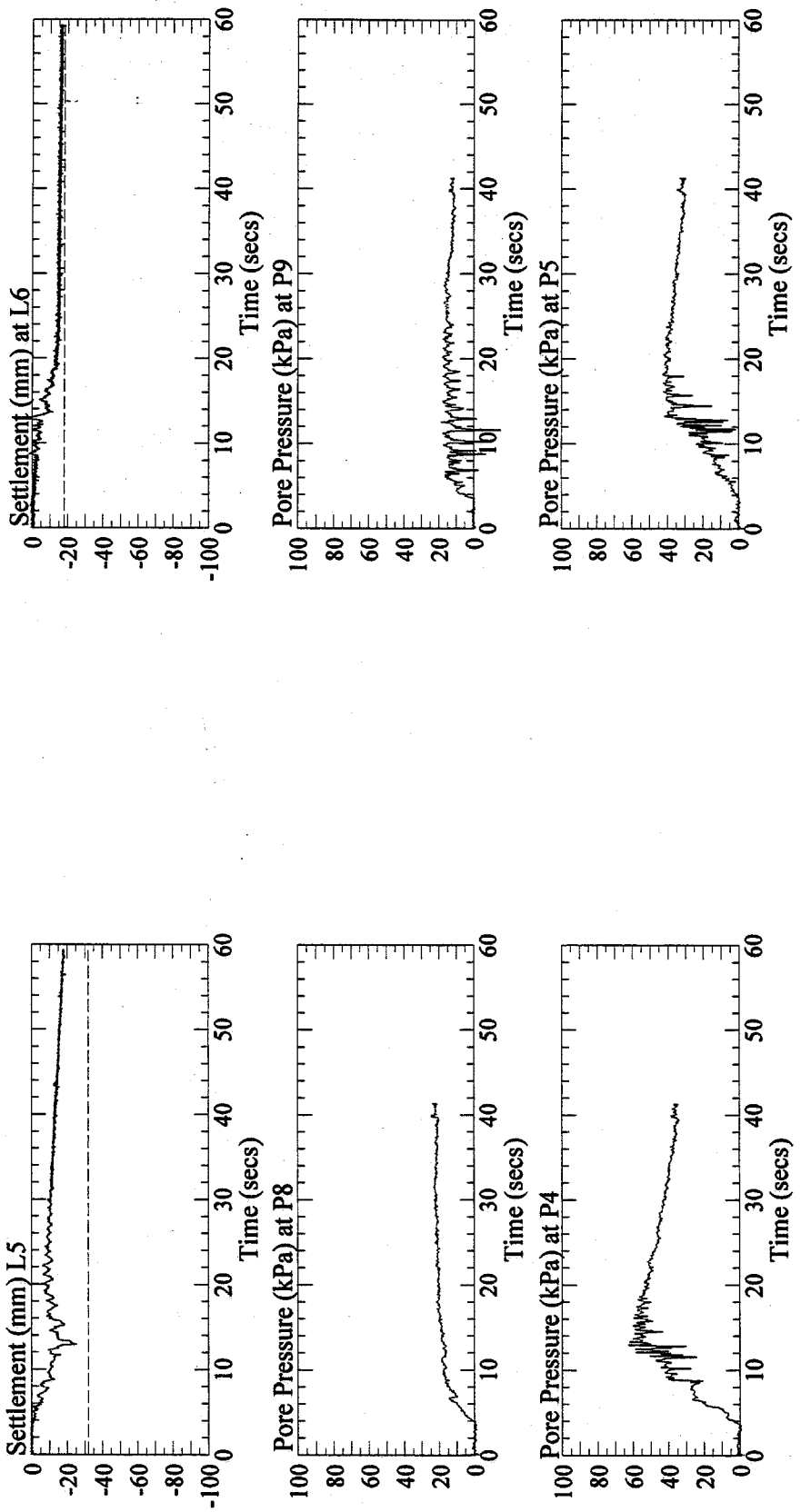

Figure 7: Vertical settlement at L5 and L6, and pore pressures at P4, P5, P8 and P9, recorded in the one-g model SM3J8. Pore pressure signals were post processed with a low pass filter of 10 Hz.

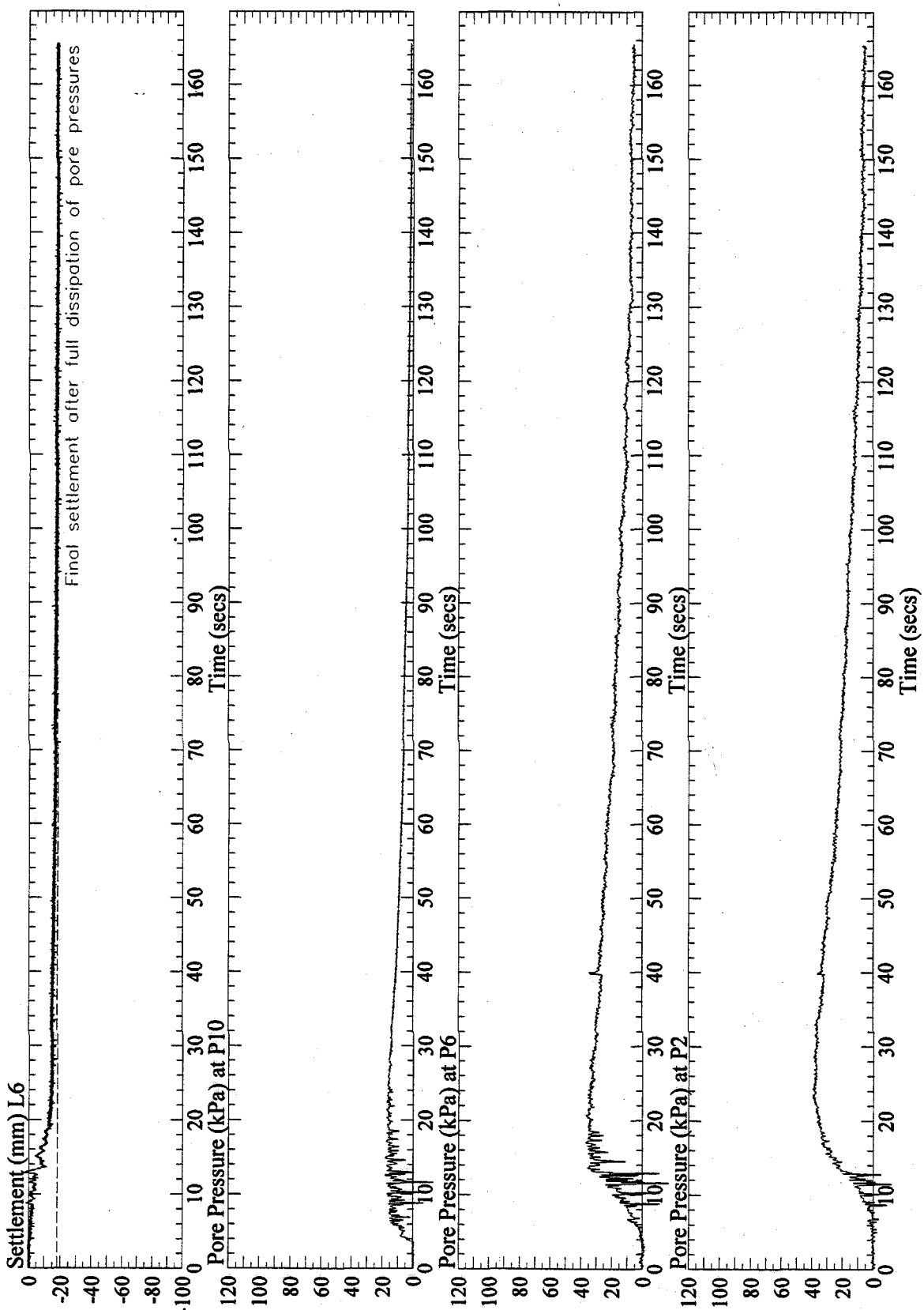

Figure 8: Vertical settlement at L6 and pore pressures at P2, P6, and P10, recorded in the one-g model SM3J8. Signal from P2 and P6 were post processed with a low pass filter of 10 Hz.

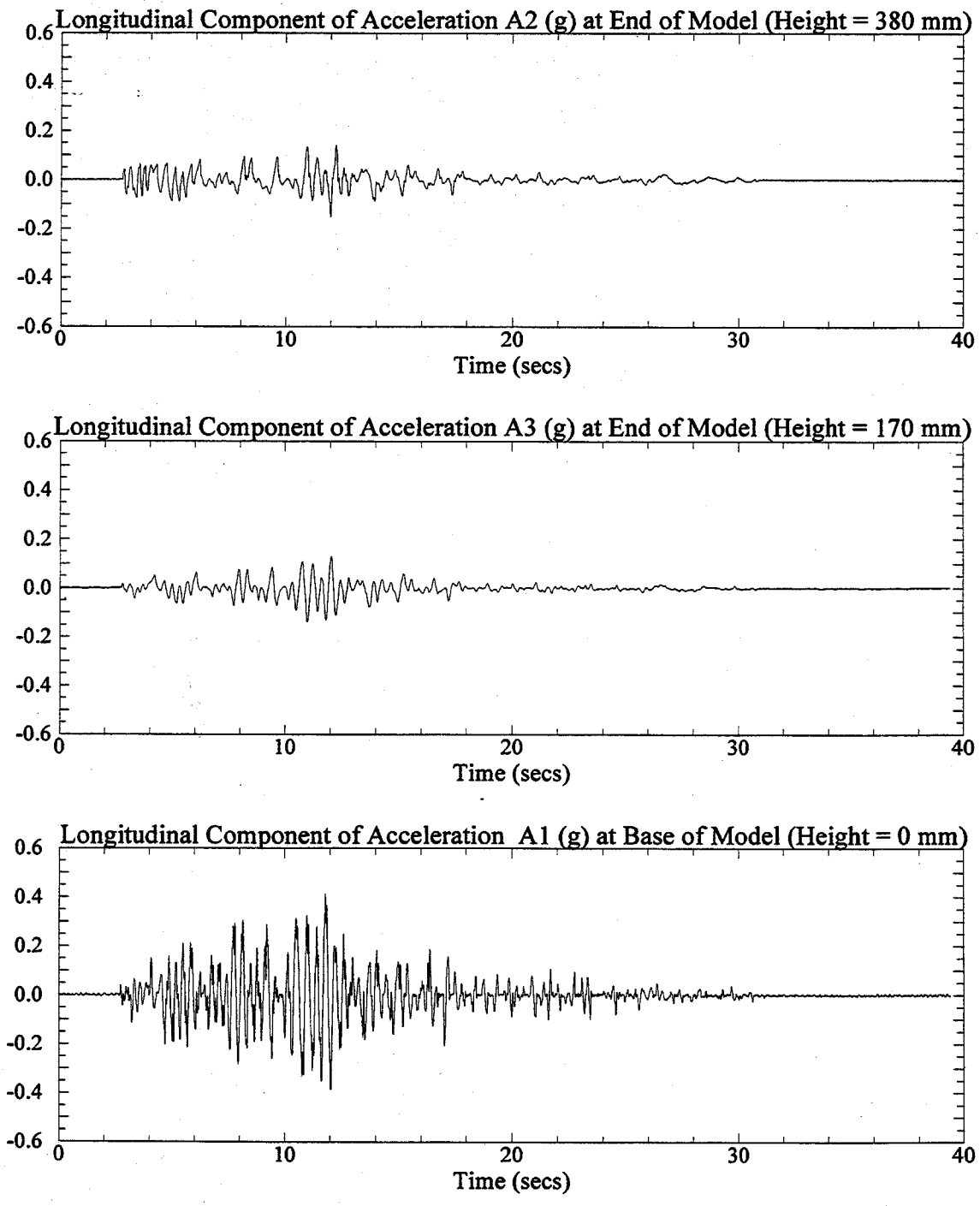

Figure 1: Longitudinal components of recorded acceleration at the base and end of the one-g model SM3K1. Signals were post processed with a low pass filter of 20 Hz.

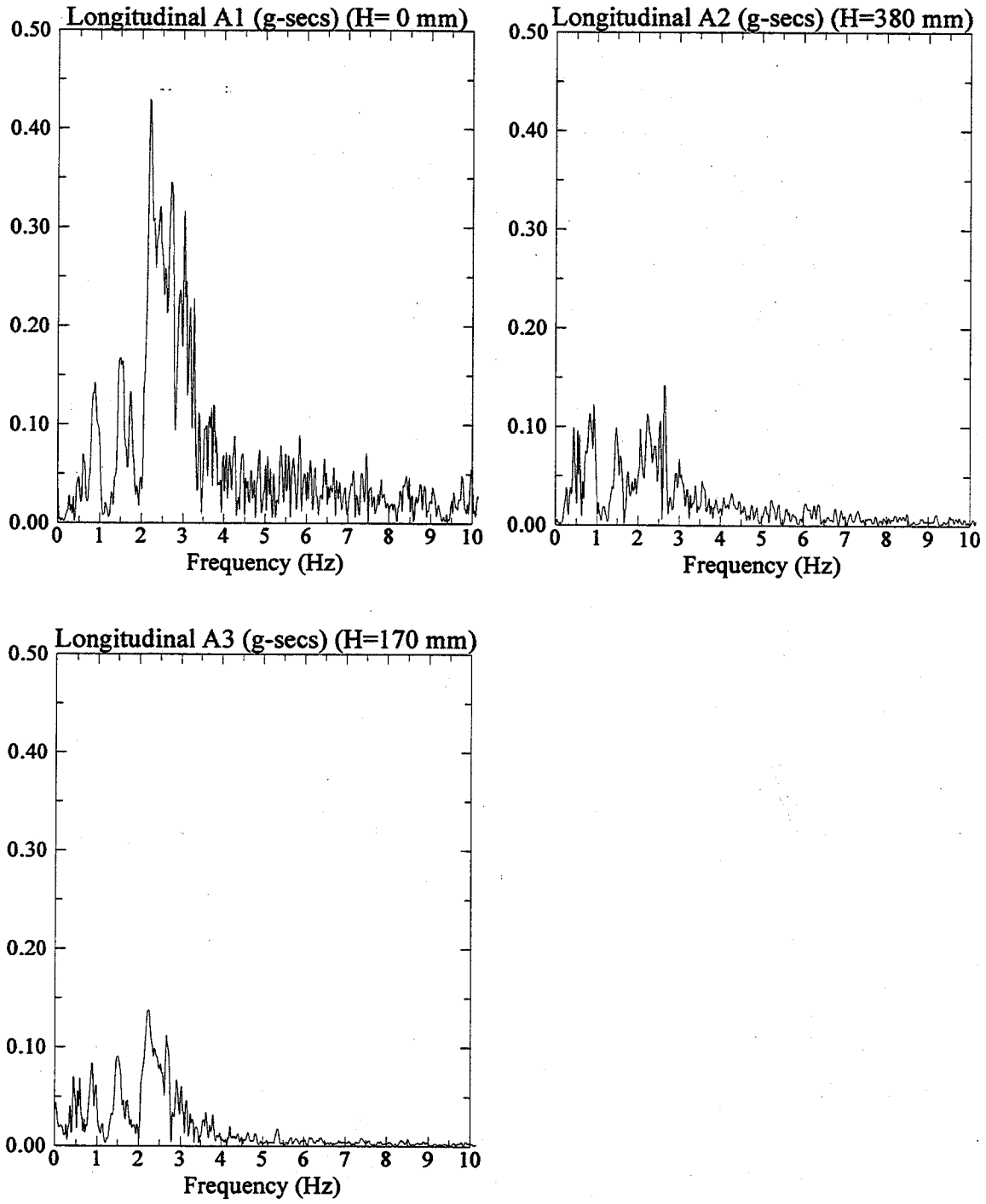

Figure 2: Fast Fourier Transform of longitudinal components of recorded acceleration at the base and end of the one-g model SM3K1.

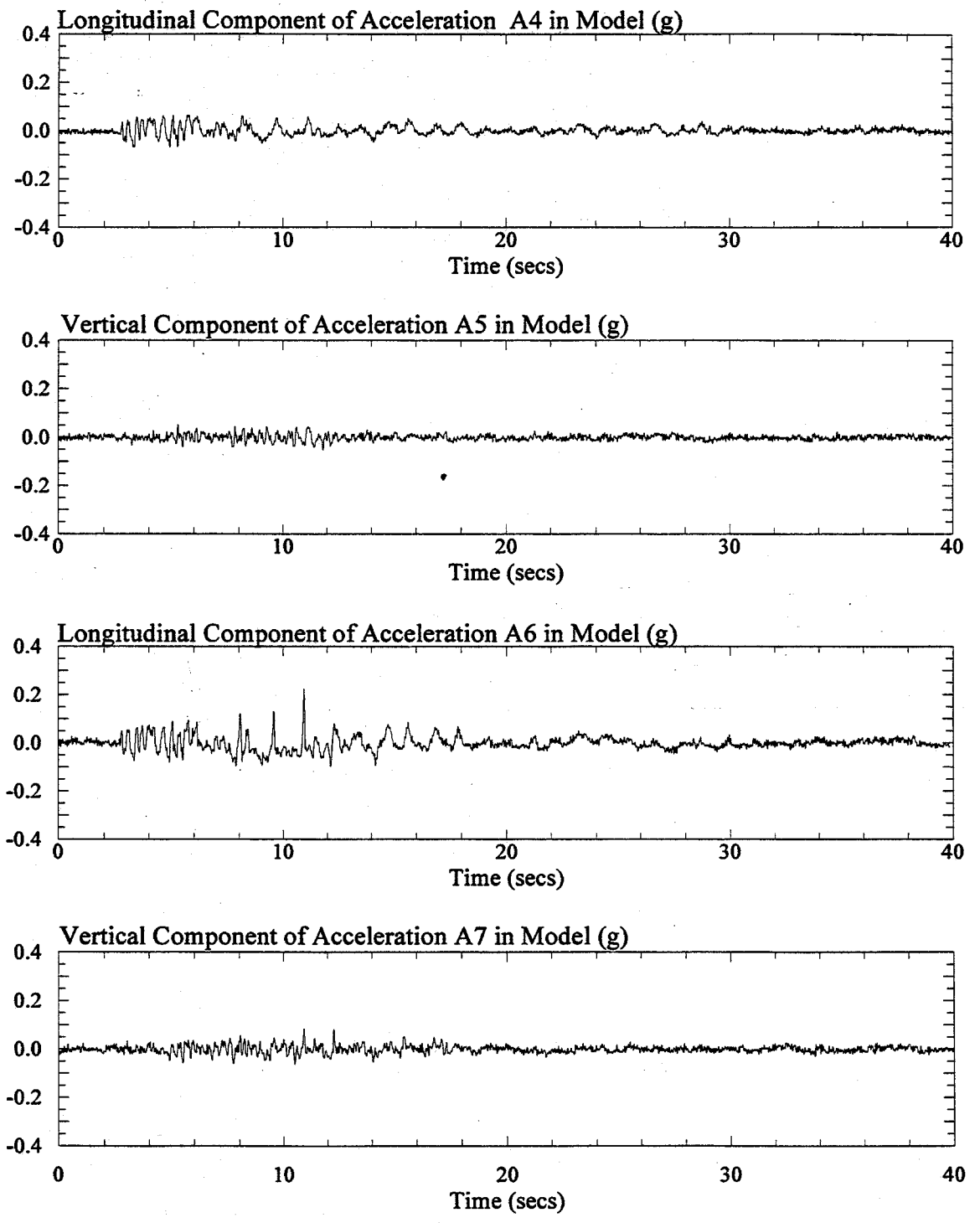

Figure 3: Longitudinal and vertical components of recorded acceleration in the one-g model SM3K1. Signals were post processed with a low pass filter of 20 Hz.

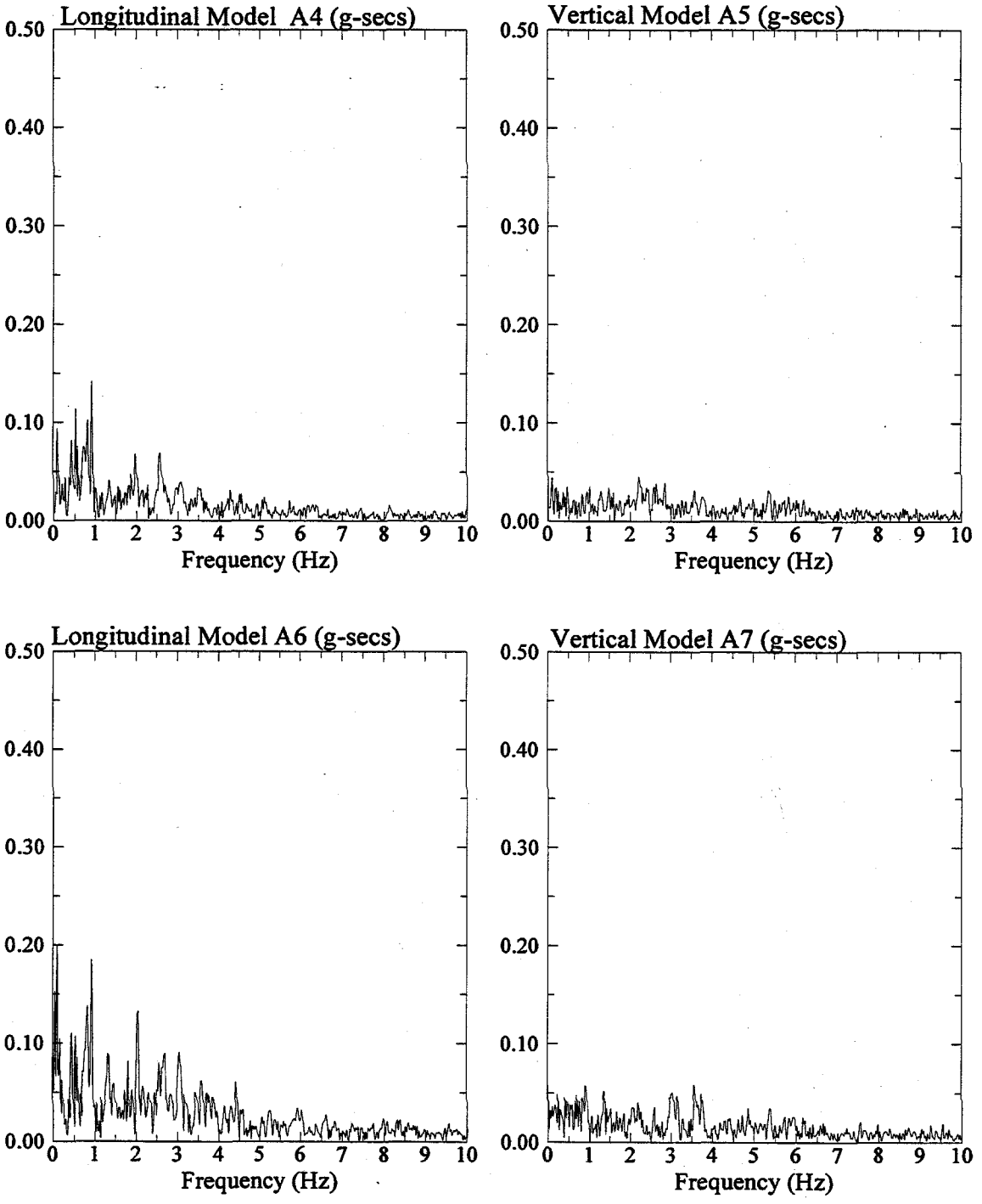

Figure 4: Fast Fourier Transform of longitudinal and vertical components of recorded acceleration in the one-g model SM3K1.

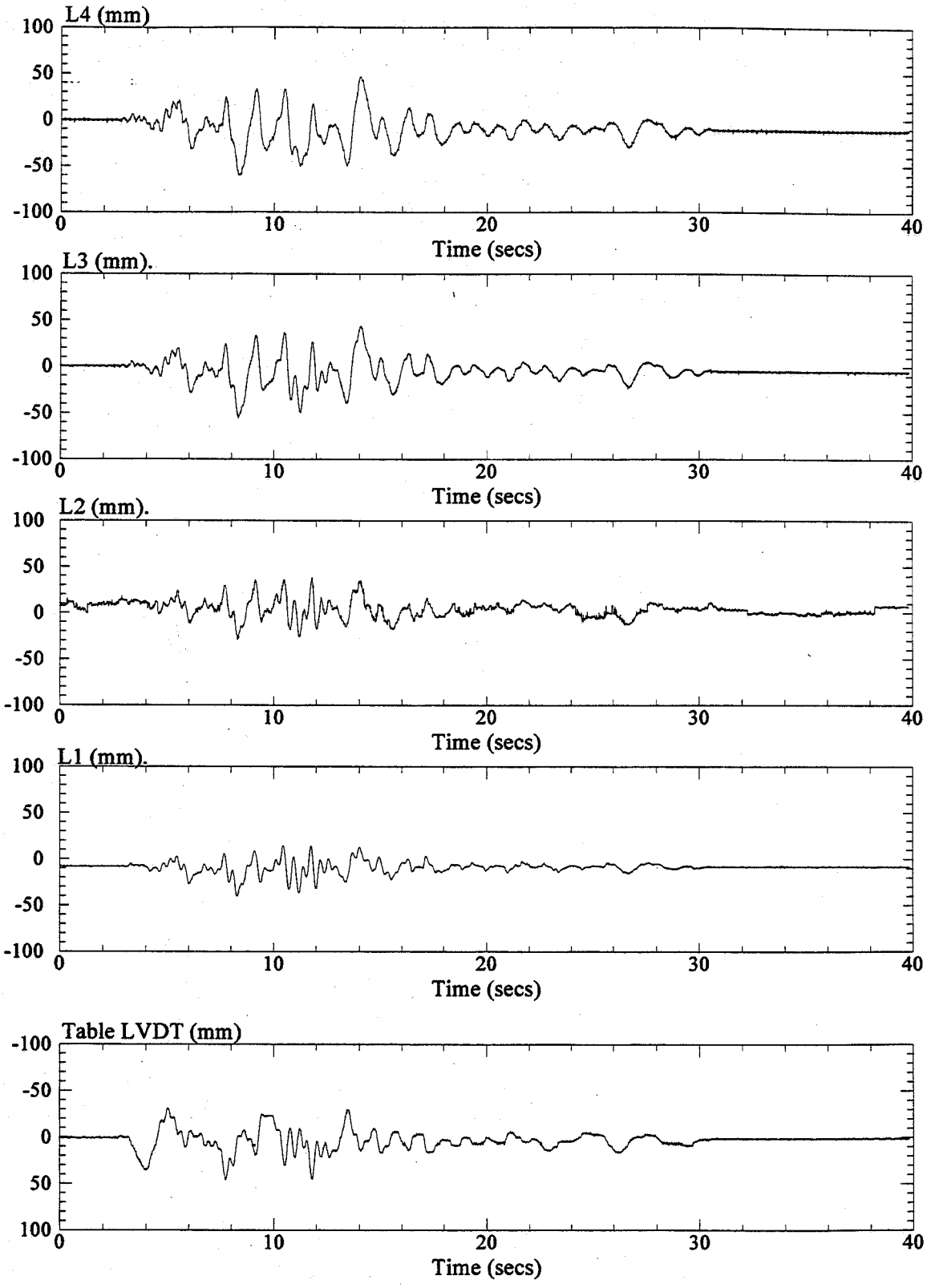

Figure 5: Longitudinal displacements recorded from the shake table LVDT and at LVDT's L1, L2, L3, and L4 in the one-g model SM3K1.

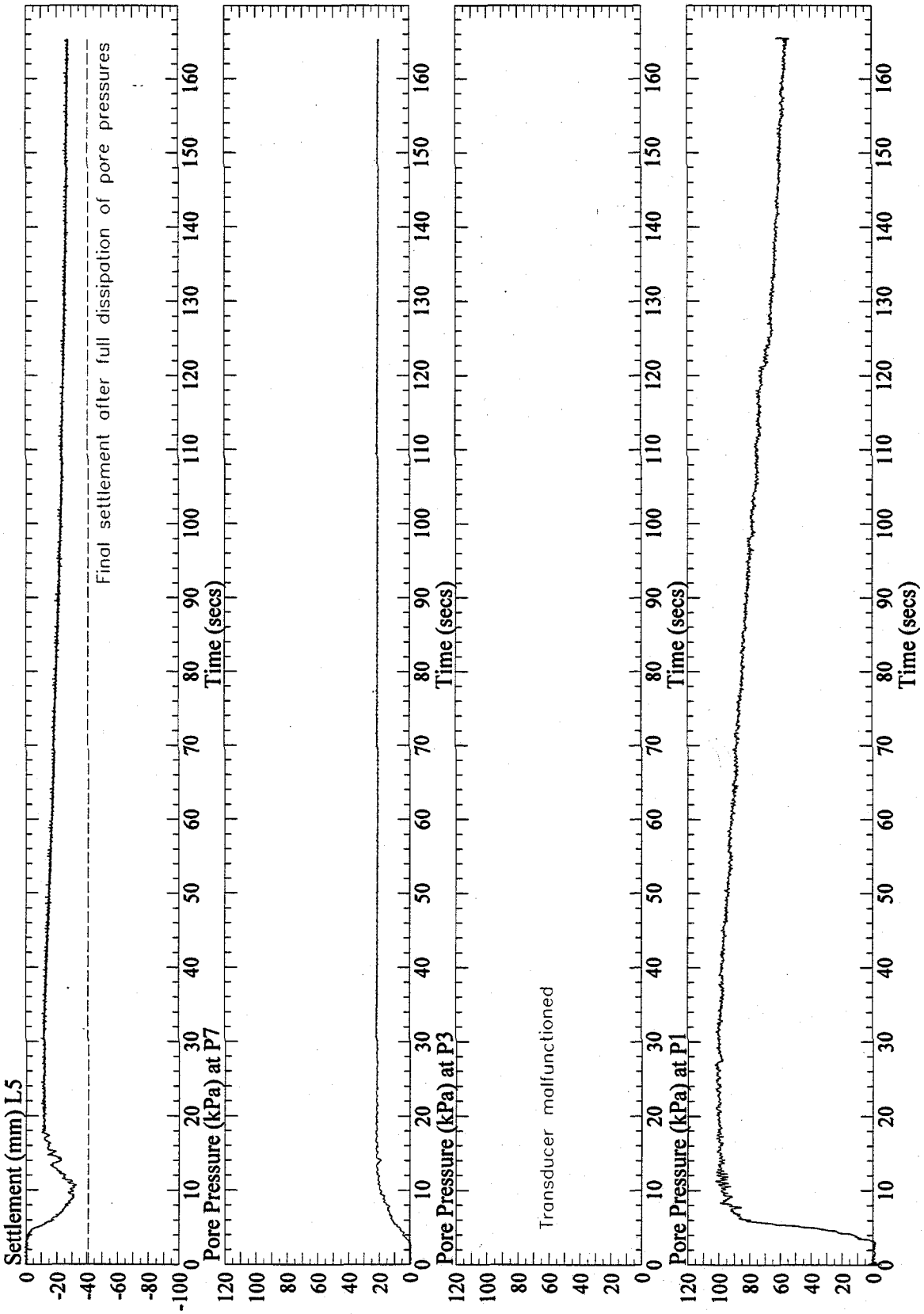

Figure 6: Vertical settlement at L5 and pore pressures at P1, P3, and P7, recorded in the one-g model SM3K1. Signals from P1 and P3 were post processed with a low pass filter of 10 Hz.

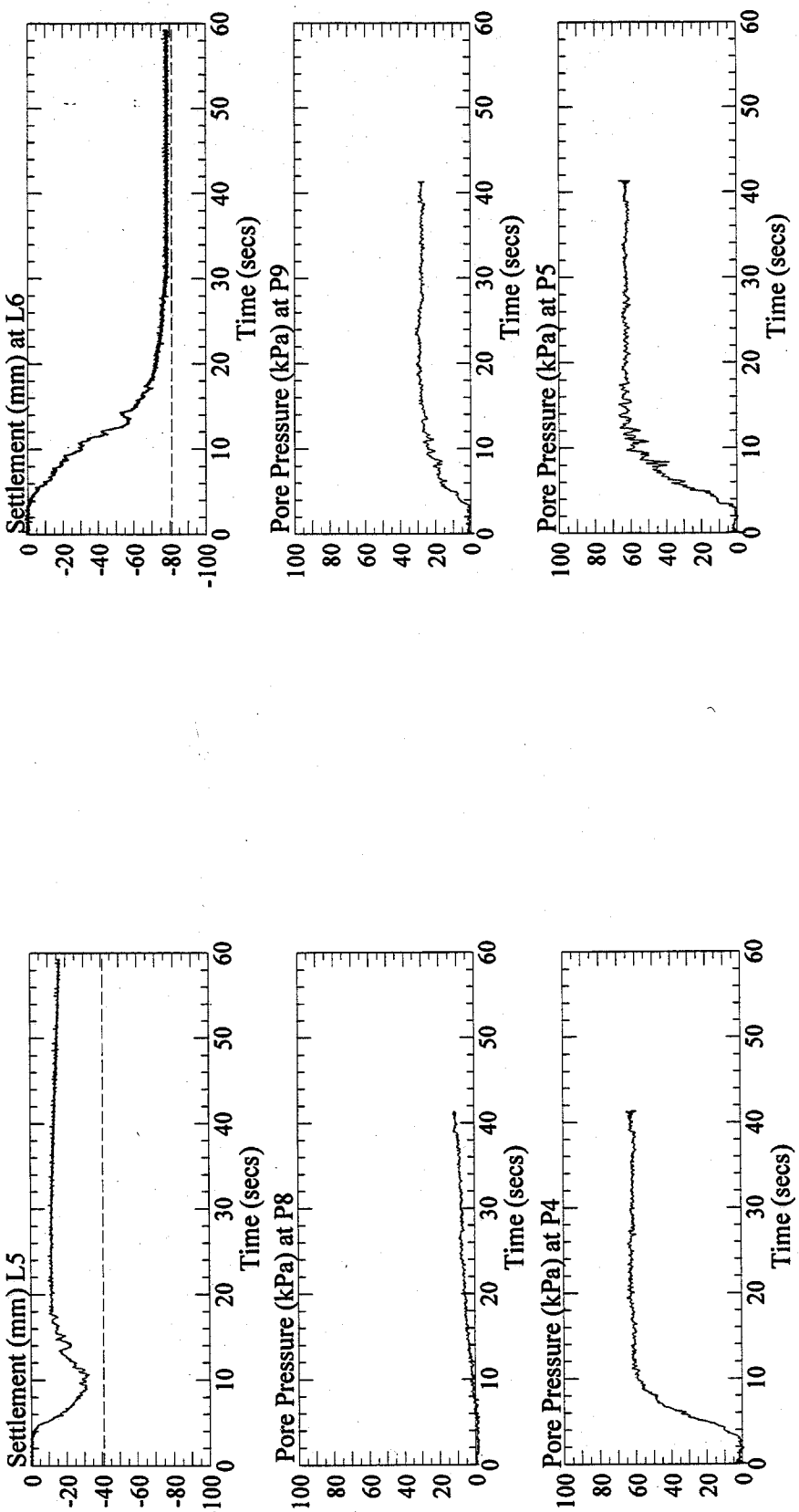

Figure 7: Vertical settlement at L5 and L6, and pore pressures at P4, P5, P8 and P9, recorded in the one-g model SM3K1. Pore pressure signals were post processed with a low pass filter of 10 Hz.

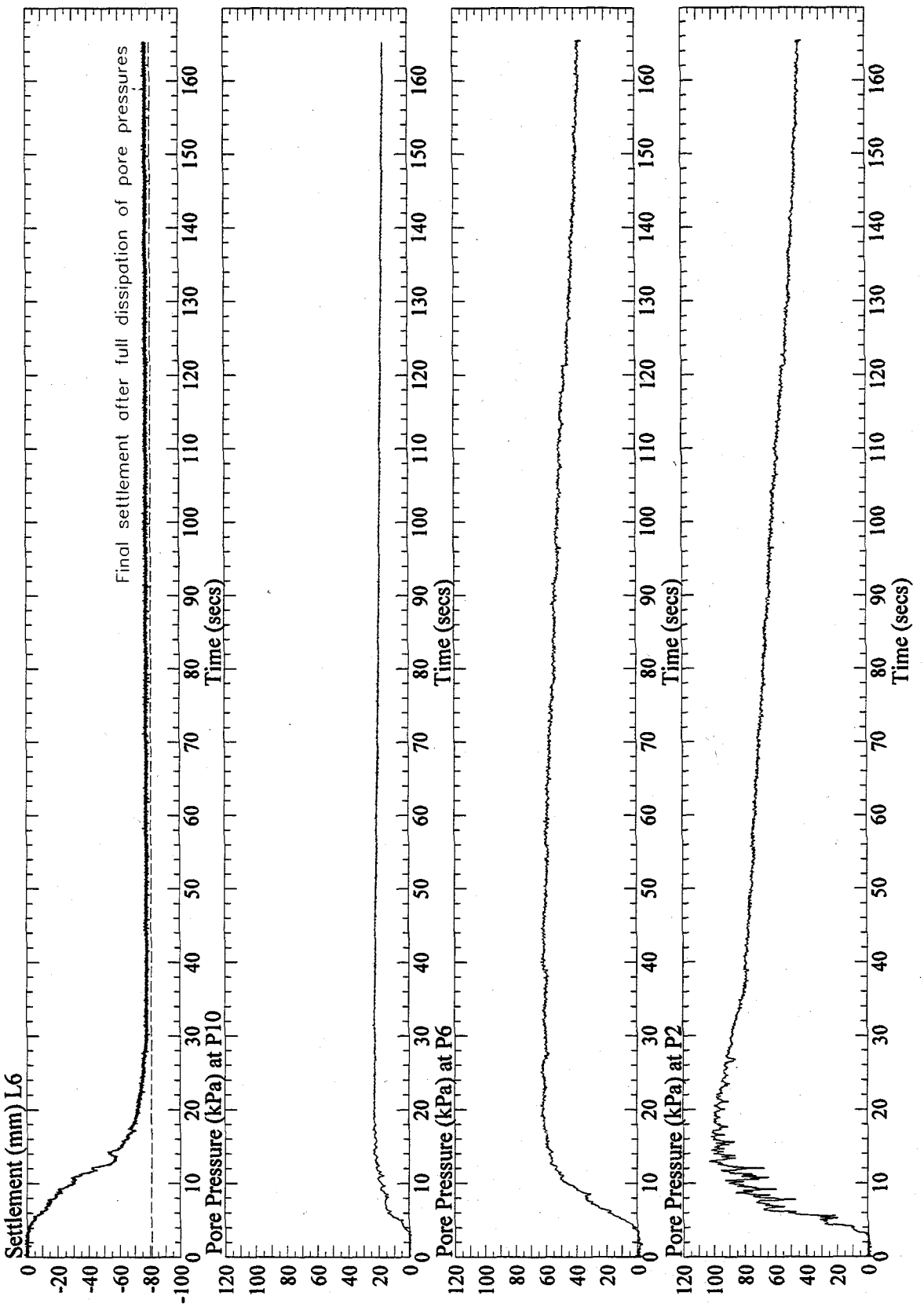

Figure 8: Vertical settlement at L6 and pore pressures at P2, P6, and P10, recorded in the one-g model SM3K1. Signal from P2 and P6 were post processed with a low pass filter of 10 Hz.

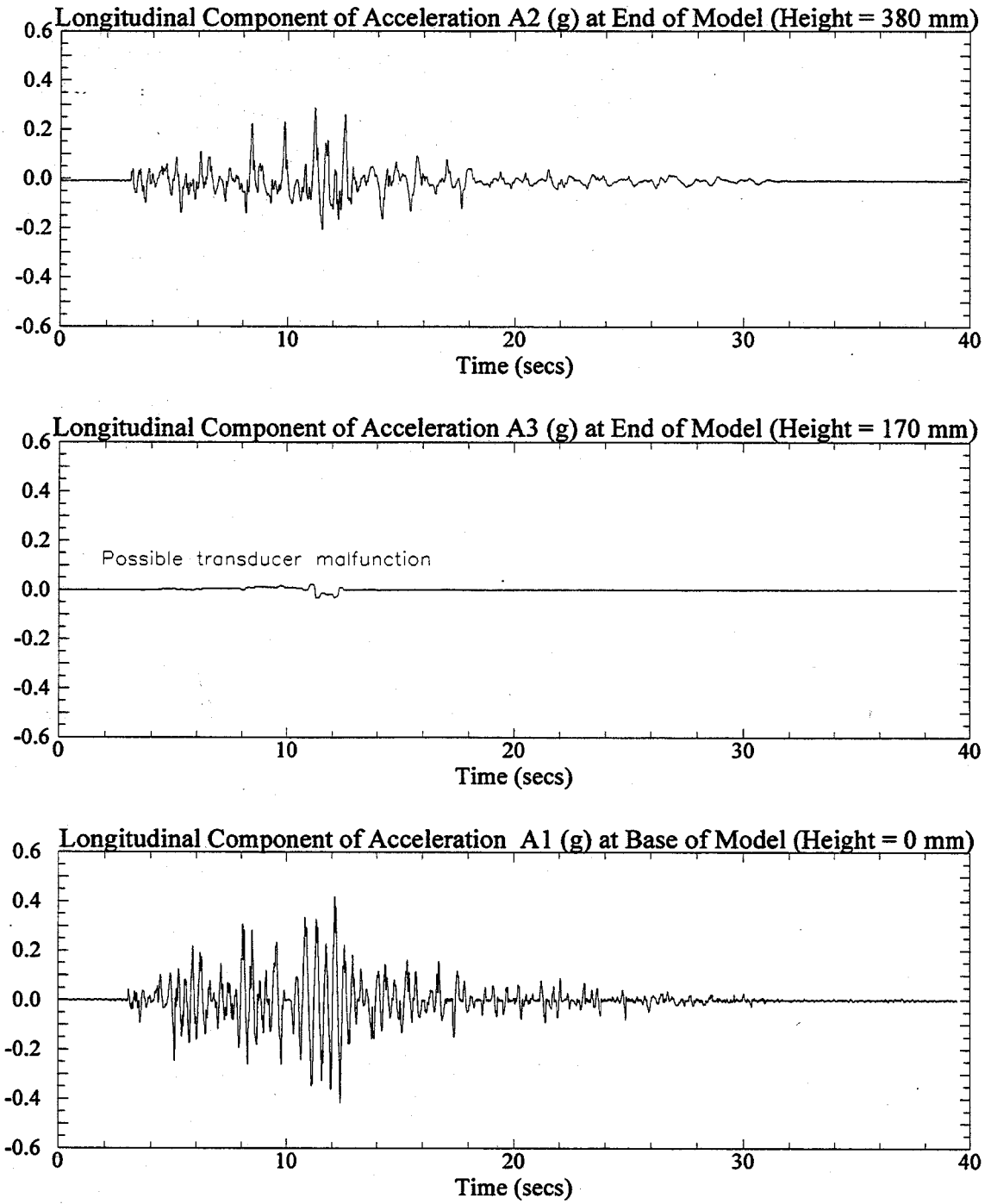

Figure 1: Longitudinal components of recorded acceleration at the base and end of the one-g model SM3K8. Signals were post processed with a low pass filter of 20 Hz.

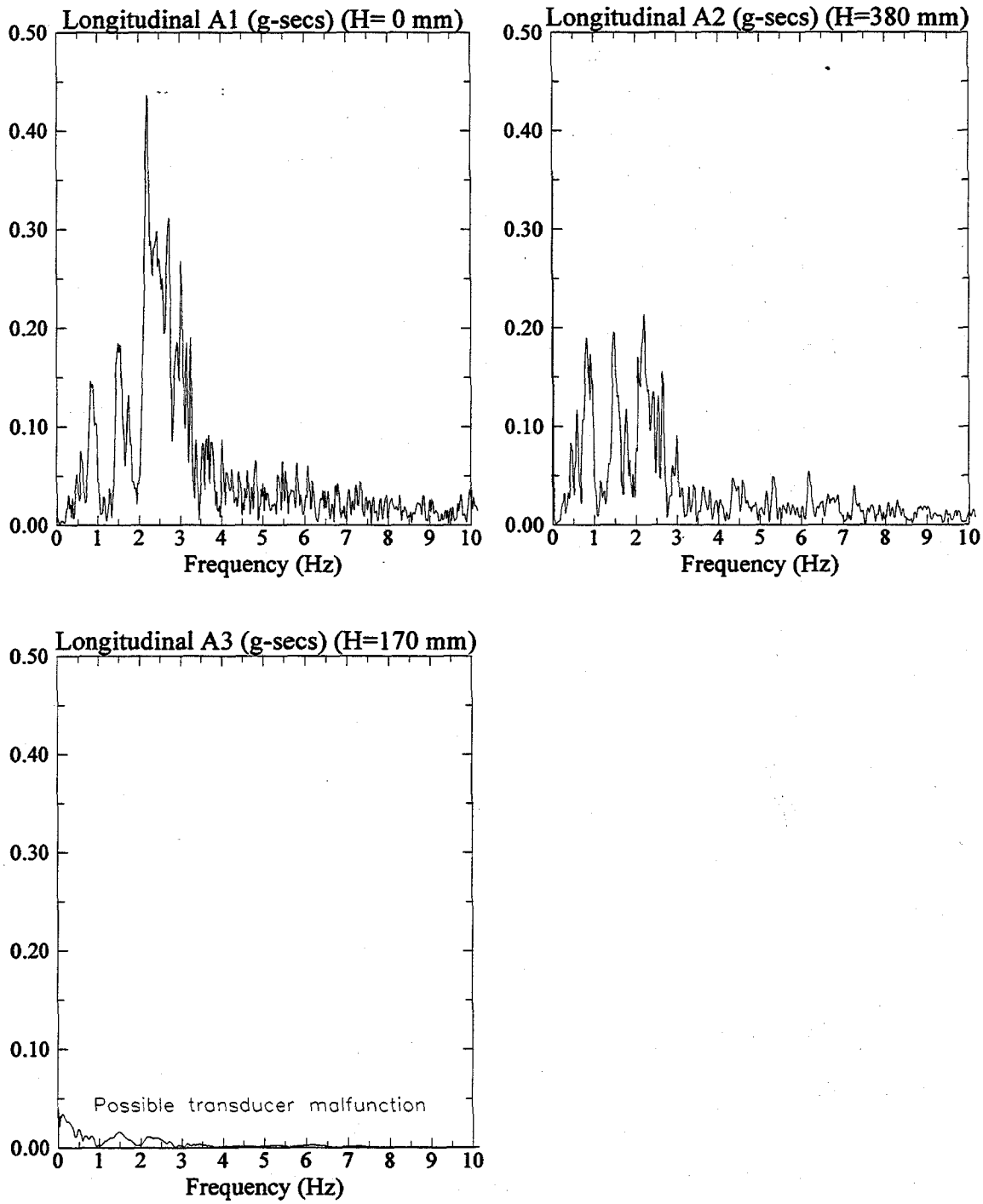

Figure 2: Fast Fourier Transform of longitudinal components of recorded acceleration at the base and end of the one-g model SM3K8.

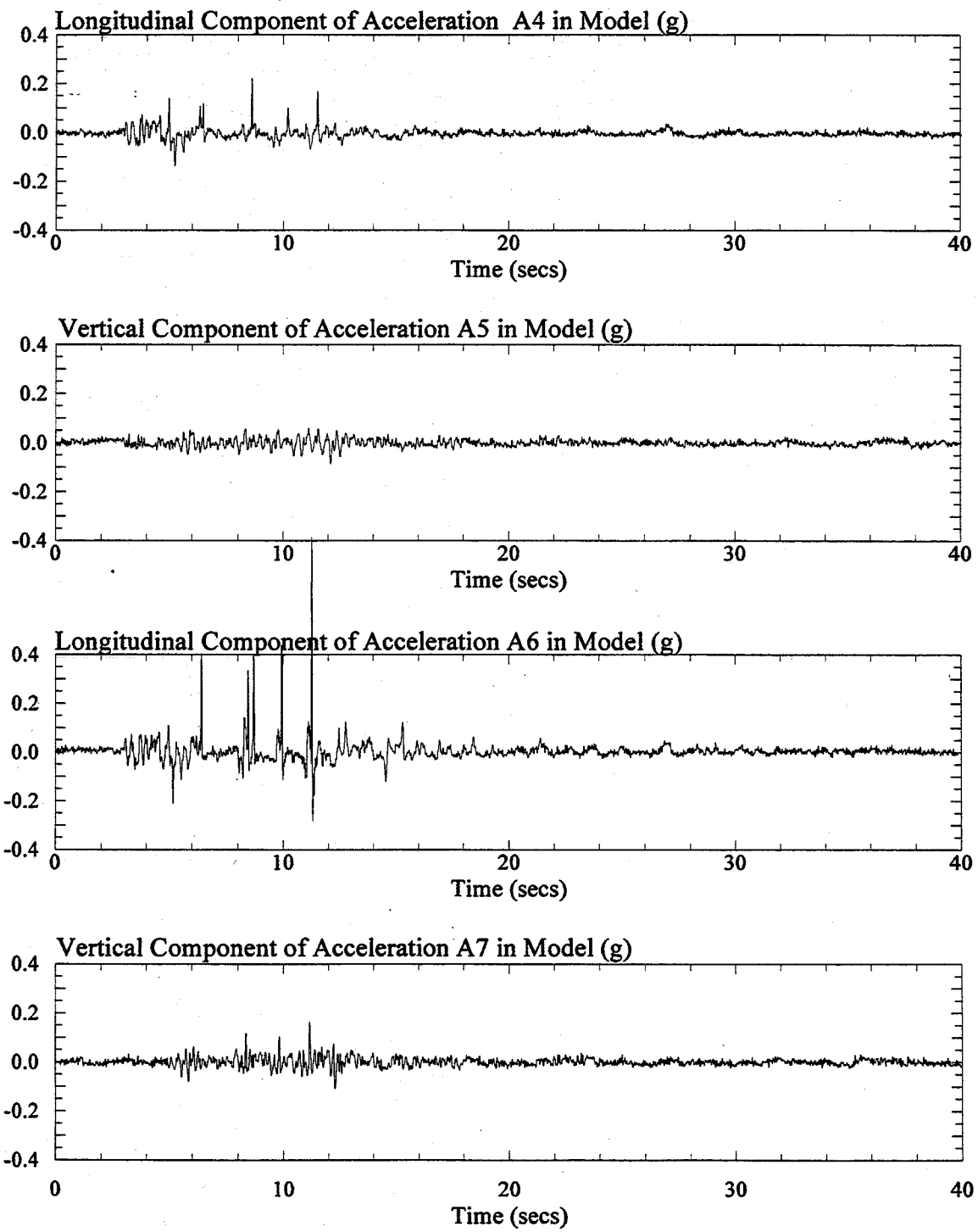

Figure 3: Longitudinal and vertical components of recorded acceleration in the one-g model SM3K8. Signals were post processed with a low pass filter of 20 Hz.

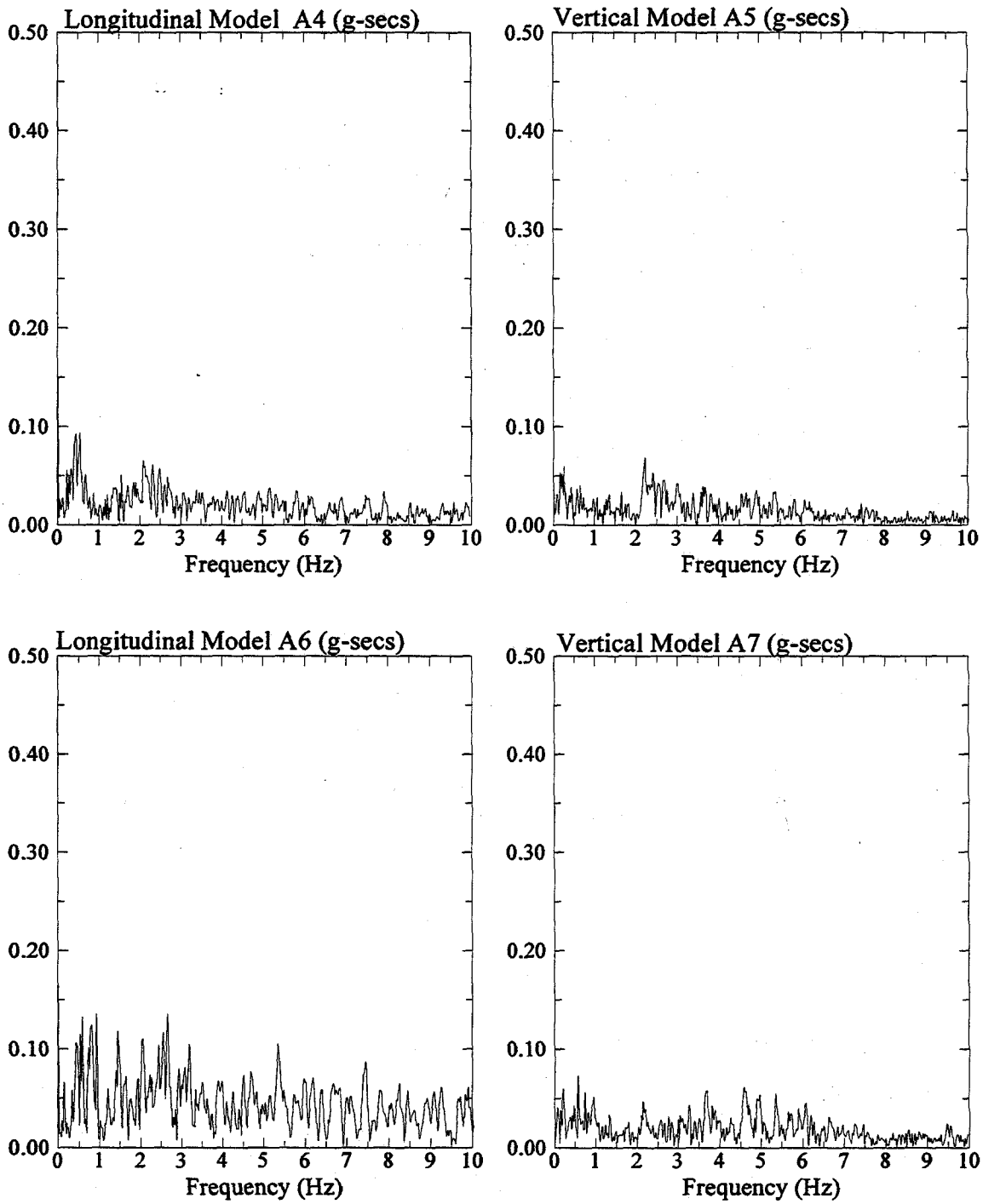

Figure 4: Fast Fourier Transform of longitudinal and vertical components of recorded acceleration in the one-g model SM3K8.

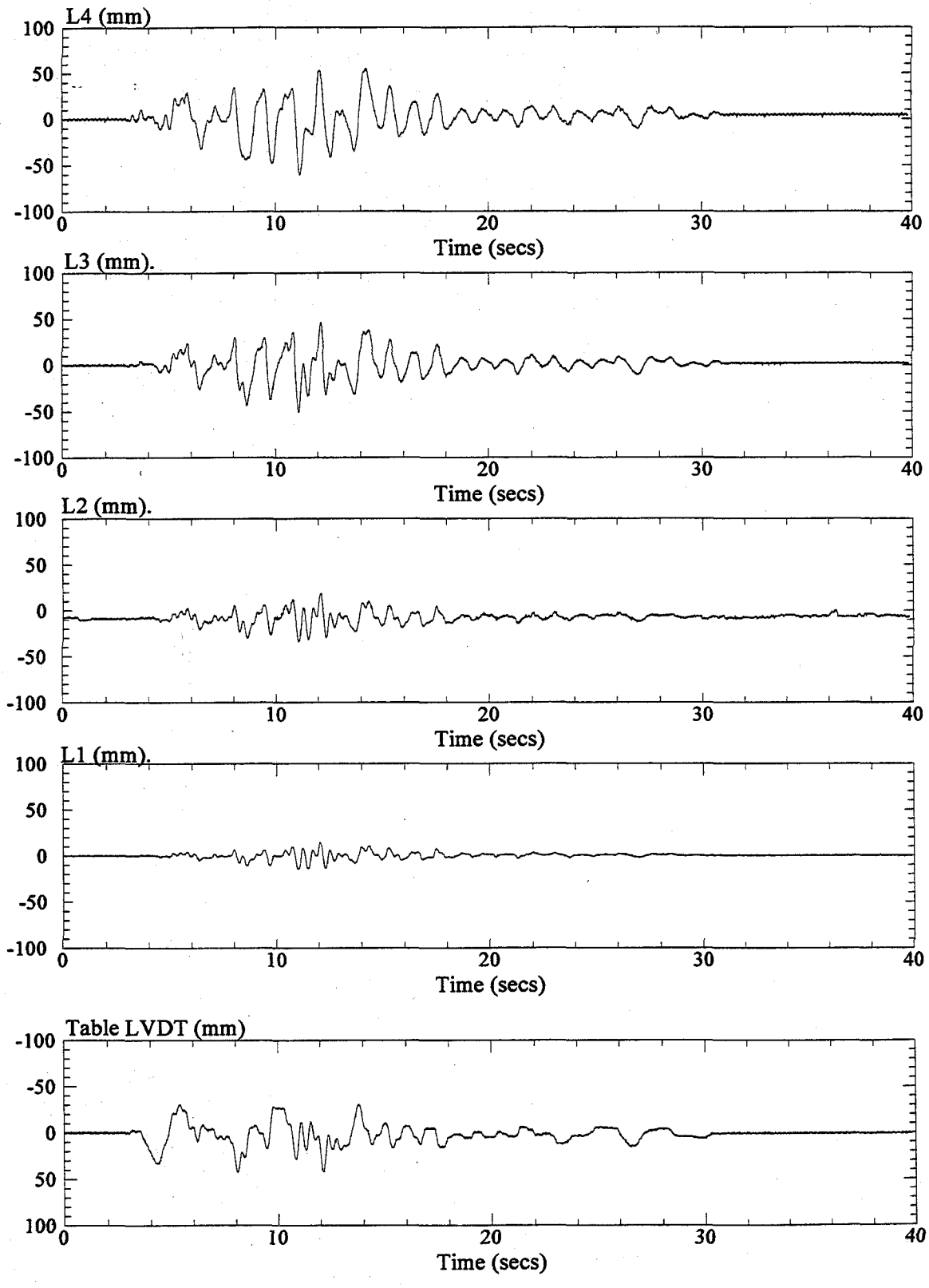

Figure 5: Longitudinal displacements recorded from the shake table LVDT and at LVDT's L1, L2, L3, and L4 in the one-g model SM3K8.

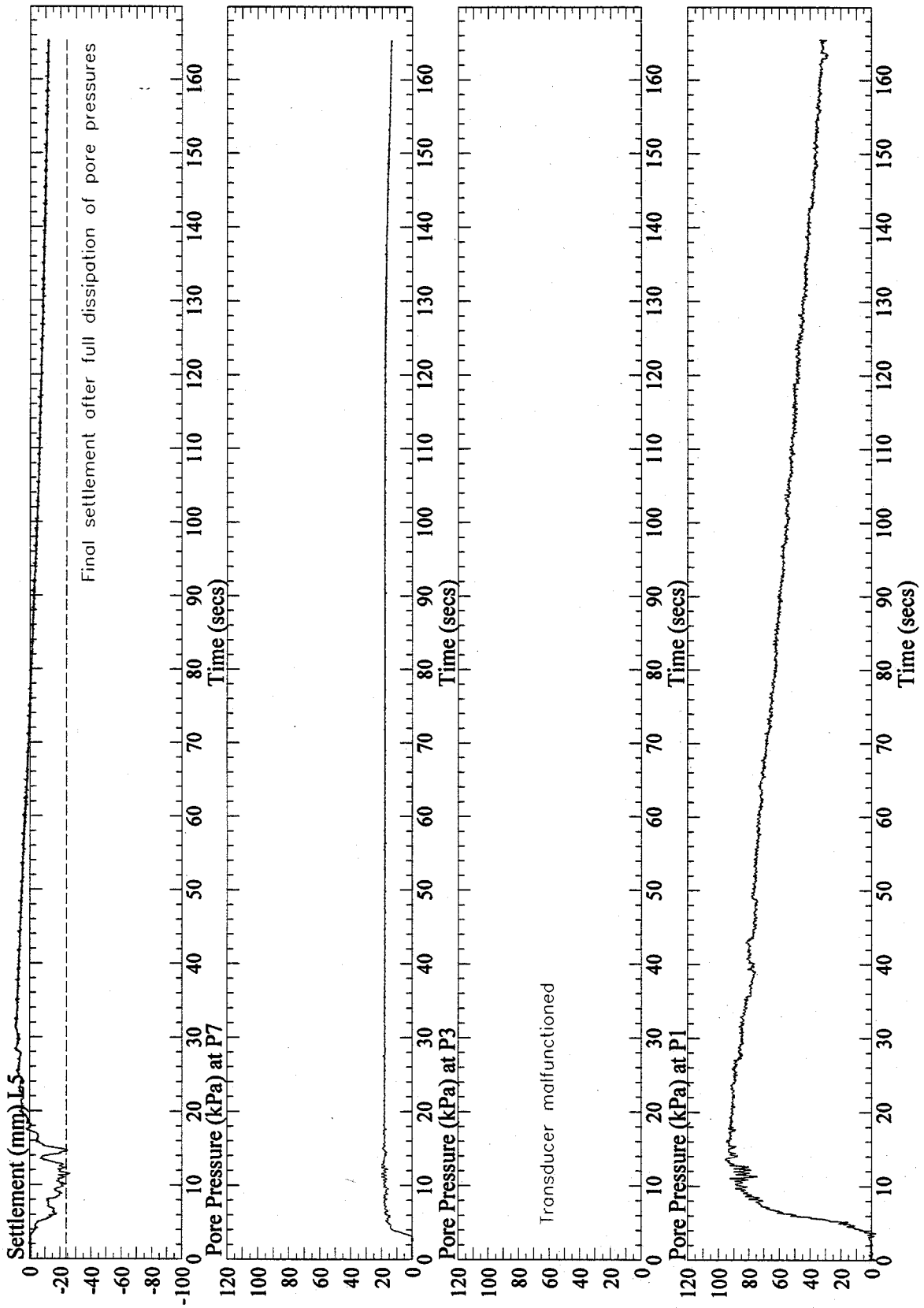

Figure 6: Vertical settlement at L5 and pore pressures at P1, P3, and P7, recorded in the one-g model SM3K8. Signals from P1 and P3 were post processed with a low pass filter of 10 Hz.

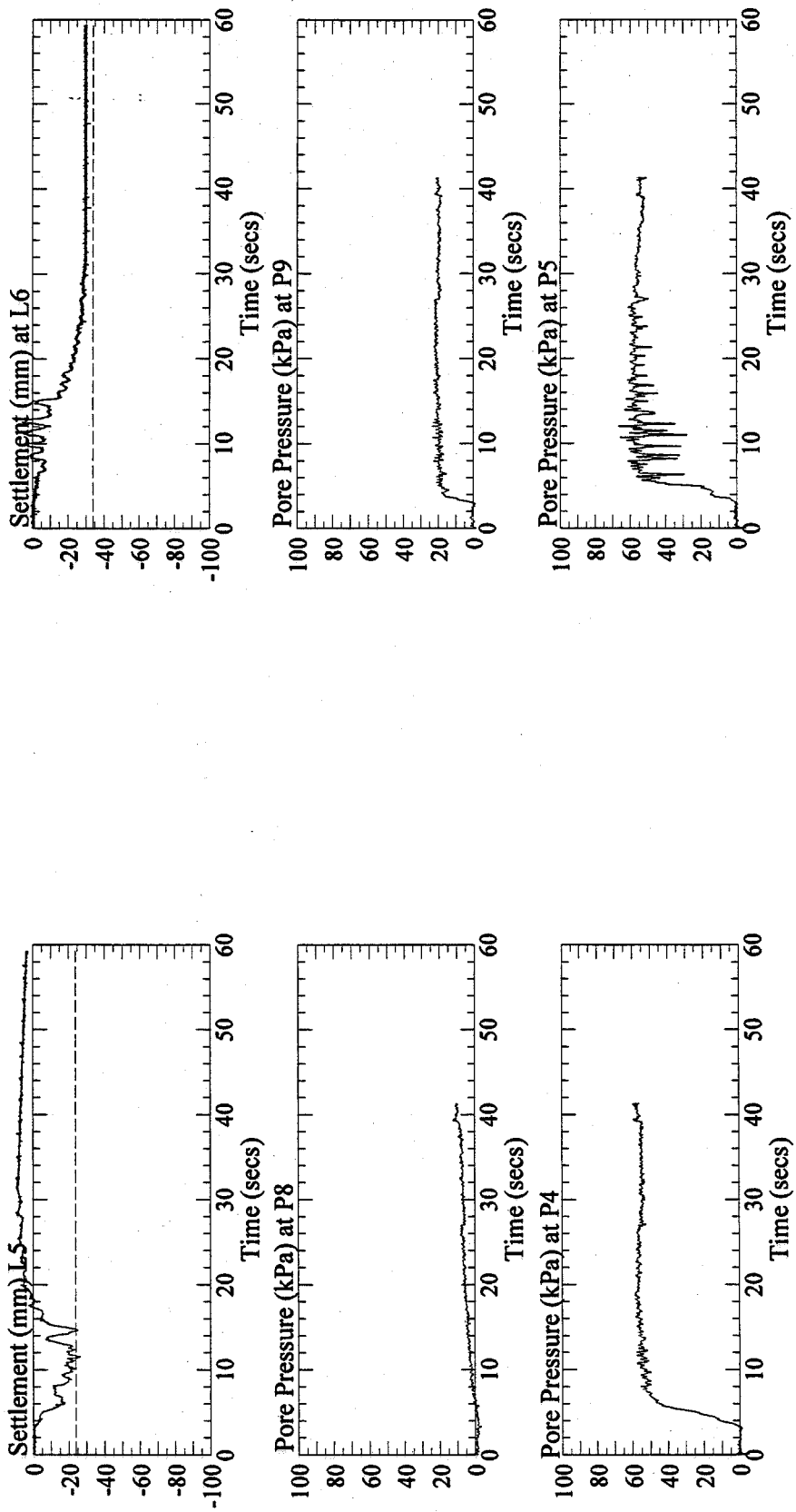

Figure 7: Vertical settlement at L5 and L6, and pore pressures at P4, P5, P8 and P9, recorded in the one-g model SM3K8. Pore pressure signals were post processed with a low pass filter of 10 Hz.

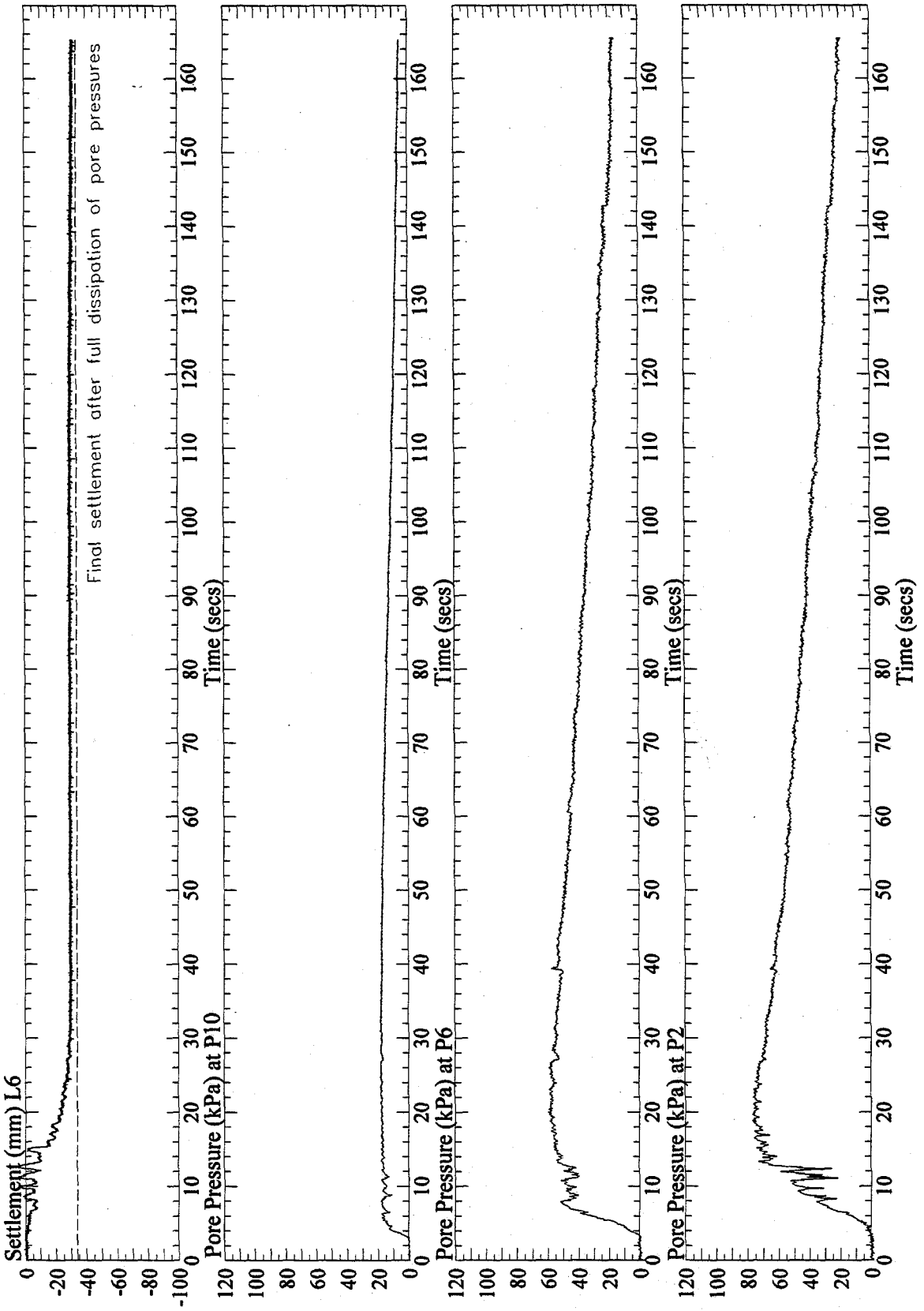

Figure 8: Vertical settlement at L6 and pore pressures at P2, P6, and P10, recorded in the one-g model SM3K8. Signal from P2 and P6 were post processed with a low pass filter of 10 Hz.